The Synthesis and Characterisation of Inorganic and Organic Luminophores Suitable for Biomolecule Conjugation

A thesis submitted to Dublin City University for the award of PhD.

By

Ciarán M. Dolan, B.Sc. (Hons)

School of Chemical Sciences,

Dublin City University,

Glasnevin,

Dublin 9.

November 2011

Supervisors: Prof. Tia Keyes / Prof. Robert Forster

Declaration

I hereby certify that this material, which I now submit for assessment on the programme of study leading to the award of PhD. is entirely my own work, that I have exercised reasonable care to ensure that the work is original, and does not to the best of my knowledge breach any law of copyright, and has not been taken from the work of others save and to the extent that such work has been cited and acknowledged within the text of my work.

Signed: _____

ID No.: _____

Date: _____

Acknowledgements

First and foremost I would like to take this opportunity to sincerely thank my supervisors; Prof. Tia Keyes, Prof. Robert Forster, Prof. Godfrey Beddard and internal supervisor Dr. Kieran Nolan for all their guidance, time and patience with me over the past few years. I would also like to thank Dr. Vladimir Gubala for taking under his wing in my first year in the lab and always making himself available to answer any questions or proof read material - it was really appreciated and I learned an awful lot. A special thanks to my two German summer students, Sebastian and Fabian, for their contribution to the fluorescent labelling of nucleosides. My gratitude also goes to IRCSET and NBIPI for providing the all important financial assistance throughout my research and Dr. Marc Devocelle for access to the peptide synthesis equipment in the RCSI.

Big thanks too to all of the technical staff: Ambrose, Damien (for running all my mass spec samples), John 'NMR' McLoughlin, Veronica, Mary x 2, Catherine, Vinny, Brendan and all of the other past and present members of staff in DCU. Your hard work is much appreciated and does not go unnoticed.

A massive thanks to all those who made my postgraduate experience so enjoyable; Zoe 'the original leafainn' Stack, Elaine 'blow it all out of proportion' Spain, Kieran 'BOBFOC' Joyce, Emma 'No!! – black is white' Harvey, Jen '2.5 day week' Manton, Nikki 'I'll be finished this year' Boyle (you kept your word, eventually!), Kellie 'Special K' Adamson, Shane 'where have you gone?' O'Carroll, Subo, Aaron, Laura '-52' Barron and Jamie 'King of Gyppos' Walsh. Thanks for keeping me going when things were down and making everyday research in the lab tolerable when nothing ever worked! Who could forget The Bray 'T-Shirt' Party, The Snow Avalanche, The Spaceship Bench, The Dolan Appreciation Club, Fun-Doley, CSI, the Christmas and Halloween decorations (every year!), the random stickers/drawings, the great nights out and weekends away to name but a few. I take with me some great memories and I'm sure we will remain the bestest buds well into the future. Sure who else can I go to McGowans with midweek?!! (stickey-out tongue face) It's been emotional to say the least!!

Not to forget all the other members of the research group, both postgraduate and postdoctoral, for all their help and discussion when called upon over the years; Colm (thanks for help with the dreaded electrochemistry), Lorraine (thanks for help with the peptide synthesis), Roisin (thanks a million for all the cell work), Tib (thanks for help with the Raman), Elena (thanks for the tips on synthesis), Chuck, Stephen, Lynda, Gavin, Jie, Gennaro, Tebo, Andrea, Damien, Una, Anita, Binci, Anitha and the many others who have moved onto bigger and better things.

Special thanks too to the Bray lads, my DIT 'real mates', the MPRG, the football lads for a kick around on a Friday evening and the larger DCU family as a whole for the great friends and the even better nights out. A special mention too for my extended family for their words of encouragement and in particular to my ever dependable housemates', cousin Rob and Elena, for taking my mind off work with talk of ladies t-shirts, silver, politics and whatever else is going on in this crazy world we live in.

Finally my biggest thanks of all, goes to my Mum, Dad, Sister and Samantha, without whom I would not be where I am today. You have been a rock of support for me throughout the years. Thank you for everything; this is as much for you as it is for me. Grá ollmhór i gconaí.

….....anois, chun cúrsa eile a aimsiú!!!

This thesis is dedicated to family and friends, past and present.

Table of Contents

Chapter 2: Experimental Methods and Instrumentation

Chapter 3: Synthesis and Characterisation of Ruthenium (II) Polypyridyl Luminophores for Conjugation

Chapter 4: Synthesis and Characterisation of Iridium (III) Luminophores Suitable for Bioconjugation

Chapter 5: Metal Luminophore-Peptide Conjugates for Cellular Imaging

Chapter 6: Model Photoantenna Based on Interfacial DNA Scaffolds

Chapter 7: Conclusions and Future Work

Abstract

Inorganic transition metal complexes have been under extensive investigation for many years in supramolecular assemblies due to their favourable photophysical and redox properties including; absorbance and emission in the visible region of the spectrum, large stokes shifts, long lifetimes, intense luminescence, good photostability and useful photosensitising properties for photodynamic therapy. Their properties make them potentially very valuable biological probes but to date relatively little application of transition metals in this area have been made. This thesis focuses on a range of novel ruthenium and iridium luminophores, their bioconjugates and nanoparticle conjugates which were prepared for applications in cell imaging. A key aim of this thesis was the synthesis, characterisation and identification of novel bioconjugates suitable for applications in cellular imaging. Some preliminary studies of their application in cell imaging are also presented.

Chapter 1 outlines how metal complexes have been used previously in cellular imaging and how conjugation of these transition metal complexes to biomolecules has lead to more targeted and improved applications in medical diagnostics, photodynamic therapy, cellular imaging and pharmaceutical drug delivery. Chapters 3 & 4 detail the synthesis and photophysical characterisation of a series of Raman and oxygen sensitive, water soluble and water insoluble ruthenium (II) and novel iridium (III) polypyridyl complexes suitable for biomolecule coupling. Following conjugation of these luminophores to gold nanoparticles in Chapter 3 and cell penetrating peptides in Chapter 5, the dye-conjugates were shown to transport efficiently across the cellular membrane of mammalian SP2 and CHO cells and locate throughout the cell's organelles. Whereas, using confocal fluorescence microscopy, the parent complexes were shown not to internalise within the cellular structures. The inherent properties of the dyes, such as Raman and lifetime sensitivity, may then be used to determine pH and oxygen levels inside the cell. This could provide critical information for the early detection of certain diseases, as abnormal pH and oxygen levels are indicative of cancerous tumours. Furthermore, the generation of singlet oxygen following light absorption by the luminophores is known to cause additional cell apoptosis.

Finally, Chapter 6 describes attempts to functionalise the nucleobase guanine with a fluorescent fluorescein molecule through a short and rigid linker. A range of synthetic techniques such as Suzuki coupling, Sonogashira coupling, click chemistry and Buchwald-Hartwig coupling were used in an effort to achieve this. Using DNA as a scaffold for the first time, the modified nucleoside may be incorporated into the sequence of DNA which may be surface immobilised. Thus, providing an efficient light harvesting supramolecular assembly for the conversion of solar energy into electrical potential.

List of Acronyms/Symbols/Complexes

8-BrdG – 8-Bromo-2'-Deoxyguanosine.

Arg - Arginine

Arg_8 – Octarginine

AuNPs – Gold Nanoparticles

bpy – 2,2'-Bipyridyl

CFM – Confocal Fluorescence Microscopy

CHO cells – Chinese Hamster Ovary cells

CPPs – Cell Penetrating Peptides

CT – Charge Transfer

CV – Cyclic Voltammetry

dG – Deoxyguanosine.

DTT - Dithiothreitol

EDC - 1-Ethyl-3-[3-dimethylaminopropyl] carbodiimide hydrochloride

Fmoc - Fluorenylmethoxycarbonyl

FRET – Fluorescence Resonance Energy Transfer

FLIM – Fluorescence Lifetime Imaging Microscopy

HOMO – Highest Occupied Molecular Orbital

IC50 – Concentration at which exhibits 50% cell population death

IC – Internal Conversion

ILCT – Inter Ligand Charge Transfer

ISC – Inter-System Crossing

LC – Ligand Centred

LUMO – Lowest Unoccupied Molecular Orbital

MLCT – Metal to Ligand Charge Transfer

MC – Metal Centred

NA – Numerical Aperture

NHS - N-Hydroxysulfosuccinimide

NMR – Nuclear Magnetic Resonance

Pbf - 2,2,4,6,7-Pentamethyldihydrobenzofuran-5-sulfonyl

PBS – Phosphate Buffered Solution

PCR – Polymerase Chain Reaction

PDT – Photo-Dynamic Therapy

PEG_8 – Polyethylene Glycol (3 nm Linker)

PEG_{32} – Polyethylene Glycol (13 nm Linker)

ROS – Reactive Oxygen Species

RR – Resonance Raman

SAMs – Self Assembled Monolayers

SERS – Surface Enhanced Raman Spectroscopy

SPPS – Solid Phase Peptide Synthesis

TEM – Transition Emission Microscopy

TCSPC – Time Correlated Single Photon Counting

ϕ_f – Fluorescent Quantum Yield

ϕ_p – Phosphorescent Quantum Yield

τ – Lifetime

π – Pi Bonding Orbital

π^* - Pi Antibonding Orbital

σ – Sigma Bonding Orbital

σ^* - Sigma Antibonding Orbital

ε - Molar Absorptivity Coefficient

Δ – Delta

k_q – Quenching Rate Constant

N_A – Avogadro's number

ΔH – Changes in Enthalpy

ΔG – Changes in the Gibbs Free Energy

h – Planks Constant

v – Frequency of Radiation

R – Gas Constant

T – Temperature in Kelvin

x^2 value – Chi Squared Distribution

[(picCOOH)] - 2-(4-Carboxylphenyl)imidazo[4,5-f][1,10]phenanthroline).

[($picNO_2$)] - 2-(4-Nitrophenyl)imidazo[4,5-f][1,10]phenanthroline).

[($picNH_2$)] - 2-(4-Aminophenyl)imidazo[4,5-f][1,10]phenanthroline).

[$Ru(bpy)_2Cl_2$] - Ruthenium-(bis-2,2-bipyridyl)dichloride.

[$Ru(bpy)_2(picCOOH)]^{2+}$ - Ruthenium (II) (bis-2,2-bipyridyl)-2(4-carboxylphenyl) imidazo[4,5-f][1,10]phenanthroline.

[$Ru(bpy)_2(picNO_2)]^{2+}$ - Ruthenium (II) (bis-2,2-bipyridyl)-2(4-Nitrophenyl) imidazo[4,5-f][1,10]phenanthroline.

[$Ru(bpy)_2(picNH_2)]^{2+}$ - Ruthenium (II) (bis-2,2-bipyridyl)-2(4-Aminophenyl) imidazo[4,5-f][1,10]phenanthroline.

[(dfpp)] - 2-(4,6-Difluorophenyl)pyridine.

[$Ir_2(dfpp)_4(Cl_2)$] - Iridium (III) di-μ-chloro-tetrakis(2-(2, 4-difluorophenyl)pyridinato-N, C2'.

[$Ir(dfpp)_2(picCOOH)]^{+}$ - Iridium (III) bis(2-(2,4-difluorophenyl)pyridinato-N, C2')-2(4-carboxylphenyl)imidazo[4,5-f][1,10]phenanthroline.

[$napthNO_2$] - 2-(Naphtho[2,3-d]oxazol-2-yl)-5-nitrophenyl.

[$napthNH_2$] - 2-(Naphtho[2,3-d]oxazol-2-yl)-5-aminophenyl.

[$Ir(dfpp)_2(napthNO_2)$] - Iridium (III) bis(2-(2,4-difluorophenyl)pyridinato-N,C2') (2-naphthoxazoyl)4-nitrophenolate).

[$Ir(dfpp)_2(napthNH_2)$] - Iridium (III) bis(2-(2,4-difluorophenyl)pyridinato-N,C2') (2-naphthoxazoyl)4-aminophenolate).

Chapter 1: Introduction

"The journey of a thousand miles begins with one step" – Lao Tsu.

1.0 Introduction to Molecular Photophysics

When a molecule absorbs a photon of light energy it is excited to higher vibration energy state. There are many ways in which the molecule may lose its excess energy in returning back to it's original ground state energy level, as illustrated by the Jablonski diagram in Figure 1.1.

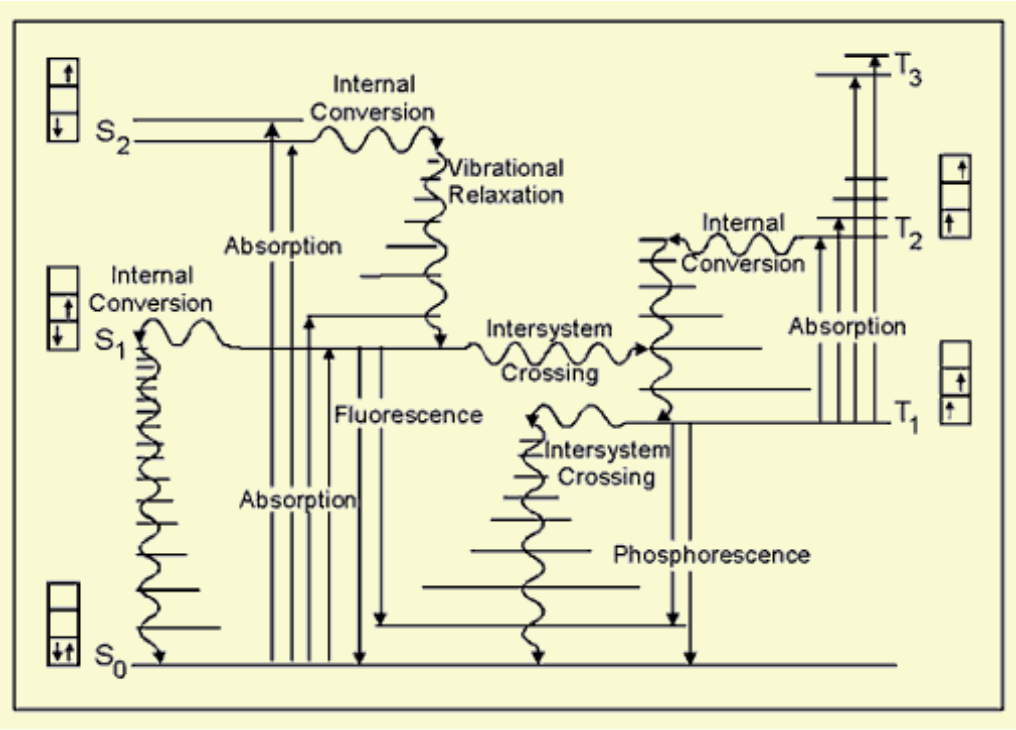

Figure 1.1: Jablonski diagram illustrating the radiative and non-radiative processes involved in the absorption and resultant relaxation of a molecule following excitation by a photon of light energy.[1]

Non-radiative deactivation processes include vibrational relaxation whereby an excited electron returns to the ground energy state without the emission of a photon through energy transfer to the environment caused by collisions. Internal conversion (IC) is a non-radiative isoenergetic process that involves the transfer of an electron between states of the same multiplicity. Intersystem crossing (ISC) is also an isoenergetic non-radiative deactivation process involving the transfer of an electron

between an excited singlet (S) and exited triplet (T) state since the vibrational energy levels within the singlet and triplet states overlap. The singlet and triplet states are electronic isomers of each other; their differences are due to the electronic spin configurations of each state. ISC is also enhanced with the presence of heavy and paramagnetic atoms such as ruthenium and iridium.

The molecule may also lose its excess energy through radiative processes known as luminescence, which may be further subdivided into fluorescence and phosphorescence. Fluorescence is a radiative deactivation process between states of the same multiplicity in a molecule (for example: $S_1 \rightarrow S_0$) and is the emission process for many organic fluorophores. Phosphorescence, on the other hand, is a radiative deactivation process between states of different multiplicity (for example: $T_1 \rightarrow S_0$) and is common for many transition metal complexes. The spin forbidden nature of this transition explains why excited state lifetimes are generally much greater for metal complexes than that seen for organic fluorophores.

Another mode of deactivation for an excited state molecule is non-radiative molecular quenching and may be described as (i) dynamic quenching; which is a process of collisional deactivation of the excited state molecule as a result of diffusion-based interactions within the system or (ii) static quenching; which is the interaction of the luminophore with the quencher molecule to form a non-emissive complex and inhibits excited state formation of the chromophore in the first place.

1.0.1 Luminescent Quantum Yields (ϕ_f) and Lifetimes (τ)

Both luminescent quantum yields and luminescent lifetimes are two important quantitative assessments of a chromophore's emission efficiency. Determining the lifetime of a molecule is important as it gives insight into how long a chromophore remains in an excited energy state and therefore, the time it has to interact with its surrounding environment. The lifetime of a chromophore may be effected by many factors including the presence of heavy atoms and the solvents used.

A molecule's quantum yield (ϕ_f) is a fractional quantity of the number of emitted photons relative to the number of photons absorbed as shown in Equation 1.1.

$$\phi_f = \text{\# photons emitted / \# photons absorbed} \quad \text{.....(Eq 1.1)}$$

Luminescent quantum yields may approach but never achieve unity as the rate of non-radiative decay decreases but there will always be some energy lost as a result of Stokes losses. The luminescent quantum yield is a key parameter in calculating quenching rate constants, energy transfer rates and radiative / non-radiative decay rate constants.[2] Together with experimentally determined emission lifetimes (τ) the quantum yield may be used to estimate unimolecular rate constants for radiationless processes such as internal conversion and intersystem crossing within the system.

In a given system all of the unimolecular phototransitions expected to occur in a molecule include the absorption of light energy (I_{abs}) followed by some or all of; internal conversion (IC), intersystem crossing (ISC), fluorescence (F) or phosphorescence (P). Steady-state approximation for the concentration of the first excited singlet energy state [S_1] assumes that the rate of absorption of light is equal to the combined rates of deactivation of S_1.

$$I_{abs} = (k_{IC} + k_{ISC} + k_f)\,[S_1] \quad \text{.....(Eq 1.2)}$$

As most of the complexes in this thesis deal with phosphorescence and therefore emission from the triplet state [T_1], steady-state approximations also assume that the rate of formation of triplet states is equal to their rates of deactivation, giving Equation 1.3.

$$k_{ISC}[S_1] = (k_{ISC} + k_P)[T_1] \text{…….(Eq 1.3)}$$

Therefore, under steady-state conditions for phosphorescent complexes, the quantum yield of key processes may be described as the ratio of the decay rates to the total deactivation rates of that state. The quantum yields for the transitions may then be expressed as.

$$\phi_{IC} = k_{IC} / (k_F + k_{ISC} + k_{IC}) \text{…….(Eq 1.4)}$$
$$\phi_{ISC} = k_{ISC} / (k_F + k_{ISC} + k_{IC}) \text{…….(Eq 1.5)}$$
$$\phi_P = \phi_{ISC} \times k_{IC} / (k_P + k_{ISC}) \text{…….(Eq 1.6)}$$

The quantum yield may also be related to the lifetime (τ) of the chromophore. The singlet (τ_S) and triplet lifetimes (τ_T) are equal to the inverse of the sum of all the rates that deactivate their respective energy levels and may be written as seen in Equations 1.7 and 1.8 respectively.

$$\tau_S = 1 / (k_F + k_{ISC} + k_{IC}) \text{…….(Eq 1.7)}$$
$$\tau_T = 1 / (k_P + k_{ISC}) \text{…….(Eq 1.8)}$$

Therefore, the expression of key quantum yield states may be defined as follows:

$$\phi_{IC} = (k_{IC})(\tau_S) \text{…….(Eq 1.9)}$$
$$\phi_{ISC} = (k_{ISC})(\tau_S) \text{…….(Eq 1.10)}$$
$$\phi_P = (\phi_{ISC})(k_P)(\tau_T) \text{…….(Eq 1.11)}$$

Hence, the measured values of τ_S does not provide information on the pure radiative lifetime of fluorescence from the singlet energy state. However, phosphorescent lifetimes provide a direct insight into the lifetime of the excited triplet energy state (τ_T) as shown in Equation 1.11.[2] An increase in temperature usually causes a decrease in both the quantum yield and lifetime of a molecule as non-radiative decay processes such as vibrations, rotations and collisions become more likely. Frequently, for ruthenium polypyridyl complexes, the population of the geometrically distorted ^{3}MC states are thermally induced leading to decomposition of the complex.[3, 4]

1.1 Charge Transfer Transitions in Metal Complexes

Most transition metal polypyridyl complexes display very intense absorption bands in the visible and near UV regions of the electromagnetic spectrum. Absorbance bands are usually assigned to electronic transitions which can be regarded as metal centred (MC) transitions, ligand centred (LC) transitions or charge transfer (CT) as illustrated in Figure 1.2. In general, in a metal complexes' ground energy state the σ_L and π_L ligand orbitals are full. The metal's d orbitals are partially filled depending on the oxidation state of the metal. Other anti-bonding σ^*_L and π^*_L ligand orbitals are usually empty.

Once light energy is absorbed the population of these orbitals change. Metal-centred (MC) transitions (or d-d transitions) are low in energy and their absorbance often corresponds to the wavelength of visible light as seen for many brightly coloured ruthenium (II) metal complexes. This involves a rearrangement of the metal d-electrons from the t_{2g} to e_g sets. Interligand charge transfer (ILCT) transitions are of much higher energy and generally occur when chromophoric ligands are coordinated to the metal centre. MLCT is particularly common since it involves promotion of an electron from the highest occupied molecular orbital (HOMO) to the lowest unoccupied molecular orbital (LUMO).[5] All of these excited energy states may have singlet or triplet multiplicity although spin-orbit coupling causes singlet-triplet mixing in MC and MLCT excited energy states.[6]

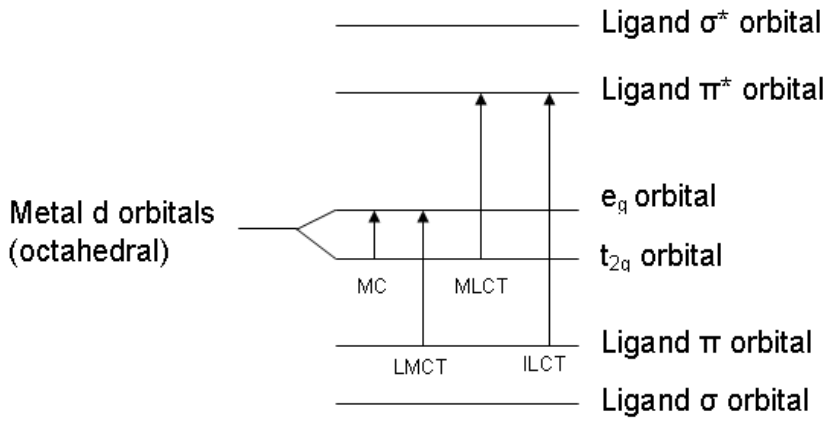

Figure 1.2: Energy level diagram for octahedral metal complexes showing the possible electronic transitions.

Many of the photophysical and redox characteristics of $[Ru(bpy)_3]^{2+}$ have been detailed extensively in the literature[3, 4, 6-8] and it may be used as a prototype to explain similar processes occurring in other ruthenium (II) polypyridyl complexes discussed in Chapter 3. Figure 1.3 shows the typical absorbance and emission profile for the $[Ru(bpy)_3]^{2+}$ complex in acetonitrile solution.

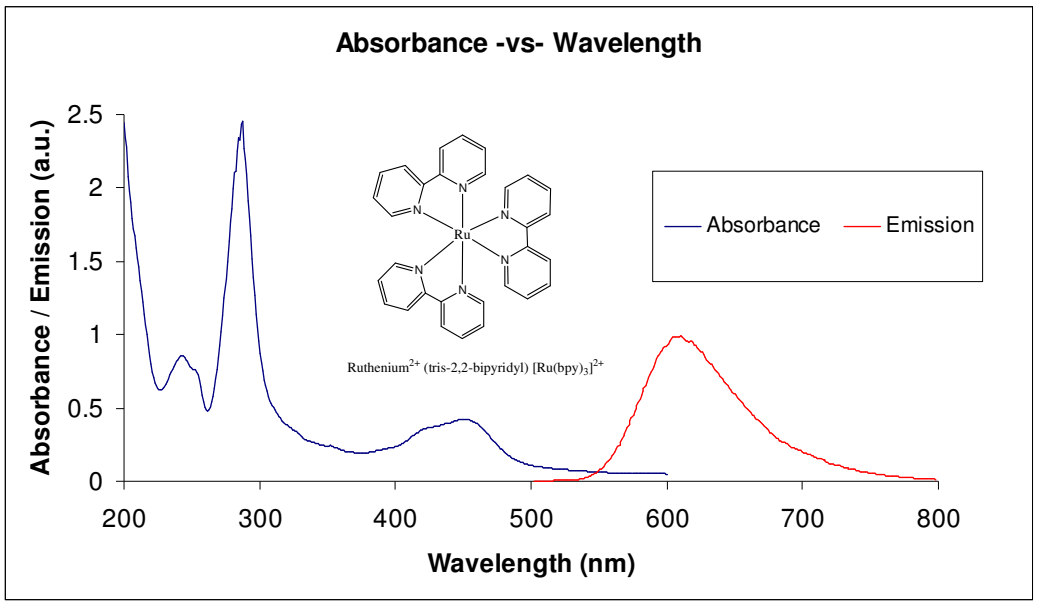

Figure 1.3: Absorbance and normalised emission spectra (excited at 451 nm, slit widths: 5 nm – normalised to 1 arbitrary unit) of 20 x 10^{-6} M $[Ru(bpy)_3]^{2+}$ in acetonitrile solution.

The UV-vis spectrum of $[Ru(bpy)_3]^{2+}$ is dominated by a spin allowed MLCT transition from the ruthenium (dπ orbital) to a bipyridyl ligand (π*) orbital at 451 nm with a further MLCT transition at a higher energy at 241 nm. The strong absorbance at 286 nm is attributed to LC (π-π*) electronic transitions within the bipyridyl ligands orbitals.[4]

The emission spectrum of $[Ru(bpy)_3]^{2+}$ has a maximum emission at 611 nm when excited into the MLCT band at 451 nm. It has a phosphorescent lifetime of 470 ns in degassed acetonitrile and 954 ns in degassed aqueous solution. It has a quantum yield of 0.0642 in aerated acetonitrile at room temperature.[9] For most ruthenium (II)

polypyridyl complexes, the lowest excited energy state is a ^{3}MLCT state which undergoes relatively slow radiationless transitions and thus a relatively long emission lifetime.[3] The intersystem crossing from singlet to triplet state has been shown to be close to unity.[4] Transient absorption spectroscopy has been used to calculate that it takes approximately 100 fs for the formation of the excited triplet state following absorption of a photon of light in acetonitrile solution.[7, 8] This does not necessarily indicate the true intersystem crossing rate as it also contains the overall evolution of the singlet excited state to the thermalised triplet excited state but presumably contains the intersystem crossing rate within the results.

UV-vis light absorption by iridium (III) complexes is mostly ligand centred (LC) and therefore light energy is absorbed at shorter wavelengths when compared to ruthenium (II) complexes and they also tend not to be as brightly coloured. A typical example of an iridium (III) absorbance and emission profile is shown in Figure 1.4.

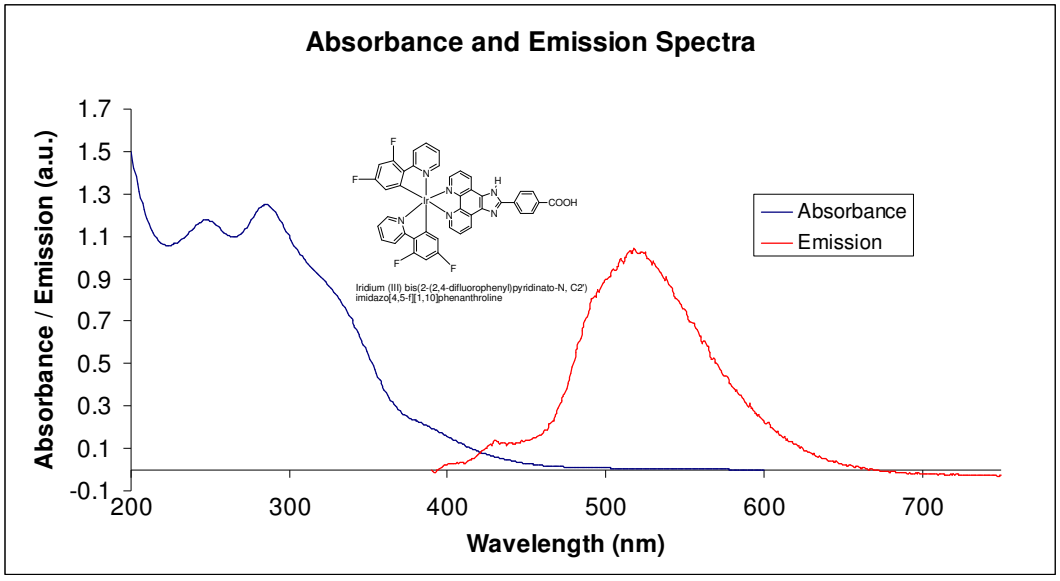

Figure 1.4: Absorbance and normalised emission spectra (excited at 381 nm, slit widths: 5 nm - normalised to 1 arbitrary unit)) of 20 x 10^{-6}M $[Ir(dfpp)_2(picCOOH)]^+$ in acetonitrile solution.

The UV-vis spectrum of $[Ir(dfpp)_2(picCOOH)]^+$ is dominated by LC difluorophenyl pyridine π-π* electronic transitions giving maximum absorbance peaks at 245 nm and 283 nm. This is consistent with reports of other iridium (III) complexes containing difluorophenyl pyridine, bipyridyl or terpyridine ligands.[10, 11] The shoulder at 324 nm may be assigned to the intraligand π-π* transition of the [picCOOH] ancillary ligand. There is evidence of a smaller peak extending down into longer wavelengths at 381 nm which is attributed to MLCT from the iridium dπ to [dfpp] π* orbital.

$[Ir(dfpp)_2(picCOOH)]^+$ has a maximum emission at 521 nm when excited into the MLCT band at 381 nm and a quantum yield of 0.103 in aerated acetonitrile at room temperature. The emission decay follows biexponential kinetics with a lifetime of 195 +/- 3 ns in aerated acetonitrile and 241 +/- 5 ns in degassed acetonitrile with the second lifetime component of around 1 ns in duration. However, its emission lifetime in degassed methanol is as long as 842 +/- 9 ns.

The optical transitions of ruthenium and iridium polypyridyl complexes may be tuned with the addition of certain electron withdrawing or donating ligands and therefore, one may control the nature of the lowest excited state energy.[3] In general, a broadening of absorption bands at lower energy levels suggests that the new ancillary ligand charge-transfer state will be the lowest triplet excited energy state.[7] To shift the t_{2g} - π* band to longer wavelengths of the spectrum one may add electron withdrawing groups to the cyclometalating ligands of ruthenium and iridium complexes in an effort to lower their π* energy level. Another technique is to introduce an electron donating ligand to stabilise the positive hole at the metal centre following MLCT. Replacement of bipyridyl (bpy) ligands with a stronger π-acceptor ligand, such as biquinoline (biq), results in a shift in absorbance to longer wavelengths because of a decrease in the ligand's π* (LUMO) energy level upon coordination. Metal d-orbitals may then also overlap with ligand π* orbitals and thus back-bonding occurs creating a strong chemical bond.

For a metal-ligand complex to be luminescent the crystal field strength must be strong enough to raise the metal d-orbitals to a higher energy level than that of the ^{3}MLCT or ^{3}LC states and hence, prevent a route for radiationless decay back to the ground state. In octahedral metal-ligand complexes LC and MLCT excited states are not usually strongly displaced compared to the ground state geometry and thus, when LC or MLCT states are the lowest excited states, the complex does not undergo fast radiationless decay to the ground state and luminescence can usually be observed.[3] The features in ruthenium (II) and iridium (III) absorbance and emission profiles may be explained by the spin-orbit coupling of the d^6 metal centres, leading to large stokes shifts. Spin-orbit coupling involves mixing of both the singlet and triplet excited energy states of the molecule. However, the lowest lying energy state responsible for emission remains largely triplet in nature. The efficiency of intersystem crossing following light absorption is known to be close to unity for ruthenium (II) and iridium (III) polypyridyl complexes.[12, 13]

Bipyridine ligands are good σ-donor ligands as the lone pair of electrons on the nitrogen is able to form a σ-bond with the unoccupied orbital of the metal ion centre. This leads to smaller ligand field strength and as a result the ^{3}MC states are closer in energy to the ^{3}MLCT states allowing thermal access. Consequently, these compounds tend to be photolabile.[14] The photostability of iridium is generally greater than that of ruthenium due to the larger ligand field splitting in iridium complexes resulting in a thermally inaccessible ^{3}MC excited energy state.[15]

1.1.1 Ruthenium (II) and Iridium (III) Polypyridyl Complexes as Biological Probes:

One of the key objectives of this thesis was the synthesis and identification of suitable transition metal probes for potential conjugation to cell penetrating biomolecules for applications in cellular imaging. With this in mind a series of ruthenium (II) and iridium (III) metal complexes were prepared and fully characterised. Transition metal complexes have been under intensive investigation for many years as sensors due to their favourable photophysical and redox properties including; absorbance and emission in the visible region of the electromagnetic spectrum, large stokes shifts, long-lived intense luminescence, good photostability and useful singlet oxygen photosensitising properties.[16] These properties make them potentially very valuable as biological probes but this has not been explored until the last 5 years.

Their long lived emission is of particular interest, allowing for discrimination from the shorter-lived background fluorescence present in many biological samples. Their large Stokes shifts also reduce the possibility of concentration quenching or self-absorption of the complex and in addition, their red shifted emission is removed from regions of the spectrum where autofluorescence of biological samples often occurs in FLIM and confocal microscopy measurements. Autofluorescence from biological samples interfere with luminescence even in the red region. Therefore, a key aim is to try and move to the NIR region > 700 nm in analysis of biological samples.[17, 18] However, time gating experiments may also remove the shorter lived autofluorescence components present in biological samples.

The majority of luminophores previously used for diagnostic purposes are organic typically with short-lived fluorescent lifetimes (<10 ns) and limited somewhat by their environmental sensitivity. As a result they are not very well suited to examine oxygen concentration or environmental sensitivity in biological samples. Furthermore, longer-lived biological processes on a microsecond timescale such as membrane diffusion, protein rotation and protein folding may be studied using luminescence anisotropy results from the inorganic transition metal probes. The emission maxima of many ruthenium (II) complexes are in the region of 600 nm to 700 nm and thus, correspond to low absorption of biological samples. Another advantage is that they

tend not to exhibit dimer formation or have associated photobleaching problems as is common for some organic based molecular probes.[19]

Iridium (III), like ruthenium (II), is a d^6 transition metal atom and as such displays many optical characteristics similar to ruthenium (II) complexes. However, many iridium complexes have shown greater emission, quantum yields and longer lifetimes. The stronger spin-orbit coupling of iridium complexes results in greater mixing singlet and triplet excited energy states, allowing for efficient intersystem crossing and largely removing the spin-forbidden nature of a phosphorescent transition.[20, 21] Furthermore, modification of ancillary ligands yields tunable emission from blue to red as illustrated in results published by Zhao *et al.*[22, 23] in Figure 1.6. Such tunable photophysical characteristics are generally not seen to the same extent for ruthenium (II) metal complexes. It has been well demonstrated that the photophysical properties, in particular emission wavelength of iridium (III) complexes, is determined by the ligand structure. The emission of iridium (III) complexes 1-5 (Figure 1.5) is significantly red-shifted with extension of the conjugated length of the ancillary ligand.

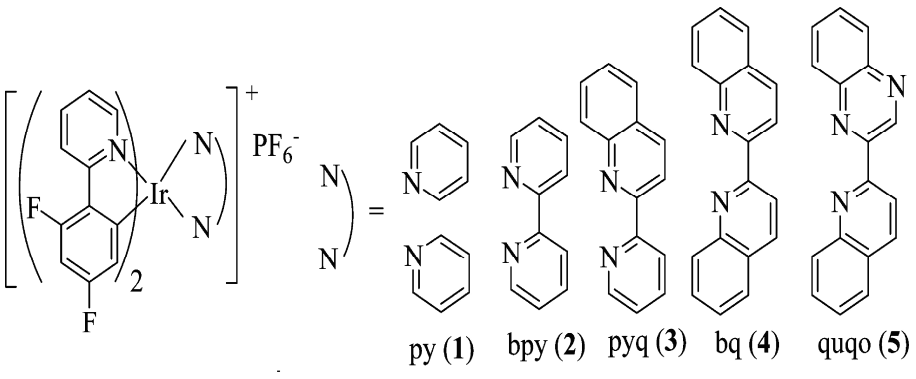

Figure 1.5: Chemical structures of iridium (III) complexes synthesised by Zhao et al.[23]

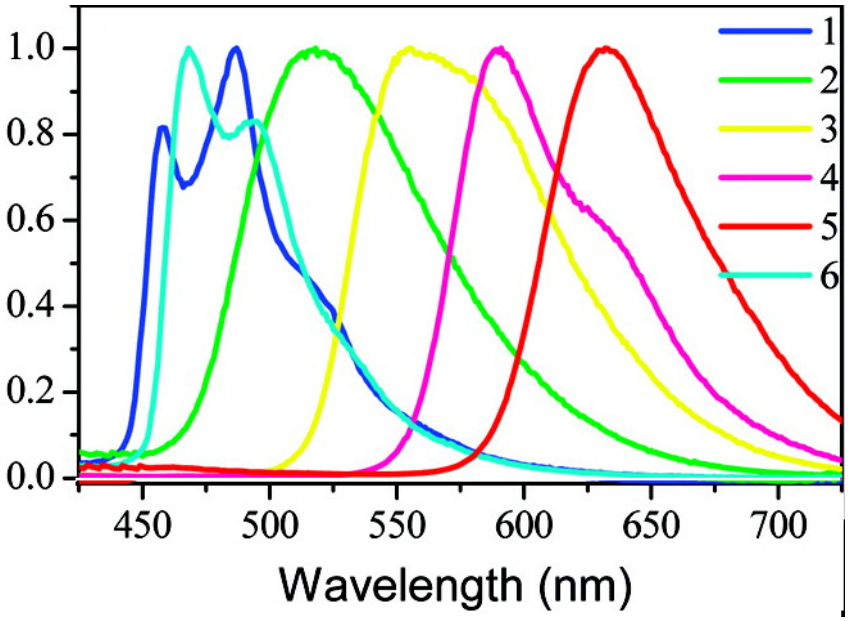

Figure 1.6: Normalised emission spectra of iridium (III) complexes 1-5 (illustrated in Figure 1.5) synthesised by Zhao et al.[23] in dichloromethane at room temperature.

The addition of ancillary ligands with environmentally sensitive functional groups, such as ionisable protons, can offer additional pH sensitivity to a metal complex which may be reproduced in their optical properties or photophysics. Recently, there has been considerable interest in the binding ability of pH sensitive ruthenium (II) polypyridyl complexes to DNA given their potential therapeutic effects.[24, 25] Bai *et al.*[25] reported how the pH sensitive $[Ru(bpy)_2(picCOOH)]^{2+}$ complex showed successful intercalation with double stranded calf-thymus DNA. This was indicated by an increase in the emission intensity and quantum yield of the molecular probe upon the addition of increasing amounts of DNA to a solution containing the metal complex. Intramolecular hydrogen bonding between luminophore and DNA offers protection to the probe from the surrounding aqueous environment as the dye intercalates within the DNA. This family of ruthenium (II) complexes could potentially be modified to exhibit pH-dependent DNA damage and therefore, display preferential selectivity towards cancerous cells.

1.1.2 Ruthenium (II) and Iridium (III) Complexes with pH Sensitive Ancillary Ligands

It is noted that there has been very limited study into metal complexes with multidentate protonatable/deprotonatable groups and their potential interactions with DNA.[26] 2-(4-Carboxylphenyl)imidazo[4,5-f][1,10]phenanthroline) [(picCOOH)], illustrated in Figure 1.7, is coordination to both ruthenium (II) and iridium (III) metal centres in this thesis. The ligand has two ionisable protons located on the imidazole ring giving rise to well defined acid-base characteristics and a terminal carboxyl functionality that allows for the efficient conjugation to biomolecules such as polypeptides. The substitution of the carboxyl functionality with either nitro or amino substituent has also been achieved and their photophysical comparison forms detailed analysis in Chapter 3.

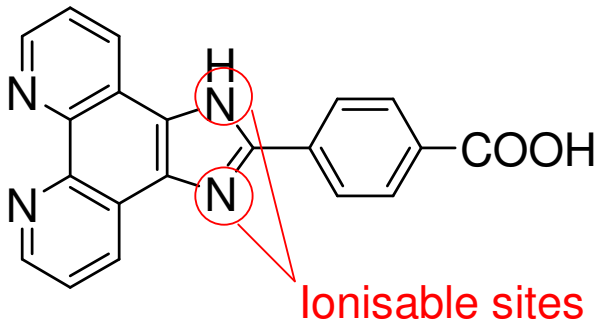

Figure 1.7: Ionisable sites on 2-(4-carboxylphenyl)imidazo[4,5-f][1,10]phenanthroline) [(picCOOH)] ligand.

One of the reasons our group is so interested in the [pic(COOH)] ligand is that remarkably, when coordinated to a metal centre the resulting luminophores displayed longer lifetimes (> 600 ns) and increased emission intensities (more than twice) in aqueous media, lending to the arguments for their use as molecular probes for biological media. Pellegrin *et al.*[27, 28] details the extensive photophysical characterisation of the ruthenium (II) polypyridyl complex, $[Ru(bpy)_2(picCOOH)]^{2+}$, containing this pH sensitive ancillary ligand.

Its subsequent conjugation to biomolecules such as polypeptides[19, 29] has shown how the acid-base characteristics of the ligand may be exploited to glean information on intracellular environments for example. Neugebauer *et al.*[19] reported how conjugation of this pH sensitive probe to a cell penetrating peptide allowed for the passive diffusion of the probe across a cell membrane (Figure 1.8). Once inside the cell membrane, the pH of the cytoplasm had a direct effect on both the lifetime and relative Raman peak intensities of the ruthenium (II) multimodal probe. As a result, by using the same molecular probe, one could efficiently determine both pH (by using the relative Raman peak intensities) and oxygen concentrations (by using the lifetime of the dye) within the cell. This could potentially provide critical information in the identification of cancerous tumours as they are known to express abnormal pH and oxygen levels.[30-32]

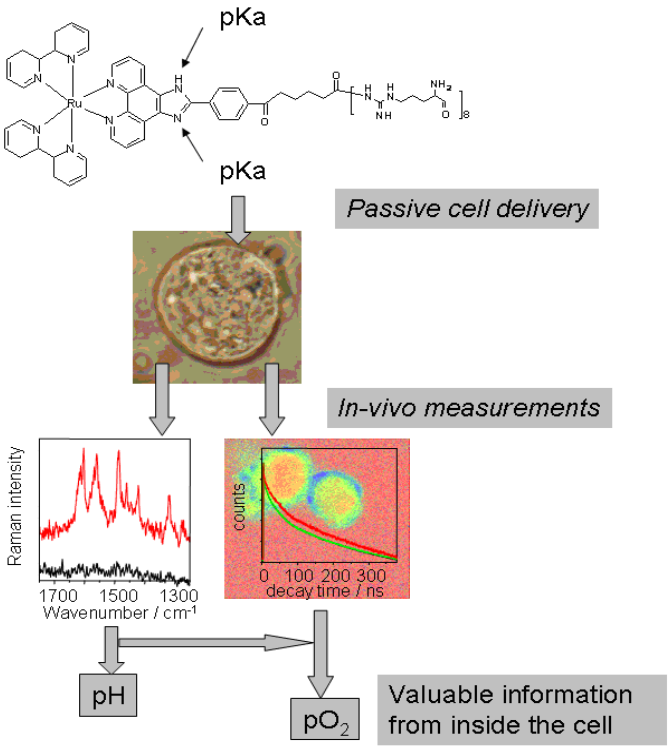

Figure 1.8: Flow diagram illustrating the cellular uptake and determination of intercellular pH (using Raman spectroscopy) and oxygen levels (using lifetimes) using the same pH sensitive $[Ru(bpy)_2(picCOOH)]^{2+}$ multimodal probe.[33]

Interestingly, the uncoordinated nitro funtionalised pH sensitive ligand 2-(4-nitrophenyl)imidazo[4,5-f][1,10]phenanthroline) [($picNO_2$)] displayed preferential selectivity towards certain anions allowing for their fast and easy colorimetric determination by the naked eye.[34] The ligand exhibited a red shift in its absorbance spectrum of up to 89 nm when bound to anions in the order of $AcO^- > H_2PO_4^- > F^-$ when performed in DMSO. Furthermore, the emission of the ligand is completely quenched upon the addition of fluoride (F^-) to the solution as shown in Figure 1.9. This lends to arguments for its potential use as an efficient fluoride sensor as high fluoride concentrations are known to be toxic and can cause fluorosis.[35]

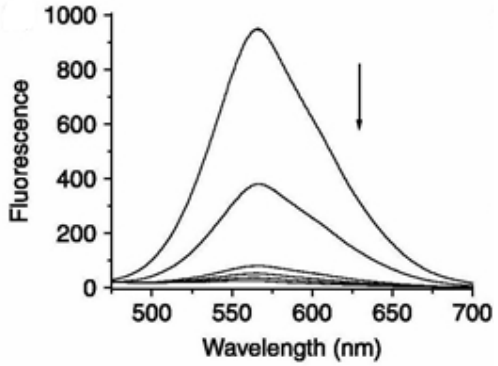

Figure 1.9: Quenching of emission of the [($picNO_2$)] ligand upon addition of F^- anion. Sample was excited at 387 nm in DMSO.[34]

^{1}H-NMR studies indicated that the mechanism of interaction between sensor and anions (such as AcO^-, $H_2PO_4^-$ or F^-) is one of deprotonation, by forming a hydrogen bond with the $H_{1'}$ proton. Whereas, Cl^-, Br^- and I^- anions formed a hydrogen bond with the NH, $H_{c'}$ and $H_{1'}$ protons as illustrated in Figure 1.10 below.

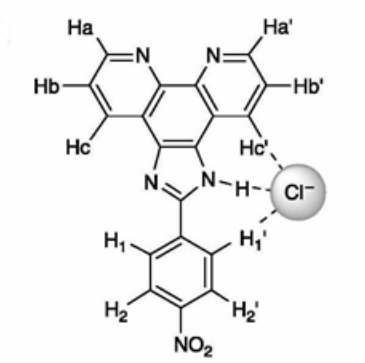

Figure 1.10: Proposed colorimetric anion binding mechanism to the [(picNO$_2$)] ligand.[34]

The [Ru(bpy)$_2$(picNO$_2$)]$^{2+}$ metal complex also demonstrated anion binding affinity, which displayed similar results to that seen for the free [(picNO$_2$)] ligand. [24, 34] Shi *et al.*[24] reported of the synthesis of ortho-, meta- and para-nitro substituted [Ru(bpy)$_2$(picNO$_2$)]$^{2+}$ complexes with the intention of examining their comparative DNA intercalating abilities in a procedure very similar to that of Bai *et al.*[25] Of particular interest is the discovery that the location of the nitro substituent has a dramatic effect on the emission intensity of the pH sensitive complex. Ortho-subsitiuted and para-substituted complexes failed to display any luminescence, whereas, the meta-functionalised nitro group showed a bright emission profile. This has implications for the compounds synthesised in this thesis and is discussed in detail in Chapter 3.

The synthesis of the amino functionalised ligand 2-(4-aminophenyl) imidazo[4,5-f][1,10]phenanthroline) [(picNH$_2$)] and coordination to a ruthenium metal centre has also been reported.[36, 37] They highlighted the complexes ability to (i) intercalate into the DNA base pairs and upon irradiation possibly photocleave the plasmid pBR 322 DNA, (ii) display anti-tumor activity against transfected cells and (iii) exhibit good antioxidant activity against hydroxyl radicals that may induce DNA damage in humans. Once again, these results were determined through a series of absorbance, luminescence, viscosity and cell viability studies.

Iridium (III) complexes containing derivatives of the protonable ligand have also previously been reported. Zhao *et al.*[22] synthesised and characterised a series of iridium (III) complexes (Figure 1.11) that were used to study the influences of protons and anions on the photophysical properties of the complexes.

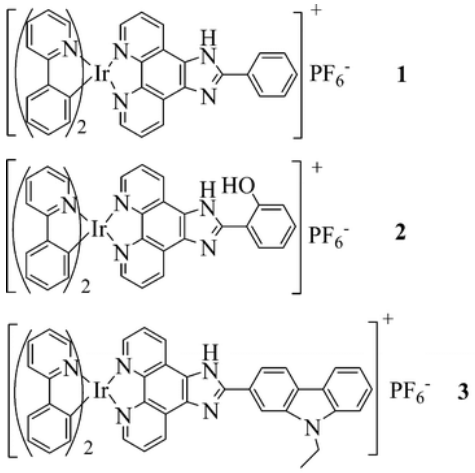

Figure 1.11: Series of cationic iridium (III) complexes 1-3 containing different pH sensitive phenanthroline derivatives.[22]

Similar to the research conducted by Chen *et al.*,[34] the addition of anions and protons to the complexes' solution had a significant effect on their photophysical properties. Following the addition of CF_3COOH, all three iridium (III) complexes show a significant change in emission from yellow to red. The addition of anions, such as F^-, CH_3COO^- or $H_2PO_4^-$, caused variations in both the absorbance and emission profiles of the complex and was characterised by a quenching of emission intensity along with a colour change from greenish-yellow to brown as shown in Figure 1.12. However, the iridium complex 1 showed the largest binding affinity towards the fluoride anion and is suggested that it too may act as a potential phosphorescent chemosensor for fluoride anions.

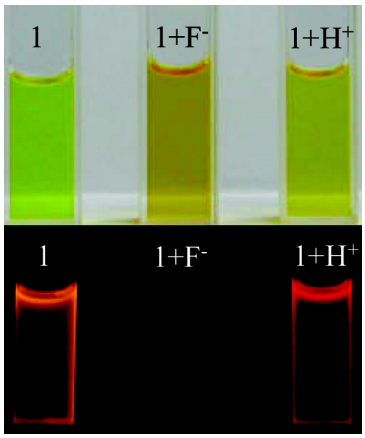

Figure 1.12: Colour (top) and emission (bottom) changes for iridium (III) complex 1 (Figure 1.11) in the presence of 2 equivalences of F^- and CF_3COOH in acetonitrile solutions.[22]

There are many examples outlined in this introduction where derivatives of the pH sensitive phenanthroline ligand have been reported to be useful in a wide range of areas from the colorimetric identification of specific ions to the determination of intracellular pH and oxygen levels. This thesis provides detailed studies on a series of ruthenium (II) and iridium (III) complexes containing the phenanthroline ligand. Due to its favourable chemical properties and ease of functionalised synthesis, this ancillary bridging ligand was also utilised as an efficient way to luminescently label other molecules. Examples of which are discussed in Chapter 3 and Chapter 5 in the luminescent labelling of gold nanoparticles and cell penetrating peptides, respectively.

1.2 Introduction to Photoactive Supramolecular Chemistry

Supramolecular chemistry derives its inspiration from many of the structural aspects of biology. A key objective is to construct well-organized assemblies from smaller molecular subunits that are held together by intermolecular non-covalent bonding interactions such as hydrogen bonding, van der Waals forces, metal coordination and electrostatic bonding. Supramolecular chemistry is described as 'chemistry beyond the molecule' and is not only concerned with the individual components but more importantly the organisation, orientation and interaction of these subunits with one another.[5, 38-40] Jean-Marie Lehn is considered to be one of the earliest innovators in the field of supramolecular chemistry. He was awarded the Nobel Prise for his work in chemistry in 1987, along with Donald Cram and Charles Pedersen, for "their development and use of molecules with structure-specific interactions of high selectivity".

Subsequent research in the area of supramolecular chemistry has led to the development of brand new classes of materials that are capable of light or electronically stimulated chemistry and long-range electronic communications.[41] Photochemically active supramolecular assemblies have potential applications that are widespread, from new photonic devices, such as solar energy conversion[42-44], to the understanding of drug-acceptor interactions[45, 46] and the study of biological processes including protein-protein interactions.[5]

In its most simplistic form, a photoactive supramolecular system may be described as A-L-B. A and B consist of two molecular components, at least one of which is photoactive, and L is a linker or bridge that allows efficient communication between the two components. Following photoexcitation, the excited assembly of A*-L-B may lose its energy through a number of photochemical and photophysical processes as illustrated in Figure 1.13.

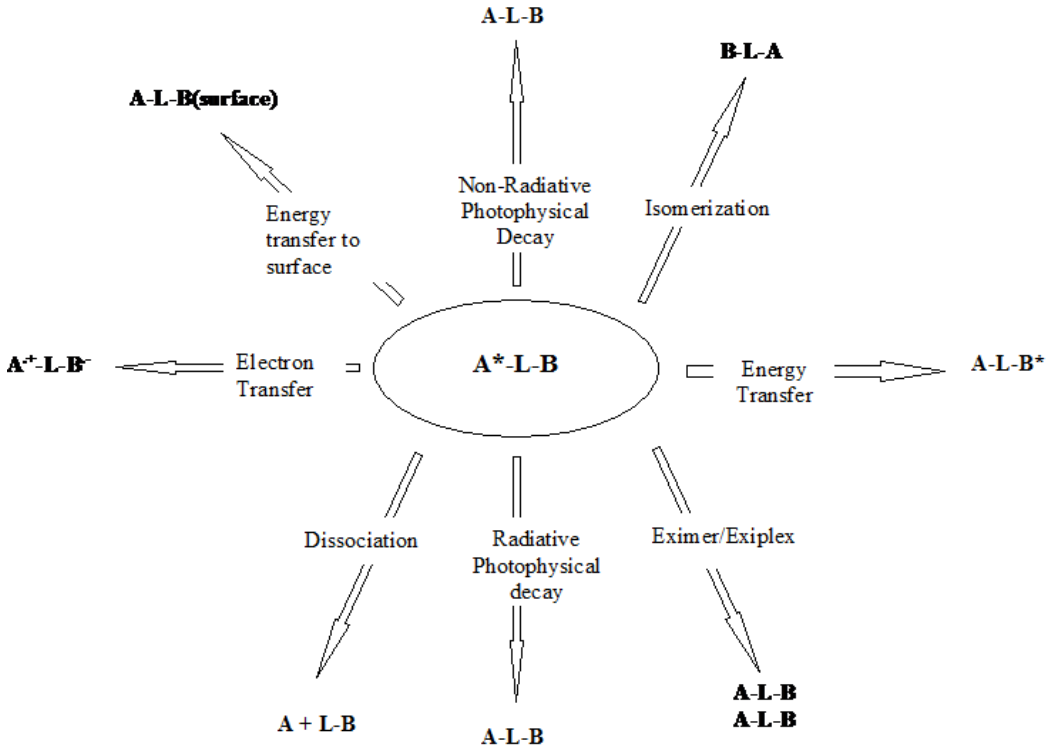

Figure 1.13: Photochemical and photophysical processes through which the photoexcited A-L-B dyad may lose its excess energy.*[41]

This concept of a photoactive supramolecular A-L-B dyad is carried throughout the work presented in this thesis. The photoactive components (A) consist mainly of inorganic, ruthenium (II) and iridium (III) polypyridyl complexes, or organic fluorophores such as fluorescein. The bridging units (L) take the shape of polyethylene glycol linkers, hexanoic acid linkers, functionalised pH sensitive phenanthroline ligands or simple carbon-carbon bonds and they are conjugated to substrates, in which the second component (B) are nanoparticles, polypeptides or nucleoside units.

The resultant A-L-B assemblies often exhibit an increase in their photophysical characteristics and their applications are above that of the sole parent photoactive subunit. All of which occurs without destroying the individual character of the subunit; a true characteristic of a supramolecular assembly.[41]

Supramolecular assemblies are often described as a 'bottom-up' approach in the manufacturing of functional electronic devices i.e. using atoms and molecules to build much larger structures. They frequently use redox centres and chromophores as building blocks to create assemblies on solid surfaces. A surface allows for potentially controllable lateral interactions between the subunits and collectively increases the strength of the intermolecular communication within the assembly. It also provides a 2-D organisation for the supramolecular adsorbate. Furthermore, the surface itself may become a part of the assembly to drive certain electronic processes.[41] Most importantly the surface provides a route to addressability through measurement or control of current and potential.

The impact of a metal surface on a luminophore may be explained under the following headings:

(i) Intermolecular interactions between surface bound molecules: the nature of the linker used to attach the luminophore to a surface provides topographical control of the surface bound molecules, affecting intermolecular communication between them. This often leads to more rigid, sheltered environments and therefore increased protection from oxygen, causing a decrease in the rate of non-radiative deactivation.[47] Conversely close packing of dyes may cause an increase in the self-quenching of the luminophore.

(ii) Energy transfer from the luminophore to metal surfaces: this is considered to be one of the major deactivation pathways for metal surface bound molecules and is highly dependent on (a) a size, shape and orientation of the molecules dipole with respect to the substrate's axis, (b) the distance between molecule and substrate and (c) the spectral overlap between the emission of the luminophore and the absorption of the substrate to which it is conjugated.[47]

(iii) Electron transfer between the luminophore and surface: the binding of a luminophore to a metal conductor may result in quenching of excited states if an electron/hole transfer occurs to the conduction/valance band of the conducting substrate.

(iv) Plasmonic enhancement of emission: the binding of a luminophore to a plasmonic / coinage metal substrate may also lead to enhanced emission intensity. The plasmonic field interacts with the absorption or emission of the dye. The magnitude of the enhancement is dependent on the type of substrate and the distance between luminophore and substrate. A balance of quenching, resulting from energy transfer to the substrate versus plasmonic enhancement from the metal substrate, must be struck. This distance dependence relationship is believed to be most enhanced at a distance of around 10 nm from luminophore to substrate.[48, 49] The process of metal enhanced luminescence is explained in more detail in section below.

1.2.1 Examples of Photoactive Supramolecular Assemblies

The separation of charge within a donor-acceptor assembly is one of the key processes exploited in photoactive supramolecular systems. Plant photosynthesis is an example of charge separation in an energy producing biological process.[11] Absorption of a photon of light by chlorophyll produces a transmembrane potential gradient allowing for the flow of electrons. Consequently, the production of protons ultimately provides the chemical energy necessary for adenosine triphosphate (ATP) synthesis. In semiconductors, surfaces undergo light induced charge separation leading to an electron-hole pair that results in a potential difference that is widely exploited in many photovoltaic devices.[7, 8]

Due to their photosensitising properties ruthenium and iridium transition metal complexes have been the subject of intensive research for many years in an effort to mimic the charge transfer process, with a view to improving existing technologies across a wide range of areas from solar energy conversion to material science to medical diagnostics.[7] There are many examples throughout the literature where ruthenium[50-56] and iridium[11, 57, 58] {{}}metal complexes have been used as subunits in supramolecular assemblies.

A recent example was reported by Sykora *et al.*,[44] who demonstrated a light induced charge separated process by mimicking antenna-electron transfer in photosynthesis using a supramolecular assembly based on derivatised polystyrene (Figure 1.14). This mimics both the light-harvesting and energy conversion steps of photosynthesis in a laboratory environment. Irradiation of the assembly by visible light leads to the excitation of the bound chromophore unit, a ruthenium (II) polypyridyl complex, which acts as an antenna fragment within the polymer. Following absorption of a photon and thermal equilibration, an excited state is formed, which can rapidly transfer energy to its neighbour leading to energy migration along the polymer chain until it reaches the reaction centre. The ruthenium reaction centre is both a metal to ligand charge transfer (MLCT) chromophore and a quencher complex with an electron transfer donor [phenothiazine (PTZ)] and acceptor [methylviologen (MV^{2+})] coordinated to the metal bound ligands. This resulted in a redox separated state with transiently stored oxidative (PTZ^{+}) and reductive (MV^{-}) redox equivalence. Subsequently this undergoes a back electron transfer returning the original ground state complex at a rate of 6.3 x 10^{6} s^{-1} (t = 160 ns), providing a primitive model for the photosynthetic conversion of light energy to chemical energy. A similar rationale was proposed for the work in Chapter 6, using DNA for the first time as the scaffold for the model photoantenna system.

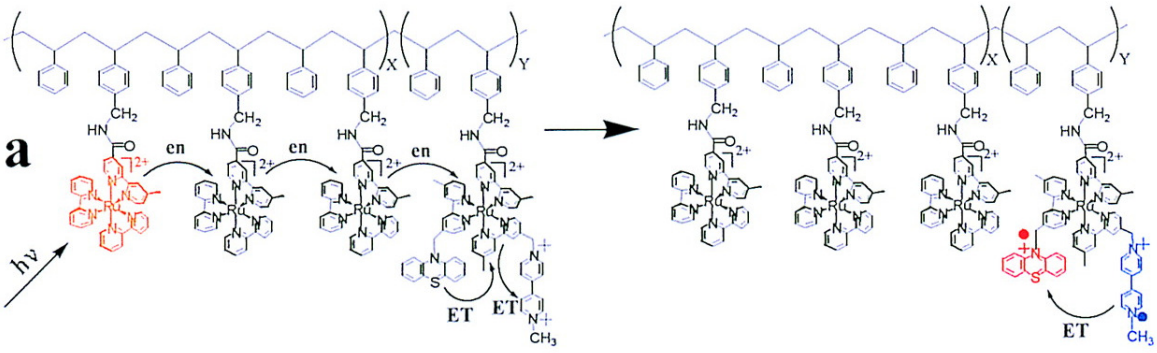

Figure 1.14: Diagram illustrating a supramolecular photoantenna assembly providing a primitive model for the photosynthetic conversion of light energy to chemical energy based on a polystyrene backbone.[44]

A recently published example by Robson *et al.*,[59] involving a ruthenium supramolecular assembly, details a series of nine bis-tridentate ruthenium (II) complexes each containing one cyclometalating ligand with terminal triphenylamine substituent shown in Figure 1.15.[59] The aim was to establish if a correlation existed between different electron donating/withdrawing substituents with the physiochemical properties of the dual chromophoric scaffold. This may potentially serve as a guide for designing future light-harvesting assemblies. They showed how they can systematically tune the redox potentials of both the ruthenium and triphenylamine units. This was in contrast with the slight changes observed in their equivalent optical transitions by simply changing the substituents. This systematic control over the redox potentials is made possible because the ground state oxidation potentials of each unit may be altered over a wide range of potentials by altering the type of substituents on the coordinated ligands. As a result, the HOMO may be directed to either the ruthenium metal centre or the triphenylamine unit. For example, the oxidation potential may be localised on the triphenylamine unit when electron donating groups are placed at position R_1 and an electron withdrawing groups at R_2, as seen for complex 6. The ability to control the redox properties, as the absorbance wavelength remains unaltered, makes it possible to induce an electronic cascade and increase the thermodynamic driving force for the reaction between the electrolyte and photoxidised dye in any potential solar cells. Whilst still maintaining a good overlap with the solar spectrum.

Complex	Ligand	Substituent		
		$-R_1$	$-R_2$	$-R_3$
1	**L1**	-H	-H	-H
2	**L2**	-Me	-H	-H
3	**L3**	-OMe	-H	-H
4	**L4**	-H	$-CF_3$	-H
5	**L5**	-Me	$-CF_3$	-H
6	**L6**	-OMe	$-CF_3$	-H
7	**L7**	-H	-H	-OMe
8	**L8**	-Me	-H	-OMe
9	**L9**	-OMe	-H	-OMe

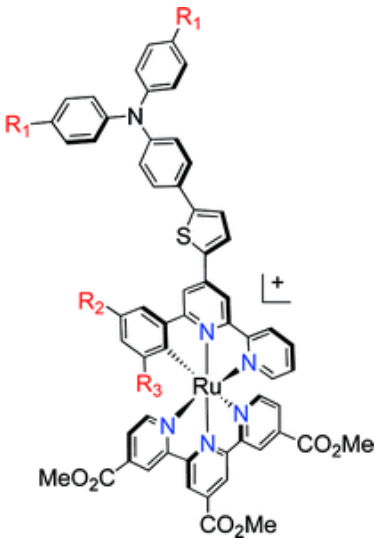

Figure 1.15: Chemical structures of the nine supramolecular bis-tridentate ruthenium (II) assemblies synthesised by Robson et al.[59]

Pellegrin *et al.*[27] described the synthesis of a self assembled supramolecular dyad system consisting of a ruthenium (II) polypyridyl complex and an anthraquinone-2-carboxylic acid subunit as shown in Figure 1.16.

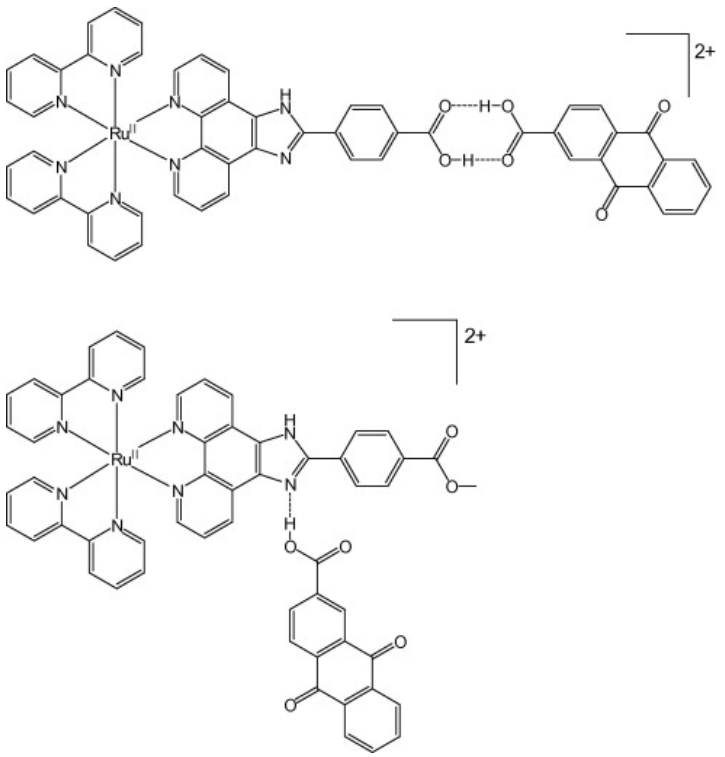

Figure 1.16: Schematic diagram of a self assembled supramolecular dyad system consisting of a ruthenium (II) polypyridyl complex and an anthraquinone-2-carboxylic acid subunit.[27]

Oxidative quenching of the excited state of the complex by anthraquinone-2-carboxylic acid was investigated for both complexes in aqueous and non-aqueous media. By measuring the redox potential, luminescence intensity and lifetimes of the complexes, the energetics and dynamics of the photoinduced electron transfer between ruthenium donor and acceptor was examined. In polar media, this was found to be a dynamic process suggesting that the quenching rate was controlled by bimolecular collisions. The quenching rate constant (k_q) was calculated to be approximately equal to 6.7×10^9 M^{-1} s^{-1} in water for the carboxyl terminated self assembled dyad. In contrast the in aprotic solvent, dichloromethane, quenching occurred through a static quenching

mechanism as determined by a Stern-Volmer plot. This indicated that the association between the luminophore and quencher was most likely through hydrogen bonding between the carboxylic acid moieties of the ruthenium complex and the anthraquinone carboxylic derivative. The rate of electron transfer between the subunits was estimated to be 4.7×10^7 s^{-1} using lifetime measurements.

In contrast, for the analogous complex in which the carboxylate was methyl protected, a mixture of static and dynamic quenching behaviour in aprotic solvent was observed by Stern-Volmer plots. This had a bimolecular quenching rate constant of 7.0×10^8 M^{-1} s^{-1}. The statically quenched ruthenium component is thought to arise from H-bonding interactions between the carboxyl of anthraquinone quencher and the nitrogen on the imidazole ancillary ligand. H-bonding, prevalent in biological systems, is known to facilitate electron transfer[27] and this is an interesting example of solvent induced switching between two electron transfer pathways, one unimolecular, most likely driven by H-bonding and one bimolecular.

Flamigni *et al.*[11] reported on the use of an iridium terpyridine, $[Ir(tpy)_2]^{3+}$, subunit in porphyrin arrays for the conversion of light energy. Initially ruthenium and osmium terpyridine units were employed as photosensitisers in triads containing organic donors and acceptors. However, the relatively low excited state energy of these complexes provided an energy sink, seriously competing with the charge separation process through recombination of the ground state energy.[11] $[Ir(tpy)_2]^{3+}$, by comparison, exhibited higher excited state energy levels favouring charge separation, longer excited state lifetimes and stronger absorption/emission profiles. The iridium complex was used in arrays containing electron accepting gold porphyrins (PAu) and electron donating base-free porphyrins (PH_2). Modification of the base-free porphyrin with zinc (PZn) allowed alteration of the photoreactivity and led to very efficient charge separation with a lifetime on the order of a microsecond.

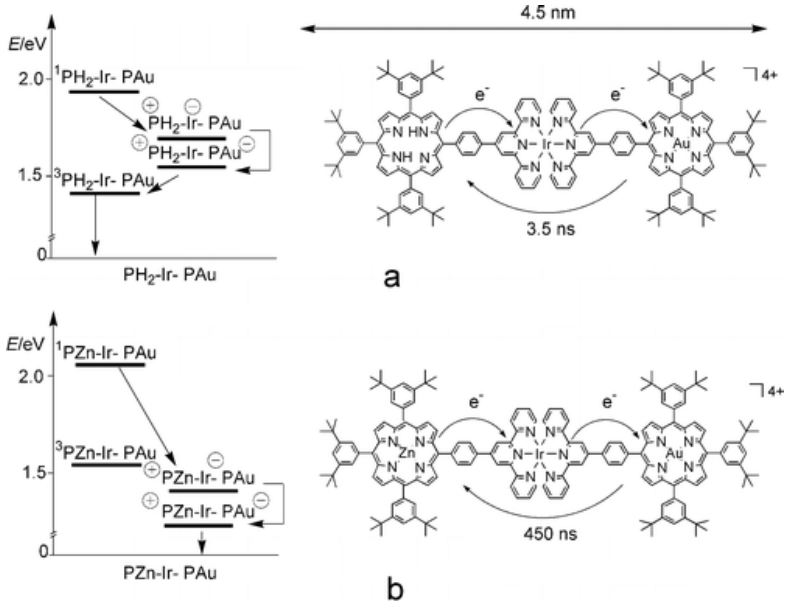

Figure 1.17: Energy level diagram and photoinduced processes in supramolecular assemblies PH_2 – I r - PAu in acetonitrile and PZn – Ir - PAu in toluene.[11]

A charge separated state of PH_2^+ -Ir- PAu^- that stored energy of about 1.5 eV was estimated. The resultant lifetime of 3.5 ns was disappointingly short due recombination of the charge separated state to a close lying triplet energy state localised on the base-free porphyrin moiety (Figure 1.17(a)). Modification to include a zinc porphyrin subunit lead to a lower energy oxidation potential and a higher triplet excited state energy of the PZn-Ir-PAu supramolecular assembly (Figure 1.17(b)). Using transient absorption spectroscopy, it was found that recombination of the triad to its ground state occurred from the charge separated intermediate state while displaying a remarkably longer lifetime of 450 ns in toluene. This charge separated state could store energy of about 1.3 eV and was formed with 100% efficiency. Considering its lifetime and stability in air, this is one of the most successful examples of charge separation based on a transition metal complex.

Lehn *et al.*[60] also described remarkable charge separated efficiencies in the synthesis of a supramolecular assembly containing multichromophoric cyclodextrins (Figure 1.18) for the conversion of light energy via the antenna effect. Energy transfer from the napthoyl antenna chromophores to the encased merocyanine dye was shown to

occur with 100% efficiency by FRET and thus mimic important features of photosynthetic units. The mechanism of homo energy transfer (between naphthoate chromophores) and hetero energy transfer (between naphthoate chromophores and the merocyanine dye) was attributed to Coulombic interactions rather than short-range interactions.

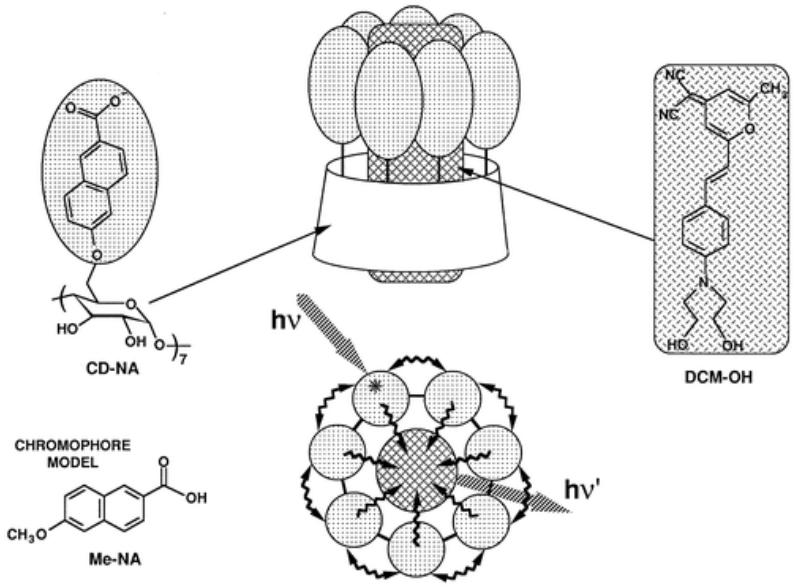

Figure 1.18: Schematic illustration of the supramolecular assembly between the hepthanapthoate β-cyclodextrin (CD-NA) and the merocyanine (DCM-OH) fluorophore.[60]

Pellegrin *et al.*[28] described the synthesis of a novel photoactive ruthenium (II) polypyridyl complex coordinated to an adamantyl pendent that formed a self-assembled supramolecular structure with β-cyclodextrins (Figure 1.19). The self-assembly was driven by the hydrophobic host-guest interaction between the adamantyl and the cyclodextrin. This association was found to be pH dependent with an association constant of 8.8 x 10^3 M^{-1} in neutral media and 2.24 x 10^4 M^{-1} in basic media. Results suggested that photoinduced electron transfer between the luminophore and methyl viologen (MV) terminus was strongly and reversibly controlled by pH. At pH above 8.5, an efficient electron transfer occurred, resulting in the oxidation of the ruthenium

centre in the charge separated state and the formation of the $MV^{+\cdot}$ radical, which was identified by transient absorbance studies and steady state photolysis. It is thought that the increased electron transfer rate under basic pH conditions was facilitated more efficiently through the anionic imidazole ligand, via what is effectively a hole transfer between donor and acceptor.

Conversely, assembly of the modified ruthenium luminophore with an unfunctionalised cyclodextrin exhibited no significant pH dependence of formation and therefore, the charge interactions between the methyl viologen and cationic ruthenium complex is thought to drive the pH dependence of the self-assembly process. Such switchable electron transfer is desirable in molecular electronics, where these materials may behave as logic gates.[28]

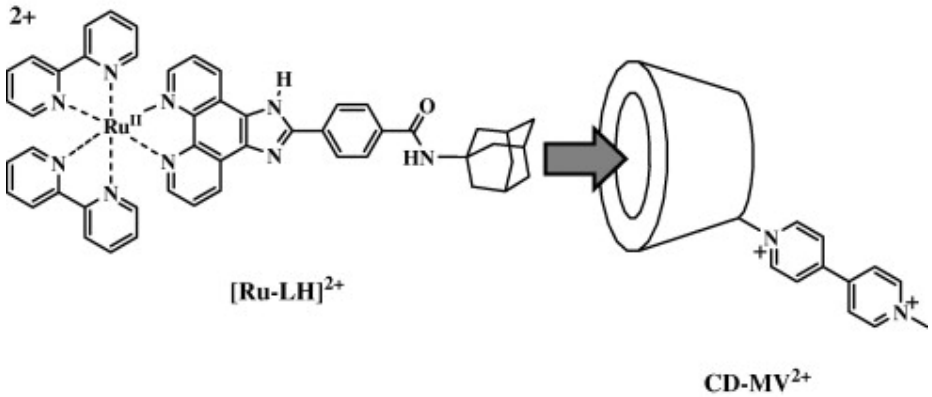

Figure 1.19: Schematic diagram illustrating the self-assembled supramolecular structure between a modified photoactive ruthenium (II) polypyridyl complex and β-cyclodextrin. [28]

1.2.2 Photoactive Self-Assembled Monolayers (SAMs) and Metal Enhanced Fluorescence

Self assembled monolayers (SAMs) offer a very easy way of controlling the chemical composition and physical structure of a substrate surface. This control has far reaching implications for many aspects of surface chemistry including; nano-scale photonic devices, wetting, solar energy conversion, catalysis and chemical sensing.[41, 61, 62] Furthermore, the introduction of photoactive SAMs is one of the most versatile ways of generating photoactive molecular devices as the surface provides a means of addressability to the SAM. As a result, light may be exploited to initiate photochemical events that may subsequently be detected by electrochemical methods or may result in the generation of photocurrents.[41]

Immobilisation of molecular dyads onto semiconductor surfaces leads to new electron transfer pathways as the solid support becomes an active contributor to the interfacial supramolecular triad.[41] Argazzi *et al.*[63] elegantly highlighted this phenomenon in a report describing the surface immobilisation of a ruthenium-phenthiazine (PTZ) dyad (similar to the sensitiser used previously in mimicking model photoantenna assembly based on a polystyrene backbone) onto TiO_2 as illustrated in Figure 1.20.

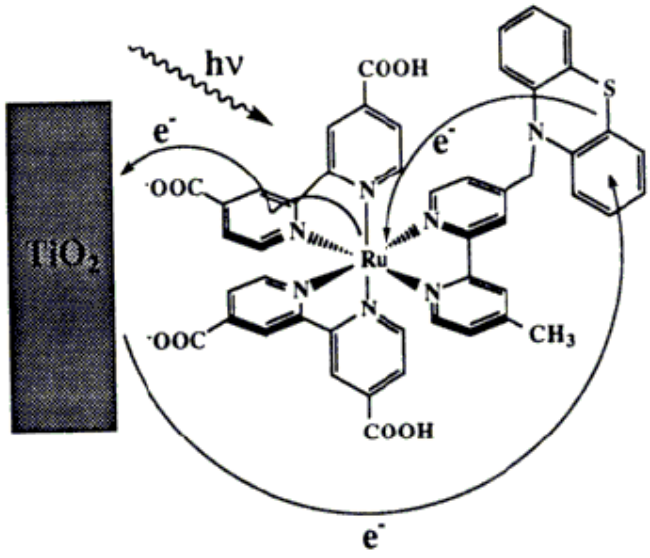

Figure 1.20: Schematic diagram illustrating the ruthenium-phenthiazine (PTZ) dyad immobilised onto a TiO_2 surface and the possible electron transfer pathways.[63]

The charge-separated state of TiO_2^- - Ru(II) – PTZ^+ was achieved by electron injection from the ruthenium unit to the TiO_2 substrate followed by electron transfer from the phenothiazine (PTZ) unit to the oxidised ruthenium metal centre.[3] The charge separated species decays to the ground state with a rate of 3.6×10^3 s^{-1} (lifetime of 300 ns). This is three orders of magnitude longer lived than the unsupported dyad in solution. This sensitiser has also been shown to efficiently convert light energy into electrical energy in regenerative solar cells using an NaI/I_2 electrolyte.[63]

Metal substrates especially gold and silver, are often used to enhance the photophysical characteristics of an attached luminophore[47, 64-67] and has already been discussed in Section 1.2. Metal-luminophore interactions can result in increased quantum yields but may also display a consequent decrease in the lifetime of a given chromophore; owing to an enhanced local electric field and an increase in the intrinsic system decay rate.[49, 68] The type and length of the bridging unit in the A-L-B assembly is critical to the electronic communication between the metal and photoactive components. Linker length should be sufficiently long to facilitate maximum emission enhancement of the luminophore preventing efficient quenching by the metal substrate. Unless energy transfer to the metal is desirable.[69, 70]

Malicka *et al*.[48] have highlighted this distance dependent relationship in a study using layers of protein to separate fluorescently labelled DNA oligomers from silver island films (SIFs) by fluorescent means. The process involved adsorption of a layer of biotinylated bovine serum albumin (BSA) followed by deposition of further layer of avidin. The treatment may be repeated many times adding a thickness of about 9 nm for each BSA-avidin layer as illustrated in Figure 1.21. The fluorescently functionalised DNA oligomers were then deposited onto the separate layers of BSA-avidin and the resulting emission intensity was measured as a function of the distance from the SIFs.

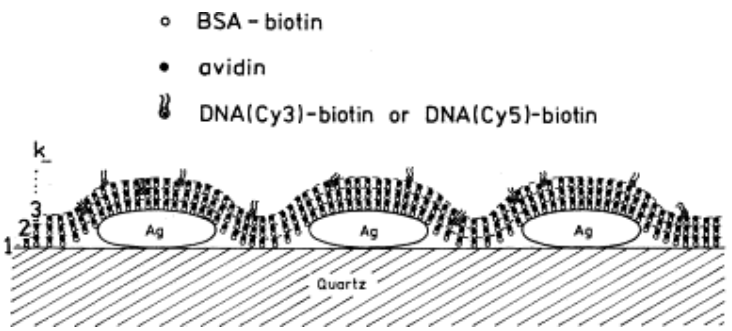

Figure 1.21: Schematic diagram illustrating the SIFs with layers of biotinylated BSA, avidin and functionalised DNA oligomers to determine the distance dependent relationship between a metal substrate and luminophore.[48]

Figure 1.22 below shows the emission intensity of the Cy3- and Cy5- labelled DNA oligomers at various distances from the SIFs. Results showed that the greatest luminescence enhancement is when one layer of BSA-avidin is present and hence, a distance of about 9 nm from metal substrate to luminophore. Any greater and the luminescence is significantly reduced for both of the fluorescently labelled DNA oligomers. However, using a BSA-avidin bilayer does not give a high degree of control over the distance from metal substrate to luminophore as there is no option to determine the metal enhanced emission at distances other than 9, 18, 27 nm etc. These results are confirmed in experiments performed in Chapter 3, where a ruthenium (II) complex at a distance of 13.2 nm (in linear conformation) from the metal nanoparticle exhibited greater emission intensity than that of the same dye located at a distance of only 3.3 nm from the substrate.

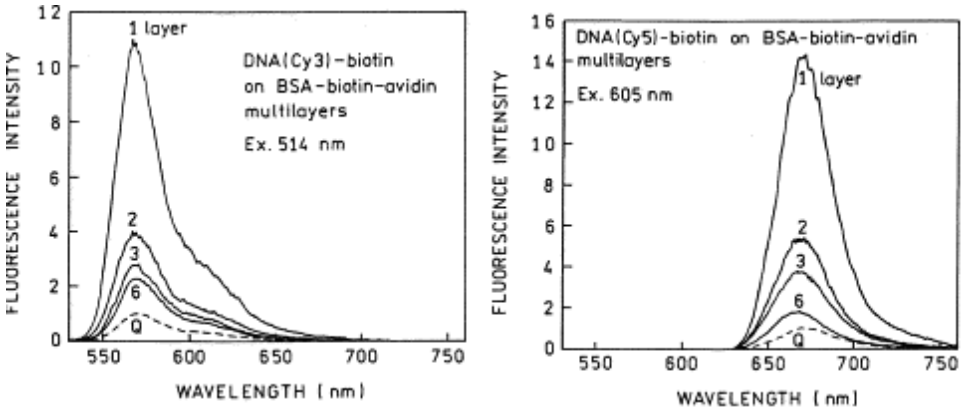

Figure 1.22: Distance dependence on emission intensities of the Cy3-(left) and Cy5-(right) labelled DNA oligomers form SIFs.[48]

Using core-shell silver colloids coated with silica gel of varying thickness Aslan *et al.*[49] also described this phenomenon of luminescent enhancement as a result of a nearby silver metal substrate. Europium and rhodamine dyes were doped inside the silica pores and an Alexa 647 fluorophore was covalently attached to the silica shell itself. The diameter of the silver nanoparticle was 130 +/- 10 nm for all preparations with silica coatings ranging from 2-35 +/- 1 nm in thickness. The silica gel surrounding the silver metal core provides (a) robustness, chemical inertness and the versatility needed for conjugation of molecules to the silver colloid, (b) protection of the metal core from ions present in solution and (c) allows for the optimum distance for metal enhanced fluorescence which was determined to be at a silica shell thickness of around 10 nm.

The significance of the silver core to the enhanced luminescence of the dyes is demonstrated in Figure 1.23 below. Here, the emission intensities of the attached luminophores are compared directly with one another using a shell-core with and without the metal nanoparticle. The europium and rhodamine doped nanoparticles displayed an enhanced emission intensity that was 8 and 20 times, respectively, that of the controlled substrate containing no silver core. Whereas, the confocal fluorescence image (Figure 1.23) of the covalently linked Alexa 647 dye showed an approximate 10 fold increase in emission intensity with the silver nanocore nearby.

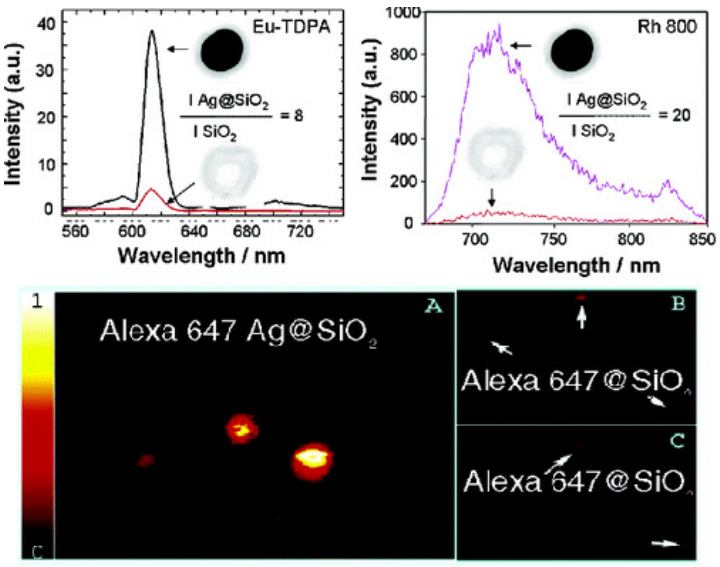

Figure 1.23: (top) Emission intensity of europium and rhodamine doped nanoparticles with and without core silver nanoparticles. All maximum enhancement values were recorded using the optimised silica shell thickness of 11 +/- 1 nm. (bottom) Confocal fluorescence microscopy images showing difference in luminescent intensity of an Alexa 647 linked supramolecular assembly in the presence and absence of the silver nanocore.[49]

By comparison, Thomas *et al.*[47, 71] used gold nanoparticles to enhance the fluorescence of 1-aminomethylpyrene by means of inducing electron transfer from the photoactive moiety directly to the metal substrate. 1-Aminomethylpyrene is an organic molecule that is weakly luminescent when dissolved in an organic solvent. This is due to intramolecular quenching of the excited energy state by electron transfer from the lone pair of electrons on the nitrogen atom to the aromatic pyrene rings. However, when bound to AuNPs the quantum yield and emission intensity of 1-aminomethylpyrene dramatically increases as binding of the amine group to the gold substrate suppresses the intramolecular electron transfer of the nitrogen lone pairs to the pyrene moiety.

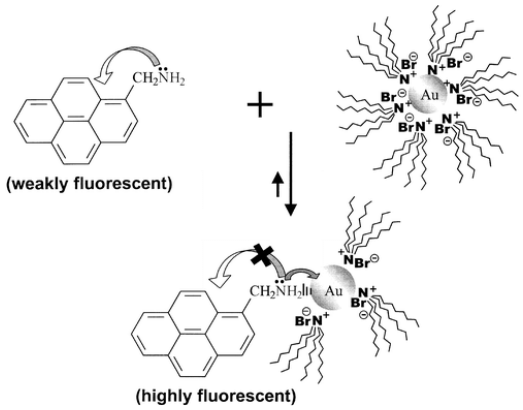

Figure 1.24: Schematic diagram illustrating the binding of 1-aminomethylpyrene to gold nanoparticles, and resultant increase in fluorescence following attachment to the metal substrate.[71]

Studies have indicated that densely packed chromophores on metal nanoparticles dramatically suppressed quenching of the excited energy state of bound molecules.[65, 72] Stellacci *et al.*[65] reported the first supramolecular assembly consisting completely of a self-assembled layer of chromophores on silver nanoparticles (Figure 1.25). It is claimed that this allows for the close packing of about 2500 chromophores on a single silver nanoparticle surface with a diameter of less then 10 nm. The resulting two-photon excited fluorescent nanobeacons were ultra-bright, exhibited higher quantum yield efficiencies and displayed a decrease in sensitivity to photobleaching compared to the individual unbound chromophores. Perhaps another interesting experiment would have been to examine the enhanced photophysics of the dye as a function of the alkane chain linker length to determine if these results were due to their proximity to the nanoparticle or the local environments in which the chromophore is located upon conjugation.

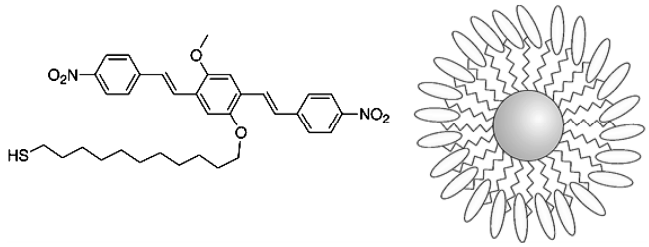

Figure 1.25: Chemical structure of 11-{4-methoxy-2,5-bis[(E)-2-(4-nitrophenyl)ethenyl]phenoxy}-1-undecanethiol (left) and schematic representation of closely packed silver nanoparticle (right).[65]

Chapter 3 discusses attempts to utilise SAMs in creating a nanoconjugate system suitable for multimodal cellular imaging. The length of the bridging linkers were varied in an effort enhance the luminescence and Raman signal of an adsorbed ruthenium luminophore. The resultant nanoconjugate displaying the superior results was then exploited for the purposes of cellular imaging of mammalian cells. Additionally, in the attempts to create a model photoantenna in Chapter 6, it was proposed to use SAMs to control the lateral spacing between adjacent oligonucleotide sequences and therefore, have a direct impact on the communication between chromophores within the supramolecular assembly.

1.3 Metal Complexes used for Cellular Uptake/Imaging

Until approximately 5 years ago, very few research groups had reported the use of phosphorescent heavy metal complexes in bioimaging.[23] However, due to their favourable optical and redox properties, metal complexes have been examined very recently as possible candidates for real-time live cell imaging, most particularly; zinc (II)[45], rhenium (I) [73], platinium (II)[74] and rhodium (III).[75]

In order for a luminophore to be a suitable candidate for cellular imaging it must be photostable, have a high quantum yield, reasonably non-toxic, cell permeable, have visible to NIR emission and depending on the application, show a preference for localisation within a certain organelle of the cell. Of the non ruthenium and iridium complexes, an interesting paper published by Kowol *et al*.[45] described the synthesis of the first zinc (II) complex containing Triapine. Triapine, or 3-aminopyridine-2-carboxaldehyde thiosemicarbazones (Figure 1.26), is one of the most promising antitumor chemotherapeutic compounds to have entered into phase I and phase II clinical trials. It has been shown to inhibit the enzyme ribonucleotide reductase which is essential for cell propagation. Coordination of the Triapine unit to a zinc (II) metal centre increased antineoplastic activity and displayed more selective affinity for the nucleoli within the nucleus of human colon carcinoma cells as shown in Figure 1.27. Co-staining studies with nucleolar protein fibrillarin and the zinc (II) complex showed preferential selectivity towards the nucleoli of these cells, as illustrated in Figure 1.27 image H below.

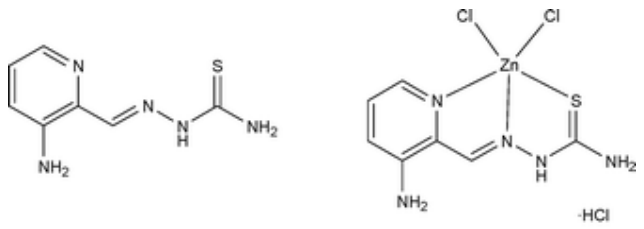

Triapine [Zn(Triapine)Cl_2]·HCl (1)

Figure 1.26: Structures of Triapine unit and zinc (II) Triapine complex.[45]

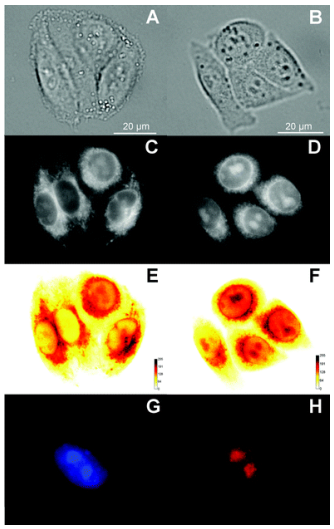

Figure 1.27: Live cell images of human colon carcinoma cells incubated with 0.25 mM Triapine (A, C, E, G) in PBS and 0.25 mM in 0.5% DMSO/PBS zinc (II) Triapine complex (B, D, F, H) representing their bright field images, luminescence images, false colour images and co-staining images from top to bottom respectively.[45]

In another study reported by Bieda *et al.*[75], the cytotoxicity of a series of rhodium (III) complexes (Figure 1.28) towards colon and breast cancer cell lines was determined. Compounds 4, 6, 8 and 9, containing polypyridyl ligands with increasing numbers of phenyl ring attached, demonstrated an increase in the antiproliferative potency with increasing surface area and hydrophobicity. It was claimed that compound 9, containing the dppz ligand, is even more potent than cisplatin. Cisplatin is the chemotherapeutic drug used most to treat many cancers but has many undesirable side effects, high toxicity and problems with drug resistance in primary and metastatic cancers.[76] As a result, research has intensified into transition metal complexes because of their favourable properties suited to anti-cancer drug design for photodynamic therapy.

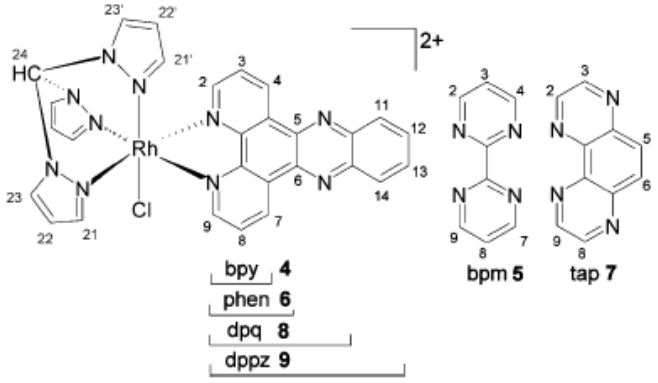

Figure 1.28: Series of rhodium (III) complexes synthesised by Bieda et al for cellular imaging.[75]

Much of the relatively limited research surrounding ruthenium (II) complexes for live cellular imaging involved compounds containing the dipyridophenazine (dppz) cyclometalating ligand. These particular complexes have been shown to act like a 'molecular light switch'. They are brightly luminescent when intercalated with DNA or protected from aqueous environments and virtually non-emissive when in aqueous solutions.[77] Svensson *et al.*[77, 78] reported the synthesis of a series of $[Ru(phen)_2(dppz)]^{2+}$ derivatives, where the dppz ligand was altered with alkyl chains of different lengths (Figure 1.29).

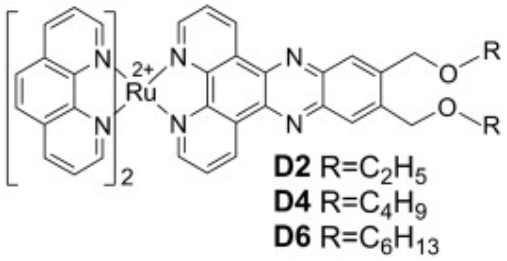

Figure 1.29: Series of ruthenium (II) derivatives containing the dppz ligand synthesised by Svensson et al. for cellular imaging.[77]

They reported how slight modifications to the lipophilicity of the dye to the dppz ligand resulted in large variations in its distribution throughout the membrane, its DNA binding ability and its cellular uptake in CHO cells. Figure 1.30 shows the distribution of the assorted dyes throughout the cell structure using confocal fluorescence microscopy. A decrease in the alkyl chain length resulted in a higher emission intensity in the nucleus compared to the cytoplasm (Figure 1.30 diagram A). While the most lipophilic complex, D6, resided mainly on the outside of the nucleus of the fixed CHO cells (Figure 1.30 diagram C). However, it must be noted that throughout their experiments and many other reported studies on coordination compounds, DMSO (1%) was used to solvate the metal complexes. Organic solvents, such as DMSO and ethanol, are frequently used in cellular uptake analysis. Alarmingly, DMSO is known to induce cell diffusion, cell differentiation and enhance the permeability of lipid membranes. DMSO also causes the cell membrane to become less ridged, making it more susceptible to facilitate membrane diffusion.[79, 80] Chapter 5 details results of the cytotoxic effect of DMSO and ethanol on SP2 myeloma and CHO cell lines.

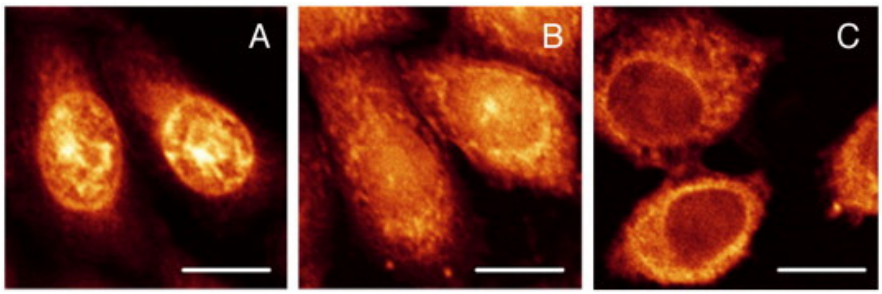

Figure 1.30: Confocal fluorescence microscopy images showing the distribution of ruthenium (II) complexes in fixed CHO cells. D2 (A), D4 (B) and D6 (C) (10μM in 1% DMSO/serum free medium) were added to cells in fixed methanol for 15 minutes and excited at 488 nm.[77]

Chen *et al.*[81] published preliminary studies on a series of water soluble ruthenium (II) polypyridyl complexes which they reported induced mitochondria mediated apoptosis in human cancer and normal cells. Included in this series of ruthenium (II) probes was the $[Ru(bpy)_2(picNO_2)]^{2+}$ complex, which is also synthesised in this thesis. One of the more interesting results found that $[Ru(bpy)_2(picNO_2)]^{2+}$

showed a greater cytotoxic effect to the human Hep G2 cell line, when compared to the widely used cisplatin anti-tumour drug. However, the complex exhibited a considerably poorer cytotoxic effect against the other cell lines under analysis.

Barton *et al.*[82] were one of the first research groups to investigate the cellular uptake of ruthenium (II) polypyridyl complexes in living cells. The metal complexes were incubated with HeLa cells in tris buffer with varying final concentrations of the ruthenium complexes. Figure 1.31 illustrates the chemical structures synthesised as part of their analysis. Uptake of these luminophores into the cells was analysed by the mean luminescence intensity of the overall cell population by flow cytometry. Results indicated that the complexes with the greater lipophilicity exhibited higher cellular uptake, with $[Ru(DIP)_2(dppz)]^{2+}$ (DIP = 4,7-diphenyl-1,10-phenanthroline) best of all. For all complexes, the greatest luminescence was evident in the cytoplasm as confirmed by co-localisation studies.

It was thought that if a complex entered a cell by means of passive diffusion, one might assume that a complex with closest to neutral charge, smaller particle size and greater hydrophilicity should display greater cellular uptake.[82] However, unexpectedly the most hydrophobic DIP ligand seemed to facilitate cellular transport despite its larger size. The dye showed distribution throughout the cells cytoplasm but without ever entering into the nuclear envelope as shown in Figure 1.32.

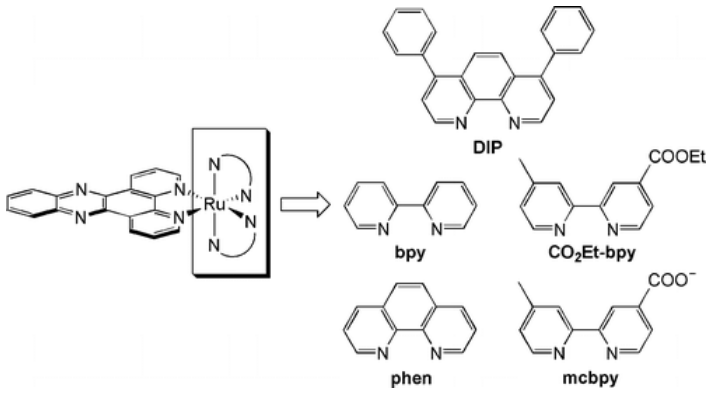

Figure 1.31: Chemical structures of the ruthenium (II) dppz derivatives synthesised by Barton et al. for cellular imaging.[82]

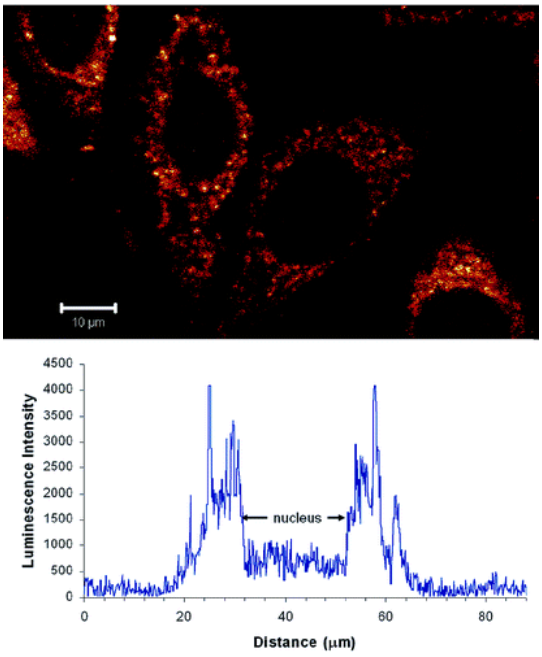

Figure 1.32: (top) Confocal fluorescence microscopy image of HeLa cells with $[Ru(DIP)_2(dppz)]^{2+}$. *Cells incubated with 5µM (in tris buffer) ruthenium for 2 hours at 37 °C, excitation wavelength of 488 nm. (bottom) Intensity profile of the ruthenium emission across HeLa cells following incubation for 12 hours with 10 µM (in tris buffer) of dye.*[82]

In a later report,[83] a mechanism of passive diffusion of the $[Ru(DIP)_2(dppz)]^{2+}$ complex into the cell was proposed, as uptake decreased when cells were depolarized with a high potassium buffer and increased when cells are hyperpolarized with valinomycin. This suggested a passive diffusion mode of cellular uptake as the membrane potential of a cell is dependent on the potassium ion concentration. Due to its lipophilicity and positive charge, $[Ru(DIP)_2(dppz)]^{2+}$ is likely to traverse the membrane in response to the membrane potential similar to other lipophilic cations such as rhodamine 123.[83]

The plasma membrane of a viable cell has a membrane potential of -50 to -70 mV, with the inside of the cell negative with respect to the outside.[83] As most transition metal complexes carry an overall positive charge, uptake of the luminophore may be driven by the potential difference across the cellular membrane. The membrane potential in animal cells depends mainly on the potassium ion concentration in the cytoplasm. Hence, in the experiments carried out by Barton *et al*. they use potassium-based buffers to alter the cells potassium concentration, which drives the cellular uptake of the dye.[83]

Tan *et al*.[84] also demonstrated how a similar series of ruthenium (II) 4,7-diphenyl-1,10-phenanthroline analogues induced apoptosis in tumour cells with even greater potency than cisplatin. Following optical irradiation, many photoactive ruthenium complexes can interact with $^3O_2$ in a process that results in the formation of reactive oxygen species (ROS). These ROS species can then cause cellular damage leading to cell apoptosis. It is already known that molecules possessing reactive electronically excited states have found clinical use as PDT agents for the treatment of cancers.[85] However, tumour cells are often hypoxic and using PDT causes further oxygen depletion within cells so using this type of treatment may be somewhat limited.[85]

Due to their high phosphorescent quantum yield, long lifetimes and visible tunable emission, iridium (III) complexes have become the most attractive class of phosphorescent heavy metal complexes in biolabelling in recent years.[23] Huang *et al.* were the first research group to investigate luminescent staining of living cells using iridium (III) complexes. In a paper published in 2008,[86] they reported the synthesis and cellular uptake of two difluorophenyl pyridine iridium (III) complexes (Figure 1.33) that showed facile internalisation within HeLa cells (Figure 1.34).

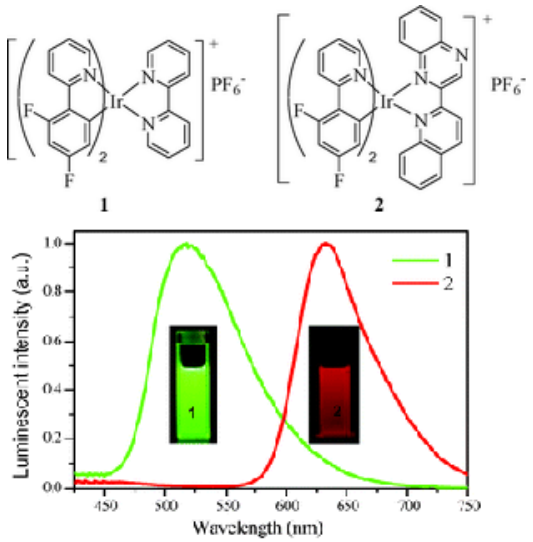

Figure 1.33: Chemical structures of iridium (III) complexes and their corresponding emission profiles in dichloromethane using 365 nm excitation wavelength.[86]

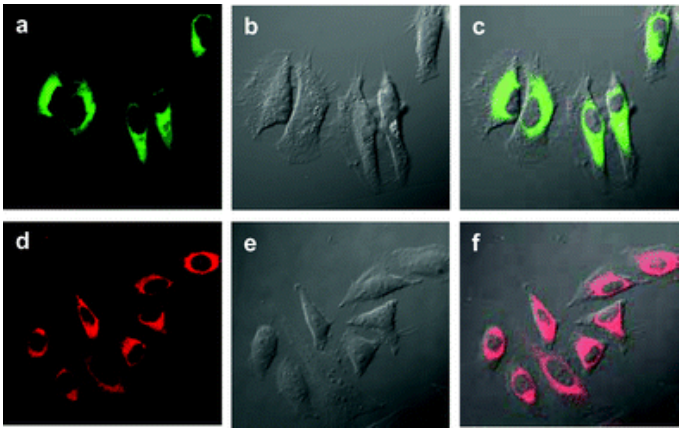

Figure 1.34: Confocal luminescence images (a and d), brightfield images (b and e) and overlaid images (c and f) of iridium (III) complexes 1 (top) and 2 (bottom) respectively. Samples are in DMSO/PBS (pH 7, 1 :49 v/v) and were incubated with HeLa cells for 10 minutes at room temperature.[86]

Membrane transportation was claimed to be as a result of the combination of the positively charged iridium (III) complexes and their increased hydrophobicity given by fluorination of the cyclometalating ligands. However, presumably due to the poor aqueous solubility of the dye, a 2% solution of DMSO was used in their cellular uptake experiments. This, once again, raises the question of whether the compounds are

genuinely cell permeable or are so because of DMSO. However, the cell viability studies were estimated to be greater than 90% for both iridium complexes. A later paper published by the same group[23] detailed the synthesis and cellular uptake of an additional four iridium (III) difluorophenyl pyridine complexes showing tunable emission from blue to red. Their results were broadly in line to what was reported in their 2008 paper but again a relatively high 2% solution of DMSO was still employed for their cell studies and it is not clear if dyes are fully cell permeable.

A potential solution to the poor aqueous solubility of iridium (III) compounds was proposed by Huang *et al.*[87] They suggested the synthesis of charge-separated zwitterionic iridium (III) complexes as shown in Figure 1.35. These displayed good luminescent character with some showing good solubility (mM) in PBS buffer pH 7.0. Table 1.1 outlines the solubility and the cellular interactions of zwitterionic iridium (III) complexes 1-5. However it is noted, that in a change from procedure by this particular research group, HeLa cells are no longer employed for the cell analysis and a KB cell line is used instead, so it is not possible to make direct comparisons.

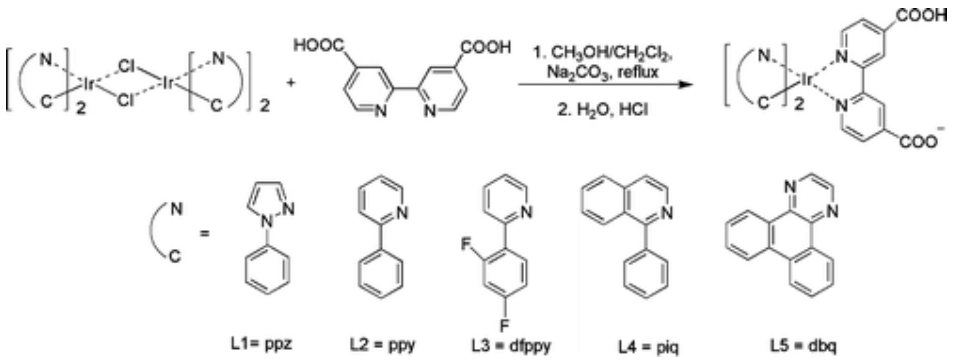

Figure 1.35: Chemical structures of zwitterionic iridium (III) complexes 1-5 for cellular imaging.[87]

complex	solubility (μM)	log $P_{o/w}$	Encapsulation efficiency (%)	Release (%)
1	2064	−1.89	49.9	39.6
2	5096	−0.88	56.1	33.5
3	559	−0.55	59.2	29.1
4	174	0.69	77.9	20.7
5	37	1.39	83.1	17.4

Table 1.1: Solubility, octanol/water partitioning coefficient (log $P_{o/w}$), encapsulation efficiency and release of zwitterionic complexes 1-5 shown in Figure 1.35.

Their results showed that complexes 1-4 had weak intercellular luminescence. However, complex 5 displayed bright luminescence inside the cell's cytoplasm, which was suggestive of transmembrane transport. Furthermore, all KB cells were still found to be alive after a 2 hour time period. Additional studies indicated that the membrane penetrating ability of fixed cells with the iridium (III) compounds was in the order of: 1 < 2 < 3-5. The more hydrophilic complexes 1 and 2 had poor cell permeability, whereas, the hydrophobic complexes 3-5 internalised within the membrane without difficulty. Once inside the cell, it was found that compounds stayed mainly in the cytoplasm of both living and fixed KB cells.

As expected the more hydrophilic complexes showed greater aqueous solubility with complex 5 only slightly soluble in aqueous PBS buffer. For the same reason, their amphiphilicity changed from hydrophilic to hydrophibic with log $P_{o/w}$ changing from -1.89 (complex 1) to 1.39 (complex 5). The ability of a cellular probe to permeate biological membranes depends strongly on its lipophilicity, which is commonly estimated by the partition coefficient of the compound in octanol/water ($P_{o/w}$).[30]

The encapsulation efficiency of the complexes into a liposome and their subsequent release reflects the complexes' permeation in and release out of the bilayer of a cell membrane, respectively.[87] According to the results, the more hydrophilic complexes were difficult to encapsulate and were easily released from the cell

membrane, whereas the hydrophobic ones were more likely to stay inside the cell. Results suggested that for the purpose of designing iridium (III) probes for cellular imaging a balance must be struck where the hydrophilic part is necessary for aqueous solubility but the lipophilic moiety is helpful in cell permeation.

Very recently, for the first time, nuclear uptake and staining within live cells by a series of iridium (III) dipyridoquinoxaline complexes was reported by Zhang *et al*.[88] However, it is noted that the use of these dyes with HeLa cells resulted in rapid and extensive cell death due to the high cytotoxicity. The more resilient MDCK cell line were used in their experiments instead. The luminophores also had to be dissolved in a solution of PBS containing 1% DMSO prior to analysis.

Not only may metal luminophores be used as potential probes for cellular imaging but they also exhibit properties that could render them very useful in the detection of certain diseases. Today, there are a couple of examples where iridium probes are already in use in medical diagnostics. Zhang *et al*.[30] used the changes in the photophysical characteristics, namely it's lifetime, of an iridium dye (Figure 1.36) to image tumour hypoxia in living animals. Hypoxia is frequently a characteristic of tumour tissue and was visible after only 5 minutes following injection of the iridium dye. However, the dye was fully metabolised by mice within a 24 hour time period. The phosphorescent lifetime of the dye was found to be 2.9 μs in the tumour tissue and 1.9 μs in the normal tissue. Thus, it may be concluded that the longer lifetime of the iridium dye in the tumour tissue was a result of the lower oxygen concentration present in the hypoxic tissue. The dye was also used to detect the oxygen concentrations within four different cell lines, including HeLa and CHO cells. However, the lipophilic dye was dissolved in a solution containing 10% DMSO prior to injection into the mice and cellular imaging analysis. This is a very high concentration of organic solvent to use and will promote cross-tissue transport and depending on its final concentration will induce cell death.

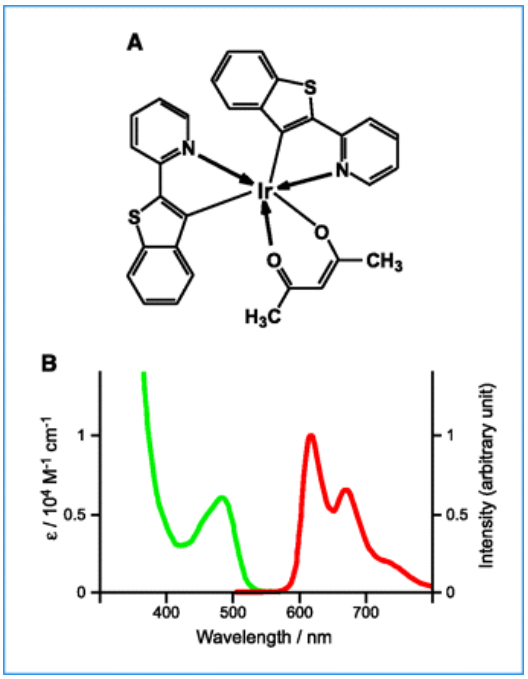

Figure 1.36: Chemical structure of iridium luminophore used to image tumour hypoxia in living animals. Its corresponding absorbance and emission profile is shown below in dichloroethene at room temperature.[30]

Xiong *et al.*[89] demonstrated the use of an iridium (III) complex for selectively targeting biomarkers such as homocysteine (Hcy) and cysteine (Cys) within living KB cells. The levels of Hcy are an important indicator for diseases including cardiovascular and Alzheimers disease, whereas, Cys deficiency is associated with slow growth, liver damage, lethargy, muscle loss and fat loss. The iridium luminophore was shown to be membrane-permeable (with a final DMSO concentration of 0.2%), displayed low cytotoxicity and can readily detect the intracellular Hcy/Cys concentrations in a ratiometric manner by a visible change in its phosphorescent emission from yellow to red as shown in Figure 1.37. The molecular design of the iridium probe is based on the selective reaction between the aldehyde on the ligand and the β,γ-aminothiol group on Hcy or Cys biomarkers to form thiazolidine and thiazine, respectively. Complexation of the metal complex to these biomarkers resulted in disruption to the π bond conjugation within the molecule, causing a switch of the excited state from an LC transition to an MLCT transition and a corresponding change in the emission

wavelength. However, it is noted that, high concentrations of amino acids are required for the successful application of such a probe.

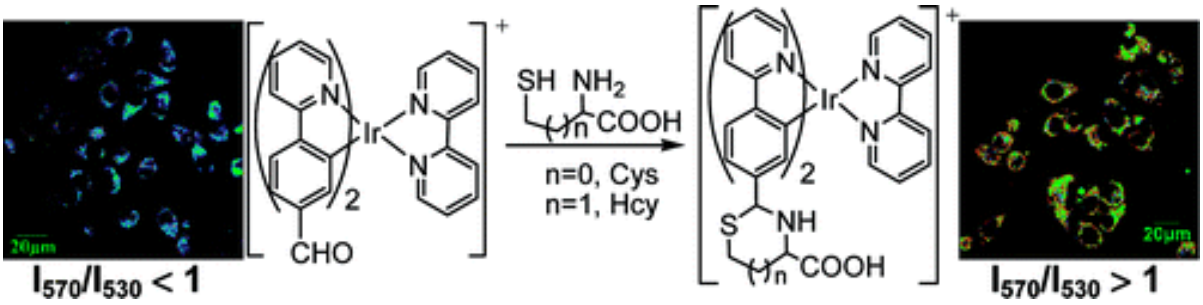

Figure 1.37: Chemical structures and resulting change in emission of the iridium (III) luminophore upon complexation with Cys or Hcy biomarker.[89]

To date there are few examples in the literature of transition metal complexes being used directly for the purpose for cell imaging. This is presumably due poor solubility issues and the low cationic charge associated with the complexes, thus prohibiting potential driven membrane diffusion of the dye across a cell membrane. Many of the luminophores reported are conjugated to polypeptides[90-92], organic luminophores[90], estradiol[93] and other biomolecules in an effort to alter the lipophilicity of the dye.

We explore the conjugation of a luminescent ruthenium (II) polypyridyl complex to thiol functionalised polyethylene glycol linkers of varied lengths. The PEGylated chromophores were then attached to 50 nm gold nanoparticles in an effort to improve their luminescent intensity as a result of metal enhanced luminescence. Furthermore, the ability of the nanoconjugate to be drawn across a lipid bilayer also increased significantly when compared to the free parent complex. In Chapter 3, it is shown how the resulting novel supramolecular nanoconjugate displays improved transmembrane capabilities and emission intensity above that of the parent dye. The probe is also used in the cellular imaging of live cells.

Chapter 5 also examines the conjugation of ruthenium (II) and iridium (III) polypyridyl luminophores to a cell penetrating peptide (CPP) to aid in its aqueous solubility and facilitate its transport across the cell membrane. This is the first time that an iridium (III) luminophore has been conjugated to a polypeptide and used as a potential multimodal probe for cellular imaging. This builds upon research published before by our group[19, 29, 33] where water soluble ruthenium (II) polypyridyl complexes are unable to transport efficiently across the cell membrane of mammalian cells. However, upon conjugation to a cell penetrating peptide, the luminophores display facile internalisation within the cellular structure without the need for organic solvents.

1.3.1 Transition Metal Complexes and Singlet Oxygen ($^1O_2$) Generation

Singlet oxygen is known to react with a number of amino acids and especially the DNA base guanosine and may lead to cell apoptosis. [16, 94-96] Furthermore, singlet oxygen is believed to be the major cytotoxic species in PDT.[96] Inorganic metal complexes are known to produce singlet oxygen typically through an energy transfer process from its excited triplet state to triplet oxygen ($^3O_2$). Therefore, an efficient generator of $^1O_2$ should have a high quantum yield of triplet formation, long triplet lifetime and a triplet state energy greater than the energy gap between singlet and triplet O_2. Djurovich *et al*.[96] showed how a series of iridium complexes they synthesised had quantum yields of singlet oxygen production ranging from 0.5-0.9. The only product observed during quenching of the excited triplet state was $^1O_2$, whose formation was promoted by contact between $^3O_2$ and the cyclometalating ligands. In general, however, little is known about how photophysical properties, such as emission energies, or changes in the electronic and geometric structures of metal complexes can effect the efficiency of $^1O_2$ production.[96]

The quenching of the excited triplet state of a luminophore (Lu) by triplet oxygen may occur via three pathways: energy transfer to give $^1O_2$ (Equation 1.12), electron transfer leading to the formation of superoxide $O_2^{\cdot -}$ (Equation 1.13) or simple deactivation (Equation 1.14).

$$Lu^* + {}^3O_2 \rightarrow Lu + {}^1O_2 \text{.....Eq 1.12}$$

$$Lu^* + {}^3O_2 \rightarrow Lu^+ + O_2^{\cdot -} \text{.....Eq 1.13}$$

$$Lu^* + {}^3O_2 \rightarrow Lu + {}^3O_2 \text{.....Eq 1.14}$$

It has been calculated that the quenching rates by triplet oxygen on ^{3}MLCT of $[Ru(bpy)_3]^{2+}$ is approximately 1/9 of the diffusion rate constant and therefore it is considered to undergo quenching exclusively by an energy transfer process.[96] However, most of the iridium complexes synthesised by Djurovich *et al*.[96] exhibited quenching rates greater then this, which is an indication of electron transfer quenching. In general however, for most iridium complexes it is thought that singlet oxygen formation is formed most likely through a combination of energy and electron transfer processes.[96] Both ruthenium and iridium luminescent probes synthesised in this thesis have previously demonstrated their triplet excited state sensitivity to dissolved oxygen and therefore, presumably their generation of $^1O_2$. This could have significant implications for the cell's viability following irradiation.

1.4 Conjugated Gold Nanoparticles for Biomedical Applications

Nanoparticles have emerged as promising materials for probing cellular processes and as such were used in this thesis in an effort to transport suitable luminescent probes across the cell's membrane. Plasmonic nanoparticles are especially useful for these applications due to their enhanced resonant absorption, scattering properties and SERS potential.[97] AuNPs appear to have good biocompatibility and may be easily modified to control their surface properties, making such nanoparticles very attractive for applications in biomedical fields such as advanced drug delivery and molecular diagnostics.[97, 98] Furthermore, there is evidence to suggest that using nanoparticles with a diameter of < 80 nm sees the excretion of the nanoparticles from the body and as a result they may be suitable for in vivo applications.[99] However, significant problems may arise due to their bio-immobilised instability and these issues must be addressed for their effective use in biomedicine. These instability issues include the adsorption of proteins and the non-specific uptake of particles by the reticular-endothelial system (RES) that may decrease the lifetime of the nanoparticles in potential medical applications.[97]

Polyethylene glycol (PEG) has proven valuable as a suitable biological linker to covalently attach to the metal nanoparticles in an effort to limit this non-specific adsorption.[97, 100] Partially coated PEG 30 nm AuNPs have already been successfully used to deliver tumour necrosis factor to solid tumours in mice, by helping to inhibit the adsorption of the functionalised nanoparticles by the RES.[101] Additionally, the attachment of PEG moieties to oligomers has also been reported to increase the circulation time of molecules in the blood stream and thus reducing the frequency when drugs must be administered. The size, shape and attachment site of the PEG linker plays a significant role in the pharmacokinetics of the functionalised pharmaceuticals.[102]

Dreaden *et al.*[100] highlighted the potential importance of PEGylated gold nanoparticles in drug delivery by reporting their selective targeting of breast cancer cells. Tamoxifen (TAM) has been widely used over the past 30 years for the treatment of breast cancer by binding to estrogen receptors and subsequently initiating programmed cell death. The TAM-PEG-AuNPs (Figure 1.38) showed selective targeting of these cells with up to 2.7 times enhanced in vitro potency versus the free drug.

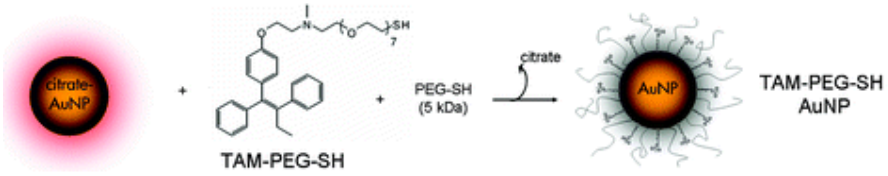

Figure 1.38: Schematic illustration showing synthesis of TAM-PEG-AuNP.[100]

The organisation and design of photoresponsive chromophores encapsulating metal nanoparticles offers exciting opportunities in the design of novel photon-based devices for sensing, switching and drug delivery.[47] Gu *et al.*[97] used modified fluorescein-PEG-AuNPs (Figure 1.39) to report the enhanced aqueous stability and efficient intracellular transport of fluorescein into the nucleus of HeLa cells possibly through the nuclear pores. The 3.7 nm monodispersed nanoparticles showed no obvious cytotoxicity to HeLa cells, making these particles ideal for improvement of nuclear targeted drug delivery. It is believed that endocytosis is the process in which the nanoconjugates are up taken by the cell as its transmembrane efficiency is greatly affected by a decrease in temperature. Prior to conjugation of the AuNPs, the free fluorescein dye did not demonstrate efficient diffusion across the cellular membrane.

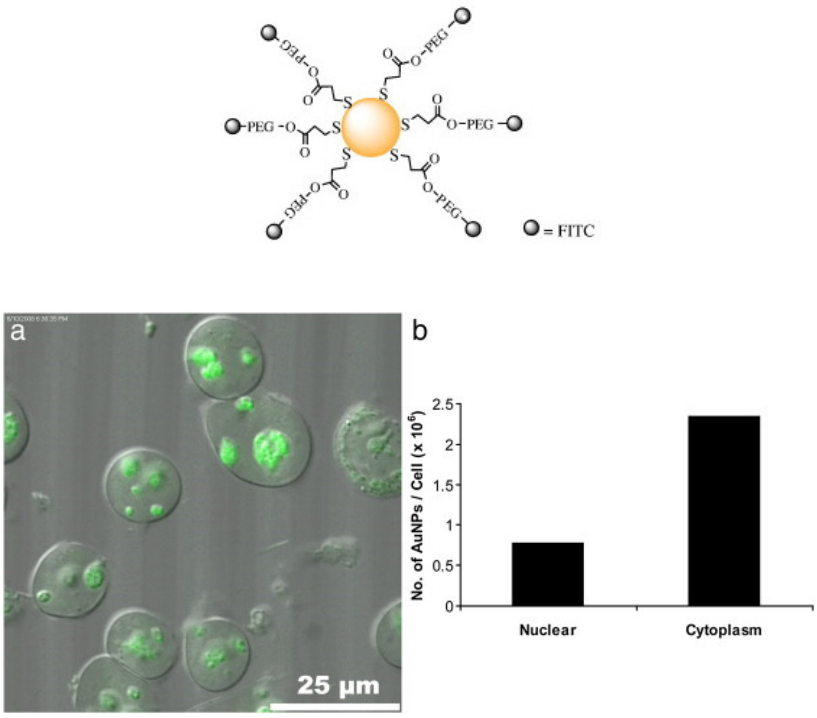

Figure 1.39: (Top) Schematic diagram illustrating AuNP-PEG-FITC (FITC = Fluorescein) nanoconjugate. (Bottom) (a) Confocal fluorescence image of isolated nucleus of HeLa cells and (b) concentration of the modified AuNPs (in PBS pH 7.4) in the nucleus and cytoplasm as measured by ICP.[97]

There are many examples in the literature of ruthenium polypyridyl functionalised gold nanoparticles.[69, 103-105] Similar to the work carried out in this thesis, Pramod *et al.*[67] reported the synthesis of $[Ru(bpy)_3]^{2+}$ functionalised gold nanoparticles with controlled separation by PEG linkers illustrated in Figure 1.40. Results demonstrated a light-induced charge shift between chromophores at higher concentrations leading to the formation of the redox products $[Ru(bpy)_3]^{3+}$ and $[Ru(bpy)_3]^{+}$. Interestingly, lowering the concentration of the ruthenium complex on the substrate resulted in a retention of the characteristic luminescence of $[Ru(bpy)_3]^{2+}$. Their results indicated that the local concentration of ruthenium complexes on the nanoparticles played a critical role in controlling the photophysics of $[Ru(bpy)_3]^{2+}$.

They also mentioned several attempts to functionalise the AuNPs with an alkane modified ruthenium complex without using PEG as a spacer. However, this resulted in the precipitation of an unfunctionalised nanoparticle. This was attributed to the non-compatibility of the non-polar alkane functionalised ruthenium moiety on the gold surface. The addition of polar PEG linkers to the reaction resulted in the formation of stable nanoparticles containing mixed monolayers on its surface.

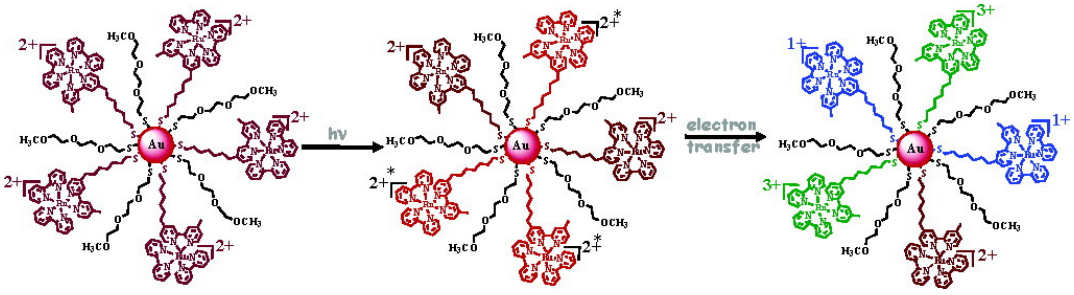

Figure 1.40: Schematic diagram showing gold nanoparticles (4.5 nm) containing mixed monolayers of an alkane functionalised ruthenium complex and PEG spacing linker for increased stability.[67]

1.5 Polypeptides as Suitable Transmembrane Transporters

1.5.1 Cell Penetrating Peptides (CPPs)

Another potential cargo-carrying molecule examined in this thesis to transport a luminophore across the cellular membrane was CPPs. Certain naturally occurring molecules may enter the cell through a facilitated transport pathway mediated by receptors on the cell's surface. An example of such a molecule is the nuclear transcription activator protein (Tat) encoded by HIV type 1 (HIV-1).[106] Octarginine is a cationic, naturally occurring derivative of the CPP Tat that has the following amino acid sequence RKKRRQRRR, where R = arginine, K = lysine and Q = glutamine. The importance of the guanidinium groups on the peptide was demonstrated by Wender *et al*.[106] who systematically changed the cationic groups with neutral alanine residues. This caused a significant decrease in the cellular uptake that was directly correlated with the number of arginines residues. Therefore, the large amount of arginine in the Tat sequence intensified research into polyarginine as a CPP. The ability of these CPPs to diffuse across the cell membrane is highly dependent on the length of the arginine chain, with a chain length of Arg_5-Arg_{11} necessary but octa- or nona-arginine showing best cargo carrying ability.[19, 107, 108] In addition, our work involving penta- and octa-arginine also showed an effect on uptake of a ruthenium (II) complex.[19, 107, 108]

The four main routes of cellular uptake are endocytosis, active transport, facilitated diffusion and passive diffusion.[83] Endocytosis is the process in which the cell membrane engulfs the extra-cellular molecules and they are brought into the cell by these tiny vesicles surrounding the substance. The various endocytotic processes are illustrated in Figure 1.41. In the process of phagocytosis the cell membrane changes shape to engulf the extracellular molecule with projections known as pseudopodia. When the plasma membrane of both projections meet membrane fusion occurs, which result in the formation of a vesicle capable of transporting the molecule inside the cell. Pinocytosis on the other hand is the process in which the cell membrane forms an invagination and whatever substance is found within the area of invagination is brought into the cell's cytoplasm by tiny vesicles. In general these materials will usually be dissolved in the extracellular fluid as pinocytosis is opposed to the ingestion of larger

particulate material such as bacteria. Receptor-mediated endocytosis is an endocytotic mechanism in which specific molecules are brought into the cell. Receptors on the cell's surface target specific molecules outside the cell. After binding an endocytotic process occurs and the molecule is ingested by the cell.

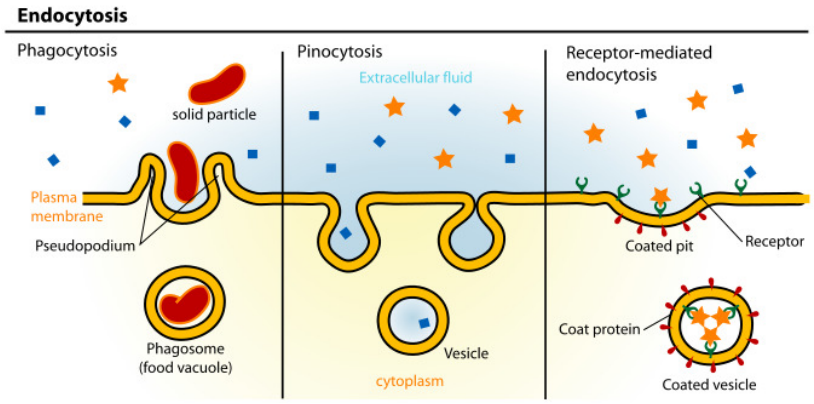

Figure 1.41: Schematic diagram illustrating different types of endocytosis.[109]

Electrostatic attraction is the first process in which the highly positively charged polypeptides are attracted to the negatively charged phosphate groups at the cell phospholipid membrane. Binding then occurs between the peptides and heparan sulphate proteoglyans (HSPGs) located on the cell membrane leading to heparin sulphate mediated endocytosis. Once the vesicle is inside the cell, the heparin sulphate is destroyed by heparanases releasing the peptide into the cell. Macropinocytosis is reported as one of the major pathways of uptake for arginine rich peptides.[107, 110]

It is widely believed that endocytosis is the most likely mechanism of cellular uptake of arginine rich cell penetrating peptides as results have shown the process to be temperature and energy dependent which is indicative of endocytosis.[19, 107, 110, 111] Fuchs *et al.*[110] reported the synthesis of a fluoroscein labelled polypeptide. Using colocalisation studies with vesicular specific markers they observed that the dye-peptide was only present in the endocytic vesicles of live cells. This confirmed that the internalisation of the dye-peptide was by entocytoic means and not by passive diffusion across the cell membrane. Furthermore, their results showed the inability of the dye-peptide to enter cells deficient in herparan sulphate, a molecule which is synonymous

with the endocytic process. In addition, treatment of cells with arginine rich peptides has been shown to promote intracellular signalling including activation of Rac protein that subsequently leads to F-actin organisation and pinocytosis.[111]

Although endocytosis is recognised by most as the main pathway involved in the cellular uptake of arginine rich peptide sequences, it has come under increased scrutiny as some conflicting results have been reported. Internalisation of polypeptides has also been observed at 4 ^{o}C; temperatures at which endocytic pathways do not function. [111] This suggested an energy independent pathway, such as passive diffusion, of cellular uptake exists.

Herce *et al.*[112] illustrate in Figure 1.42 an alternative mechanism called the translocation mechanism of polypeptides across the cell membrane via non-endocytotic pathways. As illustrated in Figure 1.42 (a) the P–N dipole vector is in the plane of the membrane. As the peptide approaches the surface of the membrane it attracts the phosphate groups and the dipole bends towards the interior of the membrane (Figure 1.42 (b)). Since this is not the best conformation for the system, the peptide inserts into the interface between the hydrophilic head groups and the carbon chains. This allows the peptide to orient away from the choline groups (Figure 1.42 (c)). As the density of peptides increases, the membrane gets thinner (Figure 1.42 (d)). An arginine amino acid translocates with a local bending of the membrane on both sides of the bilayer (Figure 1.42 (e)). This bending reduces the energetic barrier of the translocation. A pore forms and the peptide translocates bound to the interior of the bilayer surface (Figure 1.42 (f)).

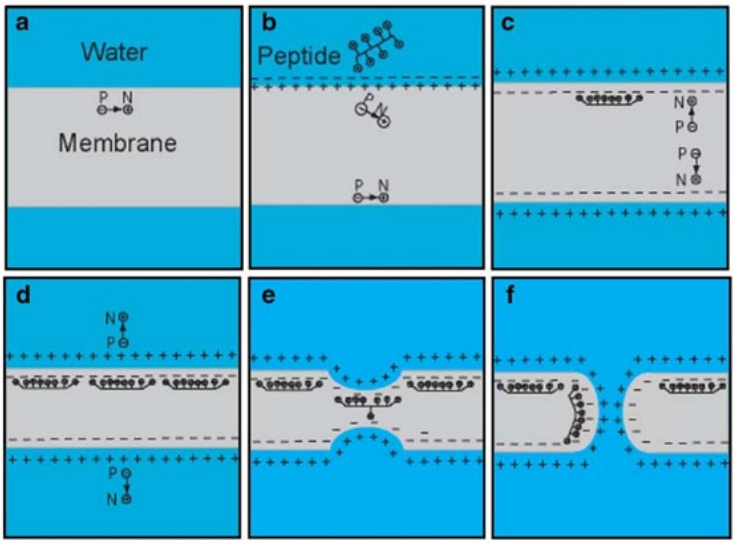

Figure 1.42: Schematic diagram illustrating qualitatively the steps involved in the translocation mechanism. The orientation of the dipole moment vector formed by the phosphate group (negatively charged) and the choline group (positively charged) denoted by P and N, respectively is shown.[112]

Either way, both endocytosis and translocation methods of cellular uptake have theoretical problems that need to be resolved: (i) the lack of cell specificity does not correlate well with the idea that peptides could be targeting any specific cell receptor and (ii) peptides are highly hydrophilic and the idea that they may directly translocate across the hydrophobic core of the membrane would need an excessive amount of energy.[112] However in reality, neither assignment of the mechanism of cellular internalisation of arginine rich polypeptides has been proven conclusively and the mechanism of uptake remains a hotly debated topic. Nonetheless, what has been clearly demonstrated is the efficiency of polyarginine as a transmembrane molecular cargo carrier.

Polypeptides have already been used to deliver a wide variety of molecular cargo to living cells such as quantum dots[113], drugs[46, 114], organic fluorophores[106, 110], proteins[115, 116] and other smaller molecules.[117, 118] Rothbard *et al.*[46] highlighted the potential applications of polyarginine sequences for drug delivery in Figure 1.43. Many drugs that prevent inflammatory skin conditions, such as cycloporin A for example, are ineffective topically because of their poor penetration into the skin. They reported the synthesis of cycloporin A coupled to a hepta-arginine peptide via a linker designed to release the active drug at physiological pH within tissue cells. Results showed that the conjugate was a great deal more soluble than the drug alone and that distribution of the drug was achieved throughout the epidermis and dermis skin layers.

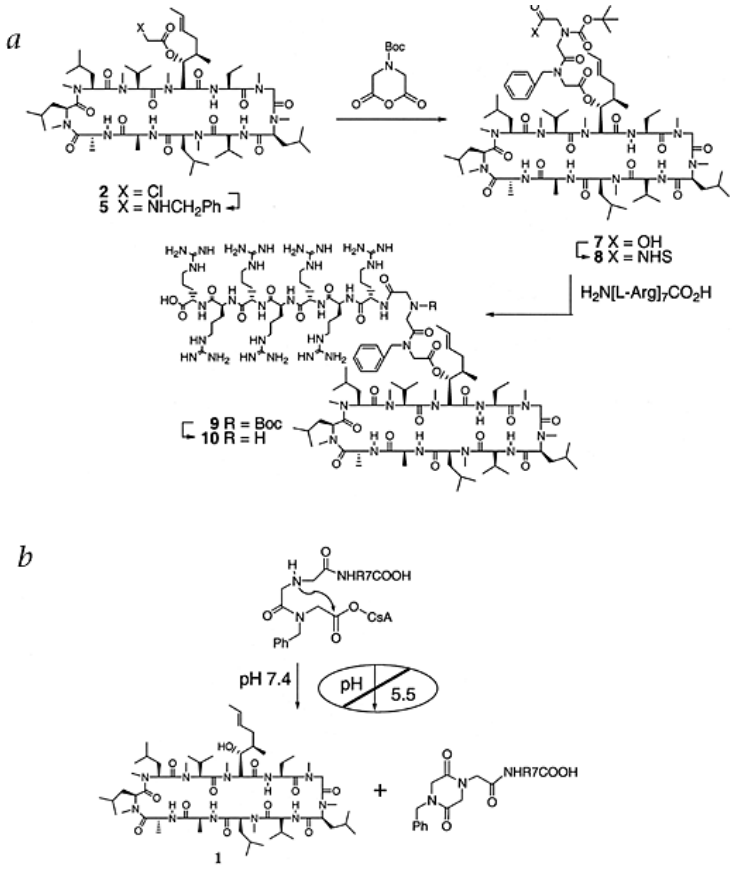

Figure 1.43: (a) Synthetic scheme for the chemical conjugation of cycloporin A and hepta-arginine peptide via a pH sensitive linker. (b) Schematic diagram illustrating the mechanism of release of the drug upon contact with tissue at physiological pH.[46]

The delivery of functional proteins within a cell also provides a powerful tool for therapeutics and the fundamental study of cell biology. Ghosh *et al.*[116] reported the synthesis of peptide coated gold nanoparticles to promote intracellular delivery of the membrane-impermeable β-galactosidase protein in aqueous media as illustrated in Figure 1.44. β-galactosidase is a hydrolase enzyme that catalyses the hydrolysis of β-galactosides into monosaccharides; a source of energy for an organism. Their initial efforts focused on the functionalisation of the nanoparticles with a short peptide sequences containing three arginine residues. This strategy, however, yielded particles that were not well dispersible in water. In an earlier study they demonstrated that lysine-coated particles were water-soluble and stable.[119] As a result, they used a sequence containing arginine and lysine residues with the addition of a histidine (His) residue, as His groups are known to facilitate endosomal escape of cargo.[120]

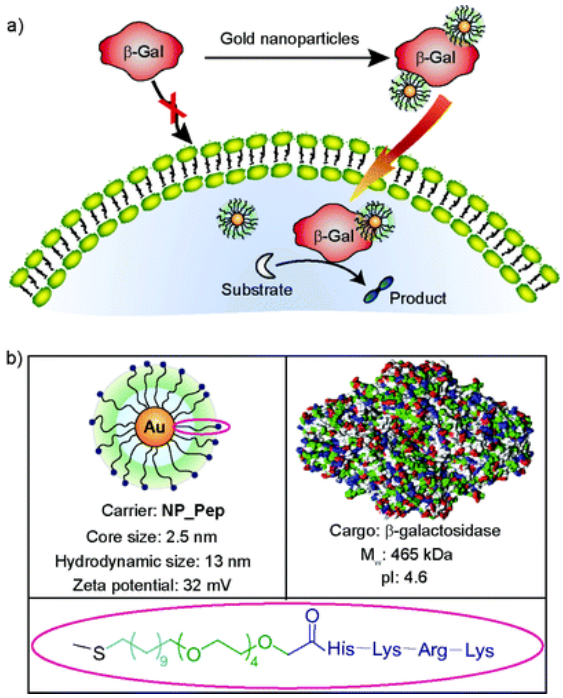

Figure 1.44: (a) Schematic representation illustrating the intracellular delivery of a functional protein using peptide/PEG coated gold nanoparticles. (b) Chemical structure of the nanoconjugate.[116]

Crucially, it was found that the transported enzyme was able to escape from the endosomes and retained its biological activity once inside the cell. The cellular delivery of the cargo was initially monitored using a fluorescent fluorescein marker. This once again demonstrated the potential applications of gold nanoparticles, PEG linkers and polypeptides, as separate entities or in conjunction with one another, as highly suitable molecules to deliver materials to intracellular environments.

1.5.2 Transition Metal Conjugated Polypeptides

Neugebauer *et al.*[19] were the first to report the synthesis of two novel ruthenium polypeptide conjugates for the purpose of cellular imaging, as illustrated in Figure 1.45.

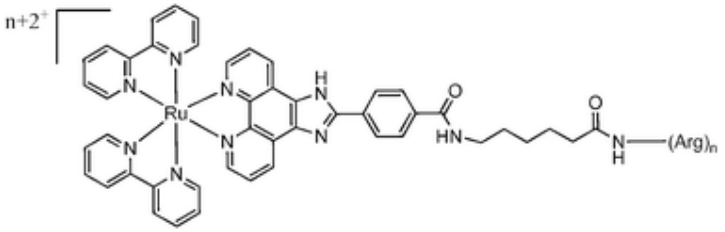

Figure 1.45: Structure of the first ruthenium (II) conjugated polypeptides suitable for cellular imaging. (where n = 5 or 8)[19]

Results highlighted the ability of the octarginine dye-conjugate $[Ru(bpy)_2(picCOOH)Arg_8]^{10+}$ to passively transport across the cell membrane of SP2 myeloma cells without the need to use organic solvents. In contrast, the parent dye and shorter pentarginine conjugate showed no evidence of distribution across the cell membrane. This suggested that the length of cell penetrating peptide is all important in determining its transmembrane capabilities. Diffusion of the parent ruthenium complex could be accomplished using the detergent Triton, DMSO or ethanol to permeabilise the cell. The migration of the octarginine dye-peptide in absence of permeabilisation proved fast and was complete after 10-15 minutes at room temperature, in a temperature dependent and an irreversible process. SP2 myeloma cells in a buffered solution were

exposed to 3.5 x 10^{-5} M of $[Ru(bpy)_2(picCOOH)Arg_8]^{10+}$ which led to bright luminescence within the cells cytoplasm after only 2 minutes as shown in Figure 1.46. Over the next 10 minutes the dye-peptide continued to distribute throughout the cell in various concentrations across the cellular plasma in a non-selective manner.

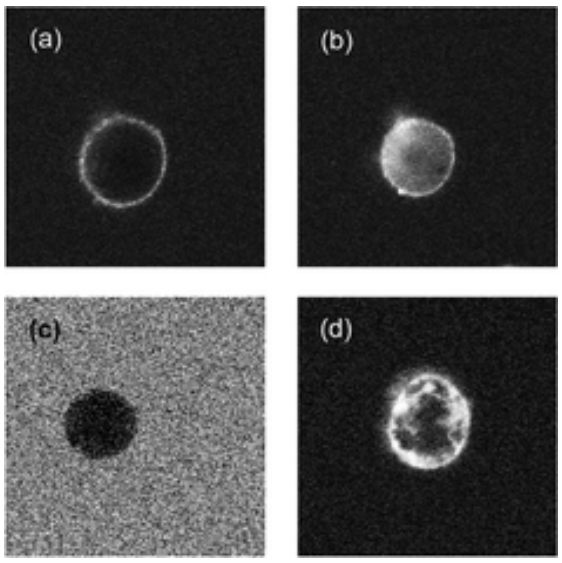

Figure 1.46: Luminescence images (λ_{ex} = 458 nm, λ_{em} = 610 nm) of SP2 myeloma cell incubated with $[Ru(bpy)_2(picCOOH)Arg_8]^{10+}$ (3.5×10^{-5} M in PBS) after (a) 3 min and (b) after 5 min. (c) Myeloma cell incubated with the parent complex $[Ru(bpy)_2(picCOOH)]^{2+}$ (3.5×10^{-5} M in PBS) for 26 min and (d) for 5 min after permeablizing the cell with Triton (1% v/v).[19]

In an effort to assess the distribution of the dye-peptide across SP2 myeloma cell organelles, Neugebauer *et al.*[19] counterstained the cells with a cell permeable localising dyes. 3,3'-Dihexyloxacarbocyanide iodide [DiOC6(3)] was chosen to selectively stain the mitochondria and at higher concentrations the membrane structures within the cell including lysozomes and endoplasmic reticulum. Analysis of both $[Ru(bpy)_2(picCOOH)Arg_8]^{10+}$ and [DiOC6(3)] in SP2 cells using confocal fluorescence microscopy showed that their luminescence did not coincide and therefore it may be concluded that the ruthenium dye-peptide does not distribute strongly within the mitochondria or endoplasmic reticulum of SP2 cells.

SP2 cells were also counterstained with Sytox green as this dye will provide information on the viability of the cells. Sytox green will only penetrate the cells with a disrupted cell membrane and additionally Sytox green will localise in the nucleus of the cells once they have been artificially permeablised. Their results suggested that the Sytox green does not enter the SP2 cells stained with $[Ru(bpy)_2(picCOOH)Arg_8]^{10+}$, indicating that the cells under investigation remain viable over the course of the experiment. These results highlighted the ability of $[Ru(bpy)_2(picCOOH)Arg_8]^{10+}$ to passively transport across the cell membrane of SP2 myeloma cells and distribute throughout the cell's cytoplasm and cell membrane without causing significant SP2 cell apoptosis. Such co-localisation studies were not performed using a CHO cell line.

In one of the first examples of its kind, FLIM measurements were used to determine the average lifetime of the dye across the various cell components. Results in Figure 1.47 indicated that the dye residing towards the outer membrane displays the shortest lifetimes. This is in good agreement with the higher solubility of molecular oxygen in the cell membrane, causing a decrease in the lifetime of the ruthenium probe. This demonstrated for the first time the potential value of these dye-conjugates for cellular oxygen sensing.

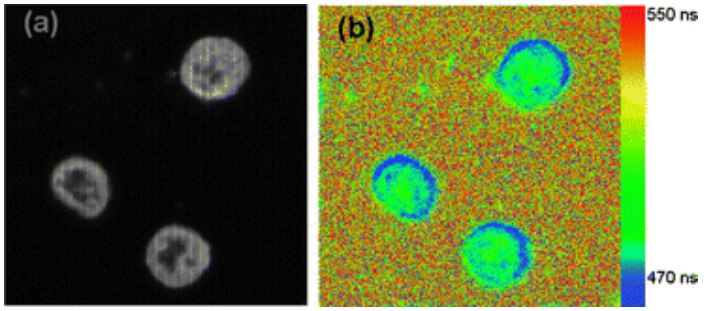

Figure 1.47: (a) Fluorescence intensity image and (b) false colour FLIM image of $[Ru(bpy)_2(picCOOH)Arg_8]^{10+}$ *(3.5 x* 10^{-5} *M in aqueous PBS buffer) in SP2 myeloma cells after 15 minutes incubation.*[19]

In a more recent paper[29] a $[Ru(dppz)_2(picCOOH)Arg_8]^{10+}$ complex (Figure 1.48) is exploited for the purposes of multimodal cellular imaging. As this dye exhibits a 'molecular switching effect' only the dye molecules protected by and associated with membrane structures emits phosphorescence and therefore, can not be used to assess the true distribution of the dye in the cell. However, resonance Raman mapping does not rely on the emission of the dye and is employed here for the first time as a complementary technique to assess the localisation of the parent dye and dye-conjugate.

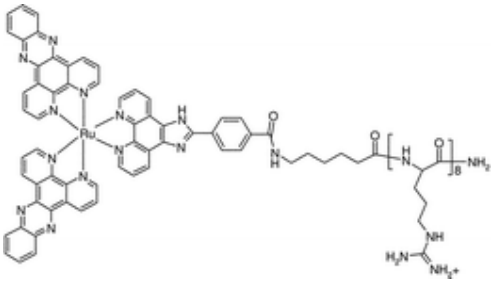

Figure 1.48: Chemical structure of $[Ru(dppz)_2(picCOOH)Arg_8]^{10+}$.[29]

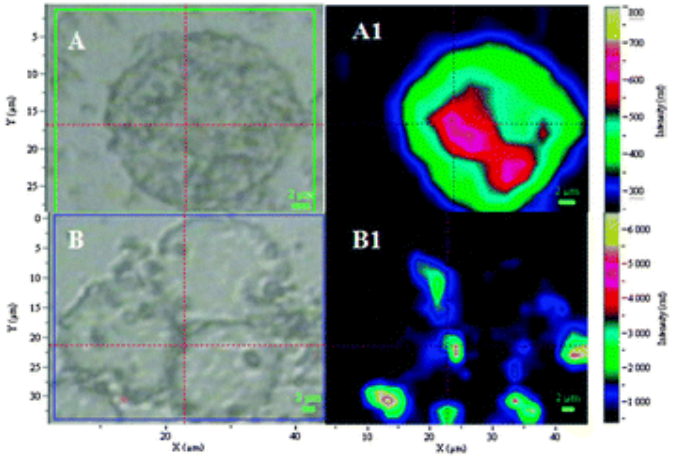

Figure 1.49: Resonance Raman intensity map of live myeloma cells after incubation with $[Ru(dppz)_2(picCOOH)Arg_8]^{10+}$ (A1) and free parent dye (B1) after excitation at 458 nm. A and B represents the brightfield images of the cells in PBS.[29]

Figure 1.49 illustrates the plot intensity of these ruthenium (II) vibrational modes and therefore the dye concentration within the cell. It can be clearly seen that the parent dye remains in the outer cell membrane (Figure 1.49, image B1), whereas, the dye peptide diffuses across the cell membrane (Figure 1.49, image A1) and is distributed throughout the entire cell.

Continuing with this idea of multimodal, mulitparameter cell imaging using polypyridyl peptide conjugates, Neugebauer *et al.*[33] used $[Ru(bpy)_2(picCOOH)Arg_8]^{10+}$ as a suitable probe for multimodal cell analysis. The conjugated ruthenium (II) dye-peptide failed to yield any significant difference the visible region of the absorption spectrum with a corresponding change in pH. This was in contrast with its Raman spectrum that is shown in Figure 1.50 below.

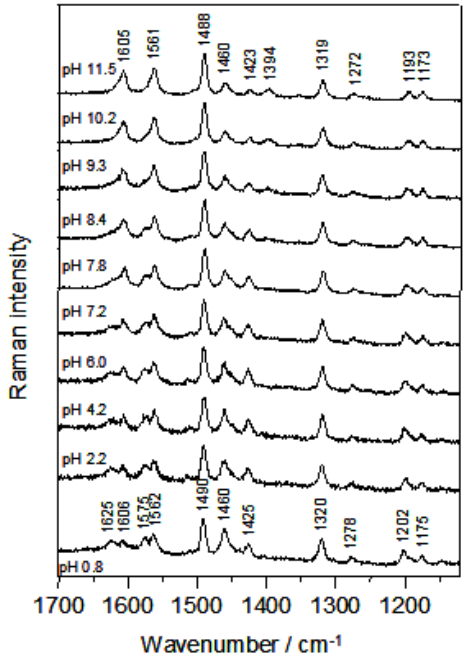

Figure 1.50: Resonance Raman spectra of $[Ru(bpy)_2(picCOOH)Arg_8]^{10+}$ at various pH values following irradiation at 458 nm.[33]

Here the ratio of the height/area of the pH dependent [picCOOH] ligand modes (at 1608 and 1550 cm^{-1}) to the height/area of the pH independent bipyridyl ligand modes (at 1488 and 1318 cm^{-1}) may be used to construct a pH plot, where any changes in concentrations may be corrected for. Resonance Raman signals were collected and

mapped from SP2 myeloma cells containing $[Ru(bpy)_2(picCOOH)Arg_8]^{10+}$ in PBS buffer. Using the pH dependent Raman calibration curve, it was found that the cellular membrane had a pH of 6.7, nucleus pH 6.8 and cytoplasm pH 7.2. These values were in good agreement with values previously published.

Intracellular pH is an important parameter in the natural synthesis of macromolecules within the cell such as DNA, RNA, protein production and in regulation of the cell cycle itself.[121] Abnormal pH levels within the cell may be an indication of disease, as often tumour cells are found to contain higher acidity levels in the cytoplasm.[31, 32]

While $[Ru(bpy)_2(picCOOH)Arg_8]^{10+}$ is highly sensitive to changes in pH, as seen previously it is also sensitive to changes in oxygen concentration. As a result, one may take advantage of the same ruthenium dye-conjugate probe to measure both parameters in a single environment. In a more detailed study, the luminescent lifetime of the ruthenium dye was used to calculate the oxygen concentration within the cell, as the lifetime is not effected by local concentrations of the dye. Fluorescence lifetime imaging microscopy (FLIM) measurements were used to determine the lifetimes of the ruthenium luminophore within the cell as shown in Figure 1.51.

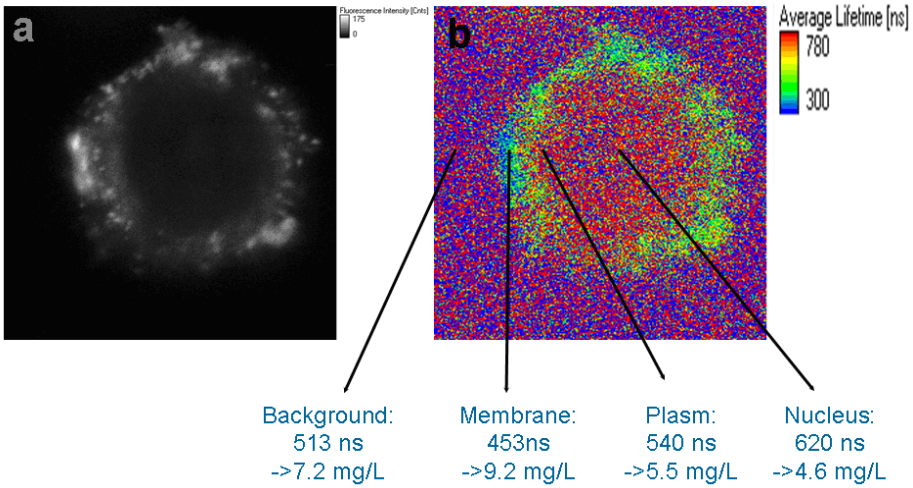

Figure 1.51: (a) Fluorescence intensity map of SP2 myeloma cell incubated for 12 minutes with $[Ru(bpy)_2(picCOOH)Arg_8]^{10+}$ in PBS for 12 minutes and (b) false colour lifetime image of the same cell.[33]

Three regions within the cell were identified by comparison with Raman spectroscopy and confocal microscopy images. The lifetimes for the background medium, cell membrane, cytoplasm and nucleus are shown in Figure 1.48 above. These lifetimes correspond to oxygen concentrations of 7.2 +/- 1.2 mg O_2/L in the background solution, 9.2 +/- 1.7 mg O_2/L in the cell membrane, 5.5 +/- 1.0 mg O_2/L in the cytoplasm and 4.6 +/- 0.8 mg O_2/L in the nucleus. These results confirm that there is a higher concentration of molecular oxygen located in the membrane of a cell, causing a decrease in the lifetime of the phosphorescent dye.

Barton *et al.*[90] are another group who have realised the potential of using a cell penetrating peptide to facilitate entry of a ruthenium dye peptide into HeLa cells. Results showed that the parent complex $[Ru(phen)(bpy)(dppz)]^{2+}$ showed no transport across a cellular membrane prior to conjugation to the octarginine peptide. Interestingly, the uptake of a dye peptide containing ruthenium-Arg_8-fluorescein is far greater at lower concentrations when compared to the ruthenium-Arg_8 conjugate alone (Figure 1.52). It is thought that due to the fluorescein moiety having a greater lipophilicity versus the ruthenium and this serves to increase the interaction of the dye conjugate with the cellular membrane.

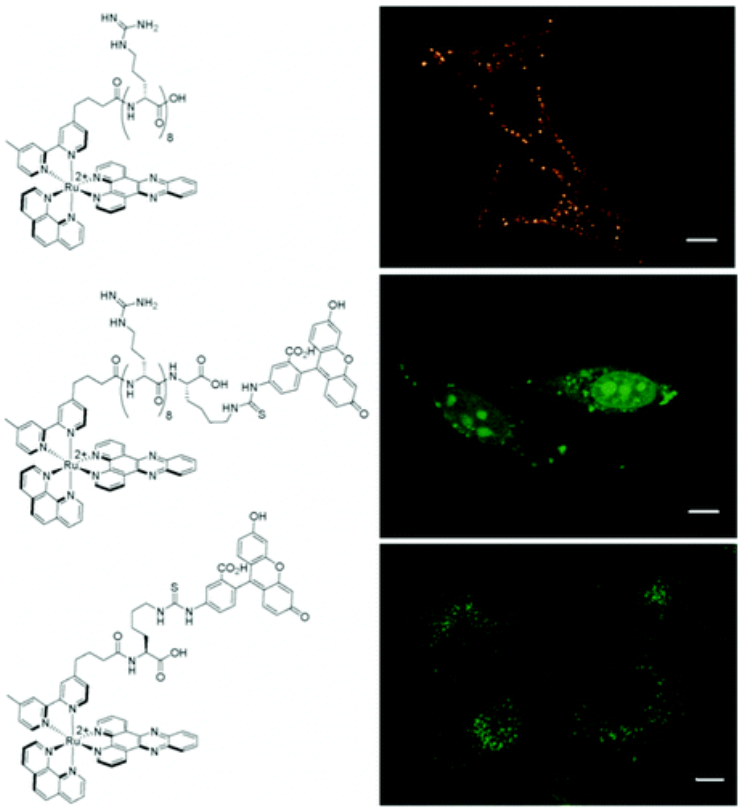

Figure 1.52: Chemical structures and corresponding cellular distribution of complexes synthesised by Barton et al. in various concentrations in HeLa cells incubated at 37°C in complete medium (σ-MEM with 10% FBS) then rinsed with HBSS solution and imaged without cell fixation.[90]

Recently Rijt *et al.*[122] reported the promising cancer cell cytotoxicity of an osmium (II) polyarginine peptide. It has been shown to induce non-repairable damage to DNA by causing a large degree of DNA unwinding. They also examined the effect of varying the polyarginine lengths (from Arg_1 to Arg_8) on the cellular uptake, toxicity and cell distribution of the dye-peptide in CHO cell lines. As previously discussed their results also highlighted a strong correlation between increased arginine length and cellular uptake, nuclear uptake, DNA binding and decreased cytotoxicity. The cellular uptake and increased activity of the osmium functionalised polypeptides showed preference in the order of Arg_8>> Arg_5> Arg_1~unfunctionalised. In addition, polyarginine peptides have been conjugated to other metal complexes including rhodium[91], gadolinium[92], europium[92], nickel[111], rhodamine[111], and terbium[123] for the purposes of cell imaging.

1.6 Conclusion

Over the past number of year's research into the potential applications of photoactive supramolecular assemblies, incorporating inorganic and organic chromophores, has exploded across a wide range of areas from medicine to energy conversion to nanoscience. However, given their large stokes shifts, long lifetimes, intense luminescence, good photostability and PDT properties inorganic probes are seen to be the way forward in terms of challenging and improving on existing technologies. In addition, the ability to fine tuning their absorbance and emission characteristics for specific purposes only adds credence to their use as potential multimodal molecular probes.

As part of this research two main series of luminescent metal complexes, that of ruthenium (II) and iridium (III), are studied to determine their suitablility as potential cellular probes. A series of water soluble ruthenium (II) polypyridyl and novel water insoluble iridium (III) complexes were synthesised and their spectroscopic, photophysical, and electrochemical properties fully characterised and compared. Iridium has been one of the most explored metal complexes in recent years but tends to be poorly water soluble and non cell permeable. This thesis addresses this issue by its conjugation to a CPP for applications in cellular imaging. Most of the assemlies outlined in this thesis are based on the supramolecular dyad system of A-L-B, where the characteristics or applications of the assembly outweigh that of the individual sole photoactive component.

To date there has been very limited research into the potential use of gold nanoparticles as suitable transmembrane transporter of molecular cargo, in particular luminescent markers. In addition, the coupling of a luminophore to a metal nanoparticle is shown to enhance its emission intensity when the distance from the nanoparticle is appropriate. Chapter 3 describes the functionalisation of gold nanoparticles with a ruthenium (II) polypyridyl complex through polyethylene glycol linkers of varied length. Not only did conjugation to the gold nanoparticles provide enhanced luminescence and lifetimes but they also facilitated the transport of an otherwise non-permeable ruthenium dye across the cell membrane of SP2 myeloma cells.

Successful conjugation of metal luminophores to polypeptides has been achieved previously, however, the synthesis of an iridium (III) polypeptide is yet to be reported. It was hoped that the use on an iridium label would exhibit enhanced quantum yields and lifetimes of the molecular probe when compared to existing transition conjugated metal polypeptides. In Chapter 5, conjugation of the ruthenium (II) and iridium (III) dyes to biomolecules builds upon previously reported work by our group and enables the analysis of biological samples through non-targeted localisation within a cell, but most importantly without destroying the cell membrane in the process. It remains to be seen how further conjugation of the dye-peptides to target specific peptides could help with concentration of the luminophore within certain tumour cells. The generation of reactive oxygen species following absorption of light energy by the transition metal luminophores may also induce cell apoptosis and could potentially make these a powerful diagnostic and photo therapeutic tool.

Numerous reports highlight attempts in creating light harvesting supramolecular assemblies capable of mimicking processes involved in plant photosynthesis. Chapter 6 discusses attempts to synthesise a light harvesting device for the efficient conversion of solar energy to electrical energy. The attachment of an organic fluorophore to a supramolecular structure, namely DNA, as the backbone is attempted for the first time. This is in keeping with the general topic of research; in building photoactive supramolecular assemblies and identifying suitable luminescent probes for conjugation to biomolecules for applications in areas from diagnostics to solar energy conversion.

One of the main aims of this thesis is to identify suitable luminophores and to demonstrate how their conjugation to cell membrane transporters enables their applications in cellular imaging. Furthermore, the inherent properties of the dyes may then be exploited for multimodal cellular imaging to determine characteristics such as pH and oxygen levels within cellular structures. This thesis provides an insight into the construction of supramolecular assemblies from its individual subunit synthesis to their combined functional applications. It also gives an idea of the work currently being undertaken across a range of disciplines and will add to the understanding of the basic principles on which these luminophores may be exploited for their potential uses in photoactive supramolecular assemblies, diagnostics and other related photochemical processes.

1.7 References

(1) Jablonski Diagram. http://www.photobiology.info/Photochem.html. (Accessed: 08/06/2011)

(2) Nicholas J. Turro, V. Ramamurthy, J. C. Scaiano. *Principles of Molecular Photochemistry - An Introduction;* University Science Books: **2009**.

(3) Campagna, S.; Puntoriero, F.; Nastasi, F.; Bergamini, G.; Balzani, V. *Photochemistry and Photophysics of Coordination Compounds: Ruthenium,* Springer Berlin / Heidelberg: **2007**, *280*, 117-214.

(4) A. Juris, V. Balzani, F. Bargelletti, S. Campagna, P. Belser, A. Von Zelewsky. *Coord. Chem. Rev.* **1988**, 85-277.

(5) Steed, A. *Supramolecular Chemistry;* Wiley: **2000**.

(6) Barigelletti, F.; Juris, A.; Balzani, V.; Belser, P.; Von Zelewsky, A. *Inorg. Chem.* **1987***, 26*, 4115-4119.

(7) McCusker, J. K. *Acc. Chem. Res.* **2003***, 36*, 876-887.

(8) Damrauer, N. H.; Cerullo, G.; Yeh, A.; Boussie, T. R.; Shank, C. V.; McCusker, J. K. *Science* **1997***, 275*, 54-57.

(9) Bhasikuttan, A. C.; Suzuki, M.; Nakashima, S.; Okada, T. *J. Am. Chem. Soc.* **2002***, 124*, 8398-8405.

(10) Ragni, R.; Plummer, E. A.; Brunner, K.; Hofstraat, J. W.; Babudri, F.; Farinola, G. M.; Naso, F.; De Cola, L. *J. Mater. Chem.* **2006***, 16*, 1161-1170.

(11) Flamigni, L.; Collin, J.; Sauvage, J. *Acc. Chem. Res.* **2008***, 41*, 857-871.

(12) Durham, B.; Caspar, J. V.; Nagle, J. K.; Meyer, T. J. *J. Am. Chem. Soc.* **1982***, 104,* 4803-4810.

(13) You, Y.; Seo, J.; Kim, S. H.; Kim, K. S.; Ahn, T. K.; Kim, D.; Park, S. Y. *Inorg. Chem.* **2008***, 47*, 1476-1487.

(14) Hartl, F.; Snoeck, T. L.; Stufkens, D. J.; Lever, A. B. P. *Inorg. Chem.* **1995***, 34*, 3887-3894.

(15) Mallick, T. K.; Das, P. K.; Sinha, S.; Ghosh, B. K. *Polyhedron* **1994***, 13*, 1817-1823.

(16) Hirohara, S.; Obata, M.; Alitomo, H.; Sharyo, K.; Ando, T.; Yano, S.; Tanihara, M. *Bioconjug. Chem.* **2009***,* 20, 944-952.

(17) Pauli, J.; Grabolle, M.; Brehm, R.; Spieles, M.; Hamann, F. M.; Wenzel, M.; Hilger, I.; Resch-Genger, U. *Bioconjug. Chem.* **2011***, 22*, 1298-1308.

(18) Welsher, K.; Sherlock, S. P.; Dai, H. *Proc. Natl. Acad. Sci. U. S. A.* **2011***, 108*, 8943-8948.

(19) Neugebauer, U.; Pellegrin, Y.; Devocelle, M.; Forster, R. J.; Signac, W.; Moran, N.; Keyes, T. E. *Chem. Commun.* **2008**, 5307-5309.

(20) Lamansky, S.; Djurovich, P.; Murphy, D.; Abdel-Razzaq, F.; Kwong, R.; Tsyba, I.; Bortz, M.; Mui, B.; Bau, R.; *Inorg. Chem.* **2001***, 40*, 1704-1711.

(21) Licini, M.; Gareth Williams, J.,A. *Chem. Commun.* **1999**, 1943-1944.

(22) Zhao, Q.; Liu, S.; Shi, M.; Li, F.; Jing, H.; Yi, T.; Huang, C. *Organometallics* **2007***, 26*, 5922-5930.

(23) Zhao, Q.; Yu, M.; Shi, L.; Liu, S.; Li, C.; Shi, M.; Zhou, Z.; Huang, C.; Li, F. *Organometallics* **2010***, 29*, 1085-1091.

(24) Shi, S.; Liu, J.; Li, J.; Zheng, K. C.; Tan, C. P.; Chen, L. M.; Ji, L. N. *Dalton Trans.* **2005**, 2038-2046.

(25) Bai, G.; Dong, B.; Lü, Y.; Wang, K.; Jin, L.; Gao, L. *J. Inorg. Biochem.* **2004***, 98*, 2011-2015.

(26) Metcalfe, C.; Thomas, J. A. *Chem. Soc. Rev.* **2003***, 32*, 215-224.

(27) Pellegrin, Y.; Forster, R. J.; Keyes, T. E. *Inorg. Chim. Acta* **2009***, 362*, 1715-1722.

(28) Pellegrin, Y.; Forster, R. J.; Keyes, T. E. *Inorg. Chim. Acta* **2008***, 361*, 2683-2691.

(29) Cosgrave, L.; Devocelle, M.; Forster, R. J.; Keyes, T. E. *Chem. Commun.* **2010**, *46*, 103-105.

(30) Zhang, S.; Hosaka, M.; Yoshihara, T.; Negishi, K.; Iida, Y.; Tobita, S.; Takeuchi, T. *Cancer Res.* **2010***, 70*, 4490-4498.

(31) Schindler, M.; Grabski, S.; Hoff, E.; Simon, S. M. *Biochemistry (N. Y.)* **1996***, 35*, 2811-2817.

(32) Švastová, E.; Hulíková, A.; Rafajová, M.; Zat'ovičová, M.; Gibadulinová, A.; Casini, A.; Cecchi, A.; Scozzafava, A.; Supuran, C. T.; Pastorek, J.; Pastoreková, S. *FEBS Lett.* **2004***, 577*, 439-445.

(33) Neugebauer, U.; Cosgrave, L.; Pellegrin, Y.; Devocelle, M.; Forster, R.; Keyes, T.,E. *unpublished results* .

(34) Chen, H.; Li, J.; Lin, H.; Cai, Z.; Lin, H. *Supramolecular Chemistry* **2009***, 21*, 401.

(35) Lin, Z.; Ou, S.; Duan, C.; Zhang, B.; Bai, Z. *Chem. Commun.* **2006**, 624-626.

(36) Liu, Y.; Zeng, C.; Huang, H.; He, L.; Wu, F. *Eur. J. Med. Chem.* **2010***, 45*, 564-571.

(37) Huang, H.; Liu, Y.; Zeng, C.; Yao, J.; Liang, Z.; Li, Z.; Wu, F. *J. Mol. Struct.* **2010**, *966*, 136-143.

(38) Micic, M., *Supramolecular Chemistry at Interfaces. Colloids and Surfaces B: Biointerfaces* **2007**, *58*, 1-2.

(39) Balzani, V.; Bergamini, G.; Marchioni, F.; Ceroni, P. *Coord. Chem. Rev.* **2006**, *250*, 1254-1266.

(40) Cozzolino, A. F.; Vargas-Baca, I. *Journal of Organometallic Chemistry* **2007**, *692*, 2654-2657.

(41) Robert J. Forster, Tia E. Keyes, Johannes G. Vos *Interfacial Supermolecular Assemblies;* Wiley: 2003.

(42) Gust, D.; Moore, T. A.; Moore, A. L. *Acc. Chem. Res.* **2001**, *34*, 40-48.

(43) Konishi, T.; Ikeda, A.; Shinkai, S. *Tetrahedron* **2005**, *61*, 4881-4899.

(44) Sykora, M.; Maxwell, K. A.; DeSimone, J. M.; Meyer, T. J. *Proceedings of the National Academy of Sciences* **2000**, *97*, 7687-7691.

(45) Kowol, C. R.; Trondl, R.; Arion, V. B.; Jakupec, M. A.; Lichtscheidl, I.; Keppler, B. K. *Dalton Trans.* **2010**, *39*, 704-706.

(46) Rothbard, J. B.; Garlington, S.; Lin, Q.; Kirschberg, T.; Kreider, E.; McGrane, P. L.; Wender, P. A.; Khavari, P. A. *Nat. Med.* **2000**, *6*, 1253-1257.

(47) Thomas, K. G.; Kamat, P. V. *Acc. Chem. Res.* **2003**, *36*, 888-898.

(48) Malicka, J.; Gryczynski, I.; Gryczynski, Z.; Lakowicz, J. R. *Anal. Biochem.* **2003**, *315*, 57-66.

(49) Aslan, K.; Wu, M.; Lakowicz, J. R.; Geddes, C. D. *J. Am. Chem. Soc.* **2007**, *129*, 1524-1525.

(50) Reger, D. L.; Gardinier, J. R.; Smith, M. D.; Pellechia, P. J. *Inorg. Chem.* **2003**, *42*, 482-491.

(51) Deshpande, M. S.; Kumbhar, A. A.; Kumbhar, A. S.; Kumbhakar, M.; Pal, H.; Sonawane, U. B.; Joshi, R. R. *Bioconjug. Chem.* **2009**, *20*, 447-459.

(52) Deshpande, M. S.; Kumbhar, A. S.; Puranik, V. G.; Selvaraj, K. *Crystal Growth & Design* **2006**, *6*, 743-748.

(53) Motiei, L.; Sassi, M.; Kaminker, R.; Evmenenko, G.; Dutta, P.; Iron, M. A.; van, d. B. *Langmuir* **2011**, *27*, 1319-1325.

(54) Swavey, S.; Brewer, K. J. *Inorg. Chem.* **2002**, *41*, 4044-4050.

(55) Schild, V.; van Loyen, D.; Bouas-Laurent, H.; Turro, C.; Warner, M.; Raj Pokhrel, M.; Bossmann, S. H. *The Journal of Physical Chemistry A* **2002**, *106*, 9149-9158.

(56) Kleverlaan, C. J.; Indelli, M. T.; Bignozzi, C. A.; Pavanin, L.; Scandola, F.; Hasselman, G. M.; Meyer, G. J. *J. Am. Chem. Soc.* **2000**, *122*, 2840-2849.

(57) Jia, W.; Han, Y.; Lin, Y.; Weng, L.; Jin, G. *Organometallics* **2009**, *28*, 3459-3464.

(58) Polson, M.; Fracasso, S.; Bertolasi, V.; Ravaglia, M.; Scandola, F. *Inorg. Chem.* **2004**, *43*, 1950-1956.

(59) Robson, K. C. D.; Sporinova, B.; Koivisto, B. D.; Schott, E.; Brown, D. G.; Berlinguette, C. P. *Inorg. Chem.* **2011**, *50*, 6019-6028.

(60) Jullien, L.; Canceill, J.; Valeur, B.; Bardez, E.; Lefavre, J.; Lehn, J.; Marchi-Artzner, V.; Pansu, R. *J. Am. Chem. Soc.* **1996**, *118*, 5432-5442.

(61) Arya, S. K.; Solanki, P. R.; Datta, M.; Malhotra, B. D. *Biosensors and Bioelectronics* **2009**, *24*, 2810-2817.

(62) Rickert, J.; Weiss, T.; Göpel, W. *Sensors Actuators B: Chem.* **1996**, *31*, 45-50.

(63) Argazzi, R.; Bignozzi, C. A.; Heimer, T. A.; Castellano, F. N.; Meyer, G. J. *J. Am. Chem. Soc.* **1995**, *117*, 11815-11816.

(64) Kuhn, S.; Hakanson, U.; Rogobete, L.; Sandoghdar, V. *Phys. Rev. Lett.* **2006**, *97*, 017402.

(65) Stellacci, F.; Bauer, C. A.; Meyer-Friedrichsen, T.; Wenseleers, W.; Marder, S. R.; Perry, J. W. *J. Am. Chem. Soc.* **2003**, *125*, 328-329.

(66) Ipe, B. I.; Thomas, K. G.; Barazzouk, S.; Hotchandani, S.; Kamat, P. V. *The Journal of Physical Chemistry B* **2002**, *106*, 18-21.

(67) Pramod, P.; Sudeep, P. K.; Thomas, K. G.; Kamat, P. V. *The Journal of Physical Chemistry B* **2006**, *110*, 20737-20741.

(68) Zhang, J.; Fu, Y.; Lakowicz, J. R. *The Journal of Physical Chemistry C* **2011**, *115*, 7255-7260.

(69) Glomm, W. R.; Moses, S. J.; Brennaman, M. K.; Papanikolas, J. M.; Franzen, S. *The Journal of Physical Chemistry B* **2005**, *109*, 804-810.

(70) Forster, R. J.; Keyes, T. E. *The Journal of Physical Chemistry B* **1998**, *102*, 10004-10012.

(71) Thomas, K. G.; Kamat, P. V. *J. Am. Chem. Soc.* **2000**, *122*, 2655-2656.

(72) Imahori, H.; Arimura, M.; Hanada, T.; Nishimura, Y.; Yamazaki, I.; Sakata, Y.; Fukuzumi, S. *J. Am. Chem. Soc.* **2001**, *123*, 335-336.

(73) Lo, K. K.; Louie, M.; Zhang, K. Y. *Coord. Chem. Rev.* **2010**, *254*, 2603-2622.

(74) Koo, C.; Wong, K.; Man, C. W.; Tam, H.; Tsao, S.; Cheah, K.; Lam, M. H. *Inorg. Chem.* **2009**, *48*, 7501-7503.

(75) Bieda, R.; Ott, I.; Gust, R.; Sheldrick, W. S. *European Journal of Inorganic Chemistry* **2009***, 2009*, 3821-3831.

(76) Schmitt, F.; Govindaswamy, P.; Sass-Fink, G.; Ang, W. H.; Dyson, P. J.; Juillerat-Jeanneret, L.; Therrien, B. *J. Med. Chem.* **2008***, 51*, 1811-1816.

(77) Svensson, F. R.; Matson, M.; Li, M.; Lincoln, P. *Biophys. Chem.* **2010***, 149*, 102-106.

(78) Matson, M.; Svensson, F. R.; Norden, B.; Lincoln, P. *J Phys Chem B* **2011***, 115*, 1706-1711.

(79) Notman, R.; Noro, M.; O'Malley, B.; Anwar, J. *J. Am. Chem. Soc.* **2006***, 128*, 13982-13983.

(80) Yu, Z.; Quinn, P. J. *Mol. Membr. Biol.* **1998***, 15*, 59-68.

(81) Chen, T.; Liu, Y.; Zheng, W.; Liu, J.; Wong, Y. *Inorg. Chem.* **2010***, 49*, 6366-6368.

(82) Puckett, C. A.; Barton, J. K. *J. Am. Chem. Soc.* **2007***, 129*, 46-47.

(83) Puckett, C. A.; Barton, J. K. *Biochemistry (N. Y.)* **2008***, 47*, 11711-11716.

(84) Tan, C.; Lai, S.; Wu, S.; Hu, S.; Zhou, L.; Chen, Y.; Wang, M.; Zhu, Y.; Lian, W.; Peng, W.; Ji, L.; Xu, A. *J. Med. Chem.* **2010***, 53*, 7613-7624.

(85) Holder, A. A.; Zigler, D. F.; Tarrago-Trani, M.; Storrie, B.; Brewer, K. J. *Inorg. Chem.* **2007***, 46*, 4760-4762.

(86) Yu, M.; Zhao, Q.; Shi, L.; Li, F.; Zhou, Z.; Yang, H.; Yia, T.; Huang, C. *Chemical Communications* **2008**, 2115-2117.

(87) Jiang, W.; Gao, Y.; Sun, Y.; Ding, F.; Xu, Y.; Bian, Z.; Li, F.; Bian, J.; Huang, C. *Inorg. Chem.* **2010***, 49*, 3252-3260.

(88) Zhang, K. Y.; Li, S. P.; Zhu, N.; Or, I. W.; Cheung, M. S.; Lam, Y.; Lo, K. K. *Inorg. Chem.* **2010***, 49*, 2530-2540.

(89) Xiong, L.; Zhao, Q.; Chen, H.; Wu, Y.; Dong, Z.; Zhou, Z.; Li, F. **2010***, 49*, 6402-6408.

(90) Puckett, C. A.; Barton, J. K. *J. Am. Chem. Soc.* **2009***, 131*, 8738-8739.

(91) Brunner, J.; Barton, J. K. *Biochemistry (N. Y.)* **2006***, 45*, 12295-12302.

(92) Allen, M.; Meade, T. *Journal of Biological Inorganic Chemistry* **2003**7746-750.

(93) Lo, K. K.; Lee, T. K.; Lau, J. S.; Poon, W.; Cheng, S. *Inorg. Chem.* **2008***, 47*, 200-208

(94) Rani-Beeram, S.; Meyer, K.; McCrate, A.; Hong, Y.; Nielsen, M.; Swavey, S. *Inorg. Chem.* **2008***, 47*, 11278-11283.

(95) Gianferrara, T.; Bergamo, A.; Bratsos, I.; Milani, B.; Spagnul, C.; Sava, G.; Alessio, E. *J. Med. Chem.* **2010***, 53*, 4678-4690.

(96) Djurovich, P. I.; Murphy, D.; Thompson, M. E.; Hernandez, B.; Gao, R.; Hunt, P. L.; Selke, M. *Dalton Trans.* **2007**, 3763-3770.

(97) Gu, Y.; Cheng, J.; Lin, C.; Lam, Y. W.; Cheng, S. H.; Wong, W. *Toxicol. Appl. Pharmacol.* **2009***, 237*, 196-204.

(98) Bhattacharya, R.; Patra, C. R.; Earl, A.; Wang, S.; Katarya, A.; Lu, L.; Kizhakkedathu, J. N.; Yaszemski, M. J.; Greipp, P. R.; Mukhopadhyay, D.; Mukherjee, P. *Nanomedicine: Nanotechnology, Biology and Medicine* **2007***, 3*, 224-238.

(99) Zhang, G.; Yang, Z.; Lu, W.; Zhang, R.; Huang, Q.; Tian, M.; Li, L.; Liang, D.; Li, C. *Biomaterials* **2009***, 30*, 1928-1936.

(100) Dreaden, E. C.; Mwakwari, S. C.; Sodji, Q. H.; Oyelere, A. K.; El-Sayed, M. *Bioconjug. Chem.* **2009***, 20*, 2247-2253.

(101) Paciotti et al. *drug deliv,* **2004***, 11*, 169.

(102) Levin, C. S.; Bishnoi, S. W.; Grady, N. K.; Halas, N. J. *Anal. Chem.* **2006***, 78*, 3277-3281.

(103) Dong, T.; Shih, H.; Chang, L. *Langmuir* **2004***, 20*, 9340-9347.

(104) Xu, X. N.; Huang, S.; Brownlow, W.; Salaita, K.; Jeffers, R. B. *The Journal of Physical Chemistry B* **2004***, 108*, 15543-15551.

(105) Akiyama, T.; Inoue, K.; Kuwahara, Y.; Niidome, Y.; Terasaki, N.; Nitahara, S.; Yamada, S. *Langmuir* **2005***, 21*, 793-796.

(106) Wender, P. A.; Mitchell, D. J.; Pattabiraman, K.; Pelkey, E. T.; Steinman, L.; Rothbard, J. B. *Proceedings of the National Academy of Sciences,* **2000***, 97*, 13003-13008.

(107) Fuchs, S.; Raines, R. *Cellular and Molecular Life Sciences,* **2006,** *16*, 1819-1822.

(108) Takechi, Y.; Yoshii, H.; Tanaka, M.; Kawakami, T.; Aimoto, S.; Saito, H. *Langmuir* **2011***, 27*, 7099-7107.

(109) Endocytosis Diagram. http://php.med.unsw.edu.au/cellbiology/index.php?title=File:Endocytosis_types.png. (Accessed 14/08/2011)

(110) Fuchs, S. M.; Raines, R. T. *Biochemistry (N. Y.)* **2004***, 43*, 2438-2444.

(111) Futaki, S.; Niwa, M.; Nakase, I.; Tadokoro, A.; Zhang, Y.; Nagaoka, M.; Wakako, N.; Sugiura, Y. *Bioconjug. Chem.* **2004***, 15*, 475-481.

(112) Herce, H.; Garcia, A. *Journal of Biological Physics,* **2007**, *5*, 345-356.

(113) Yukawa, H.; Kagami, Y.; Watanabe, M.; Oishi, K.; Miyamoto, Y.; Okamoto, Y.; Tokeshi, M.; Kaji, N.; Noguchi, H.; Ono, K.; Sawada, M.; Baba, Y.; Hamajima, N.; Hayashi, S. *Biomaterials* **2010***, 31*, 4094-4103.

(114) Wender, P. A.; Rothbard, J. B.; Jessop, T. C.; Kreider, E. L.; Wylie, B. L. *J. Am. Chem. Soc.* **2002***, 124*, 13382-13383.

(115) Fawell, S.; Seery, J.; Daikh, Y.; Moore, C.; Chen, L. L.; Pepinsky, B.; Barsoum, J. *Proceedings of the National Academy of Sciences* **1994***, 91*, 664-668.

(116) Ghosh, P.; Yang, X.; Arvizo, R.; Zhu, Z.; Agasti, S. S.; Mo, Z.; Rotello, V. M. *J. Am. Chem. Soc.* **2010***, 132*, 2642-2645.

(117) Vazquez, O.; Blanco-Canosa, J.; Vazquez, M. E.; Martanez-Costas, J.; Castedo, L.; Mascareas, J. L. *ChemBioChem* **2008***, 9*, 2822-2829.

(118) Cohen, J. L.; Almutairi, A.; Cohen, J. A.; Bernstein, M.; Brody, S. L.; Schuster, D. P.; Frachet, J. M. J. *Bioconjug. Chem.* **2008***, 19*, 876-881.

(119) Ghosh, P. S.; Han, G.; Erdogan, B.; Rosado, O.; Krovi, S. A.; Rotello, V. M. *Chemical Biology & Drug Design* **2007***, 70*, 13-18.

(120) Benns, J. M.; Choi, J.; Mahato, R. I.; Park, J.; Kim, S. W. *Bioconjug. Chem.* **2000***, 11*, 637-645.

(121) Madshus, I. H. *Biochem. J.* **1988**, *15*, 250.

(122) Rijt, S. H. v.; Kostrhunova, H.; Brabec, V.; Sadler, P. J. *Bioconjug. Chem.* **2011***, 22*, 218-226.

(123) Kielar, F.; Congreve, A.; Law, G.; New, E. J.; Parker, D.; Wong, K.; Castreao, P.; de Mendoza, J. *Chem. Commun.* **2008**, 2435-2437.

Chapter 2: Experimental Methods and Instrumentation

"In order to have a good idea…you must have lots of ideas" – Linus Pauling.

2.0 Introduction to Raman spectroscopy

Raman is a vibrational spectroscopic technique which has advantages over others, such as infrared (IR), in that low frequency modes between 10-600 cm^{-1} can be studied. These modes prove to be particularly important for metal ligand complexes and in addition resonance Raman may be used to identify optical transitions in complex molecules. In Raman a laser typically in the visible region is used to irradiate the sample. Once this light interacts with the sample it produces scattered light that may be interpreted to give bond vibrational information. The scattered light may be divided into 3 types: (i) Rayleigh scatter which has the same frequency of the incident beam, this scatter is the most intense and contributes to more than 90% of the scattered light, (ii) Stokes scattering and (iii) anti-Stokes Raman scattering. In Stokes and anti-Stokes scattering, energy is exchanged between the molecule and incident light beam and is much weaker by comparison to Rayleigh scatter. Raman spectroscopy analysis usually involves Stokes scatter as anti-Stokes signals originate from molecules in vibrational energy levels other than the lowest. Anti-Stokes scatter are usually poorly populated at room temperature leading to lower intensities.[1] The various Raman scattering processes are illustrated in Figure 2.1 below.

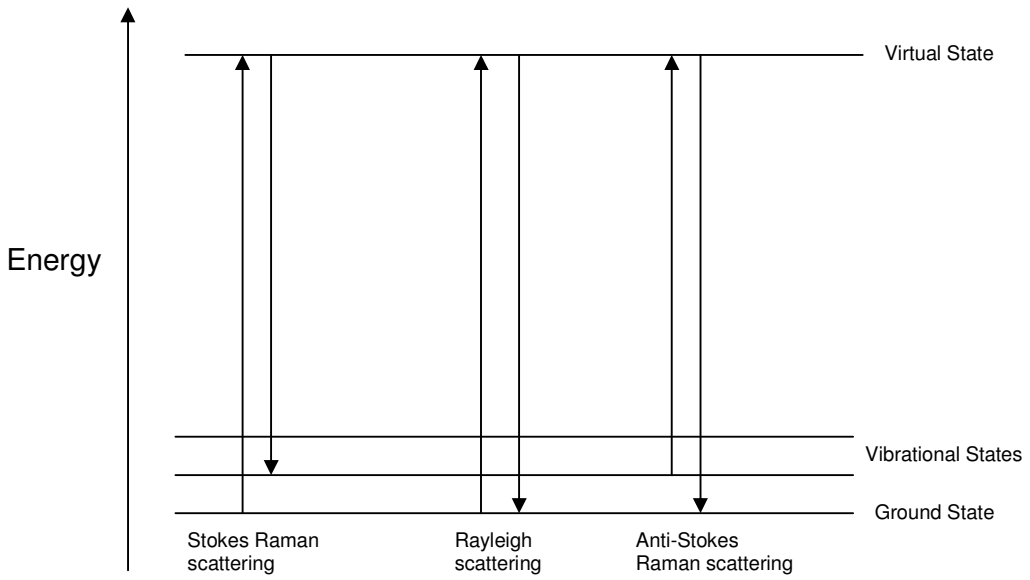

Figure 2.1: Schematic diagram showing the possible Raman and Rayleigh scattering in Raman spectroscopy.

In conventional Raman, light energy from the laser excites the molecule from the ground state into some virtual state. As the molecules relaxes back to the ground state it scatters a photon and in doing so returns to a different vibrational or rotational state. It is the difference in this energy shift from the absorbed and emitted photon that gives rise to Raman scattering. If the photon returns to a higher final vibrational state than the initial state the emitted photon will result in Stokes scattering. On the other hand, if the final state is a lower energetic state this will lead to an anti-Stokes shift. Rayleigh scatter is where the photon returns to the same vibrational energy level and there is no scattering of light following interaction between the incident beam and the sample.

2.0.1 Selection rules

For a mode to be Raman active the polarisability of the molecule must change when placed into the laser's electric field during the vibration. The incident laser may interact with the surrounding electron density of the molecule resulting in the distortion of the molecule giving rise to the Raman light scattering. Raman is a complementary technique to IR spectroscopy where, for a vibration to be IR active the dipole moment must change during the vibration. For very symmetrical molecules bands that are IR inactive are usually Raman active and visa versa. One of the main advantages of Raman over IR is that water is a poor Raman scatterer. This allows for the analysis of biological samples with less interference. The probability of Raman scattering occurring is small under most circumstances, however, two important implications of the Raman effect lead to strong enhancements of the Raman signal: resonance Raman spectroscopy and surface-enhanced Raman spectroscopy.[1]

Resonance Raman (RR) spectroscopy is more commonly exploited in this thesis. RR scattering occurs when the incident laser beam coincides with an optical transition of a compound leading to the population of an electronically excited state. RR shows a large enhancement of up to six orders of magnitude of the Raman signal originating principally from the Franck Condon modes (i.e. those distorted by the optical transition) of the compound in question.[1] Therefore, it may provide additional information on the chromophores being irradiated in an electronic transition. This technique has been used

in the past to assign the MLCT excited states for many complexes.[2] It is known that the absorbance band at around 450 nm for $[Ru(bpy)_2(picCOOH)]^{2+}$ corresponds to the MLCT transition from a ruthenium metal dπ orbital to bipyridyl ligand π* orbital. However, as the absorbance extends to slightly longer wavelengths, the vibrational modes of a MLCT from ruthenium metal centre to [picCOOH] π* orbital become evident. This suggests that a ruthenium dπ to [picCOOH] π* orbital is the lowest energy optical transition. Examples of this are demonstrated and explained in detail in Chapter 3. Hence, resonance Raman spectroscopy may be used to assign the electronic transitions within a molecule.

Fluorescence may prove to be a problem in gathering RR scattering information because when the exciting wavelength excites an emissive state or is close to its absorbance, the fluorescence signal may overcome the vibrational modes making analysis difficult. However, for metal ligand complexes, the Stokes shifts are typically 100 – 200 nm which is particularly amenable to RR.

Surface enhanced Raman spectroscopy (SERS) is a surface sensitive technique used to intensify Raman scattering signal from molecules adsorbed on a rough/irregular metal surface. Enhancement factors in the order of 10^{20} may be achieved and have been used in single molecule detection.[3] It is normally performed on silver or gold substrates with roughened nanoscale surfaces. Similar to metal enhanced fluorescence, surface plasmons of the metal are excited by the incident laser at a certain wavelength. This results in an increased electric field at the metal interface effectively enhancing the electric field of the incident light as Raman intensities are proportional to electric field strength. Chemical enhancement also may occur where a molecule is bonded to a substrate leading to resonant enhancement of charge transfer transitions between metal and analyte. While monolayers show superior surface enhancement there is evidence to suggest that SERS may operate at distances of up to tens of nanometers. Furthermore, for adsorbed species, the selection rules are relaxed and vibrational modes forbidden in the normal Raman spectrum are frequently observed when that species is adsorbed onto a roughened metal surface.[1]

2.1 Instrumentation

2.1.1 Nuclear Magnetic Spectroscopy (NMR) Spectroscopy

^{1}H-NMR was performed on a Brucker AC 400 MHz using deuterated DMSO-d_6 or $CDCl_3$ as solvent unless otherwise specified. Peak positions are relative to TMS (0 ppm chemical shift). All NMR spectra were processed and analysed using Topspin NMR software.

2.1.2 Mass Spectrometry

Mass spectrometry experiments were carried out using a Bruker Esquire LC_00050 electron spray interface (ESI) with a positive ion polarity. Samples were dissolved in one of HPLC grade methanol or acetonitrile or a mixture of both.

2.1.3 Elemental Analysis

Elemental analysis was carried out on an Exador analytical CE440 analyser at the Microanalytical Laboratory in Univeristy College Dublin. Samples were analysed by the technicians in UCD.

2.1.4 Absorption Spectroscopy

UV-Vis spectra were recorded on a Varian Cary 50 spectrophotometer. Samples were analysed in a quartz cuvette with a pathlength of 1 cm with a spectral range of 200-600 nm unless otherwise stated. The background was corrected for blank solvent absorbance prior to every measurement and was performed at room temperature.

2.1.5 Fluorescence Spectroscopy

Emission spectra were recorded on a Varian Cary Eclipse fluorescence spectrophotometer with an excitation slit width of 5 nm and an emission slit width of 5

nm. All experiments were performed using a 1 cm pathlength quartz cuvette. The background was corrected for blank fluorescence before each measurement and was performed at room temperature.

2.1.6 Lifetime Measurements

Luminescent lifetimes were obtained using a Picoquant Fluotime 100 TCSPC (Time Correlated Single Photon Counting) system exciting at 450 nm and using a 510 nm narrow band pass dielectric filter for ruthenium complexes. Excitation at 370 nm and the band pass dielectric filter was set for detection at 460 nm and above for iridium complexes. The instrument response function was determined by using ledox AM30 colloidal silica solution (Adrich) with an excitation source (picosecond pulse diode lasers) of 370 nm for iridium samples and 450 nm for ruthenium samples respectively. 10,000 counts were collected for each lifetime measurement and all measurements were performed in triplicate using Nanoharp software to confirm results. Typical pulse rates of the excitation source were $1x10^5$ s^{-1} with typical pulse widths of 300 ps. Degassed samples were degassed with nitrogen for 20 minutes prior to analysis. It is also noted that solvents were used as received and as a result may contain trace water which may have an impact on the results.

The calculation of the luminescent lifetimes was performed by fitting an exponential decay function to each decay plot to extract the lifetime information using FluoFit software. Due to the inherent long lifetimes of inorganic complexes all data was fitted to mono/bi-exponential decay functions to the baseline of the decay curve using tail-fit with an x^2 value of between 0.9-1.1.

2.1.7 Confocal Fluorescence Microscopy

Confocal fluorescence microscopy is an imaging technique that uses point illumination and a spatial pinhole to eliminate out of focus light in samples that are thicker than the focal plane as illustrated in Figure 2.2. The incident light is focused by the objective lens into a cone shaped beam of light so that the maximum intensity of the beam strikes one spot at a specific depth within the sample. The fluorescence from the sample is then focused by the dichroic mirror onto a pinhole aperture, eliminating

fluorescent light from outside the sample volume, yielding very high sensitivity and a sub-micron spatial resolution.[1]

Luminescence images were recorded using with a Zeiss LSM510 Meta confocal microscope using a 64x oil immersion objective lens (NA 1.4). The 458 nm argon ion laser excitation was used for ruthenium samples and the 375 nm laser line for iridium samples. Optical density filters were reduced to 0.1% transmission in order to reduce any effects of photobleaching. The luminescence from ruthenium was collected using 490/505 nm long pass filters and iridium samples was collected using 420/490 nm long pass filters.

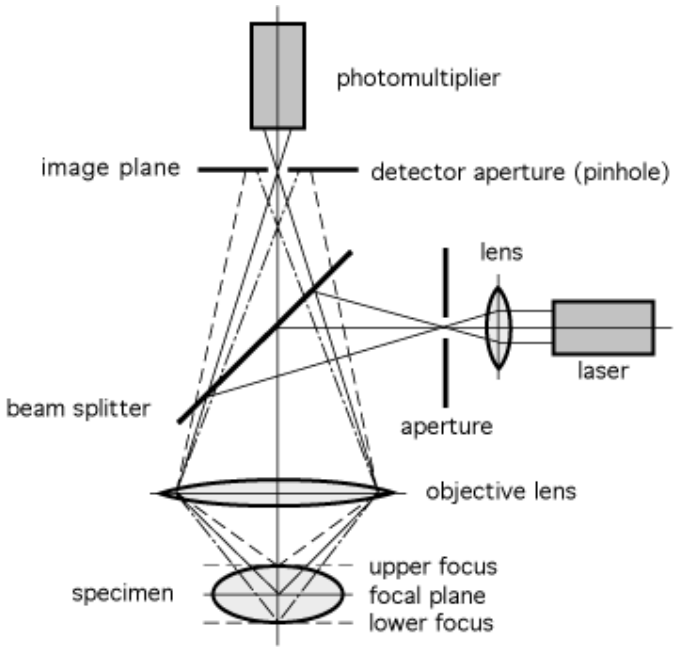

Figure 2.2: Schematic diagram illustrating the components present in a confocal microscope.[1]

2.1.8 Microwave Synthesis

Microwave experiments were performed in a CEM XP-500 Plus microwave equipped with pressure vessels, temperature control and pressure control. Pressure vessels could hold up to 10 mls of samples but no more that 3 mls were ever used in any experiment to reduce the chances of an explosion occurring.

2.1.9 Thin Layer Chromatography

Thin layer chromatography (TLC) was performed on glass silica gel (Merck, 250 μm thickness), alumina (Alumina GF, Aldrich, 250 μm thickness) or C18 (Sorbent Technologies, 250 μm thickness) plates. These were then immersed in a beaker containing mobile phase of interest and analysed under UV light (254 and 365 nm).

2.1.10 Chromatographic Techniques

All silica gel chromatography was performed using an automated flash chromatography system (Analogix-Intelliflash 310) using 50μm silica gel particle size, equipped with a UV detector (200-400 nm) and auto collector. The detection wavelength used was dependent on the maximum absorbance of the compound in between the detector limitations, with a slope sensitivity of 0.1. Alumina chromatography was performed using basic alumina pre-packed chromatographic columns (Al_2O_3, 150 mesh size).

High performance liquid chromatography (HPLC) used was a Varian LC 940 series using a Varian pursuit XRs C18 250 x 4.6 mm column along with photodiode array detector (150-900 nm), auto sampler and auto collector. The detection wavelength used was dependent on where the maximum absorbance of the compound was located. All mobile phases were of HPLC grade quality and were filtered and degassed prior to use. The wavelength of detection was set to that of the maximum absorbance of the sample and usually set up to collect the peaks at a specific retention time rather than a threshold or slope setting.

2.1.11 Electrochemistry – Cyclic Voltammetry

Cyclic voltammetry (CV) is an electrochemical technique that scans a potential region by varying the applied potential at a working electrode and recording the current produced. It may rapidly determine information on redox systems in solution and on an electrode surface. CV's were carried out using a CH Instruments CH-600 electrochemical workstation. A three electrode cell was used, with a glassy carbon

electrode (3 mm diameter Teflon shrouded) as the working electrode, silver wire a reference electrode and platinum wire as auxiliary electrode. Ferrocene was employed as an internal standard and calibrated for all results versus Ag/AgCl as reference. All CV's were performed in duplicate with different glassy carbon electrodes, scanning though the range of potentials: 1, 0.50, 0.25 and 0.05 Vs^{-1} respectively.

Electrochemistry was conducted using 1 mmol of sample dissolved in 5 cm^3 of dry acetonitrile (HPLC grade, used as received) containing 0.1 M tetrabutylammonium tetrafluoroborate (TBA) as supporting electrolyte. No additional care was taken to dry the acetonitrile solution and hence, it is noted that the presence of a protic solvent such as water may complicate the electrochemical results. All samples were degassed with nitrogen for approximately 20 minutes prior to analysis.

2.1.12 Raman Spectroscopy

Micro-Raman measurements were carried out in backscattering configuration using an Olympus confocal microscope attached to a HORIBA Jobin-Yvon Labram HR 1000 spectrometer coupled to Digital Instruments Bioscope II with an inverted microscope. Raman scattering was detected using a Peltier cooled (−70 ◦C) charge-coupled device (CCD) camera (255×1024 pixels), excited with vertically polarised excitation lines from Ar^+ laser (458/488/514 nm) or 785 nm diode laser sources. The spectrometer was equipped with diffraction gratings of 600 grooves / mm and the slit allowed the spectral resolution of 2 cm^{-1}. An appropriate edge filter was set in the spectrometer depending on the excitation source.

The area of the laser spot on the samples was 1 μm in diameter. The laser power at the sample set from 1 to 2 mW using the inbuilt laser power control. Data acquisition times used in the Raman experiments ranged from 1 to 20 s. The Raman band of a silicon wafer at 520 cm^{-1} was used to calibrate the spectrometer and the accuracy of the spectral measurement was estimated to be approximately 2 cm^{-1}. The spectral data were acquired and analysed using LabSpec software.

2.1.13 Fourier Transform Infrared Spectroscopy (FTIR)

The FTIR spectrum of the iridium (III) complexes was recorded using a Varian 610-IR microscope equipped with a nitrogen-cooled mercury cadmium telluride (MCT) and deuterated triglycine sulphate (DTG) detectors. A spatula tip full of sample was dispersed in a KBr matrix and were recorded with a 2 cm^{-1} spectral resolution with KBr used as a beam splitter. Raw spectra were manipulated by built in functions in Varian Resolution pro software, which performs corrections in atmospheric water vapour and CO_2 absorption bands, baseline and smoothing.

2.1.14 Zeta Potential Analyser

The zeta potential of the colloidal systems were analysed using a Beckmann Coulter Delsa Nano C Particle Analyser. The zeta potential is a measure of the potential difference between the colloid material and the layer of fluid surrounding the colloid, also known as the electrical double layer. The zeta potential gives an indication as to the stability and the degree of repulsion between adjacent colloids in the dispersion media. A large zeta potential value (+/- >40 mV) suggests good colloid stability and repulsion between other colloids. Whereas a smaller zeta potential value (+/- <40 mV) indicates less stable systems that will tend to coagulate and drop out of solution.[4]

2.1.15 pH Titrations

pH titrations were performed in the pH range of 0.5-12 with a VWR Symphony SP70P pH meter. The instrument was calibrated using a 3 point calibration plot using solutions of pH 3, 7 and 9. The pH titration experiments were performed by the stepwise additions of µl aliquots of concentrated perchloric acid or sodium hydroxide solutions into a 15 ml PBS buffered solution containing 20 µM of the complex under investigation. All PBS buffer solutions throughout the thesis were made using P-5368 PBS pH 7.4 in individual foil pouches purchased from Sigma unless otherwise stated. The dry powder was dissolved in 1 litre of deionised water which yielded a solution containing 0.01 M PBS, 0.138 M NaCl and 0.0027 M KCl at pH 7.4.

All pH induced spectral changes were analysed for reversibility by checking if their absorbance and emission spectra were fully recovered after restoring the pH to neutral. The resulting spectra are not corrected for dilution as the volume added to the solutions were negligible compared to its total volume. A pKa standard deviation of +/- 0.07 pH units was experimentally calculated and a +/- 0.1 pH units was applied to each pKa measurement.

It is noted that PBS is not supposed to be used over very large pH ranges and only works well over the range of approximately pH 5-9. It would have been better to use discrete buffers for each pH value to eliminate this issue and should be done for any additional pH dependence studies.

2.1.16 Cell Culture

SP2/0-Ag 14 murine Myeloma spleen cells (ATCC no. CRL-1581) and Chinese hamster ovarian (CHO) (CHO-K1, ATCC no. CCL-61) were purchased from ATCC Cell Biology Collection (UK). The suspension cell line SP2 were grown in Dulbecco's modified Eagle's medium (DMEM) with stable L-glutamine and CHO cells in DMEM/Hams F-12 both supplemented with 10% foetal calf serum (Biosera) at 37 ^{o}C with 5% CO_2. Cells were harvested or split when they reached 90% confluency for CHO cells or 1 x 10^6 cells per ml for the suspension SP2 cells.

2.1.16.1 Cellular Uptake of Complexes

In order to assess and compare the ability of the compounds to transport across the cell membrane, SP2 and CHO cells were cultured on 35 mm glass bottom culture dishes. SP2 cells were seeded at 5 x 10^5 cells in 2 ml media and CHO cells were harvested after trypsinisation (0.25% trypsin for 5 mins at 37 ^{o}C) and seeded at 8 x 10^4 cells in 2 ml media. Both cell types were grown for 48 hours before imaging. For confocal measurements the growth medium was removed by washing with PBS buffer (pH 7.4) and 20 µl of the parent complex (1.4 mM) or dye-peptide (1.4 mM) in PBS (pH 7.4, with $MgCl_2$ and $CaCl_2$) was added. The luminophores and dye-peptides were made to a final concentration of 70 µM with PBS (pH 7.4) except for the iridium parent complex which made to 70 µM in 0.05% DMSO in PBS (1:20 dilution from stock with 1% DMSO) and were imaged immediately.

The cell viability dye, DRAQ7 (Biostatus), was generally added after 1 hour of imaging as it stains the nucleus of dead cells. DRAQ7 (4 μM final concentration) in PBS was carefully added to each dish and excited at 633 nm with emission collected at 650 nm. It is also noted that the cellular imaging results reported in this thesis take place at room temperature and without a 5% CO_2 environmental control in place. This may cause additional stresses on the cells which could account for increased cell apoptosis.

2.1.16.2 Cytotoxicity Assay

Cells were seeded in a 96-well plate in 100 μl of media for 24 hours at 37 ^{o}C with 5% CO_2 before addition of compounds. SP2 cells were seeded at 1 x 10^5 and CHO cells at 1 x 10^4 cells per well. PBS solvent containing DMSO and ethanol with final concentrations of between 20 to 0.3% were added to the harvested cells and left for 16 hours at 37 ^{o}C in a 5% CO_2 incubator. 10 μl of either the MTT or resazurin reagents (PromoKine) were added and incubated for 4 hours for MTT and 7 hours for resazurin at 37 ^{o}C. Formazan was solubilised with 150 μl DMSO per well for MTT assay and absorbance was measured at 570 nm and 630 nm (background). The resazurin converted to resorufin in viable cells was detected at absorbance 570 nm with background subtracted at 600 nm. Absorbance readings were performed using a Tecan 96-well plate reader. All cytotoxicity experiments are reported in terms of % cytotoxicity, e.g. 100% cytotoxicity = 100% of cells non-viable.

2.1.17 Freeze Drier

The freeze drier used was a Labcono FreeZone 2.5. Prior to placing on the freeze drier, all samples were dissolved or dispersed in deionised water and fully frozen in liquid nitrogen. The sample was then left on the freeze drier overnight.

2.2 Instrumentation used for peptide synthesis

2.2.1 HPLC Analysis

Chromatographic purification was carried out on a Varian HPLC Chromatography Workstation using a Phenomenex Gemini (C-18) reverse-phase chromatography column. The Gemini C-18 (250mm x 2.5 mm) was used at 1 ml per minute with linear gradient programs. The UV detector was monitored for dye-peptides at dual wavelengths of 214 nm and 350 nm for iridium conjugate and 214 nm and 452 nm for ruthenium conjugate respectively. Solvent A consisted of deionised H_2O containing 0.1% TFA and solvent B consisted of CH_3CN containing 0.1% TFA. The gradient ran over 30 minutes going from 5% to 65% of solvent A.

2.2.2 Mass Spectrometry Analysis

Mass spectrometry analysis was performed on a LaserToF by Matrix Assisted Laser Desorption Ionisation-Time Of Flight (MALDI-TOF). α-Cyano-4-hydroxy cinnamic acid matrix was dissolved in 1:1 H_2O containing 0.1% TFA and CH_3CN containing 0.1% TFA at a concentration of 10mg/ml. 2µl of a 1:1 solution of the dye-peptide to matrix were applied to the MALDI plate. Measurements were kindly performed by Lorraine Blackmore and Graeme Kelly of the RCSI.

2.3 Calculating Quantum Yields

In this thesis the phosphorescent quantum yield of the metal complexes are estimated by matching the MLCT absorbance transition of both the complex and standard $[Ru(bpy)_3]^{2+}$ [$\phi_P = 0.0642$ in acetonitrile].[5] Both solutions are excited into the MLCT region of maximum absorbance and the corresponding emission recorded. The luminescent quantum yield may be calculated by using the following formula in Equation 2.1.

$$\phi_{P(x)} = (A_x/A_s)\,(F_s/F_x)\,(n_x/n_s)^2\,\phi_{P(s)} \qquad \text{(Eq 2.1)}$$

where ϕ_P is the phosphorescent quantum yield, A is the absorbance at the excitation wavelength, F is the area under the corrected emission spectrum and n is the refractive index of the solvents used. The subscripts s and x refer to the standard and unknown respectively. This procedure for quantum yield determination is a relative method and provides a quick way to estimate the quantum yields of a complex. All quantum yield experiments were performed three times and the average quantum yield is the value quoted throughout this thesis for all metal complexes.

2.4 References

(1) Robert J. Forster, Tia E. Keyes, Johannes G. Vos In *Interfacial Supermolecular Assemblies;* Wiley: **2003**.

(2) Gordon, K. C.; Al-Obaidi, A.; Jayaweera, P. M.; McGarvey, J. J.; Malone, J. F.; Bell, S. E. J. *J. Chem. Soc. , Dalton Trans.* **1996**, 1591-1596.

(3) Le Ru, E. C.; Blackie, E.; Meyer, M.; Etchegoin, P. G. *The Journal of Physical Chemistry C* **2007***, 111*, 13794-13803.

(4) Ivanov, M. R.; Bednar, H. R.; Haes, A. J. *ACS Nano* **2009***, 3*, 386-394.

(5) Bhasikuttan, A. C.; Suzuki, M.; Nakashima, S.; Okada, T. *J. Am. Chem. Soc.* **2002***, 124*, 8398-8405.

Chapter 3: Synthesis and Characterisation of Ruthenium (II) Polypyridyl Luminophores for Conjugation

"To reference one is plagiarism but to reference many is research" – Anonymous.

3.0 Introduction

Inorganic luminophores offer many advantages over organic fluorophores and their benefits in cellular imaging,[1-3] diagnostics,[4-6] and supramolecular assemblies[7-9] have been known for many years. Transition metal complexes offer significant synthetic flexibility where by changing the ligands one can fine tune the absorbance and emission characteristics of the complex. In the cases of ruthenium, osmium, iridium and rhodium their relatively high phosphorescent quantum yields permits easy detection of luminophores at low concentrations, however, many small organic dyes such as fluorescein and Alexa are used at 1 nM concentrations for fluorescence measurements. Furthermore, the addition of ligands with environmentally sensitive functional groups, such as ionisable protons, offers pH sensitivity to the complex as is the case with the functionalised phenanthroline ligand reported throughout this chapter.

Specifically, ruthenium (II) polypyridyl complexes have attracted a lot of attention due to their strong DNA-binding[10-13] and potential anti-cancer properties.[5, 14-16] Results have shown how numerous ruthenium (II) polypyridyl complexes displayed excellent anti-tumour activity towards selected transfected cell lines. More recently, several complexes were also shown to induce mitochondria-mediated apoptosis in human cancer cell lines while displaying a lower toxicity when compared to widely used cisplatin based drugs to treat certain cancers.[5]

Much of the early bio-related research into ruthenium centred around derivatives of $[Ru(phen)_3]^{2+}$ because they were known to act like a 'molecular switch', as their luminescent output intensities were dependent on their microenvironments. Olson *et al.*[17] reported this 'light switching' effect for $[Ru(phen)_2(dppz)]^{2+}$, where dppz = dipyridophenazine. Figure 3.1 illustrates how the luminescence of the complex is completely quenched in aqueous media but is highly emissive in other aprotic organic solvents. In this particular ruthenium species there are several excited states quite close in energy: (i) a MLCT state directly populated by light excitation, in which the excited electron resides on the LUMO centred on the 'bpy-like' portion of the dppz ligand, (ii) the excited electron is located on the LUMO centred on a phenazine bound state the of the dppz ligand and (iii) a ligand centred (dppz-based) excited state.[18] In aqueous

solution, data showed that MLCT charge transfer is directed from the metal centre to the phenazine of the dppz ligand. However, a major source of non-radiative deactivation of the excited state is protonation of the nitrogen atoms on the phenazine ring, here, the rapid radiationless decay is driven by hydrogen bonding. Interestingly, when the complex is solvated by an aprotic organic solvent, the MLCT excited state involving the 'bpy-like' dppz subunit becomes dominant. Since such an energy state has better emissive properties the luminescence of the complex is effectively 'switched on'.[18]

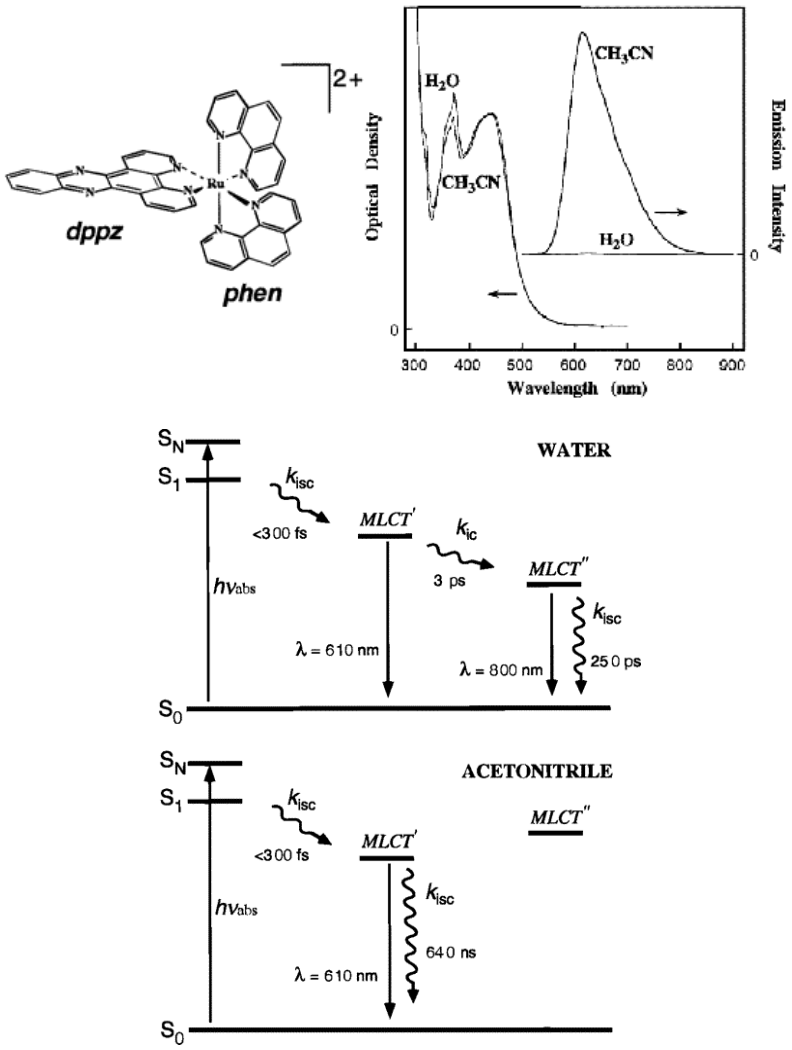

Figure 3.1: (Top) Chemical structure of $[Ru(phen)_2(dppz)]^{2+}$ and resultant photophysics in both aqueous and non-aqueous media. (Bottom) Model diagram illustrating its solvent dependent photophysics, were MLCT' and MLCT'' denotes distinct MLCT excited states distinguished by the distribution of charge on the metal-ligand framework.[17]

Furthermore, the addition of DNA to aqueous solutions containing $[Ru(phen)_2(dppz)]^{2+}$ and its derivatives also lead to a molecular 'light switching' effect as the nitrogen atoms on the dppz ligands are effectively shielded from its aqueous environment via intercalation with the DNA and H-bonding events.[10, 12, 19] This allows for the switching of excited state from the MLCT on the 'phenazine-like' to the triplet MLCT excited state located the 'bpy-like' subunit of the dppz ligand and the complex emits brightly. The interaction between ruthenium (II) polypyridyl complexes with DNA has been well documented in a series of reviews.[10, 12, 20] The exact binding mechanism between a metal complex and DNA is not well understood, however, it is believed that electrostatic interactions and groove binding within the minor groove of the DNA double helix are responsible.[10] Modification of chelating ligands can create interesting spatial configurations and electronic structures that have been shown to effect their binding interactions with DNA.[10, 12, 21] It is noted that research into ruthenium complexes containing ionisable ligands has been limited in the context of DNA and protein binding. The use of such pH sensitive metal complexes could potentially exhibit preferential selectivity towards pH-dependent damage in DNA and hence, show increased selectivity towards cancer cells.[13] In addition, use of pH sensitive ligands may also potentially provide critical information in the identification of cancerous tumours as they are known to express abnormal pH levels.[4, 22, 23]

$[Ru(bpy)_2(picCOOH)]^{2+}$ has been reported before by our research group and others[13] on its photophysical properties[24, 25] and its subsequent conjugation to biomolecules, such as polypeptides.[1, 26] Characteristics such as long aqueous lifetimes (> 800 ns), large Stokes shifts, pH dependence, photostability and increased emission in water make this and related dyes an attractive proposition for their use as molecular probes. The carboxyl functionality may be used to conjugate the luminophore to many naturally existing functional groups on biomolecules. However, of particular interest is its conjugation to amino groups located on such biomolecules which may be achieved though various coupling techniques such as PyBOP/HOBt[1, 27] or EDC/NHS[28] coupling reactions.

$R = COOH = [Ru(bpy)_2(picCOOH)]^{2+}$

$R = NO_2 = [Ru(bpy)_2(picNO_2)]^{2+}$

$R = NH_2 = [Ru(bpy)_2(picNH_2)]^{2+}$

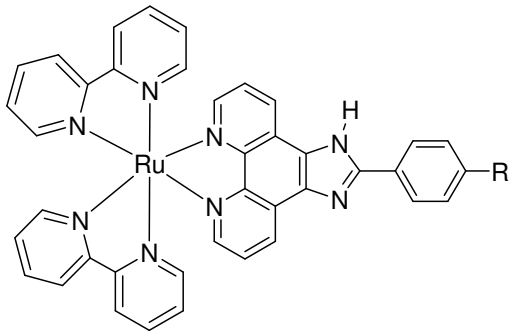

Figure 3.2: Chemical structures of ruthenium (II) polypyridyl complexes synthesised as part of this thesis.

A key aim of this chapter was to synthesise the luminophore with an amine reactive terminal functionality to take advantage of the many other reactive groups, in particular carboxyl functional groups, which are present on biomolecules. The synthetic approach taken was to synthesise 2-(4-nitrophenyl)imidazo[4,5-f][1,10]phenanthroline followed by a reduction reaction that yielded the analogous 2-(4-aminophenyl)imidazo[4,5-f][1,10]phenanthroline ligand. Since the nitro ligand was easily synthesised it too was coordinated to the ruthenium metal centre and characterised by spectroscopy, photophysics and electrochemical methods to compare electronic behaviour between all three functionalised derivatives of the ruthenium luminophore to build upon the literature already available.

Significant improvements on the synthesis of 2-(4-nitrophenyl)imidazo[4,5-f][1,10]phenanthroline are reported here, where the reaction time was decreased by 86% compared existing published methods.[29] Furthermore, coordination of the nitro functionalised ligand to the ruthenium metal centre was achieved using conditions that were not as harsh as previously reported[21] and did not required column chromatography for its purification as reported previously.[21, 30]

As discussed in Chapter 1, $[Ru(bpy)_2(picNO_2)]^{2+}$ has been shown previously to bind to DNA[21] and has been used as a luminescent sensor for anions. This has proven valuable as many biological processes involve the recognition of anionic species.[29] Interestingly, the free 2-(4-nitrophenyl)imidazo[4,5-f][1,10]phenanthroline ligand has also been used to provide colorimetric determination of anions present in samples which has enabled fast and easy detection of certain anions by the naked eye.[29] In addition, it has been reported that the location of the nitro functionality has a significant impact on the photophysics of this particular complex.[21] When the nitro group is located in the ortho- or para-positions, the compound's emission is quenched completely. Conversely, if located in the meta-position, the complex is found to be brightly luminescent. This may be explained in terms of the differences in bond polarity and its implications are discussed later in this chapter.

Unfortunately, whilst developing our novel synthesis of $[Ru(bpy)_2(picNH_2)]^{2+}$, Liu *et al.*[11] published a similar procedure on its synthesis and demonstrated how this particular amino functionalise ruthenium polypyridyl dye has been found to (i) intercalate into the DNA base pairs and upon irradiation may photocleave the plasmid pBR 322 DNA, (ii) display anti-tumor activity against transfected cells and (iii) exhibit good antioxidant activity against hydroxyl radicals that may induce DNA damage in humans. One of their major findings from IC50 values on selected cell lines indicated that coordination of the free amino ligand to the ruthenium metal centre resulted in a lowering of its antitumor activity. However, the cytotoxic effect of the luminophore came close but did not match that of cisplatin against certain cell lines.

For the first time a detailed and comparative photophysical, spectroscopic and electrochemical study is presented here on all three ruthenium functionalised complexes which extends on studies already reported for these models. All inorganic dyes synthesised are fully characterised by NMR, mass spectrometry and elemental analysis.

3.1 Acid-Base Chemistry of Metal Complexes

The excited state and ground state acid-base properties may differ significantly in a metal complex and any changes may be explained by differences in electron distribution within the complex between both states. In most transition metal complexes the coordinating ligand is more acidic than that of the free ligand. This may be explained by σ-donation from the ligand to the metal which reduces electron density around the ligand.[31]

Studying the effects of protonation / deprotonation of metal-ligand complexes on the both absorbance and emission spectra may give valuable insight into the extent of electronic communication within the metal complex and provide information on the location of the excited state. This is of particular interest in mixed ligand complexes where the nature of the lowest MLCT π* level is not necessarily known. It is generally accepted that if the acidity of the excited state increases with respect to the ground state that the ligand involved in the acid-base process is not directly involved in the emissive process. On the other hand, if the acidity decreases typically by 2 or more pH units, the excited state is thought to be localised on the ligand with the acid-base chemistry. These assumptions are based on the observation that upon excitation of ruthenium (II) polypyridyl complexes an electron is promoted from the metal centre d-orbital to a ligand π* orbital leaving a valence of +3 on the metal centre. An increase in basicity on the ligand is explained by increased electron density on the ionisable ligand due to electron donation from the metal centre and hence, one may predict the location of the excited state on mixed ligand complexes.[31, 32]

For example, it was found that the LUMO of the ruthenium (II) polypyridyl complexes synthesised in this thesis was located on the bpy ligands and not on the ionisable ligand involved in the acid-base chemistry. This was confirmed by similar ground and excited state pKa values. Had the excited state been located on the ionisable ligand, the excited state pKa* value would have been less acidic due to the increase in electron density on that ligand.

3.1.1 Background Theory:

Protonation of a complex will change the electronic levels within the molecule leading to changes in its electronic spectroscopy, particularly if the ligand participates in absorbance. The ground state pKa of a molecule may be calculated by monitoring absorbance of a complex at a wavelength that shows good acid-base variation plotted against the corresponding change in pH. The resultant first derivative of the pH titration may be determined in order to extract the ground state pKa values.

The excited state acidity of a complex may be evaluated using the Förster cycle. An acid-base equilibrium may be written for the $[Ru(bpy)_2(picCOOH)]^{2+}$ complex as follows in Equation 3.1:

$$[Ru(bpy)_2(picCOOH)]^{2+} \rightleftharpoons [Ru(bpy)_2(picCOOH)]^{+} + H^{+} \quad \text{.....(Eq 3.1)}$$

Where $[Ru(bpy)_2(picCOOH)]^{2+}$ and $[Ru(bpy)_2(picCOOH)]^{+}$ signify the acid and conjugate base respectively. In the relationship between the enthalpy changes and electronic transitions within the molecule it is arbitrarily assumed that the protonated compound absorbs at a higher energy than that of the deprotonated species and this is confirmed by the pH titrations for this particular complex.[31] Figure 3.3 demonstrates the relationship that may be used to determine the energy band gap between the ground and excited states of the $[Ru(bpy)_2(picCOOH)]^{2+}$ complex for example.

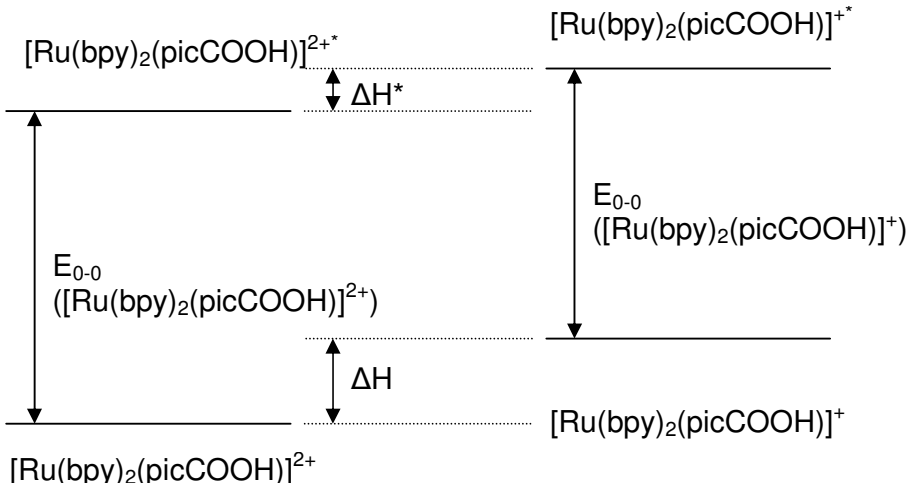

Figure 3.3: Relationship between enthalpy and electronic transitions for $[Ru(bpy)_2(picCOOH)]^{2+}$.
Where, $[Ru(bpy)_2(picCOOH)]^{2+}$ *= [Ru] and* $[Ru(bpy)_2(picCOOH)]^{1+}$ *= [Ru-L].*

$$\Delta H^{*} + E_{0\text{-}0}([Ru]) = \Delta H + E_{0\text{-}0}([Ru\text{-}L]) \text{…….Eq 3.2}$$

$$\Delta H^{*} + N_A h v_{[Ru]} = \Delta H + N_A h v_{[Ru\text{-}L]} \text{…….Eq 3.3}$$

$$\Delta H^{*} - \Delta H = N_A h (v_{[Ru\text{-}L]} - v_{[Ru]}) \text{…….Eq 3.4}$$

where ΔH^{*} and ΔH are the enthalpy changes caused by protonation in the excited and ground state, $v_{[Ru]}$ and $v_{[Ru\text{-}L]}$ are the frequencies of the lowest absorption or emission bands of [Ru] and [Ru-L], N_A is Avogadro's number and h is Plank's constant. If experiments are conducted under conditions where ΔH approximates the standard ΔH^{o} and if equal reaction entropies are assumed then;

$$\Delta H^{o} \sim \Delta G^{o} = RT \ln K = 2.303\ RT\ pK \text{…….Eq 3.5}$$

Then this gives;

$$pKa^{*} = pKa + (0.625/T)\ (v_{[Ru\text{-}L]} - v_{[Ru]}) \text{…….Eq 3.6}$$

where Ka and Ka^{*} are the ground and excited state equilibrium constants, R is the gas constant and T is the temperature in Kelvin. It is now possible to estimate excited state pKa^{*} values from ground state values and spectroscopic parameters.

When considering whether absorption or emission data should be used in calculating the pKa^* it is important to take into account the nature of the complex in question. Many organic fluorophores emit from their lowest singlet excited state and for such compounds absorbance or emission data may be used as lifetimes are generally short. However, for many inorganic based compounds the main absorption is in the visible part of the spectrum corresponding to the lowest singlet MLCT level. Internal conversion then occurs to the triplet MLCT excited energy state and phosphorescent emission of the photon occurs and hence, lifetimes are longer. It is then important to use the emission data of such species in calculating excited state pKa* values.

When proton exchange is much faster than the excited-state decay of both protonated and deprotonated species an equilibrium may be established in the excited state and meaningful results can be obtained from the Förster cycle between $\nu_{[Ru\text{-}L]}$ - $\nu_{[Ru]}$. If the rate of emission decay is less then the rate of (de)protonation then the following Equation 3.7 holds true.

$$pKa^* = pH_i + \log (\tau_{HB} / \tau_B^-) \text{.....Eq 3.7}$$

Where pH_i is the point of inflection on the pH titration emission curve (as determined using the first derivative function in Origin 6.0 software) and τ_{HB} and τ_B^- are the lifetimes of the protonated and deprotonated species respectively. As a result one may use the equation above to calculate the excited state pKa* of a luminophore using its emission data and in turn determine the location of the excited state on the molecule under analysis. However to use this particular equation, it is necessary for the complexes to have relatively long lifetimes.

Figure 3.4 illustrates the four possible protonation states for the $[Ru(bpy)_2(picCOOH)]^{2+}$ complex and may be used to illustrate similar processes occurring in all the organic luminophores synthesised in this thesis with changes in pH. Formation of the $[Ru(bpy)_2(picCOOH)]^{3+}$ species was found to have a ground state pKa value of 1.5 +/- 0.1. The effect of solvents on the pKa of this particular ruthenium polypyridyl complex is highlighted in a paper published previously.[24] Here, it was determined that the formation of the protonated $[Ru(bpy)_2(picCOOH)]^{3+}$ species, using acetonitrile as solvent, had a much higher ground state pKa value of 5. Furthermore, it

was also shown that the ground state pKa values for the formation of $[Ru(bpy)_2(picCOOH)]^+$ and $[Ru(bpy)_2(picCOOH)]^0$ was 8.9 and 9.5, respectively.

However, in the aqueous based experiments carried out in this thesis only two ground state pKa values are evident, that of the formation of $[Ru(bpy)_2(picCOOH)]^{3+}$ and $[Ru(bpy)_2(picCOOH)]^+$ at 1.5 +/- 0.1 and 8.5 +/- 0.1, respectively. This is further supported by similar experiments performed by Pellegrin *et al.*[25] in an earlier published paper. (De)protonation of the carboxyl functionality is no longer evident in aqueous environments as it is involved in solvation of the complex through H-bonding.

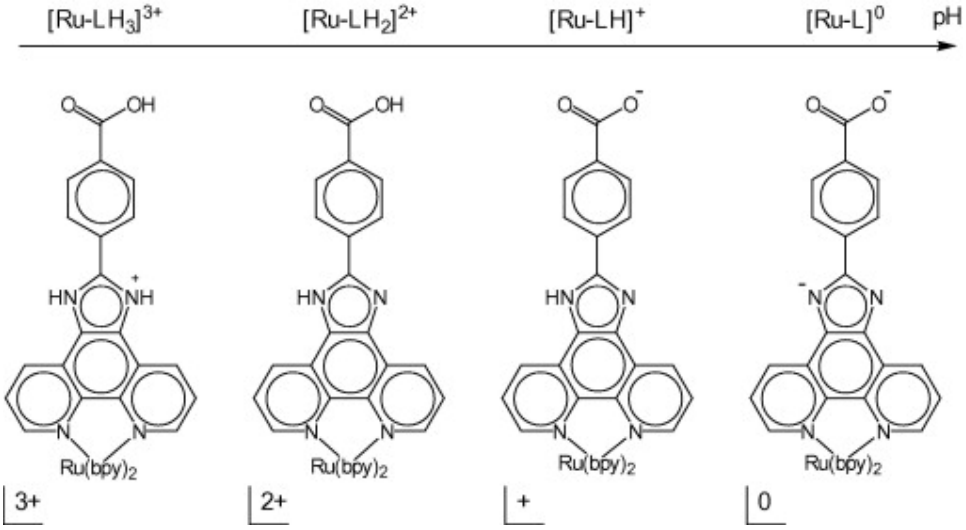

Figure 3.4: Schematic diagram illustrating the different protonation states for $[Ru(bpy)_2(picCOOH)]^{2+}$.[24]

The likely acid-base equilibrated equations for the protonation/deprotonation of this complex (and other similar complexes) may be described as follows:

$[Ru(bpy)_2(picCOOH)]^{2+} + H^+ \leftrightarrow [Ru(bpy)_2(picCOOH)]^{3+}$ (pKa = 1.5 +/- 0.1) …….Eq 3.8

$[Ru(bpy)_2(picCOOH)]^{2+} \leftrightarrow [Ru(bpy)_2(picCOOH)]^+ + H^+$ (pKa = 8.5 +/- 0.1) …….Eq 3.9

In the determination of pKa/pKa* values for the metal complexes, one full pH titration experiment was performed in triplicate to calculate the standard deviation for the calculated pKa values. This standard deviation of +/- 0.07 units (or +/- 0.1 units [rounded to one significant figure]) was to be applied to all pKa/pKa* figures.

3.2 Ruthenium Conjugated Gold Nanoparticles

In the second part of this chapter, the amino functionalised ruthenium complex, whose peptide conjugate was previously shown to be useful as a multimodal probe in cellular imaging,[1] was conjugated to gold nanoparticles in an effort to enhance its emission intensity and lifetime. This was achieved using 50 nm gold nanoparticles as substrate onto which an amino functionalised ruthenium (II) dye was attached via thiol-PEG-carboxyl bifunctionalised linkers. This is the first time to our knowledge that a ruthenium complex has been directly immobilised on to a gold nanoparticle surface via PEG linkers.

As discussed in Chapter 1, water soluble PEG linkers have been shown before to provide additional stability to nanoparticles[33, 34] and it was hoped that it would help in drawing the nanoconjugate across the cell membrane. The length of the PEG linkers were varied (from PEG_8 = 3.3 nm to PEG_{32} = 13.2 nm approximately, when in linear conformation) in an effort to increase the distance between chromophore and substrate and thus, have a direct impact on the luminescent output of the dye as a result of metal enhanced emission. It has also been previously shown in Chapter 1 that a distance of approximately 10 nm from substrate to dye exhibited the best balance between surface quenching and enhancement.[35, 36]

In addition, the nanoconjugate that demonstrated superior luminescence and lifetimes was then used in the cellular imaging of SP2 myeloma cells. This nanoparticle probe has the potential to be used as a multimodal probe in determining both intracellular pH levels and oxygen concentrations as its photophysics are very similar to that of the carboxyl functionalised parent dye complex. This parent dye has previously been conjugated to a cell penetrating peptide for multimodal cellular imaging purposes.[1, 26] Furthermore, the ability of the luminophore to generate singlet oxygen means that the ruthenium nanoconjugate could prove critical in the early detection and subsequent apoptosis of tumour cells.

3.3 Experimental Procedure

Chemicals

All chemicals and reagents were purchased from Sigma-Aldrich (Ireland) and were used without any further purification unless otherwise stated. Polyethylene glycol (PEG) linkers were supplied by Quanta Biodesign (except for COOH-PEG_{24}-NH_2 [Aldrich]) and 50 nm gold nanoparticles (AuNPs) by BBInternational. All reactions were performed in air unless otherwise stated.

The preparation of ruthenium-(bis-2,2-bipyridyl)dichloride. [$Ru(bpy)_2Cl_2$]

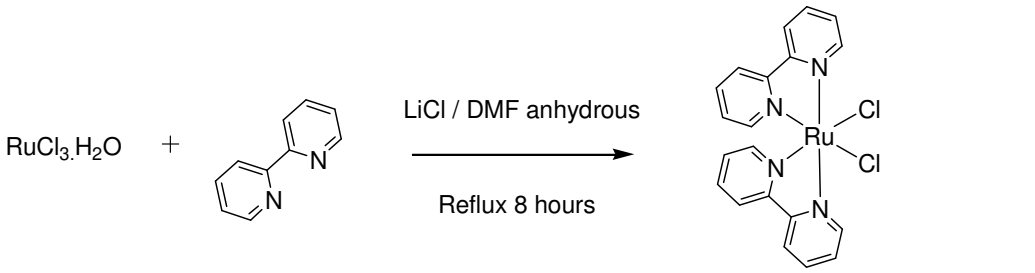

Ruthenium tri chloride hydrate

2,2-bipyridine

Ruthenium-(bis-2,2-bipyridyl)dichloride

The compound was prepared according to a method modified from the literature.[37] $RuCl_3.3H_2O$ (500 mg, 1.91 mmol) was dissolved in anhydrous DMF (7 ml) in a three neck round bottomed flask. Next lithium chloride (551 mg, 13.00 mmol) was added to the solution followed by 2,2-bipyridine (597 mg, 3.82 mmol) in three equal portions. The reaction was then refluxed under a nitrogen environment at 160 ^{0}C for 8 hours.

The reaction mixture was then allowed to cool to room temperature and acetone was added to promote precipitation and left in the fridge overnight. The precipitate was then collected by vacuum filtration and washed well with acetone and diethyl ether to leave a dark purple coloured solid.

The product was then purified on an alumina (basic) chromatographic column using 10 % methanol ; dichloromethane as mobile phase to yield the product as a dark purple solid (301 mg, 62 %).

^{1}H NMR (400MHz, DMSO-d_6): **δ (ppm) 9.94** (d, 2H, J = 4.8 Hz), **8.60** (d, 2H, J = 8 Hz), **8.45** (d, 2H, J = 8.4 Hz), **8.03** (t, 2H, J = 6.4 Hz), **7.74** (t, 2H, J = 6.4 Hz), **7.64** (t, 2H, J = 6.4 Hz), **7.47** (d, 2H, J = 5.2 Hz), **7.07** (t, 2H, J = 6.4 Hz).

The preparation of 2-(4-carboxylphenyl)imidazo[4,5-f][1,10]phenanthroline). [(picCOOH)]

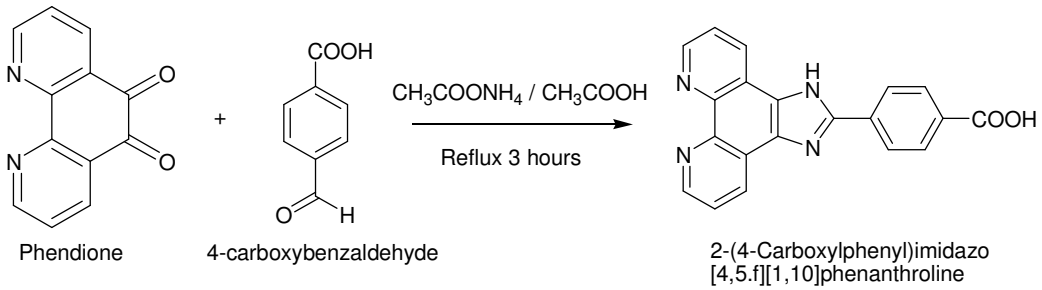

Phendione 4-carboxybenzaldehyde 2-(4-Carboxylphenyl)imidazo [4,5.f][1,10]phenanthroline

The ligand was prepared according to a method modified from the literature.[24] 1,10-Phenanthroline 5,6-dione (210 mg, 1 mmol), 4-carboxy-benzaldehyde (180 mg, 1.2 mmol), ammonium acetate (1540 mg, 20 mmol) and glacial acetic acid (25 ml) were added to a 100ml round bottomed flask and left refluxing at 130 ^{0}C for 3 hours. The solution was then cooled to room temperature and excess water added to induce recrystallisation and was kept in the fridge overnight at 4 ^{o}C.

The precipitate was collected by vacuum filtration and washed with deionised water, methanol and diethyl ether to afford the ligand as a yellow solid (231 mg, 68%).

^{1}H NMR (400 MHz, DMSO-d_6): **δ (ppm) 13.96** (s, 1H), **13.09** (s-broad, 1H), **9.05** (d, 2H), **8.95** (d, 2H, J = 2.4 Hz), **8.40** (d, 2H, J = 8.4 Hz), **8.17** (d, 2H, J = 8.4 Hz), **7.87** (m, 2H).

The preparation of ruthenium (II) (bis-2,2-bipyridyl)-2(4-carboxylphenyl) imidazo[4,5-f][1,10]phenanthroline. $[Ru(bpy)_2(picCOOH)]^{2+}. (ClO_4^-)_2$

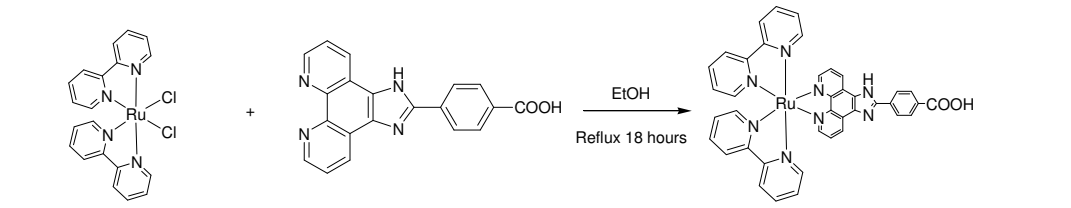

The compound was prepared according to a method modified from the literature.[24] $[Ru(bpy)_2Cl_2]$ (50 mg, 0.103 mmol), 2-(4-carboxylphenyl)imidazo[4,5-f][1,10]phenanthroline [(picCOOH)] (31 mg, 0.123 mmol) and ethanol (15 ml) were placed in a 50 ml round bottomed flask and left refluxing for 18 hours.

The solvent was evaporated under reduced pressure and the crude product was suspended in a saturated solution of $NaClO_4$ and filtered. The precipitate was then washed with deionised water, diethyl ether and dichloromethane to yield reddish solid. The product was then taken and dissolved in acetonitrile. The precipitate was then removed and the solvent was evaporated to dryness to give a red coloured product (69 mg, 87 %).

^{1}H NMR (400 MHz, DMSO-d_6): **δ (ppm) 14.43** (s, 1H), **9.11** (d, 2H, J = 8.4 Hz), **8.85** (d, 2H, J = 8 Hz), **8.81** (d, 2H, J = 8 Hz), **8.43** (d, 2H, J = 8.4 Hz), **8.20** (m, 4H), **8.11** (t, 2H, J = 6.4 Hz), **8.08** (m, 2H), **7.92** (m, 2H), **7.83** (d, 2H, J = 5.2 Hz), **7.59** (m, 4H), **7.33** (t, 2H, J = 6 Hz).

ESI-MS (CH_3OH, m/z): 952.77, ($[M- 2ClO_4]^{2+}$): 753.2.

Elemental analysis calculated for $C_{40}H_{28}N_8O_2Ru.(ClO_4^-)_2.(CH_2Cl_2)_2$: C, 44.94; H, 2.87; N, 9.98%. Found: C, 43.41; H, 2.67; N, 10.00%.

Melting point: 274 ^oC

The preparation of 2-(4-nitrophenyl)imidazo[4,5-f][1,10]phenanthroline. [(picNO$_2$)]

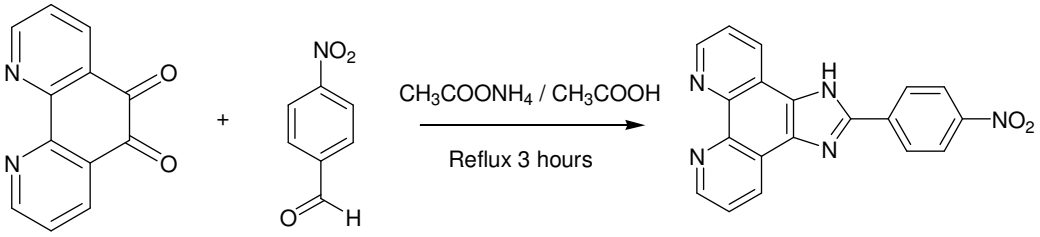

1,10-Phenanthroline 5,6-dione (500 mg, 2.38 mmol), 4-nitro-benzaldehyde (432 mg, 2.86 mmol), ammonium acetate (3669 mg, 47.6 mmol) and glacial acetic acid (40 ml) were added to a 100ml round bottomed flask and left refluxing at 130 ^{0}C for 5 hours. The solution was then cooled to room temperature and water added to induce recrystallisation and was left in the fridge overnight.

The precipitate was then collected by vacuum filtration and washed with water, diethyl ether, acetonitrile and acetone to yield the product as a yellow solid (612 mg, 75 %).

^{1}H NMR (DMSO-d$_6$): **δ (ppm) 14.13** (s, 1H), **9.06** (d, 2H, J = 1.6 Hz), **8.89** (dd, 2H, 1.6 Hz, 1.6 Hz), **8.51** (q, 4H, J = 8.8 Hz, J = 7.2 Hz, J = 9.2 Hz), **7.86** (m, 2H).
MALDI-TOF (CH_3CN, m/z): 341.09, ([M-H$^+$]): 340.57.

The preparation of ruthenium (II) (bis-2,2-bipyridyl)-2(4-Nitrophenyl) imidazo[4,5-f][1,10]phenanthroline. $[Ru(bpy)_2(picNO_2)]^{2+}.(ClO_4^-)_2$

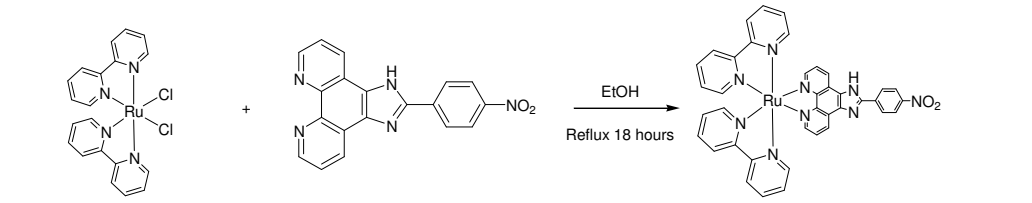

$[Ru(bpy)_2Cl_2]$ (237 mg, 0.488 mmol), 2-(4-nitrophenyl)imidazo[4,5-f][1,10]phenanthroline $[(picNO_2)]$ (200 mg, 0.586 mmol) and ethanol (20 ml) were placed in a 100 ml round bottomed flask and left refluxing for 18 hours.

The reaction was cooled to room temperature and the solvent was evaporated under reduced pressure. The crude product was suspended in a saturated solution of $NaClO_4$ and filtered. The precipitate was then washed with deionised water, dichloromethane and diethyl ether to yield bright red coloured solid (377 mg, 90 %).

^{1}H NMR (400 MHz, DMSO-d_6): **δ (ppm) 14.69** (s, 1H), **9.07** (d, 2H, J = 8 Hz), **8.85** (d, 2H, J = 8 Hz, J = 8 Hz), **8.83** (d, 2H, J = 8 Hz, J = 8 Hz), **8.53** (s, 4H), **8.21** (t, 2H, J = 8 Hz), **8.17** (m, 4H), **7.93** (m, 2H), **7.81** (d, 2H, J = 5.2 Hz), **7.59** (m, 4H), **7.33** (t, 2H, J = 8 Hz).

ESI-MS (CH_3OH, m/z): 854.3 ($[M- ClO_4]^{2+}$): 754.3.

Elemental analysis calculated for $C_{39}H_{27}N_9O_2Ru.(ClO_4^-)_2.(CH_2Cl_2)$: C, 46.26; H, 2.81; N, 12.14%. Found: C, 45.77; H, 2.70; N, 12.09%.

Melting point: 285-287 ^oC

The preparation of 2-(4-aminophenyl)imidazo[4,5-f][1,10]phenanthroline. [(picNH$_2$)]

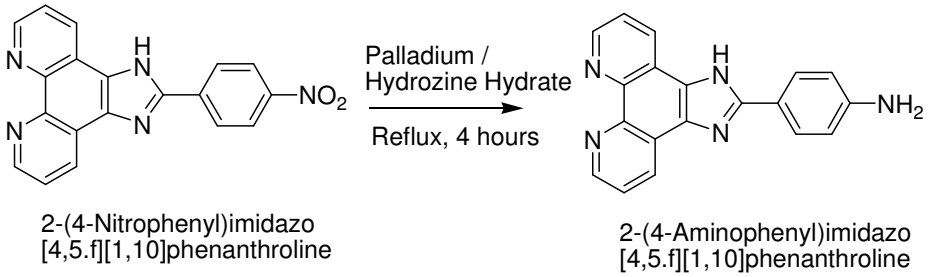

2-(4-Nitrophenyl)imidazo
[4,5.f][1,10]phenanthroline

2-(4-Aminophenyl)imidazo
[4,5.f][1,10]phenanthroline

2-(4-Nitrophenyl)imidazo[4,5-f][1,10]phenanthroline [(picNO$_2$)] (100 mg, 0.293 mmol), palladium 5 % wt on activated carbon (18.8 mg) and absolute ethanol (5 ml) were added to a 25 ml round bottomed flask. Hydrazine hydrate (73 µl was added dropwise to the reaction and left refluxing at 90 ^{o}C for 4 hours.

The solution was then filtered through celite and the solvent was evaporated to dryness. Diethyl ether was added and the precipitate was collected by vacuum filtration and washed with diethyl ether. The solid was then purified using an alumina (basic) chromatographic column using 10 % methanol ; dichloromethane as mobile phase to yield a brown coloured product (72 mg, 79 %).

^{1}H NMR (DMSO-d$_6$): **δ (ppm) 13.35** (s, 1H), **8.99** (d, 2H), **8.88** (d, 1H, J = 2 Hz), **8.86** (d, 2H, J = 1.6 Hz), **7.97** (d, 2H, J = 8.8 Hz), **7.80** (m, 2H), **6.71** (d, 2H, J = 8.4 Hz), **5.61** (s, 2H).

ESI-MS (CH_3OH, m/z): 311.34 ([M+Na^{+}]): 334.5.

The preparation of ruthenium (II) (bis-2,2-bipyridyl)-2(4-aminophenyl) imidazo[4,5-f][1,10]phenanthroline. $[Ru(bpy)_2(picNH_2)]^{2+}.(ClO_4^-)_2$

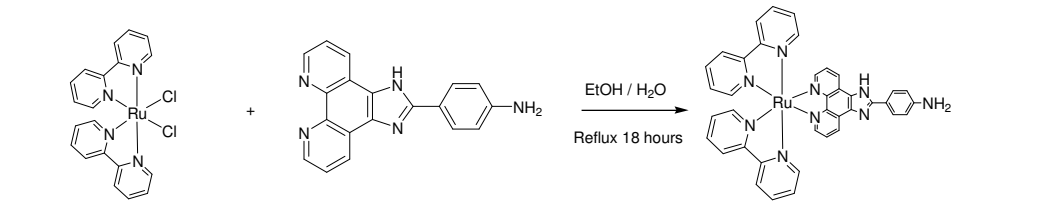

Ruthenium-(bis-2,2-bipyridyl)dichloride

2-(4-Aminophenyl)imidazo [4,5.f][1,10]phenanthroline

Ruthenium^{2+} (bis-2,2-bipyridyl)-2(4-Aminophenyl) imidazo[4,5-f][1,10]phenanthroline. $[Ru(bpy)_2(picNH_2)]^{2+}$

$[Ru(bpy)_2Cl_2]$ (38.8 mg, 0.08 mmol), 2-(4-aminophenyl)imidazo[4,5-f][1,10]phenanthroline [$(picNH_2)$] (30 mg, 0.096 mmol), deionised water (5 ml) and ethanol (5 ml) were placed in a 50 ml round bottomed flask and left refluxing for 18 hours under a nitrogen atmosphere. After cooling, a saturated solution of $NaClO_4$ was added and the red precipitate was collected. The crude product was then purified on an alumina (basic) chromatographic column using 10 % methanol ; dichloromethane as mobile phase, to leave the product as a red powder (27 mg, 46 %).

^{1}H NMR (400 MHz, DMSO-d_6): **δ (ppm) 14.34** (s, 1H), **9.35** (d, 1H, J = 8.4 Hz), **9.06** (d, 1H, J = 8.4 Hz), **9.02** (d, 2H, J = 8.4 Hz), **8.87** (d, 2H, J = 8.4 Hz), **8.22** (t, 2H, J = 8 Hz), **8.12** (m, 4H), **8.03** (d, 1H, J = 4 Hz), **7.98** (d, 1H, J = 5.2 Hz), **7.91** (m, 2H), **7.84** (d, 2H, J = 5.6 Hz), **7.58** (m, 4H), **7.34** (t, 2H, J = 6.4 Hz), **6.73** (d, 2H, J = 6 Hz), **5.78** (d, 2H, J = 6.4 Hz).

ESI-MS (CH_3OH, m/z): 824.3 ($[M- ClO_4]^{2+}$): 724.2.

Elemental analysis calculated for $C_{39}H_{29}N_9Ru.(ClO_4^-)_2$: C, 50.71; H, 3.16; N, 13.65%. Found: C, 51.25; H, 3.81; N, 13.58%.

Melting point: >300 ^oC

The preparation of AuNP-PEG$_8$-Ru. (linear linker length approximately 3.3 nm)

Thiol-PEG$_8$-COOH (20 mg, 0.045 mmol) and 1-ethyl-3-[3-dimethylaminopropyl] carbodiimide hydrochloride [EDC] (42 mg, 0.218 mmol) were added to PBS buffer pH 7.0 (1 ml) in an eppendorf tube and left shaking for 5 minutes. Next N-hydroxysulfosuccinimide [NHS] sodium salt (47 mg, 0.218 mg) was added to the solution and left stirring for a further 20 minutes. $[Ru(bpy)_2(picNH_2)]^{2+}.(ClO_4^-)_2$ (25 mg, 0.030 mmol) was then added and the reaction mixture was left shaking gently overnight.

Dithiothreitol [DTT] (2mg, 0.013 mmol) was added to the solution and left stirring for a further 10 minutes. A concentrated solution of the 50 nm AuNPs (1 ml) was then added and left to shake gently overnight. The eppendorf tube was then centrifuged at 9,000 rpm and the precipitate was washed with deionised water (x 8 times), with sonication each time prior to centrifugation, to yield a reddish brown coloured precipitate. The conjugated gold nanoparticles were then resuspended in a PBS solution (pH 7.4).

The preparation of AuNP-PEG$_{32}$-Ru. (linear linker length approximately 13.2 nm)

The general procedure for the preparation of AuNP-PEG$_{32}$-Ru was performed as outlined above for the AuNP-PEG$_8$-Ru nanoconjugate. The only exception was an additional EDC/NHS coupling reaction step between the COOH-PEG$_{24}$-NH$_2$ linker and thiol functionalised, SH-PEG$_8$-COOH, linker prior to conjugation to $[Ru(bpy)_2(picNH_2)]^{2+}$ complex.

3.4 Results and Discussion

3.4.1 Synthesis

In the formation of the imidazole ligand derivatives it is the acid catalysed reaction of 1,10-phenanthroline 5,6-dione with the ammonium acetate which provides the critical 1,10-phenanthroline 5,6-di-imine intermediate (1) necessary for synthesis. This intermediate is then reacted with the appropriate aldehyde and undergoes an aldol-type of condensation to form a second intermediate which is then followed by a two hydrogen shift and subsequent loss of a water molecule to form the desired imidazole complex as illustrated in Figure 3.5.[38]

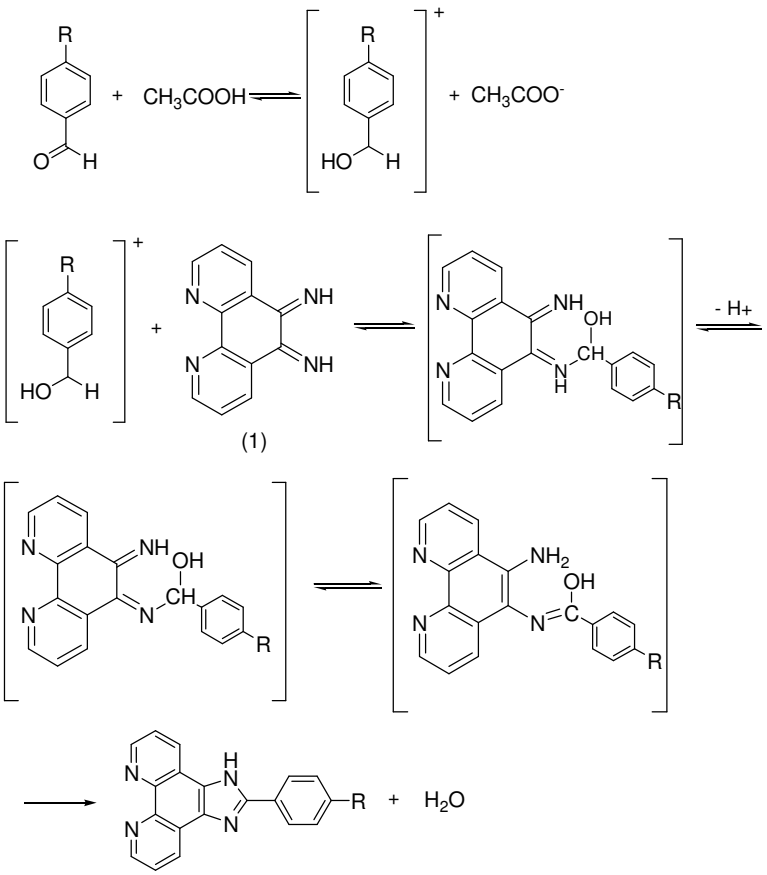

Figure 3.5: Mechanism illustrating the formation of the imidazole ligand.[38]

The synthesis of $[Ru(bpy)_2(L\text{-}L)]^{2+}$ [where L-L = bidentate polypyridyl ligands] complexes from $[Ru(bpy)_2Cl_2]$ is based on the propensity of this complex to replace the two chloride ligands with water molecules initially. This results in a labile complex that may undergo further reaction with an incoming ligand to give the final product. The first chloride ligand may be removed relatively easily using organic solvents and may be preformed at low temperatures (< 70 ^oC). The replacement of the second chloride ligand however requires higher boiling point solvents and higher temperatures (> 70 ^oC).[39] Adding a slight excess of ligand to the reactions gave the best results for the synthesis of the desired complex and products were easily purified by washing or column chromatography. The synthesis of the ruthenium complexes proved relatively straight forward and the associated high yields only lend to its use as a suitable multimodal molecular probe.

There are a couple of approaches to the synthesis of $[Ru(bpy)_2(picNH_2)]^{2+}$. The initial preference was the reduction of $[Ru(bpy)_2(picNO_2)]^{2+}$ to give the corresponding $[Ru(bpy)_2(picNH_2)]^{2+}$, however, this did not prove successful. Therefore, it was decided therefore to reduce the ligand initially before coordination of the metal centre and this approach proved more successful with a yield of 46%.

The amino functionalised complex also proved valuable in the labelling of the gold nanoparticles. The polyethylene glycol (PEG) linkers are expensive, particularly a thiol-PEG-amine bifunctionalised linker ($500 for 100 mg), which would have been necessary should the $[Ru(bpy)_2(picCOOH)]^{2+}$ complex have been used. Consequently, a cheaper thiol-PEG-carboxyl linker ($250 for 100 mg) was purchased and used for the conjugation of ruthenium luminophore to the gold nanoparticles via an EDC/NHS coupling reaction.

3.4.2 ^{1}H-NMR Discussion

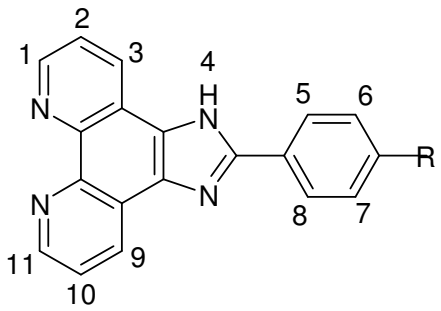

Figure 3.6: [pic-R] ligand illustrating numbering scheme for ^{1}H-NMR analysis.

Proton	**[picCOOH] ppm**	**Proton**	**[picNO$_2$] ppm**	**Proton**	**[picNH$_2$] Ppm**
H_4 (N-H)	13.96 (s, 1H)	*H_4 (N-H)*	14.13 (s, 1H)	*H_4 (N-H)*	13.35 (s, 1H)
Carboxyl-H	13.09 (s, 1H)	*H_1, H_{11}*	9.06 (d, 2H)	*H_1, H_{11}*	8.99 (d, 2H)
H_1, H_{11}	9.05 (d, 2H)	*H_3, H_9*	8.89 (dd, 2H)	*H_3, H_9*	8.88 (dd, 2H)
H_3, H_9	8.95 (d, 2H)	*H_5, H_6, H_7, H_8*	8.51 (q, 4H)	*H_5, H_8*	7.97 (d, 2H)
H_6, H_7	8.40 (d, 2H)	*H_2, H_{10}*	7.86 (m, 2H)	*H_2, H_{10}*	7.80 (m, 2H)
H_5, H_8	8.17 (d, 2H)			*H_6, H_7*	6.71 (d, 2H)
H_2, H_{10}	7.87 (m, 2H)			*Amino-NH_2*	5.61 (s, 2H)

Table 3.1: ^{1}H-NMR resonances for [pic-R] ligand with various functional groups, carried out in DMSO-d_6. The integration and peak splitting are shown in brackets.

Mass spectrometry and elemental analysis were combined with NMR (^{1}H-NMR / COSY) to confirm the purity and structure of the complexes synthesised. Table 3.1 shows the full ^{1}H-NMR data for the peak shifts for the various [pic-R] ligands. Due to the electron donating and electron withdrawing constituents of the ligand's R-group, the protons that show the most change in chemical shifts are located on the phenyl ring. Having an electron withdrawing substituent on the ligand has the effect of drawing

electron density away from nearby protons, thus, causes a deshielding effect resulting in a chemical shift downfield. On the other hand when an electron donating group is present, it has the opposite effect causing a shift upfield in its NMR spectrum. This is most effectively demonstrated by comparison of the electron donating amino group versus the electron withdrawing nitro group. The protons located at positions H_6 and H_7 on the amino functionalised ligand are shifted upfield to 6.71 ppm, whereas, the corresponding protons on the nitro functionalised ligand have chemical shift of 8.40 ppm.

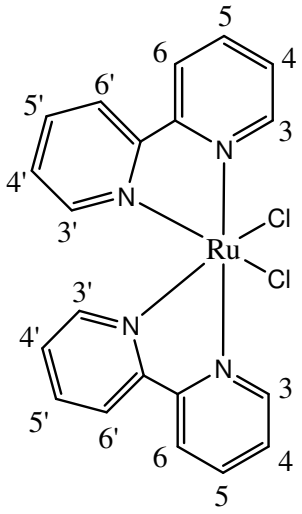

Figure 3.7: [Ru(bpy)$_2$Cl$_2$] complex illustrating numbering scheme for ^{1}H-NMR analysis.

Table 3.2 below shows the complete proton assignments for the ^{1}H-NMR spectra of the three ruthenium (II) compounds synthesised. As expected, due to the displacement of the chlorine atoms on the [Ru(bpy)$_2$Cl$_2$] complex, the protons in the H_3 position on the bpy ligands experience a change in their chemical environments. This results in a shift of around 1 ppm upfield due to the shielding effect of the incoming imidazole ligand. It must also be noted that the protons on the imidazole ring (H_4) were not always observed, presumably because these protons are very active and may be easily exchanged between the two nitrogens on the imidazole ring in solution.[11]

$[Ru(bpy)_2picCOOH]^{2+}$		$[Ru(bpy)_2picNO_2]^{2+}$		$[Ru(bpy)_2picNH_2]^{2+}$	
Bpy protons. ppm	**[picCOOH] protons. ppm**	**bpy protons. ppm**	**[$picNO_2$] protons ppm**	**bpy protons. ppm**	**[$picNH_2$] protons. ppm**
H_3 8.85 (d, 2H)	H_4 *(N-H)* 14.43 (s, 1H)	H_3 8.85 (d, 2H)	H_4 *(N-H)* 14.69 (s, 1H)	H_3 9.02 (d, 2H)	H_4 *(N-H)* 14.34 (s, 1H)
$H_{3'}$ 8.81 (d, 2H)	H_1, H_{11} 9.11 (d, 2H)	$H_{3'}$ 8.81 (d, 2H)	H_1, H_{11} 9.07 (d, 2H)	$H_{3'}$ 8.87 (d, 2H)	H_1 9.35 (d, 1H)
H_4 8.20 (m, 4H)	H_6, H_7 8.43 (d, 2H)	H_4 8.21 (t, 2H)	H_5, H_6, H_7,H_8 8.53 (m, 4H)	H_4 8.22 (t, 2H)	H_{11} 9.06 (d, 1H)
$H_{4'}$ 8.11 (t, 2H)	H_5, H_8 8.20 (m, 4H)	$H_{4'}$ 8.17 (m, 4H)	H_3, H_9 8.08 (m, 4H)	$H_{4'}$ 8.12 (m, 4H)	H_5, H_8 8.12 (m, 4H)
H_6 7.83 (d, 2H)	H_3, H_9 8.08 (m, 2H)	H_6 7.81 (d, 2H)	H_2, H_{10} 7.93 (m, 2H)	H_6 7.84 (d, 2H)	H_3 8.03 (d, 1H)
$H_{6'}$, H_5 7.59 (m, 4H)	H_2, H_{10} 7.92 (m, 2H)	$H_{6'}$, H_5 7.59 (m, 4H)		$H_{6'}$, H_5 7.58 (m, 4H)	H_9 7.98 (d, 1H)
$H_{5'}$ 7.33 (t, 2H)		$H_{5'}$ 7.33 (t, 2H)		$H_{5'}$ 7.34 (t, 2H)	H_2, H_{10} 7.91 (m, 2H)
					H_6, H_7 6.73 (d, 2H)
					NH_2 5.78 (d, 2H)

Table 3.2: ^{1}H-NMR resonances for the ruthenium compounds synthesised, carried out in DMSO-d_6. The integration and peak splitting are shown in brackets.

Table 3.3 shows the relative shifts in ppm of the free [pic] ligand versus the coordinated [pic] ligand. The protons located at H_3 and H_9 of the [pic-R] ligands show the greatest chemical shifts of 0.9 ppm following coordination to the ruthenium metal centre. This may be explained by the increased electron density around the [pic-R] ligands due to the donation of 2 electrons from the binding ruthenium centre. This causes a delocalised shielding effect which seems to be mostly concentrated on the H_3 and H_9 protons and hence, results in an upfield chemical shift. It is also considered that there may be possible anisotropic effects on these protons as a result of the 3-D

configuration of the complex and the proximity of cyclometalating ligands to one another.

The chemical shift of the imidazole H_4 proton demonstrates remarkable sensitivity to the identity of the carboxyl, nitro and amino substituents. It is also noted that ^{1}H-NMR analysis of $[Ru(bpy)_2(picNH)_2]^{2+}$ shows that protons at positions H_1, H_{11}, and H_3, H_9 split into their own individual doublets with an integration of one proton. It is speculated that this splitting of peaks is caused by the increased delocalisation of electron density over the [pic-NH_2] ligand. This may result in resonance structures within the phenanthroline section of the ligand as the double bond character is shifted from bond to bond and hence, differences in the effective magnetic field are experienced by the protons.

Proton	**$[Ru(bpy)_2picCOOH]^{2+}$ Δ ppm**	**$[Ru(bpy)_2picNO_2]^{2+}$ Δ ppm**	**$[Ru(bpy)_2picNH_2]^{2+}$ Δ ppm**
H_1	0.06	0.01	0.36
H_2	0.05	0.07	0.11
H_3	-0.87	-0.81	-0.85
H_4	-0.47	0.83	0.99
H_5	0.03	0.02	0.15
H_6	0.03	0.02	0.02
H_7	0.03	0.02	0.02
H_8	0.03	0.02	0.15
H_9	-0.87	-0.81	-0.90
H_{10}	0.05	0.07	0.11
H_{11}	0.06	0.01	0.07

Table 3.3: Δ ppm of the coordinated complexes compared to the free [pic-R] ligand.

3.4.3 Optical and Acid-Base properties of Ruthenium (II) Complexes

Compound	Absorbance [a] λ_{max} (ε, $dm^3mol^{-1}cm^{-1}$)	Emission [a] λ_{max}	τ (ns) [b] (aerated/ degassed)	ϕ [c]	pKa [d] (+/-0.1)	pKa* [d] (+/-0.1)
$[Ru(bpy)_2(picCOOH)]^{2+}$	457 nm (13,033) 330 nm (23,946) 285 nm (61,318)	608 nm	158/ 502	0.068	1.5, 8.5	2.2, 8.7
$[Ru(bpy)_2(picNO_2)]^{2+}$	455 nm (17,220) 346 nm (25,034) 282 nm (58,376)	608 nm	55/ 66	0.028	3.7[e], 8.0	1.5[e], 8.0
$[Ru(bpy)_2(picNH_2)]^{2+}$	460 nm (15,917) 333 nm (32,737) 285 nm (71,344)	611 nm	379/ 550	0.035	1.5, 8.8	3.2, 9.1

Table 3.4: Optical and Acid-Base properties of Ruthenium (II) Complexes Synthesised.

[a] Measured in acetonitrile at room temperature at concentrations of 20 x 10^{-6} M.

[b] Monoexponential decays measured in aerated/degassed acetonitrile at room temperature

[c] Photoluminescent quantum yield (ϕ) measured in degassed acetonitrile at room temperature, using $[Ru(bpy)_3]^{2+}$ as a standard.

[d] Ground (pKa) and excited state (pKa) values, measured in PBS buffer solution at room temperature. (standard deviation calculated +/- 0.1 units). [e] has a larger associated pKa calculation standard deviation.*

3.4.4 Characterisation of Ruthenium (II) Complexes

3.4.4.1 Absorbance

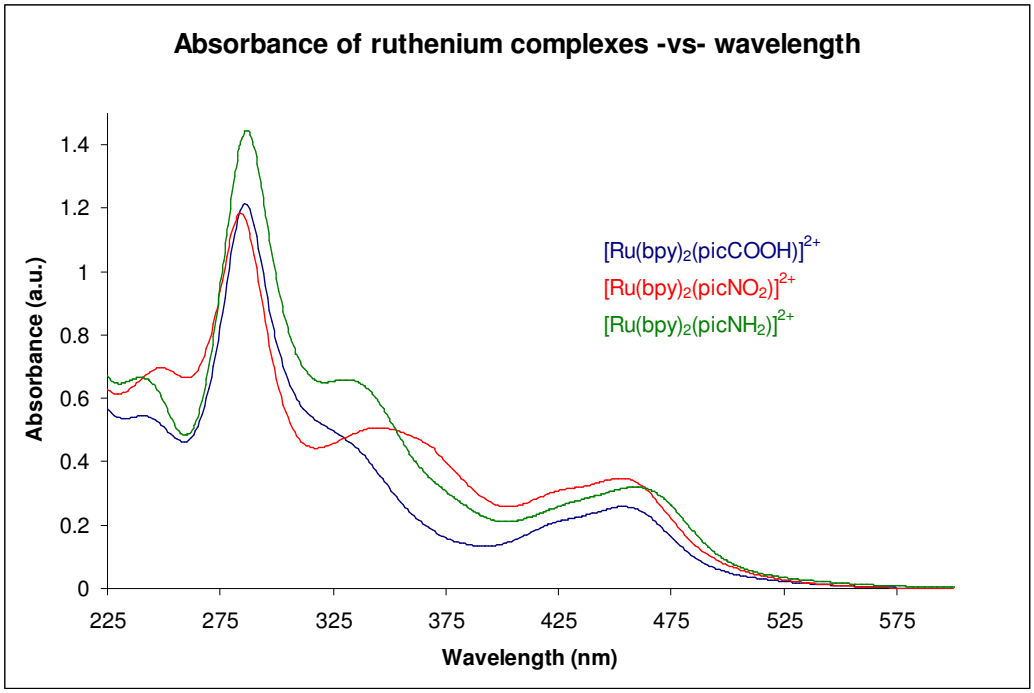

Figure 3.8: Overlaid absorbance spectra of ruthenium (II) polypyridyl complexes synthesised (20 x 10^{-6}M) in acetonitrile solution.

Figure 3.8 above shows the overlaid absorbance spectra for the ruthenium (II) polypyridyl complexes synthesised. The UV-vis spectra of all three complexes are distinguished by a ruthenium dπ to ligand π* MLCT transition at 457 nm (carboxyl), 455 nm (nitro) and 460 nm (amino) respectively. For the amino complex there is ca. 4 nm shift to a longer wavelength in this transition when compared to the others, suggesting that the amino ancillary ligand is a slightly better σ-donating ligand.[30] There is also evidence of a further MLCT transition within the complexes at around 245 nm.

The strong absorbance band at approximately 285 nm may be assigned to π-π* transitions within the bpy ligands, whereas the shoulder at approximately 330 nm is attributed to the π-π* transitions of the [pic-R] ligands containing the two ionisable protons on the imidazole ring as this transition exhibits a strong pH dependence, vide infra. The benzimidazole spacer has little effect on the absorbance spectra of the complex as the energies and absorbance profile of these transitions are almost identical to that of $[Ru(bpy)_3]^{2+}$ and $[Ru(bpy)_2(phen)]^{2+}$, which indicates a weak interaction between ruthenium bis-bipyridyl and benzimidazole moieties.[25, 40]

However, the absorbance peak at 346 nm for the nitro functionalised complex, assigned to the ILCT π-π* transitions of the $[picNO_2]$ ligand, has shifted 16 nm to a longer wavelength when compared to $[Ru(bpy)_2(picCOOH)]^{2+}$. This confirms that this is a π-π* transition of the $[picNO_2]$ ligand. It is known that the nitro substituent has a more pronounced effect on the HOMO-LUMO band gap of a molecule. The dπ-π* and π-π* interactions permit hyperconjugation between the electronic structures and aromatic rings causing a decrease in the energy gap. This is may be seen by a decrease in the HOMO-LUMO energy gap resulting in shift to longer wavelengths.[41, 42]

3.4.4.2 Emission Properties

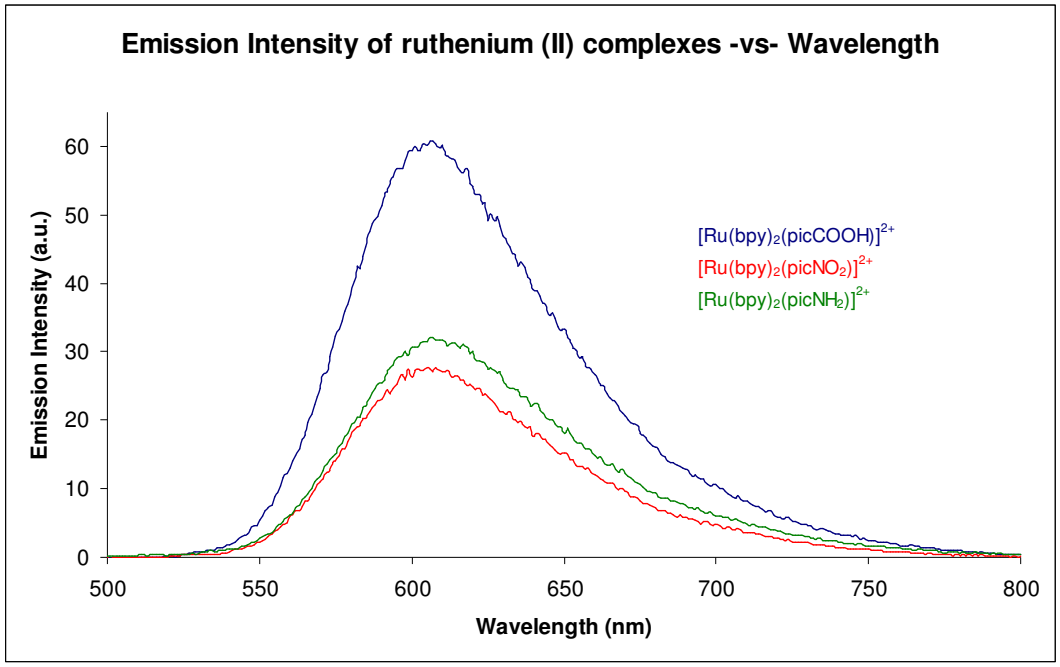

Figure 3.9: Overlaid emission spectra of 20 x 10^{-6}M acetonitrile solutions of $[Ru(bpy)_2(picCOOH)]^{2+}$ (excited at 457 nm), $[Ru(bpy)_2(picNO_2)]^{2+}$ (excited at 455 nm) and $[Ru(bpy)_2(picNH_2)]^{2+}$ (excited at 460 nm). Slit widths: 5 nm. Samples are not absorbance matched.

The emission spectrum of $[Ru(bpy)_2(picCOOH)]^{2+}$, in Figure 3.9, exhibits a maximum emission at 608 nm when excited into the MLCT absorbance band at 457 nm with a quantum yield of 0.068 in aerated acetonitrile. This complex also exhibits the highest quantum yield of the three ruthenium complexes synthesised. The emission decays follow monoexponential kinetics with a lifetime of 158 +/- 2 ns in aerated and 502 +/- 4 ns in degassed acetonitrile solutions. The increase in lifetime in absence of oxygen is also indication of the triplet MLCT character of the emission.[1] Unusually, this lifetime dramatically increases in degassed aqueous PBS buffer solutions, compared with acetonitrile, with luminescent lifetimes of 878 +/- 6 ns at pH 1.0, 811 +/- 4 ns at pH 6.9 and 526 +/- 4 ns at pH 12.0. The longer lifetimes in aqueous media may be explained by stabilisation of the emissive ^{3}MLCT of the carboxyl complex as a result of H-bonding between the solvent and complex. The decrease in lifetimes of the deprotonated species in aqueous media may be due to the extension of the π system across the imidazolate or dissipation of the excited ruthenium-bpy state energy into low

lying less radiative ruthenium-[picCOOH] acceptor states on the imidazolate ligand, as determined by resonance Raman spectroscopy later in the chapter.[24] Many other metal complexes exhibit a decrease in lifetimes when measured in aqueous solution and this demonstrates the importance of H-bonding in controlling the properties of the complex.[24]

The emission spectrum of $[Ru(bpy)_2(picNO_2)]^{2+}$ has a maximum emission at 608 nm when excited at 455 nm with a quantum yield of 0.028 in aerated acetonitrile. The emission decays once again follow monoexponential kinetics with a lifetime of 55 +/- 2 ns in aerated acetonitrile and 66 +/- 3 ns in degassed acetonitrile. The low sensitivity to oxygen is typical of shorter lived complexes. In stark contrast to $[Ru(bpy)_2(picCOOH)]^{2+}$, the lifetime dramatically decreases in acetonitrile and in degassed aqueous PBS buffer solutions, with a lifetime of 22 +/- 0.4 ns at pH 1.0, 6 +/- 0.2 ns at pH 6.9 and 7 +/- 0.3 ns at pH 12.0. It is thought that the H-bonding between the carboxylate and water (or some constituent within the PBS) brings about a more stabilised excited energy state by the polar solvent giving rise to the dramatic increase in lifetimes. This stabilisation of the excited state is further supported by a slight red shift (4 nm) in the aqueous emission spectrum of $[Ru(bpy)_2(picCOOH)]^{2+}$ at higher pH values. Of the three ruthenium complexes synthesised $[Ru(bpy)_2(picNO_2)]^{2+}$ displayed the lowest aqueous emission intensity and is also the most sensitive to solvent. This is discussed in further detail in Section 3.4.4.2.1 below.

The emission spectrum of $[Ru(bpy)_2(picNH_2)]^{2+}$ exhibited a maximum at 611 nm when excited into the MLCT band at 460 nm and a quantum yield of 0.035 in aerated acetonitrile. This slight shift to a longer wavelength of emission is explained by the electron donating nature of the amino substituent causing a slight decrease in the LUMO for the $[picNH_2]$ ligand. The emission decays, again, follow monoexponential kinetics with a lifetime of 379 +/- 4 ns in aerated acetonitrile and 550 +/- 4 ns in degassed acetonitrile. The lifetime increases in degassed aqueous PBS buffer solutions with a lifetime of 905 +/- 8 ns at pH 1.0, 543 +/- 6 ns at pH 6.9 and 580 +/- 6 ns at pH 12.0. This once again may be attributed to the solvation of the amine functionality in aqueous solvent. These values are comparable to the $[Ru(bpy)_2(picCOOH)]^{2+}$ complex and a similar decrease in lifetimes also accompanies a decrease in emission intensity at higher pH values.

3.4.4.2.1 Solvatochromism

Solvatochromism may be described as the changes in the absorption and emission characteristics of a chromophore brought about by the solvent environment. Charge-transfer transitions in metal complexes are sensitive to solvents as the separation of charge is expected to induce dynamics in the solvent itself. This is due to the changes in the local electric field associated with the solute following absorption of a photon.[43] Solvent effects on electronic spectra may be complicated and can include; a broadening of the spectral band, a change in intensity of absorption/emission (ε) and the change in the shape of a band which is related to the various rotational and vibrational energy levels within the molecule. Specific solute-solvent interactions are known to play an important role in the optical and thermal electron transfer process involving metal complexes and these may influence both the redox potentials and photophysics significantly.[44]

As illustrated in Figures 3.10 and 3.11, $[Ru(bpy)_2(picNO_2)]^{2+}$ shows a strong solvent dependence in it's absorption and emission spectra respectively. The polar protic solvent of methanol induces the most drastic change in its absorbance spectrum with a red shift in the π-π* [$picNO_2$] transition from 347 nm to 378 nm. This is attributed to the hydrogen bonding interactions between complex and solvent molecules leading to the efficient stabilisation of the polar charge transfer state. However, this effect is relatively weak for other solvents and the polar compound is insoluble in non-polar solvents.

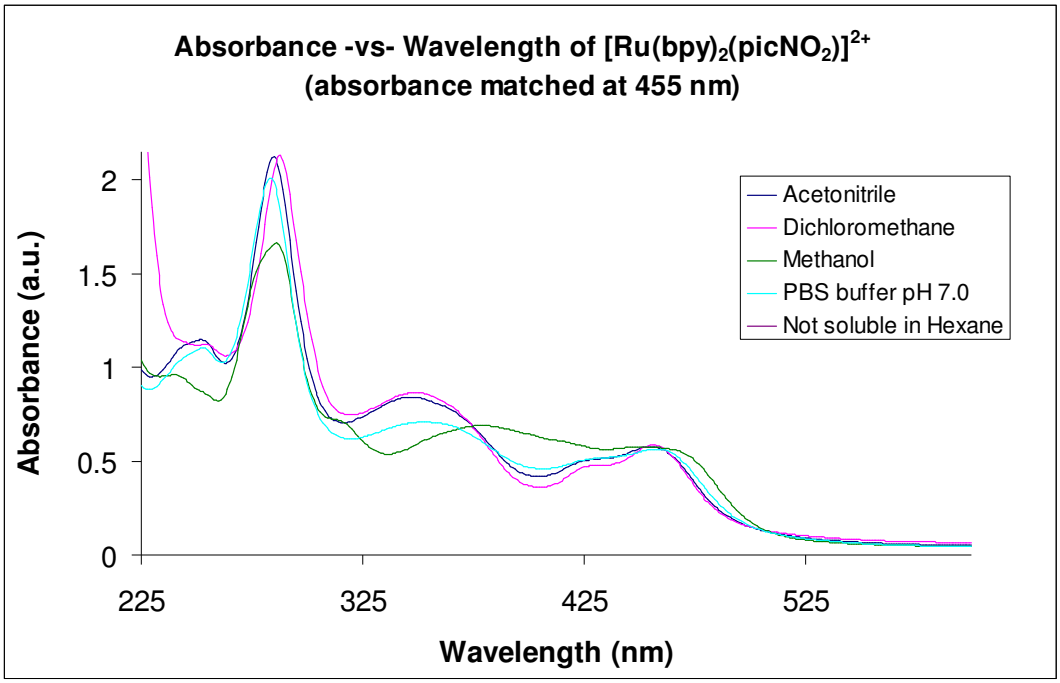

Figure 3.10: Absorbance spectra of $[Ru(bpy)_2(picNO_2)]^{2+}$ in different solvents. All spectra are absorbance matched at 455 nm.

Following excitation it is known that solvent molecules may reorient and relax around the excited state complex which proceeds in lowering the energy of the excited state.[15, 45] $[Ru(bpy)_2(picNO_2)]^{2+}$ shows significant differences in emission intensities between polar protic and polar aprotic solvents (Figure 3.11). This is attributed to an alternative non-radiative deactivation pathway via solvent relaxation from the triplet MLCT excited energy state provided by the polar protic solvent.

Emission spectra are generally more sensitive to solvent effects than absorbance spectra. This is because absorption occurs at a timeframe too short for motion of the solvent to have an effect. In contrast, the emitting excited state complex is exposed to the relaxed solvent environment, whose solvent molecules may be orientated around the dipole moment of the excited state luminophore.[45] Nitro functionalised systems tend to have higher internal conversion rates as a result of mixing of vibronic states as well as solvent interactions that effectively quenches luminescence.[46]

For Figure 3.11 all $[Ru(bpy)_2(picNO_2)]^{2+}$ samples were absorbance matched at 455 nm. The strong solvent dependence on emission intensity observed would lend support to the use of this dye as a possible polarity sensor for future work and the nitro complex has already been used before as an efficient anion sensor.[29] There are unexpected considerable differences in the emission intensities of the nitro functionalised complex in dichloromethane and acetonitrile. As previously explained, all solvents were used as received and any trace elements of water, in particular in the acetonitrile solution, may explain its significantly lower emission intensity.

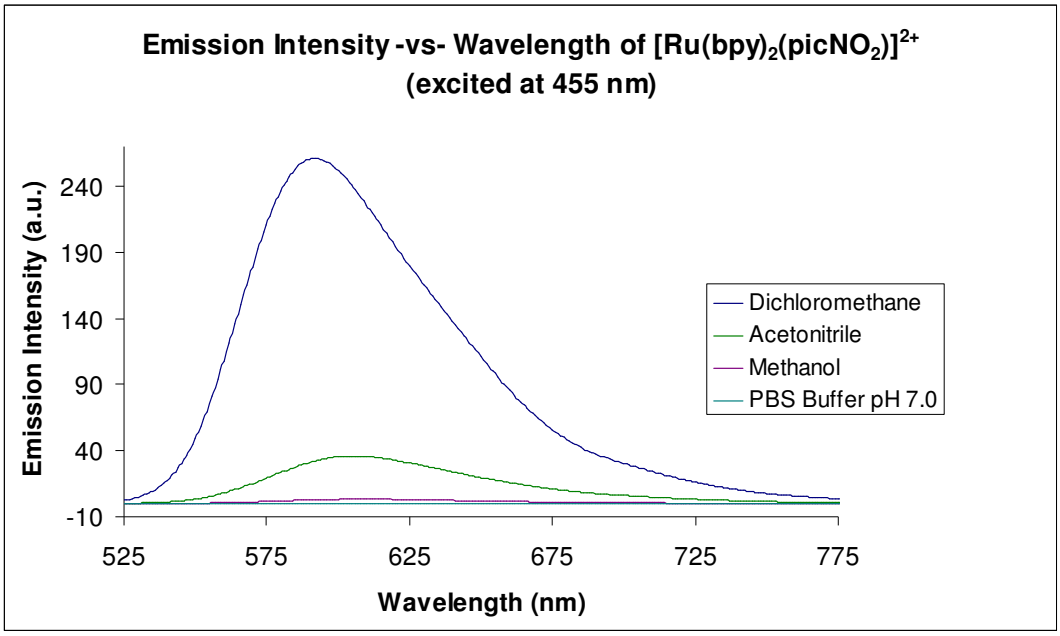

Figure 3.11: Relative emission intensities of $[Ru(bpy)_2(picNO_2)]^{2+}$ in various solvents. All samples were absorbance matched and excited at 455 nm. Slit widths: 5 nm.

This poor luminescence of $[Ru(bpy)_2(picNO_2)]^{2+}$ in aqueous solution has been reported previously.[21] In addition, merely changing the position of the nitro substituent on the phenyl ring plays a critical role in the emission of the complex itself.[21] When the nitro group is located in the ortho-position or para-position, the compound's luminescence is almost completely quenched. However, if the nitro group is located in the meta-position the complex is found to be brightly luminescent. This decrease in luminescence is usually explained by the capture of the photoexcited electron by the strong electron withdrawing nitro group. The electron withdrawing

ability of the ortho- and para-nitro substituent is greater than that of the meta-substituent and results in a deactivation to the ground state by non-emissive pathways. Shi *et al.*[21] proposed that this may be explained more effectively by the law of polarity alteration where the idea of polarity interface as well as the calculated net charge populations is applied.

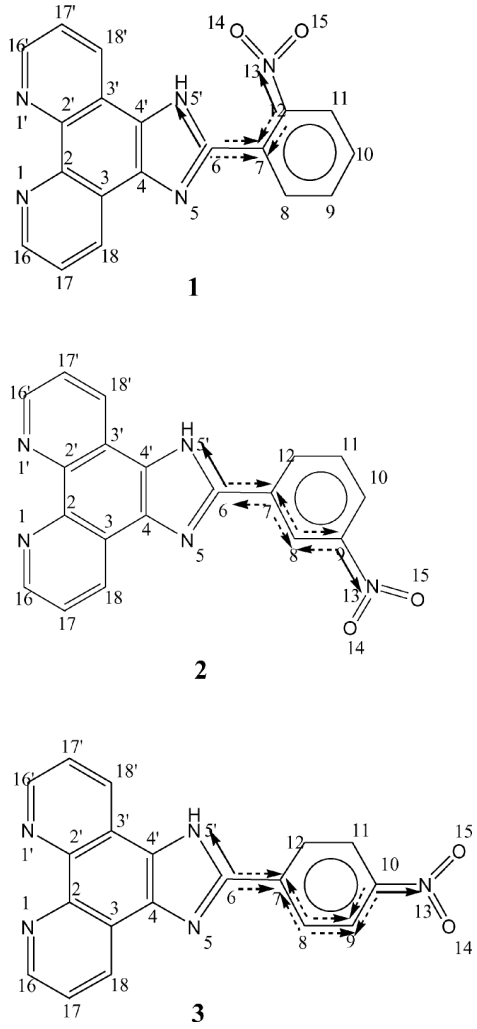

Figure 3.12: Schematic diagram of [picNO$_2$] ligand with nitro substituent at 1) ortho- 2) meta- and 3) para- positions of the phenyl ring. The arrow heads show the directions of the moving negative charges.[21]

As illustrated in Figure 3.12 the direction interferences for the poorly emissive ortho (1) and para (3) functionalised ligands are the same and as a result the polarity of every bond is strengthened from N13-N5. On the other hand, for the luminescent meta functionalised species (2) the direction interferences are opposing in nature and this leads to a weakening in the bond polarity from N13-N5. As a result the electron withdrawing ability of the ortho- and para-substituted ligands is greater. This provides a reasonable explanation for the differences in luminescent intensities between compounds based solely on the position of the substituent. Neither the carboxyl nor amino functionalised complexes show such sensitive emission characteristics according to their substituent locations, presumably because their bond polarities are not altered significantly.

3.4.4.3 pH Dependence Studies

3.4.4.3.1 $[Ru(bpy)_2(picCOOH)]^{2+}$

For the protonated species $[Ru(bpy)_2(picCOOH)]^{3+}$ the LC [picCOOH] π-π* transition at 330 nm is slightly shifted towards a shorter wavelength compared with the deprotonated species as shown in Figure 3.13. This suggests that formation of the carboxylate leads to an increase in the HOMO-LUMO energy gap. This transition also begins to overlap with the bpy π-π* transition, which itself has shifted from 284 to 280 nm upon protonation. The MLCT region does not change wavelength upon protonation, however, the relative intensities of the contributing bands do alter. This decreasing relative intensity of the band at 458 nm has been described in previous reports as evidence of a benzo-carboxylate to phenanthroline ILCT (interligand charge transfer).[24]

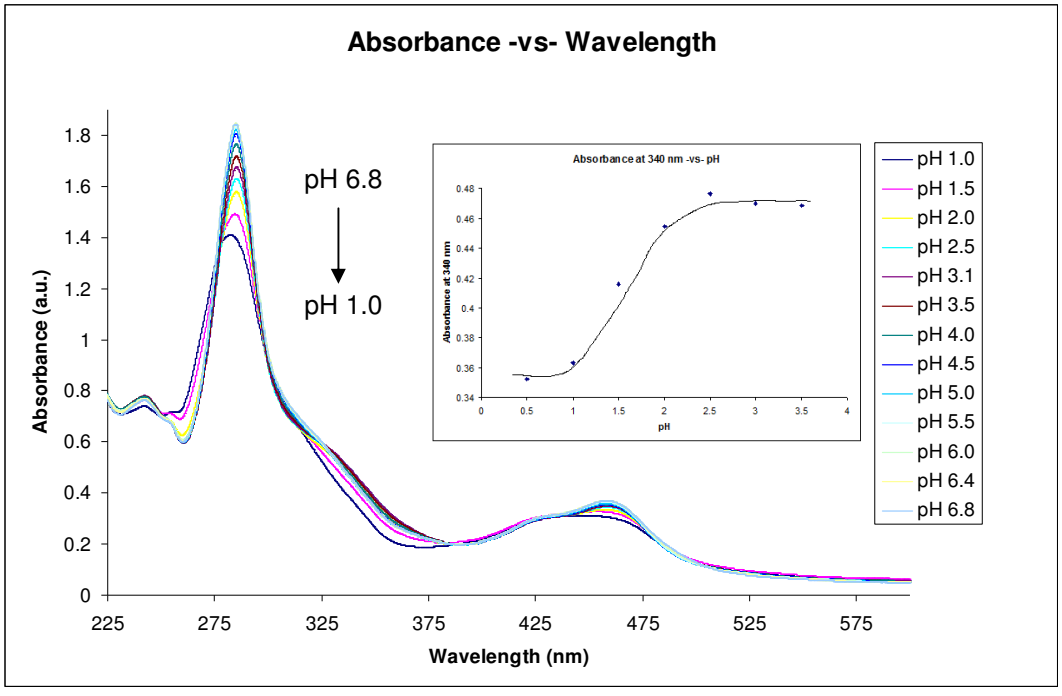

Figure 3.13: Absorbance spectra of 20 x 10^{-6} M (15 cm^3) $[Ru(bpy)_2(picCOOH)]^{2+}$ in PBS buffer solution, upon addition of µl aliquots of percholric acid solution. (inset) pH titration curve of $[Ru(bpy)_2(picCOOH)]^{2+}$ in PBS solution, monitoring the changes in absorbance at 340 nm upon addition of perchloric acid.

Formation of the imidazolate $[Ru(bpy)_2(picCOOH)]^0$ at pH > 8.7 (Figure 3.14) sees red shift in the MLCT to 468 nm, LC [picCOOH] π-π* transition to 340 nm and bpy π-π* transition to 287 nm. This suggests a more extended π system which is consistent with deprotonation of the imidazole leading to an enhanced electronic communication between the phenanthroline and imidazole ligand components. These effects have been previously noted in imidazole and triazole ligands.[24]

The spectral changes brought about by a change in pH have a relatively small effect on the MLCT transition and are mostly confined to the ligand, suggesting that the LUMO for the MLCT transition lies mainly on the bipyridine ligands. This is found to be the case in calculating its pKa/pKa* values and it is also consistent with the excited state pKa* studies on comparable benzimidazole complexes.[25, 47]

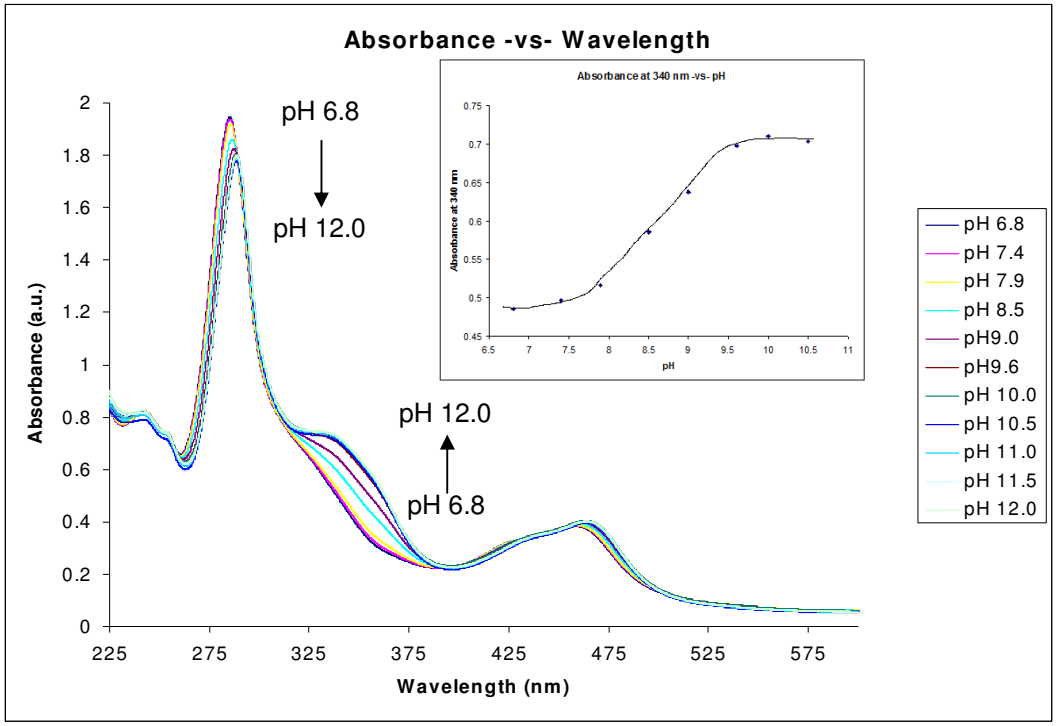

Figure 3.14: Absorbance spectra of 20 x 10^{-6} M (15 cm^3) $[Ru(bpy)_2(picCOOH)]^{2+}$ in PBS buffer solution, upon addition of μl aliquots of sodium hydroxide solution. (inset) pH titration curve of $[Ru(bpy)_2(picCOOH)]^{2+}$ in PBS solution monitoring the changes in absorbance at 340 nm upon addition of sodium hydroxide solution.

The ground state pKa values of the imidazole ligand were determined by monitoring the spectral changes of the absorbance spectrum at 340 nm over a pH range of 1.0-12.0 (Figures 3.13 inset and 3.14 inset). The data was then fitted to a plot of absorbance at 340 nm -vs- pH and the point of inflection was determined by differentiation. This yielded pKa values of 1.5 +/- 0.1 and 8.5 +/- 0.1 respectively. Protonation of the imidazole, to give the imidazolium, only occurs at very low pH values and as a result only an estimate of this pKa value may be given. This is thought to be a result of the coulombic repulsion between the positively charged imidazolium ring and the positive metal centre.[24] Furthermore, as discussed in the introduction to Chapter 3 the pKa values are also solvent dependent. From the pH titration curve it is the $[Ru(bpy)_2(picCOOH)]^{2+}$ complex that is the major species in solution between pH 4-7, whereas, the $[Ru(bpy)_2(picCOOH)]^{+}$ complex dominates between pH 10-12. Interestingly, the pH dependence of the visible MLCT region is minimal under these changes in pH. This is important to note because it is usually between the wavelengths 405-488 nm that are exploited for excitation in both FLIM and confocal microscopy measurements.

Protonation of the imidazole on the ancillary ligand has a large impact on both its luminescent intensity and emission wavelength. Both $[Ru(bpy)_2(picCOOH)]^{3+}$ and $[Ru(bpy)_2(picCOOH)]^{+}$ exhibited red shifted emission maxima when compared to $[Ru(bpy)_2(picCOOH)]^{2+}$. It is thought in the case of $[Ru(bpy)_2(picCOOH)]^{3+}$ that the red shift may be a result of a stabilising electrostatic interaction between the MLCT generated bpy anion radical and the extra positive charge of the imidazolium since the shift is greater than that observed in the equivalent absorbance spectra.[24]

Figures 3.15 and 3.16 below illustrate the pH dependence on the emission spectrum of the dye in aqueous PBS buffer solution. In acidic media the spectral changes are more dramatic with a red shifted emission maximum from 605 nm to 624 nm at pH 1.0 upon the formation of the imidazolium species. It is also proposed that the increase in the shoulder in the absorbance of the MLCT, assigned to ILCT of benzo-carboxylate to phenanthroline, may cause self absorption of emitted radiation through energy transfer.[24] This would account for the loss of emission intensity without a significant decrease in luminescent lifetimes as seen for this complex at low pH values. There is also a loss of luminescent intensity and red shift in emission maximum from

604 nm to 613 nm when the complex is deprotonated at pH 12.0 as a result of the extended π delocalisation across the complex. The excitation wavelengths used for the pH dependence studies corresponds to (or is as close as possible to) the isosbestic point in the MLCT region of the absorbance spectra for all the complexes.

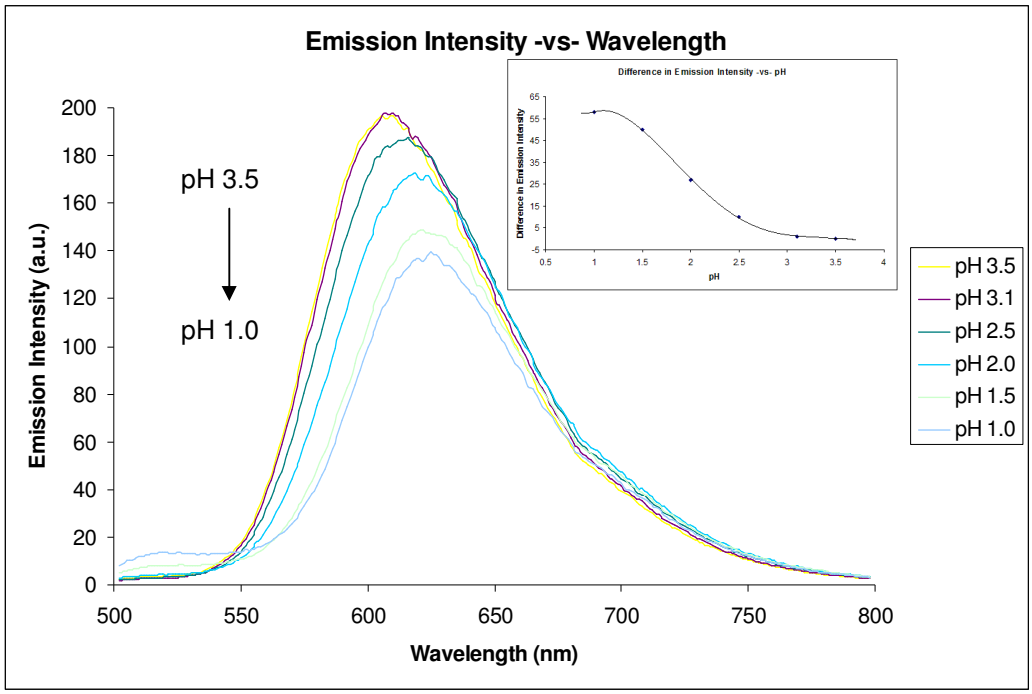

Figure 3.15: Emission spectra of 20 x 10^{-6} M (15 cm^3) $[Ru(bpy)_2(picCOOH)]^{2+}$ in PBS buffer solution, upon addition of µl aliquots of perchloric acid solution. (437 nm excitation wavelength, slit widths: 5 nm). (inset) pH titration curve of $[Ru(bpy)_2(picCOOH)]^{2+}$ in PBS solution monitoring the difference in emission intensity (excited at 437 nm) –vs- pH upon addition of perchloric acid solution.

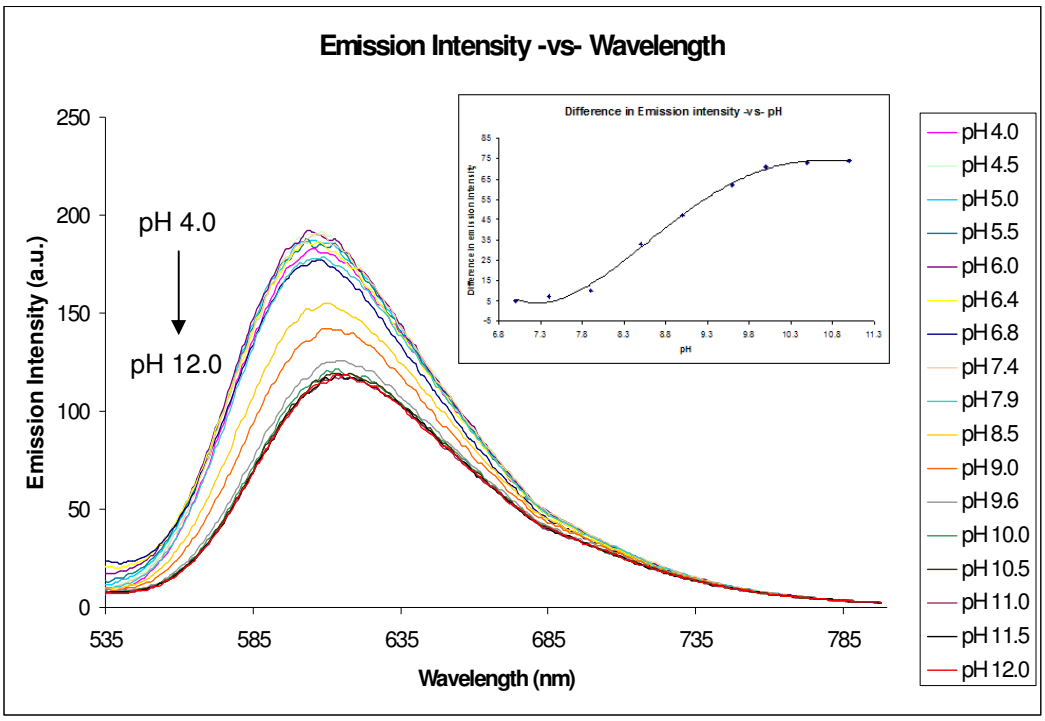

Figure 3.16: Emission profile of 20 x 10^{-6} M (15 cm^3) $[Ru(bpy)_2(picCOOH)]^{2+}$ in PBS buffer solution, upon addition of µl aliquots of sodium hydroxide solution. (448 nm excitation wavelength, slit widths: 5nm). (inset) pH titration curve of $[Ru(bpy)_2(picCOOH)]^{2+}$ in PBS solution monitoring the difference in emission intensity (excited at 448 nm) –vs- pH upon addition of sodium hydroxide solution.

The excited state pKa* values were calculated using the maximum emission intensity to plot titration curves (Figures 3.15 inset and 3.16 inset) and were fitted to an expression for the Förster cycle in Equation 3.10:

$$pKa^* = pH_i + \log(\tau_{HB} / \tau_B^-) \text{.....Eq 3.10}$$

where pH_i is the point of inflection on the pH emission titration plot, τ_{HB} is the lifetime of the protonated species and τ_B^- is the lifetime of the deprotonated species. The excited state pKa* values were calculated to be 2.2 +/- 0.1 and 8.7 +/- 0.1 respectively for the (de)protonation of the nitrogen moieties on the ancillary ligand. These values are similar to those calculated for ground state pKa values suggesting that the excited state lies on the bpy ligands of the complex. As the emissive state is one of charge transfer,

one of the ligands carries the excited electron. If the excited electron was located on the [picCOOH] ligand, because of the nominal charge induced by the excited state, it would be considered to be more basic than that of the corresponding ground state value by as much as 3 pH units.[31, 48] These pKa and pKa* results are in good agreement with values determined previously.[25] In this case, the ground state pKa values were estimated to be 1.3 and 8.4 and the excited state pKa* values were calculated to be equal to 1.3 and 8.5 respectively. Any slight variation in the pKa values may be explained by the different PBS or ionic strength of the buffers used which will have an effect on pKa values. All absorbance and emission spectral changes are fully reversible between pH 0.5 to pH 12.0 indicating that the compound is stable at extreme pH values and does not undergo chemical decomposition.

3.4.4.3.2 $[Ru(bpy)_2(picNO_2)]^{2+}$

To date, the pKa/pKa* values have not yet been reported for the nitro and amino functionalised ruthenium (II) complexes. Due to the poor aqueous emission characteristics of $[Ru(bpy)_2(picNO_2)]^{2+}$ the spectral changes brought about by varying the pH was difficult to assess when compared to the other ruthenium complexes synthesised. However, changing the solvent to acetonitrile for example, made it very difficult to control the pH of the solution because it fluctuated significantly. Nevertheless, the absorbance profile changed in going from basic to acidic media in aqueous conditions but without evidence of an isosbestic point is shown in Figure 3.17. The formation of a precipitate of the nitro complex within the solution at lower pH values leads to changes in the absorbance baseline. Protonation of the nitro group leads to a redistribution of charge and many resonance structures within the $[picNO_2]$ ligand, promoting hydrogen bonding between molecules and the possible formation of dimers in solution. It has been noted before that nitro groups display a significant degree of intermolecular self-association due to π-stacking enhancement between molecules at lower pH.[46] Unlike the other ruthenium complexes, all spectral changes of $[Ru(bpy)_2(picNO_2)]^{2+}$ were confirmed to be irreversible and the initial absorbance and emission profile intensities were not re-established on restoring neutral pH [data not shown] due to the formation of a precipitate in solution.

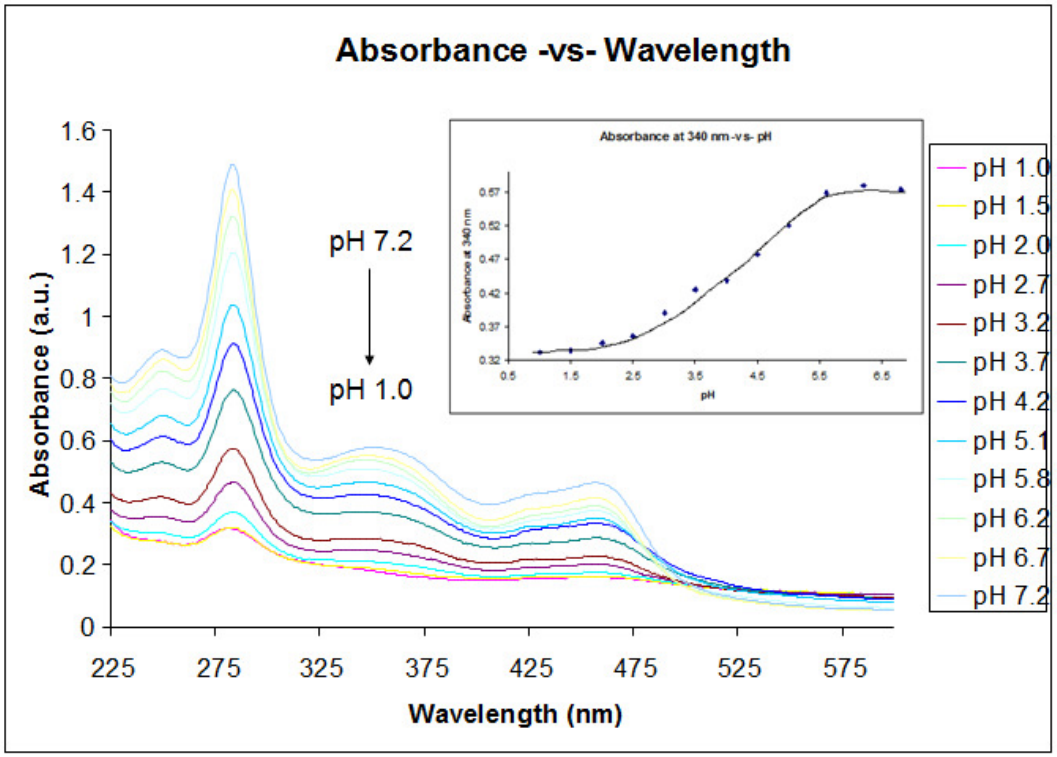

Figure 3.17: Absorbance of 20 x 10^{-6} M (15 cm^3) $[Ru(bpy)_2(picNO_2)]^{2+}$ in PBS buffer solution, upon addition of µl aliquots of perchloric acid solution. (inset) pH titration curve of $[Ru(bpy)_2(picNO_2)]^{2+}$ in PBS solution, monitoring the changes in absorbance at 340 nm upon addition of perchloric acid solution.

Upon increasing pH from neutral (Figure 3.18), the absorbance spectra are better behaved but are considerably different to that seen previously for the carboxyl functionalised complex. Of particular interest are the regions of the $[picNO_2]$ π-π* transition and the MLCT transition. Upon formation of the imidazolate the absorbance maximum shifts from 357 nm to form an isobestic point at 368 nm. An increase in the absorbance intensity and corresponding red shift in the MLCT peak to 463 nm is attributed to an increased σ-donor ability of the anionic ligand upon deprotonation. Once again at higher pH values it is noted that the relative intensities of the ILCT on the shoulder of the MLCT has increased. Unlike for $[Ru(bpy)_2(picCOOH)]^{2+}$ the MLCT region is strongly influenced by changes in pH.

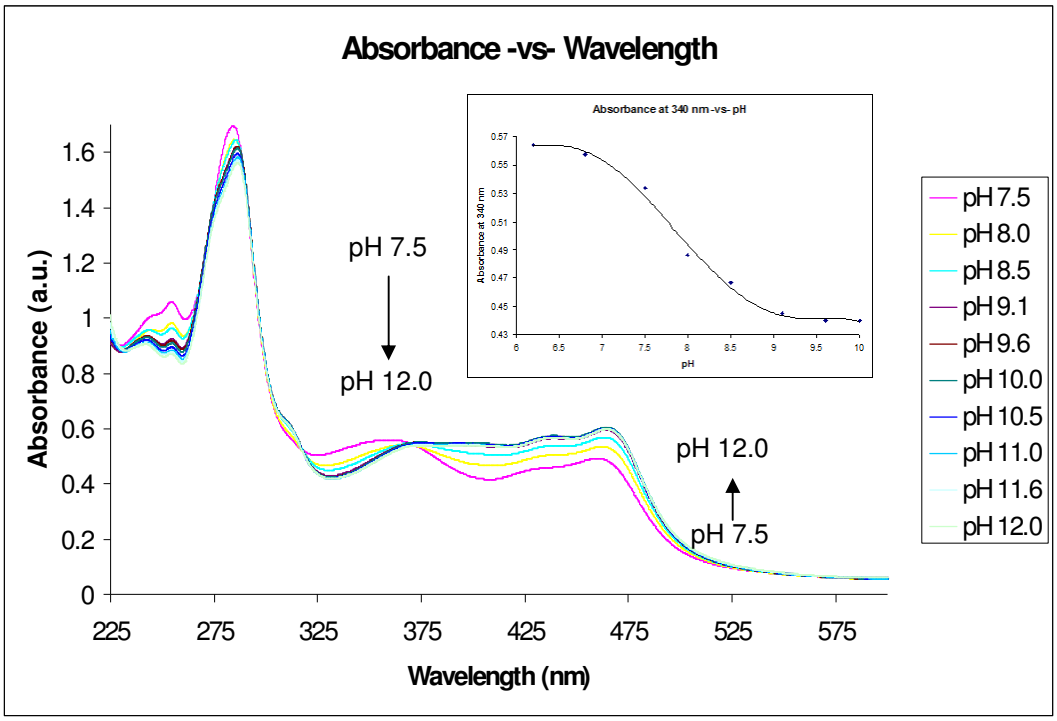

Figure 3.18: Absorbance of 20 x 10^{-6} M (15 cm^3) $[Ru(bpy)_2(picNO_2)]^{2+}$ in PBS buffer solution, upon addition of µl aliquots of sodium hydroxide solution. (inset) pH titration curve of $[Ru(bpy)_2(picNO_2)]^{2+}$ in PBS solution, monitoring the changes in absorbance at 340 nm upon addition of sodium hydroxide solution.

The ground state pKa values of the nitrogen atoms on the benzimidazole ligand were estimated to be equal to 3.7 and 8.0 +/- 0.1 as illustrated in Figures 3.17 (inset) and 3.18 (inset) respectively. However, it is noted that the lower pKa value of 3.7 will have a large associated error as acidification leads to the unavoidable formation of a precipitate of the complex within the solution.

Similar to the luminescence spectra for $[Ru(bpy)_2(picCOOH)]^{2+}$, there is a slight shift in the emission maximum of $[Ru(bpy)_2(picNO_2)]^{2+}$ to longer wavelengths with protonation/deprotonation (Figures 3.19 and 3.20). However, the spectral shifts are not as dramatic. It is proposed, as in the case of $[Ru(bpy)_2(picCOOH)]^{3+}$, that the red shift may be a result of a stabilising electrostatic interaction between the MLCT generated bpy anion radical and the extra positive charge of the imidazolium.

The emission spectrum in the formation of $[Ru(bpy)_2(picNO_2)]^{1+}$ at pH > 8.0 (Figure 3.20) showed little change in the maximum wavelength of emission, which is interesting considering the equivalent absorbance spectrum of $[Ru(bpy)_2(picNO_2)]^{1+}$ showed significant changes upon deprotonation.

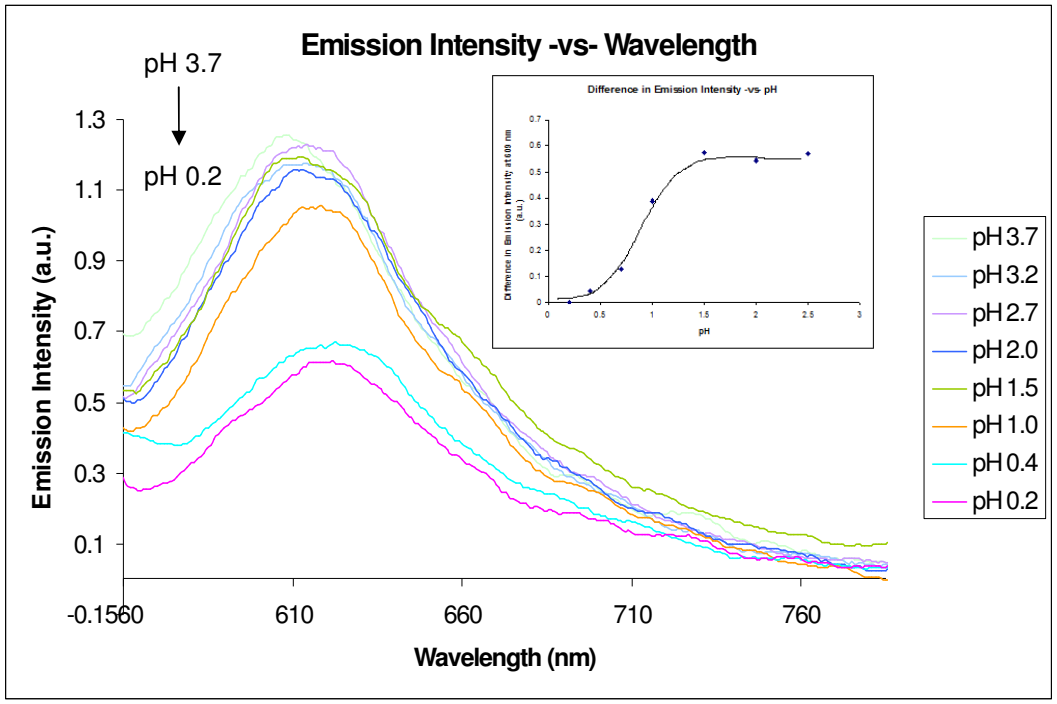

Figure 3.19: Emission spectra of 20 x 10^{-6} M (15 cm^3) $[Ru(bpy)_2(picNO_2)]^{2+}$in PBS buffer solution, upon addition of µl aliquots of perchloric acid solution. (487 nm excitation wavelength, slit widths: 5 nm). (inset) pH titration plot of $[Ru(bpy)_2(picNO_2)]^{2+}$ in PBS solution monitoring the difference in emission intensity (excited at 487 nm) –vs- pH upon addition of perchloric acid solution.

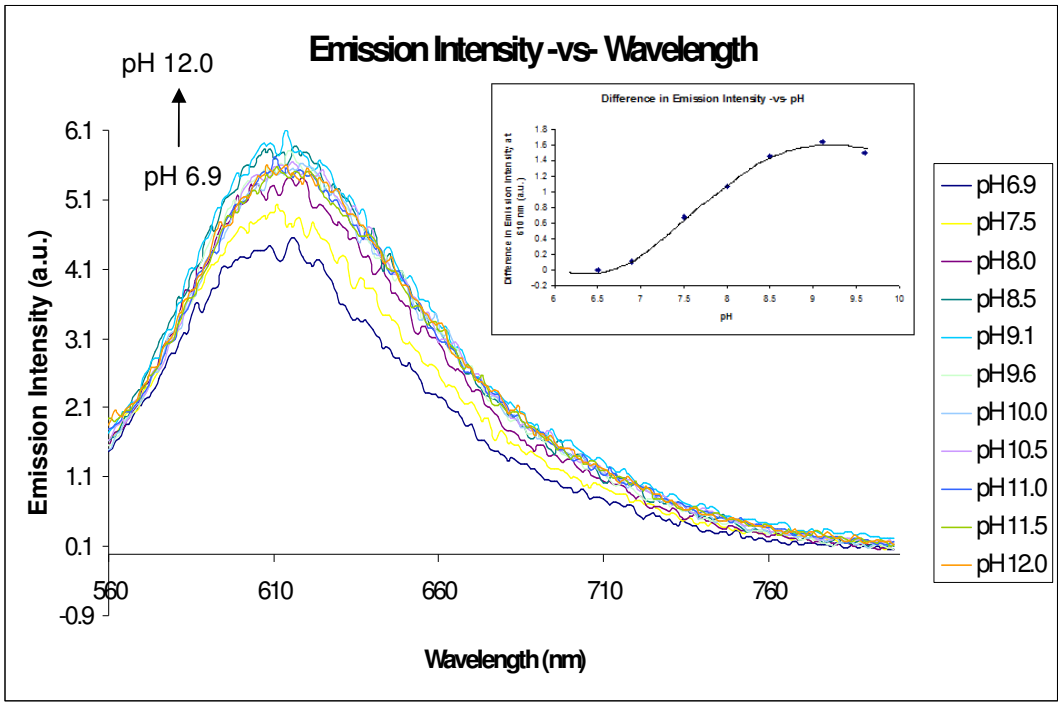

Figure 3.20: Emission spectra of 20 x 10^{-6} M (15 cm^3) $[Ru(bpy)_2(picNO_2)]^{2+}$ in PBS buffer solution, upon addition of µl aliquots of sodium hydroxide solution.(447 nm excitation wavelength, slit widths: 5 nm. (inset) pH titration plot of $[Ru(bpy)_2(picNO_2)]^{2+}$ in PBS solution monitoring the difference in emission intensity (excited at 447 nm) –vs- pH upon addition of sodium hydroxide solution.

The excited state pKa* values of the benzimidazole ligand were calculated to be equal to 1.5 and 8.0 +/- 0.1, respectively, from the graphs in Figures 3.19 (inset) and 3.20 (inset). The excited state pKa* value of 8.0 +/- 0.1 is identical to that of the ground state pKa indicating that once again the excited state lies on the bpy ligands of the complex. Protonation of the second nitrogen on the imidazole gives two significantly different pKa and pKa* values based on the absorption and emission profiles respectively. This reveals a change to the trends seen previously and may suggest that when it is protonated the excited state may lie on the benzimidazole ligand. However, due to precipitation of the protonated nitro complex at low pH, the pKa calculations there are large errors and it may be assumed that the excited state does indeed lie on the LUMO of the bpy ligands. The pKa/pKa* values calculated here are similar to those calculated for the carboxyl functionalised complex, which again supports the assumption that the excited state lies on the bpy ligand of the complexes.

Density functional theory (DFT) calculations performed by Shi *et al.*[21] on this particular nitro complex indicated that the LUMO was located on the bpy ligands. However the pKa values were not reported.

3.4.4.3.3 $[Ru(bpy)_2(picNH_2)]^{2+}$

Changes in absorbance spectra due to variations in pH for the $[Ru(bpy)_2(picNH_2)]^{2+}$ complex (Figures 3.21 and 3.22) are very similar to those of $[Ru(bpy)_2(picCOOH)]^{2+}$. The only exception is relatively smaller changes in absorbance for the bpy π-π* transition following a change in pH. Ground state pKa values were calculated to be 1.5 +/- 0.1 and 8.8 +/- 0.1 as illustrated in Figures 3.21 (inset) and 3.22 (inset) respectively, which are similar to ground state pKa results for the $[Ru(bpy)_2(picCOOH)]^{2+}$ complex. The induced spectral changes are also fully reversible in going from a neutral to basic pH and back again. However interestingly, following acidification approximately 65 % of the emission intensity was lost irreversibly upon returning to a neutral pH.

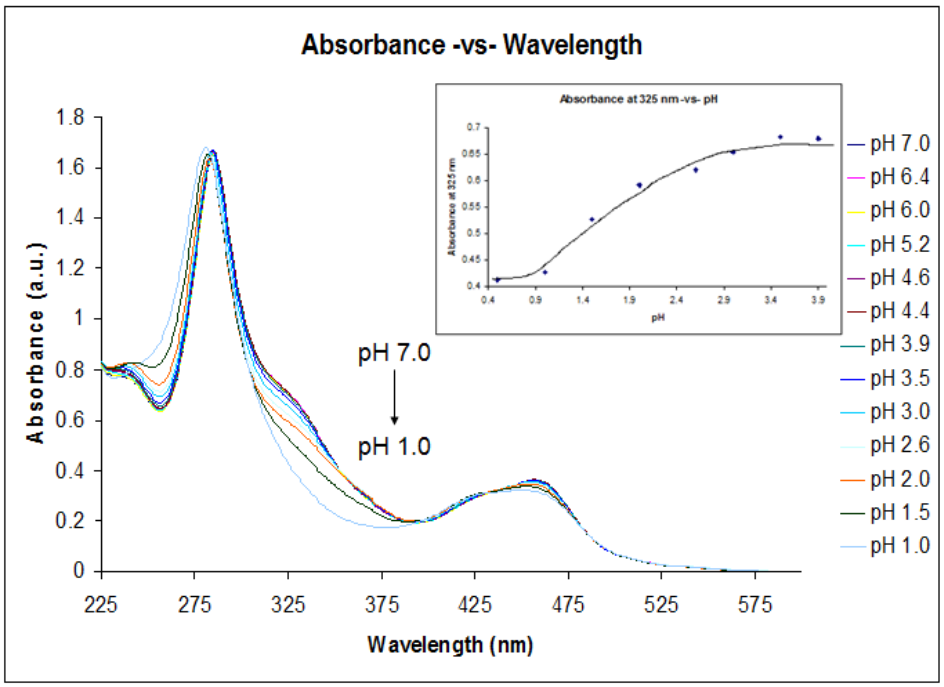

Figure 3.21: Absorbance spectra of 20 x 10^{-6} M (15 cm^3) $[Ru(bpy)_2(picNH_2)]^{2+}$ in PBS buffer solution, upon addition of μl aliquots of perchloric acid solution. (inset) pH titration curve of $[Ru(bpy)_2(picNH_2)]^{2+}$ in PBS solution, monitoring the changes in absorbance at 325 nm upon addition of perchloric acid solution.

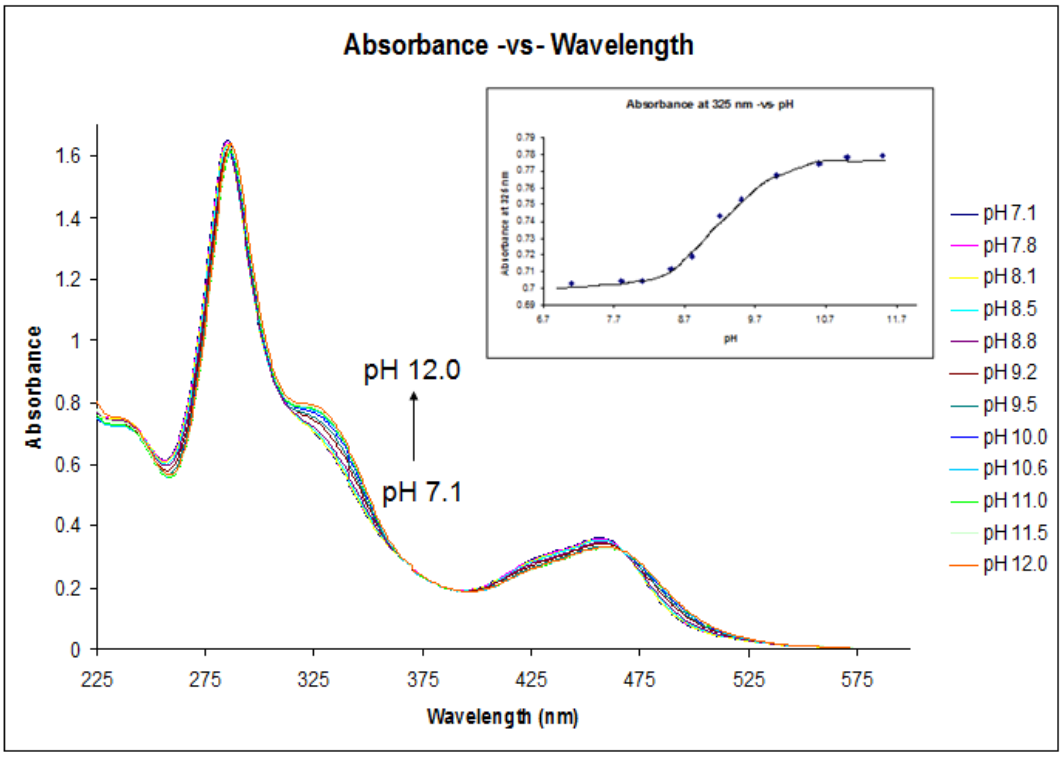

Figure 3.22: Absorbance spectra of 20 x 10^{-6} M (15 cm^3) $[Ru(bpy)_2(picNH_2)]^{2+}$ in PBS buffer solution, upon addition of µl aliquots of sodium hydroxide solution. (inset) pH titration curve of $[Ru(bpy)_2(picNH_2)]^{2+}$ in PBS solution monitoring the changes in absorbance at 325 nm upon addition of sodium hydroxide solution.

The emission of $[Ru(bpy)_2(picNH_2)]^{2+}$ is extremely pH sensitive with a maximum emission at a pH of 1.0 and a minimum emission at a pH of 12.0 as shown in Figures 3.23 and 3.24 respectively. Unlike $[Ru(bpy)_2(picCOOH)]^{2+}$, acidification to form the imidazolium species ($[Ru(bpy)_2(picNH_2)]^{3+}$) sees an increase in emission intensity. However, as seen before for $[Ru(bpy)_2(picCOOH)]^{3+}$, a significant spectral red shift in the emission maximum from 607 nm to 620 nm of the $[Ru(bpy)_2(picNH_2)]^{3+}$ complex is observed. Once again, it is speculated that this is due to the stabilising electrostatic interaction between the MLCT generated bpy anion radical and the extra positive charge of the imidazolium. Deprotonation of the imidazole ring to form $[Ru(bpy)_2(picNH_2)]^{+}$ sees little change in the wavelength of emission maximum. However, in contrast to $[Ru(bpy)_2(picCOOH)]^{+}$ the emission intensity is almost reduced to zero at high pH values (Figure 3.24). Any changes in the protonation state of the amino terminal functionality were not observed in the acid-base titration experiments.

The pKa of the NH_2 group is approximately 9.9 and it is speculated that the lack of an observed pKa may be as a result of its involvement in the solvation of the $[Ru(bpy)_2(picNH_2)]^{2+}$ complex.

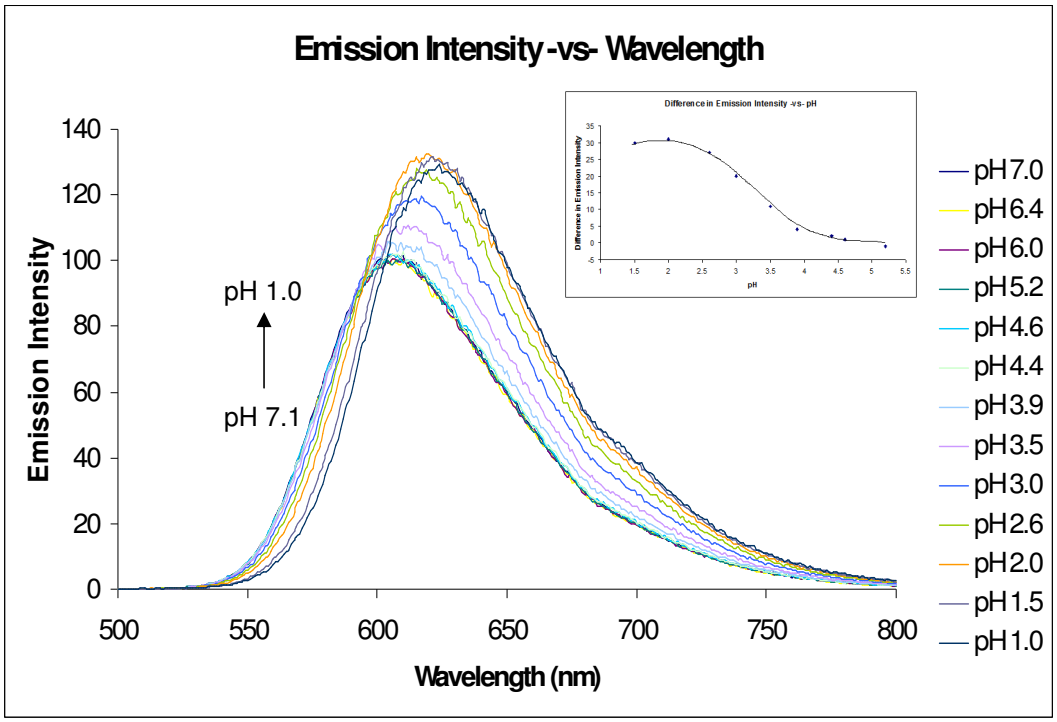

Figure 3.23: Emission spectra of 20 x 10^{-6} M (15 cm^3) $[Ru(bpy)_2(picNH_2)]^{2+}$ in PBS buffer solution, upon addition of µl aliquots of perchloric acid solution. (440 nm excitation wavelength, slit widths: 5 nm). (inset) pH titration curve of $[Ru(bpy)_2(picNH_2)]^{2+}$ in PBS solution monitoring the difference in emission intensity (excited at 440 nm) –vs- pH, upon addition of perchloric acid solution.

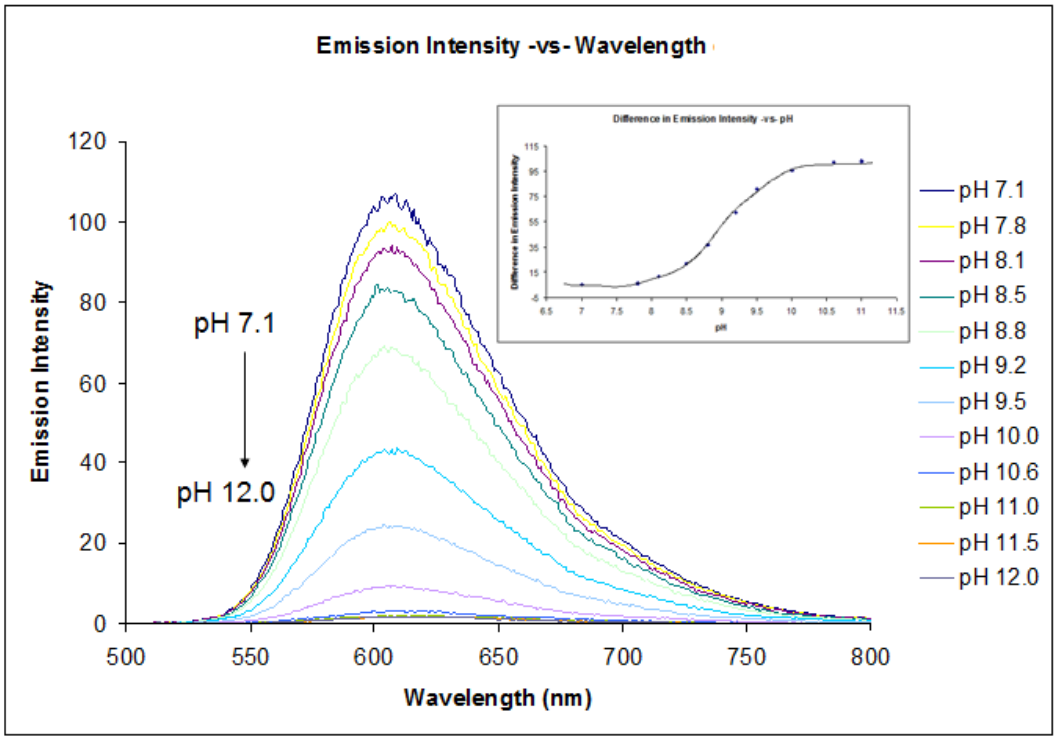

Figure 3.24: Emission spectra of 20 x 10^{-6} M (15 cm^3) $[Ru(bpy)_2(picNH_2)]^{2+}$in PBS buffer solution, upon addition of µl aliquots of sodium hydroxide solution. (467 nm excitation wavelength, slit widths: 5 nm). (inset) pH titration curve of $[Ru(bpy)_2(picNH_2)]^{2+}$ in PBS solution monitoring the difference in emission intensity (excited at 467 nm) –vs- pH, upon addition of sodium hydroxide solution.

The excited state pKa* values were calculated to be 3.2 +/- 0.1 and 9.1 +/- 0.1 as shown in Figures 3.23 (inset) and 3.24 (inset) respectively. This is the largest difference calculated between pKa and pKa* values for protonation of the complex and may be explained by the more efficient electron donating ability of the amino functionalised ligand. This causes an increase in the basicity of the ligand, thus, making it easier to protonate. However, both ground state pKa and excited state pKa* values are within 3 pH units of each other suggesting that the excited state remains on the bpy ligands. This has been the trend seen for all three ruthenium (II) complexes irregardless of the coordinated ancillary ligand.

3.4.4.4 Electrochemistry – Cyclic Voltammetry

The redox behaviour of the three ruthenium (II) polypyridyl complexes synthesised were investigated by cyclic voltametry and their redox potentials are shown in Table 3.5 below. The electrochemistry of $[Ru(bpy)_2(picNO_2)]^{2+}$ and $[Ru(bpy)_2(picNH_2)]^{2+}$ has not been reported previously.

Compound	***Metal-centred redox potential (V)***	***Ligand based redox potentials (V)***
$[Ru(bpy)_2(picCOOH)]^{2+}$	+1.32 (r)	-0.72 (qr) -1.30 (qr)*, -1.61 (r)* -1.74 (qr).
$[Ru(bpy)_2(picNO_2)]^{2+}$	+1.29 (r)	-0.64 (ir), -0.86 (r), -1.22 (qr), -1.40 (ir)*, -1.51 (ir), -1.65 (qr)*.
$[Ru(bpy)_2(picNH_2)]^{2+}$	+1.37 (qr)	-0.67 (ir), -0.84 (r), -1.15 (qr), -1.40 (r)*, -1.57 (r)*, -1.97 (r).

*Table 3.5: Redox properties of ruthenium (II) complexes measured in acetonitrile (containing 0.1M TBA as electrolyte) with a 1.5 mm glassy carbon working electrode and referenced against Ag/AgCl. (r) – reversible reaction, (ir) – irreversible reaction and (qr) – quasi-reversible reaction. All CV's were performed in duplicate with different glassy carbon electrodes, scanning though the range of potentials (multiple scans): 1, 0.50, 0.25 and 0.05 Vs^{-1} respectively. Electrochemistry was conducted using 1 mmol of sample dissolved in 5 cm^3 of dry acetonitrile (HPLC grade, used as received) containing 0.1 M tetrabutylammonium tetrafluoroborate (TBA) as supporting electrolyte. All samples were degassed with nitrogen prior to analysis. * denotes bpy ligand reduction potentials.*

Figure 3.26 below illustrates the cyclic voltammogram for the $[Ru(bpy)_2(picCOOH)]^{2+}$ complex over negative potentials and Figure 3.26 (inset) also shows the well behaved redox couple attributed to the reversible metal centred oxidation (Ru^{2+}/Ru^{3+}) of the compound at +1.32 V versus Ag/AgCl.[25, 42] This is in good agreement with previously published results for this carboxyl complex[25] as illustrated in Figure 3.25.

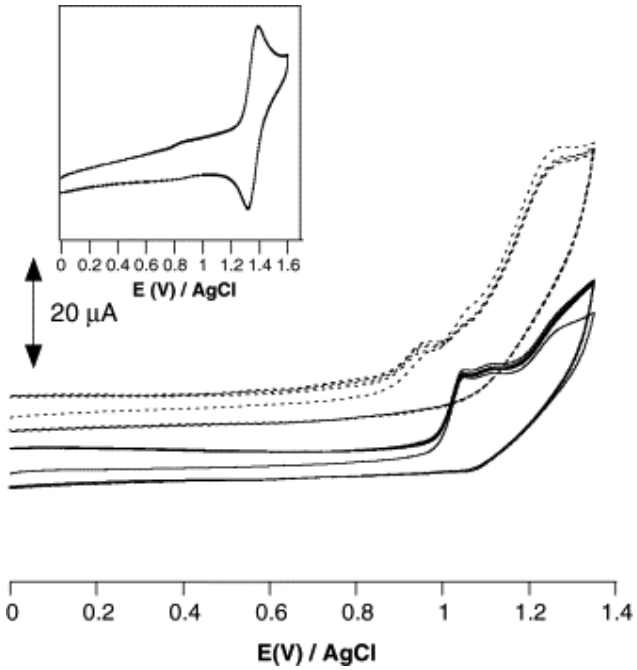

Figure 3.25: Cyclic voltammograms of $[Ru(bpy)_2(picCOOH)]^{2+}$ (pH 7, solid line) and $[Ru(bpy)_2(picCOOH)]^{+}$ (pH 12.0, dotted line), in phosphate buffer (0.1 M). Sweep rate: 100 mV s^{-1}; working electrode: glassy carbon disk (2 mm diameter); auxiliary electrode: platinum wire; reference electrode: aqueous Ag/AgCl. Inset: cyclic voltammogram of $[Ru(bpy)_2(picCOOH)]^{2+}$ in dry acetonitrile.[25]

In an ideal, fully reversible electrochemical based process the redox peak separations should be equal to 59 mV for a one electron process. The metal centred peak separation for (Ru^{2+}/Ru^{3+}) is 115 mV. As this peak separation value increases the redox process of a complex becomes slower and more irreversible, making regeneration of the original species more difficult. The peak areas for both oxidation and reduction are similar in values showing a chemically reversible redox process.

Two quasi-reversible bpy-centred reductions were observed at -1.30 V and -1.61 V versus Ag/AgCl respectively as identified by previously published literature.[25, 49] Pellegrin *et al*.[25] reported of a further irreversible ligand reduction peak assigned to a [picCOOH] ligand-centred reduction at -1.74 V in phosphate buffer solution (0.1 M). However, upon addition of TBA to the phosphate buffered solution, this redox peak disappears but leaves both bpy reduction peaks unaffected. Unfortunately this particular negatively scanned ligand reduction CV region is not published. However, this is probably the case seen here as the addition of TBA to the electrolyte solution causes the disappearance of the peak at -1.74 V. The redox couple at -0.72 V is also assigned to a further [picCOOH] ligand reduction.[50] This suggests that the LUMO of the complex lies on the ancillary [picCOOH] ligand and not on the cyclometalating bpy ligands as determined by ground and excited state pKa* values previously. This observation is consistent throughout the electrochemistry of all the ruthenium (II) complexes synthesised. However it is thought that the higher lying LUMO, which determines the T_1 state of the complexes, and therefore its emission, are dominated by the cyclometalating bpy ligands.

It is likely that the reduction peak at -1.30 V also contains some [picCOOH] ligand character, or the possible adsorption of the complex onto the electrode, given the non-uniform areas of the peak. Adsorption of molecules onto glassy carbon electrodes with oxygen containing functional groups has been observed before.[51] During the potential sweep the electrode may be anodised with the complex as a result of the interaction between the oxygen and electrode surface. This observation is supported by the cyclic voltammetry results here showing possible adsorption processes for both carboxyl and nitro functionalised complexes, whereas, there is little evidence of significant adsorption for the amino functionalised complex. It is also considered that

any trace elements of water within the solution could cause a water ingress effect that may also affect the electrochemical results.

Bracketing experiments were performed to isolate a particular potential window in the scanning process. This may provide additional information on what redox processes are coupled in the full CV. For the carboxyl and nitro functionalised ruthenium complexes, bracketing experiments indicated when the potential is only applied in a positive direction (starting at 0 V), and ligand reduction potentials not applied, the Ru^{2+}/Ru^{3+} metal redox couple is well defined and reversible as shown in Figure 3.26 and Figure 3.28 respectively. However, once the ligands have been reduced, the metal redox couple no longer displays well defined character and other oxidation peaks are evident in the positive region of the potential scan as illustrated in Figure 3.27. This indicates that upon ligand reduction, a chemical reaction or adsorption of the complex onto the electrode occurs during the negative potential sweep.

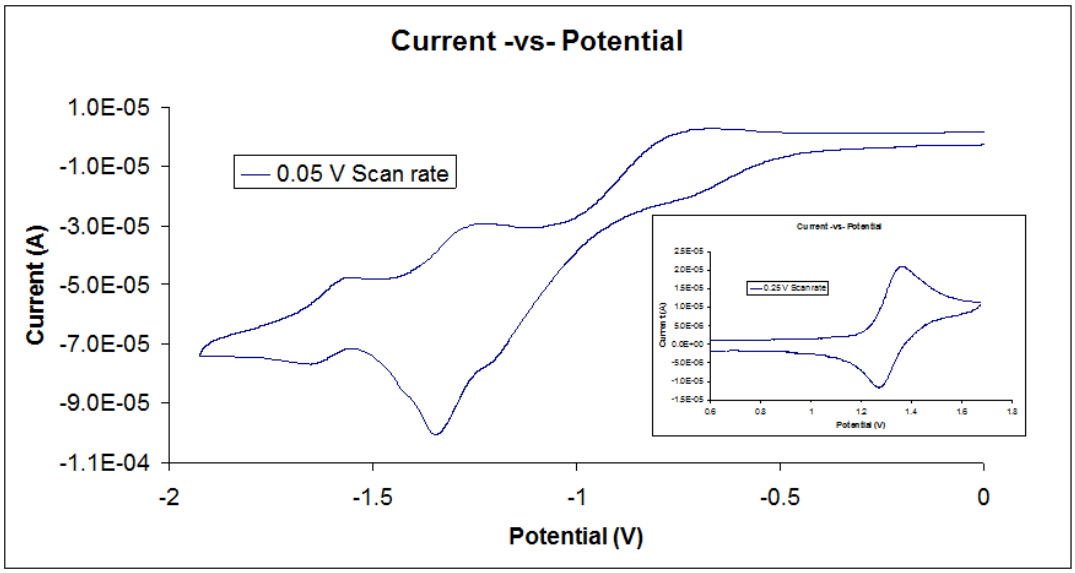

Figure 3.26: Cyclic voltammogram of $[Ru(bpy)_2(picCOOH)]^{2+}$ in acetonitrile (containing 0.1M TBA as electrolyte) with 1.5 mm glassy carbon working electrode and referenced against Ag/AgCl. Scans were started in a positive direction from an initial potential of 0 V. (Inset) Bracketed positive region of CV.

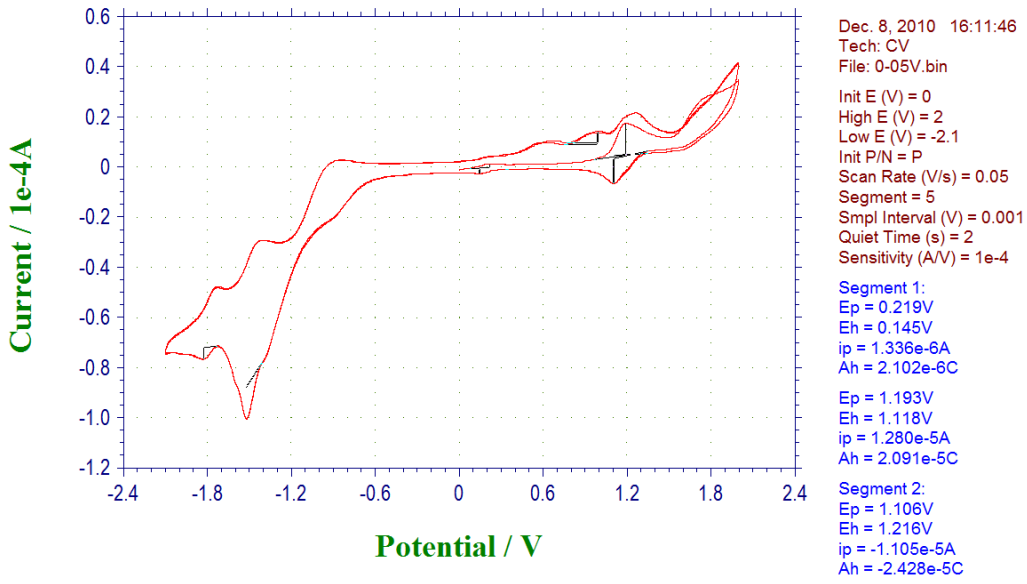

Figure 3.27: Full cyclic voltammogram of $[Ru(bpy)_2(picCOOH)]^{2+}$ in acetonitrile (containing 0.1M TBA as electrolyte) with 1.5 mm glassy carbon working electrode and referenced against Ag/AgCl. Scans were started in a positive direction from an initial potential of 0 V with a scan rate of 0.05 Vs^{-1}.

Figure 3.28 shows the cyclic voltammogram of $[Ru(bpy)_2(picNO_2)]^{2+}$. Once again it displayed a well defined redox couple (Ru^{2+}/Ru^{3+}) in Figure 3.38 (inset) at +1.29 V versus Ag/AgCl, when this redox couple is isolated. The presence of the electron withdrawing nitro group has the effect of shifting the metal redox potential to slightly more negative potentials as shown in Table 3.5. This is surprising as increasing the electron withdrawing nature of a ligand would be expected to make the metal oxidation more difficult and reduction of the ligands easier.[52] However, the impact of the electron withdrawing group on the ligand is thought to be minimal due to the distance from the ruthenium metal centre. Here, the metal redox peak separation is 116 mV, which is almost identical to that observed for the carboxyl complex.

Some six reduction processes were also observed when the window of analysis was widened to include negative potentials. The bpy ligand reduction peaks are tentatively assigned to the peaks present at -1.40 V and -1.65 V respectively.[25, 53] All other reduction peaks may be attributed to $[picNO_2]$ ligand reductions on the imidazole hetrocyclic ring, the bipyridyl ring or on the substituted phenyl ring. It is very difficult

to distinguish between the ligands responsible for each of the reduction peaks as there is likely to be a mixture of peaks, judging by the peak areas, caused by the reduction and adsorption of the compound onto the electrode surface. Furthermore, the reduction peak at -1.51 V is thought be as a result of adsorption of the complex as explained before.

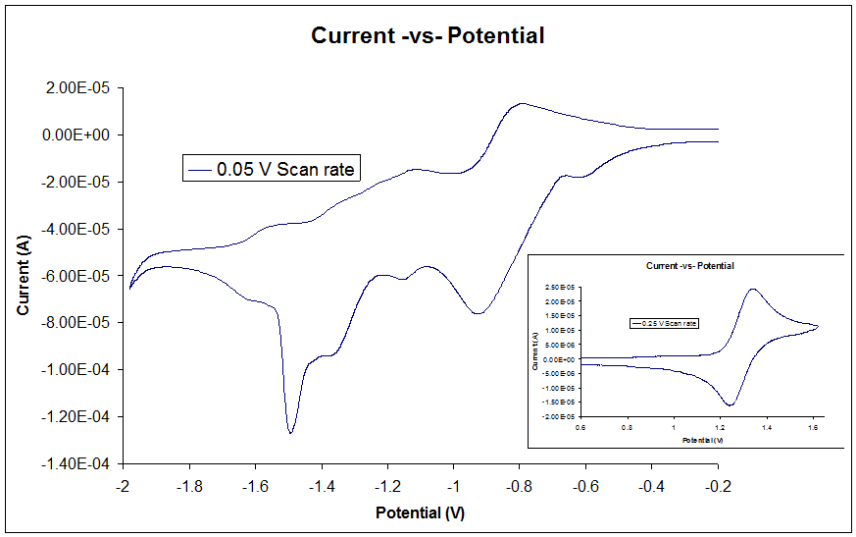

Figure 3.28: Cyclic voltammogram of $[Ru(bpy)_2(picNO_2)]^{2+}$ in acetonitrile (containing 0.1M TBA as electrolyte) with 1.5 mm glassy carbon working electrode and referenced against Ag/AgCl. Scans were started in a positive direction from an initial potential of 0 V. (Inset) Bracketed positive region of CV.

Finally, the cyclic voltammogram of $[Ru(bpy)_2(picNH_2)]^{2+}$ is shown in Figures 3.29 and 3.30. It exhibits a quasi-reversible metal centred redox couple (Ru^{2+}/Ru^{3+}) (Figure 3.29 inset) at 1.37 V versus Ag/AgCl and even when isolated in a positive potential sweep this feature does not become reversible as seen for the other two complexes. However, it is considered that this ruthenium oxidation peak may be preceeded by NH_2 oxidation which may lead to polymerisation.[54]

Once again this CV shows six ligand based reductions at negative potentials, however, they are more reversible in nature when compared to the nitro complex. These are tentatively assigned to; -0.67 V ([$picNH_2$] reduction), -0.84 V ([$picNH_2$] reduction), -1.15 V ([$picNH_2$] reduction), -1.40 V ([bpy reduction), -1.57 V (bpy reduction) and -1.97 V ([$picNH_2$] reduction) versus Ag/AgCl respectively. Reduction

peaks at -0.84 V, -1.40 V, -1.57 V and -1.97 V seem to be fully reversible in a single electron or multi-electron transfer process. Furthermore, the adsorption peaks seen previously at around -1.5 V is not evident for the $[Ru(bpy)_2(picNH_2)]^{2+}$ complex. For comparison, the three bpy ligand reduction peaks for $[Ru(bpy)_3]^{2+}$ are reported to be present at -1.35 V, -1.61 V and -1.80 V and the metal centred redox couple (Ru^{2+}/Ru^{3+}) is at +1.28 V versus Ag/AgCl in acetonitrile solution.[49] The replacement of a bpy ligand with the [picNH$_2$] ligand has the largest effect on the (Ru^{2+}/Ru^{3+}) redox potential. This suggests that the amino ligand exhibits the greater electron withdrawing potential from the ruthenium centre and the metal centre becomes slightly more difficult to oxidise. In addition, the introduction of the nitro functionalised ligand has had the effect of moving the reduction of the bpy ligands to more negative potentials.

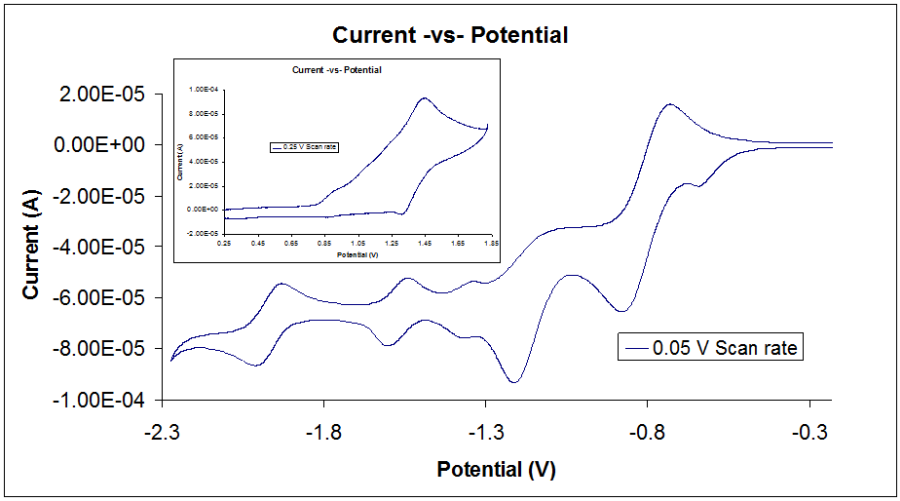

Figure 3.29: Cyclic voltammogram of $[Ru(bpy)_2(picNH_2)]^{2+}$ in acetonitrile (containing 0.1M TBA as electrolyte) with 1.5 mm glassy carbon working electrode and referenced against Ag/AgCl. Scans were started in a positive direction from an initial potential of 0 V. (Inset) Bracketed positive region of CV.

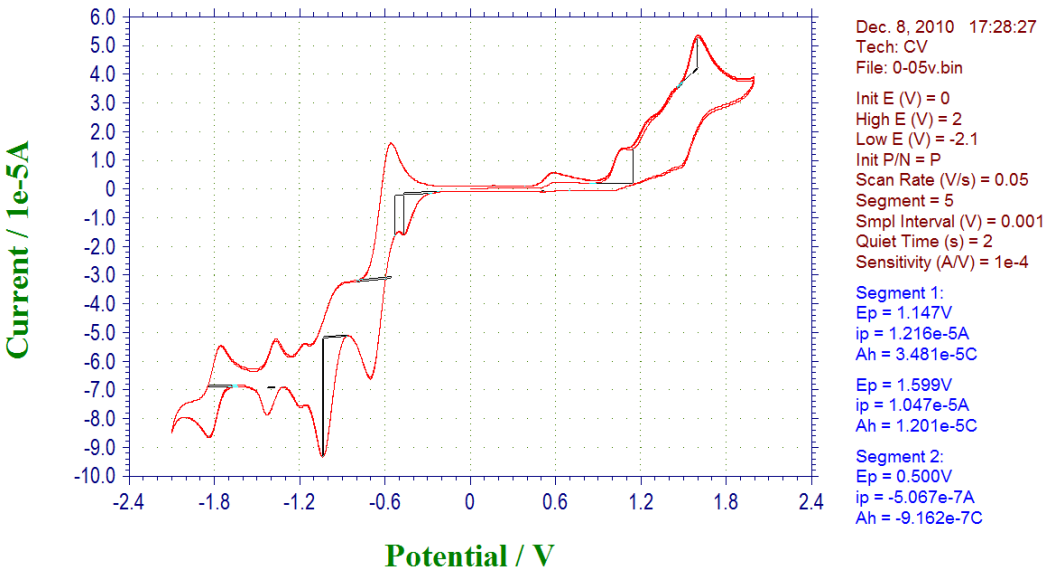

Figure 3.30: Full cyclic voltammogram of $[Ru(bpy)_2(picNH_2)]^{2+}$ *in acetonitrile (containing 0.1M TBA as electrolyte) with 1.5 mm glassy carbon working electrode and referenced against Ag/AgCl. Scans were started in a positive direction from an initial potential of 0 V with a scan rate of 0.05* Vs^{-1}.

Ventatanarayanan *et al.*[54] reported the production of an interfacial polymer film through the oxidative electropolymerisation of the amino functionality on a $[Ru(aphen)_3]^{2+}$ complex shown in Figure 3.31 below. In acetonitrile two oxidation processes were observed on the first scan, that of the irreversible oxidation of the amine functionalised phenanthroline ligand at + 1.13 V and reversible $Ru^{2+/3+}$ couple at + 1.25 V. For the $[Ru(bpy)_2(picNH_2)]^{2+}$ system analysed here, there is also evidence of an irreversible oxidation peak of the $[picNH_2]$ ligand at + 0.91 V. Depending on the mechanism of interaction, the NH· radical is thought to either dimerise with an adjacent NH· radical to form a diazo bond or the radical proceeds to react with an adjacent carbon atom on a neighbouring complex to form an imine bond.[54] Their results suggested the formation of the diazo bond as the aromaticity of the ligand is preserved upon electropolyperisation. It is likely that similar electropolymerisation is occurring here for the $[Ru(bpy)_2(picNH_2)]^{2+}$ complex and also following the reduction of $[Ru(bpy)_2(picNO_2)]^{2+}$ to the corresponding amino complex.

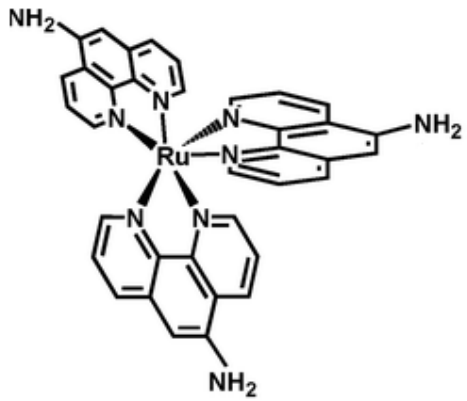

Figure 3.31: Schematic diagram illustrating the $[Ru(aphen)_3]^{2+}$ complex.[54]

3.4.4.5 Raman Spectroscopy

Raman spectroscopy is a fundamentally weak phenomenon, but the signal may be considerably enhanced if the laser of excitation coincides with an intense optical transition within the molecule. The resonance Raman effect can lead up to a 6 fold enhancement of the Raman signal of vibrations associated with the chromophores involved in the optical transition of a complex.[55] Resonance with the MLCT transitions of ruthenium (II) polypyridyl complexes yield intense Raman spectra with excellent signal-to-noise ratio. The three ruthenium (II) polypyridyl complexes were irradiated with 458, 514 and 785 nm laser lines. The 458 nm laser line is coincident with the main visible MLCT absorption of the complexes (as shown in the UV-vis absorbance profiles before) and under these resonance conditions the vibrational modes associated only with the chromophores are enhanced.[25] The post resonance laser line at 514 and non-resonant laser line at 785 nm are then used to determine the lowest energy state and general vibrational spectra respectively. No pre-resonance laser lines of higher energies were used in the analysis of the complexes.

Figure 3.32 displays the stacked resonance Raman spectra for $[Ru(bpy)_2(picCOOH)]^{2+}$ at the three wavelengths of irradiation. Following excitation of $[Ru(bpy)_2(picCOOH)]^{2+}$ at 458 nm the signature bipyridyl vibrational modes are also marked in Figure 3.32 and assigned in Table 3.6. This suggests that the optical

transition at 458 nm arises mainly from a ruthenium (dπ) to bipyridyl ligand (π*) MLCT transition. Although, there is evidence of additional peaks suggestive of a ruthenium (dπ) to [picCOOH] ligand (π*) MLCT transition. There is also evidence of a weak ruthenium-nitrogen stretch at 340 cm^{-1}. The two Raman peak at 1457 and 1427 cm^{-1} throughout every Raman spectrum are not attributed to bpy ligand and are most likely due to post-resonance with the heteroligand based optical transition at around 330 nm.[56]

As the energy of excitation is decreased using the 514 and 785 nm laser lines more complex Raman spectra with overlapping bands were observed. This was expected because in the case of the 785 nm laser line no resonance Raman is present and only the normal Raman spectrum of the complex is observed. The decrease in Raman intensity of the bpy modes, in the 514 nm spectrum, along with the introduction of more intense, lower energy Raman signals (due to phenyl or pyridyl in-plane twisting modes) suggests that the optical transitions at shorter wavelengths consists mainly of a ruthenium (dπ) to [picCOOH] ligand (π*) MLCT transition. This is consistant for all Raman spectra for the three ruthenium complexes. This indicates that the lowest ^{1}MLCT is [picCOOH] based, even though pKa results suggest that ^{3}MLCT seems to originate from the bpy ligands. It is also considered that vibrational modes observed following irradiation at 514 nm originate from an ILCT and this is further supported by the evidence of an ILCT absorbance band on the shoulder for the MLCT transition for the complexes. The intensity of the C-C and C-N stretching vibrations of the aromatic rings under higher irradiation energies indicates that such stretching modes are the dominant accepting modes for deactivation of the triplet MLCT excited state.[18]

The Raman analysis was performed using solid state samples placed onto glass microscopy slides. Judging by elemental analysis results of the synthesised complexes two perchlorate counterions are evident suggesting an overall charge of 2+ on the ruthenium complexes. All peaks are tabulated and given assigned vibrational modes in Table 3.6 below. All the Raman modes were assigned according to the published data.[25, 56-59]

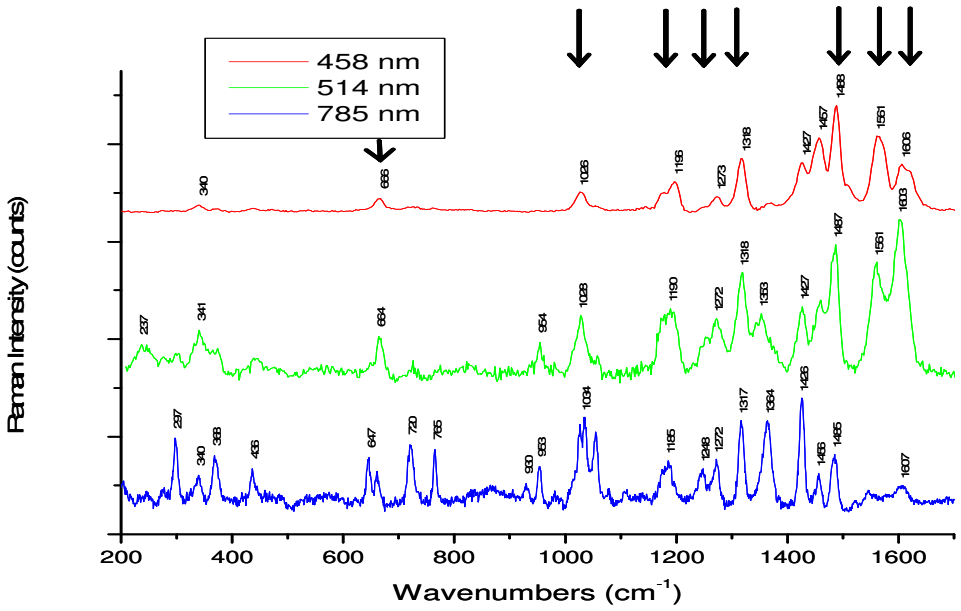

Figure 3.32: Stacked Raman spectra of $[Ru(bpy)_2(picCOOH)]^{2+}$. Solid state analysis of the samples was conducted using 458 nm (top), 514 nm (middle) and 785 nm (bottom) excitation laser lines. All spectra were gathered with 5 acquisitions and an exposure time of 3 seconds with a laser power of 2 mW. Arrows indicate signature bipyridyl vibrational modes.

$[Ru(bpy)_2(picR)]^{2+}$		
458 nm	***(cm^{-1})***	***Assignment***
Bipyridyl vibrational modes:	~1606 ~1561 ~1488 ~1318 ~1273 ~1196 ~1026 ~666	C=C stretch C=C stretch C=N stretch C=N stretch C-C (inter-ring bending) CCH (in-plane bending) Ring breathing Pyridyl in-plane twisting
[picR] ligand vibrational modes:	n/a	n/a
Ruthenium – Ligand vibrational modes:	~340	Metal-Ligand stretching
Other vibrations:	~1457 ~1427	Post resonance vibrations
514 nm		
Bipyridyl vibrational modes:	~1603 ~1561 ~1487 ~1318 ~1272 ~1190 ~1026 ~664	C=C stretch C=C stretch C=N stretch C=N stretch C-C (inter-ring bending) CCH (in-plane bending) Ring breathing Pyridyl in-plane twisting
[picR] ligand vibrational modes:	~1353 ~954 ~664	C=N stretch Ring breathing Phenyl or pyridyl in-plane twisting
Ruthenium – Ligand vibrational modes:	~340 ~237	Metal-Ligand stretching
Other vibrations:	~1457 ~1427	Post resonance vibrations
785 nm		
Bipyridyl vibrational modes:	~1607 ~1561 ~1485 ~1317 ~1272 ~1185 ~1034 ~647	C=C stretch C=C stretch C=N stretch C=N stretch C-C (inter-ring bending) CCH (in-plane bending) Ring breathing Pyridyl in-plane twisting
[picR] ligand vibrational modes:	~1354 ~953 ~765 ~720 ~647	C=N stretch Ring breathing Phenyl or pyridyl bending Phenyl or pyridyl bending Phenyl or pyridyl in-plane twisting
Ruthenium – Ligand vibrational modes:	~436 ~368 ~297	Metal-Ligand stretching
Other vibrations:	~1456 ~1426	Post resonance vibrations

Table 3.6: General assignment of Raman vibrational modes of the ruthenium (II) complexes synthesised using 458, 514 and 785 nm excitation wavelengths.

The Raman spectra for $[Ru(bpy)_2(picNO_2)]^{2+}$ are similar to the carboxyl functionalised equivalent. Once again, under irradiation at 458 nm the bipyridyl vibrational modes mainly dominate and excitation at longer wavelengths sees the introduction of vibrational modes that suggest that the lowest ^{1}MLCT is may also be located on the $[picNO_2]$ ligand. One significant difference between the non-resonant spectra at 785 nm is the noticeable enhancement of the intensity of a pyridine ring stretch at 1603 cm^{-1} as revealed in Figure 3.33.

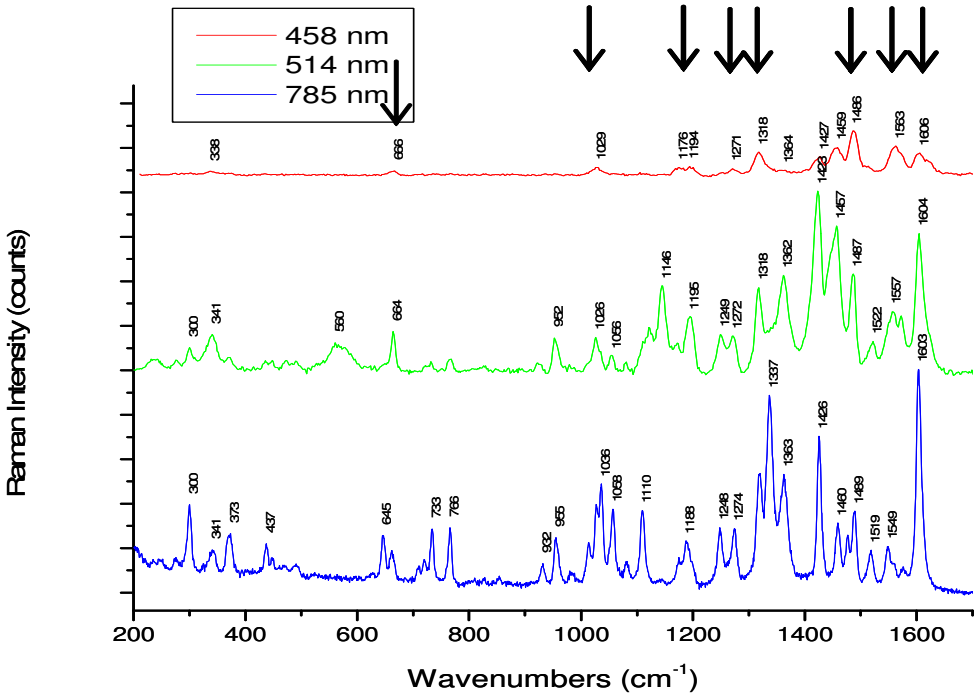

Figure 3.33: Stacked Raman spectra of $[Ru(bpy)_2(picNO_2)]^{2+}$. Solid state analysis of the samples was conducted using 458 nm (top), 514 nm (middle) and 785 nm (bottom) excitation laser lines. All spectra were gathered with 5 acquisitions and an exposure time of 3 seconds with a laser power of 2 mW. Arrows indicate signature bipyridyl vibrational modes.

Raman results for the amino functionalised $[Ru(bpy)_2(picNH_2)]^{2+}$ complex are shown in Figure 3.34. Surprisingly, under irradiation at 458 nm, there is evidence of additional peaks at 1352, 1178, 1140 and 947 cm^{-1} that suggestive of a stronger

contribution of a ruthenium (dπ) to [picNH$_2$] ligand (π*) MLCT transition at this wavelength of excitation. Excitation at 514 nm yields similar spectra as seen following excitation at 458 nm, however, there is a slight change in the relative intensities of the peaks.

As can be seen below, the relative intensity of the Raman bands are weaker and show a significantly smaller number bands under investigation at 785 nm. However, this is with the exception of an intense broad peak at 545 cm^{-1} which was evident in many different spectral accumulations. It is speculated that this might a result of the in-plane twisting of the more delocalised phenyl ring on the [picNH$_2$] ligand and this is further correlated with the experimental data previously reported by Pellegrin *et al.*[25] on a similar complex. It is also noted that the use of glass slides in gathering the Raman spectra may have resulted in contamination of the sample signal by the glass Raman signal.

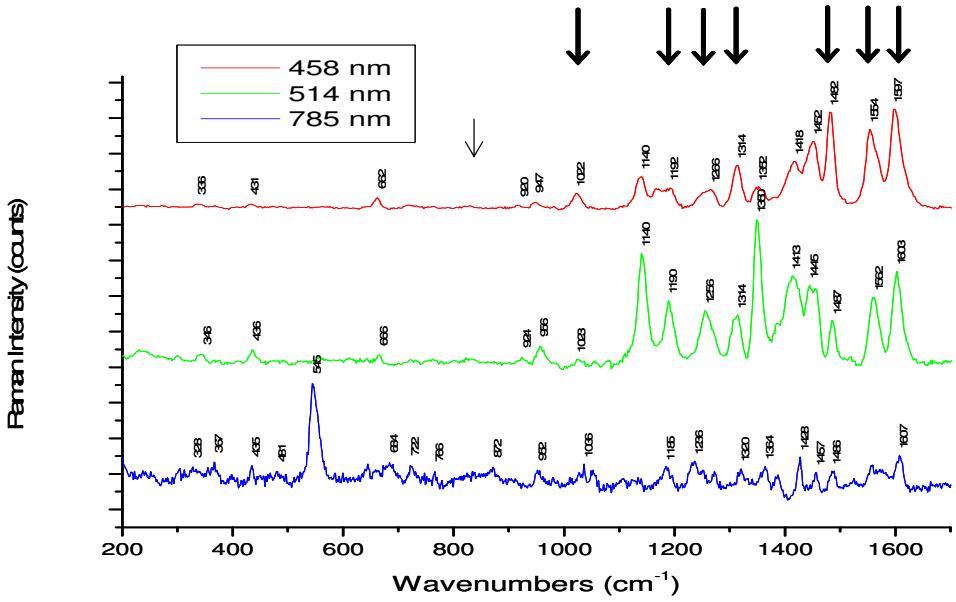

Figure 3.34: Stacked Raman spectra of [Ru(bpy)$_2$(picNH$_2$)]$^{2+}$. Solid state analysis of the samples was conducted using 458 nm (top), 514 nm (middle) and 785 nm (bottom) excitation laser lines. All spectra were gathered with 5 acquisitions and an exposure time of 3 seconds with a laser power of 2 mW. Arrows indicate signature bipyridyl vibrational modes.

3.5 Ruthenium Conjugated Gold Nanoparticles

3.5.1 Synthesis

The amino functionalised luminophore was prepared in order to exploit this group for EDC/NHS coupling to a carboxyl functionalised PEG linker. In the cross coupling reaction the water soluble carbodiimide crosslinker activates the carboxyl group for spontaneous reaction with primary amines. Figure 3.35 shows how the EDS initially reacts with the carboxyl group to form an unstable amine-reactive O-acylisourea intermediate, which is susceptible to hydrolysis, making it unstable and short lived in aqueous environments. If this intermediate does not encounter an amine it will proceed to hydrolyse resulting in the regeneration of the carboxyl functionality. The efficiency of the EDC cross-coupling reaction is increased with the addition of NHS to form a more semi-stable amine reactive NHS-ester intermediate that may be coupled with an amine to produce the desired stable amide bond. EDC couplings are best performed at slightly acidic pH (pH 4.5), however, the addition of NHS to the reaction allows for an efficient conjugation reaction to be performed at physiological pH.

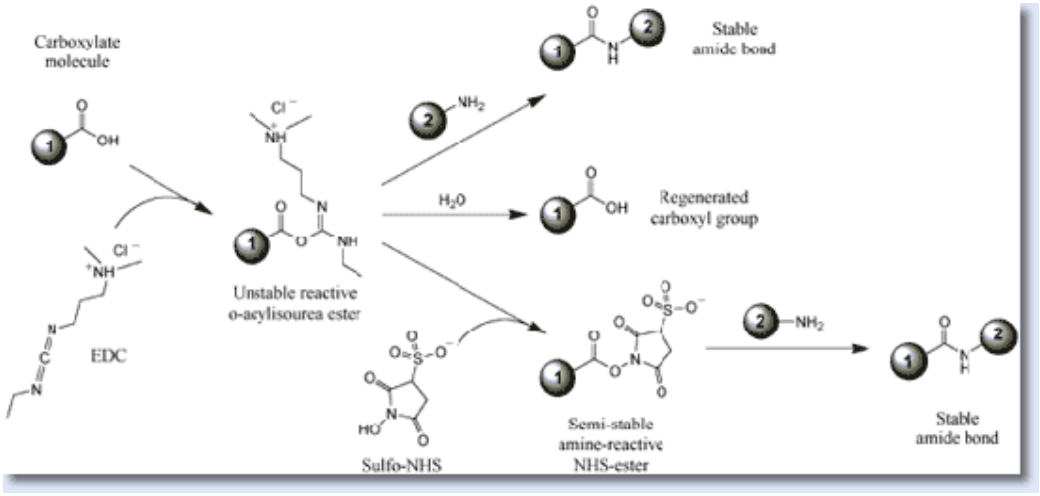

Figure 3.35: Schematic diagram illustrating the mechanism for EDC/NHS coupling reactions.[60]

Without isolation of the PEGylated ruthenium complex a disulphide reducing agent [DTT (0.3 equivalences)] was added to the solution in an effort to disrupt any disulphide bonds that may have formed between the thiol functionalised PEGylated ruthenium molecules (Figure 3.36). Its concentration was deliberately kept low as DTT in solution will compete with the PEGylated ruthenium complex for conjugation to the gold nanoparticles.

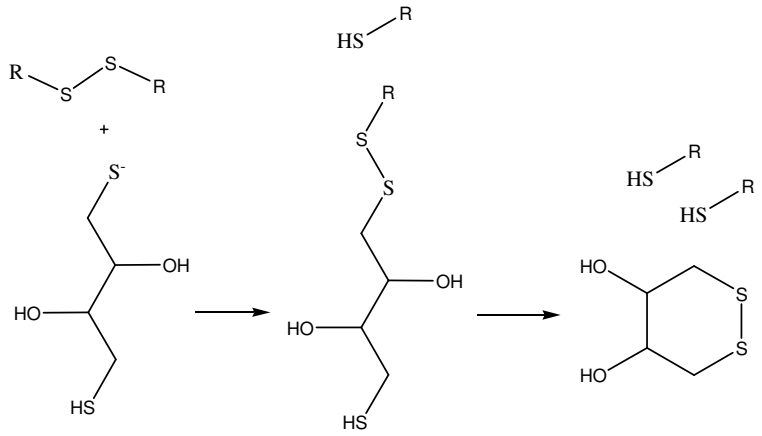

Figure 3.36: Schmetic diagram illustrating the disruption of disulphide bonds by dithiothreitol (DTT).

The free thiol groups located on the PEG linker covalently binds to the gold substrate with gentle shaking overnight. Lateral Van der Waals interactions between the tails are expected to ensure a close-packed, crystalline or semi-crystalline structure on the surface substrate. Simple purification of the functionalised nanoparticles was performed through a series of washing and centrifugation steps. The conjugated gold nanoparticles were then resuspended in a PBS solution (pH 7.4) for analysis. Characterisation of the modified nanoparticles was performed using absorbance, emission, Raman, TEM and zeta potential techniques.

3.5.2 Characterisation

UV-Vis absorption spectroscopy is the most widely used technique to characterise nanoparticles. Solutions of colloid gold nanoparticles have a distinctive red colour that is caused by excitation of electronic plasmon absorption bands of the metal nanoparticles as a consequence of moving electrons on the particle's surface. Chemical modifications to nanoparticle surfaces change the dielectric at the interface leading to shifts in the absorption bands of the metal nanoparticle.[61]

Figure 3.37 compares that the absorbance of the free parent dye, the PEGylated ruthenium complex, the unmodified AuNPs and ruthenium modified AuNPs. The spectrum of the unmodified AuNPs exhibits an intense gold plasmon absorbance band at 527 nm. Upon adsorption of the PEGylated ruthenium moieties the size and shape of the plasmon band changes which is attributed to changes in the surface dielectric of the nanoparticle.[62] The absorbance maximum for both AuNP-PEG_8-Ru and AuNP-PEG_{32}-Ru is shifted to 522 nm and 529 nm respectively. The characteristic absorbance wavelengths of the amino functionalised ruthenium (II) polypyridyl dye are also noted at 285 nm (π-π^* transition of the bpy ligand), 325 nm (π-π^* transition of the [picNH_2] ligand) and 455 nm (MLCT transition) respectively. However, the electronic transitions of the ruthenium complex are partially obscured by the strong plasmon absorbance of the gold nanoparticles. Care was taken to ensure that roughly the same amount of nanoparticles were present in the AuNP control to that of the functionalised AuNPs for all spectroscopic measurements.

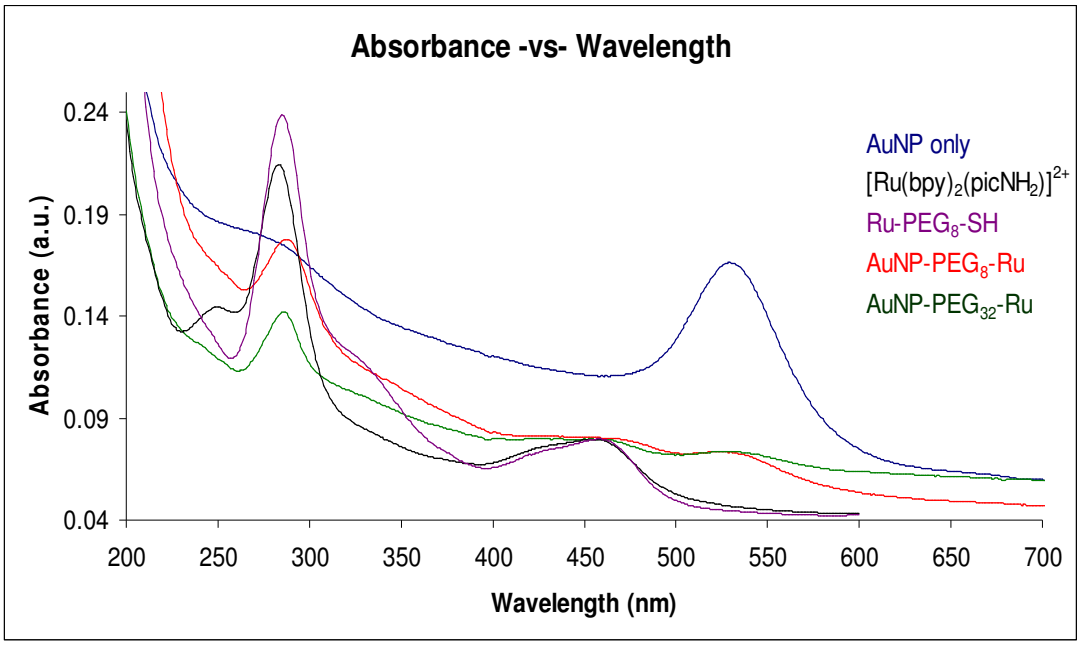

Figure 3.37: Overlaid absorbance spectra of the unmodified 50 nm AuNPs, free $[Ru(bpy)_2(picNH_2)]^{2+}$, Ru-$PEG_8$-SH, AuNP-$PEG_8$-Ru and AuNP-$PEG_{32}$-Ru nanoconjugates in PBS (pH7.4) solutions. Solutions containing the ruthenium (II) complex were absorbance matched at 455 nm.

The PEGylation of the ruthenium complex did not result in significant alterations to the emission wavelength of the luminophore as shown in Figure 3.38. The photophysical data are presented in Table 3.7. The number of dye molecules on the gold colloid surface proved difficult to quantify given the small amounts of conjugated materials under analysis. In an effort to ascertain the consequence of the metal enhanced emission on both nanoconjugates, the samples were absorbance matched at 455 nm. This assumes that the number of photons absorbed by ruthenium is the same i.e. the ruthenium surface coverage is approximately the same per nanoparticle and that no plasmon optical transition contributes to the absorbance at this wavelength. Therefore, this approach makes an underestimation of the actual emission intensity as a result of the conjugated ruthenium dye. In order to separate the effects of quenching and dilution due to absorption/scattering by the AuNPs, the emission intensity was corrected for such variations using the following formula in Equation 3.11. This formula has been used previously to correct for the absorption of incident light by a cobalt (III) complexes in quenching studies with $[Ru(bpy)_3]^{2+}$.[63]

$$(I_o/I)_{corr} = (I_o/I)_{app}\,[1\text{-}10^{-(Ad+Aq)}/1\text{-}10^{-Ad}]\,(A_d/A_d+A_q)\text{…….Eq 3.11}$$

where $(I_o/I)_{app}$ is the observed ratio of the emission intensity from the unquenched sample to that of the quenched one, and A_d and A_q are the absorbances of the donor and quencher, respectively, at the excitation wavelength of 455 nm.

Figure 3.38 compares the corrected emission spectra of the free parent ruthenium (II) dye, the PEGylated ruthenium complex, the modified AuNPs and unmodified AuNPs following excitation into the MLCT absorbance band of $[Ru(bpy)_2(picNH_2)]^{2+}$ at 455 nm of the absorbance matched solutions. As expected the unmodified AuNPs showed no evidence of luminescence, whereas, the modified AuNP-PEG_8-Ru and AuNP-PEG_{32}-Ru have an emission maxima at 605 nm and 608 nm respectively. This is interesting as one of the main concerns was that the nanoparticle might quench the luminescence of the surface bound luminophore completely, particularly for the shorter linker. However, the emission of the longer PEGylated nanoconjugate, AuNP-PEG_{32}-Ru, is over 5 times that of the shorter AuNP-PEG_8-Ru modified nanoparticle. The close proximity of the dye to the metal surface, as a result of the shorter linker, leads to a greater quenching of luminescence as energy is transferred to the metal and the rate of non-radiative decay increases. Furthermore, interestingly the emission intensity of AuNP-PEG_{32}-Ru is greater than that of the free $[Ru(bpy)_2(picNH_2)]^{2+}$ dye in PBS (pH 7.4) solution. The emission wavelength also remains unaltered indicating that the nanoparticle has little impact on the wavelength of emission. Any free, unbound ruthenium dye was removed from the conjugated nanoparticle solution by centrifugation and washing with deionised water approximately 8 times until the supernatant showed no evidence of ruthenium emission. Therefore, it can be concluded that free ruthenium contributes very little if at all to the emission shown in Figure 3.38.

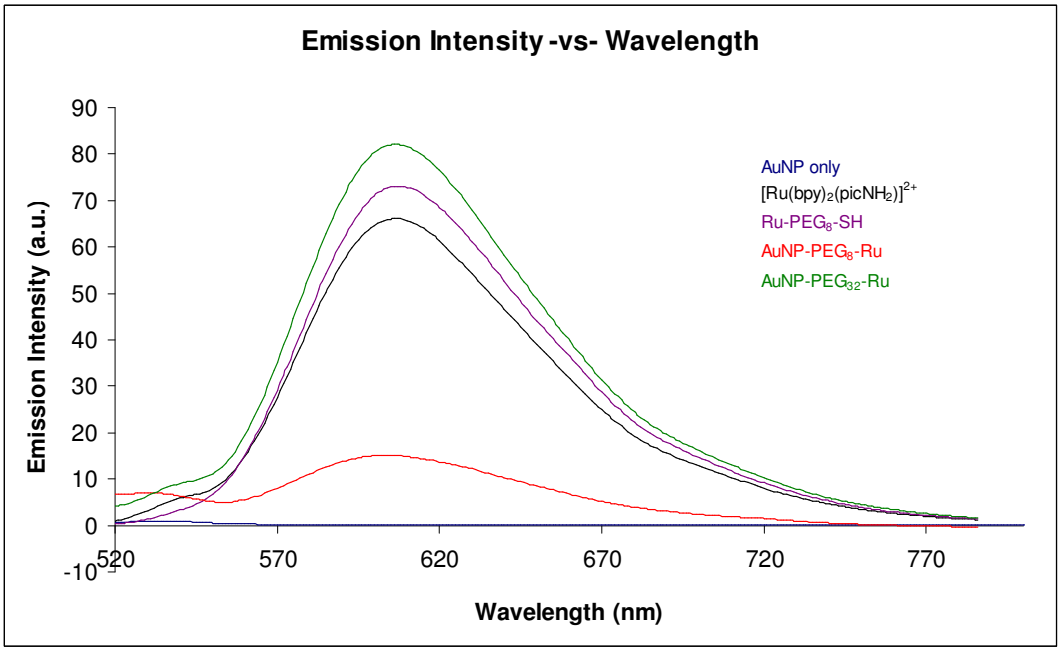

Figure 3.38: Overlaid corrected emission spectra of the unmodified 50 nm AuNPs, free $[Ru(bpy)_2(picNH_2)]^{2+}$, Ru-$PEG_8$-SH, AuNP-$PEG_8$-Ru and AuNP-$PEG_{32}$-Ru nanoconjugates in PBS (pH 7.4) solutions. Samples were excited at 455 nm using 10 nm slit widths. All ruthenium samples were absorbance matched at 455 nm.

The lifetimes of the nanoconjugates also vary significantly as shown in Table 3.7 below. The longer PEGylated nanoparticle exhibited a lifetime that is twice that of the shorter AuNP-PEG_8-Ru complex and 1.3 times that of the free $[Ru(bpy)_2(picNH2)]^{2+}$ complex in aerated PBS (pH 7.4) buffered solution as illustrated in Figure 3.39. It is thought that the increased lifetime of the AuNP-PEG_{32}-Ru nanoconjugate is a result of the more protected and restricted environment provided by the longer PEG_{32} linker surrounding the luminophore. This would result in a decrease in oxygen quenching of the ^{3}MLCT state of the ruthenium complex and thus, lead to increased lifetimes. This suggests that plasmonic enhancement of ruthenium emission is minimal. It is also acknowledged that luminescent anisotropy experiments would be of particular interest in this context. It is considered that the AuNP-PEG_{32}-Ru nanoparticles might be better suited to multimodal cellular imaging given their enhanced luminescence and phosphorescent lifetimes. The actual PEG linker lengths of 3 nm and 13 nm are thought to be less than reported as they do not exist in linear conformation upon binding to a substrate and often form self-coiled structures.[64]

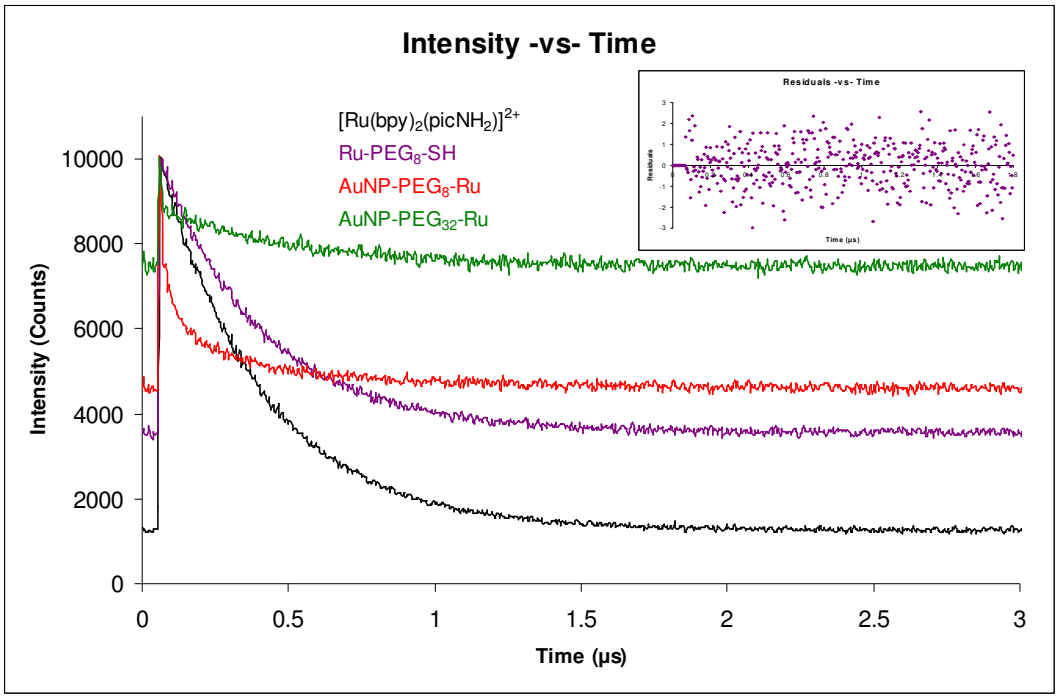

Figure 3.39: Overlaid TCSPC lifetime results of the free $[Ru(bpy)_2(picNH_2)]^{2+}$, Ru-$PEG_8$-SH, AuNP-$PEG_8$-Ru and AuNP-$PEG_{32}$-Ru nanoconjugates in aerated PBS (pH 7.4) solutions. (Inset) example of the monoexponential residual decay -vs- time plot for Ru-PEG_8-SH (lifetime = 351 +/- 3 ns, x^2 = 0.989).

Compound	Lifetime	x^2 value	Quantum Yields
$[Ru(bpy)_2(picNH_2)]^{2+}$	357 +/- 3 ns	0.993	0.044
Ru-PEG_8-SH	351 +/- 3 ns	0.989	0.047
AuNP-PEG_8-Ru	277 +/- 9 ns	1.07	n/a
AuNP-PEG_{32}-Ru	448 +/- 17 ns	0.988	n/a

Table 3.7: Lifetimes and quantum yields of the free ruthenium (II), PEGylated ruthenium complex and the conjugated ruthenium (II) dyes measured in aerated PBS (pH 7.4) solutions. All lifetimes displayed monoexponential kinetics.

Figure 3.40 shows the Raman spectra of the free ruthenium (II) complex and the functionalised gold nanoparticles following irradiation at 514 nm. This wavelength of excitation was chosen as it coincides with the surface plasmon absorbance of the gold nanoparticles and hence, was most likely to lead to surface enhanced Raman spectroscopy (SERS). In general, all of the characteristic Raman peaks for the ruthenium (II) complex are present for the ruthenium modified nanoparticles at 514 nm. From the Raman spectra it appears that resonance Raman of the luminophore is dominating the signal, as PEG vibrations would be expected to be strongly enhanced under SERS conditions. Furthermore, the Raman spectra for the modified AuNPs are not significantly different to the resonance Raman spectrum for the free ruthenium complex.

The main differences between the Raman spectrum for the free ruthenium complex and the modified AuNP spectra are located at 1445 cm^{-1} (post resonance vibration), 1415 cm^{-1} (post resonance vibration), 1350 cm^{-1} (C=N stretch-bpy), 1256 cm^{-1} (C-C inter ring bending-bpy), 1140 cm^{-1} (CCH in-plane bending-bpy), 956 cm^{-1} (ring breathing-[picNH$_2$] and 436 cm^{-1} (metal-ligand stretching). Conjugation to the AuNP has had the effect of reducing the post resonant modes and a few bpy vibrational modes within the complex probably due to a shift in the ruthenium MLCT. Furthermore, conjugation of the ruthenium sees the elimination of a metal ligand stretch and ring breathing within the [picNH$_2$] ligand possibly as a result of the more constrained environment of the attached luminophores.

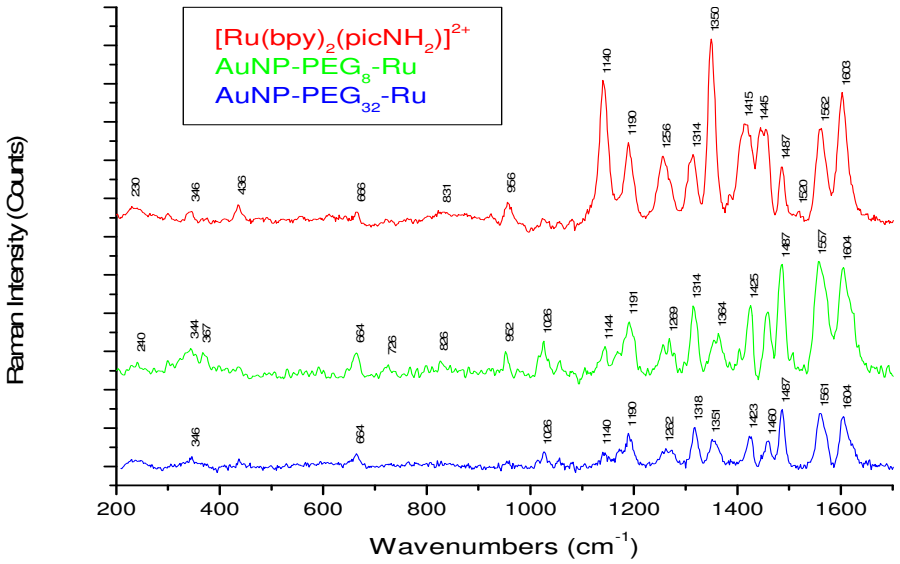

Figure 3.40: Stacked Raman spectra of the unmodified free $[Ru(bpy)_2(picNH_2)]^{2+}$ complex (top), AuNP-PEG_8-Ru (middle) and AuNP-PEG_{32}-Ru (bottom) nanoconjugates. Samples were deposited onto glass slides and solvent allowed to evaporate prior to analysis. Samples were irradiated using a 514 nm laser line. All spectra were gathered with 5 acquisitions and an exposure time of 3 seconds with a laser power of 2 mW.

The Zeta potential of the citrate stabilised AuNPs was also determined to be equal to -38.66 +/- 0.9 mV in PBS pH 7.4, indicating a good colloidal stability within the solution. This zeta potential is comparable to other citrate stabilised gold nanoparticles.[65] The Zeta potential of the modified AuNP-PEG_8-Ru nanoparticles increased to + 47.97 +/- 1.3 mV in PBS (pH 7.4), indicating improved nano-stability and attenuation of charge around the nanoparticle surface. This stability is also confirmed by the Uv-Vis spectrum in Figure 3.37 which shows no longitudinal absorbance modes indicative of aggregation of the nanoparticles. In addition, the shifting to positive Zeta potentials is further indication of the presence of the positively charged $[Ru(bpy)_2(picNH_2)]^{2+}$ complex.

3.5.3 Cellular Uptake of AuNP-PEG$_{32}$-Ru Nanoparticles

A key objective in preparing a ruthenium conjugated nanoparticle was their potential use as Stokes shifted Raman and luminescent probes for cellular imaging. In addition, the AuNP-PEG$_{32}$-Ru nanoconjugate exhibited many favourable photophysical properties including longer aqueous lifetimes and greater emission intensity when compared to the lone parent ruthenium complex.

In order to assess and compare the ability of the free $[Ru(bpy)_2(picNH_2)]^{2+}$ complex (prepared as the ClO_4 salt to improve aqueous solubility) and ruthenium (II) conjugated gold nanoparticles to transport across the cell membrane, cells were harvested after 2 days growth period. The growth medium was removed by centrifugation at 2000 rpm for 2 minutes, washed twice and resuspended in PBS buffer (pH 7.4) solution. For confocal measurements, 100 μl aliquots of the cell solution was used and mixed with 3 μl of the parent ruthenium complex (20 μM) or nanoconjugate (~0.7 μM) in PBS (pH 7.4). Confocal measurements were performed at room temperature with a final $[Ru(bpy)_2(picNH_2)]^{2+}$ complex concentration of 6 x 10^{-7} M or final nanoconjugate concentration of approximately 2 x 10^{-8} M.

Figure 3.41 shows the confocal luminescent images of $[Ru(bpy)_2(picNH_2)]^{2+}$, Ru-PEG$_{32}$-SH and AuNP-PEG$_{32}$-Ru which show the capacity of both parent and conjugates to cross the cell membrane. The water soluble $[Ru(bpy)_2(picNH_2)]^{2+}$ dye showed accumulation of the dye within the cell's membrane but poor migration into the cells cytoplasm (Figure 3.41 (a)), which is consistent with similar cell experiments carried out with $[Ru(bpy)_2(picCOOH)]^{2+}$ in Chapter 5. Following conjugation of the PEG linker to the metal complex (Figure 3.41 (b)), the moiety showed significant transmembrane transport and localisation within the cell's cytoplasm after a period of 10 minutes. As was initially hoped, the water soluble PEG linker aided in drawing the dye into the cell's cytoplasm. As mentioned in Chapter 1, PEG has proven valuable before as a suitable biological linker to covalently attach to the molecules in an effort to limit non-specific adsorption by the cell and increase aqueous solubility.[28, 66] The only other report on the potential benefits of PEGylation of metal complexes in cellular imaging is reported by Li *et al*.[67] They described the synthesis of a series of PEG_{23} functionalised iridium (III) polypyridine complexes. The PEGylated complexes

exhibited increased water solubility when compared to the parent iridium complex and considerably reduced cytotoxicity in HeLa cells when compared to both cisplatin and the iridium control. It is claimed thet even after 2 hours incubation with a relatively high concentration of PEGylated iridium complex (200 μM) the HeLa cells remained viable.

Similarly for the nanoconjugate synthesised here, AuNP-PEG_{32}-Ru (Figure 3.41 (c)), the confocal luminescent images shows permeation of the probe across the membrane and into the cytoplasm following incubation with the SP2 myeloma cells at room temperature for 10 minutes. Z-stacks of each cell confirm the dispersity of the luminophore throughout the cellular structure. No further changes were detected inside the cells over a 60 minute timeframe. Similarly, Gu *et al.*[28] described the synthesis of a fluorescein-PEG-AuNP probe that was reported to enhance the aqueous stability and efficient intracellular transport of the fluorescein dye into the nucleus of HeLa cells. The 3.7 nm monodispersed nanoparticles showed no obvious cytotoxicity to HeLa cells, making these particles ideal for improvement of nuclear targeted drug delivery. It is believed that endocytosis is the process in which the nanoconjugates are up taken by the cell as its transmembrane efficiency is greatly affected by a decrease in temperature and this is discussed in detail in Chapter 1.

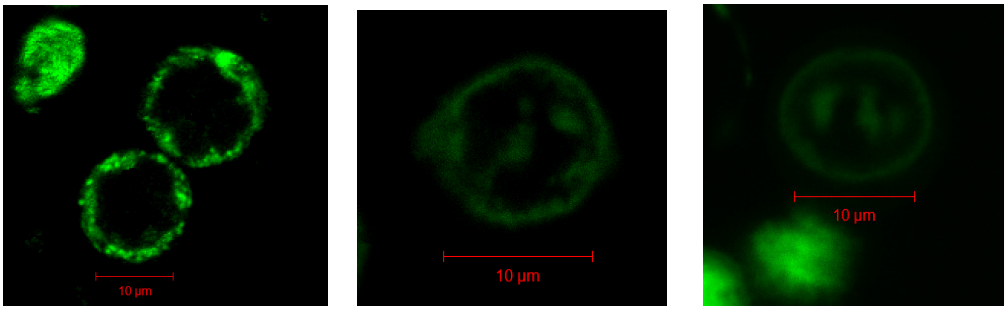

(a) ***(b)*** ***(c)***

Figure 3.41: (a) Ruthenium dye only after 10 minutes [final concentration of 6 x10^{-5} M in PBS buffer (pH 7.4)], (b) ruthenium conjugated to the PEG linker after 10 minutes [final concentration of 6 x10^{-5} M in PBS buffer (pH 7.4)] and (c) AuNP-PEG_{32}-Ru ruthenium after 10 minutes [final approx. concentration of 2 x10^{-7} M in PBS buffer (pH 7.4)]. Images taken using SP2 myeloma cells at room temperature using 458 nm excitation laser line.

These preliminary qualitative experiments serve to demonstrate the capacity of a metal complex to be transported across the cell membrane when conjugated to PEG linkers and AuNPs. The linker length between luminophore and metal substrate was varied in an effort to increase the photophysical characteristics of the dye. It was found that the larger linker length of approximately 13 nm exhibited superior emission intensity and aqueous lifetimes when compared to the shorter 3 nm PEGylated nanoparticle. In addition, following conjugation of the novel non-membrane permeable ruthenium (II) complex to AuNPs, transmembrane transport was possible and localisation within cell organelles was achieved. Furthermore, as discussed in Chapter 1, a major problem up until now has been the successful internalisation of transition metal complexes within cells without the use of organic solvents. It has been shown here that following conjugation to PEG linkers, or attachment to AuNPs, that the functionalised ruthenium (II) polypyridyl complexes may be easily transported across the cell membrane and exploited for cellular imaging without the need for organic solvents that are known to disrupt the cellular membrane.[68, 69]

3.6 Conclusion

The synthesis and characterisation of three ruthenium polypyridyl (II) complexes containing carboxyl, nitro and amino functionalised benzimidazole ancillary ligands is described. The carboxyl functionalised $[Ru(bpy)_2(picCOOH)]^{2+}$ has been used for many years by our research group for the luminescent labelling of biomolecules.[1, 24, 25] In the case of the $[Ru(bpy)_2(picNO_2)]^{2+}$ complex the synthetic procedures are improved upon in comparison to the existing literature. However, the synthesis of the novel $[Ru(bpy)_2(picNH_2)]^{2+}$ complex was reported in the literature shortly after its synthesis as part of this research. Even though the ruthenium complexes only differ by their substituent functionality on the benzimidazole ligand many contrasting results are obtained. Not least with the $[Ru(bpy)_2(picNO_2)]^{2+}$ complex that exhibited out of characteristic absorbance, emission, aqueous lifetime (~ 20 ns) , pH and solvent dependence. Nevertheless, many of these abnormal results were explained by the para-substituted nitro substituent causing a strengthening in the bond polarity of the $[picNO_2]$ ligand. As a result the electron withdrawing ability is greater, having an increased affect on its photophysical properties.

Both the carboxyl and amino functionalised complexes behave very similarly and may be characterised by long aqueous lifetimes (> 800 ns), comparable absorbance, emission, Raman profiles and similar pH dependence. For all three ruthenium complexes the pKa/pKa* calculations suggested that the ^{3}MLCT excited state of the complexes reside on the bipyridyl ligands. The ancillary ligands are not expected to have a large influence on its excited state as the functionalised phenyl group lies some distance from the metal centre to have any influence the HOMO-LUMO energy gap. However, resonant Raman spectroscopy indicates that the lower energy MLCT optical transition is a result of a ruthenium ($d\pi$) to bpy / [pic-R] (π^*) ligands following irradiaton at 458 and 514 nm.

Despite all three ruthenium complexes having been synthesised previously, this is the first time that the three have been compared and contrasted spectroscopically, photophysically and cyclic voltammetry with one another. Furthermore, it is the first time that the $[Ru(bpy)_2(picNO_2)]^{2+}$ and $[Ru(bpy)_2(picNH_2)]^{2+}$ complexes have been

characterised by pKa titrations, Raman spectroscopy and electrochemistry. The use of the pH dependant benzimidazole ligand adds extra flexibility to its potential use as a diagnostic tool. The various functionalities used here will also allow for coupling of the ruthenium (II) polypyridyl dye to almost any biomolecule or assembly. In Chapter 5 the conjugation of the $[Ru(bpy)_2(picCOOH)]^{2+}$ complex to a cell penetrating peptide octarginine is also described and its facile entry and localisation within the cell examined.

The synthesis of a novel luminescent-nanoparticle multimodal probe is also achieved. The $[Ru(bpy)_2(picNH_2)]^{2+}$ complex was used for the luminescent labelling of 50 nm AuNPs. The length of the PEG linker, between dye and nanoparticle, was varied and it was determined that the longest linker length of 13.2 nm (in linear conformation) showed enhanced luminescence and increased lifetimes, more than twice, that of the shorter (3.3 nm) modified AuNP. This nanoconjugate was then used for cellular imaging of transfected SP2 myeloma cells. The parent dye alone remains in the outer membrane of the cell wall, whereas, PEGylation to gold nanoparticles helps draw the luminophore across the cell membrane and is shown to locate throughout cell organelles without the need for organic solvents such as DMSO to help with solubility.

Furthermore, not only has the original parent complex $[Ru(bpy)_2(picCOOH)]^{2+}$, been shown to be useful in cell imaging but it has also served as a multimodal molecular probe for determining intracellular pH levels and oxygen concentrations.[1] Here, similar spectroscopic and photophysical results between the amino and carboxyl functionalised complexes were determined, lending to arguments supporting the potential use of AuNP-PEG_{32}-Ru as a potential multimodal transmembrane imaging probe.

3.7 References

(1) Neugebauer, U.; Pellegrin, Y.; Devocelle, M.; Forster, R. J.; Signac, W.; Moran, N.; Keyes, T. E. *Chem. Commun.* **2008**, 5307-5309.

(2) Brunner, J.; Barton, J. K. *Biochemistry (N. Y.)* **2006***, 45*, 12295-12302.

(3) Puckett, C. A.; Barton, J. K. *J. Am. Chem. Soc.* **2009***, 131*, 8738-8739.

(4) Zhang, S.; Hosaka, M.; Yoshihara, T.; Negishi, K.; Iida, Y.; Tobita, S.; Takeuchi, T. *Cancer Res.* **2010***, 70*, 4490-4498.

(5) Chen, T.; Liu, Y.; Zheng, W.; Liu, J.; Wong, Y. *Inorg. Chem.* **2010***, 49*, 6366-6368.

(6) Kowol, C. R.; Trondl, R.; Arion, V. B.; Jakupec, M. A.; Lichtscheidl, I.; Keppler, B. K. *Dalton Trans.* **2010***, 39*, 704-706.

(7) Balzani, V.; Bergamini, G.; Marchioni, F.; Ceroni, P. *Coord. Chem. Rev.* **2006***, 250*, 1254-1266.

(8) Deshpande, M. S.; Kumbhar, A. S.; Puranik, V. G.; Selvaraj, K. *Crystal Growth & Design* **2006***, 6*, 743-748.

(9) Daniel, M.; Astruc, D. *Chem. Rev.* **2004***, 104*, 293-346.

(10) Metcalfe, C.; Thomas, J. A. *Chem. Soc. Rev.* **2003***, 32*, 215-224.

(11) Liu, Y.; Zeng, C.; Huang, H.; He, L.; Wu, F. *Eur. J. Med. Chem.* **2010***, 45*, 564-571.

(12) Erkkila, K. E.; Odom, D. T.; Barton, J. K. *Chem. Rev.* **1999***, 99*, 2777-2796.

(13) Bai, G.; Dong, B.; Lü, Y.; Wang, K.; Jin, L.; Gao, L. A *J. Inorg. Biochem.* **2004***, 98*, 2011-2015.

(14) Huang, H.; Liu, Y.; Zeng, C.; Yao, J.; Liang, Z.; Li, Z.; Wu, F. *J. Mol. Struct.* **2010***, 966*, 136-143.

(15) Wu, J.; Li, L.; Zeng, T.; Ji, L.; Zhou, J.; Luo, T.; Li, R. *Polyhedron* **1997***, 16*, 103-107.

(16) Rani-Beeram, S.; Meyer, K.; McCrate, A.; Hong, Y.; Nielsen, M.; Swavey, S. *Inorg. Chem.* **2008***, 47*, 11278-11283.

(17) Olson, E. J. C.; Hu, D.; Harmann, A.; Jonkman, A. M.; Arkin, M. R.; Stemp, E. D. A.; Barton, J. K.; Barbara, P. F. *J. Am. Chem. Soc.* **1997***, 119*, 11458-11467.

(18) Campagna, S.; Puntoriero, F.; Nastasi, F.; Bergamini, G.; Balzani, V. *Photochemistry and Photophysics of Coordination Compounds: Ruthenium,* Springer Berlin / Heidelberg, **2007**, *280*,117-214.

(19) Liu, X.; Shen, Y.; Lu, J.; Chen, Y.; Li, L.; Zhang, D. *Spectrochimica Acta Part A: Molecular and Biomolecular Spectroscopy* **2010**, *77*, 522-527.

(20) Xiong, Y.; Ji, L. *Coord. Chem. Rev.* **1999**, *185-186*, 711-733.

(21) Shi, S.; Liu, J.; Li, J.; Zheng, K. C.; Tan, C. P.; Chen, L. M.; Ji, L. N. *Dalton Trans.* **2005**, 2038-2046.

(22) Schindler, M.; Grabski, S.; Hoff, E.; Simon, S. M.. *Biochemistry (N. Y.)* **1996**, *35*, 2811-2817.

(23) Švastová, E.; Hulíková, A.; Rafajová, M.; Zat'ovičová, M.; Gibadulinová, A.; Casini, A.; Cecchi, A.; Scozzafava, A.; Supuran, C. T.; Pastorek, J.; Pastoreková, S. *FEBS Lett.* **2004**, *577*, 439-445.

(24) Pellegrin, Y.; Forster, R. J.; Keyes, T. E. *Inorg. Chim. Acta* **2009**, *362*, 1715-1722.

(25) Pellegrin, Y.; Forster, R. J.; Keyes, T. E. *Inorg. Chim. Acta* **2008**, *361*, 2683-2691.

(26) Neugebauer, U.; Cosgrave, L.; Pellegrin, Y.; Devocelle, M.; Forster, R.; Keyes, T.,E. *unpublished results* .

(27) Cosgrave, L.; Devocelle, M.; Forster, R. J.; Keyes, T. E. *Chem. Commun.* **2010**, *46*, 103-105.

(28) Gu, Y.; Cheng, J.; Lin, C.; Lam, Y. W.; Cheng, S. H.; Wong, W. *Toxicol. Appl. Pharmacol.* **2009**, *237*, 196-204.

(29) Chen, H.; Li, J.; Lin, H.; Cai, Z.; Lin, H. *Supramolecular Chemistry* **2009**, *21*, 401.

(30) Chao, H.; Li, R.; Ye, B.; Li, H.; Feng, X.; Cai, J.; Zhou, J.; Ji, L. *J. Chem. Soc. , Dalton Trans.* **1999**, 3711-3717.

(31) Vos, J. G. *Polyhedron* **1992**, *11*, 2285-2299.

(32) Su, C.; Chen, H.; Tsai, K. Y.; Chang, I. *J Phys Chem B* **2007**, *111*, 6857-6860.

(33) Pramod, P.; Sudeep, P. K.; Thomas, K. G.; Kamat, P. V. *The Journal of Physical Chemistry B* **2006**, *110*, 20737-20741.

(34) Shenoy, D. *International Journal of Nanomedicine* **2006**, *1*, 51.

(35) Malicka, J.; Gryczynski, I.; Gryczynski, Z.; Lakowicz, J. R. *Anal. Biochem.* **2003**, *315*, 57-66.

(36) Aslan, K.; Wu, M.; Lakowicz, J. R.; Geddes, C. D. *J. Am. Chem. Soc.* **2007**, *129*, 1524-1525.

(37) Sullivan, P. *Inorganic Chemistry* **1978**, *12*, 3334.

(38) Steck, E. A.; Day, A. R. *J. Am. Chem. Soc.* **1943**, *65*, 452-456.

(39) Buchanan, B. E.; Degn, P.; Velasco, J. M. P.; Hughes, H.; Creaven, B. S.; Long, C.; Vos, J. G.; Howie, R. A.; Hage, R.; van Diemen, J. H.; Haasnoot, J. G.; Reedijk, J. *J. Chem. Soc. , Dalton Trans.* **1992**, 1177-1183.

(40) Atmeh, M.; Russell, N.; Forster, R.; Keyes, T. *Journal of Inclusion Phenomena and Macrocyclic Chemistry* **2007,** 1607-612.

(41) Veith, G. D.; Mekenyan, O. G.; Ankley, G. T.; Call, D. J. *Chemosphere* **1995***, 30*, 2129-2142.

(42) Ackermann, M. N.; Interrante, L. V. *Inorg. Chem.* **1984***, 23*, 3904-3911.

(43) McCusker, J. K. Femtosecond Absorption Spectroscopy of Transition Metal Charge-Transfer Complexes. *Acc. Chem. Res.* **2003***, 36*, 876-887.

(44) Curtis, J. C.; Sullivan, B. P.; Meyer, T. J. *Inorg. Chem.* **1983***, 22*, 224-236.

(45) Joseph R. Lakowicz In *Principles of Fluorescence Spectroscopy;* Springer: 2006.

(46) Spitler, E. L.; Haley, M. M. *Org. Biomol. Chem.* **2008***, 6*, 1569-1576.

(47) Quaranta, A.; Lachaud, F.; Herrero, C.; Guillot, R.; Charlot, M.; Leibl, W.; Aukauloo, A. *Chemistry - A European Journal* **2007***, 13*, 8201-8211.

(48) Madshus, I.H. *Biochem. J.*, **1988**, *250*, 1.

(49) A. Juris, V. Balzani, F. Bargelletti, S. Campagna, P. Belser, A. Von Zelewsky *Coord. Chem. Rev.* **1988**, 85-277.

(50) Sun, Y.; Collins, S. N.; Joyce, L. E.; Turro, C. *Inorg. Chem.* **2010***, 49*, 4257-4262.

(51) Maeda, H.; Yamauchi, Y.; Yoshida, M.; Ohmori, H. *Analytical Sciences* **1995***, 11*, 947-952.

(52) Liu, X.; Liu, J.; Jin, K.; Yang, X.; Peng, Q.; Sun, L. *Tetrahedron* **2005***, 61*, 5655-5662.

(53) Dodsworth, E. S.; Vlcek, A. A.; Lever, A. B. P. *Inorg. Chem.* **1994***, 33*, 1045-1049.

(54) Venkatanarayanan, A.; Spehar-De leize, A.; Dennany, L.; Pellegrin, Y.; Keyes, T. E.; Forster, R. J. *Langmuir* **2008***, 24*, 11233-11238.

(55) Robert J. Forster, Tia E. Keyes, Johannes G. Vos *Interfacial Supermolecular Assemblies;* Wiley: **2003**.

(56) Keyes, T.,E.; Jayaweera, P.,M.; McGarvey, J.,J.; Vos, J.,G. *J. Chem. Soc., Dalton Trans.* **1997**, 1627-1632.

(57) Adam Webb, M.; Knorr, F. J.; McHale, J. L. *J. Raman Spectrosc.* **2001***, 32*, 481-485.

(58) Ma'nuel, D. J.; Strommen, D. P.; Bhuiyan, A.; Sykora, M.; Kincaid, J. R. *J. Raman Spectrosc.* **1997***, 28*, 933-938.

(59) Lai, S.; Ling, J.; Huang, Y.; Huang, M.; Cheng, C. H.; Chen, I. *J. Raman Spectrosc.* **2011**, *42*, 332-338.

(60) EDC/NHS coupling mechanism. http://www.piercenet.com/browse.cfm?fldID=02030312 (Accessed 07/25, 2011).

(61) Thomas, K. G.; Kamat, P. V. *Acc. Chem. Res.* **2003**, *36*, 888-898.

(62) Glomm, W. R.; Moses, S. J.; Brennaman, M. K.; Papanikolas, J. M.; Franzen, S. *The Journal of Physical Chemistry B* **2005**, *109*, 804-810.

(63) Navon, G.; Sutin, N. *Inorg. Chem.* **1974**, *13*, 2159-2164.

(64) Levin, C. S.; Bishnoi, S. W.; Grady, N. K.; Halas, N. J. *Anal. Chem.* **2006**, *78*, 3277-3281.

(65) Ivanov, M. R.; Bednar, H. R.; Haes, A. J. *ACS Nano* **2009**, *3*, 386-394.

(66) Dreaden, E. C.; Mwakwari, S. C.; Sodji, Q. H.; Oyelere, A. K.; El-Sayed, M. *Bioconjug. Chem.* **2009**, *20*, 2247-2253.

(67) Li, S.; Liu, H.; Zhang, K.; Lo, K. *Chemistry - A European Journal* **2010**, *16*, 8329-8339.

(68) Notman, R.; Noro, M.; O'Malley, B.; Anwar, J. *J. Am. Chem. Soc.* **2006**, *128*, 13982-13983.

(69) Yu, Z.; Quinn, P. J. *Mol. Membr. Biol.* **1998**, *15*, 59-68.

Chapter 4: Synthesis and Characterisation of Iridium (III) Luminophores for Bioconjugation

"If we knew what we were doing, it wouldn't be research" – Albert Einstein.

4.0 Introduction

Iridium (III) complexes are of particular interest because of their high phosphorescent quantum yields and long lifetimes. Furthermore, their spectroscopy can be fine tuned leading to emission from blue to red by simply adjusting the chelating ligands. Such behaviour has not been observed to the same extent for ruthenium (II) complexes, whose emission by comparison, is rather insensitive to ligand adjustments and is mainly confined to the red region of the visible spectrum.[1] However, there is a general lack of understanding of the correlation between triplet state energy and the molecular structure of ligands for iridium (III) complexes in comparison with other transition metal complexes.[2]

The luminescent properties of iridium (III) complexes are strongly related to the σ-donating and π-accepting capabilities of the coordinating ligands. Their colour tunability arises because emission from the excited state may be MLCT in nature, or as is more often the case, a mixture of MLCT and LC states.[3] A further consequence of the mixing of states is that the iridium (III) complexes can have very long excited state lifetimes.[1] The various advantages of iridium (III) complexes as molecular probes have already been outlined previously in Chapter 1.

The synthetic chemistry available to iridium (III) is somewhat limited in contrast to ruthenium (II) complexes. This is partly due to the more complicated synthetic procedures required due to the greater chemical inertness of the iridium (III) coordination sphere.[4] It has also been reported that the synthesis of iridium (III) tris-chelates are difficult due to their steric hinderences and electronic effects.[5-7] However, in recent years, the use of iridium (III) chloride bridged dimers as a starting material has significantly simplified the synthesis of tris-chelates. Thompson *et al.*[5, 6, 8] have also demonstrated the synthesis of many iridium (III) complexes containing mixed chelating ligands with relative ease using the cyclometalated iridium (III) chloride bridged dimer as illustrated in Figure 4.1.

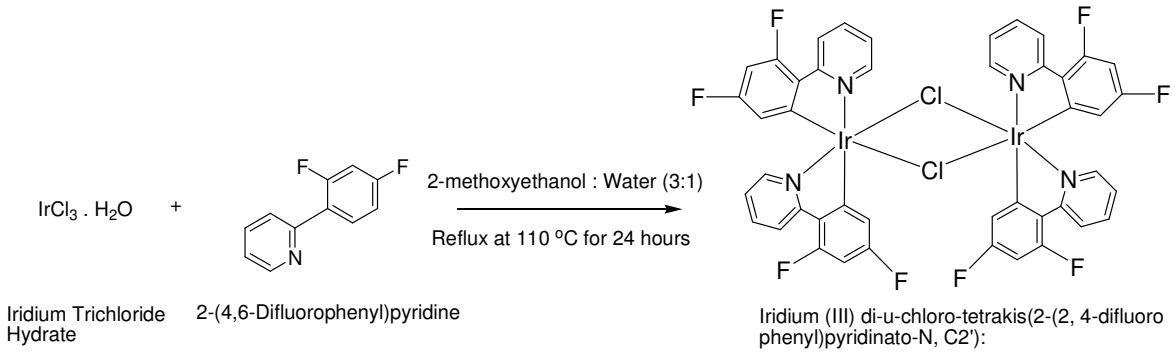

Figure 4.1: The synthesis of iridium (III) chloride bridged dimers as starting material has led to the facile synthesis of iridium (III) tris-chelates, which may display intense and long lived phosphorescence in the visible region.

Cyclometalated iridium (III) complexes have already shown significant potential for use as singlet oxygen sensors[8], DNA probes[7] and in biological labelling.[3, 9] Their use as DNA molecular probes was recently described by Lo *et al*.[7, 10] who designed a series of iridium (III) doquinoxaline and dipyridophenazine complexes as luminescent intercalators with DNA (Figure 4.2). These luminophores displayed intense and long lived green to orange phosphorescence from triplet MLCT or triplet LC transitions in aprotic organic solvents. However, in aqueous solution some complexes exhibited weak phosphorescence due to the effects of hydrogen bonding interactions between the phenazine nitrogen atoms and the aqueous solvent. Upon intercalation with synthetic double stranded oligonucleotides the probe luminesced strongly when protected from the water. This is not unlike observations previously for well known ruthenium (II) complexes containing dppz ligands.[11-13] However, the emission at 591 nm of the iridium dipyrido[3,2-f:2',3'-h]quinoxaline (dpq) complex (Figure 4.2 complex 1) exhibited a 33-fold emission intensity enhancement in the presence of double stranded calf thymus DNA.

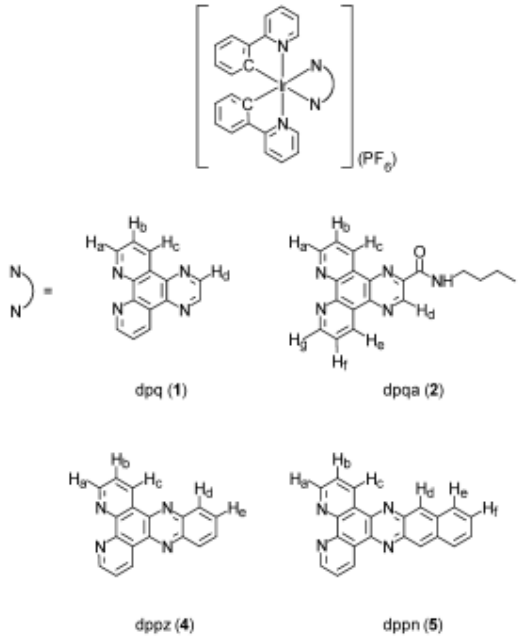

Figure 4.2: Series of iridium (III) doquinoxaline and dipyridophenazine complexes synthesised by Lo et al.[10] to determine their intercalating ability with DNA.

Another intensely researched application of iridium (III) polypyridyl complexes is their use as phosphors in organic light emitting diodes (OLEDs). The excited state generated in electroluminescence is trapped in the phosphor, where spin-orbit coupling ensures efficient population of the triplet state at room temperature. This leads to phosphorescent efficiencies of greater than 80% reported for iridium phenylpyridine based OLEDs.[6] Iridium phosphors containing phenylpyridine may also be easily functionalised to change the energies of the excited states that may result in different colour emitting diodes. The most sought after and yet most challenging accomplishment is the synthesis of blue emitting diodes. This is due to their high energy requirements whilst trying to maintain good quantum yields and photostability.[1] The ultimate aim is to achieve full colour OLED displays[2] that may be used in diverse applications from traffic lights to bill boards to remote controls.

Recently, iridium (III) complexes have been prepared using difluorophenyl pyridine ligands instead of bpy ligands commonly used in ruthenium complexes. It had been suggested that the difluorophenyl ligands led to higher quantum yield efficiencies, better photostability and longer phosphorescent lifetimes in iridium complexes.[3, 9, 14] As emission characteristics are governed by the electron density of the cyclometalating ligand[15] increasing the number of electron withdrawing fluorine substituents on the ligand causes a decrease in the HOMO energy level. This results in an increase of the HOMO-LUMO band gap and hence, a blue shift in emission maxima for the metal complex.[9, 14]

Most of the research to date has centred on chemical modification to the cyclometalating ligands (e.g. bpy / [dfpp] ligands) in an effort to fine tune their optical characteristics. For mixed ligand systems, little attention has thus far been dedicated to the ancillary ligand (e.g. [picCOOH] / [napth-R] ligands) which was thought to play an insignificant role in the phosphorescence of a complex as the LUMO generally lies on cyclometalating ligands themselves. In addition, changing the cyclometalating ligands has often proven difficult due to side reactions and steric crowding.[2]

However, You *et al.*[2] reported one of the first successful colour tuning of iridium (III) complexes by modification of the ancillary ligand. They reported the synthesis of iridium (III) complexes containing 2-(2-hydroxyphenyl)oxazole-based ancillary ligands with a lower energy ancillary ligand triplet state and higher energy cyclometalating ligand triplet state as illustrated in Figure 4.3 case III. They observed the direct optical excitation of both cyclometalating and ancillary ligands, thus identifying two excited species. This double excitation allowed for favourable interligand energy transfer processes because phosphorescence is generated from the chromophoric ancillary ligand only as a result of efficient intersystem crossing to the lower lying ancillary ligand excited energy state.

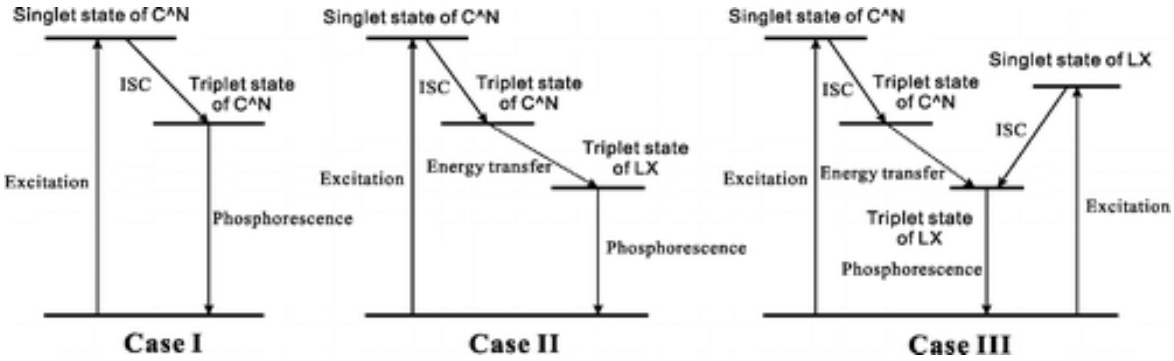

Figure 4.3: Schematic representation of the potential photophysical process of phosphorescent iridium (III) complexes, where C^N = cyclometalating ligand, LX = ancillary ligand and ISC = intersystem crossing.[2]

Their results demonstrated that the energy of LUMO on the ancillary ligand was lowered with increasing number of phenyl rings attached to the oxazole unit. Furthermore, this also occurred without any significant changes to the HOMO energy level. These novel 2-(2-hydroxyphenyl)oxazole-based compounds and related absorbance and emission spectra are illustrated in Figure 4.4 below. They exhibited broad ranging phosphorescent lifetimes (1.65-9.88 μs) and high phosphorescent quantum yields (0.36-0.43).

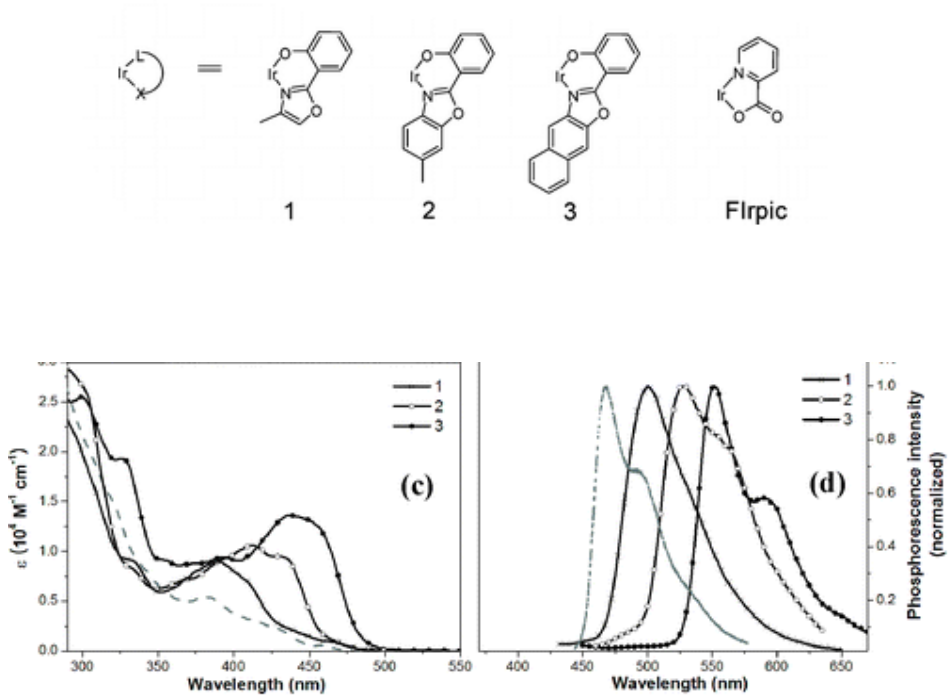

Figure 4.4: (Top) Schematic diagram illustrating the iridium (III) complexes containing 2-(2-hydroxyphenyl)oxazole-based ancillary ligands (complexes 1-3). (Bottom) Corresponding absorbance (left) and emission (right) spectra for the iridium (III) complexes 1-3. For comparison purposes the iridium (III) bis(2-(2,4-difluorophenyl)pyridinato-N,C2')pinolinate) [FIrpic] complex is also illustrated. [dashed grey line in the photophysics corresponds to the FIrpic complex].[2]

The iridium (III) complex containing the 2-(naphthoxazolyl)phenolate ancillary ligand (Figure 4.4 complex 3) displayed the longest lifetimes and largest quantum yields of the three compounds synthesised. With this in mind, in an effort to create long-lived visible emission iridium complexes for cellular imaging, two novel derivatives of the 2-(naphthoxazolyl)phenolate ligands containing nitro and amino substituents were synthesised and coordinated to the iridium (III) metal centre in this thesis. These complexes were characterised and their spectroscopic, photophysical and electrochemical properties compared. It was hoped that these new iridium (III) luminophores would display good photophysical characteristics as seen previously for their parent complex. In addition, the functionalised ligands would allow for conjugation for other molecules.

Williams *et al.*[16] also described the synthesis of a series of benzothiazole, benzoxazole and benzimidazole ligand derivatives (Figure 4.5) and examined their photophysics as a result of changing certain substituent groups. They demonstrated that the hydroxyl group located on the free ligand is essential for ligand fluorescence and that the oxazoles have higher quantum yield efficiency, greater UV stability and a more structured blue shifted fluorescence when compared to the benzothiazole or the benzimidazole derivatives.

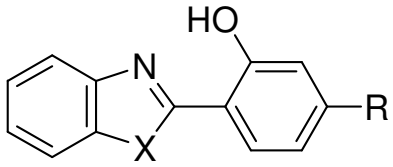

Figure 4.5: Schematic diagram illustrating series of benzothiazole (X = S), benzoxazole (X = O) and benzimidazole (X = NH) ligand derivatives synthesised by Williams et al.[16]

The inter-proton transfer capability of such ligands has been highlighted before for 2-(2'hydroxyphenyl)benzoxazole in solution phase luminescence studies and may be used to explain their basic mechanism of fluorescence. The stable ground state of the benzoxazole has the proton predominantly on the oxygen atom, whereas, following UV absorbance to an excited singlet configuration the proton is transferred to the nitrogen atom. It is this state which emits the visible fluorescence and decays back to the ground electronic state with the proton remaining on the nitrogen. The configuration with the hydrogen on the oxygen atom is its most stable form and as such completes the cycle by thermally relaxing to this arrangement. The importance of the proton associated with nitrogen to the fluorescence of the ligand is highlighted when the hydroxyl group is absent resulting in a non-fluorescent molecule.[16]

Attachment of an amino substituent to the 2-(2'hydroxyphenyl)benzoxazole ligand has the effect of shifting its absorbance and emission maximum to longer wavelengths when compared to the analogous nitro functionalised ligand as illustrated in Figure 4.22. This suggests that the electron donating amino substituent has increased density around the ligand resulting in a decrease in the π-π* HOMO-LUMO energy gap. This is further supported by results in Chapter 3 for amino and nitro functionalised ruthenium (II) polypyridyl complexes. Furthermore, the addition of the substituents does not impair the ligands ability to fluoresce in acetonitrile at room temperature.

Additionally, because of its enhanced aqueous emission, the pH sensitive ligand 2-(4-carboxylphenyl)imidazo[4,5-f][1,10]phenanthroline) [(picCOOH)] used in Chapter 3 is also coordinated to an iridium metal centre in the synthesis of the tris-chelating $[Ir(dfpp)_2(picCOOH)]^+$ dye (Figure 4.6). This novel water insoluble dye was fully characterised and conjugated to an octarginine peptide. Conjugation dramatically increased the aqueous solubility of the iridium dye which allowed for its use in the cellular imaging in SP2 myeloma and CHO cells. Direct comparisons were then made between the iridium dye-peptide, its parent and the analogous ruthenium (II) dye-conjugate in terms of detection and localisation within the cellular structure and form the basis of discussion in Chapter 5.

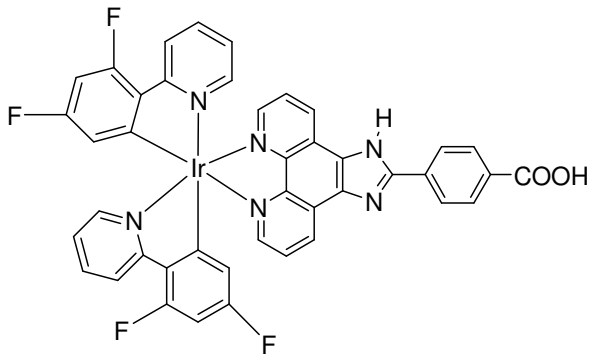

Figure 4.6: Schematic diagram illustrating the $[Ir(dfpp)_2(picCOOH)]^+$ complex synthesised in this thesis.

4.1 Experimental Procedure

Chemicals

All chemicals and reagents were purchased from Sigma-Aldrich (Ireland) and were used without any further purification unless otherwise stated.

The preparation of 2-(4,6-difluorophenyl)pyridine: [(dfpp)]

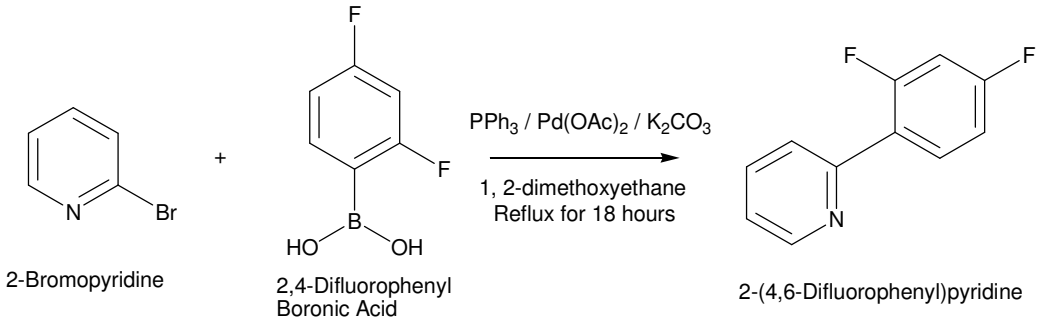

This procedure was adapted from the literature.[2] 2-Bromopyridine (2.0 g, 12.6 mmol), 2,4-diflorophenyl boronic acid (2.5 g, 15.2 mmol), triphenylphosphine (332 mg, 1.2 mmol), 1,2-dimethoxyethane (15 ml) and 2 M potassium carbonate (15 ml) were added to a round bottomed flask and degassed with stirring under a nitrogen environment. Next palladium (II) acetate (71 mg, 0.317 mmol) was added and left refluxing at 110 ^{o}C for 18 hours.

The solution was left to cool to room temperature and the aqueous phase was separated and extracted with ethyl acetate (25 ml x 3 times). The organic layers were combined and washed with deionised water and brine and finally dried on anhydrous $MgSO_4$. The solvent was then removed under reduced pressure to leave a transparent oily product.

The crude product was then purified on an alumina (neutral) chromatographic column using a mobile phase of hexane; 10% ethyl acetate to leave the product as a clear, oil-like substance (1.377 g, 57 %).

^{1}H NMR (400 MHz, DMSO-d_6): **δ (ppm) 8.72** (d, 1H, J = 4.5 Hz), **7.98** (dd, 1H, J = 2 Hz, J = 6.8 Hz), **7.92** (td, 1H, J = 2 Hz, J = 8 Hz), **7.78** (d, 1H, 4.8 Hz), **7.45-7.36** (m, 2H), **7.24** (td, 1H J = 2.4 Hz, J = 8 Hz).
Density: 1.258 g/cm^3.

The preparation of iridium (III) di-μ-chloro-tetrakis(2-(2, 4-difluorophenyl)pyridinato-N, C2'): [Ir$_2$(dfpp)$_4$(Cl$_2$)]

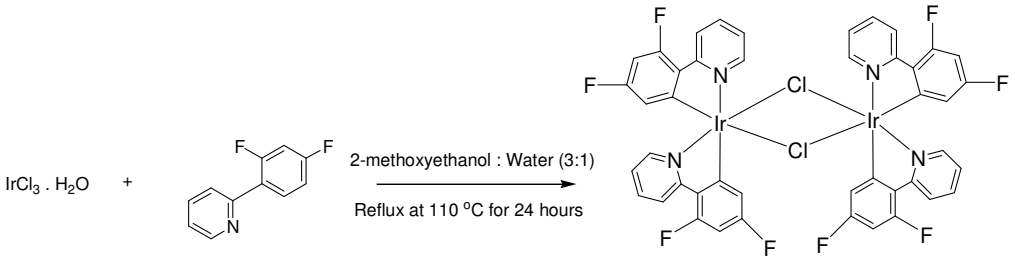

Iridium Trichloride Hydrate

2-(4,6-Difluorophenyl)pyridine

Iridium (III) di-u-chloro-tetrakis(2-(2, 4-difluoro phenyl)pyridinato-N, C2'):

This procedure was modified from the literature.[5] Iridium trichloride hydrate (842 mg, 2.66 mmol) was dissolved in a mixture of 2-methoxyethanol; water (60 ml, 3:1 v/v). 2-(4, 6-difluorophenyl) pyridine (1.066 g, 5.58 mmol) was then added and was left stirring overnight under a nitrogen environment.

Next the solution was left refluxing at 110 °C for 24 hours under a nitrogen environment. The solution was allowed cool to room temperature and water was added. The precipitate was collected by vacuum filtration and washed with ethanol. The solid was then dissolved in chloroform and washed with deionised water (10 ml x 3 times). The organic phase was dried on anhydrous $MgSO_4$ and evaporated to dryness to yield a yellow coloured product (862 mg, 27 %).

^{1}H NMR (400 MHz, $CDCl_3$): **δ (ppm) 9.78** (d, 2H, J = 5.2 Hz), **9.56** (d, 2H, J = 4.8 Hz), **8.32** (d, 2H, J = 8 Hz), **8.26** (d, 2H, J = 8.8 Hz), **8.21** (t, 2H, J = 8.4 Hz), **8.14** (t, 2H, J = 8.4 Hz), **7.69** (t, 2H, J = 7.2 Hz), **7.58** (t, 2H, J = 7.2 Hz), **6.90-6.77** (m, 4H), **5.73** (dd, 2H, J = 2.4 Hz, J = 6 Hz), **5.07** (dd, 2H, J = 2.4 Hz, J = 6 Hz).

The preparation of iridium (III) bis(2-(2,4-difluorophenyl)pyridinato-N, C2')-2(4-carboxylphenyl)imidazo[4,5-f][1,10]phenanthroline.(ClO_4^-) [Ir(dfpp)$_2$(picCOOH)]$^+$

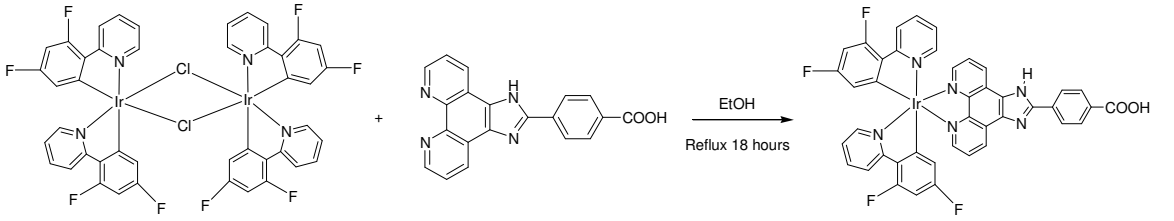

Iridium di-μ-chloro-tetrakis(2-(2, 4-difluorophenyl)pyridinato-N, C2') (220 mg, 0.181 mmol), 2-(4-Carboxylphenyl)imidazo[4,5-f][1,10]phenanthroline [(picCOOH)] (130 mg, 0.380 mmol) and ethanol (30 ml) were added to a round bottomed flask and left refluxing at 95 ^{o}C overnight.

The reaction was allowed cool to room temperature and the solvent removed by warming under reduced pressure. The solid was suspended in a saturated solution of sodium perchlorate and sonicated. The precipitate was collected by vacuum filtration and washed with deionised water. The precipitate was then dissolved in methanol and filtered once again. The filtrate was taken and evaporated to dryness to yield a yellow coloured solid (285 mg, 78 %).

^{1}H NMR (400 MHz, DMSO-d_6): **δ (ppm) 9.22** (d, 2H, 8 Hz), **8.41** (d, 2H, J = 8 Hz), **8.29** (d, 2H, J = 9.2 Hz), **8.22** (d, 2H, J = 4.4 Hz), **8.17** (d, 2H, J = 8.4 Hz), **8.07** (dd, 2H,

J = 5.2 Hz, J = 8 Hz), **7.98** (t, 2H, J = 7.6 Hz), **7.58** (d, 2H, J = 5.6 Hz), **7.09-6.99** (m, 4H), **5.71** (dd, 2H, J = 2 Hz, 2.4 Hz).

ESI-MS (CH_3OH, m/z): 1012.39, ($[M^+ - ClO_4]$): 913.1.

Elemental analysis calculated for $C_{42}H_{24}F_4IrN_6O_2.(ClO_4^-).(H_2O)_2$: C, 48.12; H, 2.69; N, 8.02%. Found: C, 48.35; H, 2.31; N, 7.86%.

Melting point: >300 ^oC

The preparation of 2-(naphtho[2,3-d]oxazol-2-yl)-5-nitrophenyl:

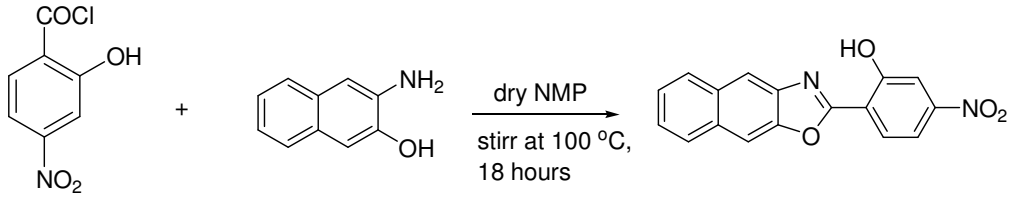

2-hydroxy-4-nitrobenzoyl chloride

3-amino-2-naphthol

2-(naphtho[2,3-d]oxazol-2-yl)-5-nitrophenyl

2-Hydroxy-4-nitrobenoyl chloride (2.75 g, 15 mmol, supplied by Dr. Elena Lestini and used as received) was added in portions to a solution of 3-amino-2-naphthol (2.38 g, 15 mmol) in dry NMP (120 ml). The mixture was stirred at 100 ^oC for 18 hours. After cooling to room temperature, the reaction was poured into deionised water and the pH adjusted to 8-9 by addition of aqueous ammonia. The precipitate formed was collected by vacuum filtration and washed with methanol to afford the product as a brown solid (1.47 g, 32 %).

^1H NMR (400 MHz, DMSO-d_6): **δ (ppm) 8.30** (d, 1H, J = 8.8 Hz), **7.83** (d, 2H, J = 8.8 Hz), **7.76** (d, 1H, J = 7.6), **7.66** (d, 1H, J = 8 Hz), **7.35** (m, 4H).

ESI-MS (CH_3OH, m/z): 306.26, ($[M+K^+]$): 347.5.

The preparation of iridium (III) bis(2-(2,4-difluorophenyl)pyridinato-N,C2') (2-naphthoxazoyl)4-nitrophenolate). [Ir(dfpp)$_2$(napthNO$_2$)]

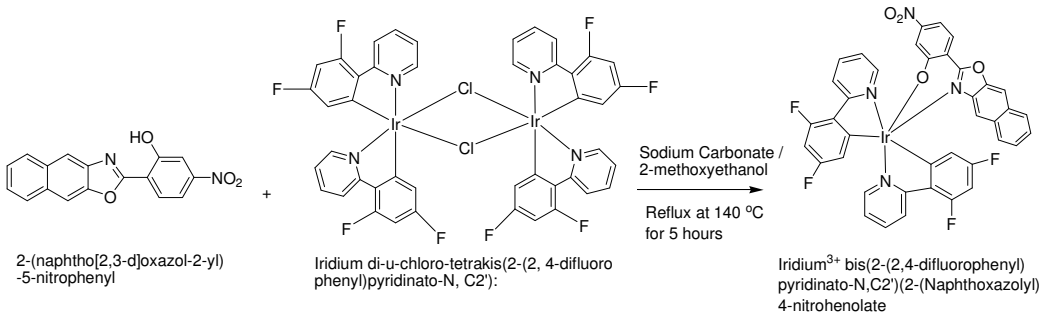

2-(naphtho[2,3-d]oxazol-2-yl) -5-nitrophenyl

Iridium di-u-chloro-tetrakis(2-(2, 4-difluoro phenyl)pyridinato-N, C2'):

Iridium^{3+} bis(2-(2,4-difluorophenyl) pyridinato-N,C2')(2-(Naphthoxazolyl) 4-nitrohenolate

Iridium di-μ-chloro-tetrakis(2-(2, 4-difluorophenyl)pyridinato-N, C2') (400 mg, 0.33 mmol), 2-(naphtho[2,3-d]oxazol-2-yl)-5-nitrophenyl (260 mg, 0.850 mmol) and sodium carbonate (350 mg, 3.2 mmol) were dissolved in 2-methoxyethanol (30 ml) and left stirring bubbling under nitrogen at room temperature for 20 minutes. The temperature was then raised to 140 ^{o}C and the reaction was refluxed under a nitrogen environment for 5 hours.

The reaction was cooled to room temperature and precipitated with a saturated solution of sodium perchlorate. The crude product was then filtered and purified on a silica gel column using a mobile phase of hexane; 20% ethyl acetate and was recrystallised in methanol to yield a red solid (150 mg, 20 %).

^{1}H NMR (400 MHz, $CDCl_3$): **δ (ppm) 8.67** (d, 1H, J = 6 Hz), **8.27** (d, 1H, J = 8.4 Hz), **8.13** (m, 2H), **8.02** (d, 1H, J = 6.8 Hz), **7.80** (d, 2H, J = 10.8 Hz), **7.68** (m, 2H), **7.51-7.34** (m, 4H), **7.21** (d, 1H, J = 2.4), **7.08** (t, 1H, J = 7.2 Hz), **6.86** (t, 1H, J = 7.2 Hz) **6.58** (m, 1H), **6.51** (s, 1H), **6.39** (m, 1H), **5.92** (dd, 1H, J = 6 Hz, J = 2.4 Hz), **5.52** (dd, 1H, J = 6 Hz, J = 2.4 Hz).

ESI-MS (CH_3OH, m/z): 877.8, ([M- NO_2ligand]): 573.2, ([M+Na^+]$^{3+}$): 901.0.

Elemental analysis calculated for $C_{39}H_{21}F_4IrN_4O_4.(CH_3OH)$: C, 52.80; H, 2.77; N, 6.16%. Found: C, 52.26; H, 2.55; N, 6.60%.

Melting point: >300 ^{o}C

The preparation of 2-(naphtho[2,3-d]oxazol-2-yl)-5-aminophenyl: [(NapthNH$_2$)]

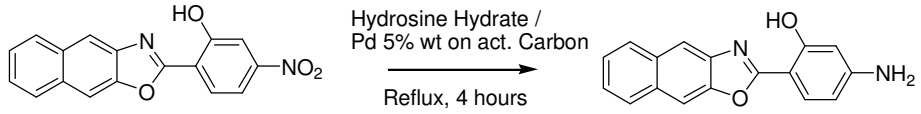

2-(naphtho[2,3-d]oxazol-2-yl)-5-nitrophenyl — 2-(naphtho[2,3-d]oxazol-2-yl)-5-aminophenyl

2-(Naphtho[2,3-d]oxazol-2-yl)-5-nitrophenyl (100 mg, 0.327 mmol), palladium 5% weight on activated carbon (21 mg) and absolute ethanol (5 ml) were added to a round bottomed flask. Next hydrazine hydrate (100 µl, 3.2 mmol) was added to the reaction in three equal amounts while stirring and left refluxing at 100 ^{o}C for 5 hours.

The solution was then cooled to room temperature and filtered through celite. The filtrate was collected and evaporated to dryness to yield a light brown coloured product (85 mg, 94 %).

^{1}H NMR (400 MHz, DMSO-d$_6$): **δ (ppm) 7.70** (d, 1H, J = 8.0 Hz), **7.67** (d, 1H, J = 8 Hz), **7.60** (d, 1H, J = 8 Hz), **7.26** (m, 4H), **6.15** (d, 1H, J = 6.4 Hz), **6.10** (s, 1H), **5.78** (s, 2H).

ESI-MS (CH_3OH, m/z): 276.29, ([M+K$^+$]): 317.4.

The preparation of iridium (III) bis(2-(2,4-difluorophenyl)pyridinato-N,C2') (2-naphthoxazoyl)4-aminophenolate). [Ir(dfpp)$_2$(napthNH$_2$)]

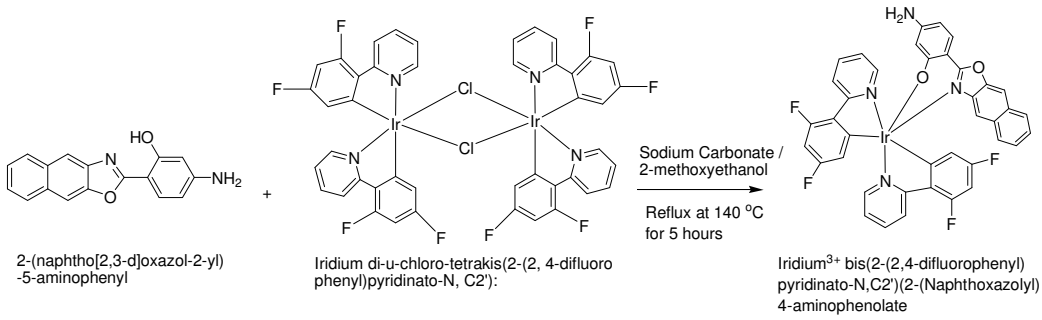

Iridium di-μ-chloro-tetrakis(2-(2, 4-difluorophenyl)pyridinato-N, C2') (168 mg, 0.138 mmol), 2-(naphtho[2,3-d]oxazol-2-yl)-5-aminophenyl (80 mg, 0.290 mmol) and sodium carbonate (146 mg, 1.38 mmol) were dissolved in 2-methoxyethanol (15 ml) and left stirring under nitrogen at room temperature overnight. The temperature was then raised to 140 ^{o}C and the reaction was refluxed under a nitrogen environment for 5 hours.

The reaction was cooled to room temperature and precipitated with a saturated solution of sodium perchlorate. The crude product was then filtered and purified on a silica gel column using a mobile phase of 10% methanol; dichloromethane to yield a yellow coloured solid (37 mg, 31 %).

^{1}H NMR (400 MHz, $CDCl_3$): **δ (ppm) 8.82** (d, 1H, J = 4.8 Hz), **8.30** (d, 1H, J = 8.4 Hz), **8.18** (m, 2H), **7.87** (d, 1H, J = 8.8 Hz), **7.80** (d, 1H, J = 8 Hz), **7.74-7.66** (m, 3H), **7.39-7.33** (m, 4H), **7.11** (t, 1H, J = 6 Hz), **6.91** (t, 1H, J = 6.8 Hz), **6.60** (m, 1H), **6.44** (m, 2H), **6.03** (d, 1H, J = 2.4), **5.98** (dd, 1H, J = 6.4 Hz, J = 2.4 Hz), **5.63** (dd, 1H, J = 6.4 Hz, J = 2.4 Hz), **3.86** (s, 2H).

MALDI-TOF (CH_3CN, m/z): 848.14, ([M+H$^+$]): 849.52, ([M- NH_2ligand]): 573.42.

Elemental analysis calculated for $C_{39}H_{23}F_4IrN_4O_2.(H_2O)$: C, 54.01; H, 2.91; N, 8.78%. Found: C, 55.96; H, 2.80; N, 8.11%.

Melting point: >300 ^{o}C

4.2 Results and Discussion

4.2.1 Synthesis

The Suzuki coupling of the difluorophenyl boronic acid and bromopyridine to give the [dfpp] ligand as starting material proceeded with a moderate yield of 57%. The full mechanism of reaction for Suzuki coupling is explained in detail in Chapter 6. Next the chlorine bridged iridium dimer was synthesised by refluxing the [dfpp] ligand and iridium trichloride overnight to give the yellow product with a relatively low yield of 27%. Identical reaction conditions as used previously to synthesise the $[Ru(bpy)_2(picCOOH)]^{2+}$ complex were also used to give $[Ir(dfpp)_2(picCOOH)]^{+}$ in good yields of 78%. This iridium (III) complex also had the added advantage of a facile purification procedure without a need for column chromatography when compared to other inorganic metal complexes.

In the synthesis of the two iridium (III) complexes containing the 2-(2-hydroxyphenyl)oxazole-based ancillary ligands, the initial chlorination of 2-hydroxyl-4-nitrobenzoic acid to give 2-hydroxyl-4-nitrobenzoyl chloride was performed using thionyl chloride in almost quantitative yields. Next, the one-step condensation reaction between 2-hydroxyl-4-nitrobenzoyl chloride and 3-amino-2-naphthol yielded the ancillary nitro functionalised ligand with a conversion of 32%. Reduction of the nitro ligand to the analogous 2-(naphtho[2,3-d]oxazol-2-yl)-5-aminophenyl ligand with hydrazine hydrate and palladium on activated carbon proceeded in a very efficient yield of 94%. Finally, the ligand exchange reaction between the chlorine bridged iridium dimer and the ancillary ligands was performed by refluxing in methoxyethanol under a nitrogen environment to give the corresponding nitro and amino functionalised iridium (III) complexes in yields of 20% and 31% respectively.

4.2.2 ^{1}H-NMR Discussion

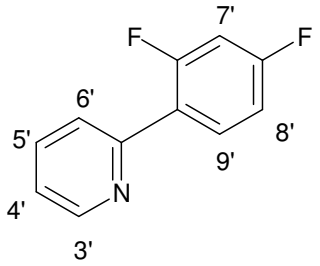

Figure 4.7: [dfpp] ligand illustrating numbering scheme for ^{1}H-NMR analysis.

Proton	**[dfpp] ppm**	**Proton**	**[$Ir_2(dfpp)_4(Cl_2)$] ppm**
$H_{3'}$	8.72 (d, 1H)	$H_{3'}$	9.78 (d, 2H)
$H_{9'}$	7.98 (dd, 1H)	$H_{3'}$	9.56 (d, 2H)
$H_{5'}$	7.92 (td, 1H)	$H_{6'}$	8.32 (d, 2H)
$H_{6'}$	7.78 (d, 1H)	$H_{6'}$	8.26 (d, 2H)
$H_{4'}, H_{8'}$	7.45-7.36 (m, 2H)	$H_{5'}$	8.21 (t, 2H)
$H_{7'}$	7.24 (td, 1H)	$H_{5'}$	8.14 (t, 2H)
		$H_{4'}$	7.69 (t, 2H)
		$H_{4'}$	7.58 (t, 2H)
		$H_{8'}$	6.90-6.77 (m, 4H)
		$H_{7'}$	5.73 (dd, 2H)
		$H_{7'}$	5.07 (dd, 2H)

Table 4.1: ^{1}H-NMR resonances for [dfpp] ligand and [$Ir_2(dfpp)_4(Cl_2)$] carried out in DMSO-d_6. The integration and peak splitting are shown in brackets.

As seen previously in Chapter 3, the proton located at $H_{3'}$ in Figure 4.7 showed the greatest shift downfield to 8.72 ppm due to the deshielding effects of the nitrogen atom on the cyclometalating ligand. The $H_{7'}$ proton, surrounded by the fluorine atoms is shifted upfield in the NMR spectrum to 7.24 ppm (Table 4.1). The increased shielding effect provided by fluorine on nearby protons has been reported previously.[17] This was in contrast to conventional thinking, that the presence of an electron withdrawing halide atom would generally show a shift in the peak further downfield. This may be explained by the stronger electronegativity of the smaller fluorine atom when compared to a larger chlorine atom. The resonance dipole is also superior for fluorine atoms because of the more efficient π-π overlapping with carbon. In the case of fluorine, it is speculated that the two dipoles effectively cancel out giving a net dipole of zero and the fluorine atom does not act like an electron withdrawing substituent.[18]

The ^{1}H-NMR spectrum of $[Ir_2(dfpp)_4(Cl_2)]$ (Figure 4.8) is not as easy to interpret as previous NMR spectra as the same protons on the four [dfpp] ligands are not always in the same chemical environments due to their spatial orientation around the coordinated metal centre. Hence, like all complexes synthesised in this thesis, ^{1}H-COSY 45 spectra (see Appendix 1) were used to aid in the assignment of all protons. Table 4.1 also outlines the individual proton chemical shifts for the $[Ir_2(dfpp)_4(Cl_2)]$ complex.

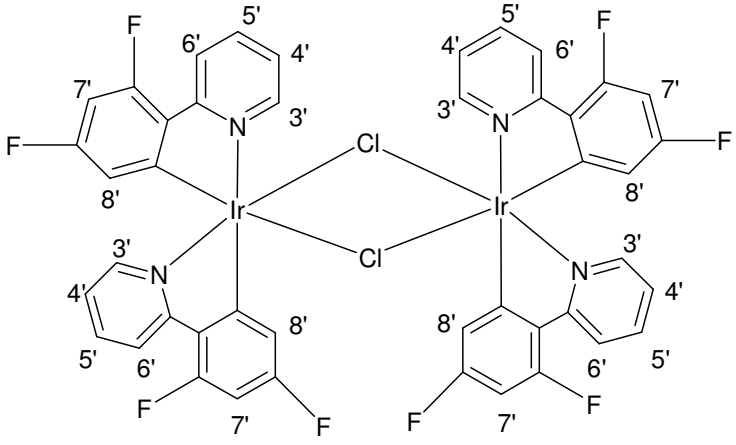

Figure 4.8: $[Ir_2(dfpp)_4(Cl_2)]$ illustrating numbering scheme for ^{1}H-NMR analysis.

For $[Ir(dfpp)_2(picCOOH)]^{2+}$ (Figure 4.9), the largest change in chemical shift (Δ ppm) between the free [dfpp] ligand and the iridium (III) coordinated [dfpp] ligand is associated with the proton located at position $H_{7'}$. This proton sees a chemical shift of -1.53 ppm upfield by comparison in Table 4.3. This may be explained by the donation of electrons from the iridium (III) metal centre to the [dfpp] ligands during bonding, thus, causing increased delocalisation of electrons around the ligand that is concentrated mainly on the $H_{7'}$ proton. All of the remaining protons are assigned in Table 4.2 below.

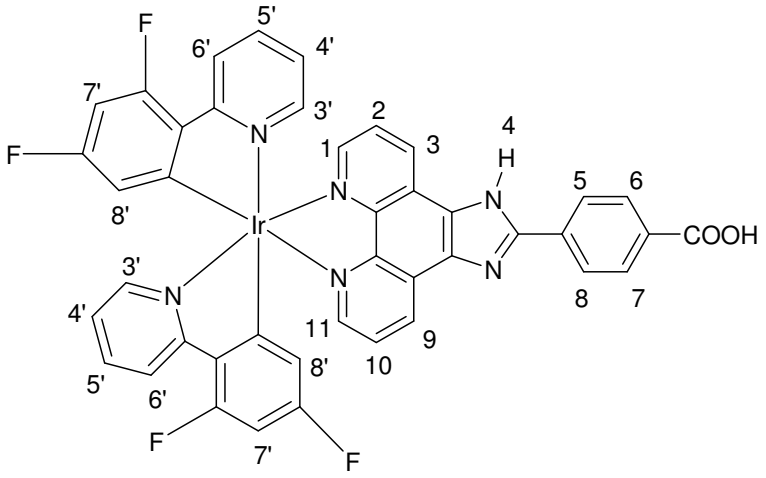

Figure 4.9: $[Ir(dfpp)_2(picCOOH)]^+$ illustrating numbering scheme for ^{1}H-NMR analysis.

Proton	**$(dfpp)_2$ ppm**	**Proton**	**[picCOOH] ppm**
$H_{3'}$	8.29 (d, 2H)	H_1, H_{11}	9.22 (d, 2H)
$H_{4'}$	7.98 (t, 2H)	H_6, H_7	8.41 (d, 2H)
$H_{6'}$	7.58 (d, 2H)	H_3, H_9	8.22 (d, 2H)
$H_{5'}$, $H_{8'}$	7.09-6.99 (m, 4H)	H_5, H_8	8.17 (d, 2H)
$H_{7'}$	5.71 (dd, 2H)	H_2, H_{10}	8.07 (dd, 2H)

Table 4.2: ^{1}H-NMR resonances for $[Ir(dfpp)_2(picCOOH)]^+$ carried out in DMSO-d_6. The integration and peak splitting are shown in brackets.

Proton	$[dfpp]_2$ Δ ppm	Proton	[picCOOH] Δ ppm
$H_{3'}$	-0.43	H_1, H_{11}	0.17
$H_{4'}$	0.58	H_2, H_{10}	0.20
$H_{5'}$	0.87	H_3, H_9	-0.73
$H_{6'}$	-0.20	H_4	n/a
$H_{7'}$	-1.53	H_5, H_8	0
$H_{8'}$	0.35	H_6, H_7	0.01
$H_{9'}$	n/a		

Table 4.3: Δ ppm of the free ligands compared to the coordinated complex.

Following coordination to the iridium metal centre, the protons at positions H_3 and H_9 of the [picCOOH] ancillary ligand exhibited the greatest change in their chemical shifts (Table 4.3). There was a slightly larger shift in ppm values for the [picCOOH] H_1 and H_{11} protons for the iridium complex compared to the ruthenium complex. This may be explained by the larger iridium atom, which has a greater electron density and greater propensity for π back donation due to the higher energy dπ orbital. There is also no indication of the amine H_4 or carboxyl protons in the $[Ir(dfpp)_2(picCOOH)]^+$ complex, presumably due to the resonance structures within the benzimidazole ligand or the deprotonation state in which the complex was synthesised.

The effects on the proton NMR of the amino and nitro substituents located on the ancillary ligand have been highlighted before in ruthenium (II) compounds in Chapter 3. The general trend is upheld here following the analysis of the iridium complexes with the 2-(naphtho[2,3-d]oxazol-2-yl)phenyl ligand (Figure 4.10). Protons located at the H_8 and H_9 positions showed an upfield chemical shift to around 6.12 ppm when the amino functionality was present. However, the same protons may be found further downfield at 7.83 ppm when the electron withdrawing nitro group is present. Protons H_2-H_5 are at similar chemical shifts values and are evident as a multiplet in the

NMR spectrum. All other protons are assigned in Table 4.4, with the exception of the O-H proton which is not evident in either NMR spectra probably due to proton exchanging.

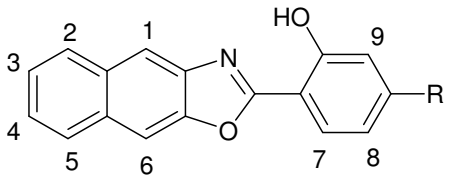

Figure 4.10: 2-(naphtho[2,3-d]oxazol-2-yl)phenyl ligand illustrating numbering scheme for ^{1}H-NMR analysis.

Proton	**[NapthNO$_2$] Ppm**	**Proton**	**[NapthNH$_2$] Ppm**
H_7	8.30 (d, 1H)	H_7	7.70 (d, 1H)
H_8, H_9	7.83 (d, 2H)	H_6	7.67 (d, 1H)
H_6	7.76 (d, 1H)	H_1	7.61 (d, 1H)
H_1	7.66 (d, 1H)	H_2, H_3, H_4, H_5	7.26 (m, 4H)
H_2, H_3, H_4, H_5	7.35 (m, 4H)	H_8	6.15 (d, 1H)
		H_9	6.10 (s, 1H)
		Amino-NH$_2$	5.78 (s, 2H)

Table 4.4: ^{1}H-NMR resonances for 2-(naphtho[2,3-d]oxazol-2-yl)phenyl ligand with nitro and amino functional groups carried out in DMSO-d_6. The integration and peak splitting are shown in brackets.

Due to its solubility the proton NMR for the coordinated iridium (III) complexes were performed in $CDCl_3$ rather than DMSO-d_6. As a result the changes in chemical shifts of the ancillary ligands are affected both by coordination to the iridium metal centre and to the solvent. Nevertheless, many of the trends observed before apply.

Coordination of the free 2-(naphtho[2,3-d]oxazol-2-yl)phenyl ligands to the iridium centre (Figure 4.11) results in the deprotonation of the ligand leading to an electron rich oxygen atom. Upon coordination of the ancillary ligand the protons are located further upfield than protons on the free ligand. The most affected protons are located at $H_{7,}$ H_8 and H_9 on the benzene ring of the napthoxazoyl ancillary ligand and they exhibited a chemical shift of up to 1.3 ppm upfield. However, as expected, the nitro withdrawing group causes a further chemical shift downfield of protons $H_{7,}$ H_8 and H_9 on the phenolate ligand in comparison with the amino substituted ligand as shown in Table 4.5. In general, the remaining protons are not as strongly affected as they are not within the three or four bonds of the electronegative oxygen site.

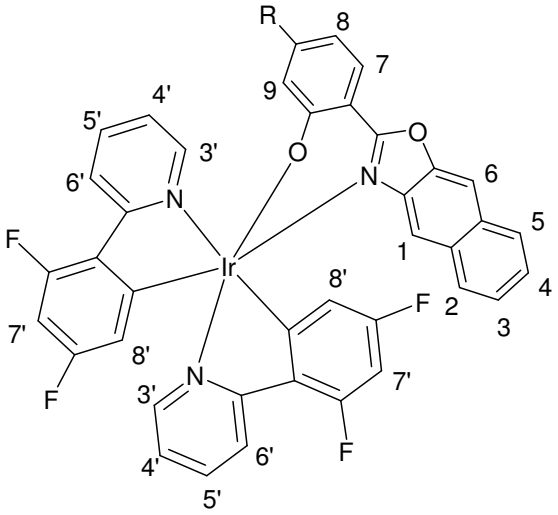

Figure 4.11: Iridium (III) bis(2-(2,4-difluorophenyl)pyridinato-N,C2') (2-naphthoxazoyl)4-phenolate) illustrating numbering scheme for ^{1}H-NMR analysis.

[Ir(dfpp)$_2$(napthNO$_2$)]		**[Ir(dfpp)$_2$(napthNH$_2$)]**	
[dfpp]$_2$ protons. ppm	**(napthNO$_2$) protons. ppm**	**[dfpp]$_2$ protons. ppm**	**(napthNH$_2$) protons Ppm**
$H_{3'}$ 8.67 (d, 1H)	H_7 8.13 (m, 2H)	$H_{3'}$ 8.82 (d, 1H)	H_7 7.87 (d, 1H)
$H_{6'}$ 8.27 (d, 1H)	H_1, H_6 7.80 (d, 2H)	$H_{6'}$ 8.30 (d, 1H)	H_1 7.80 (d, 1H)
$H_{6'}$ 8.13 (m, 2H)	H_2, H_3, H_4, H_5 7.51-7.34 (m, 4H)	$H_{3'}, H_{6'}$ 8.18 (m, 2H)	H_6 7.70 (m, 3H)
$H_{3'}$ 8.02 (d, 1H)	H_8 7.21 (d, 1H)	$H_{5'}$ 7.70 (m, 3H)	H_2, H_3, H_4, H_5 7.33-7.39 (m, 4H)
$H_{5'}$ 7.68 (m, 2H)	H_9 6.51 (s, 1H)	$H_{4'}$ 7.11 (m, 1H)	H_9 6.44 (m, 2H)
$H_{4'}$ 7.08 (t, 1H)		$H_{4'}$ 6.91 (m, 1H)	H_8 6.03 (d, 1H)
$H_{4'}$ 6.86 (t, 1H)		$H_{8'}$ 6.60 (m, 1H)	*Amino-*NH_2 3.86 (s, 2H)
$H_{8'}$ 6.58 (m, 1H)		$H_{8'}$ 6.44 (m, 2H)	
$H_{8'}$ 6.39 (m, 1H)		$H_{7'}$ 5.98 (m, 2H)	
$H_{7'}$ 5.92 (dd, 1H)		$H_{7'}$ 5.63 (m, 2H)	
$H_{7'}$ 5.52 (dd, 1H)			

Table 4.5: ^{1}H-NMR resonances for the iridium (III) bis(2-(2,4-difluorophenyl)pyridinato-N,C2') (2-naphthoxazoyl)4-phenolate compounds synthesised carried out in $CDCl_3$. The integration and peak splitting are shown in brackets.

4.2.3 Raman Spectroscopy of Iridium (III) Complexes

Figure 4.12 shows the overlaid Raman spectra of the iridium (III) complexes under non-resonant 785 nm excitation. The key bands are tabulated and tentatively assigned in Table 4.6 below according to published data on related iridium polypyridyl complexes.[19]

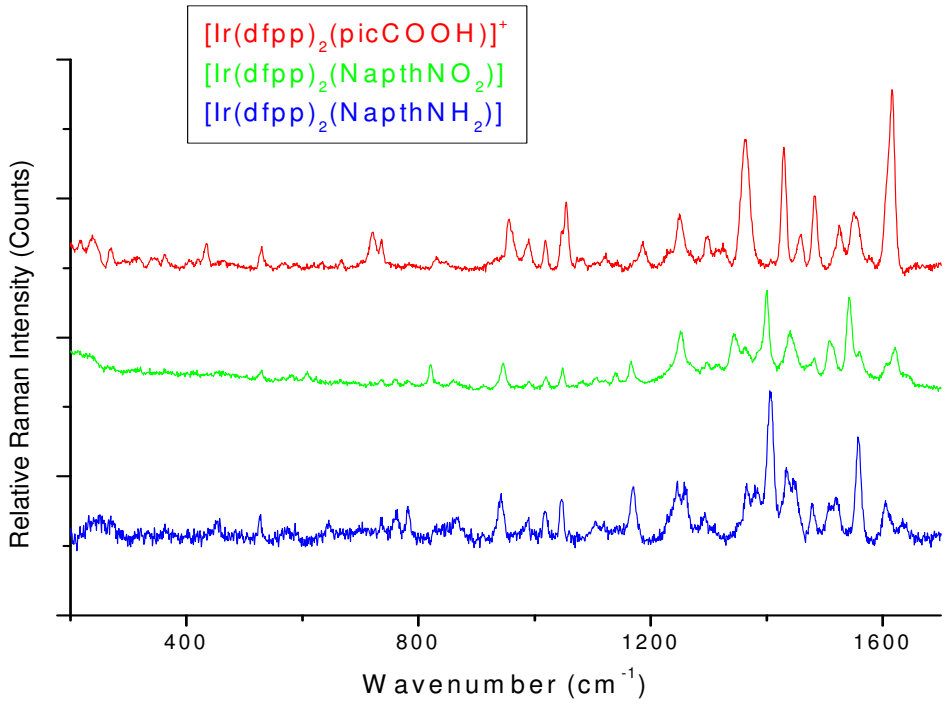

Figure 4.12: Stacked Raman spectra of the three iridium (III) complexes synthesised. Solid state samples were irradiated with 785 nm laser line. All spectra were gathered with 5 acquisitions and an exposure time of 5 seconds with a laser power of 2 mW.

Iridium - Raman peak identification		
785 nm laser	***(cm^{-1})***	***Assignment***
[dfpp] ligand vibrational modes:	~1611 ~1555 ~1520 ~1482 ~1363 ~1250 ~1170 ~1115 ~1050 ~945 ~530	C=C stretch C=C stretch C=C stretch C=N stretch C=N stretch C-C (inter-ring bending) CCH (in-plane bending) CCH (in-plane bending) Ring breathing Ring breathing Pyridyl in-plane twisting
[picCOOH] ligand vibrational modes:	~1300 ~990 ~772	C=N stretch Ring breathing Phenyl or pyridyl in-plane twisting
[napth-R] ligand vibrational modes	~1404 ~821	C=N stretch Phenyl or pyridyl in-plane twisting
Iridium – Ligand vibrational modes:	< ~450	Metal-Ligand stretching
Other vibrations:	~1450 ~1432	Post resonance vibrations

Table 4.6: Raman peak identification of the three iridium (III) complexes synthesised.

As expected, $[Ir(dfpp)_2(napthNO_2)]$ and $[Ir(dfpp)_2(napthNH_2)]$ display very similar Raman spectra with evidence of vibrational modes from both [dfpp] and [napth-R] ligands. In addition, vibrational modes containing contributions from both the [dfpp] and [picCOOH] ligands are also evident for the $[Ir(dfpp)_2(picCOOH)]^+$ complex following irradiation at 785 nm.

4.2.4 FTIR Spectroscopy of Iridium (III) Complexes

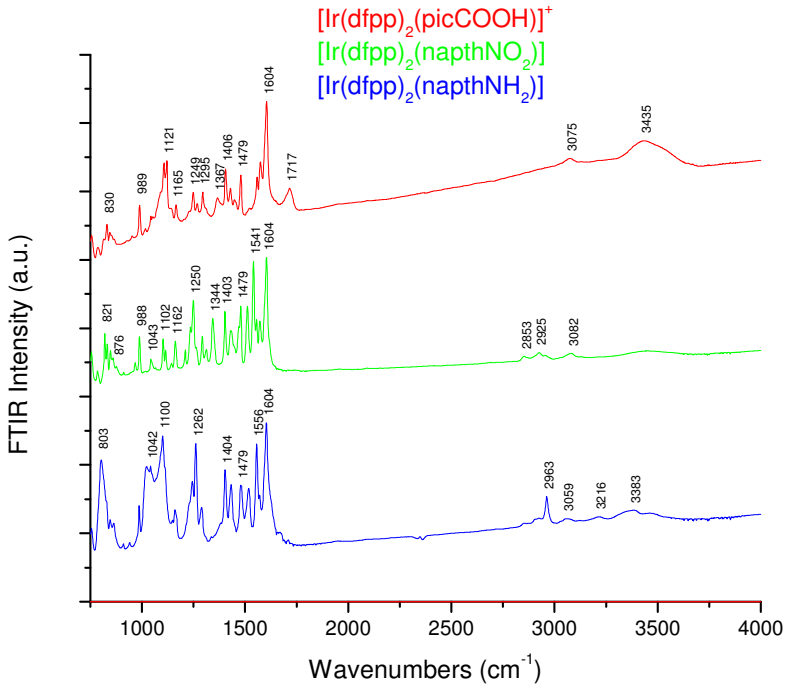

Figure 4.13: Stacked FTIR spectra of the three iridium (III) complexes synthesised. Samples were dispersed in a KBr matrix prior to analysis.

Further structural characterisation was performed using FTIR and their resulting spectra for the three iridium (III) complexes synthesised are shown in Figure 4.13 above. Common features between all three complexes include modes at ~3400 cm^{-1} (O-H stretch), ~2960 cm^{-1} (C-H stretch), ~1604 cm^{-1} (C=C stretch), ~1250 cm^{-1} (C-N stretch), ~1100 cm^{-1} (C-F stretch) and ~820 cm^{-1} (C-H phenyl ring stretch). For the $[Ir(dfpp)_2(picCOOH)]^+$ complex some of the more interesting features of the FTIR spectrum include vibrational modes at 3075 cm^{-1} (N-H stretch) and 1717 cm^{-1} (COOH stretch). For the $[Ir(dfpp)_2(napthNO_2)]$ complex the nitro symmetrical stretching mode is evident at 1262 cm^{-1} and the asymmetrical stretching mode at ~1500 cm^{-1}. Finally for the $[Ir(dfpp)_2(napthNH_2)]$ complex the two primary amine stretching vibrations are observed at 3216 cm^{-1} and 3059 cm^{-1} respectively. FTIR shows the distinctive functional groups of each complex quite clearly, which is unlike that seen in their corresponding ^{1}H-NMR spectra.

4.2.5 Electrochemical Studies of Iridium (III) Complexes

The voltammetric data for the three novel iridium (III) polypyridyl complexes are shown in Table 4.7 below.

Compound	***Metal-centred redox potential (V)***	***Ligand based redox potentials (V)***
$[Ir(dfpp)_2(picCOOH)]^+$	+1.70 (qr)	-0.85 (qr), -1.47 (qr)*, -2.09 (r)*.
$[Ir(dfpp)_2(napthNO_2)]$	+1.96 (ir)	-1.47 (ir)*, -2.47 (ir)*, -2.68 (ir).
$[Ir(dfpp)_2(napthNH_2)]$	+2.36 (ir)	-1.27 (ir)*, -2.12 (ir)*, -2.35 (ir), -2.75 (ir).

Table 4.7: Redox properties of iridium (III) complexes synthesised measured in acetonitrile (containing 0.1M TBA as electrolyte) with 1.5 mm glassy carbon working electrode and referenced against Ag/AgCl. (r) – reversible reaction, (ir) – irreversible reaction and (qr) – quasi-reversible reaction. All CV's were performed in duplicate with different glassy carbon electrodes, scanning though the range of potentials (multiple scans): 1, 0.50, 0.25 and 0.05 Vs^{-1} respectively. Electrochemistry was conducted using 1 mmol of sample dissolved in 5 cm^3 of dry acetonitrile (HPLC grade, used as received) containing 0.1 M tetrabutylammonium tetrafluoroborate (TBA) as supporting electrolyte. All samples were degassed with nitrogen prior to analysis.
** denotes the reduction potential of the [dfpp] ligands.*

Bracketing experiments in Figure 4.14 (inset) shows the quasi reversible $Ir^{3+/4+}$ redox couple for the $[Ir(dfpp)_2(picCOOH)]^+$ complex which is centred at +1.70 V versus Ag/AgCl and has a peak separation of 142 mV. The oxidation of iridium metal centres generally occurs at more positive potentials than ruthenium centres owing to less electron density around the metal centre.[4] In the full cyclic voltammogram for $[Ir(dfpp)_2(picCOOH)]^+$, there are two quasi-reversible ligand based redox potentials at -

0.85 V assigned to the [picCOOH] ligand, -1.47 V attributed to the [dfpp] ligand and a further reversible redox peak at -2.09 V attributed to the [dfpp] ligand versus Ag/AgCl respectively.[20] In contrast, the first [picCOOH] ligand reduction of the $[Ru(bpy)_2(picCOOH)]^{2+}$ complex is at a potential of -0.72 V versus Ag/AgCl, however, due to the sharpness and intensity of this peak it is thought to be as a result of adsorption or film formation on the electrode surface. Furthermore, as previously mentioned in Chapter 3, the carboxyl functional group may adsorb to an anodized glassy carbon electrode surface.[21]

There is also a peak at +1.44 V versus Ag/AgCl, which appears just before the metal redox couple in a full potential sweep. During bracketing experiments, this peak was found to be related to a ligand reduction peak at -1.02 V as it is not present unless the negative reduction voltage (and thus adsorption of the complex) has been reached. Furthermore, this peak remains present for multiple scans at various scan rates. There is no evidence of this particular oxidation peak in blank solution when the iridium complex is not present as shown in the control cyclic voltammogram in Appendix 1-Figure A39. However, it is noted that identification of redox peaks are only tentatively assigned based on the available literature for similar complexes.

Once again, as seen for the ruthenium complexes in Chapter 3, this suggests that the LUMO of the complex lies on the ancillary [picCOOH] ligand and not on the cyclometalating [dfpp] ligands as the pKa results indicated, vide infra. However it is thought that the higher lying LUMO, which determines the T_1 state of the complex, is dominated by the cyclometalating [dfpp] ligands. Theoretical calculations of cyclometalated iridium (III) complexes have also shown that reduction is generally considered to mainly occur on the heterocyclic portion of the cyclometalating (bpy or [dfpp] ligands). [14]

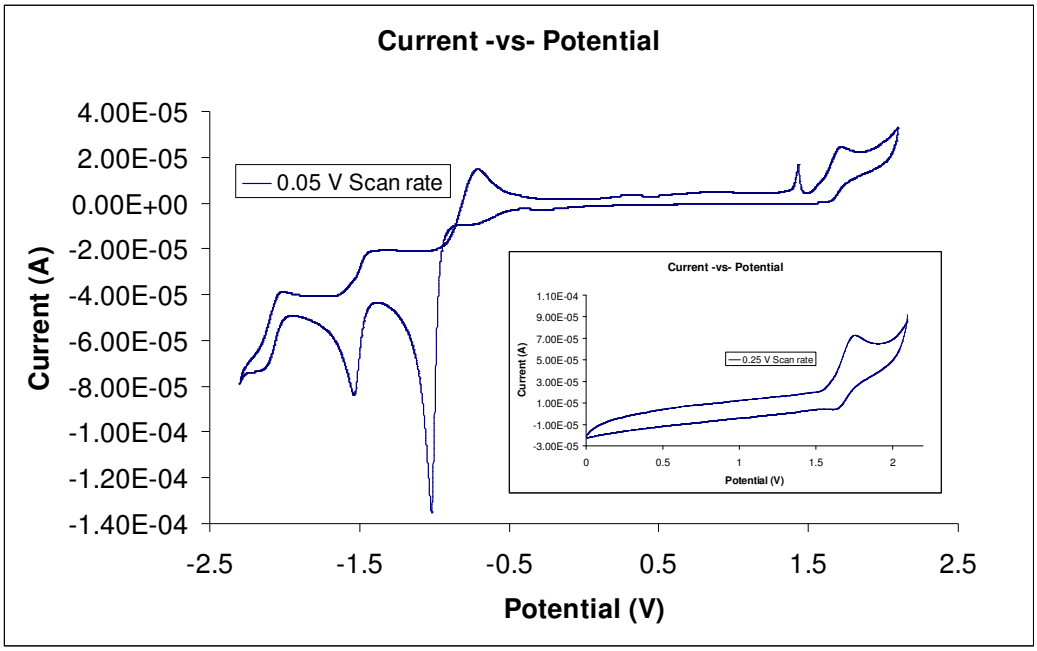

Figure 4.14: Cyclic voltammogram of $[Ir(dfpp)_2(picCOOH)]^+$ in acetonitrile (containing 0.1M TBA as electrolyte) with 1.5 mm glassy carbon working electrode and referenced against Ag/AgCl. Scans were started in a positive direction from an initial potential of 0 V. (Inset) isolated positive region of CV.

The metal centered oxidation of $[Ir(dfpp)_2(napthNO_2)]$ at +1.96 V versus Ag/AgCl is irreversible with little evidence of the corresponding reduction peak for the $Ir^{3+/4+}$ redox couple even when only scanning in the bracketed positive potential region window (Figure 4.15). The ligand based redox couples are also irreversible processes. The ligand based reductions are tentatively assigned to -1.47 V [dfpp] ligand, -2.47 V [dfpp] ligand and -2.68 V $[napthNO_2]$ ligand versus Ag/AgCl, whereas, there is slight evidence of the corresponding ligand oxidation peaks is at -0.57 V, -2.26 V and -2.77 V versus Ag/AgCl respectively.

It has been noted that a one electron oxidation of an iridium metal centre results in a lengthening of the iridium-oxygen bond length.[22] It is likely that the $Ir^{3+/4+}$ couple leads to disruption of the iridium ligand bond. However, narrowing the potential window and changing scan rates revealed no further improvement to the CVs upto a scan rate of 1 Vs^{-1}, which indicates that the bond disruption is fast. The delicate nature of the iridium (III) (naphthoxazolyl) phenolate complexes was further replicated in their

mass spectra analysis where fragmentation of the iridium-ligand bond was evident. This proved unlike any other coordinated metal complex synthesised as part of this research where mass spectra fragmentation patterns of the ligands, under electron spray ionisation conditions, were not typically observed.

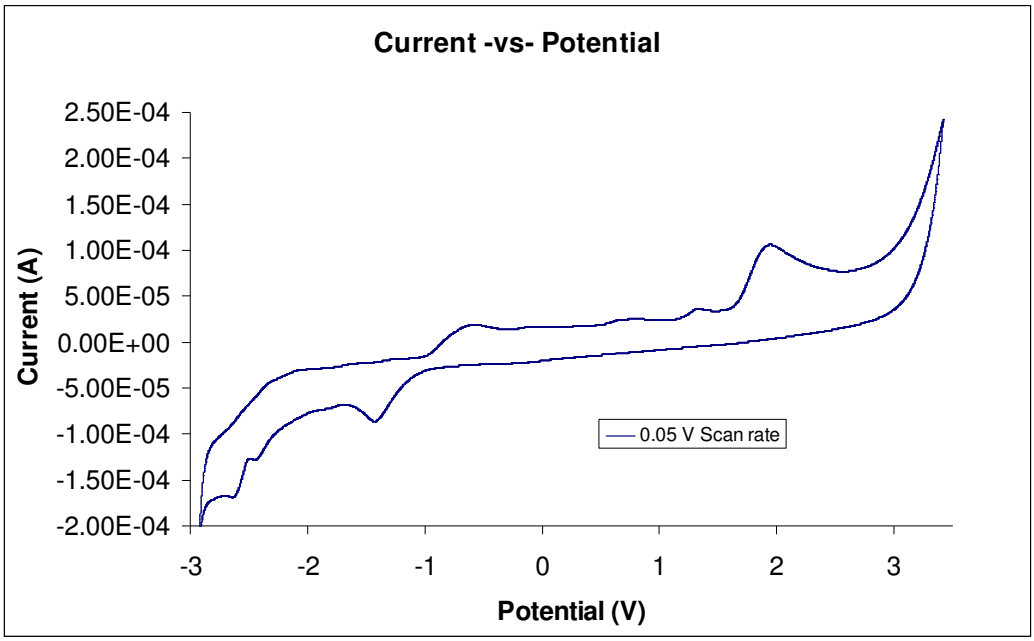

Figure 4.15: Cyclic voltammogram of [Ir(dfpp)$_2$(napthNO$_2$)] in acetonitrile (containing 0.1M TBA as electrolyte) with 1.5 mm glassy carbon working electrode and referenced against Ag/AgCl. Scans were started in a positive direction from an initial potential of 0 V.

Again the cyclic voltammogram of [Ir(dfpp)$_2$(napthNH$_2$)] contains an irreversible metal oxidation. The $Ir^{3+/4+}$ occurs at +2.36 V versus Ag/AgCl in Figure 4.16. Additionally, there is no evidence of a reversible couple when only positive potentials are isolated. Such high metal oxidation potentials are caused by low electron density available around the iridium (III) atom making coordinating bonds unstable. The ligand redox couples are also irreversible. Ligand reduction peaks are evident at -1.27 V [dfpp] ligand, -2.12 V [dfpp] ligand, -2.35 V [napthNH$_2$] ligand and -2.75 V [napthNH$_2$] ligand versus Ag/AgCl respectively and irreversible oxidation peak values at -0.78 V, -1.45 V, -2.19 V and -2.74 V versus Ag/AgCl. As explained previously, the irreversible electrochemistry is attributed to bond breakage between iridium centre and

ancillary ligand moiety when placed under electrochemical stress. As seen previously for amino functionalised complexes,[23] it is possible that electropolymerisation is occurring here for the [Ir(dfpp)$_2$(napthNH$_2$)] complex and also following the reduction of [Ir(dfpp)$_2$(napthNO$_2$)] to the corresponding amino complex during the electrochemical potential sweep. Furthermore, adsorption is not really obvious for the nitro or amino functionalised complexes.

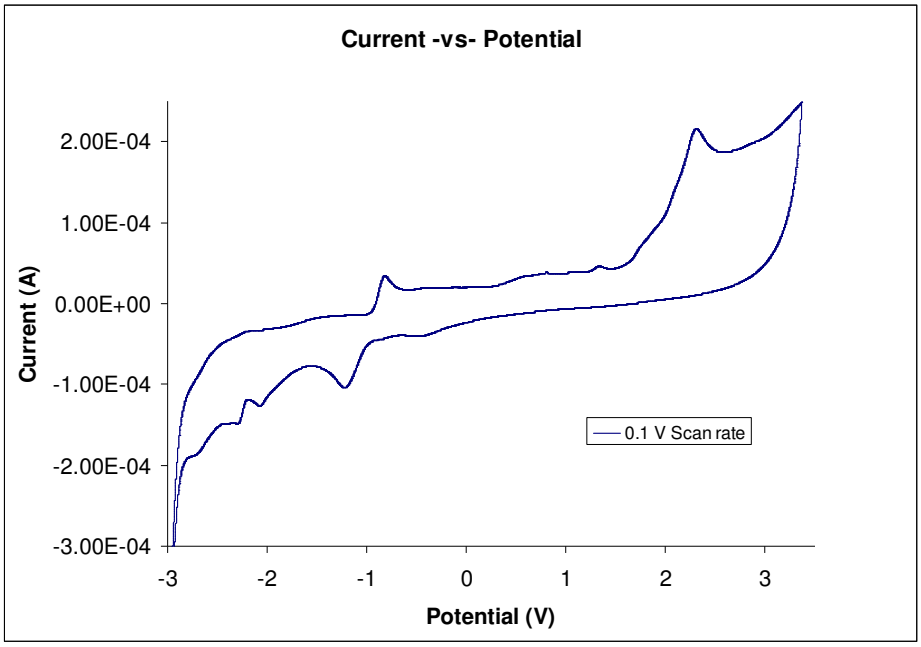

Figure 4.16: Cyclic voltammogram of [Ir(dfpp)$_2$(napthNH$_2$)] in acetonitrile (containing 0.1M TBA as electrolyte) with 1.5 mm glassy carbon working electrode and referenced against Ag/AgCl. Scans were started in a positive direction from an initial potential of 0 V.

4.3 Optical and Acid-Base properties of Iridium (III) Complexes

Compound	Absorbance [a] λ_{max} (ε, $dm^3mol^{-1}cm^{-1}$)	Emission [a] λ_{max}	ϕ [b]	pKa [c] (+/- 0.1)	pKa* [c] (+/- 0.1)
$[Ir(dfpp)_2(picCOOH)]^+$	381 nm (12,390) 324 nm (44,084) 283 nm (54,847)	521 nm	0.103	3.7, 11.5	3.1, 11.1
$[Ir(dfpp)_2(napthNO_2)]$	450 nm (6,271) 338 nm (21,563) 243 nm (56,300)	516 nm 539 nm	0.0009	n/a	n/a
$[Ir(dfpp)_2(napthNH_2)]$	418 nm (20,800) 348 nm (19,650) 245 nm (56,700)	524 nm 564 nm	0.0056	n/a	n/a

Table 4.8: Optical and Acid-Base properties of Iridium (III) Complexes Synthesised.

[a] *Measured in acetonitrile at room temperature using concentrations of 20 x 10^{-6} M.*

[b] *Photoluminescent quantum yield (ϕ) measured in degassed acetonitrile at room temperature, using $[Ru(bpy)_3]^{2+}$ as standard.*

[c] *Ground (pKa) and excited state (pKa*) values, measured in PBS buffer solution at room temperature.*

Complex	**τ (ns)** [a] ***(percentage component)***	**τ (ns)** [a] ***(percentage component)***	***x^2 value***
$[Ir(dfpp)_2(picCOOH)]^+$	241 +/- 5 (95%)	20 +/- 3 (5%)	0.897
$[Ir(dfpp)_2(napthNO_2)]$	11 +/- 3 (79%)	3 +/- 1 (21%)	0.942
$[Ir(dfpp)_2(napthNH_2)]$	189 +/- 6 (84%)	7 +/- 2 (16%)	0.871

Table 4.9: Biexponential lifetime results for the iridium (III) complexes synthesised.

[a] *Biexponential lifetimes measured in degassed acetonitrile at room temperature*

4.3.1 Absorbance and Emission of [Ir(dfpp)$_2$(picCOOH)]$^+$

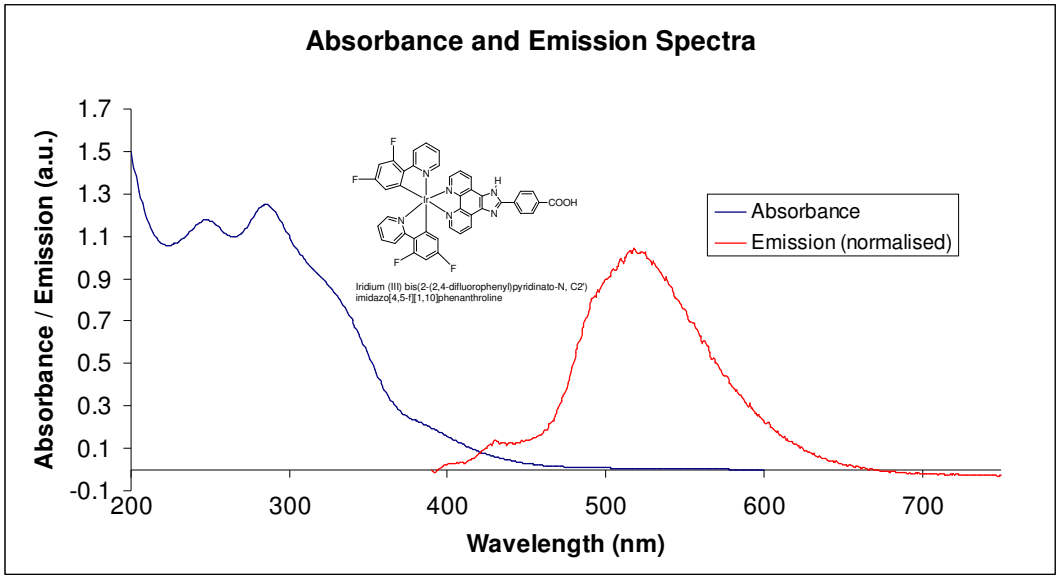

Figure 4.17: Absorbance and normalised emission spectra (excited at 381 nm, slit widths: 5 nm, normalised to 1 arbitrary unit) of 20 x 10^{-6}M [Ir(dfpp)$_2$(picCOOH)]$^+$ in acetonitrile solution.

Figure 4.17 shows the absorbance and emission spectra for the [Ir(dfpp)$_2$(picCOOH)]$^+$ complex. The UV-vis spectrum of [Ir(dfpp)$_2$(picCOOH)]$^+$ is dominated by LC difluorophenyl pyridine π-π* electronic transitions giving maximum absorbance peaks at 245 nm and 283 nm. This is consistent with reports of other iridium (III) complexes containing difluorophenyl pyridine, bipyridyl or terpyridine ligands.[1, 24] The shoulder at 324 nm may be assigned to the intraligand π-π* transition of the [picCOOH] ligand. A weaker, broad feature extending down into longer wavelengths at 381 nm is attributed to the MLCT from the iridium dπ to [dfpp] π* orbital.

[Ir(dfpp)$_2$(picCOOH)]$^+$ is strongly luminescent and exhibits an emission maximum at 521 nm when excited into the MLCT band at 381 nm with a quantum yield of 0.103 in aerated acetonitrile. This compares favourably with increased quantum yield when compared to the [Ru(bpy)$_2$(picCOOH)]$^{2+}$ complex (ϕ = 0.068). Interestingly, the emission decay follows biexponential kinetics as outlined in Table 4.9.

Furthermore, the lifetimes in degassed PBS buffer solutions (containing 5% acetonitrile) are 207 +/- 7 ns at pH 1.0, 168 +/- 6 ns at pH 6.9 and 5 +/- 1 ns at pH 12.0. The decrease in lifetimes of the deprotonated imidazolate species may be explained by the dissipation of the excited state energy into lower lying non-radiative acceptor states on the imidazolate ligand.[25] Although the lifetimes are shorter, the quantum yield of the iridium (III) complex is 40% greater than $[Ru(bpy)_2(picCOOH)]^{2+}$ and its lifetime in degassed methanol is as long as 842 +/- 9 ns. $[Ir(dfpp)_2(picCOOH)]^{+}$ is only partially soluble in PBS buffer and initially had to be dissolved in acetonitrile (5%) to aid solubility.

4.3.2 pH Dependence Studies of $[Ir(dfpp)_2(picCOOH)]^{+}$

Protonation of the $[Ir(dfpp)_2(picCOOH)]^{+}$ complex had little effect on the wavelength of the absorbance of the iridium complex suggesting that there is no change in the HOMO-LUMO energy gap or in the distribution of π electrons across the system upon acidification (Figure 4.18). This is in contrast to the ruthenium (II) complex as the formation of the protonated species leads to an increase in the HOMO-LUMO as indicated by a blue shift in the absorbance at 330 nm in Figure 3.13. The formation of an isobestic point at 370 nm is an indication that changes its absorbance intensity is not just due to changes in its solubility upon protonation. In particular, the relative intensities of the two LC transitions at 245 nm and 283 nm vary significantly with a decrease in pH.

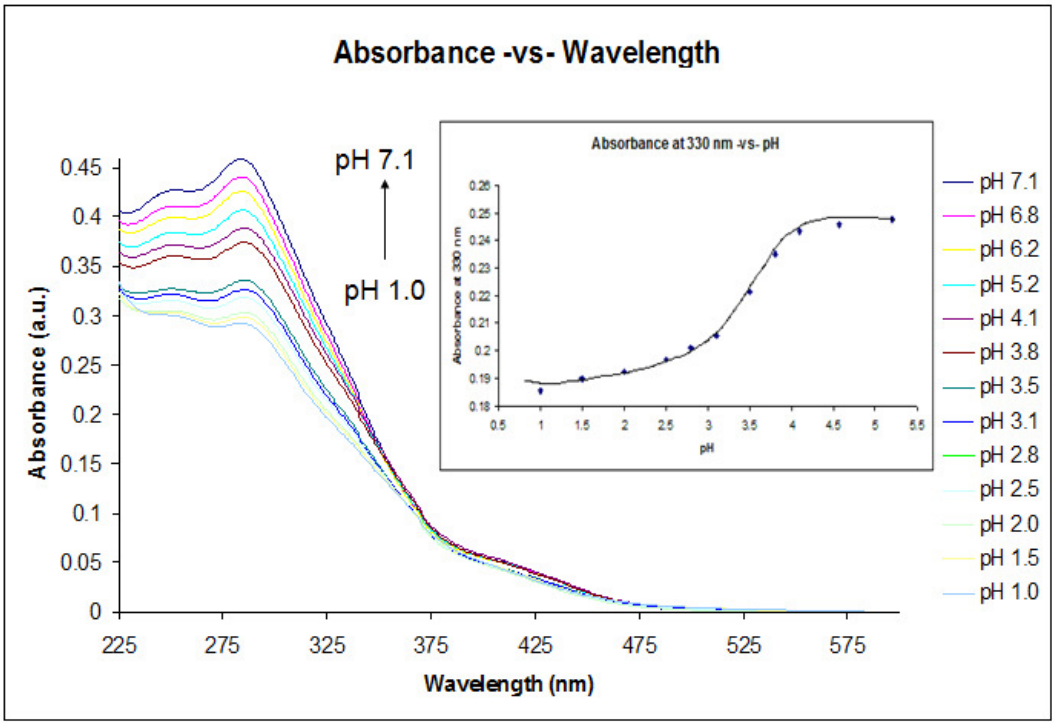

Figure 4.18: Absorbance spectra of 20 x 10^{-6} M (15 cm^3) $[Ir(dfpp)_2(picCOOH)]^+$ in PBS buffer solution (containing 5% acetonitrile) upon addition of µl aliquots of percholric acid solution. (inset) pH titration curve of $[Ir(dfpp)_2(picCOOH)]^+$ in PBS solution (containing 5% acetonitrile) monitoring the changes in absorbance at 330 nm upon addition of perchloric acid.

Upon addition of base to the iridium (III) complex the absorbance intensity decreases with little change to absorbance wavelengths as shown in Figure 4.19. However when deprotonation of the imidazole, to form $[Ir(dfpp)_2(picCOOH)]$, occurs at around pH 10.5 where there is a dramatic shift in absorbance wavelengths to lower energies. This suggests a more extended π system which is consistent with deprotonation of the imidazole leading to enhanced electronic communication between the phenanthroline and imidazole components.[25] The spectral changes brought about by a change in pH have relatively little effect on the MLCT because this transition is mostly concentrated on LC cyclometalating ligand transitions at higher energies. This seems good confirmation that the LUMO for the MLCT lies mainly on the difluorophenyl pyridine ligands, which is also confirmed in calculating ground and excited state pKa values, vide infra.

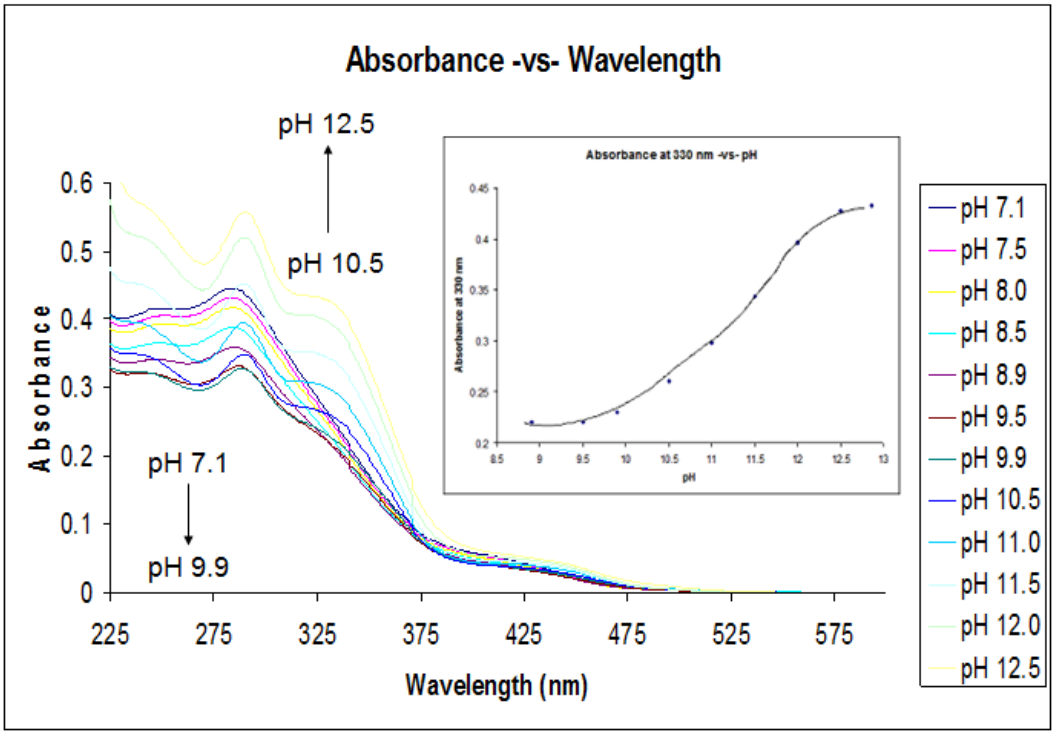

Figure 4.19: Absorbance spectra of 20 x 10^{-6} (15 cm^3) $[Ir(dfpp)_2(picCOOH)]^+$ in PBS buffer solution (containing 5% acetonitrile) upon addition of µl aliquots of sodium hydroxide solution. (inset) pH titration curve of $[Ir(dfpp)_2(picCOOH)]^+$ in PBS solution (containing 5% acetonitrile) monitoring the changes in absorbance at 330 nm upon addition of sodium hydroxide solution.

The ground state pKa values of the pH sensitive imidazole ligand were determined by monitoring the spectral changes at 330 nm over a pH range of 1.0-12.0 (Figures 4.18 inset and 4.19 inset). The pKa/pKa* spectroscopy was irreversible and was not fully recovered on returning to the initial pH. The ground state pKa values were calculated to be equal to 3.7 +/- 0.1 and 11.5 +/- 0.1 respectively. These ground state values are higher than that seen before for the same benzimidazole ligand on the $[Ru(bpy)_2(picCOOH)]^{2+}$ complex. It is considered that the calculated pKa values for the iridium (III) complex are higher in comparison with the ruthenium (II) complex as a result of the acetonitrile (5%) used to solvate the iridium complex in PBS (pH7.4) buffer. Previous papers have highlighted the significant differences in pKa values for the $[Ru(bpy)_2(picCOOH)]^{2+}$ complex when performed in acetonitrile[26] and aqueous[25] media.

The luminescent profile of $[Ir(dfpp)_2(picCOOH)]^+$ showed a small spectral shift in their emission maxima to longer wavelengths upon deprotonation from 536 nm at pH 1.5 to 564 nm at pH 9.9 as shown in Figures 4.20 and 4.21. This suggested an increase in the HOMO-LUMO energy gap at lower pH values which may be due to the electrostatic repulsion between the positively charged iridium 4+ metal centre and the extra positive charge on the imidazolium ligand.[25]

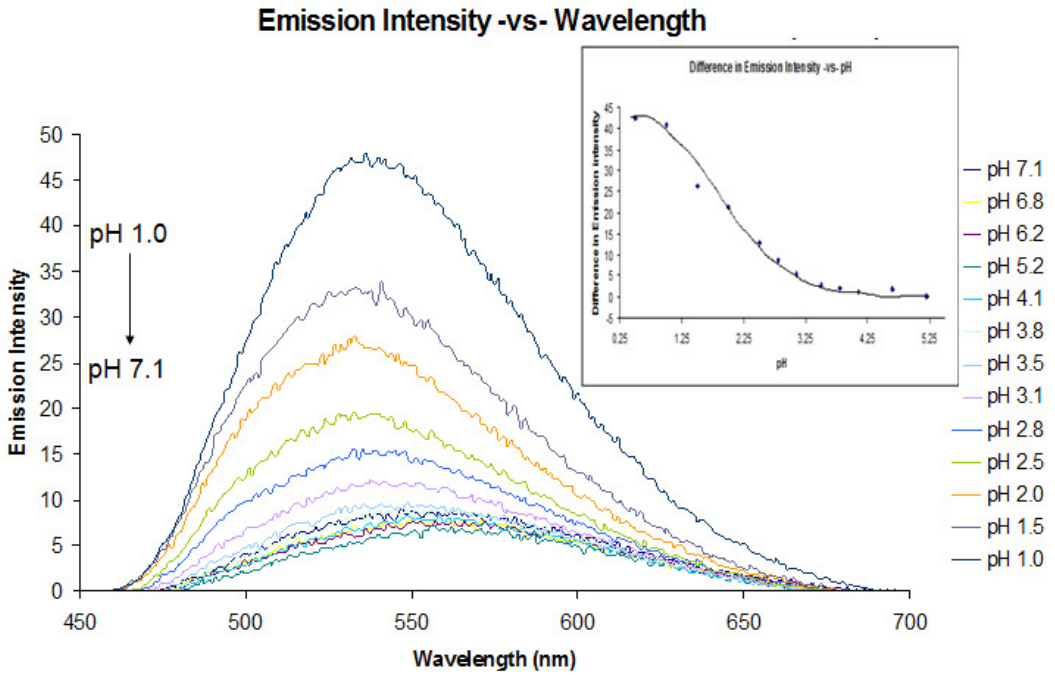

Figure 4.20: Emission spectra of 20 x 10^{-6} M (15 cm^3) $[Ir(dfpp)_2(picCOOH)]^+$ in PBS buffer solution (containing 5% acetonitrile) upon addition of µl aliquots of perchloric acid solution. (370 nm excitation wavelength, slit widths: 5 nm). (inset) pH titration curve of $[Ir(dfpp)_2(picCOOH)]^+$ in PBS solution (containing 5% acetonitrile) monitoring the differences in maximum emission intensity (excited at 370 nm) versus pH, upon addition of perchloric acid.

However, from pH 10 to pH 12, there is a reverse in this general trend and the emission maximum is slightly blue shifted as shown in Figure 4.21. This also corresponded with the dramatic change in the absorbance profile of the complex over similar pH ranges (Figure 4.19). The excited state pKa* values of the complex were

calculated to be 3.1 +/- 0.1 and 11.1 +/- 0.1 respectively (Figures 4.20 inset and 4.21 inset), which are somewhat lower than those calculated for the ground state pKa values (3.7 +/- 0.1 and 11.5 +/- 0.1). This suggests that the excited state lies on the [dfpp] ligands because had the excited state been located on the ionisable ligand, the excited state pKa* value would have been more basic (by more than 3 pH units) due to the increase in electron density on that ligand.[27] As seen for the pH dependence studies for $[Ru(bpy)_2(picCOOH)]^{2+}$ there is only evidence of two pKa values corresponding to formation of $[Ir(dfpp)_2(picCOOH)]^{2+}$ and $[Ir(dfpp)_2(picCOOH)]^{0}$ in a process very similar to that discussed in the introduction to Chapter 3. However, the emission intensity of the iridium complex is not recovered on returning to neutral pH which is unlike that seen for the corresponding $[Ru(bpy)_2(picCOOH)]^{2+}$ complex.

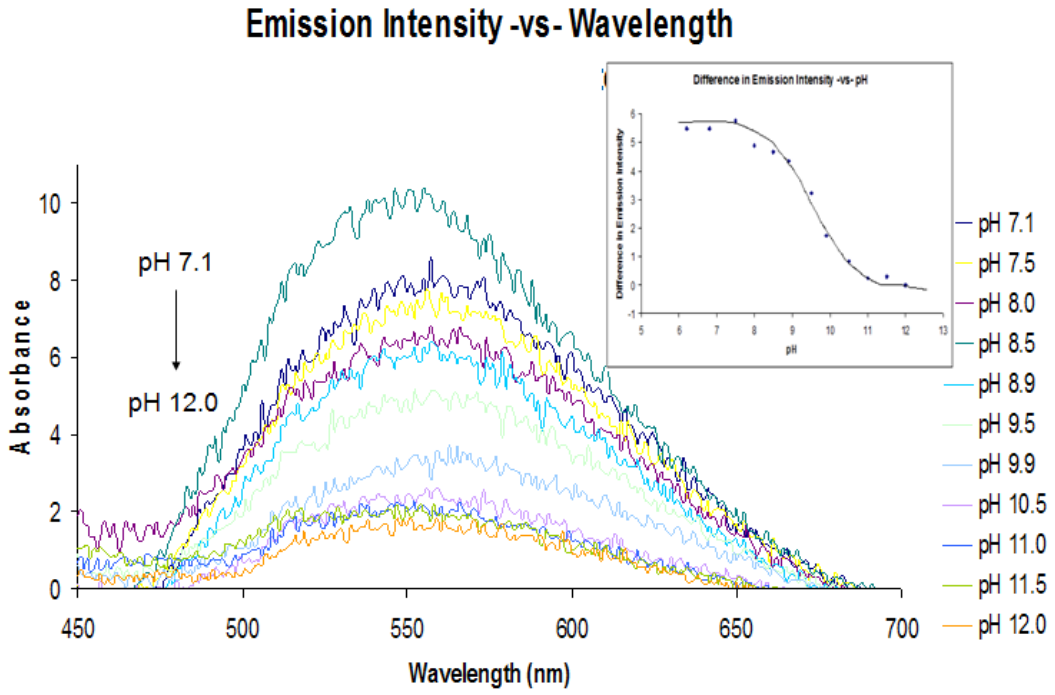

Figure 4.21: Emission spectra of 20 x 10^{-6} M (15 cm^3) $[Ir(dfpp)_2(picCOOH)]^+$ in PBS buffer solution (containing 5% acetonitrile) upon addition of µl aliquots of sodium hydroxide solution. (375 nm excitation wavelength). (inset) pH titration curve of $[Ir(dfpp)_2(picCOOH)]^+$ in PBS solution (containing 5% acetonitrile) monitoring the differences in maximum emission intensity (excited at 370 nm) versus pH, upon addition of sodium hydroxide solution.

4.4 Absorbance and Emission of Novel 2-(Naphthoxazolyl) phenolate Ancillary Ligands

Figure 4.22 below illustrates the absorbance and emission profiles for the novel uncoordinated [napthNO$_2$] and [napthNH$_2$] ligands in acetonitrile solutions. The shapes of the vibronic absorption spectra of the free ligands strongly resemble the absorption of the coordinated iridium (III) complexes (Figure 4.24) suggesting a direct excitation of the ancillary ligands. Therefore, it may be inferred that the ancillary ligands are related to the optical excitation responsible for this absorption behaviour. This allows for the complexes to absorb strongly over a large spectral range making them potentially useful as components in solar cells or OLEDs.[2]

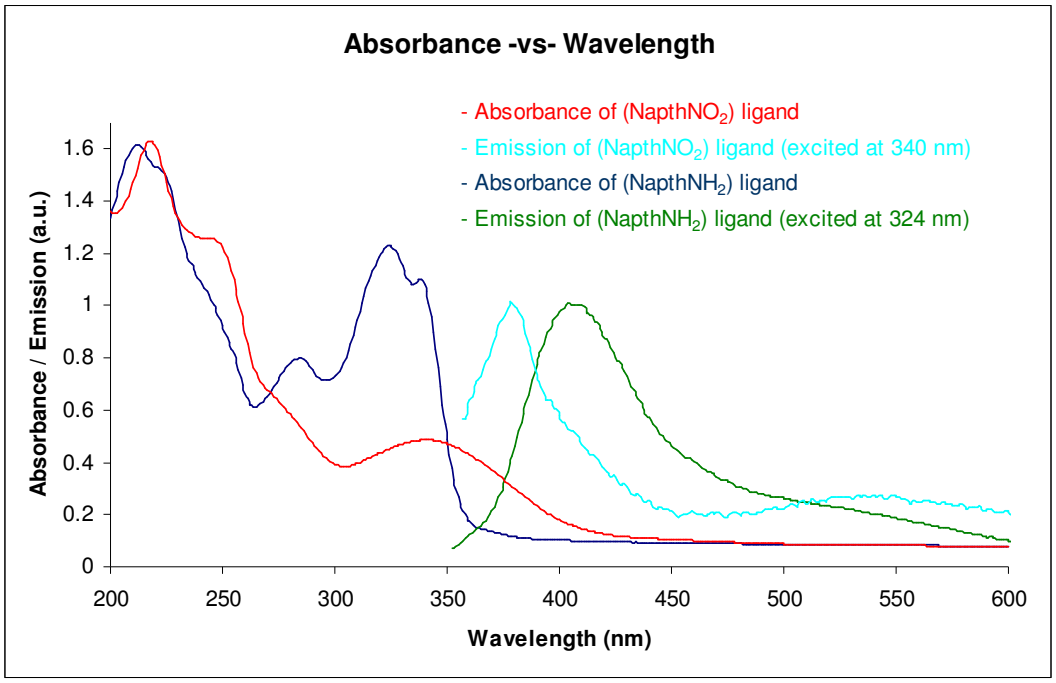

Figure 4.22: Overlaid absorbance and emission spectra of 20 x 10^{-6} M [napthNO$_2$] (excited at 345 nm) and [napthNH$_2$] (excited at 320 nm) free ligands in acetonitrile. Emission spectra are normalised to 1 arbitrary unit and slit widths of 10 nm were used in gathering emission data.

4.4.1 Absorbance of [Ir(dfpp)$_2$(napthNO$_2$)] and [Ir(dfpp)$_2$(napthNH$_2$)]

In most iridium (III) complexes containing phenylpyridine ligands the HOMO is spread over the iridium centre and anionic phenyl ring and the LUMO is mostly localised on the neutral pyridine ring of the cyclometalating ligand.[2] As mentioned in the introduction the most efficient way of altering the colour tunability of heteroleptic iridium (III) complexes is by lowering the ancillary ligand LUMO without significantly effecting the HOMO energy level. This can be achieved by controlling functionality on the chromophoric ancillary ligands. Furthermore, results by You *et al*.[2] indicated that the LUMO of the ancillary ligand is lowered with increasing numbers of phenyl rings fused to the oxazole unit while the HOMO level showed a relatively small change in energy by comparison. Results suggested that a related iridium (III) bis(2-(2,4-difluorophenyl)pyridinato-N,C2') (2-naphthoxazoyl)phenolate), shown in Figure 4.23, exhibited good photophysical characteristics including long phosphorescent lifetimes and quantum yields.[2]

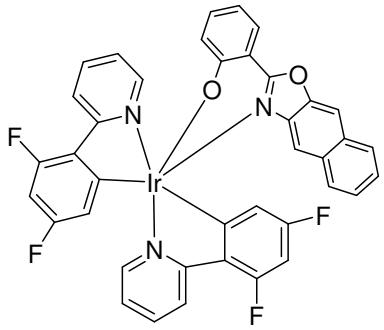

Figure 4.23: Schematic diagram of iridium (III) bis(2-(2,4-difluorophenyl)pyridinato-N,C2') (2-naphthoxazoyl)phenolate).

Indeed the author proposed the emission so bright that they are useful OLED materials. As such, we were intended in applying them as cellular probes, however, this required functional groups for bioconjugation so the novel nitro and amino functionalised derivatives of this iridium luminophore were synthesised. It was hoped that they would exhibit good photophysics as observed from their parent complex. The resultant absorbance spectra of [Ir(dfpp)$_2$(napthNO$_2$)], [Ir(dfpp)$_2$(napthNH$_2$)] and the iridium (III) parent complex ([Ir(dfpp)$_2$(napth)]) are shown in Figure 4.24 below.

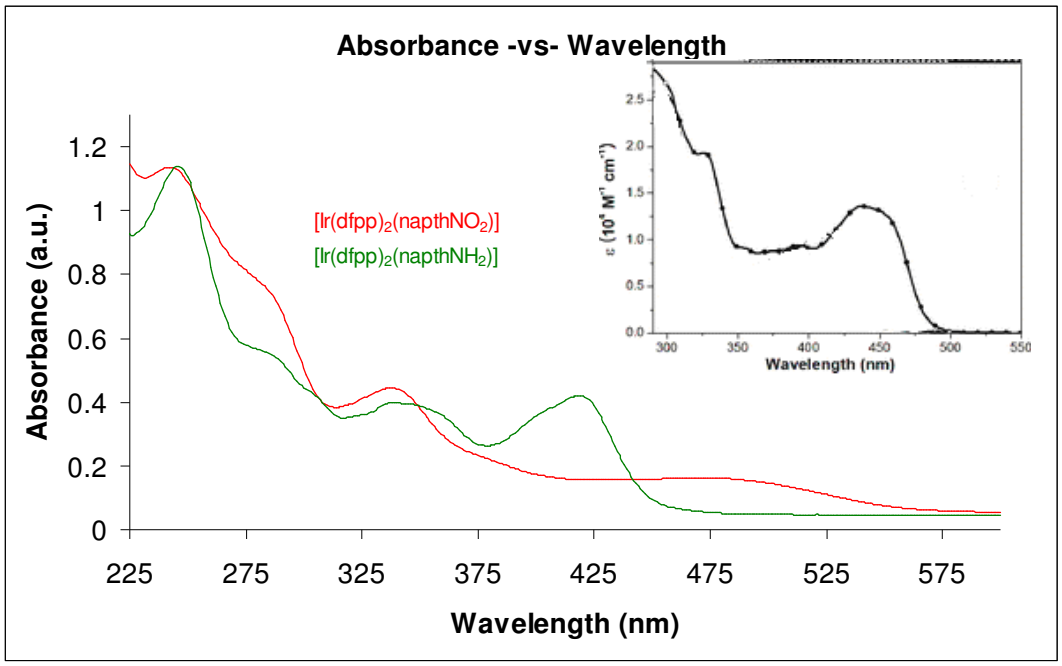

Figure 4.24: Overlaid absorbance profiles of [Ir(dfpp)$_2$(napthNO$_2$)] and [Ir(dfpp)$_2$(napthNH$_2$)] (20 x 10^{-6}M) in acetonitrile solution. (inset) Absorbance profile of the parent [Ir(dfpp)$_2$(napth)] complex, 1.0 x 10^{-5} M in toluene.[2]

The UV-vis spectrum of [Ir(dfpp)$_2$(napthNO$_2$)] is dominated by LC cyclometalating [dfpp] π-π* ligand transitions giving maximum absorbance peaks at 243 nm and a shoulder at 279 nm. The lower energy peak at 338 nm is assigned to the π-π* [NapthNO$_2$] ancillary ligand transition. There is a significant degree of overlapping of electronic transitions and the absorbance band that extends into the visible region at 450 nm is believed to be a MLCT (spin-forbidden) iridium dπ to difluorophenyl pyridine ligand π* transition. MLCT spin-forbidden transitions are known for complexes containing heavy atoms, such as iridium, due to strong spin-orbit coupling.[3] The spin-orbit coupling for iridium (III) complexes is 50% larger than that of ruthenium (II) complexes and this leads to an enhanced triplet character for iridium (III) complexes.[2, 28]

The UV-vis spectrum of [Ir(dfpp)$_2$(napthNH$_2$)] is also dominated by LC π-π* difluorophenyl pyridine ligand electronic transitions giving maximum absorbance peak at 245 nm and a shoulder at 283 nm. As seen previously for the uncoordinated ligands, the π-π* ancillary [NapthNH$_2$] ligand transition is red-shifted to 348 nm in comparison to the [NapthNO$_2$] ligand iridium complex. In addition, a more defined and blue-shifted spin-allowed MLCT peak from the iridium (dπ) to difluorophenyl pyridine ligand (π*) orbital is also present at 418 nm for the amino functionalised complex which is perhaps due to the increase in the π acceptor state of the [napthNH$_2$] ligand.

As observed in Chapter 3, it is known that the nitro substituent has an effect on the HOMO-LUMO band gap of a compound. The dπ-π* and π-π* interactions permit hyperconjugation between the electronic structures and aromatic rings causing a decrease in the energy gap. This is may be seen by a decrease in the HOMO-LUMO energy gap of the [Ir(dfpp)$_2$(napthNO$_2$)] complex resulting in shift to longer wavelengths (450 nm) when compared to the amino functionalised (418 nm) and parent iridium (III) complexes (445 nm). The absorbance profile of the parent [Ir(dfpp)$_2$(napth)] complex is very similar to that of the [Ir(dfpp)$_2$(napthNH$_2$)] complex as shown in Figure 4.24 (inset), with the exception of the absorbance peak at 348 nm which is attributed to the π-π* transition as a result of the [napthNH$_2$] ligand.

4.4.2 Emission of $[Ir(dfpp)_2(napthNO_2)]$ and $[Ir(dfpp)_2(napthNH_2)]$

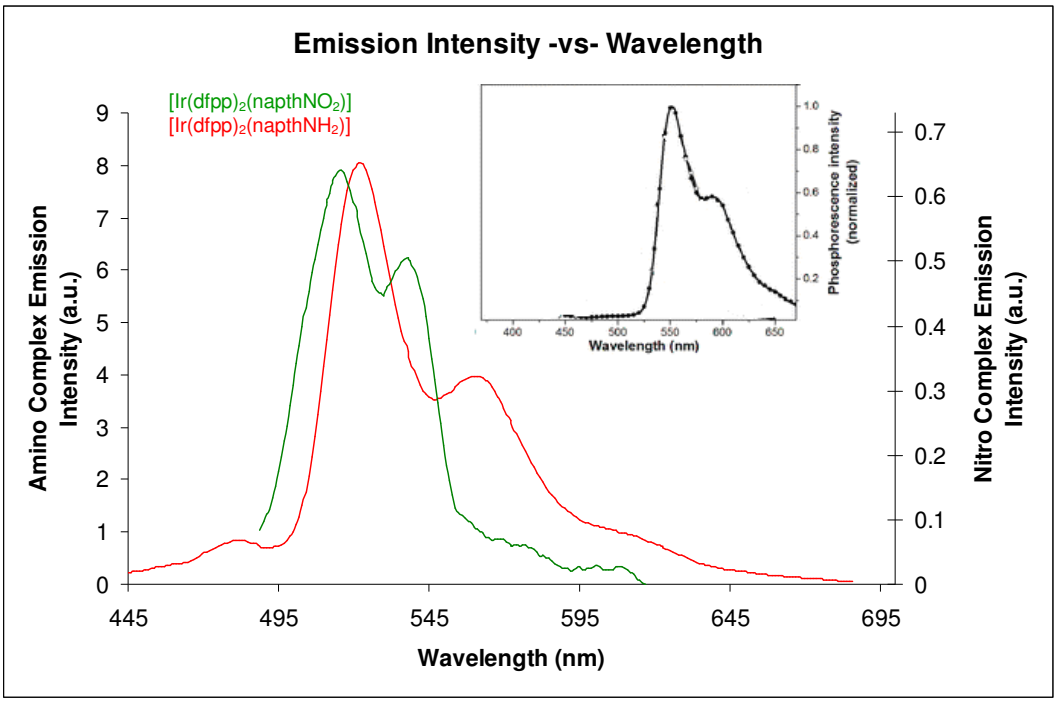

Figure 4.25: Overlaid emission spectra of 20 x 10^{-6}M solutions of $[Ir(dfpp)_2(napthNO_2)]$ (right hand side scale bar, excited at 475 nm) and $[Ir(dfpp)_2(napthNH_2)]$ (left hand side scale bar, excited at 418 nm) in acetonitrile. Slit widths: 5 nm. (inset) Emission profile of the parent $[Ir(dfpp)_2(napth)]$ complex, 1.0 x 10^{-5} M in toluene.[2]

Figure 4.25 above shows the emission spectra for the novel iridium dyes and parent iridium complex inset. The emission spectrum of $[Ir(dfpp)_2(napthNO_2)]$ exhibits vibronic structure in its emission profile with emission maxima at 516 nm and 539 nm when excited into the MLCT transition band at 475 nm respectively. The luminescence of the nitro functionalised complex is considerably less than that of the other iridium complexes synthesised. The quantum yield was very low at 0.0009 and had a short biexponential lifetime as shown in Table 4.9. The excitation spectra of all iridium (III) complexes containing 2-(2-hydroxyphenyl)oxazole-based ancillary ligand displayed strong absorbance profiles in both the π-π* difluorophenyl pyridine and π-π* [Napth-R] ligand regions [results not shown] when excited at into the emission maxima of the

complexes. As a result it is considered that dual excitation of both ligands occurs simultaneously and results in the emission of the luminophores from a single emissive centre.

On the other hand, the [Ir(dfpp)$_2$(napthNH$_2$)] complex exhibited a more intense red-shifted luminescence maximum, when compared to [Ir(dfpp)$_2$(napthNO$_2$)], and showed emission at 524 nm and 564 nm respectively. It is thought that this is as a result of the slight decrease in the emissive ligand LUMO due to the electron donating amino substituent caused by an improved π delocalisation of electrons. The red shift in the emission of the amino functionalised iridium complex, in comparison to [Ir(dfpp)$_2$(napthNO$_2$)], has also been observed in Chapter 3 when comparing both nitro and amino functionalised ruthenium (II) complexes. The quantum yield of [Ir(dfpp)$_2$(napthNH$_2$)] was calculated to be equal to 0.0056 and had a biexponential decay kinetics (Table 4.9) which showed a significant improvement on its nitro functionalised counterpart, but nonetheless very weak in comparison to the [picCOOH] functionalised iridium (III) complex.

These photophysical results proved to be far inferior to the parent [Ir(dfpp)$_2$(napth)] complex, whose lifetime was determined to be 9.88 μs with quantum yields of 0.43.[2] The emission profile of the parent complex is shown in Figure 4.25 (inset) for comparative purposes. It is proposed that the poor photophysical results in comparison are due to the increase in energy of the lower-lying π* ancillary ligand orbitals as a result of the introduction of the nitro and amino substituents on the ligand. As a result population of the lowest lying triplet state, which is responsible for phosphorescence, is prohibited and excited state energy is dissipated through lower-lying non-luminescent molecular orbitals on the cyclometalating [dfpp] ligands. It is also considered that similar to results in the previous chapter, that the poor photophysical characteristics of the nitro complex might be due to the para functionalised nitro substituent. However, unlike the ruthenium (II) functionalised nitro complex, there are no significant differences in the luminescence or lifetimes of [Ir(dfpp)$_2$(napthNO$_2$)] when the solvent is changed.

You *et al.*[2] have previously shown with the parent iridium (III) complex how the excited state energy of the cyclometalating ligand is almost quantitatively transferred to the chromophoric ancillary ligand. Furthermore, as the number of fused phenyl units on the ancillary ligand is increased, the phosphorescent emission displayed more vibronic structure in its emission profile as seen for the iridium (III) complexes synthesised in Figure 4.25. The triplet transition of the $[Ir(dfpp)_2(napth)]$ complex is afforded by the LUMO of the ancillary ligand. However, as the phosphorescence mainly involves the triplet transition, ancillary-ligand-mediated phosphorescence was expected. This was consistent with their observed results as revealed by a single ancillary ligand centred phosphorescence and double excitation to both ancillary and cyclometalating ligands. It was also calculated that the excited state energy of the cyclometalating ligand is transferred to the chromophoric ancillary ligand (through ILET – interligand energy transfer) where phosphorescence is generated with an efficiency of > 99%.[2]

Dual emission of iridium (III) complexes with diimine ligands are unusual but not unprecedented as emission may occur from both MLCT and LC excited states.[29, 30] However, for similar difluorophenyl pyridine complexes the HOMO has been shown to be primarily located on the iridium centre and the phenyl ring of the difluoropyridine ligands.[3, 9] The HOMO-LUMO transition is MLCT with a relatively large LC component involving the difluoropyridine pyridine ligand. This results in the more pronounced vibronic structure and smaller stokes shift of the emission spectra as seen for the iridium (III) complexes synthesised in this thesis. However, due to the disappointing photophysics of the nitro and amino derivatives, it was decided not to continue efforts in using this particular series of iridium (III) dyes containing 2-(2-hydroxyphenyl)oxazole-based ancillary ligands as luminescent markers to label biomolecules.

4.5 Conclusion

The synthesis and characterisation of three novel iridium (III) polypyridyl complexes is described. Iridium complexes have been shown to display many favourable photophysical characteristics, above those of other transition metal complexes, including microsecond scale phosphorescent lifetimes, high quantum yields and the ability to tune its emission wavelength from blue to red by changing the coordinated ligands. $[Ir(dfpp)_2(picCOOH)]^+$ exhibited improved lifetimes (842 +/- 9 ns in degassed organic media) and quantum yields (0.103) when compared with the ruthenium luminescent probes synthesised in Chapter 3. Furthermore, like the ruthenium (II) complexes, $[Ir(dfpp)_2(picCOOH)]^+$ exhibited lifetime and Raman sensitivity with changes in oxygen concentration and pH respectively. The location of the excited state was also found to be on cyclometalating [dfpp] ligands.

The $[Ir(dfpp)_2(napthNO_2)]$ complex had a disappointing lifetime of 11 +/- 3 ns and a quantum yield of 0.0009. Whereas, the nitro functionalised $[Ir(dfpp)_2(napthNH_2)]$ complex had an improved lifetime of 189 +/- 6 ns and a quantum yield of 0.0056. The poor photophysical properties, when compared to the parent complex, is attributed to an increase in energy of the lower-lying π^* ancillary ligand orbitals as a result of the introduction of the nitro and amino substituents on the ligand. As a result population of the lowest lying triplet state, which is responsible for phosphorescence, is prohibited and excited state energy is dissipated through lower-lying non-emissive molecular orbitals on the cyclometalating [dfpp] ligands. Therefore, it was decided not to continue efforts in using this particular series of iridium (III) dyes as luminescent markers to label biomolecules.

However, given the superior photophysical results observed for the $[Ir(dfpp)_2(picCOOH)]^+$ complex, in Chapter 5 its conjugation to a cell penetrating peptide was conducted in an effort to increase its aqueous solubility and potential to be used as a multimodal probe for cellular imaging.

4.6 References

(1) Ragni, R.; Plummer, E. A.; Brunner, K.; Hofstraat, J. W.; Babudri, F.; Farinola, G. M.; Naso, F.; De Cola, L. *J. Mater. Chem.* **2006***, 16*, 1161-1170.

(2) You, Y.; Seo, J.; Kim, S. H.; Kim, K. S.; Ahn, T. K.; Kim, D.; Park, S. Y. *Inorg. Chem.* **2008***, 47*, 1476-1487.

(3) Orselli, E.; Kottas, G. S.; Konradsson, A. E.; Coppo, P.; Frahlich, R.; De Cola, L.; van Dijken, A.; Bachel, M.; Barner, H. *Inorg. Chem.* **2007***, 46*, 11082-11093.

(4) Yoshikawa, N.; Sakamoto, J.; Takashima, H.; Tsukahara, K.; Kanehisa, N.; Kai, Y. *Analytical Sciences* **2004***, 20*, 711-716.

(5) Lamansky, S.; Djurovich, P.; Murphy, D.; Abdel-Razzaq, F.; Kwong, R.; Tsyba, I.; Bortz, M.; Mui, B.; Bau, R.; Thompson, M. E. *Inorg. Chem.* **2001***, 40*, 1704-1711.

(6) Lamansky, S.; Djurovich, P.; Murphy, D.; Abdel-Razzaq, F.; Lee, H.; Adachi, C.; Burrows, P. E.; Forrest, S. R.; Thompson, M. E. *J. Am. Chem. Soc.* **2001***, 123*, 4304-4312.

(7) Lo, K. K.; Louie, M.; Zhang, K. Y. *Coord. Chem. Rev.* **2010***, 254*, 2603-2622.

(8) Gao, R.; Ho, D. G.; Hernandez, B.; Selke, M.; Murphy, D.; Djurovich, P. I. *J. Am. Chem. Soc.* **2002***, 124*, 14828-14829.

(9) Dedeian, K.; Shi, J.; Shepherd, N.; Forsythe, E.; Morton, D. C. *Inorg. Chem.* **2005***, 44*, 4445-4447.

(10) Lo, K. K.; Chung, C.; Zhu, N. *Chemistry - A European Journal* **2006***, 12*, 1500-1512.

(11) Metcalfe, C.; Thomas, J. A. *Chem. Soc. Rev.* **2003***, 32*, 215-224.

(12) Erkkila, K. E.; Odom, D. T.; Barton, J. K. *Chem. Rev.* **1999***, 99*, 2777-2796.

(13) Liu, X.; Shen, Y.; Lu, J.; Chen, Y.; Li, L.; Zhang, D. *Spectrochimica Acta Part A: Molecular and Biomolecular Spectroscopy* **2010***, 77*, 522-527.

(14) Zhang, X.; Gao, J.; Yang, C.; Zhu, L.; Li, Z.; Zhang, K.; Qin, J.; You, H.; Ma, D. *Journal of Organometallic Chemistry* **2006***, 691*, 4312-4319.

(15) Wu, L.; Yang, C.; Sun, I.; Chu, S.; Kao, P.; Huang, H. *Organometallics* **2007***, 26*, 2017-2023.

(16) Heller, A.; Williams, D. L. *J. Phys. Chem.* **1970***, 74*, 4473-4480.

(17) Ernst, L.; Ibrom, K. *Magn. Reson. Chem.* **1999***, 37*, 441-444.

(18) Jean-Pierre Begue; Daniele Bonnet-Delpon *General Remarks on Structural, Physical and Chemical Properties of Fluorinated Compounds;* John Wiley & Sons, Inc., Ed.; Bioorganic and Medicinal Chemistry of Fluorine; **2008**; Vol. 1, 1-22.

(19) Lai, S.; Ling, J.; Huang, Y.; Huang, M.; Cheng, C. H.; Chen, I. *J. Raman Spectrosc.* **2011***, 42*, 332-338.

(20) Kahl, J. L.; Hanck, K. W.; DeArmond, K. *J. Phys. Chem.* **1978***, 82*, 540-545.

(21) Maeda, H.; Yamauchi, Y.; Yoshida, M.; Ohmori, H. *Analytical Sciences* **1995***, 11*, 947-952.

(22) Mo, Y.; Stefan, I. C.; Cai, W.; Dong, J.; Carey, P.; Scherson, D. A. *The Journal of Physical Chemistry B* **2002***, 106*, 3681-3686.

(23) Venkatanarayanan, A.; Spehar-De leize, A.; Dennany, L.; Pellegrin, Y.; Keyes, T. E.; Forster, R. J. *Langmuir* **2008***, 24*, 11233-11238.

(24) Flamigni, L.; Collin, J.; Sauvage, J. *Acc. Chem. Res.* **2008***, 41*, 857-871.

(25) Pellegrin, Y.; Forster, R. J.; Keyes, T. E. *Inorg. Chim. Acta* **2008***, 361*, 2683-2691.

(26) Pellegrin, Y.; Forster, R. J.; Keyes, T. E. *Inorg. Chim. Acta* **2009***, 362*, 1715-1722.

(27) Vos, J. G. *Polyhedron* **1992***, 11*, 2285-2299.

(28) Yoshikawa, N.; Matsumura-Inoue, T.; Sakamoto, J.; Takashima, H.; Tsukahara, K.; Kanehisa, N.; Kai, Y. *Analytical Sciences* **2004***, 20*, 1639-1644.

(29) Wilde, A. P.; King, K. A.; Watts, R. J. *J. Phys. Chem.* **1991***, 95*, 629-634.

(30) Goodall, W.; Williams, J. A. G. *J. Chem. Soc. , Dalton Trans.* **2000**, 2893-2895.

Chapter 5: Metal Luminophore-Peptide Conjugates for Cellular Imaging

"The reasonable man adapts himself to the world; the unreasonable man persists in trying to adapt the world to himself. Therefore all progress depends on the unreasonable man" - George Bernard Shaw

5.0 Introduction

A major limitation to date has been the inability of such inorganic dyes to passively diffuse across a cell membrane without membrane permeabilisation. The relatively low cationic charge associated with many of these metal complexes means that they are unable to effectively use the cell's membrane potential as a driving force for cellular entry.[1] Common methods for permeabilisation include electroporation, organic solvents, the use of detergents and all lead to questions about the cell viability. Aprotic solvents, such as DMSO, have been shown before to induce water pores in lipid bilayers.[2, 3] Molecular dynamic simulations indicated a number of features that were significant for the effects of DMSO on a cell membrane. The solvent was shown to readily partition into the bilayer occupying a position beneath the lipid headgroups, reduce the bilayer thickness, increase headgroup area, markedly reduce both the area compressibility modulus and the bending ridgity of the membrane, which led to induced water pore formation. The remarkable event of water pore formation was observed at a 27 mol% concentration of DMSO after 240 ns. Furthermore, an important application of DMSO is in topical drug delivery where its powerful ability to increase the skins permeability is exploited, however, exactly how it increases the skins permeability is not fully understood.[2]

However, research published by our group[4, 5] demonstrated that conjugation of a metal complex to a CPP, like octarginine, facilitates the efficient diffusion of the luminescent probe across mammalian cell membranes without destroying the lipid bilayer. Furthermore, once inside the cell's membrane, the environmentally sensitive photophysics and spectroscopic properties of the dye-peptide may be exploited to report on the intracellular environment. Cosgrave *et al*.[5] have previously exploited the multimodal imaging capability of a related ruthenium dye-peptide synthesised here to give information on the intracellular pH and oxygen concentrations and this is discussed in detail in Chapter 1. Chapter 1 also reviewed examples where polyarginine CPPs have been used for the internalisation of inorganic luminophores into cellular structures for live cellular imaging and the processes by which these biomolecules are uptaken by the cell.

5.1 Solid Phase Peptide Synthesis (SPPS)

Synthetic peptides are playing an increasing role in biological, medical and pharmaceutical research and therefore the synthesis of such polyamide molecules is of major interest. The introduction of SPPS has offered many important advantages over conventional solution phase peptide synthesis. Advantages include the fact that coupling reactions may be carried out more rapidly and to completion on a solid support that leads to easier purification procedures.[6] Furthermore, the introduction of Fmoc-protecting groups by Carpino in 1970 allowed for the process of SPPS to be conducted under milder conditions.[6] Peptide coupling chemistry was then further improved with the use of novel side-chain protecting groups, such as Arg(Pbf) used throughout this chapter as shown in Figure 5.1.

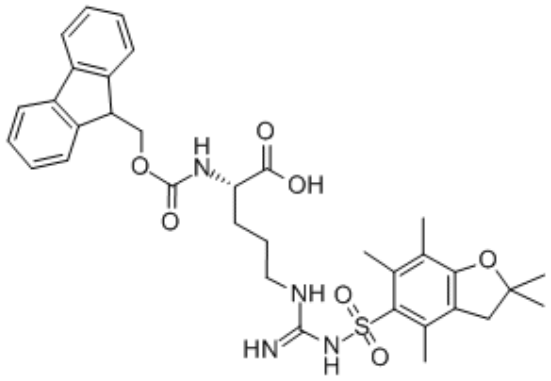

Figure 5.1: Chemical structure of Fmoc-Arg-Pbf used in the SPPS of octarginine.

The first step is to couple the peptide unit to the solid support resin. 2-(1H-Benzotriazole-1-yl)-1,1,3,3-tetramethyl uronium hexafluorophosphate (HBTU) (Figure 5.2) is used as the coupling reagent for the automated peptide synthesis of this polypeptide. It is one of the most common coupling reagents used that forms an active hydroxybenzotriiazole (HOBt) ester and its general mechanism of coupling is shown in Figure 5.3. HBTU in the presence of a base converts carboxylic acids to the corresponding HOBt ester.[7] It is the base N,N-diisopropylethylamine (DIEA) that initiates this coupling reaction.

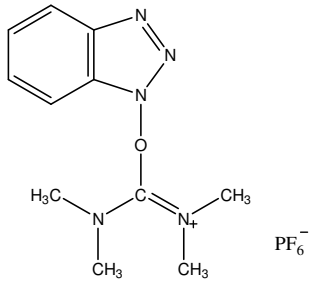

Figure 5.2: Schematic diagram of the HBTU coupling reagent.

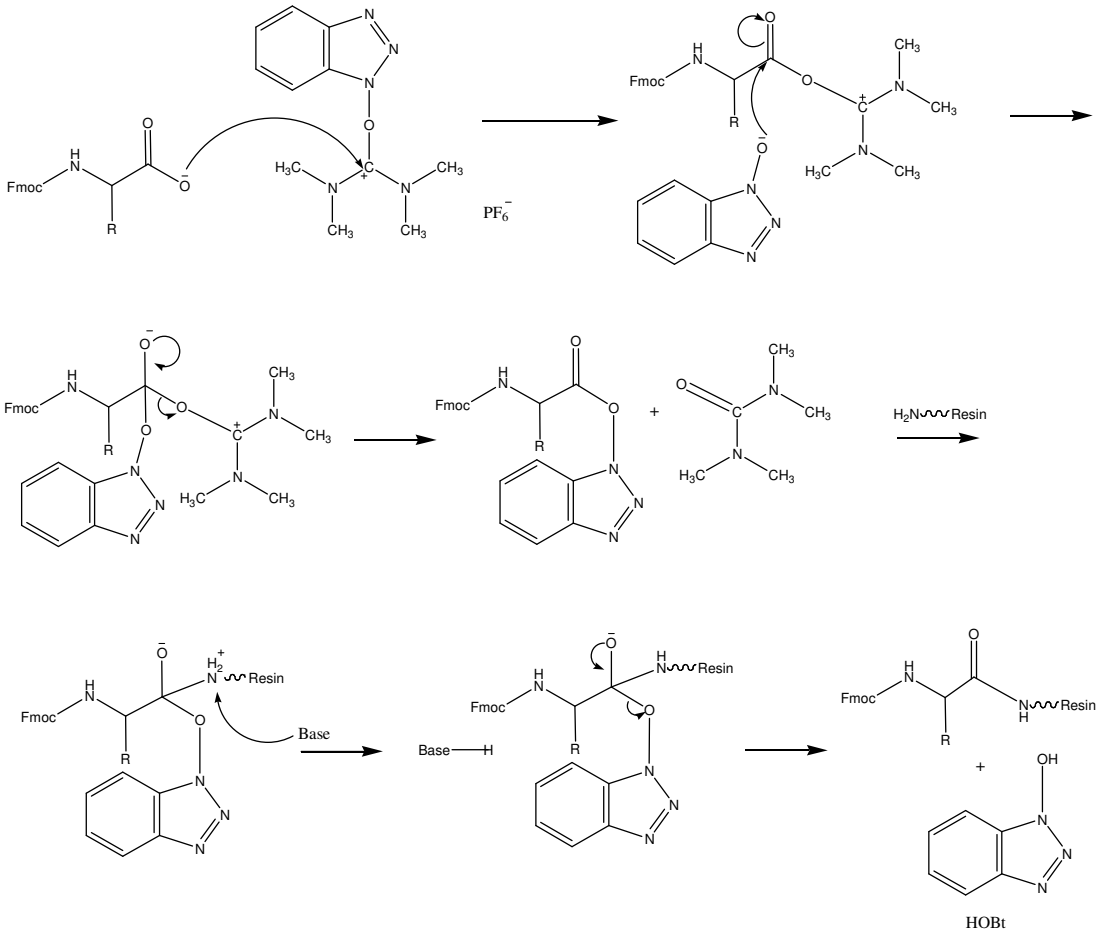

Figure 5.3: General mechanism for the HBTU/HOBt mediated coupling reaction of peptides in SPPS. (Illustrated in the above diagram is the mechanism for the HBTU/HOBt mediated coupling reaction of a peptide to the solid support resin).

Following Fmoc deprotection by piperidine in NMP the amine group on the resin is available for amino acid coupling. The general mechanism of Fmoc deprotection using piperidine as strong base is illustrated in Figure 5.4 below. The peptide is then elongated from the C-terminus (carboxylic acid functional group) to the N-terminus (amino functional group) via HBTU/HOBt/DIEA mediated coupling reactions similar to that illustrated in Figure 5.3 above.

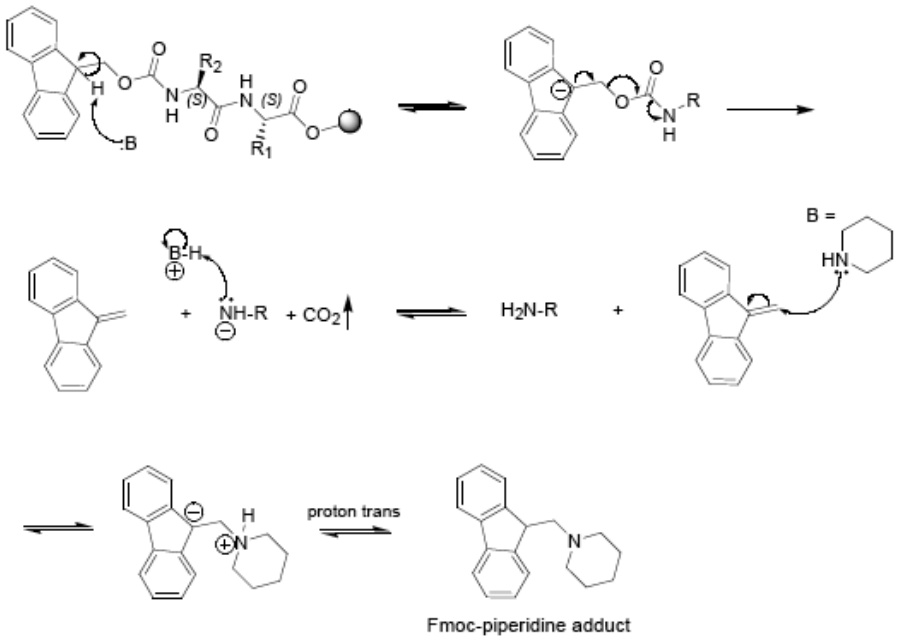

Figure 5.4: General mechanism for deprotection of Fmoc using piperidine (B) as the strong base.[8]

Following SPPS of the octarginine polypeptide, the remaining Fmoc protecting group on the hexanoid acid spacer is removed manually using piperidine. The inorganic molecular probes were then manually conjugated to the polypeptide using HBTU/PyBOP/DIEA coupling reagent in a procedure described in the experimental section. Finally the dye-peptides were removed from the resin and the amino acid side-chains (Pbf) groups deprotected using a cleavage cocktail. The reaction between the carboxyl group on the inorganic dyes and amino group on the peptide results in the formation of a stable amide bond. The bond stability may be explained by a resonance contributor in which the nitrogen shares its lone pair with the carbonyl carbon. This overlapping of molecular orbitals lowers the energy of the lone pair and raises the energy of the π^* orbital of the carbonyl, making it less reactive to nucleophiles.

5.2 Resazurin and MTT Cell Viability Assays

In order to assess and compare the viability of the cells, two cell viability assays were performed; the resazurin and MTT cell viability assays. Resazurin is a colorimetric assay performed to determine the viability of cells and was also used in the cytotoxicity studies previously. Resazurin (7-hydroxy-3H-phenoxazin-3-one-10-oxide) is a non-fluorescent blue coloured dye when exposed to green light. However, upon reduction of the dye to form resorufin (pink in colour) the dye is brightly fluorescent under green light. The dye is mainly used as an oxidation-reduction indicator in cell viability assays for bacteria and mammalian cells. The resazurin assay is based on the ability of viable, active cells to reduce resazurin to resorufin and dihydroresorufin, and can be readily applied to both fixed and live cell cultures. This redox conversion is intracellular and is facilitated by mitochondrial, microsomal and cytosolic oxidoreductases. The rate of dye reduction is directly proportional to the amount of viable cells present in a given assay.[9] An advantage of the resazurin assay over other cell viability assays include its low toxicity to living cells allowing for the study of cells over longer time periods. Figure 5.5 illustrates the conversion of resazurin to resorufin following reduction by active cell enzymes.

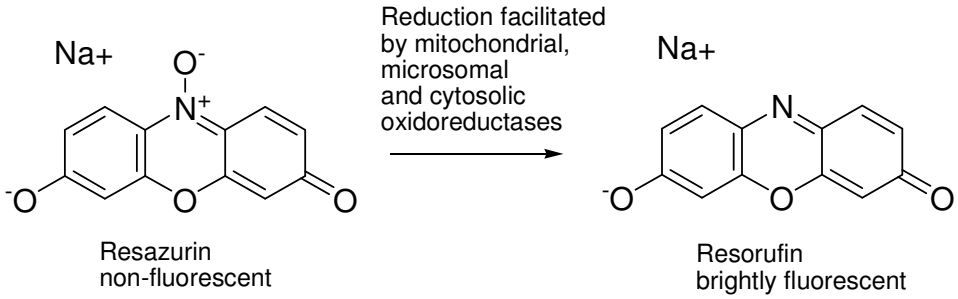

Figure 5.5: Schematic diagram illustrating the conversion of resazurin to resorufin following reduction by active cell enzymes.

The MTT assay is another colorimetric assay that measures the activity of enzymes that cause the reduction of MTT ((3-(4,5-Dimethylthiazol-2-yl)-2,5-diphenyltetrazolium bromide – yellow in colour) to formazan (purple in colour).

Reduction of tetrazolium salts by dehydrogenases and reductases present in living cells results in the production of the artificial dye formazan that may be monitored by UV-Vis spectroscopy. The assay detects living, but not dead cells and the signal generated is dependent on the degree of activation of the cells.[10] Figure 5.6 illustrates the conversion of the MTT tetrazolium salt to formazan following reduction by active cell enzymes.

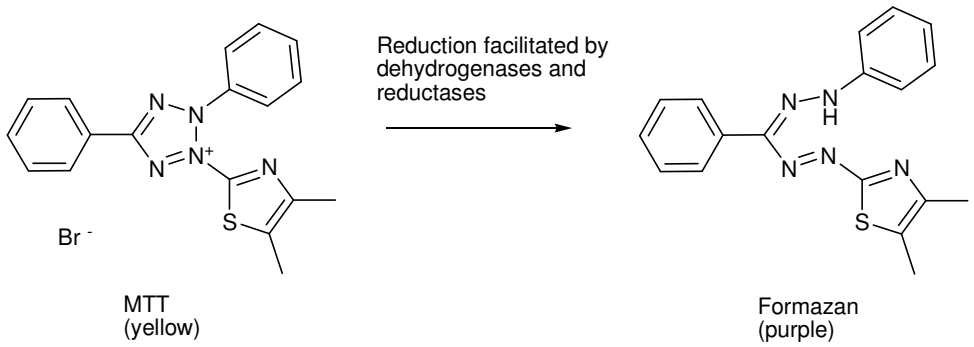

Figure 5.6: Schematic diagram illustrating the conversion of the MTT tetrazolium salt to formazan following reduction by active cell enzymes.

5.3 SP2 Myeloma and CHO Cells

The two cell lines used throughout this thesis are SP2 myeloma and CHO cell lines. SP2 myeloma cells are formed by fusing BALB/c spleen cells (from mice immunised with sheep red blood cells) with the P3X63Ag8 myeloma. Chinese hamster ovary (CHO) cells are epithelial cells which grow as an adherent monolayer in culture in many academic research laboratories. Furthermore, they are the most widely used mammalian cells for transfection, expression and protein production. From a biochemical perspective, one of the main differences between both cell lines is that SP2 cells are a suspension cell line, whereas, CHO are an adhesive cell line. Consequently, there are likely to be significant differences in the surface expression proteins on the cell membranes, potentially leading to very different interactions between both cell lines and the luminophores/dye-peptides. This is of course assuming that the surface proteins interact with the dyes and octarginine polypeptides.

Throughout the literature cells are commonly imaged as live cells or fixed cells. Live cells involve taking a sample of cells directly from the cell culture and imaging under the microscope immediately. In contrast, fixed cells are essentially adhered to and preserved on a surface so that the imaging of these cells may take place over longer periods of time.

This chapter details the synthesis of ruthenium (II) and novel iridium (III) inorganic metal luminophores conjugated to polyarginine peptides. There luminophores have been shown to be highly luminescent, singlet oxygen generating, have intense resonance Raman spectra and are oxygen / pH sensitive. Conjugation of the dyes to the CPP octarginine allows for the passive and non-destructive entry of the molecular probes, without the need for permeabilisation, into living mammalian cells and these dye-peptides may then be used for cellular imaging. As discussed to in Chapter 1, metallo dye-peptides hold significant potential for use as molecular probes suitable for multimodal cellular imaging. Due to their large stokes shifts, photostability, long aqueous lifetimes and pH / oxygen sensitivity not only can these metallo dye-peptides image cells but they may also provide critical information on the intracellular pH levels and the oxygen concentrations using a single multimodal molecular probe. Furthermore, this is the first time that an iridium (III) luminophore has been conjugated to a polyarginine peptide and been used as a molecular probe for cellular imaging with the potential for multimodal imaging applications.

In addition to the research carried out in this thesis, work is currently underway by our research group to conjugate target-peptides to existing cell penetrating dye-peptides to help with targeted localisation within cell organelles. This may prove very useful in the detection of certain diseases as targets may be synthesised to detect specific gene sequences known to be of harm. Additionally, the intrinsic photophysical properties of these metal complexes, with their triplet excited states allowing for the generation of singlet oxygen and other reactive oxygen species may lead to induced apoptosis in cells,[11-13] thus, making these dye-peptides potentially valuable in the area of photodynamic therapy.

5.4 Experimental Procedure

Chemicals

Protected amino acids, HBTU, PyBOP and Rink-amide MBHA resin were purchased from Novabiochem (Merck Biosciences). HOBt was purchased from Iris Biotech GmbH. Synthesizer filters (in-line and reactor) and solvents (DCM, NMP) were sourced from Applied Biosystems. All other chemicals were reagent grade purchased from Sigma-Aldrich and were used without further purification unless otherwise stated.

Peptide Synthesis

Automatic Peptide Synthesis

The synthesis was carried out by automated Solid Phase Peptide Synthesis (SPPS) performed on an Applied Biosystem ABI 433A Synthesizer. 1 mmol (10 fold molar excess) quantities of each protected amino acids was used. The amine group on the resin is Fmoc protected initially but is available for amino acid coupling following piperidine (20% in NMP) deprotection. The peptide was elongated from the C-terminus (carboxylic acid functional group) to the N-terminus (amino group). The sequence was assembled with monitoring of the Fmoc deprotection by UV at 301 nm.

Manual Deprotection

Manual deprotection was used after automated peptide coupling to remove the remaining Fmoc protecting group. The manual deprotection was performed in a syringe fitted with a filter. Piperidine (20%) in DMF (v/v) was then added to the syringe and placed on the shaker for 10-15 minutes. The syringe was then drained and 20% piperidine in DMF (v/v) was added again and shaken for a further 10 minutes. This process was performed twice.

Manual Coupling

Manual peptide synthesis was used to label the peptides with the inorganic dye probes. The resin was placed into a 5 ml syringe fitted with a Teflon filter and a stopcock. The resin was allowed to swell for 1 hour in DMF. Coupling reagent PyBop was used in 5 molar equivalents to the resin and DIEA was used in 10 molar equivalents to initiate the reaction. The coupling reagents, inorganic dye and the protected amino acid were dissolved in 4ml of DMF and then DIEA was added. The solution was then added to the syringe and placed on the shaker for overnight. The resin was filtered and then washed twice with NMP and then a third time with DCM (3 x 5 ml aliquots of each, for 2 minutes agitation).

Cleavage

A cleavage procedure was used to remove the dye-peptide from the resin and deprotect the amino acid side-chains (Pbf) once assembly of the sequence was complete. The resin was placed in a test tube with a magnetic stirrer and the cleavage cocktail was added. The cleavage cocktail consisted of trifluoroacetic acid (6 ml, TFA 80%) while scavenging of the cationic species formed from the protecting groups was achieved by using; water (450 µl, 5%), triisopropylsilane (450 µl, TIS or TIPS, 5%), thioanisole (450 µl, TA, 5%), ethandithiol (450 µl, EDT, 5%). The mixture was left to stir for 4 hours at room temperature.

After stirring, the solution was filtered into a plastic centrifuge tube using a teflon tube fitted with a filter. To the centrifuge tube, diethyl ether (10 ml) was added to precipitate the peptide. The centrifuge tube was then placed in the freezer for 5-10 minutes to aid the precipitation process. The product was centrifuged five minutes at 2.8×10^3 rpm. The acidic liquid supernatant was removed. The peptide was then washed twice using diethyl ether (15 ml) before being air dried for 1 hour. Finally the product was left on the freeze drier overnight.

The preparation of $[Ru(bpy)_2(picCOOH)Arg_8]^{10+}$ bioconjugate

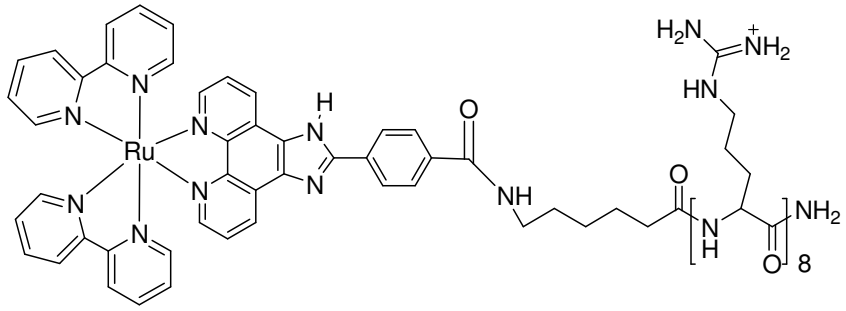

Figure 5.7: Schematic diagram of $[Ru(bpy)_2(picCOOH)Arg_8]^{10+}$.

Eight vials each containing Fmoc-Arg(Pbf)-OH (650 mg, 1 mmol) and one vial containing an hexanoic acid spacer Fmoc-6-Ahx-OH (354 mg, 1 mmol) were weighed out and placed into the SPPS. The peptide was assembled using Rink Amide Resin (172 mg, 0.36 mmol) and was performed on the SPPS as described previously. Following the reaction, the resin was transferred into DMF (4 ml) to allow for swelling of the resin.

Half of this solution (2 ml) was added to a vial already containing PyBOP (78 mg, 0.15 mmol), $[Ru(bpy)_2(picCOOH)]^{2+}.(ClO_4^-)_2$ (150 mg, 0.16 mmol) and DMF (2 ml). Finally, DIEA (40 µl, 0.23 mmol) was added and the solution was left shaking overnight. The resin precipitated and was washed with NMP (5 ml x 3 times) and DMF (5 ml x 3 times) allowing for 2 minutes agitation before each filtering. The remaining resin was then left to dry. The peptide was cleaved by standard methods and then purified by RP-HPLC as described previously. The fractions collected by semi-preparative HPLC were analysed by mass spectrometry and it's purity confirmed by HPLC analysis (conditions as outlined in Chapter 2 with a retention time of 28.41 minutes). The synthesis yielded an orange coloured solid (2.8 mg, 34%). The purity of the dye-peptide was confirmed by mass spectrometry and HPLC analysis. A stock solution (20 µM) in PBS buffer pH 7.4 was then made up and kept in the freezer.

MALDI-TOF ($[Ru(bpy)_2(picCOOH)Arg_8]^{10+}$ m/z): 2120.3, ([M]) 2120.5.
HPLC single peak retention time of 28.41 minutes. (HPLC conditions as described in Chapter 2)

The preparation of $[Ir(dfpp)_2(picCOOH)Arg_8]^{9+}$ bioconjugate

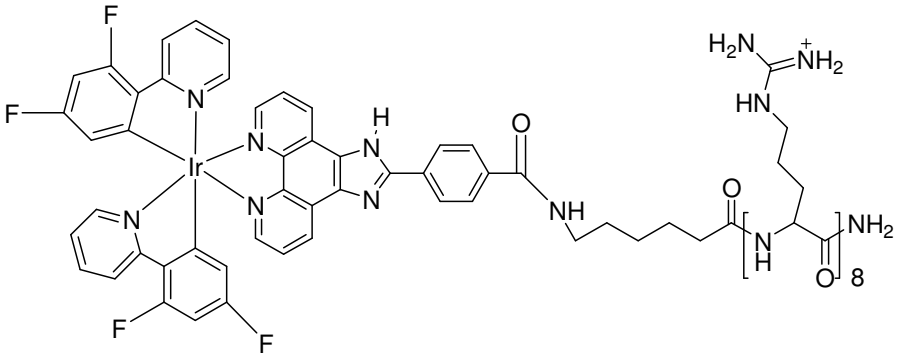

Figure 5.8: Schematic diagram of $[Ir(dfpp)_2(picCOOH)Arg_8]^{9+}$

Eight vials each containing Fmoc-Arg(Pbf)-OH (650 mg, 1 mmol) and one vial containing an hexanoic acid spacer Fmoc-6-Ahx-OH (354 mg, 1 mmol) were weighed out and placed into the SPPS. The peptide was assembled using Rink Amide Resin (172 mg, 0.36 mmol) and was performed on the SPPS as described previously. Following the reaction, the resin was transferred into DMF (4 ml) to allow for swelling of the resin.

Half of this solution (2 ml) was added to a vial already containing PyBOP (78 mg, 0.15 mmol), $[Ir(dfpp)_2(picCOOH)]^+.(ClO_4^-)$ (200 mg, 0.20 mmol) and DMF (2 ml). Finally, DIEA (40 µl, 0.23 mmol) was added and the solution was left shaking overnight. The resin precipitate was washed with NMP (5 ml x 3 times) and DMF (5 ml x 3 times) allowing for 2 minutes agitation before each filtering. The remaining resin is then left to dry. The peptide was cleaved by standard methods and then purified by RP-HPLC as described previously only this time using 5% TFA instead of 0.1% TFA. The fractions collected by semi-preparative HPLC were analysed by mass spectrometry. The synthesis yielded a yellow coloured solid (3.0 mg, 34%). The purity of the dye-peptide was confirmed by mass spectrometry and HPLC analysis. A stock solution (20 µM) in PBS buffer pH 7.4 was then made up and kept in the freezer.

MALDI-TOF ($[Ir(dfpp)_2(picCOOH)Arg_8]^{9+}$ m/z): 2279.4, ([M-H_5]) 2274.0.

HPLC single peak retention time of 30.27 minutes. (HPLC conditions as described in Chapter 2)

5.5 Results and Discussion

5.5.1 Ruthenium (II) Conjugated Polypeptide

This particular dye-peptide had been synthesised previously by our group[4, 14] and it was synthesised here again to understand the basic principles involved in SPPS, the bioconjugation of a luminophore to a peptide and uptake of a dye-peptide in mammalian cells. Furthermore, for the first time the uptake of this ruthenium molecular probe in CHO cells is examined. Coupling of $[Ru(bpy)_2(picCOOH)]^{2+}$ to the polypeptide gave a moderate yield (2.8 mg, 34%). This is far lower than the conjugated percentage yield of 85% quoted by Neugebauer *et al.*[4] in their synthesis of this particular ruthenium polypeptide. Mass spectrometry and HPLC analysis were used as standard to confirm the purity of both dye-conjugates. The ruthenium (II) and iridium (III) polypyridyl dyes used were conjugated through a single reactive carboxyl group on the pH sensitive ancillary ligand with the amino functionality on the protected polypeptide. As a result of the selective coupling reactivity they generally do not contain isomers or other competing functional groups that may in turn lower the synthetic yields further.[4, 15]

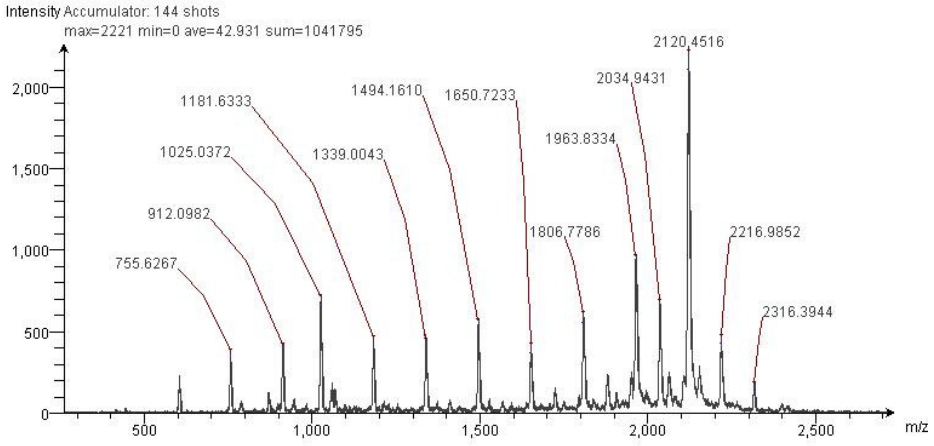

Figure 5.9: MALDI-TOF m*ass spectrum of* $[Ru(bpy)_2(picCOOH)Arg_8]^{10+}$ *with the molecular ion of interest at 2120.45 m/z.*

MALDI-TOF mass spectrum (Figure 5.9) of the ruthenium (II) bioconjugate reveals the molecular ion of interest at 2120 m/z along with a stepwise fragmentation pattern associated with the loss of individual arginine moieties. This sequential stepwise mass spectrum fragmentation for the ruthenium dye-peptide is in contrast to that seen for the iridium dye-peptide. However, fragmentation of peptide bonds by transition metals has been observed previously.[26] The purity of this conjugate was confirmed by HPLC analysis which showed a single peak with a retention time of 28.41 minutes using HPLC conditions as set out in the Chapter 2. Conjugation of the ruthenium (II) dye to the peptide did not cause any significant alterations to the wavelength of absorbance and emission of the conjugate when compared to the parent dye as shown in Figure 5.10 below. Previous results[4] also indicated that conjugation of the dye did not cause any variations in the pKa of the dye-peptide when compared to the free parent complex.

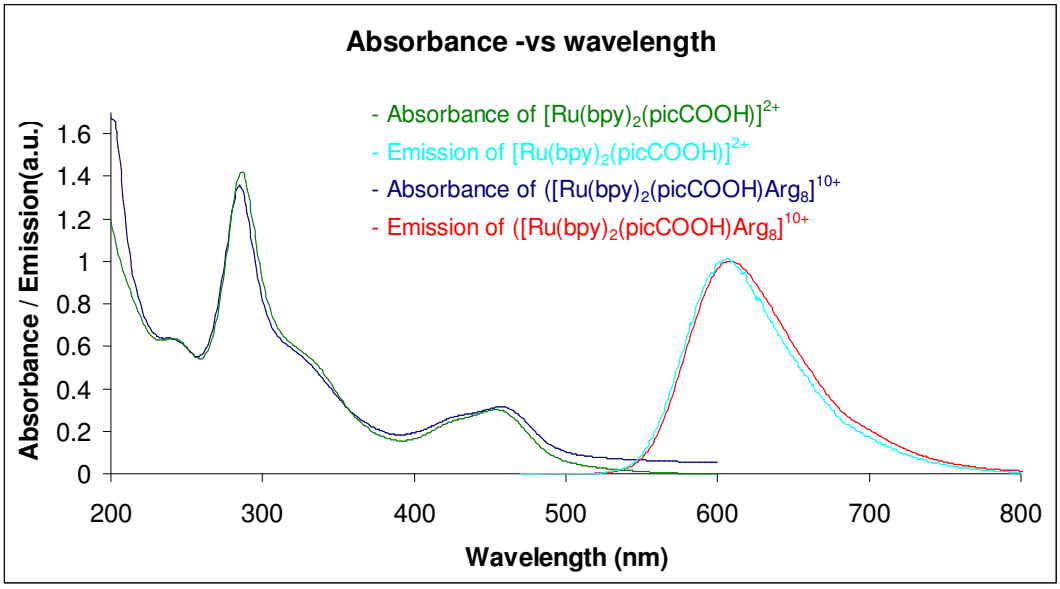

Figure 5.10: Overlaid absorbance and normalised emission spectra (excited at 458 nm, slit widths: 5 nm, normalised to 1 arbitrary unit) of 20 x 10^{-6} M $[Ru(bpy)_2(picCOOH)]^{2+}$ and $[Ru(bpy)_2(picCOOH)Arg_8]^{10+}$ in PBS buffer (pH 7.4) solutions.

The UV-vis spectrum of $[Ru(bpy)_2(picCOOH)Arg_8]^{10+}$ and its parent dye displays a MLCT with a maximum absorbance at 457 nm as described in Chapter 3. However, the absorbance tail of the dye-peptide extends slightly further into longer wavelengths. The absorbance band at 285 nm is assigned to π-π* transitions within the bpy ligands, whereas the shoulder at 330 nm is assigned to the π-π* transitions of the [picCOOH] ligand containing the two ionisable protons on the imidazole ring.

The emission spectrum of $[Ru(bpy)_2(picCOOH)]^{2+}$ has a maximum at 608 nm, whereas, $[Ru(bpy)_2(picCOOH)Arg_8]^{10+}$ has an emission maximum that is slightly red-shifted to 611 nm when excited into the MLCT band at 457 nm. Table 5.1 compares the photophysical results of the parent ruthenium dye and the ruthenium-peptide conjugate. Both the lifetimes and the quantum yields are very similar for that of the free ruthenium (II) dye and the conjugated complex indicating that the peptide had little effect on the photophysics of the luminophore. These photophysical results correspond well with what has been reported in Chapter 3 and has already been published.[4]

Compound	Lifetime[a]	x^2 value	Quantum Yield[b]
$[Ru(bpy)_2(picCOOH)]^{2+}$	820 +/- 6 ns	0.986	0.074
$[Ru(bpy)_2(picCOOH)Arg_8]^{10+}$	838 +/- 8 ns	0.107	0.071

Table 5.1: Photophysical comparison of parent ruthenium dye versus dye-conjugate.

[a] *Monoexponential lifetimes measured in degassed PBS buffer solution (pH 7.4) at room temperature*

[b] *Photoluminescent quantum yield (ϕ) in PBS buffer solution (pH 7.4) at room temperature, using* $[Ru(bpy)_3]^{2+}$ *as standard .*

5.5.1.1 Cellular Uptake of $[Ru(bpy)_2(picCOOH)]^{2+}$ and $[Ru(bpy)_2(picCOOH)Arg_8]^{10+}$

In order to assess and compare the ability of the compounds to transport across the cell membrane of two different cell lines, SP2 and CHO cells were cultured separately on 35 mm glass bottom culture dishes. SP2 cells were seeded at 5 x 10^5 cells in 2 ml media and CHO cells were harvested after trypsinisation (0.25% trypsin for 5 minutes at 37^{o}C) and seeded at 8 x 10^4 cells in 2 ml media. Both cell types were grown for 48 hours before imaging. For confocal measurements the growth medium was removed by washing with PBS buffer (pH 7.4) and 20 µl of the ruthenium parent complex (1.4 mM) or ruthenium dye-peptide (1.4 mM) in PBS (pH 7.4, with $MgCl_2$ and $CaCl_2$) was added. The luminophore and dye-peptide were made to a final concentration of 70 µM with PBS (pH 7.4) and were imaged immediately. Cell imaging throughout this chapter was performed by Dr. Roisin Moriarty, a postdoctoral researcher for the Prof. Tia Keyes research group.

The cellular imaging results shown below highlight the ability of $[Ru(bpy)_2(picCOOH)Arg_8]^{10+}$ to passively transport across the cell membrane of SP2 myeloma and CHO cells, whereas, the parent dye alone showed no evidence of capacity to diffuse across either cell line as shown in Figure 5.11 below. Furthermore, the parent ruthenium complex showed no strong luminescence within cell lines after a 40 minute time period. However, diffusion of the ruthenium parent dye into SP2[4] and CHO cells could be accomplished using a 0.1% Triton solution, to permeabilise the membrane, as illustrated for CHO cells in Figure 5.12.

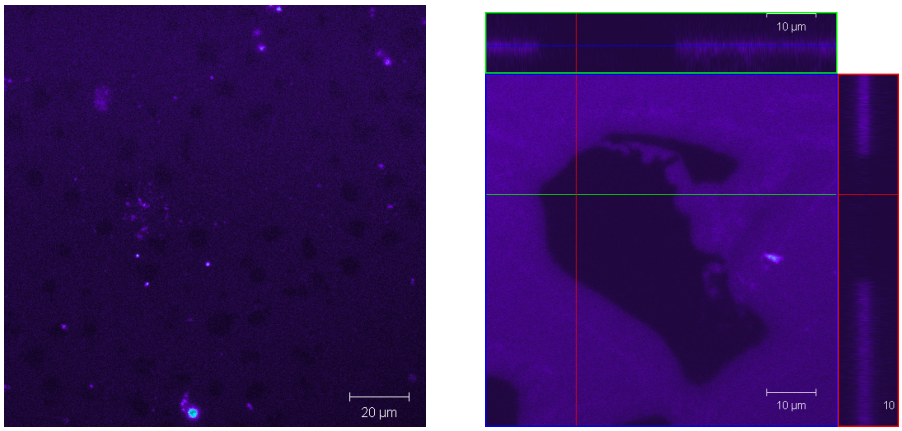

(a) ***(b)***

Figure 5.11: Luminescencent confocal rainbow images (λ_{ex} = 458 nm, λ_{em} = 610 nm) of (a) live SP2 myeloma cells incubated with $[Ru(bpy)_2(picCOOH)]^{2+}$ (70×10^{-6} M) after 15 minutes and (b) live CHO cells incubated with $[Ru(bpy)_2(picCOOH)]^{2+}$ (70×10^{-6} M) after 15 minutes in PBS buffer (pH7.4) at room temperature. (Images courtesy of Dr. Roisin Moriarty)

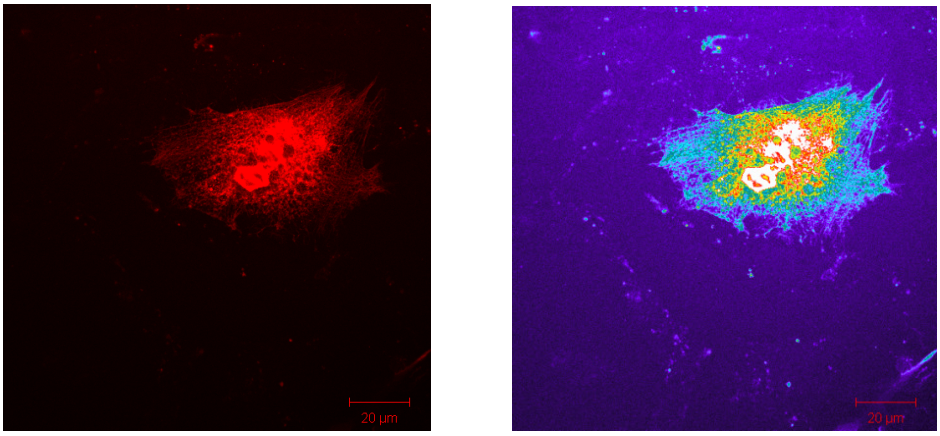

Figure 5.12: Luminescencent confocal image (left) and rainbow image (right) (λ_{ex} = 458 nm, λ_{em} = 610 nm) of fixed CHO cells incubated with $[Ru(bpy)_2(picCOOH)]^{2+}$ (70×10^{-6} M) in 0.1% triton in PBS solution (pH 7.4) after 15 minutes at room temperature. (Images courtesy of Dr. Roisin Moriarty)

As discussed in detail in Chapter 1 Neugebauer et at.[4] have previously demonstrated the ability of $[Ru(bpy)_2(picCOOH)Arg_8]^{10+}$ to transport across the cell membrane of SP2 cells. This material was prepared here to extend these studies and examine its uptake for the first time in CHO cells. As shown previously in Chapter 1, it was confirmed that the migration of the ruthenium dye-peptide in SP2 cells was quick and was complete after 10-15 minutes at room temperature in an irreversible process. All SP2 myeloma cells in a buffered solution were exposed to a final concentration of 70 μM of $[Ru(bpy)_2(picCOOH)Arg_8]^{10+}$ which led to bright luminescence within the cellular membrane and cell's cytoplasm after only 2 minutes with minimal intensity from the background by comparison. Over the next 10 minutes the dye-peptide continues to distribute throughout the cellular plasma with little evidence for targeted localisation within specific cell organelles as shown in Figure 5.13. The z-stack images confirming the distribution of the ruthenium dye-peptide throughout the different SP2 cell organelles is also shown in Figure 5.14.

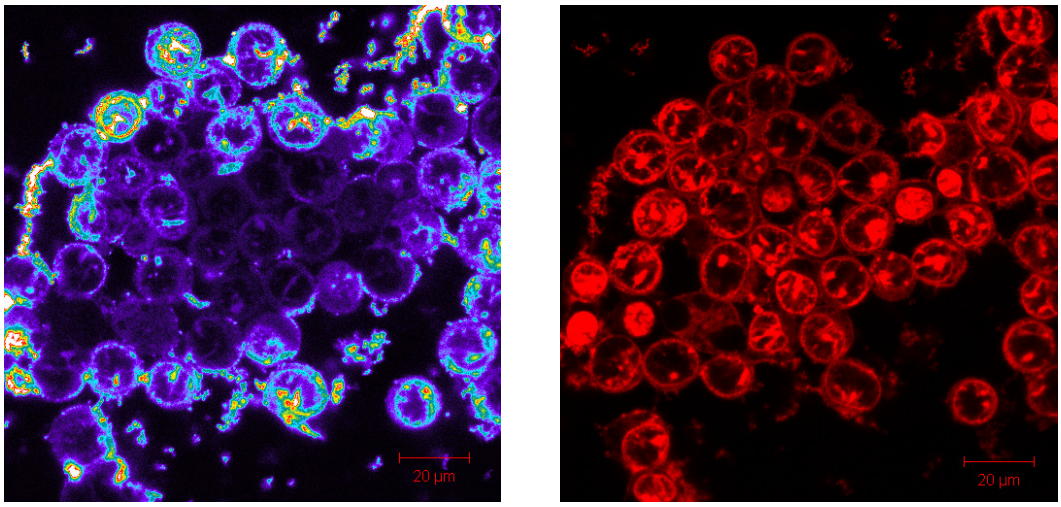

(a) ***(b)***

Figure 5.13: Luminescencent confocal images (λ_{ex} = 458 nm, λ_{em} = 610 nm) of live SP2 myeloma cells incubated with $[Ru(bpy)_2(picCOOH)Arg_8]^{10+}$ (70×10^{-6} M) after (a) after 10 minutes (rainbow image) and (b) after 48 minutes (luminescent image) in PBS (pH 7.4) at room temperature. (Images courtesy of Dr. Roisin Moriarty)

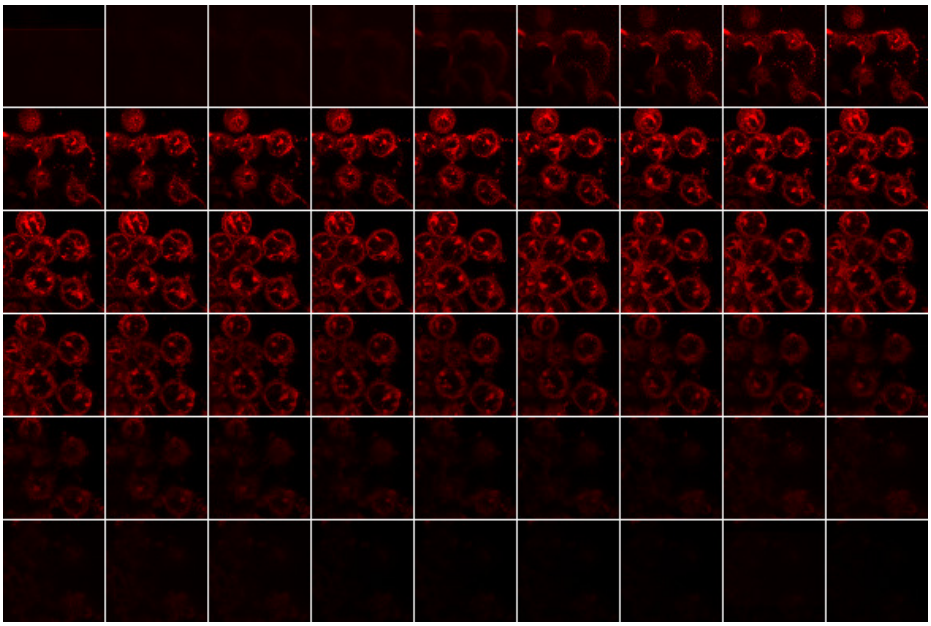

Figure 5.14: Luminescencent confocal z-stack images (λ_{ex} = 458 nm, λ_{em} = 610 nm) of live SP2 myeloma cells incubated with $[Ru(bpy)_2(picCOOH)Arg_8]^{10+}$ (70×10^{-6} M) after 30 minutes in PBS (pH 7.4) at room temperature. (Images courtesy of Dr. Roisin Moriarty)

By comparison, uptake of the ruthenium dye-peptide in CHO cells does not appear to be as efficient as that for SP2 cells. Internalisation of the ruthenium dye-peptide in SP2 cells was complete after 10-15 minutes, whereas under the same conditions, uptake of the ruthenium probe in CHO cells was observed to the same extent over time frames of upwards of 40 minutes as shown in Figure 5.15 as indicated by the luminescent intensity of the dye inside the cells. Even then distribution of the dye within cell organelles is not the same as seen for SP2 cells. The ruthenium probe seems to distribute throughout the cellular plasma with little localisation in any CHO cell organelles. The longer uptake times of $[Ru(bpy)_2(picCOOH)Arg_8]^{10+}$ may partially account for their decreased cytotoxicity in CHO cells when compared to other transition metal probes as discussed in Section 5.5.3.

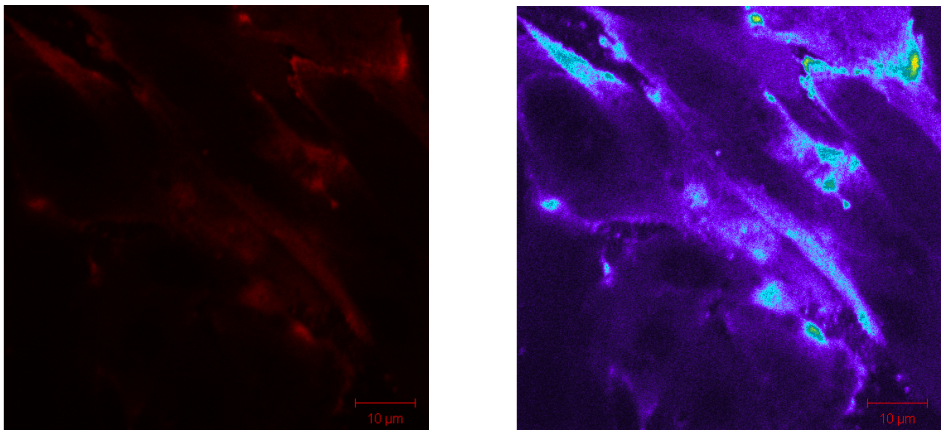

Figure 5.15: Luminescencent confocal image (left) and rainbow image (right) (λ_{ex} = 458 nm, λ_{em} = 610 nm) of live CHO cells incubated with $[Ru(bpy)_2(picCOOH)Arg_8]^{10+}$ (70 × 10^{-6} M) after 40 minutes in PBS (pH 7.4) at room temperature. (Images courtesy of Dr. Roisin Moriarty)

5.5.2 Iridium (III) Conjugated Peptide

The synthesis of the iridium (III) conjugated peptide proved more problematic than the ruthenium (II) conjugated polypeptide. This was largely due the poor aqueous solubility of the iridium dye, however, the isolated yield was identical to that of the ruthenium peptide. Many solvent combinations were tried to dissolve the unpurified dye peptide including DMSO, methanol, water and DMF for HPLC purification purposes. Finally, it was found that a mixture of 5% trifluoroacetic acid (TFA) in water was a suitable solvent mixture for the HPLC purification of the iridium peptide. MALDI-TOF mass spec analysis of the product is shown in Figure 5.16 below with the molecular dye-peptide ion of interested present at 2274 m/z. HPLC confirmed the purity of the iridium dye-peptide with a single peak retention time of 30.27 minutes with the HPLC conditions as outlined in Chapter 2.

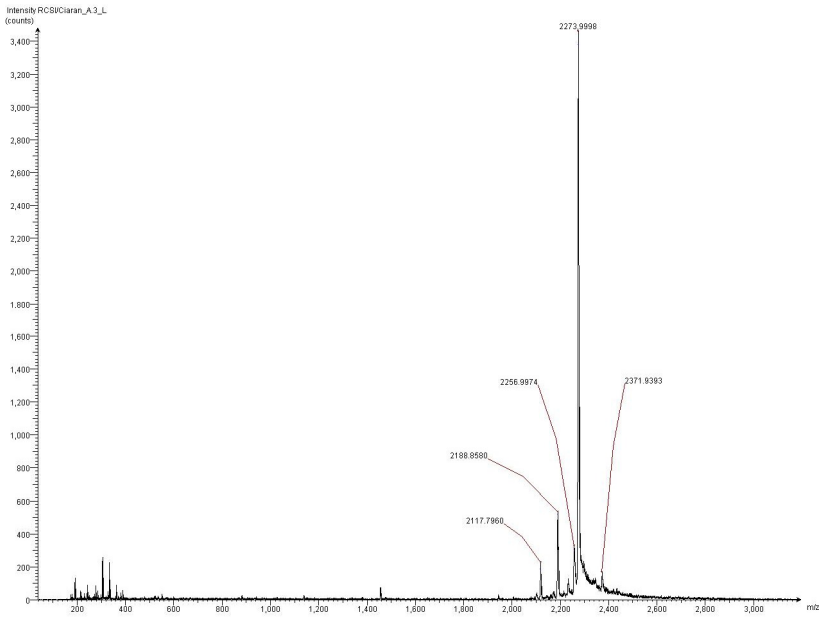

Figure 5.16: MALDI-TOF mass spectrum of $[Ir(dfpp)_2(picCOOH)Arg_8]^{9+}$ with the molecular ion of interest at 2274 m/z.

Figure 5.17 illustrates the absorbance and emission spectra of the free iridium (III) polypyridyl parent dye and the corresponding iridium dye-peptide. As seen previously in Chapter 4, the UV-vis spectrum of $[Ir(dfpp)_2(picCOOH)]^+$ displays a LC difluorophenyl pyridine π-π* electronic transitions giving maximum absorbance peaks at 246 nm and 282 nm. The shoulder at 325 nm may be assigned to the intraligand π-π* transition of the [picCOOH] ligand and is pH dependent, as are the π-π* transitions at 246 nm and 282 nm. There is evidence of a MLCT transition from the iridium dπ to [dfpp] π* orbital at 416 nm in PBS buffered (pH7.4) solution containing 1% DMSO, which is red shifted when compared to the corresponding complex in acetonitrile solution.

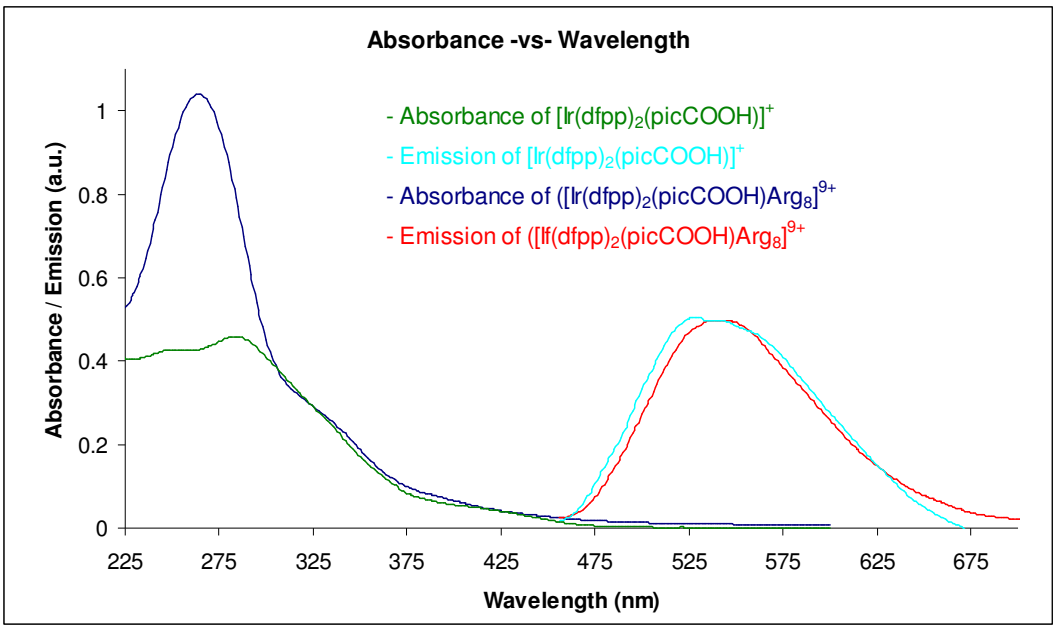

Figure 5.17: Overlaid absorbance and normalised emission spectra (excited at 380 nm, slit widths: 5 nm, normalised to 0.5 arbitrary units) of 20 x 10^{-6}M $[Ir(dfpp)_2(picCOOH)]^+$ in PBS buffer (pH 7.4 + 1% DMSO) solution and $[Ir(dfpp)_2(picCOOH)Arg_8]^{9+}$ in PBS buffer (pH 7.4) solution.

The UV-vis spectra of $[Ir(dfpp)_2(picCOOH)Arg_8]^{9+}$ is dominated by a peptide absorbance peak at 262 nm. There is evidence of a shoulder at 330 nm due to the intraligand π-π* transition of the [picCOOH] ligand. There is also evidence of a slight MLCT absorbance peak at 387 nm. The emission spectrum of the free iridium dye has a maximum emission at 537 nm and the corresponding dye-peptide has a slightly red shift emission at 543 nm in comparison. Table 5.2 outlines both the lifetimes and quantum yields of the free iridium and coupled iridium dye-peptide. It shows that there are no significant differences between the lifetimes and quantum yields following conjugation to octarginine and the values are similar to those already determined in Chapter 4.

Compound	Lifetime[a] (percentage component)		x^2 Value	Quantum Yield[b]
$[Ir(dfpp)_2(picCOOH)]^+$	142 +/- 5 ns (92%)	13 +/- 2 ns (8%)	0.897	0.115
$[Ir(dfpp)_2(picCOOH)Arg_8]^{9+}$	153 +/- 7 ns (94%)	10 +/- 3 ns (6%)	0.921	0.109

Table 5.2: Photophysical comparison of parent iridium dye versus dye-conjugate.

[a] *Biexponential lifetimes measured in degassed PBS buffer solution (pH 7.4) at room temperature.*

[b] *Photoluminescent quantum yield (ϕ) in PBS buffer solution (pH 7.4) at room temperature, using* $[Ru(bpy)_3]^{2+}$ *as standard .*

**(Buffer contains 1% DMSO in the case of the free dye measurements)*

A key difficulty in the application of inorganic dyes to cellular imaging is their inability to penetrate the cytoplasmic membrane of the living cell. This is greatly amplified by the poor aqueous solubility of the $[Ir(dfpp)_2(picCOOH)]^+$ dye. As discussed in Chapter 1, iridium (III) dyes have been used before to image cells, however, solvents such as DMSO have been employed in the imaging process to aid with solubility issues.[16] Low concentrations of DMSO (< 1%) have been reported in the study of SP2 myeloma cells without significant adverse effects on the cells themselves.[17-19] However, it is noted that due to the toxic nature of such a solvent, it calls into question the viability of the cells.[2, 3] The implications of using organic solvents, in particular ethanol and DMSO, on the viability of a cell during cellular imaging is discussed in Section 5.5.3.2.

5.5.2.1 Cell Uptake of $[Ir(dfpp)_2(picCOOH)]^+$ and $[Ir(dfpp)_2(picCOOH)Arg_8]^{9+}$

As preformed previously for the ruthenium cellular uptake experiments, SP2 and CHO cells were cultured separately on 35 mm glass bottom culture dishes and 20 µl of the iridium parent complex (1.4 mM) or iridium dye-peptide (1.4 mM) in PBS (pH 7.4, with $MgCl_2$ and $CaCl_2$) was added. The luminophore and dye-peptide were made to a final concentration of 70 µM with PBS (pH 7.4) except for the iridium parent complex which made to 70 µM in 0.05% DMSO in PBS (1:20 dilution from stock with 1% DMSO) and were imaged immediately.

As Figure 5.18 shows, surprisingly, the iridium (III) parent dye transports across the membrane passively after less than 10 minutes. Initially the dye is located in the cell's membrane after approximately 10 minutes at room temperature in PBS (pH 7.4 containing 0.05% DMSO) as shown in Figure 5.18 (a). However, it is thought that the use of DMSO as co-solvent, to help with solubility of the dye, has permeabilised the cell membrane.

The vesicles observed in the SP2 cell after 30 minutes (Figure 5.18 (b)) is an indication of cell death. Vesicle formation also occurs in endocytosis, however as discussed in Section 5.5.3, the iridium (III) complex exhibits extremely high cytotoxicity in comparison to the ruthenium parent luminophore which does not display any signs of vesicle formation in SP2 cells following 30 minutes at room temperature. This is further confirmed when the nuclear staining dye of dead cells, DRAQ7, showed some penetration of SP2 cells without the iridium luminophore present after 30 minutes in PBS (pH 7.4 containing 0.05% DMSO). However, under identical conditions with the iridium (III) complex present, the DRAQ7 dye displayed evidence of the nuclear staining of cells indicating cell death. In contrast, the ruthenium luminophore showed little evidence of DRAQ7 nuclear staining both with and without the ruthenium complex present in PBS (pH 7.4) after 30 minutes. Following incubation with the dye overnight at 37^{o}C the iridium luminophore has completely permeated the cell's cytoplasm. Z-stack images of the cells confirm the distribution of the dye throughout the whole cell [images not shown].

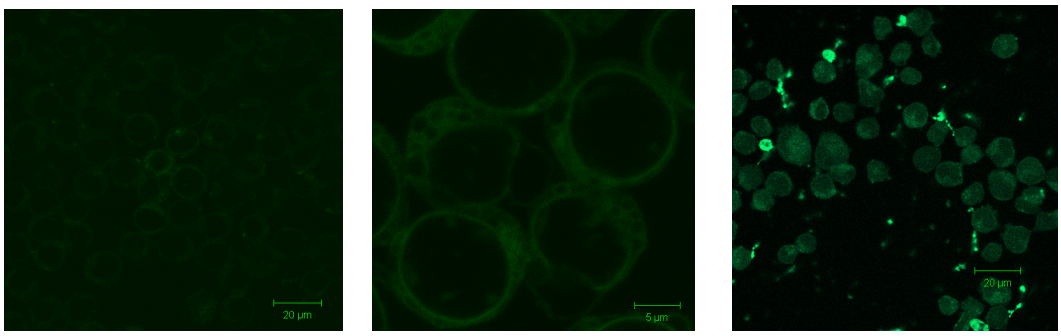

(a) ***(b)*** ***(c)***

Figure 5.18: Luminescencent confocal images (λ_{ex} = 375 nm, λ_{em} = 520 nm) of live SP2 myeloma cells incubated with $[Ir(dfpp)_2(picCOOH)]^+$ (70×10^{-6} M) after (a) 10 minutes at room temperature, (b) 30 minutes at room temperature and (c) overnight at 37 ^oC in PBS (pH 7.4 containing 0.05% DMSO). (Images courtesy of Dr. Roisin Moriarty)

Longer uptake times and results are observed for the interaction of the $[Ir(dfpp)_2(picCOOH)]^+$ complex with CHO cells as illustrated in Figure 5.19. Figure 5.19 (a) shows little uptake of the iridium dye following 5 minutes incubation, however, after a time period of 40 minutes (Figure 5.19 (b) and (c)) at room temperature the dye is distributed throughout the cell's cytoplasm but without ever entering the nucleus of the cell. Once again there is evidence of cellular vesicles indicating potential cell death. In contrast the ruthenium parent complex did not exhibit transmembrane transport after 40 minutes incubation time as seen here for the iridium equivalent. Figure 5.20 demonstrates the emission profile and luminescent image of the iridium dye in a CHO cell compared with the surrounding media. Luminescence from inside the cellular structure corresponds to the characteristic emission of $[Ir(dfpp)_2(picCOOH)]^+$ at ~520 nm (Figure 5.20 - region of interest 2). Furthermore, minimal emission intensity is detected this wavelength as a result of the background luminescence in Figure 5.20 - region of interest 1.

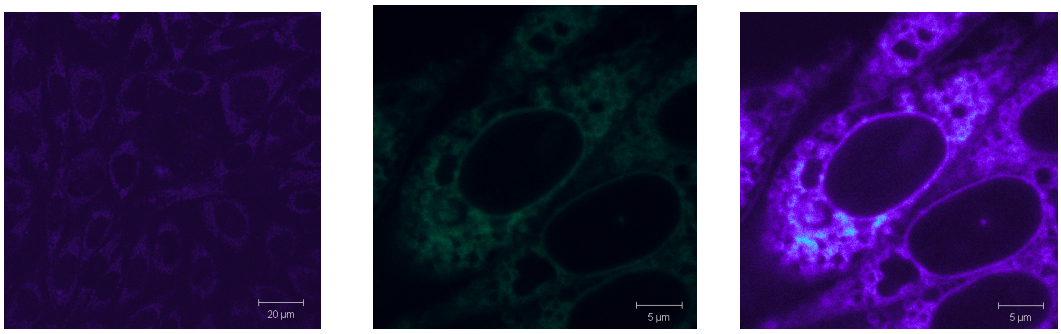

(a) ***(b)*** ***(c)***

Figure 5.19: Confocal images (λ_{ex} = 375 nm, λ_{em} = 520 nm) of live CHO cells incubated with $[Ir(dfpp)_2(picCOOH)]^+$ (70 × 10^{-6} M) after (a) 5 minutes at room temperature (rainbow image), (b) 40 minutes at room temperature (luminescent image) and (c) 40 minutes in PBS (pH 7.4 containing 0.05% DMSO) at room temperature (rainbow image). (Images courtesy of Dr. Roisin Moriarty)

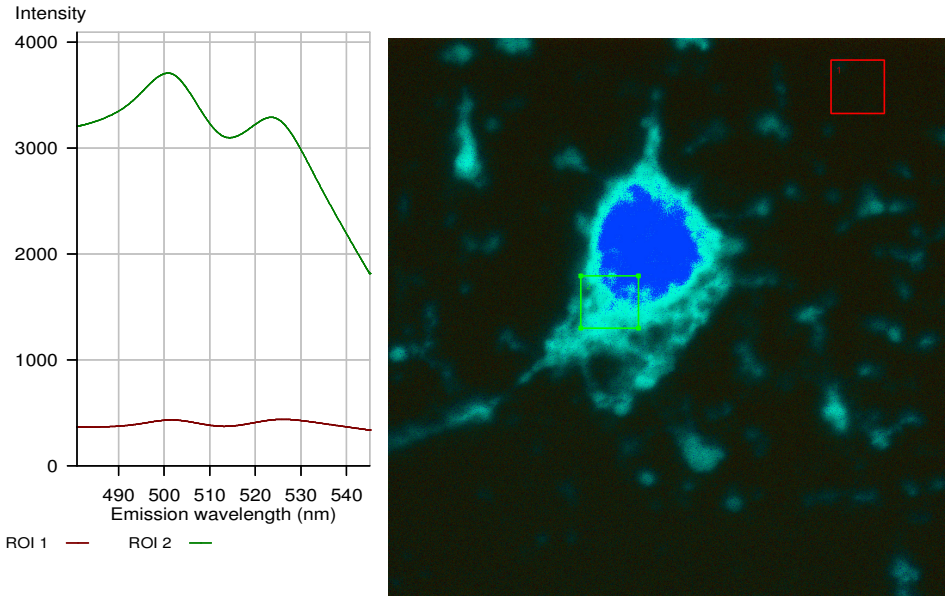

Figure 5.20: Emission intensity profile and luminescent confocal image (λ_{ex} = 375 nm, λ_{em} = 520 nm) of live CHO cells incubated with $[Ir(dfpp)_2(picCOOH)]^+$ (70 × 10^{-6} M) after 30 minutes in PBS (pH 7.4 containing 0.05% DMSO) at room temperature. (Image courtesy of Dr. Roisin Moriarty)

Importantly, the distribution of the iridium dye-conjugate in both SP2 and CHO cells is different to that of the parent iridium dye complex. Figure 5.21 displays the distribution of the iridium peptide in SP2 myeloma cells. Figure 5.21 (a) shows that the dye-peptide is initially concentrated in the cell membrane after 5-10 minutes at room temperature. The centre of this particular group of cells in Figure 5.21 (a) is protected from the iridium dye-peptide and therefore the observed uptake in these cells is less then that of the cells located around the edges. After approximately 40 minutes at room temperature complete internalisation of the dye is observed in the cell's cytoplasm and what appears to be the nuclear membrane as shown in Figure 5.21 (b). However, Figure 5.21 (c) suggests that the cellular walls of the SP2 cells have been disrupted following incubation with the parent dye for 50 minutes at room temperature. This finding is supported by DRAQ7 staining of the SP2 cells after 50 minutes, which localises in the nucleus confirming cell death. The high mortality rate of SP2 cells following incubation with the iridium-peptide is further confirmed by cytotoxicity studies of the dye-peptide in Section 5.5.3. Z-stack images in Figure 5.22 shows the distribution of the dye-peptide in the SP2 cell membrane over a time frame of 18-24.5 minutes whilst imaging at room temperature.

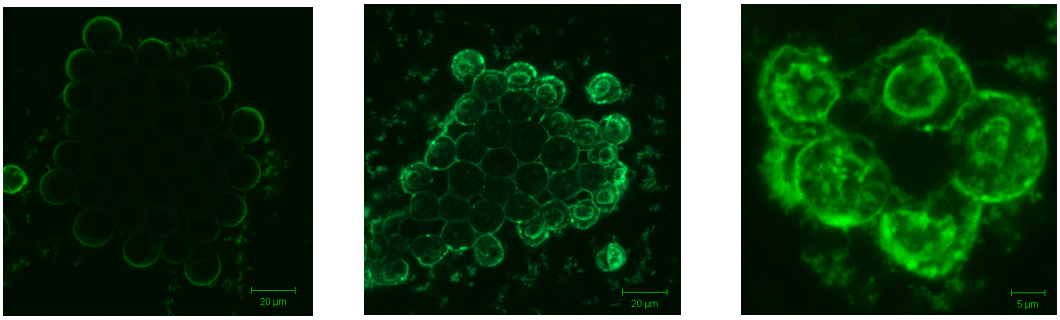

(a) ***(b)*** ***(c)***

Figure 5.21: Luminescent confocal images (λ_{ex} = 375 nm, λ_{em} = 520 nm) of live SP2 myeloma cells incubated with $[Ir(dfpp)_2(picCOOH)Arg_8]^{9+}$ (70×10^{-6} M) after (a) 5 minutes, (b) and (c) 50 minutes in PBS (pH 7.4) at room temperature. (Images courtesy of Dr. Roisin Moriarty)

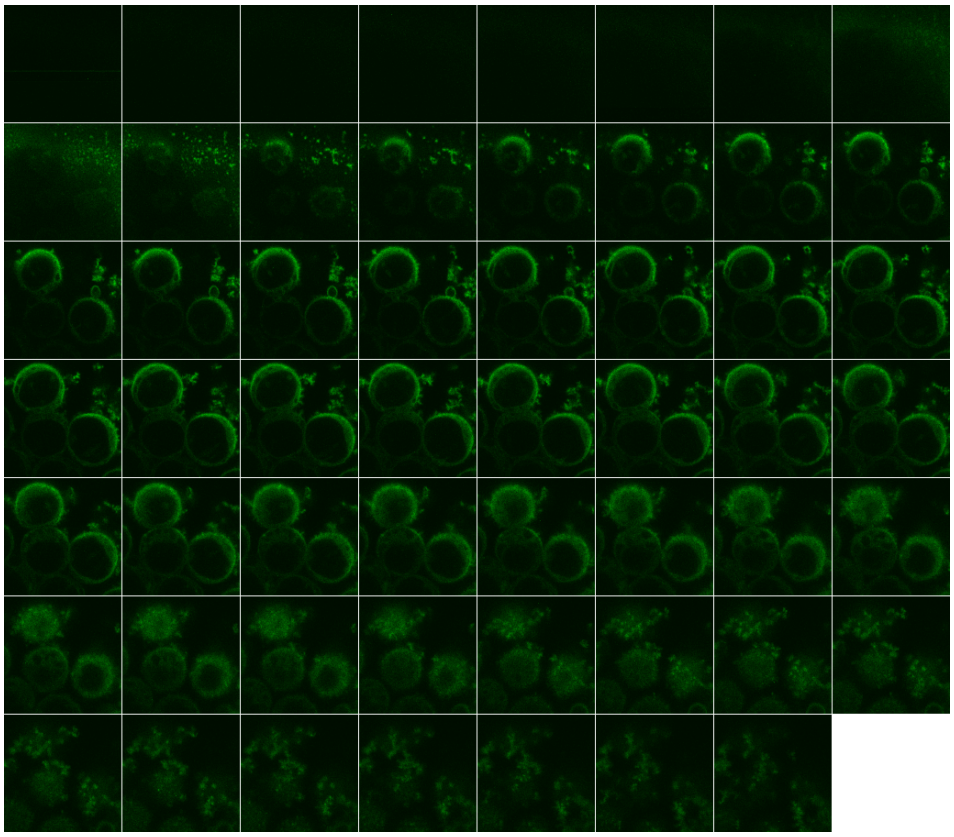

Figure 5.22: Luminescent confocal z-stack images (λ_{ex} = 375 nm, λ_{em} = 520 nm) of live SP2 myeloma cells incubated with $[Ir(dfpp)_2(picCOOH)Arg_8]^{9+}$ (70×10^{-6} M) after 18-24.5 minutes in PBS (pH 7.4) at room temperature. (Images courtesy of Dr. Roisin Moriarty)

As expected, the transmembrane transport of the iridium dye-peptide into CHO cells proved to be much quicker than for the corresponding $[Ir(dfpp)_2(picCOOH)]^+$ complex and full penetration of the cell membrane is evident after only 10 minutes (Figure 5.23 (b)). As seen previously in SP2 cells, the dye-peptide is initially concentrated in the cell membrane of the CHO cells. Following a period of about 10 minutes the dye-peptide is located throughout the CHO cell's membrane, cytoplasm, nuclear membrane and inside the nucleus itself. However, following an incubation time of 30 minutes at room temperature the iridium conjugate permeates the whole CHO cell, making identification of internal cell organelles difficult as illustrated in Figure 5.23 (c). Once again there is evidence of the formation of vesicles inside the cellular structure after only 10 minutes indicating the start of cell death.

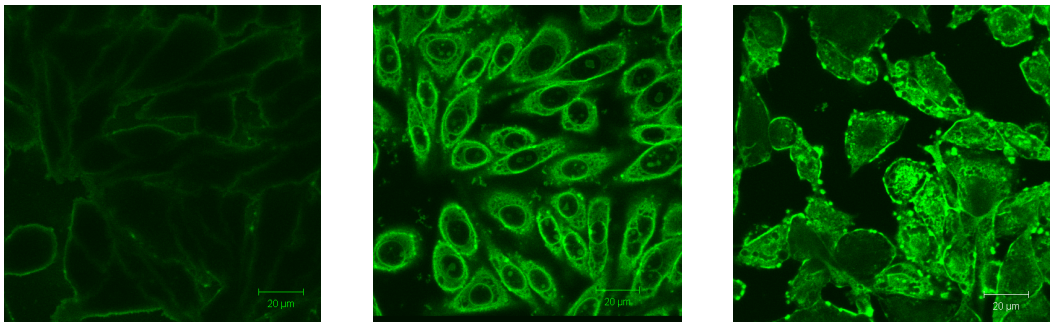

(a) ***(b)*** ***(c)***

Figure 5.23: Luminescent confocal images (λ_{ex} = 375 nm, λ_{em} = 520 nm) of live CHO cells incubated with $[Ir(dfpp)_2(picCOOH)Arg_8]^{9+}$ (70×10^{-6} M) after (a) 5 minutes, (b) 10 minutes and (c) 30 minutes in PBS (pH 7.4) at room temperature. (Images courtesy of Dr. Roisin Moriarty)

Figure 5.24 shows the luminescent cross section of the iridium-peptide in live CHO cells after 25 minutes at room temperature. A z-stack image in Figure 5.25 confirms the distribution of the dye-peptide throughout the CHO cells. In comparison the ruthenium peptide also exhibits a bright a luminescence from inside the CHO cells and is distributed throughout the cell's cytoplasm, however, it is not localised as noticeably in specific cell organelles after a 40 minutes as shown in Figure 5.15. However the cytotoxicity for the iridium-peptide is far greater than the ruthenium-peptide in CHO cells, vide infra.

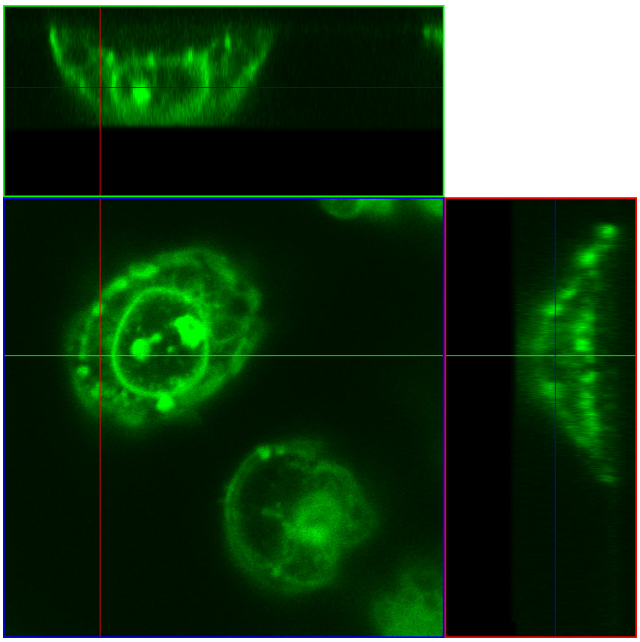

Figure 5.24: Luminescent confocal image (λ_{ex} = 375 nm, λ_{em} = 520 nm) showing luminescent cross section of a live CHO cell incubated with $[Ir(dfpp)_2(picCOOH)Arg_8]^{9+}$ (70 × 10^{-6} M) after 25 minutes in PBS (pH 7.4) at room temperature. (Image courtesy of Dr. Roisin Moriarty)

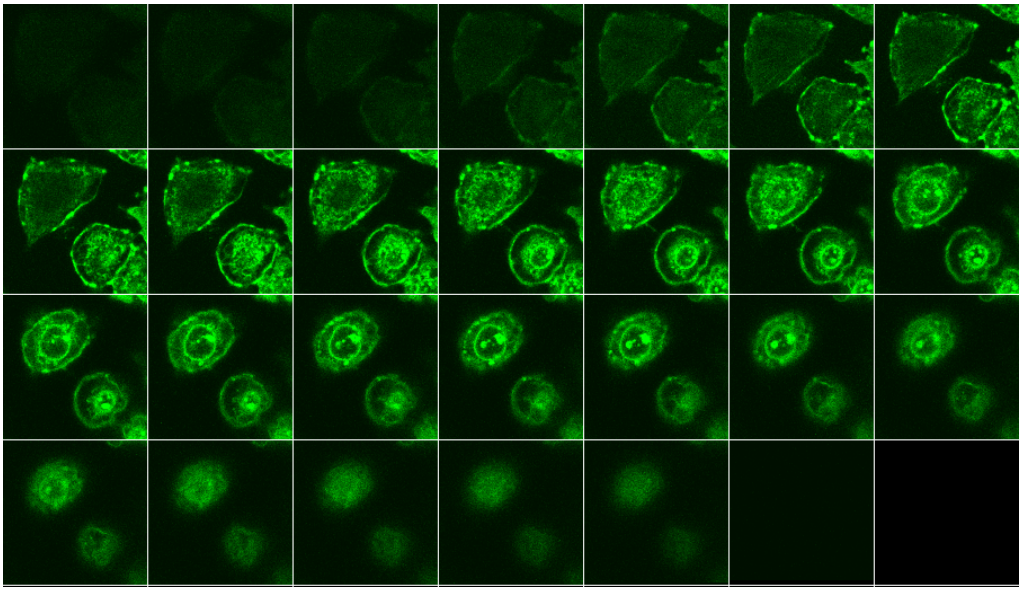

Figure 5.25: Luminescent confocal z-stack images (λ_{ex} = 375 nm, λ_{em} = 520 nm) of live CHO cells incubated with $[Ir(dfpp)_2(picCOOH)Arg_8]^{9+}$ (70 × 10^{-6} M) after 18-24.5 minutes in PBS (pH 7.4) at room temperature. (Images courtesy of Dr. Roisin Moriarty)

5.5.3 Cytotoxicity Studies

With the evidence of vesicle formation, in particular in both SP2 and CHO cells following incubation with the iridium (III) complex, it is important to assess the potential toxic effects of the metal complexes on the cell lines. The cytotoxic effect of the parent luminophores and dye-peptides was determined using the reasazurin viability assay which is explained in detail in the introduction. Both cell lines were incubated with parent luminophores and dye-peptides in PBS (pH 7.4) overnight at 37^{o}C in the dark over a range of concentrations and their cell viability results were determined the following day.

Figures 5.26 and 5.27 below illustrate the cytotoxic effect of the parent luminophores and conjugated dye-peptides on SP2 myeloma and CHO cell lines respectively. It is evident from both sets of results that the iridium (III) complex exhibits a toxic effect on the cells well above that of the ruthenium (II) complexes. Since the cytotoxicity experiments were performed in the dark, the cell death as a result of the singlet oxygen generating ability of the complex is considered to be minimal. Other factors that may explain the increased cytotoxicity of the iridium probe include the fluorination of the cyclometalating iridium (III) ligands as any potential reduction in the ligand in the cells may lead to the formation of fluoride, which is known to be highly toxic at high concentrations.[20] In addition, the iridium metal centre is much larger than that of the ruthenium metal centre and as a result is not as well protected by the coordinated ligands from potential interactions with the surrounding cell. This may result in increased cytotoxicity in cells due to the toxic iridium metal centre.

The iridium polypeptide shows the greatest cytotoxicity of all the complexes analysed even above that of the iridium parent using DMSO as a solvent. This is thought to be due to the more localised, increased and faster cellular uptake of the iridium peptide when compared to the iridium parent dye. Previous results have indicated significant uptake of the iridium peptide occurs after only after 10 minutes, whereas, much longer time periods are required for similar uptake by the parent iridium complex, facilitated by the use of DMSO as co-solvent.

By comparison, the ruthenium moieties display much lower cytotoxicity in both SP2 and CHO cell lines when compared to the iridium equivalents. This may be due to a number of things including a smaller ruthenium metal centre and no fluorination of cyclometalating ligands. The ruthenium polypeptide displayed very similar cytotoxicity to that of the ruthenium parent dye in both cell lines. This is very interesting considering that the ruthenium parent dye has been shown previously not to transport across the cell membrane of either cell lines without permeabilisation, whereas, the ruthenium dye-peptide showed internalisation inside SP2 cells after 10 minutes and CHO cells after approximately 50 minutes. The relatively low cytotoxicity, up to a concentration of 140 μM, of the ruthenium polypeptide probe further supports its use as a molecular probe for multimodal imaging purposes.

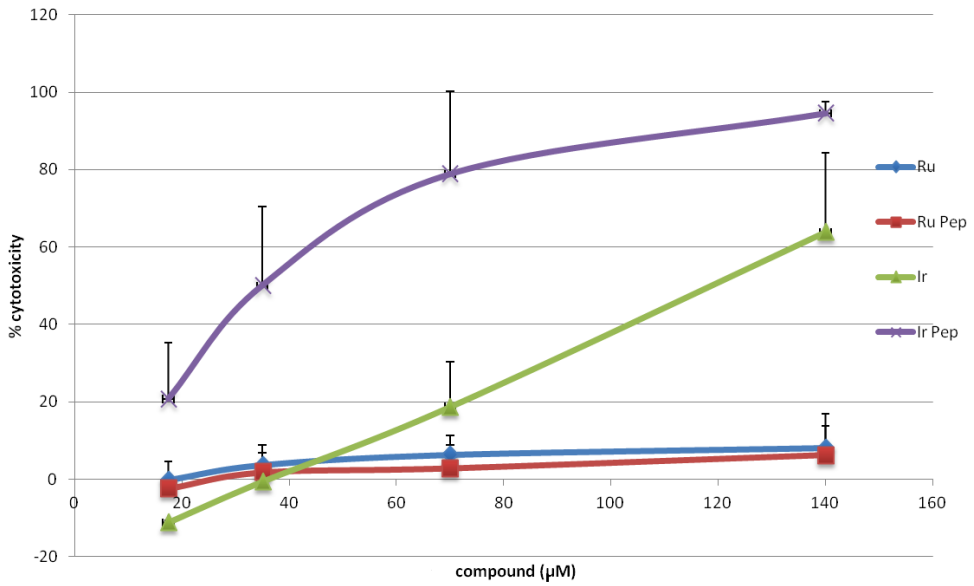

Figure 5.26: SP2 myeloma cell cytotoxicity at different concentrations of the parent luminophore and dye-peptide complex. Resazurin assay (n=4) was used to determine the cytotoxic effects of the complexes on the cell line following incubation overnight at 37°C. (Data courtesy of Dr. Roisin Moriarty)

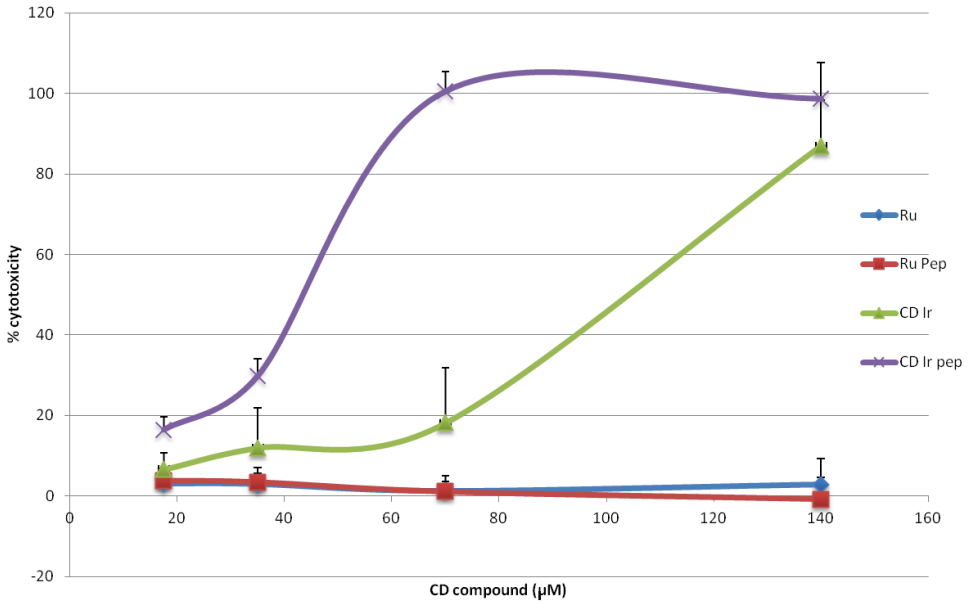

Figure 5.27: CHO cell cytotoxicity at different concentrations of the parent luminophore and dye-peptide complex. Resazurin assay (n=4) was used to determine the cytotoxic effects of the complexes on the cell line following incubation overnight at 37°C. (Data courtesy of Dr. Roisin Moriarty)

The increased cytotoxicity of the iridium (III) peptide when compared to the ruthenium (II) peptide in CHO cell lines is highlighted again in Figure 5.28 below. Following incubation with the dye-peptides in the dark for approximately 35 minutes, DRAQ7, was added to the cells under analysis for approximately 15 minutes. DRAQ7 is a far red fluorescent DNA dye that only stains the nuclei of dead and permeabilised cells and does not enter intact live cells. Furthermore, it is also non-toxic to cells. Figure 5.28 shows no luminescence from the DRAQ7 in the CHO cells and only the emission from $[Ru(bpy)_2(picCOOH)Arg_8]^{10+}$ is detected. This suggests that the CHO cells remain alive during the analysis of the ruthenium conjugate of up to 50 minutes. This observation is also seen for the ruthenium-peptide in SP2 cells [image not shown] and this is further supported by co-localisation studies performed by Neugebauer *et al.*[4] involving the distribution of the ruthenium (II) peptide in SP2 cells as discussed in Chapter 1.

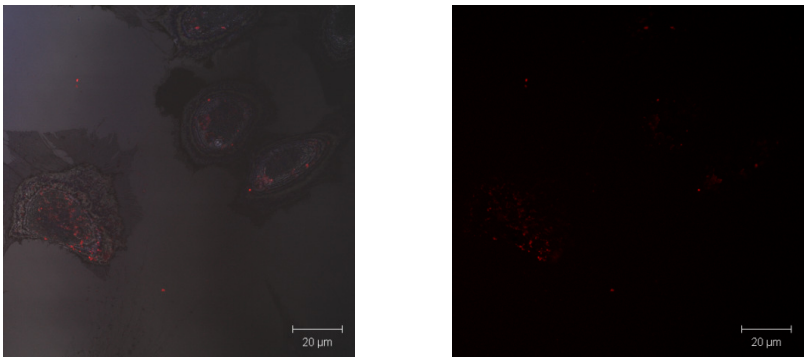

(a) ***(b)***

Figure 5.28: Confocal images (λ_{ex} = 458 nm, λ_{em} = 610 nm) of fixed CHO cells incubated with $[Ru(bpy)_2(picCOOH)Arg_8]^{10+}$ (70×10^{-6} M) and DRAQ 7 (4×10^{-6} M – excited at 633 nm) after 50 minutes in PBS (pH7.4) at room temperature. (a) Backscatter image and (b) luminescent image. (Images courtesy of Dr. Roisin Moriarty)

On the other hand, Figure 5.29 displays bright luminescence inside the nucleus of both SP2 and CHO cells following 50 minutes incubation with the $[Ir(dfpp)_2(picCOOH)Arg_8]^{9+}$ conjugate at room temperature in the dark. This signals the unquestionable cell death of CHO cells as a result of incubation with the iridium molecular probe even without scanning continuously at 375 nm.

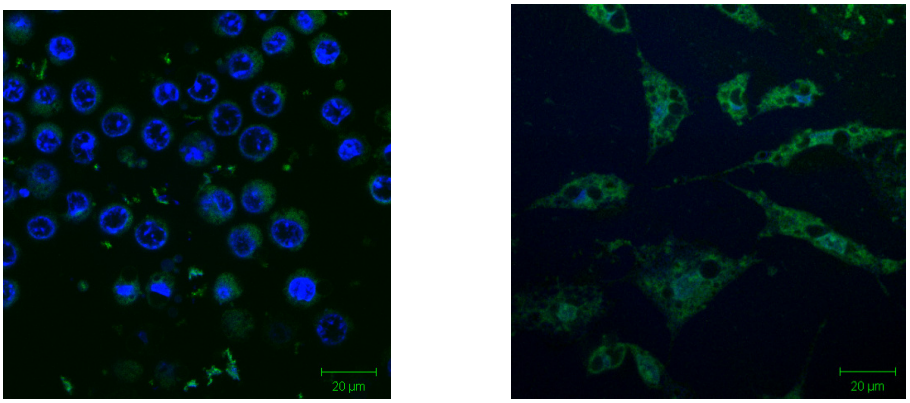

(a) ***(b)***

Figure 5.29: Luminescent confocal image (λ_{ex} = 375 nm, λ_{em} = 520 nm) of (a) SP2 and (b) CHO cells incubated with $[Ir(dfpp)_2(picCOOH)Arg_8]^{9+}$ (70×10^{-6} M) and DRAQ 7 (4×10^{-6} M – excited at 633 nm) after 50 minutes in PBS (pH7.4) at room temperature. (Images courtesy of Dr. Roisin Moriarty)

The resazurin cytotoxicity studies performed involve incubating the complexes with the cells overnight in the dark at 37°C and determining cell death by absorbance of resorufin produced at 570 nm. Hence, one critical factor yet to be fully considered is the continuous wavelength of excitation used for both iridium complexes (375 nm) and ruthenium complexes (458 nm). The higher energy of excitation of the iridium complexes, when compared to the ruthenium complexes, also accounts for its visible signs of increased cell death in both SP2 and CHO cells. This is found to be the case as DRAQ7 staining is evident for both ruthenium and iridium luminophores in SP2 and CHO cells after 50 minutes following continuous irradiation at 375 nm. Figure 5.30 shows extensive DRAQ7 nuclear staining of SP2 cells when incubated with $[Ru(bpy)_2(picCOOH)Arg_8]^{10+}$ at room temperature for 50 minutes following constant irradiation at 375 nm. In general, such extensive cell death was not observed under identical conditions using a continuous excitation wavelength of 458 nm [image not shown].

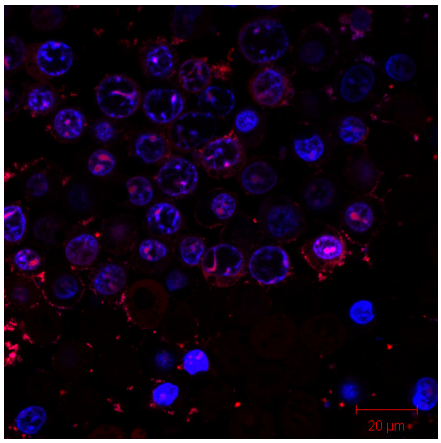

Figure 5.30: Confocal images (λ_{ex} = 375 nm, λ_{em} = 610 nm) of SP2 cells incubated with $[Ru(bpy)_2(picCOOH)Arg_8]^{10+}$ (70×10^{-6} M) and DRAQ 7 (4×10^{-6} M – excited at 633 nm) after 50 minutes in PBS (pH7.4) at room temperature. (Image courtesy of Dr. Roisin Moriarty)

Interestingly, when no dye is present under continuous excitation at 375 nm there is minimal evidence of cell death, as observed with the viability dye DRAQ7 nuclear stain as shown in Figure 5.31 for CHO cells. Therefore, it may be concluded that the iridium complex itself and in particular excitation of the iridium dye at 375 nm at shorter time frames causes a significant contribution to cell death. Furthermore, after image acquisition and continuous 375 nm laser scanning for 60 minutes of the iridium dye-peptide, 90% of the cells were dead as observed with DRAQ7 nuclear dye. In addition, when moving to a different field of view there is less evidence of staining for DRAQ7. This suggests that the increased cell death is due to a light activated process, which most likely considered to be the generation of singlet oxygen ($^1O_2$). This is further supported by preliminary experiments using ascorbic acid as a singlet oxygen scavenger[21] which has resulted in a reduction in cell cytotoxicity of the iridium peptide from 50% to 5% under similar experimental conditions outlined here.

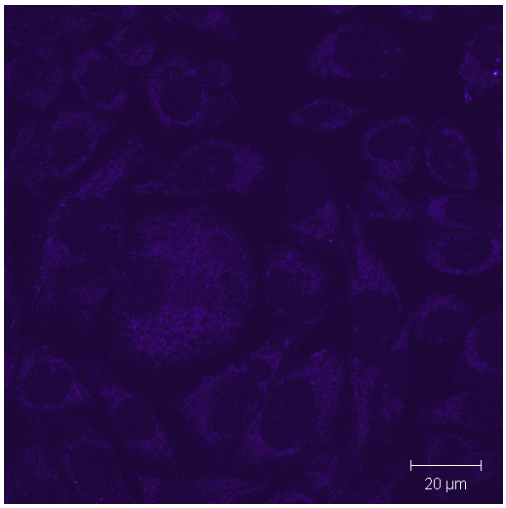

Figure 5.31: Confocal rainbow image (λ_{ex} = 375 nm, λ_{em} = 610 nm) of CHO cells with DRAQ 7 (4×10^{-6} M – excited at 633 nm) after 50 minutes in PBS (pH 7.4) following continuous irradiation at 375 nm at room temperature. (Image courtesy of Dr. Roisin Moriarty)

In general however, the ruthenium peptide (when excited at 458 nm) also appears to be inducing some cell death but this is not necessarily due to the laser as different fields of view have different cell death populations. Similarly, the iridium peptide (when excited with the 375 nm laser) is inducing cell death but this is dependent on the laser at shorter time frames as different fields of view have different cell death as observed by DRAQ7 nuclear staining. It has been shown the iridium induces cell death after 16 hours exposure at 37^{o}C in the dark in the cytotoxicity studies, but one of the main contributing factor to cell death following 1 hour exposure time at room temperature seems to be the 375 nm laser excitation. The rapidly induced cell death using the iridium probe at 375 nm excitation is highlighted by the fact that the DRAQ7 mean pixel intensity goes from 1.41 to 5.94 after only 4 scans on the confocal microscope.

In general, it also appears that upon increased light exposure to cells containing dye, the emission intensity also increases with time. The cause of this could be two fold: firstly, the effect of the 375 nm laser when the dye is present is known to damage cell viability and could cause membrane disruption leading to further dye leakage into the cells. Or secondly, light exposure of the inorganic complexes can cause an increased production of singlet oxygen, and therefore a decrease in molecular oxygen in the cell, which could in turn induce changes in pH of the cells. This will have an impact on the emission intensity of the luminophores as they have been shown previously in Chapters 3 & 4 to be very pH sensitive. For example, the emission intensity of the iridium dye increases with decreasing pH and this could also account for the increases in emission intensity in the observed confocal images after 15 minutes incubation and peaking at 40/60 minutes [images not shown]. A further factor yet to be fully considered is the fact that imaging of the cells takes place at room temperature and without a 5% CO_2 controlled environment. This may cause additional stresses on the cells which could also lead to increased apoptosis.

Overall, however, it can be concluded that phototoxicity of the luminophores is having a dramatic impact on the cell viability under the imaging conditions. The damaged cell is either up-taking more dye than an intact one or changes in pH and singlet oxygen generation of these dyes is causing an increase in the overall intensity of the luminophore within the cells. In light of the research reported by Djurovich *et*

al.[22], it is also considered that the increased cytotoxicity of the iridium luminophore in both SP2 and CHO cell lines following photoexcitation, when compared to the ruthenium luminophore, is potentially due to its longer triplet state lifetimes, higher quantum yield efficiencies and that its $^1O_2$ generation may be a result of both energy and electron transfer processes. Additional experiments in the near future intend to use FLIM measurements to help in determining any variations in the oxygen concentrations in SP2 and CHO cell lines using both ruthenium and iridium molecular probes as a result of experimental conditions.

Other factors that may attribute to the overall cell death could be the decreased ability of endogenous enzymes, such as superoxide dismutase and catalase to combat the increase in free radical generation as seen with the iridium dye due to imaging conditions at room temperature. In reality however, there are many different biological processes happening on a sub-cellular level that may have a significant effect on the luminophores once inside the cell and systematically examining all possibilities entails a great body of work that will be studied over the coming months.

5.5.3.1 IC50 Values

In order to assess and compare the effects of drugs / molecular cargo on a particular cell line it is important to determine their IC50 value. The IC50 value is the concentration at which 50% cell death has occurred in the cell population under analysis. The IC50 values for the luminophores and dye-peptides synthesised here were calculated using Prism statistic analysis software using the cytotoxicity results determined previously. The IC50 for the ruthenium parent and conjugate could not be determined as there was minimal inhibition up to a concentration of 140 μM in SP2 and CHO cell lines. For comparison, Liu *et al.*[23] reported IC50 values of 95.33 μM (in BEL-7402 cells), 22.77 μM (in C-6 cells), 102.01 μM (in hepG-2 cells) and 23.00 μM (in MCF-7 cells) for the $[Ru(bpy)_2(picNH_2)]^{2+}$ complex in Chapter 3. All of which exhibited less cytotoxicity towards the selected cell lines when compared to cisplatin and therefore, would not be considered as a potential anti cancer agent. There is not much published on the IC50 values on either ruthenium or iridium and their conjugates, particularly in SP2 and CHO cell lines.

IC50 Values	SP2	CHO
$[Ir(dfpp)_2(picCOOH)]^+$	118.7 μM	102.3 μM
$[Ir(dfpp)_2(picCOOH)Arg_8]^{9+}$	63.9 μM	85.5 μM

Table 5.3: IC50 values for $[Ir(dfpp)_2(picCOOH)]^+$ and $[Ir(dfpp)_2(picCOOH)Arg_8]^{9+}$ in SP2 and CHO cell lines.

The IC50 values for the iridium complexes are shown in Table 5.3 above. As expected, the iridium conjugate displayed lower IC50 values when compared with $[Ir(dfpp)_2(picCOOH)]^+$ due to more efficient and faster uptake times as a result of the attached peptide. Interestingly, the cytotoxicity of the iridium peptide is greater in SP2 cells in comparison to CHO cells. These results also have implications for the cell experiments performed here as a final concentration of 70 μM is used for confocal measurements throughout this chapter. This implies that approximately 50% of cell

death may be attributed to the iridium complex prior to any analysis being undertaken. Therefore, it is suggested that future cell experiments should be performed at concentrations lower than 70 μM. The majority of the cell experiments performed in the literature use final concentrations of between 20-50 μM.

Zhang *et al*.[24] reported of the considerable cytotoxicity of a series of iridium complexes towards HeLa and MDCK cell lines as the majority of complexes had a IC50 value < 10 μM.. Rijt *et al*.[25] also supported results here that an osmium conjugate exhibited more cytotoxicity when compared to the parent complex as seen for the iridium conjugate. This particular osmium conjugate showed very promising activity with an IC50 of only 4.5 μM towards the A2780 human ovarian cancer cell line.

5.5.3.2 Effects of Organic Solvents on SP2 Myeloma and CHO Cell Viability

As DMSO was used in the media to encourage dissolution of the iridium (III) parent complex it was decided to examine any potential effect such an organic solvent might have on the viability of SP2 and CHO cell lines. To our knowledge this is the first systematic study of its kind to highlight the potential implications of using commonly reported solvents, such as DMSO and ethanol, in cellular imaging. In order to asses the cytotoxicity of organic solvents on a particular cell line, an assay for measuring the activity of the cell population must be performed. The assays used here included the resazurin and MTT cell viability assays respectively, which are fully discussed in the introduction.

PBS solvent containing DMSO and ethanol with final concentrations of between 20 to 0.3 % were added to the harvested cells and left for 16 hours at 37^{o}C in a 5% CO_2 incubator. 10 µl of either the MTT or resazurin reagents were added and incubated for 4 hours for MTT and 7 hours for resazurin at 37^{o}C. Formazan was solubilised with 150 µl DMSO per well for MTT assay and absorbance was measured at 570 nm and 630 nm (background). The resazurin converted to resorufin in viable cells was detected at absorbance 570 nm with background subtracted at 600 nm. Figures 5.32 and 5.33 illustrate the cytotoxic effect on SP2 myeloma cell lines of ethanol and DMSO using the resazurin and MTT assays respectively. The cytotoxicity of DMSO proved to be far greater towards SP2 cells with 100% cell cytotoxicity at a DMSO concentration of 20% in PBS buffer using the resazurin assay. These results are confirmed using a MTT assay that yielded a comparable cell death at a DMSO concentration of 20%. Conversely, a solution containing 20% ethanol only exhibited a SP2 cell population death of approximately 60% using the resazurin assay.

Several papers published on metal complexes used for the purpose of cellular imaging used a 1% DMSO solution as standard in the cellular uptake analysis. According to the results obtained here, a 1% DMSO solution would correspond to a cell population death ranging from on average from 10-20%. This could prove significant as the potential toxicity of the transition metal complex and its singlet oxygen generating ability is not taken into account as this could lead to additional significant cell apoptosis.

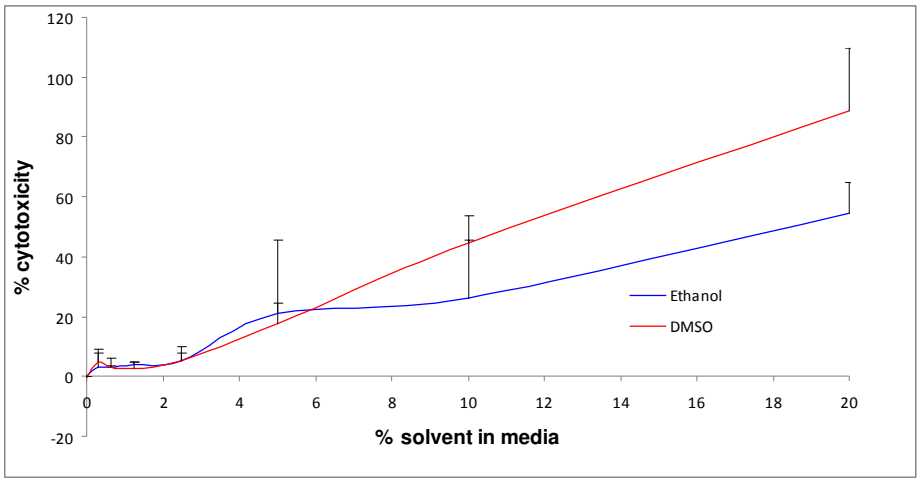

Figure 5.32: SP2 myeloma cell cytotoxicity with various concentrations of ethanol and DMSO. Measurements were performed using a resazurin assay (n=3). Experiments were performed in PBS solution following incubation for 16 hours at 37°C. (Data courtesy of Dr. Roisin Moriarty)

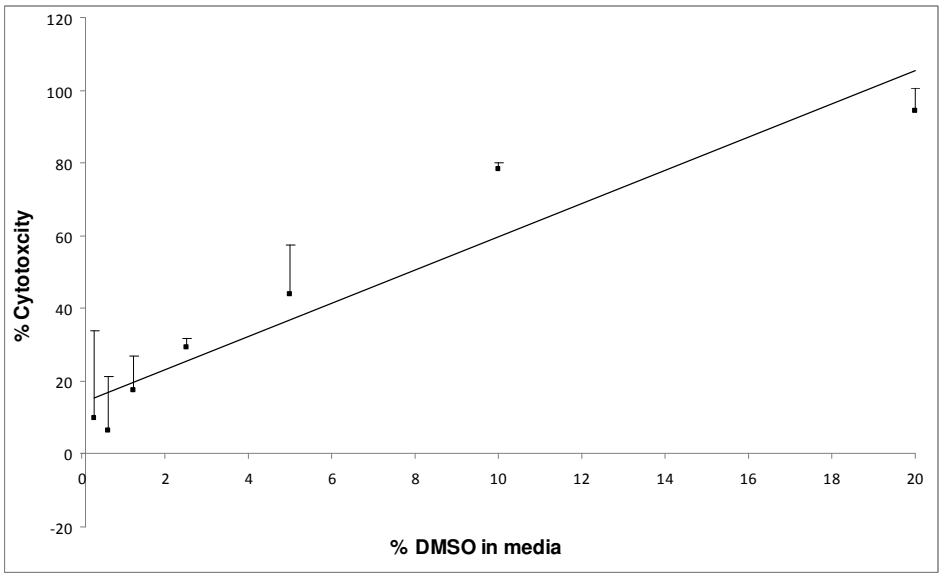

Figure 5.33: SP2 myeloma cell cytotoxicity with various concentrations of DMSO. Measurements were performed using a MTT assay (n=3). Experiments were performed in PBS solution following incubation for 16 hours at 37°C. (Data courtesy of Dr. Roisin Moriarty)

Similar cytotoxicity studies were performed using CHO cells. The cytotoxicity of ethanol proved to be far greater towards CHO cells when compared to SP2 cell lines, with 100% cell death with an ethanol concentration of ~20% as illustrated in Figure 5.34. Additionally, at lower concentrations of DMSO (1%) there is a considerable increase in the cytotoxicity towards CHO cells to approximately on average 30% when compared to the SP2 cell line at similar DMSO concentrations as illustrated by the MTT assay in Figure 5.35.

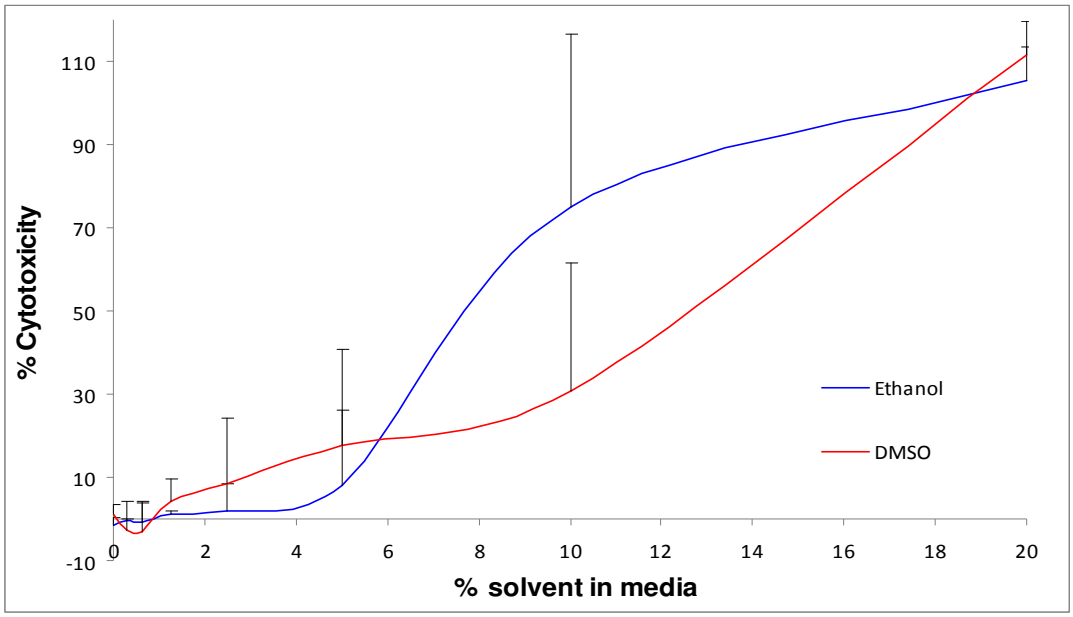

Figure 5.34: CHO cell cytotoxicity with various concentrations of ethanol and DMSO. Measurements were performed using a resazurin assay (n=3). Experiments were performed in PBS solution following incubation for 16 hours at 37°C. (Data courtesy of Dr. Roisin Moriarty)

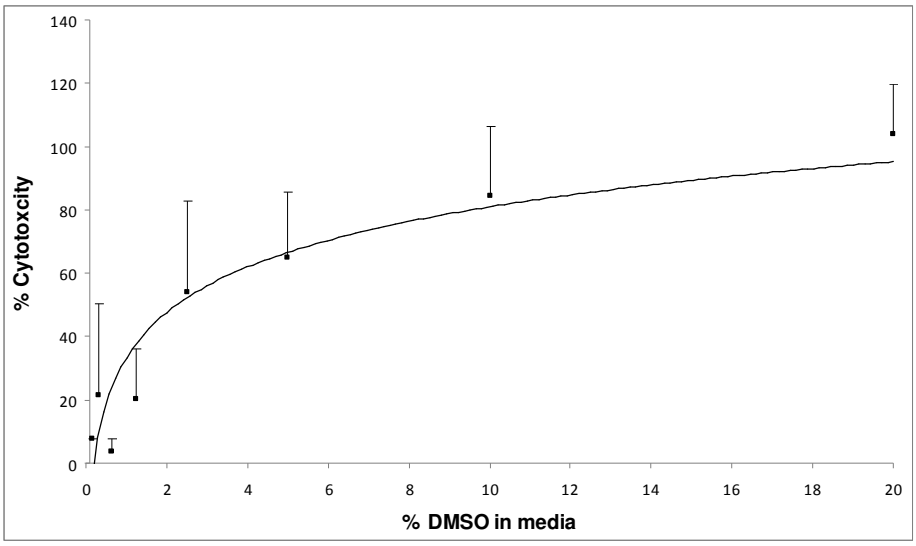

Figure 5.35: CHO cell cytotoxicity with various concentrations of DMSO. Measurements were performed using a MTT assay (n=3). Experiments were performed in PBS solution following incubation for 16 hours at 37^{o}C. (Data courtesy of Dr. Roisin Moriarty)

The effects of using DMSO as solvent in cellular imaging is also confirmed using the water soluble $[Ru(bpy)_2(picCOOH)]^{2+}$ dye in a solution containing 1% DMSO. It has been seen before how this particular ruthenium complex probe failed to transfer efficiently across the cellular membrane of SP2 myeloma cells in aqueous conditions. However, upon addition of 1% DMSO to the solution, the dye showed signs of transport across the cellular membrane [results not shown]. The presence of the dye throughout the whole cell cytoplasm was confirmed by z-stack images of the cell. Unfortunately, the use of very low concentrations of organic solvent remains unavoidable as solubility of the parent iridium (III) dye in aqueous buffer is extremely poor. Thus a key advantage, as outlined in this chapter, for the conjugation of a metal complex to a polypeptide is the increased water solubility, membrane penetrating ability and localisation of the dye-conjugate in SP2 and CHO cells. This allows for the molecular probe to be exploited for cellular imaging analysis. Further experiments are currently underway to determine the suitability of the iridium dye-peptide in determining intracellular pH (using Raman spectroscopy) and oxygen (using FLIM) levels as this luminophore has also been shown to be both pH and oxygen sensitive. Other worthwhile experiments would include studying at the photostability and bleaching of the luminophores inside the cells following excitation.

5.6 Conclusion

This chapter details the conjugation of ruthenium (II) and novel iridium (III) polypyridyl luminophores to the cell penetrating peptide octarginine. The synthesis of the dye-peptides proceeded with relatively low yields (34%) and the purification of the iridium-conjugate proved to be more challenging due to its aqueous solubility issues. Prior to biomolecule conjugation, neither parent complex exhibited efficient transport across the cell membrane of SP2 myeloma and CHO cell lines. However, internalisation of the $[Ir(dfpp)_2(picCOOH)]^+$ parent complex was achieved in both cell lines after approximately 40 minutes at room temperature when DMSO was used as co-solvent. This is due to the disruption of the cell membrane caused by this solvent. Studies to determine the effects of DMSO on a cell's viability indicated that a 1% DMSO solution resulted in approximately a 10-20% cell death in SP2 cells and approximately a 30% cell death in CHO cells.

However, once both inorganic luminophores were coupled to the CPP this permitted their dissolution in buffered aqueous media without the need for an organic solvent. Both complex conjugates underwent diffusion across the cell membrane of both SP2 and CHO cells after only 10-15 minutes incubation time at room temperature. In general, this led to the localisation of the dyes within the cell's membrane, cytoplasm and nuclear membrane of SP2 and CHO cells. Confocal fluorescence microscopy and z-stack images were used to determine the distribution of the dyes throughout the cells.

Following conjugation of the luminophores to the CPPs, the ruthenium probe remains the more attractive proposition for use as a molecular probe when compared to the iridium equivalent. The ruthenium conjugate displayed an aqueous lifetime more then five times greater, however, its quantum yield is only 60% that seen for the iridium conjugate. For the free dye in organic solvents, this situation is generally reversed with the iridium (III) polypyridyl complex displaying longer lifetimes and greater quantum yields. Unfortunately in aqueous media, the iridium (III) complex does not exhibit lifetimes that are comparable with that of the ruthenium (II) complex.

Furthermore, the cytotoxicity of the iridium probe is far greater when compared to the ruthenium conjugate. Extensive cell death was also exhibited in both SP2 and CHO cells at a final iridium conjugate concentration of 70 μM in times as short as 10 minutes under 375 nm irradiation. This was confirmed using a DRAQ7 localising dye, which only stains the nucleus of dead cells. However, the ruthenium dye-peptide also exhibited increased cell death as a result of 375 nm irradiation when compared with 458 nm excitation. Interestingly, when no dye is present under continuous excitation at 375 nm and 458 nm there is minimal evidence of cell death, as observed with the viability dye DRAQ7. This suggests that the increased cell death of the iridium complexes is a result of the energy of excitation and also potentially due to a light activated process, which most likely thought to be the generation of singlet oxygen ($^1O_2$) through an electron and energy transfer process. This is further supported by preliminary experiments using ascorbic acid as a singlet oxygen scavenger which has resulted in a reduction in cell cytotoxicity of the iridium peptide from 50% to 5% under similar experimental conditions preformed here. Other explanations for its increased cytotoxicity may include the fluorination of the cyclometalating ligands, the larger iridium metal centre and longer phosphorescent quantum yields and lifetimes under particular conditions that will also have an impact on the generation of singlet oxygen.

The next step, currently being undertaken by our group, is to attach target specific peptides to the dye-conjugates in an effort to localise the dye within certain organelles of the cell. It is proposed that the ruthenium probe synthesised in this chapter may be more useful for imaging cells. However, the iridium probe may be useful in targeting with a nuclear probe that could potentially result in the apoptosis of cancer cells. However, the wavelength of excitation of the iridium probe is not as amiable to biological samples when compared with the ruthenium probe.

5.7 References

(1) Puckett, C. A.; Barton, J. K. *J. Am. Chem. Soc.* **2009***, 131*, 8738-8739.

(2) Notman, R.; Noro, M.; O'Malley, B.; Anwar, J. *J. Am. Chem. Soc.* **2006***, 128*, 13982-13983.

(3) Yu, Z.; Quinn, P. J. *Mol. Membr. Biol.* **1998***, 15*, 59-68.

(4) Neugebauer, U.; Pellegrin, Y.; Devocelle, M.; Forster, R. J.; Signac, W.; Moran, N.; Keyes, T. E. *Chem. Commun.* **2008**, 5307-5309.

(5) Cosgrave, L.; Devocelle, M.; Forster, R. J.; Keyes, T. E. *Chem. Commun.* **2010,** *46,* 103-105.

(6) Coin, I.; Beyermann, M.; Bienert, M. *Nat. Protocols* **2007***, 2*, 3247-3256.

(7) Greg T. Hermanson, *Bioconjugate Techniques;* Academic Press: **1996**.

(8) Fmoc deprotection. http://web.whittier.edu/people/webpages/personalwebpages/Hashemzadeh/Solid%20Phase%20Peptide%20Synthesis.pdf. (Accessed 16/05/2011)

(9) Anoopkumar-Dukie, S.; Carey, J. B.; Conere, T.; O'Sullivan, E.; van Pelt, F. N.; Allshire, A. *Br. J. Radiol.* **2005***, 78*, 945-947.

(10) Tim, M. *J. Immunol. Methods* **1983***, 65*, 55-63.

(11) Rani-Beeram, S.; Meyer, K.; McCrate, A.; Hong, Y.; Nielsen, M.; Swavey, S. *Inorg. Chem.* **2008***, 47*, 11278-11283.

(12) Hirohara, S.; Obata, M.; Alitomo, H.; Sharyo, K.; Ando, T.; Yano, S.; Tanihara, M. *Bioconjug. Chem.* **2009***, 20*, 944-952.

(13) Gianferrara, T.; Bergamo, A.; Bratsos, I.; Milani, B.; Spagnul, C.; Sava, G.; Alessio, E. *J. Med. Chem.* **2010***, 53,* 4678-4690.

(14) Neugebauer, U.; Cosgrave, L.; Pellegrin, Y.; Devocelle, M.; Forster, R.; Keyes, T.,E. *unpublished results* .

(15) Fischer, R.; Mader, O.; Jung, G.; Brock, R. *Bioconjug. Chem.* **200***3, 1*4, 653-660.

(16) Yu, M.; Zhao, Q.; Shi, L.; Li, F.; Zhou, Z.; Yang, H.; Yia, T.; Huang, C. *Chemical Communications* **2008**, 2115-2117.

(17) Doshi, J. M.; Tian, D.; Xing, C. *Molecular Pharmaceutics* **2007***, 4*, 919-928.

(18) Cuendet, M.; Pezzuto, J. M. *J. Nat. Prod.* **2004***, 67*, 269-272.

(19) Hossain, M. M.; Smith, P. G.; Wu, K.; Jin, J. *Biochemistry (N. Y.)* **2006***, 45*, 15670-15683.

(20) Lin, Z.; Ou, S.; Duan, C.; Zhang, B.; Bai, Z. *Chem. Commun.* **2006**, 624-626.

(21) Bodannes, R. S.; Chan, P. C. *FEBS Lett.* **1979***, 105*, 195-196.

(22) Djurovich, P. I.; Murphy, D.; Thompson, M. E.; Hernandez, B.; Gao, R.; Hunt, P. L.; Selke, M. *Dalton Trans.* **2007**, 3763-3770.

(23) Liu, Y.; Zeng, C.; Huang, H.; He, L.; Wu, F. *Eur. J. Med. Chem.* **2010***, 45*, 564-571.

(24) Zhang, K. Y.; Li, S. P.; Zhu, N.; Or, I. W.; Cheung, M. S.; Lam, Y.; Lo, K. K. *Inorg. Chem.* **2010***, 49*, 2530-2540.

(25) Rijt, S. H. v.; Kostrhunova, H.; Brabec, V.; Sadler, P. *J. Bioconjug. Chem.* **2011***, 22*, 218-226.

(26) Milovic, N. M.; Kostic N. M. *J. Am. Chem. Soc.,* **2002**, *124,* 4759-4769.

Chapter 6: Model Photoantennas Based on Interfacial DNA Scaffolds

"Science….never solves a problem without creating ten more" – George Bernard Shaw.

6.0 Introduction

Many of the supramolecular assemblies studied today derive their inspiration from or directly include biological molecules. Deoxyribonucleic acid (DNA) contains all the genetic information needed for the operation of every living organism. DNA is a polymer of nucleotides, consisting of a phosphodiester and sugar backbone, to which one of four bases is attached. It is the sequence of these bases that determines the type of genetic information encoded.

The base units of DNA include adenine (A), guanine (G), cytosine (C) and thymidine (T). Single stranded DNA has the unique ability to recognise and hybridise with its complementary base sequence to form a double stranded structure. All of which is possible due to the capacity of each individual base unit to recognise its complementary base pair, for example A binds with T and G binds with C (Figure 6.1). This hybridising phenomenon has been used previously to synthetically assemble modified DNA sequences that are capable of detecting abnormalities in complementary DNA sequences.[1-5]

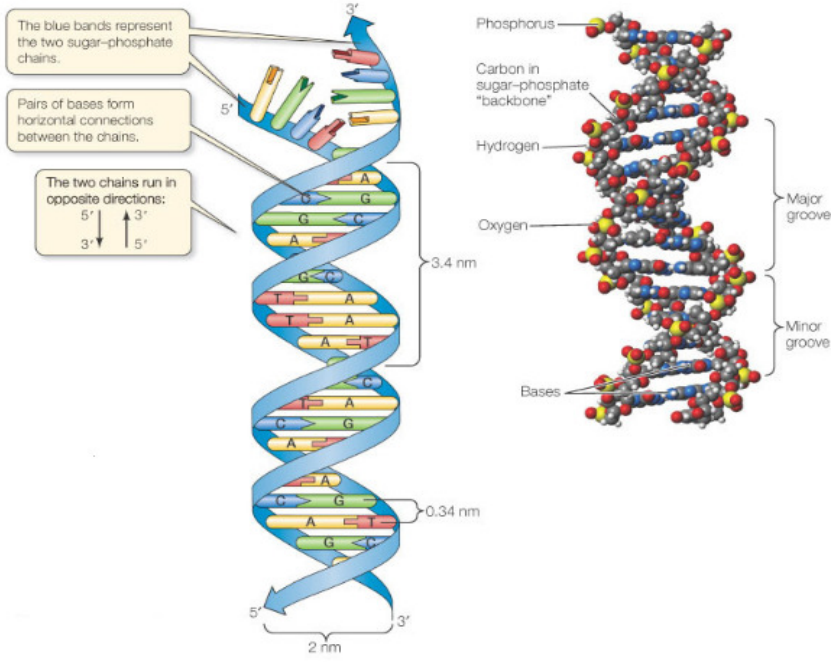

Figure 6.1: Chemical structure of DNA double helix.[6]

6.1 Model Photoantennas based on Interfacial DNA Scaffolds

This chapter outlines attempts to functionalise deoxyguanosine with a fluorescent marker in an effort to create a supramolecular photoantenna system. It was hoped to exploit the self-assembly of single stranded DNA to its complementary strand to control the distance and orientation of the fluorophores in relation to one another. For example, if every 5-7 base pairs in a sequence were tagged with a fluorescent label, one could ensure that the chromophores would be located every half turn within the DNA double helix. Using DNA as the interfacial scaffold, which has not been attempted before, allows an element of control with the interspatial separation between fluorescent moieties and therefore directly affect their photochemical properties to ensure efficient energy migration through the system. The ability of DNA to support single-step energy transfer using single molecule spectroscopy has already been demonstrated.[7]

It was anticipated that the functionalised DNA oligonucleotides could then be self-assembled on either gold or platinum if a thiol terminated DNA strand had been employed. Single strands of alkane thiols or thiol terminated polyethylene glycol may be used to separate these DNA strands in an effort to help to prevent a lateral approach taken by the functionalised dyes and reduce quenching. Electrostatic repulsion of the adjacent oligonucleotides should also aid in the lateral separation of the DNA double helixes.

The ideal situation arises where the chromophores are close enough together to facilitate efficient energy transfer but also far enough apart to prevent self-quenching. Such quenchers are formed by close contact (<1 nm) of two or more chromophores. In the completed system (Figure 6.2), the energy would migrate between the dyes arriving at the redox centre to create an electronically excited state. This may then act as an energy readout for energy migration through the system, thus, hopefully providing an efficient method for the conversion of light energy into electrical energy using DNA as the backbone for the model photoantenna.

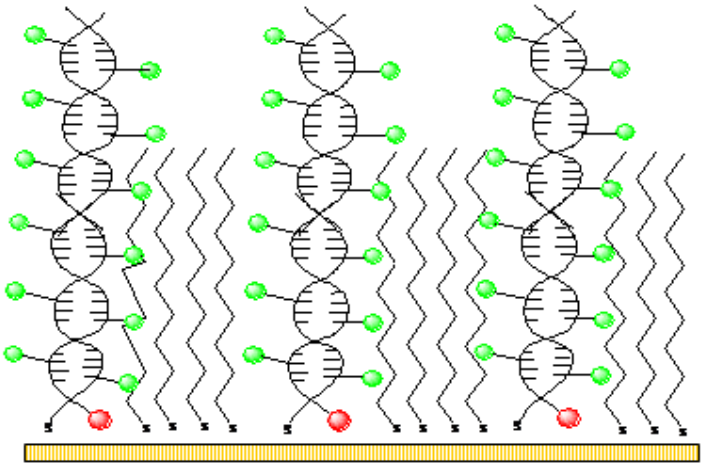

Figure 6.2: Schematic illustrating the model system: A thiol terminated oligonucleotide and its complimentary oligonucleotide which has been functionalised with a single chromophore with appropriate R_0 for energy transfer to self at value at set sequences, typically every 5 to 7 bases. The 3' or 5' end of the nucleotide will be functionalised with an acceptor chromophore and these will be incorporated into SAMs on gold. Alkane thiols or thiol-terminated polyethylene glycol will be used as an inert diluent in the SAM.

With the push to find alternative fuels, the potential of artificial light-harvesting systems for the conversion of solar energy has been widely discussed for many years. It has also been recognised that artificial photosynthesis has potential uses in molecular scale optoelectronics, photonics, sensor design, and other areas of nanotechnology.[8-10]

6.2 Internal Fluorescent Labelling of 2'-Deoxyguanosine

There are many examples in the literature of the internal labelling of molecules to the C-8 position of unprotected (deoxy)guanosine[11-16], fully protected deoxyguanosine[17-24], and the conjugation of ruthenium (II) luminophores[2, 25, 26] and fluorescein[5, 27-30] to nucleobases. These publications serve as a good starting point for the synthetic aim of this chapter. However, to the best of our knowledge, nobody has yet managed to internally tag a fluorescein molecule to the C-8 position of a purine base via a short rigid linker. Many other smaller electron withdrawing and donating groups have been synthesised in the C-8 position with the inference that any molecule may be linked to the nucleoside using such chemistry.

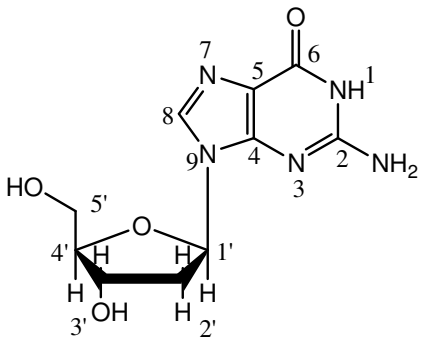

2'-Deoxyguanosine

Figure 6.3: 2'-Deoxyguanosine illustrating numbering scheme for ^{1}H-NMR analysis.

Interestingly, Salic *et al.*[5] described the incorporation of fluorescent molecules into a double stranded sequence of DNA. Here, 5-ethynyl-2'-deoxyuridine was initially integrated into a single strand of DNA as shown in Figure 6.4. Following hybridisation to its complementary DNA strand, using click chemistry, the available alkyne group was reacted with fluorescent azides, such as azidofluorescein, to give the fluorescently labelled nucleoside.

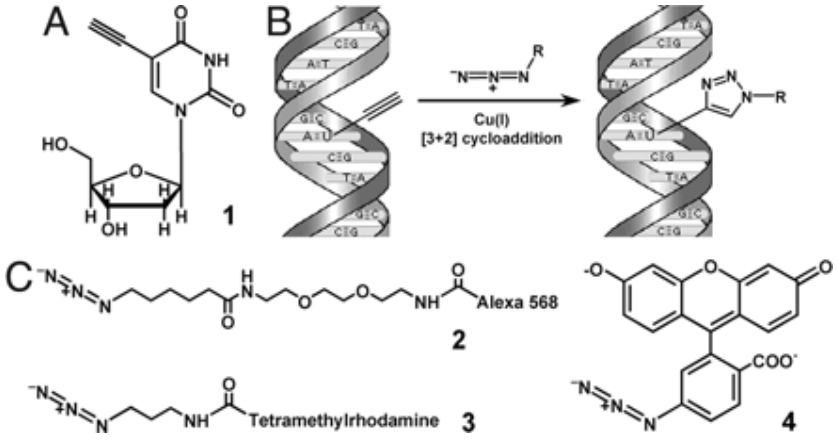

Figure 6.4: (A) Structure of 5-ethynyl-2'-deoxyuridine, (B) schematic diagram illustrating click reaction chemistry for the incorporation of a fluorescent azide to the terminal alkyne group available in the DNA double helix and (C) chemical structures of the fluorescent azides conjugated to the DNA double helix.[5]

However, most applicably to work carried out in this chapter, it is only very recently that a group in Japan[22, 23] have successfully managed to couple the fluorescent 2-bromofluorene molecule to deoxyguanosine in the C-8 position via a relatively short linker using the Stille method of coupling. This luminophore-bioconjugate system exhibited fully reversible luminescent photoswitching characteristics when light of a certain wavelength was applied as shown in Figure 6.5. This was then used in the photoregulation of G-quadruplex formation using cis-trans photoisomerisation of the nucleobase at room temperature. G-quadruplexes are formed by stacked G-quartets, a planar association of four guanines, by hydrogen bonding. They are found in guanine rich sequences and are involved in several key biological processes. To demonstrate the potential application of this technology they reported the switching of molecular structures between a very stable quadruplex state bound to thrombin and a non-structured state that disrupted and suppressed binding to thrombin, in a process that is totally reversible as shown in Figure 6.5 below.

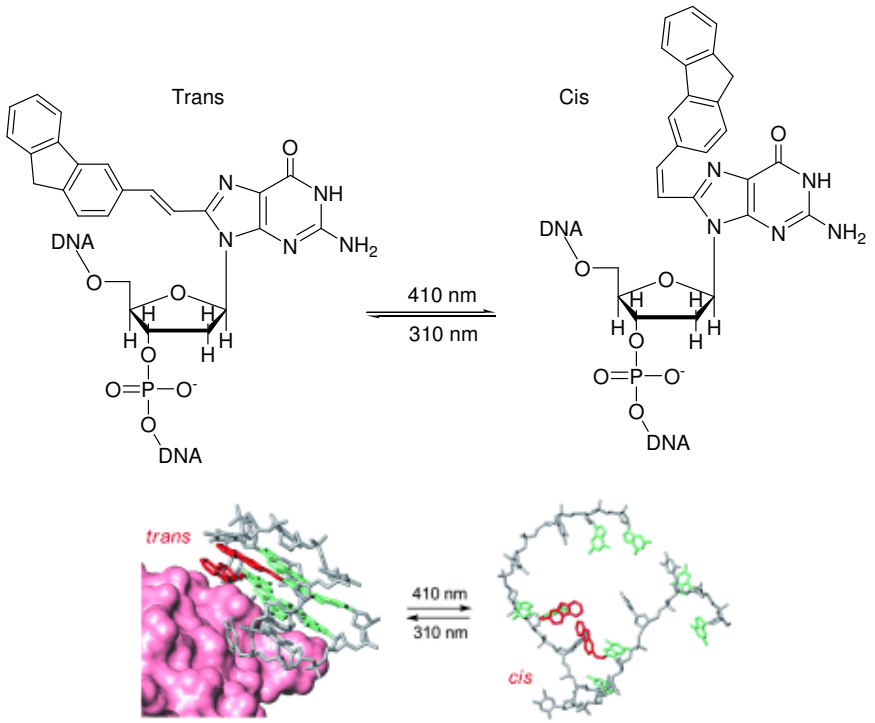

Figure 6.5: (Top) Photoinduced cis-trans isomerisation of 8-fluorenylvinyl-2'-deoxyguanosine. (Bottom) Photoregulation of the thrombin aptamer G-quadruplex by cis-trans photoisomerisation of the photochromic nucleobase.[22]

This chapter discusses attempts to use recent advances in DNA chemistry[3, 5, 11-13, 20, 27, 30-33] to create a novel internally labelled 2'-deoxyguanosine molecule with a common fluorophore, fluorescein, via a short rigid linker to the C-8 position of the nucleobase. Another significant application of these internally labelled nucleobases is their potential use in biomedical fields. Much of the research into the early detection of biomarkers related to illnesses, such as cancer, is based on the use of a fluorescently modified DNA sequence binding to its complementary base sequence and monitoring the output of the attached fluorescent dye. To date many of these detection systems have the fluorescent markers linked to the terminal of the sequence or through long linkers internally.[4, 26, 32] The ability to have the fluorophore so close to the modified DNA strand could lead to a reduction in the outside interferences associated with medical diagnostics and may lead to increased sensitivity and detection.

6.3 Experimental Procedure

Chemicals

All chemicals used were purchased from Sigma-Aldrich (Ireland) without further purification except for 2'- deoxyguanosine (TCI Europe), 4-bromophthalic anhydride (TCI Europe), tris(3-sulfonatophenyl)phosphine (ABCR), 5-aminofluorescein (ABCR), amyl nitrite (ABCR), diisopropyl azodicarboxylate (ABCR) and 4-cyanophenyl boronic acid (Fisher Scientific). All solvents were fully degassed prior to use. All experiments were performed using oven-dried glassware under an N_2 environment.

The preparation of 8-bromo-2'-deoxyguanosine

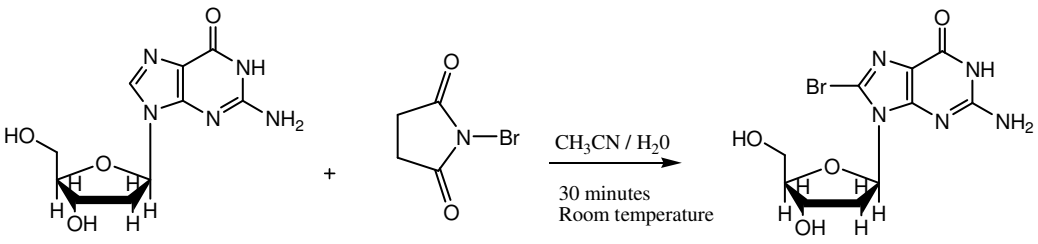

2'-Deoxyguanosine N-Bromosuccinimide 8-Bromo-2'-deoxyguanosine

8-Bromo-2'-deoxyguanosine was prepared according to a method modified from the literature.[20] 2'- Deoxyguanosine (2.0 g, 7.5 mmol) and N-bromosuccinimide [NBS] (2.0 g, 11.2 mmol) were added to a mixture of acetonitrile (80 ml) and water (20 ml). The NBS was added to the mixture in three equal portions, and it was then stirred for 30 minutes at room temperature. The precipitate was collected by vacuum filtration and was then suspended in a solution of acetone (40 ml) and stirred at room temperature for 2 hours. The mixture was then cooled overnight in the freezer at -20 ^{o}C.

The precipitate was collected by vacuum filtration, washed with cold acetone and dried to give a creamy white product (2.05 g, 79%).

^{1}H NMR (400 MHz, DMSO-d_6): **δ (ppm) 10.81** (s, 1H, N_1-H), **6.50** (s, 2H, N_2-H_2), **6.15** (t, 1H, J = 7.2 Hz, $C_{1'}$-H), **5.27** (d, 1H, J = 4.4 Hz, $C_{3'}$-OH), **4.87** (t, 1H, J = 6 Hz, $C_{5'}$-OH), **4.39** (m, 1H, $C_{3'}$-H), **3.79** (m, 1H, $C_{4'}$-H), **3.61** (m, 1H, $C_{5'}$-H), **3.50** (m, 1H, $C_{5'}$-H), **3.16** (m, 1H, $C_{2'}$-H), **2.10** (m, 1H, $C_{2'}$-H).

The preparation of 5-bromofluorescein diacetate

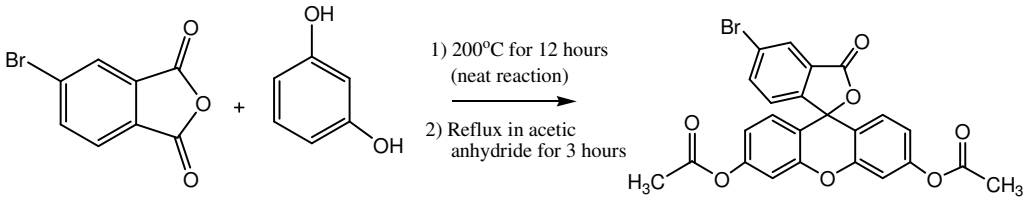

4- Bromophthalic anhydride Rescorcinol 5-Bromofluorescein diacetate

5-Bromofluorescein diacetate was prepared according to a method modified from the literature.[34] A mixture of 4-bromophthalic anhydride (5.01 g, 22.03 mmol) and resorcinol (4.87 g, 44.06 mmol) were heated, as a neat reaction, at 200 °C with stirring for 12 hours. The solidified shiny, rusty, green product was crushed and ground in a mortar to yield a mixture of 5- and 6-bromofluorescein.

Without any further purification the mixture was refluxed for 3 hours in acetic anhydride (35 ml). The solution was then cooled to induce recrystallisation. This was then filtered by vacuum and washed with cold acetic anhydride and ethanol, successively.

The filtrate was collected and concentrated to half volume with warming under reduced pressure and was then placed in an ice bath and allowed to stand for a day to induce recrystallisation, which was then collected by filtration.

The first and second set of pale yellow crystals were combined and dissolved in hot acetic anhydride (9 ml) and cooled to allow recrystallisation. The product was filtered by vacuum and washed with cold acetic anhydride and ethanol successively, to yield a pale yellow powder. Further recrystallisation in acetic anhydride gave the regioisomerically pure 5-bromofluorescein diacetate as a yellow solid (1.80 g, 16 %).

^{1}H NMR (400 MHz, DMSO-d_6): **δ (ppm) 8.25** (s, 1H, H_6), **8.00** (d, 1H, J = 8.0 Hz, H_4), **7.43** (d, 1H, J = 8.0 Hz, H_3), **7.29** (s, 2H, $H_{C/C'}$), **6.98** (m, 4H, $H_{A/A'}$, $H_{B/B'}$), **2.29** (s, 6H, acetyl protons).

6.3.1 Synthetic Strategy 1: Suzuki Coupling

The preparation of 5-(4,4,5,5-tetramethyl-1,3,2-dioxaborolan-2-yl)fluorescein diacetate

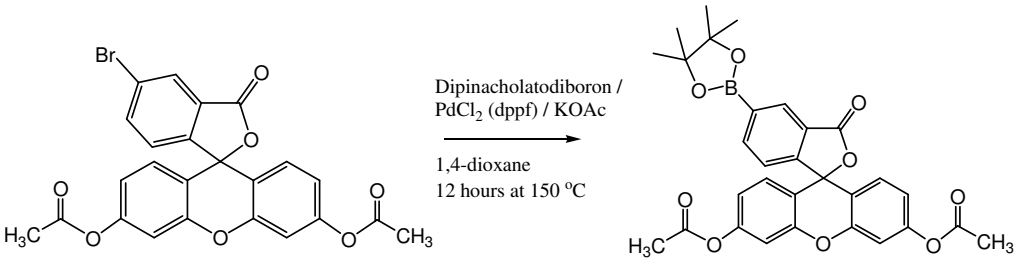

5-Bromofluorescein diacetate

5-(4,4,5,5-Tetramethyl-1,3,2-dioxaborolan-2-yl) fluorescein diacetate

5-(4,4,5,5-Tetramethyl-1,3,2-dioxaborolan-2-yl)fluorescein diacetate was prepared according to methods modified from the literature.[35-37] To a pressure tube filled with nitrogen, 5-bromofluorescein diacetate (500 mg, 1 mmol), dipinacholatodiboron (279 mg, 1.1 mmol), [1,1'-bis(diphenylphosphino) ferrocene] dichloropalladium(II) [$PdCl_2$(dppf)] (8.2 mg, 0.01 mmol), potassium acetate (294 mg, 3 mmol) and 1,4-dioxane (4 ml) were added. The reaction was then heated at 85 ^oC for 48 hours with stirring.

After cooling, the mixture was poured into a 0.1M NH_4Cl (10 ml) solution. The mixture was then extracted with benzene (2x20 ml) and the organic layer was washed with 0.1M $NaHCO_3$ and 0.1M NaCl solutions successively. The organic layer was then dried over anhydrous $MgSO_4$ and the solvent evaporated under reduced pressure. The product was then recrystalised from benzene/ethanol (1:1) to give the pure boronated fluorescein ester as a white solid (207 mg, 38 %).

^1H NMR (400 MHz, DMSO-d_6): **δ (ppm) 8.21** (s, 1H, H_6), **8.07** (d, 1H, J = 8.0 Hz, H_4), **7.43** (d, 1H, J = 8.0 Hz, H_3), **7.37** (s, 1H, carboxyl-OH), **7.29** (s, 2H, $H_{C/C'}$), **6.93** (m, 4H, $H_{A/A'}$, $H_{B/B'}$), **2.29** (s, 6H, acetyl protons), **1.34** (s, 12H, CH_3 protons x 4).

The preparation of 5-fluorescein boronic acid

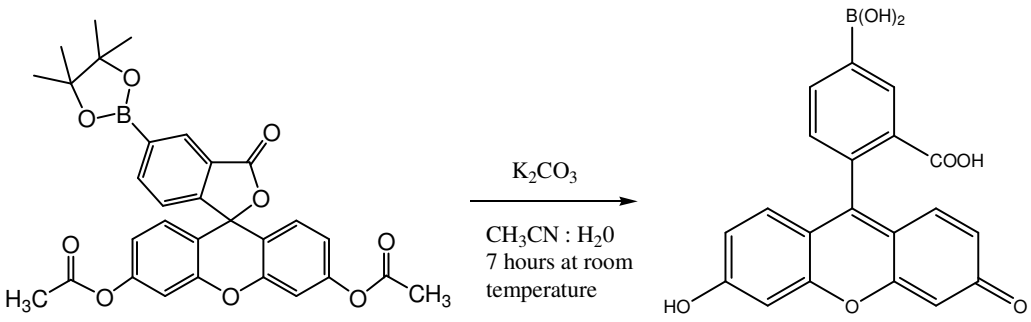

5-(4,4,5,5-Tetramethyl-1,3,2-dioxaborolan-2-yl) fluorescein diacetate

5-Fluorescein boronic acid

5-Fluorescein boronic acid was prepared according to a method modified from the literature.[36] 5-(4,4,5,5-Tetramethyl-1,3,2-dioxaborolan-2-yl)fluorescein diacetate (217 mg, 0.5 mmol), potassium carbonate (346 mg, 2.5 mmol) were added to a mixture of acetonitrile / water (1:1) (4 ml) and left stirring at room temperature for 7 hours.

The mixture was then acidified with concentrated HCl and the resulting yellow precipitate was filtered and washed successively with deionised water and diethyl ether. The solid was dried under reduced pressure to give a yellow solid product (125 mg, 66%).

[**note:** isolation of the pure product proved very difficult and no clean ^{1}H-NMR spectrum was obtained. Therefore, in an effort to overcome this problem, the Suzuki coupling was performed after in-situ hydrolysis of the boronated fluorescein ester and direct Suzuki coupling to 8-BrdG without isolation of the starting material.]

The preparation of 8-(5-fluorescein)-2'-deoxyguanosine: (Suzuki Coupling)

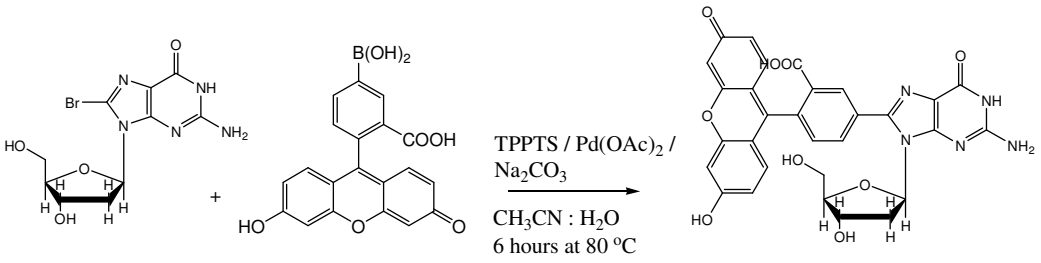

8-Bromo 2'-deoxyguanosine

5-Fluorescein boronic acid

8-(5-Fluorescein)-2'-deoxyguanosine

8-Bromo 2'-deoxyguanosine (87 mg, 0.25 mmol), 5-fluorescein boronic acid (113 mg, 0.30 mmol [not isolated-theoretical value]), tris(3-sulfonatophenyl)phosphine (TPPTS) (8.9 mg, 0.016 mmol), palladium acetate (1.5 mg, 0.006 mmol), and sodium carbonate (53 mg, 0.5 mmol) were placed in a round-bottomed flask under nitrogen. Degassed water : acetonitrile (2:1) (3.5 ml) was added and the mixture was heated at 80 ^{o}C for 6 hours until reverse-phase TLC (1:1, water : methanol) showed no further conversion of starting materials.

The reaction mixture was diluted with MilliQ water (10 ml) and its pH adjusted to 6-7 using 10 % aqueous HCl. The mixture was then heated to dissolve and solid precipitates and allowed to cool to 0 ^{o}C, and left to stand for several hours. The product was then recovered by filtration as a fine yellow powder (31 mg, 20 %, impure). However, NMR and mass spectrometry analysis failed to show any evidence of the coupled product having being formed.

6.3.2 Synthetic Strategy 2: Sonogashira Coupling

The preparation of 5-(2-trimethylsilylethynyl)fluorescein diacetate

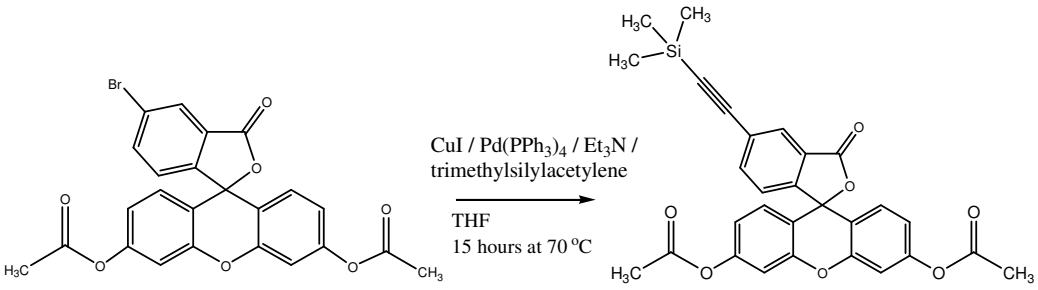

5-Bromofluorescein diacetate

5-(2-Trimethylsilylethynyl)fluorescein diacetate

5-(2-trimethylsilylethynyl)fluorescein diacetate was prepared according to a method modified from the literature.[36, 38] 5-Bromofluorescein diacetate (500 mg, 1 mmol), copper (I) iodide (9.5 mg 0.05 mmol), tetrakis(triphenylphosphine) palladium(0) (58 mg, 0.05 mmol) and anhydrous THF (1 ml) were placed in a round-bottomed flask. Triethylamine (1.4 ml, 10 mmol) followed by trimethylsilylacetylene (280 µl, 2 mmol) were added to the above reaction and stirred at 70 ^{o}C for 15 hours.

The mixture was allowed to cool to room temperature and stirring continued overnight. The solution was then filtered over Celite and washed with THF. The solvent was then evaporated under reduced pressure, diethyl ether (40 ml) was added, sonicated and extracted with 0.1M HCl (3x40 ml). The aqueous layers were extracted once with diethyl ether (25 ml) and the organic layers were combined, dried over anhydrous $MgSO_4$, and the solvent evaporated under reduced pressure. The crude product was then recrystallised from ethanol to give 5-(2-trimethylsilylethynyl)fluorescein diacetate as a light brown powder (361 mg, 70 %).

^{1}H NMR (400 MHz, DMSO-d_6): **δ (ppm) 7.97** (s, 1H, H_6), **7.78** (d, 1H, J = 8 Hz, H_4), **7.37** (d, 1H, J = 8 Hz, H_3), **7.22** (s, 2H, $H_{C/C'}$), **6.88** (s, 4H, $H_{A/A'}$, $H_{B/B'}$), **2.26** (s, 6H, acetyl protons), **0.21** (s, 9H, methyl protons x 3).

The preparation of 5-ethynylfluorescein

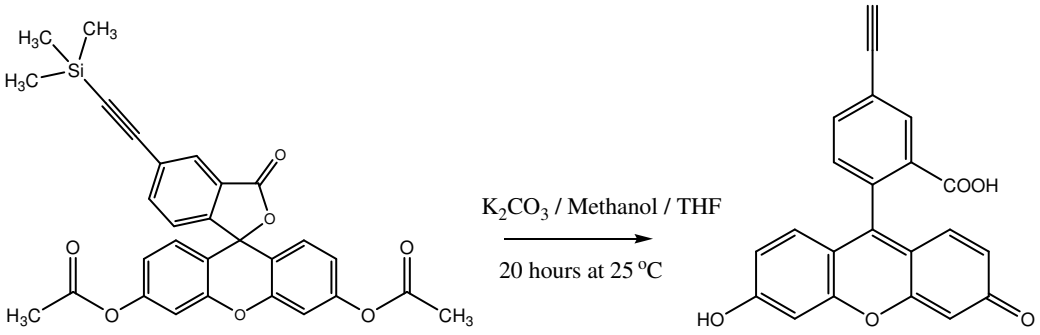

5-(2-Trimethylsilylethynyl)fluorescein diacetate

5-Ethynylfluorescein

5-Ethynylfluorescein was prepared according to a method modified from the literature.[36, 38] 5-(2-Trimethylsilylethynyl)fluorescein diacetate (150 mg, 0.30 mmol), potassium carbonate (207 mg, 1.5 mmol) were dissolved in a mixture of methanol/THF (1:1) (3 ml) and stirred at 25 °C for 20 hours. The solution was then poured into MilliQ water (20 ml) and acidified to pH 2 with concentrated HCl. The precipitate was collected by vacuum filtration, rinsed with water and dried under vacuum to yield 5-ethynylfluorescein as an orange solid (101 mg, 0.28 mmol, 93 % yield).

^{1}H NMR (400 MHz, DMSO-d_6): **δ (ppm) 10.12** (s, 1H, carboxyl-H), **7.97** (s, 1H, H_6), **7.80** (d, 1H, J = 8 Hz, H_4), **7.23** (d, 1H, J = 8 Hz, H_3), **6.63** (s, 2H, $H_{C/C'}$), **6.49** (m, 4H, $H_{A/A'}$, $H_{B/B'}$), **4.42** (s, 1H, ethynyl-H).

ESI-MS (CH_3OH, m/z): 356.33, ([M+H^+]): 357.4.

The preparation of 8-acetylene-(5-fluorescein)-2'-deoxyguanosine (Sonogashira Coupling)

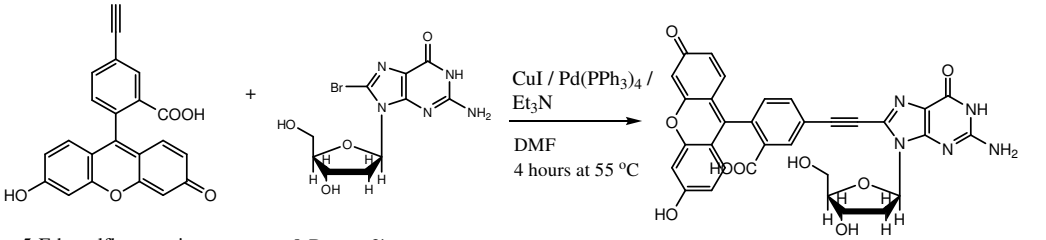

5-Ethynylfluorescein

8-Bromo 2'-deoxyguanosine

8-Acetylene-(5-fluorescein)-2'-deoxyguanosine

To a round-bottomed flask, 8-bromo-2'-deoxyguanosine (24 mg, 0.07 mmol), 5-ethynylfluorescein (30 mg, 0.08 mmol), tetrakis(triphenylphosphine) palladium(0) (8 mg, 0.007 mmol), copper (I) iodide (6.7 mg, 0.035 mmol), triethylamine (20 µl, 0.14 mmol) and anhydrous DMF (2 ml) were added and heated at 55 ^{o}C for 4 hours. The mixture was then left stirring at 25 ^{o}C overnight. The reaction was followed by TLC (silica gel) using MeOH : CH_2Cl_2 as mobile phase until there was no further conversion of the starting materials. The solution was evaporated to dryness and purified by HPLC chromatography using a mobile phase of methanol : water to leave a light orange coloured product. However an NMR of the pure product was never isolated effectively, even though mass spectrometry analysis showed evidence of the final coupled product.

ESI-MS (CH_3OH, m/z): 621.55, ([M+H^+]): 622.3, ([M-dG]): 356.3.

6.3.3 Synthetic Strategy 3: Click Reactions

The preparation of 8-(4-ethynylphenyl)-2'-deoxyguanosine

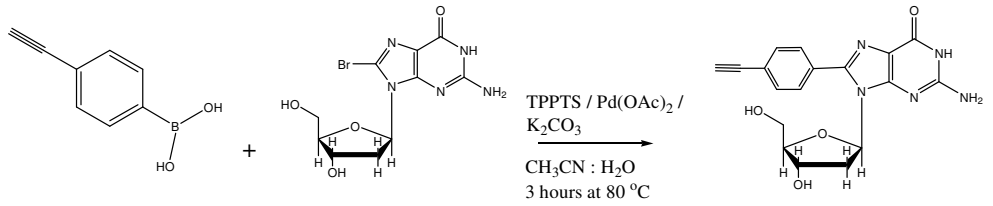

4-ethynylphenylboronic Acid + 8-Bromo-2'-deoxyguanosine → 8-(4-Ethynylphenyl)-2'-deoxyguanosine

8-Bromo-2'-deoxyguanosine (250 mg, 0.72 mmol), 4-ethynylphenyl boronic acid (168 mg, 1.152 mmol), palladium acetate (4 mg, 0.018 mmol, 2.5 mol%), tris(3-sulfonatophenyl)phosphine (TPPTS) (25.6 mg, 0.045 mmol, 6.25 mol%), potassium carbonate (299 mg, 2.16 mmol) and milliQ water: acetonitrile 2:1 (3 ml) were all placed into a dry vial in the dry box and left stirring at 80 ^{o}C for 3 hours.

The mixture was then poured onto milliQ water (10 ml) and its pH adjusted to pH 6-7 with 10 % HCl. The reaction was then left in the fridge overnight and the precipitate was collected by vacuum filtration. The product was then recrystallised from a water/methanol mixture to yield a light brown solid product (129 mg, 35 %).

^{1}H NMR (400 MHz, DMSO-d_6): **δ (ppm) 10.91** (s, 1H, H_1-H), **7.89** (d, 2H, J = 8 Hz, Ph protons), **7.57** (d, 2H, J = 8 Hz, Ph protons), **6.62** (s, 2H, N_2-H_2), **6.35** (t, 1H, J = 2.4 Hz, $C_{1'}$-H), **5.33** (d, 1H, J = 1.6 Hz, $C_{3'}$-OH), **4.92** (t, 1H, J = 1.6 Hz, $C_{5'}$-OH), **4.44** (m, 1H, $C_{3'}$-H), **3.81** (m, 1H, $C_{4'}$-H), **3.67** (m, 1H, $C_{5'}$-H), **3.56** (m, 1H, $C_{5'}$-H), **3.33** (s, 1H, ethynyl-H), **3.12** (m, 1H, $C_{2'}$-H), **2.15** (m, 1H, $C_{2'}$-H).

The preparation of 8-(4-cyanophenyl)-2'-deoxyguanosine

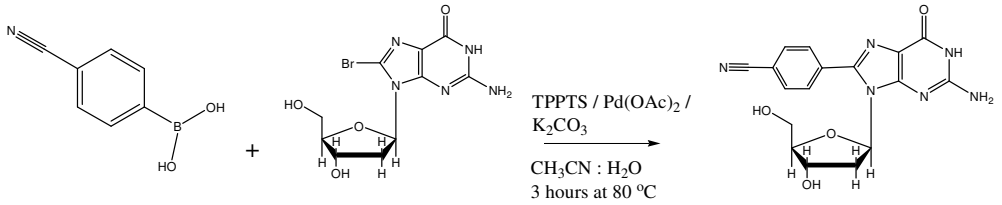

4-Cyanophenylboronic Acid + 8-Bromo-2'-deoxyguanosine → 8-(4-Cyanophenyl)-2'-deoxyguanosine

8-Bromo-2'-deoxyguanosine (250 mg, 0.72 mmol), 4-cyanophenyl boronic acid (169 mg, 1.152 mmol), palladium acetate (4 mg, 0.018 mmol, 2.5 mol%), tris(3-sulfonatophenyl)phosphine (TPPTS) (25.6 mg, 0.045 mmol, 6.25 mol%), potassium carbonate (299 mg, 2.16 mmol) and milliQ water: acetonitrile 2:1 (3 ml) were all placed into a dry vial in the dry box and left stirring at 80 ^{o}C for 3 hours.

The mixture was then poured onto milliQ water (10 ml) and its pH adjusted to pH 6-7 with 10 % HCl. The reaction was then left in the fridge overnight and the precipitate was collected by vacuum filtration to yield a grey/blue solid product (256 mg, 96 %).

^{1}H NMR (400 MHz, DMSO-d_6): **δ (ppm) 7.99** (d, 2H, J = 8 Hz, Ph protons), **7.84** (d, 2H, J = 8 Hz, Ph protons), **6.58** (s, 2H, N_2-H_2), **6.09** (t, 1H, J = 6.4 Hz, C_1-H), **5.91** (s, 1H, $C_{3'}$-OH), **5.17** (s, 1H, $C_{5'}$-OH), **4.37** (m, 1H, $C_{3'}$-H), **3.85** (m, 1H, $C_{4'}$-H), **3.68** (m, 1H, $C_{5'}$-H), **3.56** (m, 1H, $C_{5'}$-H), **3.18** (m, 1H, $C_{2'}$-H), **2.04** (m, 1H, $C_{2'}$-H).

The preparation of 5-azidofluorescein

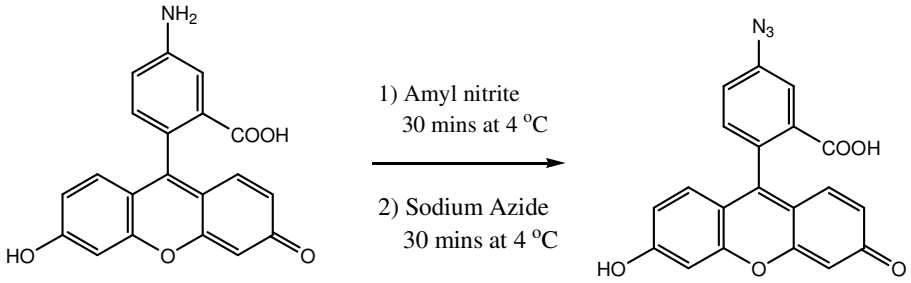

5-Aminofluorescein

5-Azidofluorescein

5-Azidofluorescein was prepared according to a method modified from the literature[39, 40], and was performed in a dark room under red light. 5-Aminofluorescein (100 mg, 0.29 mmol) was dissolved in DMF anhydrous (5 ml) in a round-bottomed flask. MilliQ water (5 ml) was then added to the mixture and adding more DMF dropwise to the reaction then dissolved any precipitate formed.

The solution was acidified with concentrated H_2SO_4 (1 ml) and amyl nitrite (200 µl) was added and left stirring at 4°C for 30 minutes. Sodium azide (200 mg, 3 mmol in 4 ml MilliQ water) was added and the reaction was continued stirring at 4 °C for a further 30 minutes.

After this, a solution of brine was used to make the reaction up to 20 ml and the solution was left in the fridge overnight. The precipitate was collected by vacuum filtration and washed with a cold saturated NaCl solution to leave 5-azidofluorescein as a red solid (80 mg, 72 %).

^{1}H NMR (400 MHz, DMSO-d_6): **δ (ppm) 10.12** (s, 1H, carboxyl-H), **7.98** (d, 1H, J = 8 Hz, H_4), **7.40** (d, 1H, J = 8, H_3), **7.03** (d, 1H, J = 1.6, H_6), **6.67** (d, 2H, J = 2, $H_{C/C'}$), **6.55** (m, 4H, $H_{A/A'}$, $H_{B/B'}$).

The preparation of 8-(4-phenyl(1,3-triazole))-5-fluorescein-2'-deoxyguanosine (Click reactions)

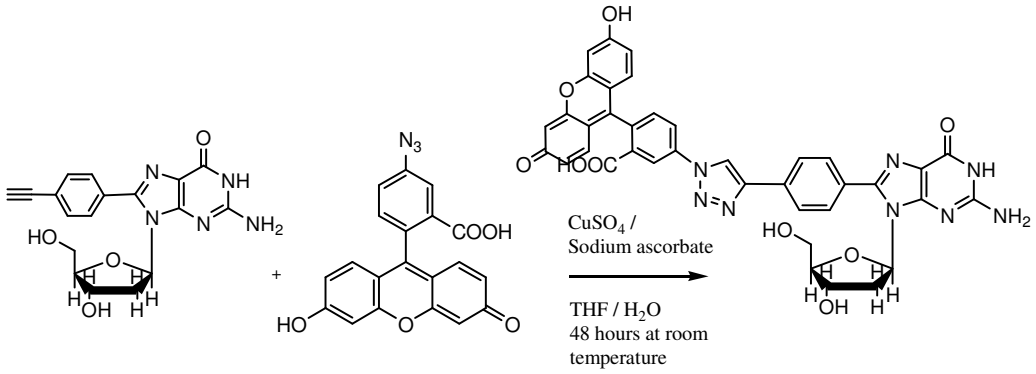

8-(4-Ethynylphenyl)-2'-deoxyguanosine

5-Azidofluorescein

8-(4-phenyl(1,3-triazole))-5-fluorescein-2'-deoxyguanosine

Triazole linker formation

8-(4-Ethynylphenyl)-2'-deoxyguanosine (40 mg, 0.107 mmol) was first dissolved in tetrahydrofuran:water (1:1) (3 ml). Then 5-azidofluorescein (40 mg, 0.107 mmol), copper sulphate pentahydrate (2.7 mg, 0.0107 mmol) and sodium ascorbate (4.2 mg, 0.0214 mmol) were added to the reaction and left stirring at room temperature for 48 hours. Pure product was not isolated.

The preparation of 8-(4-phenyl(1,5-tetrazole))-5-fluorescein-2'-deoxyguanosine

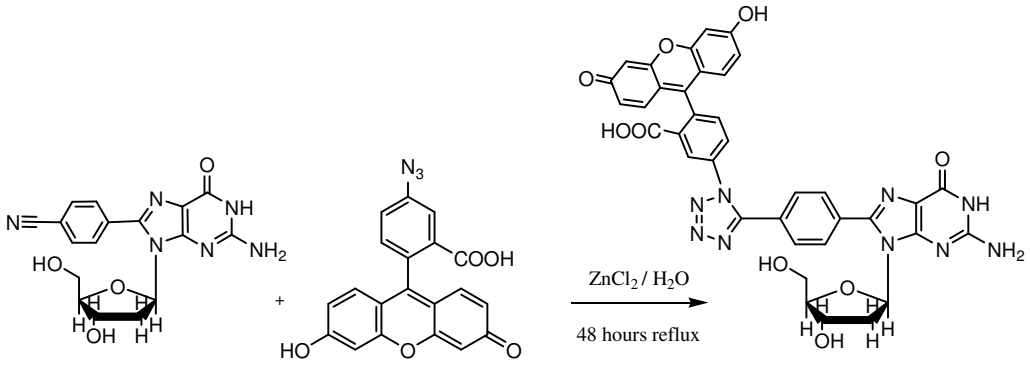

8-(4-Cyanophenyl)-2'-deoxyguanosine

5-Azidofluorescein

8-(4-phenyl(1,5-tetrazole))-5-fluorescein-2'-deoxyguanosine

Tetrazole linker formation

8-(4-Cyanophenyl)-2'-deoxyguanosine (40 mg, 0.109 mmol) was dissolved in deionised water. 5-Azidofluorescein (41 mg, 0.110 mmol) and anhydrous $ZnCl_2$ (58 mg, 0.424 mmol) were added and the reaction mixture was refluxed for 48 hours. The solution was then cooled and acidified slightly to pH 4 and left in the fridge over night to promote precipitation. The precipitate was then collected by vacuum filtration. Pure product was not isolated.

6.3.4 Synthetic Strategy 4: Buchwald-Hartwig coupling

The preparation of 8-bromo-3',5'-O-bis(tert-butyldimethylsilyl)-2'-deoxyguanosine

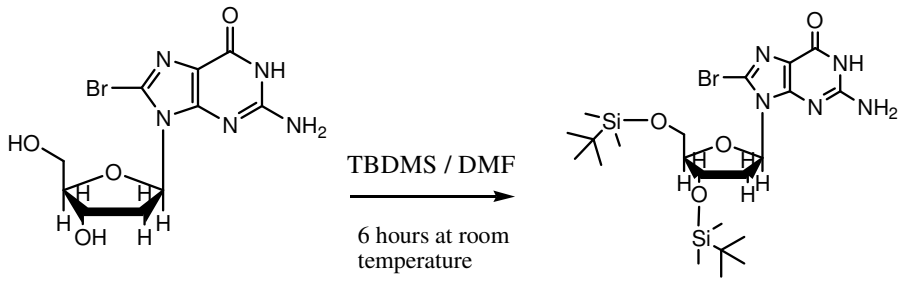

8-Bromo-2'-deoxyguanosine

8-Bromo-3',5'-O-bis(tert-butyldimethylsilyl)-2'-deoxyguanosine

8-bromo-3',5'-O-bis(tert-butyldimethylsilyl)-2'-deoxyguanosine was prepared according to a method modified from the literature.[20] 8-Bromo 2'-deoxyguanosine (362 mg, 1.04 mmol) and imidazole (340 mg, 5 mmol) were suspended in anhydrous DMF (2.3 ml). To this tert-butyldimethyl-chlorosilane (TBDMS) 1 M in dichloromethane (3 ml, 3 mmol) and was left stirring at room temperature for 6 hours.

The end of the reaction was confirmed by TLC (silica gel) analysis using $CHCl_3$:MeOH (10:1) as mobile phase. The reaction was taken and evaporated to dryness by warming under reduced pressure and then re-suspended in MilliQ water (12 ml) to produce a white precipitate. The mixture was then extracted with EtOAc (2x20 ml). The organic layers were combined, dried over $MgSO_4$ anhydrous and evaporated to dryness to leave an off-white coloured crude compound. The crude mixture was then taken and dissolved purified by silica gel chromatography using $CHCl_3$: 10% MeOH as mobile phase to give the product as a white solid (464 mg, 78 %).

^{1}H NMR (400 MHz, DMSO-d_6): **δ (ppm) 10.81** (s, 1H, N_1-H), **6.40** (s, 2H, N_2-H_2), **6.15** (t, 1H, J = 7.4, $C_{1'}$-H), **4.60** (m, 1H, $C_{3'}$-H), **3.75** (m, 2H, $C_{5'}$-H_2), **3.63** (m, 1H, $C_{4'}$-H), **3.38** (m, 1H, $C_{2'}$-H), **2.14** (m, 1H, $C_{2'}$-H), **0.87** (s, 9H, tBu-H), **0.81** (s, 9H, tBu-H), **0.09** (s, 6H, methyl group x 2), **-0.04** (s, 3H, methyl group), **-0.05** (s, 3H, methyl group).

The preparation of O^6-benzyl-8-bromo-3',5'-O-bis(tert-butyldimethylsilyl)-2'-deoxyguanosine

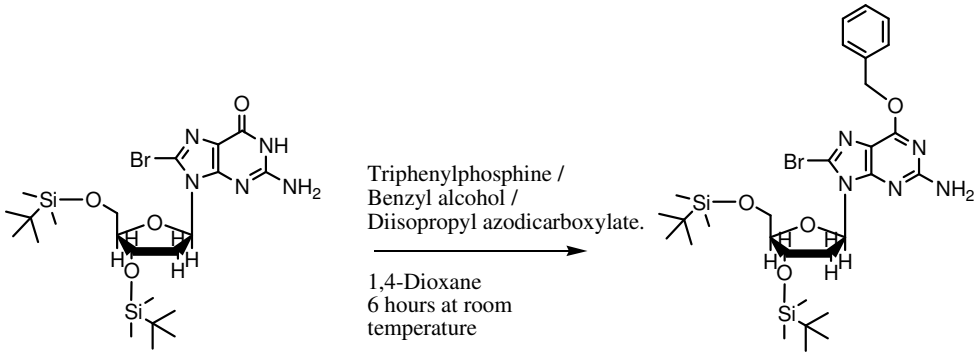

8-Bromo-3',5'-O-bis(tert-butyldimethylsilyl)-2'-deoxyguanosine

O^6-benzyl-8-Bromo-3',5'-O-bis (tert-butyldimethylsilyl)-2'-deoxyguanosine

O^6-benzyl-8-bromo-3',5'-O-bis(tert-butyldimethylsilyl)-2'-deoxyguanosine was prepared according to a method modified from the literature.[20] 8-Bromo-3',5'-O-bis(tert-butyldimethylsilyl)-2'-deoxyguanosine (620 mg, 1.08 mmol) and triphenylphosphine (850 mg, 3.24 mmol) were added to 1,4-dioxane (12.5 ml). To this suspension benzyl alcohol (559 µl, 5.4 mmol) and diisopropyl azodicarboxylate (632 µl, 3.24 mmol) were added and sonicated to dissolve all substances.

The reaction mixture was then left stirring at room temperature for 6 hours. The end of the reaction was confirmed by TLC (silica gel) analysis using a mobile phase of Hexane : EtOAc (4:1).

The solution was then concentrated and purified by silica gel chromatography using a mobile phase of Hexane : EtOAc (4:1) to give the product as a white solid (434 mg, 60 %).

^{1}H NMR (400 MHz, DMSO-d_6): **δ (ppm) 7.46-7.44** (m, 2H, Bz-H), **7.37-7.33** (m, 3H, Bz-H), **6.45** (s, 2H, N_2-H_2), **6.14** (t, 1H, J = 7.4 Hz, $C_{1'}$-H), **5.44** (s, 2H, Bz-CH_2), **4.64** (m, 1H, $C_{3'}$-H) **3.73** (m, 2H, $C_{5'}$-H_2), **3.60** (m, 1H, $C_{4'}$-H), **3.48** (m, 1H, $C_{2'}$-H), **2.17** (m, 1H, $C_{2'}$-H), **0.90** (s, 9H, tBu-H), **0.82** (s, 9H, tBu-H), **0.12** (s, 6H, methyl group x 2), **-0.06** (s, 3H, methyl group), **-0.09** (s, 3H, methyl group).

The preparation of N^2-Isobutyryl- O^6-benzyl-8-bromo-3',5'-O-bis(tert-butyldimethylsilyl)-2'-deoxyguanosine

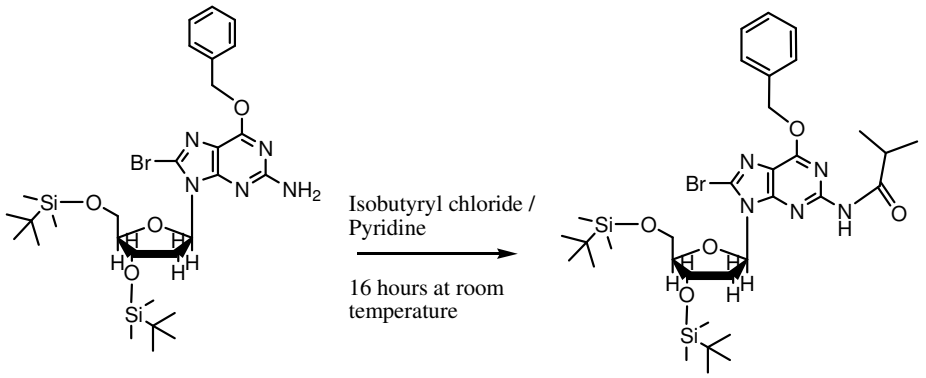

O^6-benzyl-8-Bromo-3',5'-O-bis (tert-butyldimethylsilyl)-2'-deoxyguanosine

N^2-Isobutyryl-O^6-benzyl-8-Bromo-3',5'-O-bis(tert-butyldimethylsilyl)-2'-deoxyguanosine

N^2-Isobutyryl- O^6-benzyl-8-bromo-3',5'-O-bis(tert-butyldimethylsilyl)-2'-deoxyguanosine was prepared according to a method modified from the literature.[18] O^6- Benzyl- 8-bromo 3',5'-O- bis(tert-butyldimethylsilyl) -2'-deoxyguanosine (575 mg, 0.87 mmol) was twice coevaporated with pyridine (2x2 ml) and then dissolved in anhydrous pyridine (5 ml). Then isobutyryl chloride (228 µl, 2.18 mmol) was added slowly by syringe and the reaction mixture was left stirring at room temperature for 16 hours. Methanol (0.5 ml) was added, to dissolve any remaining precipitate, and was left stirring at room temperature for a few more minutes. The solvent removed and was then coevaporated with toluene (5 ml).

The crude product was dissolved in MilliQ water (10 ml) and CH_2Cl_2 (10 ml) and the layers were separated. The aqueous layer was extracted with CH_2Cl_2 (2x20 ml) and the combined organic layers were then washed once with MilliQ water (20 ml), dried over $MgSO_4$ anhydrous and evaporated to dryness. The residue was purified by silica gel chromatography using a mobile phase of Hexane:EtOAc (20:1) to give the product as a colourless foam (341 mg, 53 %).

^{1}H NMR (400 MHz, DMSO-d_6): **δ (ppm) 10.44** (s, 1H, Iso-H), **7.52** (m, 2H, Bz-H), **7.45-7.34** (m, 3H, Bz-H), **6.25** (t, 1H, J = 6 Hz, $C_{1'}$-H), **5.57** (s, 2H, Bz-CH_2), **4.95** (m, 1H, $C_{3'}$-H), **3.76** (m, 2H, $C_{5'}$-H_2), **3.64** (m, 1H, $C_{4'}$-H), **3.49** (m, 1H, $C_{2'}$-H), **2.77**(m, 1H, Iso-CH), **2.24** (m, 1H, $C_{2'}$-H), **1.09** (d, 3H, J = 6.8 Hz, Iso-CH_3), **1.07** (d, 3H, J = 6.8, Iso-CH_3), **0.90** (s, 9H, tBu-H), **0.82** (s, 9H, tBu-H), **0.12** (d, 6H, J = 8.8 Hz, methyl group x 2), **-0.13** (d, 6H, J = 8.8 Hz, methyl group x 2).

The preparation of N^2-isobutyryl- O^6-benzyl-8N-(5-aminofluorescein)-3',5'-O-bis(tert-butyldimethylsilyl)-2'-deoxyguanosine (Buchwald-Hartwig coupling)

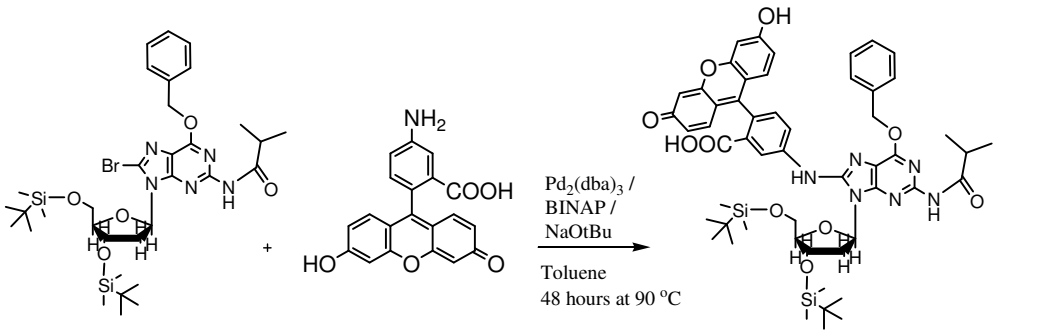

N^2-Isobutyryl-O^6-benzyl-8-bromo-3',5'-O-bis(tert-butyl dimethylsilyl)-2'-deoxyguanosine

5-Aminofluorescein

N^2-isobutyryl- O^6-benzyl-8N-(5-aminofluorescein)-3',5'-O-bis (tert-butyldimethylsilyl)-2'-deoxyguanosine

N^2-Isobutyryl- O^6-benzyl-8-bromo3',5'-O-bis(tert-butyldimethylsilyl)-2'-deoxyguanosine (100 mg, 0.136 mmol), 5-aminofluorescein (71 mg, 0.204 mmol), tris(dibenzylideneacetone) dipalladium(0) [$Pd_2(dba)_3$] (12 mg, 0.0136, 10 mol %), rac-2, 2'-bis(diphenylphosphino)-1, 1'-binaphtyl (BINAP) (25 mg, 0.0408 mmol, 30 mol %) and fully degassed anhydrous toluene (1 ml) were added to a dry glass vial in the dry box and left stirring at 90^{o}C for 40 minutes. NaOtBu (20 mg, 0.204 mmol) was added and the reaction mixture was left stirring at 90 ^{o}C for another 48 hours or until the starting material had disappeared as indicated by TLC (silica gel) analysis using a mobile phase of MeOH : Chloroform (1:10).

The reaction mixture was then allowed cool down to room temperature and diluted with diethylether (4 ml) and filtered. Methanol was then added to the filtrate and the white precipitate was removed. The filtrate was then concentrated and purified by HPLC using water : MeOH as mobile phase. Pure product was never isolated.

6.4 Results and Discussion

6.4.1 Fluorescein and Suitable FRET Pair

A further important aspect of this work was to find an appropriate fluorescent donor-acceptor pair for the model photoantenna based on the interfacial DNA scaffold. If a suitable acceptor is found, the energy may be transferred from the donor to the acceptor, in a process known as FRET, and as a result the emission is observed at a longer wavelength that is characteristic of the acceptor molecule. In addition, it would also be important to conduct experiments to demonstrate what quenching effects, if any, that the base may have on the fluorophores emission characteristics.

Fluorescein is widely used as an organic fluorescent label due to its characteristically high quantum yields. It may exist in several ionisation states (cation, neutral, anion, and dianion) each with unique spectral properties as illustrated by Margulies *et al.*[41] in Figure 6.6.

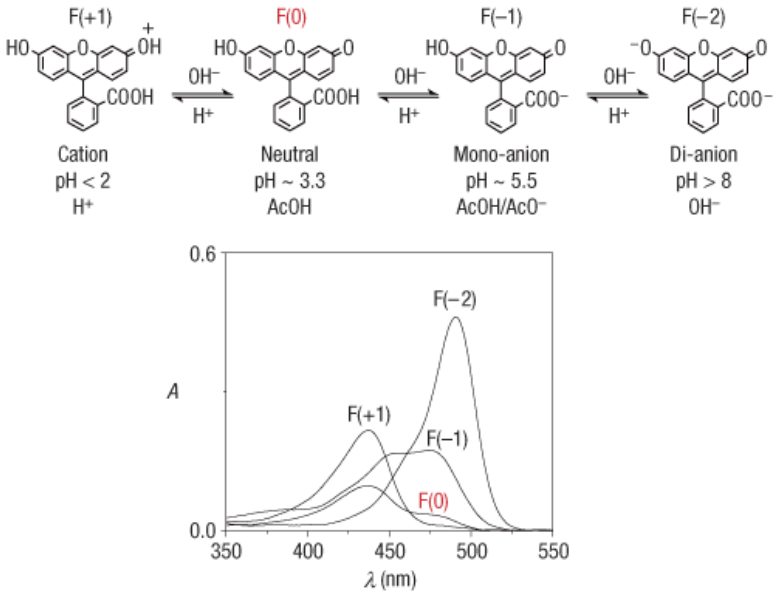

Figure 6.6: Chemical structures and corresponding absorbance spectra of fluorescein in different ionic states.[41]

In the experiments carried out here, the fluorescein was dissolved in 0.1M NaOH and exists in the dianionic state, which shows an absorption maximum at 490 nm and an emission maximum at 515 nm. The fluorescence lifetimes for the protonated and deprotonated fluorescein are approximately 3ns and 4ns respectively and the quantum yield is close to unity.[42]

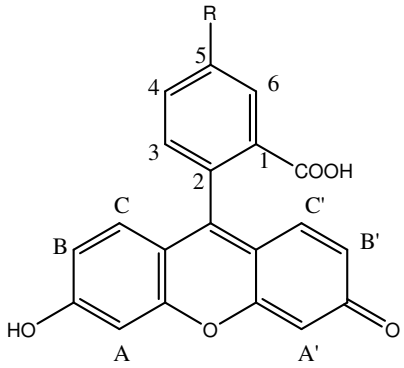

Figure 6.7: Schematic diagram illustrating the assigned protons for the general fluorescein molecule for ^{1}H-NMR analysis.

5-Carboxytetramethylrhodamine (TAMRA) (Figure 6.8) has long been used as a suitable acceptor for FRET with a donor fluorescein molecule. Its overlapping absorbance and emission are shown in Figure 6.9. The Förster distance, at which FRET is 50% efficient between both donor and acceptor fluorophores, is 55 Å.[38, 43, 44] The idea here was to use TAMRA as the 'black hole' quencher in facilitating charge transfer through the DNA scaffold. Once the charge separated state has arrived at the TAMRA molecule, a potential may be applied to the gold substrate, and thus, achieve the conversion of light energy into electrical energy.

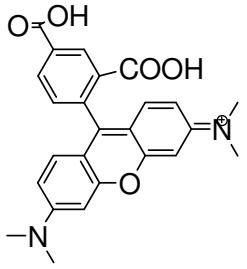

Figure 6.8: Chemical structure of TAMRA.

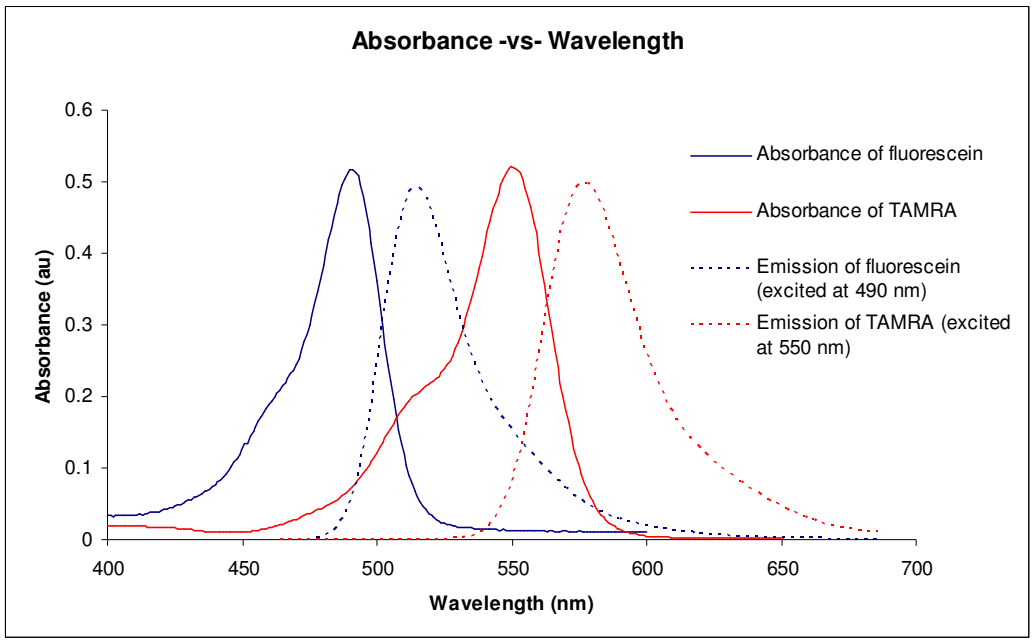

Figure 6.9: Overlapping absorbance spectrum and emission spectra of fluorescein (excited at 490 nm in 0.1 M NaOH solution) and TAMRA (excited at 550 nm in deionised water). All spectra are normalised.

Figure 6.10 outlines the various synthetic procedures performed and materials synthesised in an effort to internally label deoxyguanosine with fluorescein. The four main reactions attempted were: Suzuki couplings, Sonogashira couplings, Click chemistry and Buchwald-Hartwig couplings.

6.4.2 Synthetic Strategy Overview – internal fluorescent labelling of 2'-deoxyguanosine.

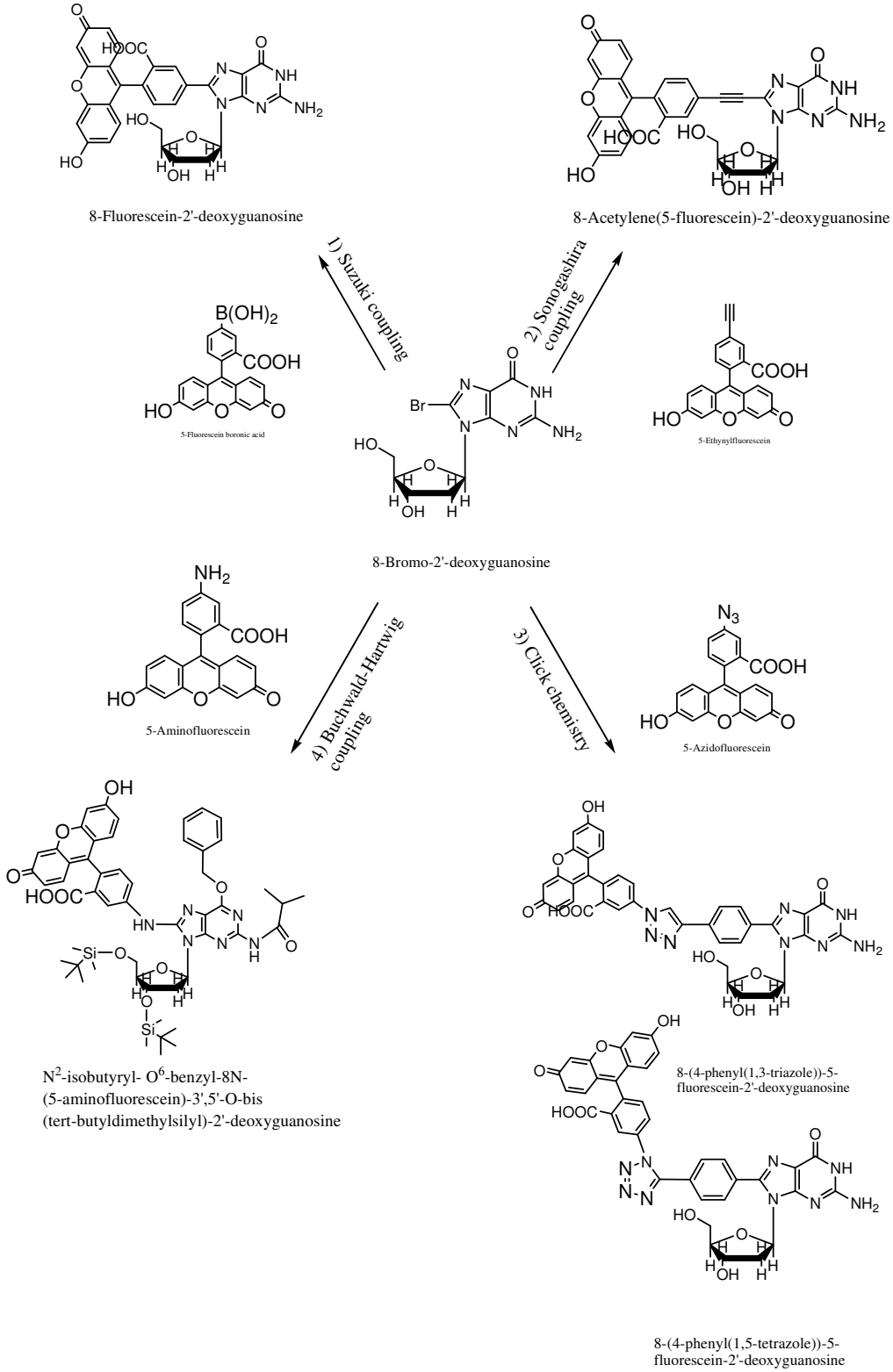

Figure 6.10: Synthetic strategy overview.

6.4.3 Synthetic Results

The starting material of 8-bromo-2'-deoxyguanosine was synthesised with a good yield of 79%. Prior to the electrophilic aromatic halogenation reaction, the 2'deoxyguanosine exists in a mixture of both cis and trans isomers, however, following the bromination of the nucleoside the majority of molecules are in the cis-configuration[14, 15] thus making the site of reaction slightly more accessible to other incoming molecules. [note: that all deoxyguanosine molecules are drawn in the trans confirmation for ease of illustration].

5-Bromofluorescein diacetate is the fluorescein precursor for many of the coupling strategies and was produced by the direct condensation reaction between the rescorcinol and 4-bromophthalic anhydride to give a mixture of the 5- and 6-bromofluorescein isomers. Further recrystallisation in acetic anhydride gave the regioisomerically pure 5-bromofluorescein diacetate as a yellow solid in a 16% yield.

6.4.3.1 Synthetic Strategy 1: Suzuki Coupling

Initially Suzuki coupling was used in an effort to label the nucleoside as this provided the shortest and most rigid linker in the final coupled product. The borylation of 5-bromofluorescein proved to be challenging, resulting in low yields and poor quality ^{1}H-NMR spectra. However, having experimented with many different reaction conditions as outlined in Table 6.1 and Table 6.2 below, a suitable method of synthesis was identified. Microwave synthesis proved relatively successful with all reactions producing some product, however, it was the conventional heating method used in experiment 6 of Table 6.1 that gave the best reaction yields.

Chemical	*Exp. 1*	*Exp. 2*	*Exp. 3*	*Exp. 4*	*Exp. 5*	*Exp. 6*
5-Bromo-fluorescein	100 mg / 0.02 mmol	100 mg / 0.02 mmol	100 mg / 0.02 mmol	100 mg / 0.02 mmol	100 mg / 0.02 mmol	500 mg / 1 mmol
Bis(pinacol-ato)diboron	56 mg / 0.22 mmol	56 mg / 0.22 mmol	56 mg / 0.22 mmol	78 mg / 0.31 mmol	76 mg / 0.30 mmol	280 mg / 1.1 mmol
NaOAc	30 mg / 0.36 mmol	-	-	-	-	-
[$PdCl_2$(dppf)]	1.6 mg / 0.002 mmol	5 mg / 0.006 mmol	5 mg / 0.006 mmol	5 mg / 0.006 mmol	5 mg / 0.006 mmol	8.2 mg / 0.01 mmol
Toluene anhydrous	5 ml	-	-	-	-	-
KOAc	-	59 mg / 0.6 mmol	59 mg / 0.6 mmol	-	59 mg / 0.6 mmol	295 mg / 3 mmol
DMSO anhydrous	-	5 ml	-	-	-	-
DMF anhydrous	-	-	5 ml	-	-	-
Triethyl-amine	-	-	-	0.08 ml / 0.6 mmol	-	-
1,4-Dioxane anhydrous	-	-	-	3 ml	3 ml	4 ml
Conditions	150 °C 16 hours	150 °C 16 hours	150 °C 24 hours	100 °C 16 hours	150 °C 48 hours	85 °C 48 hours
Yields	0%	0%	0%	0%	0%	207 mg / 38 %

Table 6.1: Summary of the experiments performed in the synthesis of 5-(4,4,5,5-tetramethyl-1,3,2-dioxaborolan-2-yl)fluorescein diacetate using conventional heating methods. All reactions were monitored by silica gel TLC analysis until no further conversion of starting material was evident (mobile phase: hexane / ethyl acetate (4:1)).

Chemical	***Exp. 1***	***Exp. 2***	***Exp. 3***	***Exp. 4***
5-Bromo-fluorescein	500 mg / 1 mmol	500 mg / 1 mmol	500 mg / 1 mmol	500 mg / 1 mmol
Bis(pinacol-ato)diboron	280 mg / 1.1 mmol	280 mg / 1.1 mmol	280 mg / 1.1 mmol	280 mg / 1.1 mmol
[$PdCl_2$(dppf)]	8.2 mg / 0.01 mmol	8.2 mg / 0.01 mmol	8.2 mg / 0.01 mmol	8.2 mg / 0.01 mmol
KOAc	295 mg / 3 mmol	295 mg / 3 mmol	295 mg / 3 mmol	295 mg / 3 mmol
1,4-Dioxane anhydrous	-	4 ml	-	4 ml
Toluene anhydrous	4 ml	-	6 ml	-
Conditions	300 W 30 minutes	600 W 30 minutes	600 W 40 minutes	900 W 20 minutes
Yields	37 mg / 7 %	106 mg / 20 %	86 mg 16 %	170 mg 32 %

Table 6.2: Summary of the experiments performed in the synthesis of 5-(4,4,5,5-tetramethyl-1,3,2-dioxaborolan-2-yl)fluorescein diacetate using microwave heating methods. All reactions were monitored by silica gel TLC analysis until no further conversion of starting material was evident (mobile phase: hexane / ethyl acetate (4:1)).

Mechanism for the borylation of 5-bromofluorescein:

The Miyaura borylation reaction allows the synthesis of boronates by the cross-coupling of bispinacolatodoboron with aryl halides[35, 37, 45, 46] and many of the processes are outlined in the section that follows for Suzuki coupling reactions.

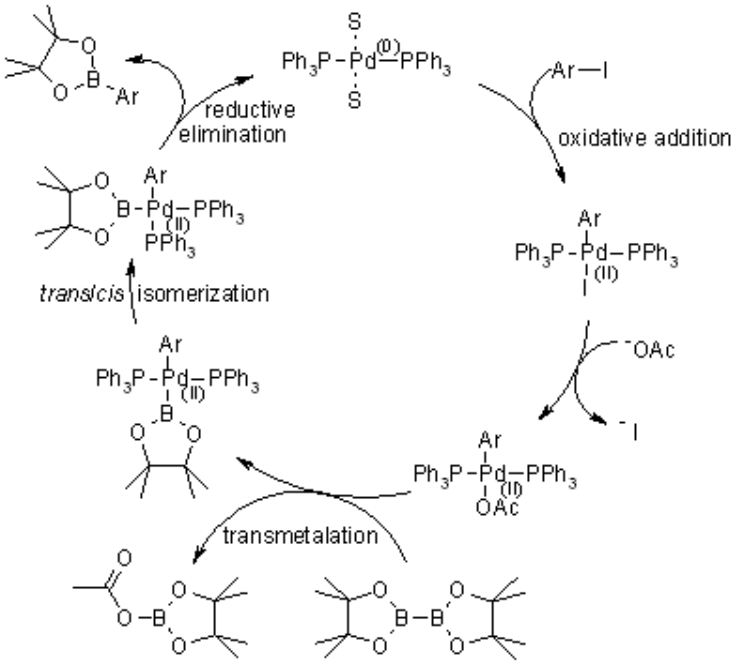

Figure 6.11: Schematic diagram illustrating the general mechanism of reaction in the borylation of compounds.[47]

The hydrolysis of the boronated fluorescein ester to the corresponding 5-fluorescein boronic acid also proved less than straight forward, and no clean NMR spectrum of the pure product was obtained. It is proposed that this is due to the cyclotrimerisation of 5-fluorescein boronic acid, which would prevent the molecule being involved in any further coupling reactions, and would also account for the inability to isolate the pure product.[27] It is also known that pinacol esters can be difficult to hydrolyse and critical for the success of the reaction is the choice of base used, all of which may have added to the difficulties in isolating this product. A summary of the experiments performed are presented in Table 6.3 below.

Chemical	***Exp. 1***	***Exp. 2***	***Exp. 3***
Boronated fluorescein	109 mg / 0.20 mmol	217 mg / 0.50 mmol	100 mg / 0.18 mmol
K_2CO_3	55 mg / 0.40 mmol	346 mg / 2.5 mmol	-
Na_2CO_3	-	-	127 mg / 1.20 mmol
Deionised H_2O	1.5 ml	1.5 ml	2 ml
Acetonitrile	3.5 ml	1.5 ml	1 ml
Conditions	2 hours at room temperature	7 hours at room temperature	3 hours at 30 ^oC
Yields	0%	0%	0%

Table 6.3: Summary of the experiments performed in the synthesis of 5-fluorescein boronic acid. All reactions were monitored by silica gel TLC analysis until no further conversion of starting material was evident (mobile phase: hexane / ethyl acetate (4:1)).

In an effort to overcome these issues, the hydrolysis was performed in-situ without isolating the product and was immediately coupled with the 8-bromo-2'-deoxyguaonsine in a 'one pot' Suzuki coupling reaction. Suzuki-Miyaura coupling involves a palladium cross coupling reaction between organoboronic acids and halides.[13, 25, 48-52] This synthetic approach has many advantages: most noticeably the production of a short rigid linker as possible between base and fluorophore, the low toxicity and the supposed relative ease of preparation of boronic acid compounds. Suzuki coupling also allows for the aqueous phase modification of an unprotected halonucleoside,[11, 12, 49, 53] which is of interest due to the environmental benefits of such reactions, furthermore, no protection chemistry is required prior to the coupling. It was also found that using the water-soluble catalytic mixture of $Pd(OAc)_2$ and tris(3-sulfonatophenyl)phosphine (TPPTS) as ligand gave the highest conversion rates for the arylation of 8-bromo-2'-deoxyguanosine that was in the region of 97 % after 2 hours.[12] Figure 6.12 below shows the general mechanism of reaction for the Suzuki coupling.

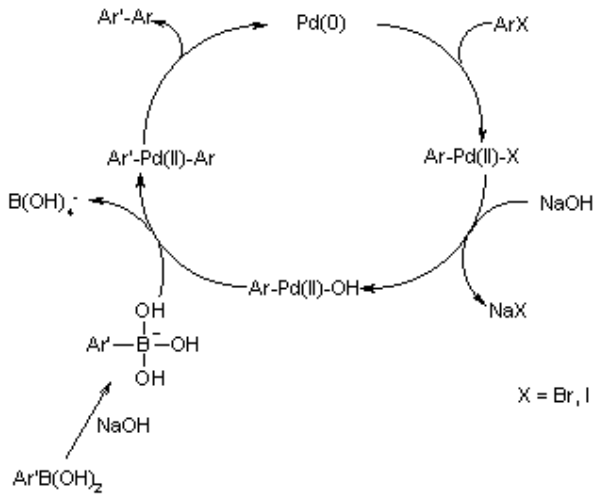

Figure 6.12: Schematic diagram illustrating the general mechanism of Suzuki coupling reactions.[54]

$Pd(II)(OAc)_2$ has an oxidation state of 2^+ and as a result must undergo ligand exchange with the TPPTS prior to entry into the Suzuki catalytic cycle to produce the corresponding Pd(0). Once this has taken place the Suzuki reaction may proceed in a number of different steps:

1) *Oxidative addition:* The first step in the Suzuki coupling cycle is oxidative addition in which a neutral ligand (8-BrdG) adds to the metal centre (Pd catalyst) and in doing so the metal centre is oxidised, usually by 2 electrons. In transferring the 2 electrons from the metal centre to the incoming 8-BrdG, this breaks a bond to produce two new anionic ligands (dG^- and Br^-), which will then go on to form new bonds to the metal centre and produce the organo-palladium compound.

2) *Transmetallation:* this involves the exchanging of ligands between two metal centres. Here the base sodium carbonate (and not NaOH as illustrated in Figure 6.12 above) is used to exchange ligands with the metal centre having already undergone oxidative addition. This results in the elimination of sodium bromide (NaBr) from the reaction and the production of another organo-palladium species.

3) *Boronic acid activation:* The boronic acid must first be activated by the presence of the base in the reaction. The activated boron improves the polarisation of the organic ligand and helps with transmetallation. This step sees the elimination of a boronic acid species and the formation of yet another organo-palladium compound.

4) *Reductive elimination:* The final step in the cycle regeneration Pd(0) and the elimination of the coupled compound of interest by a reductive elimination process. This is the opposite of oxidative addition in which two anionic ligands from the metal centre couple together to produce a neutral molecule and dissociate from metal centre. Thus, leaving the metal centre in its original oxidation state of 0 and the Suzuki coupled product.

6.4.3.1.1 Suzuki Coupling Results

Chemical	***Exp. 1***	***Exp. 2***	***Exp. 3***	***Exp. 4***
8-BrdG	45 mg / 0.13 mmol	87 mg / 0.25 mmol	58 mg / 0.17 mmol	35 mg / 0.1 mmol
5-fluorescein boronic acid*	76 mg / 0.20 mmol	113 mg / 0.30 mmol	75 mg / 0.20 mmol	45 mg / 0.12 mmol
Pd(II)(OAc)$_2$	2.2 mg / 0.01 mmol	1.5 mg / 0.006 mmol	1 mg / 0.004 mmol	0.6 mg / 0.0025 mmol
TPPTS	14 mg / 0.025 mmol	9 mg / 0.016 mmol	6 mg / 0.011 mmol	3.6 mg / 0.00625 mmol
K_2CO_3	103 mg / 0.75 mmol	-	-	42 mg / 0.30 mmol
Na_2CO_3	-	53 mg / 0.5 mmol	54 mg / 0.5 mmol	-
Deionised H_2O	1.5 ml	2.3 ml	2 ml	1 ml
Acetonitrile	3.5 ml	1.2 ml	2 ml	1 ml
Conditions	16 hour at 80 ^oC	6 hours at 80 ^oC	16 hours at 80 ^oC	3 hours at 80 ^oC, 16 hours at R.T.
Yields	0%	0%	0%	0%

*Table 6.4: Summary of the experiments performed in the synthesis of 8-(5-fluorescein)-2'-deoxyguanosine. All reactions were monitored by silica gel TLC analysis until no further conversion of starting material was evident (mobile phase: chloroform / methanol (10%)). * 5-fluorescein boronic acid was not isolated, these values represent a theoretical value based on published literature.*

Table 6.4 above outlines the various experiments performed in the synthesis of 8-(5-fluorescein)-2'-deoxyguanosine. Analysis of the recovered product, which included NMR and mass spectrometry, showed that the reaction failed to produce the final fluorescently coupled product. This could have been due to a number of reasons including; the in-situ preparation of the 5-fluorescein boronic acid had also failed to work efficiently, or the steric hindrance associated with the short rigid linker between both base and fluorophore moieties.

It is known that guanine is much less reactive than the other bases when undergoing palladium catalysed reactions. This has been attributed to the coordination of the transition metal catalyst to the guanine base under basic conditions (Figure 6.13) and guanine has also been shown to inhibit the coupling of both halopurine nucleosides and simple arly bromides.[13]

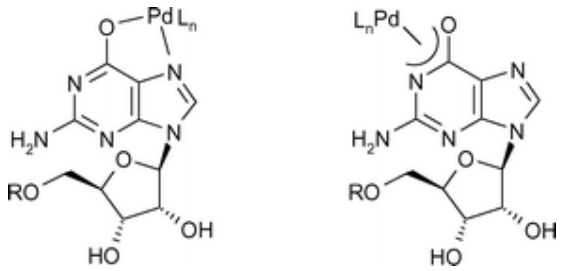

Figure 13: Possible coordination of guanosine derivatives to palladium catalysts under basic reaction conditions.[13]

Even though guanine is the most unreactive of the four DNA bases it was decided to continue with deoxyguanosine as nucleoside due to the expertise within the research group,[49] and the time already spent working with the compound. In another effort to achieve the coupling of fluorophore to nucleoside using a relatively short linker another synthetic approach was examined, that of Sonogashira couplings.

6.4.3.2 Synthetic Strategy 2: Sonogashira Coupling

Sonogashira coupling, much like Suzuki coupling, would have resulted in a short and rigid linker between fluorophore and nucleoside moieties. In the synthesis of the starting materials, Sonogashira coupling may be used to describe the alkynylation of 5-bromofluorescein and trimethylsilylacetylene to give the corresponding 5-(2-trimethylsilylethynyl)fluorescein diacetate in a 70 % yield, and the mechanism of reaction is discussed in detail below. Desilylation of the trimethylsilyl group is achieved by the addition of the base potassium carbonate to the reaction to afford the acetylene product 5-ethynylfluorescein in a 93 % yield, however, carrying out this reaction again under identical conditions would yield completely inconsistent results. The reproducibility of this reaction is somewhat questionable as the reaction only worked approximately 20% of the time. Even though NMR and mass spectrometry results may have suggested a clean product, HPLC analysis (shown in Figure 6.17) shows three separate peaks in the chromatogram. The poor quality of the NMRs produced may be explained by the possible the formation of dimers of ethynyl fluorescein under the synthetic conditions described.

Sonogashira Coupling

Sonogashira coupling is the reaction between terminal alkynes with arly halides or vinyl halides and is a robust and versatile C-C reaction.[3, 15, 25, 55-59] Not only will it provide the short linker necessary between base and fluorescent marker, but in comparison to the previous Suzuki coupling, this linker will be slightly longer and therefore more accessible to the site of reaction. Protection of the sugar hydroxyl groups is not necessary in most cases for this reaction as doing so might effect the purification of such products.[24] Firth *et al.*[16] also demonstrate that the ratio of palladium catalyst to copper additive is very important in Sonogashira cross coupling reactions.

Typically two catalysts are required for this reaction: a zerovalent palladium complex (tetrakis(triphenylphosphine) palladium(0)) and a copper (I) halide additive (CuI). Many of the processes in Sonogahsira couplings are very similar to that of Suzuki couplings already discussed in the previous section. Conditions of both reactions include the presence of a base to neutralise the hydrogen halide produced as a byproduct that may affect the reaction and run the risk of breaking the glycosidic bond between the sugar and base. In the Suzuki coupling, the base also helps to reduce the palladium catalyst to an oxidation state of 0, however, the palladium catalyst used here for the Sonogashira coupling is already a zerovalent complex and may enter directly into the catalytic cycle (Figure 6.14). All solvents used were fully degassed and the reaction performed under a nitrogen environment as the palladium catalyst is air sensitive and oxygen may also promote the homocoupling of acetylenes.[24]

The Palladium Cycle:

The palladium catalyst proceeds in activating the aromatic halide (8-BrdG) by oxidative addition to form the aromatic halide palladium complex. This may then go on to react with the copper acetylide produced in the copper cycle in the rate limiting transmetallation step and expels the copper halide. The organic ligands are then orientated in the cis-conformation during the trans/cis isomerisation step. In the last step the product is eliminated from the cycle by reductive elimination with the regeneration of the Pd(0) to the catalytic cycle.

The Copper Cycle:

Deprotonation of the terminal alkyne occurs with the presence of a strong base such as triethylamine. Although there are a few doubts as to whether or not this base is indeed strong enough to cause the deprotonation. The organocopper complex formed after the reaction with base continues to react with the aromatic halide palladium complex and see the regeneration of the copper halide (CuI).

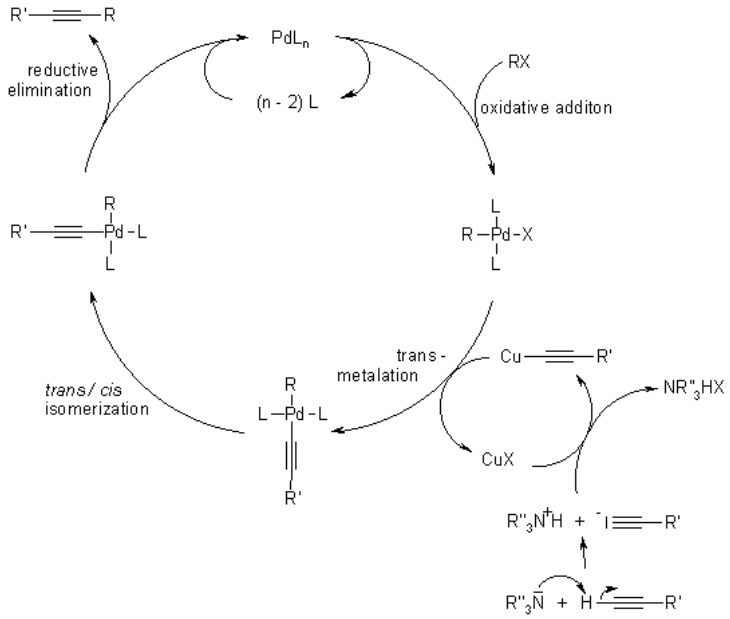

Figure 6.14: Schematic diagram illustrating the general mechanism of reaction for Sonogashira couplings.[60]

6.4.3.2.1 Sonogashira Coupling Results

Mass spectrometry of the crude 8-acetylene-(5-fluorescein)-2'-deoxyguanosine (Figure 6.15) shows evidence of the fluorescently coupled nucleoside at 622.3 m/z along with some of the starting material 5-ethynyl fluorescein at 356.3 m/z.

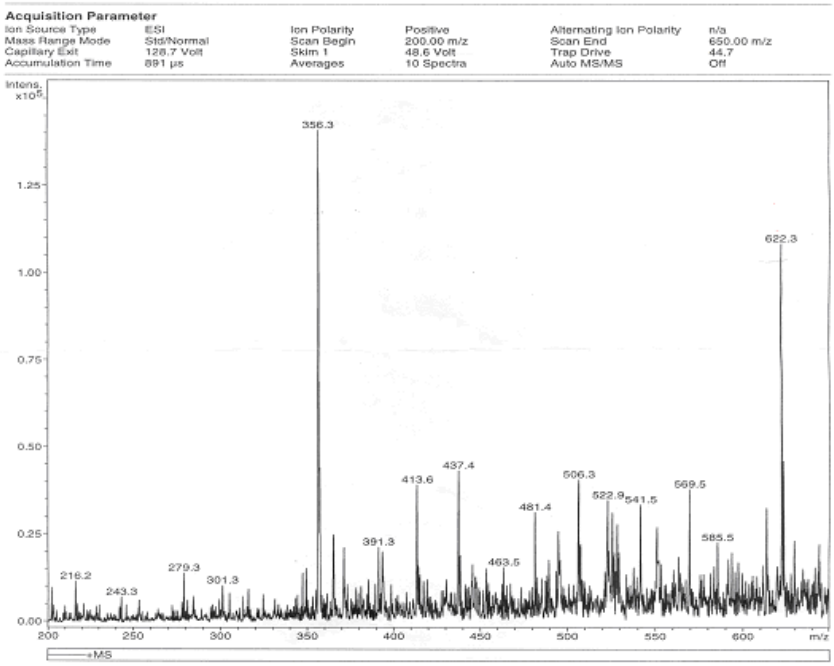

Figure 6.15: Mass spectra showing the potential presence of coupled product, 8-acetylene-(5-fluorescein)-2'-deoxyguanosine, at 622.3 m/z and 5-ethynyl fluorescein at 356.3 m/z.

Initially, silica gel chromatography was employed in an effort to purify the compound, however this proved to be unsuccessful as the strong polarity of the compound, and hence, its strong affinity for the polar silica gel (Si-O bonds) stationary phase failed to yield any elution of the compound of interest. During this purification the methanol content of the mobile phase was increased to 70%, triethylamine and even water were also added unsuccessfully to the mobile phase in an effort to remove the product. A reverse-phase HPLC method was then developed in an effort to isolate the product in favourable yields.

HPLC method development: Isolation of 8-acetylene-(5-fluorescein)-2'-deoxyguanosine.

The following HPLC conditions were found to be the best conditions for the analysis of the Sonogashira coupled compound.

HPLC: Varian LC 940 with automatic fraction collector.
Column used: Varian C18 Pursuit XRs 250x4.6 mm analytical column.
Injection volume: 60 µl. (automatic injection)
Detector Wavelengths: 254 nm and 490 nm PDA detector.
Equilibration time: 7 mins between injections.

Time (min)	Flow Rate (ml/min)	% Methanol	% MilliQ Water
0	1.0	20	80
30	1.0	20	80
40	1.0	50	50
70	1.0	100	0
90	1.0	100	0

Table 6.5: Mobile phase composition used for the isolation of 8-acetylene-(5-fluorescein)-2'-deoxyguanosine.

Firstly, the starting materials were injected in order to determine their respective retention times (Rt) and to ensure sufficient separation to allow for detection of other substances that may be present in the sample. The splitting of the chromatographic peak for 8-bromo-2'-deoxyguanosine below may suggest the presence of both cis- and trans- isomers of the nucleoside in Figure 6.16 below.

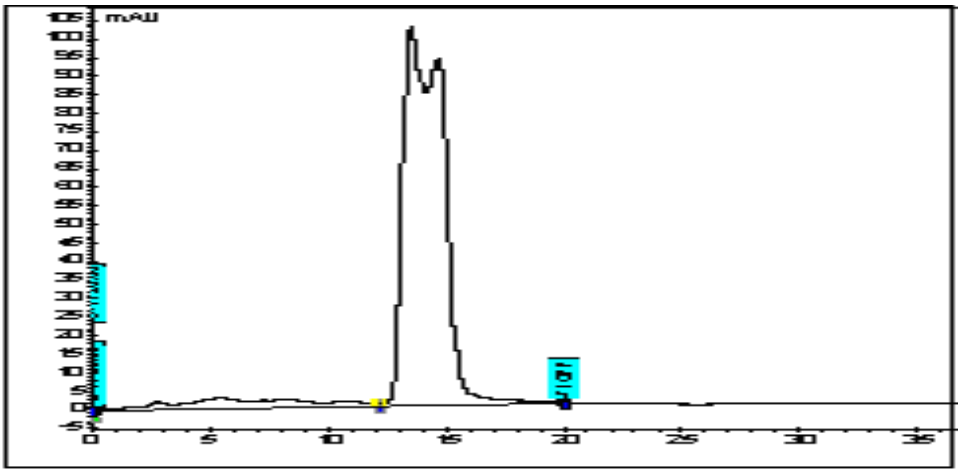

Figure 6.16: HPLC chromatogram of 8-bromo-2'-deoxyguanosine using a detection wavelength of 254 nm. Rt = 13.5 mins.

The chromatographic purity of the 5-ethynyl fluorescein is somewhat questionable (Figure 6.17), even though NMR and mass spectrometry analysis indicated a relatively clean product. Such a marked difference in the purity could have been detected by HPLC as the ε of any possible impurities at certain wavelengths may vary, and therefore, have a more intense absorbance profile in comparison to the pure product. Nevertheless, the poor chromatographic nature of 5-ethynyl fluorescein only served to increase difficulties in the detection and isolation of the coupled product.

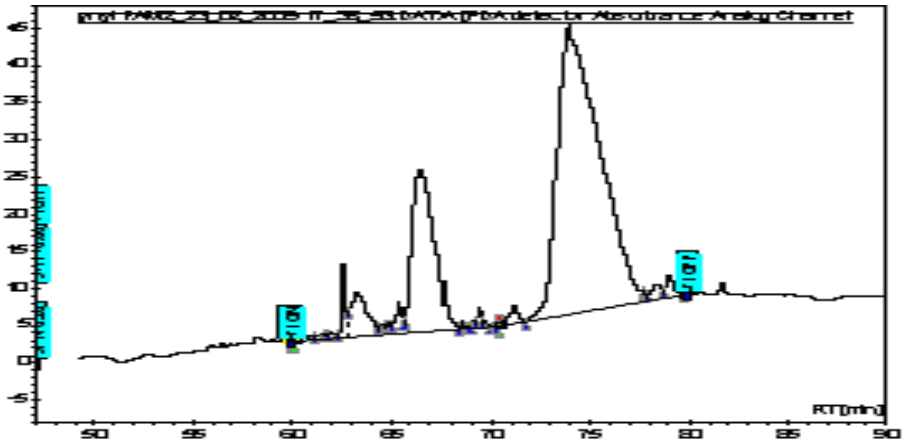

Figure 6.17: HPLC chromatogram of 5-ethynyl fluorescein using a detection wavelength of 490nm. Rt = 63-79 mins.

Injection of the crude sample onto the system yielded the chromatogram shown in Figure 6.18 below, and there was no evidence of elution of a nucleoside component at shorter retention times. Subsequent NMR and mass spectrometry of the peaks failed to give any indication of the fluorescent nucleoside that was worth further investigation.

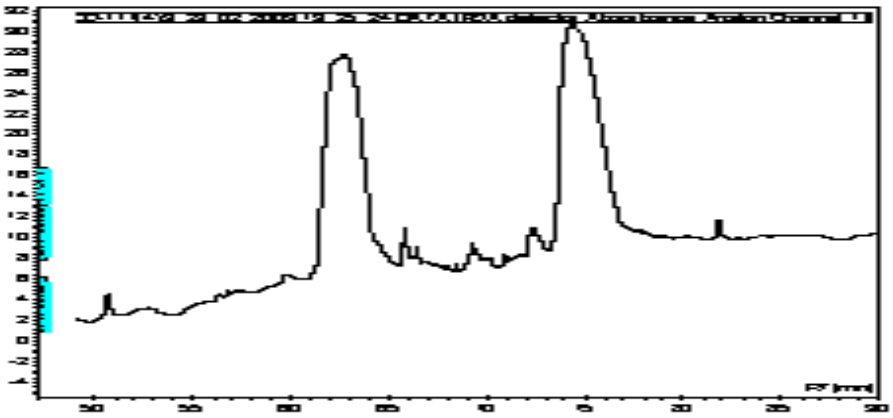

Figure 6.18: HPLC chromatogram of 8-acetylene-(5-fluorescein)-2'-deoxyguanosine using a detection wavelength of 254nm. Rt = 62 and 75 mins.

Chromatographic conditions and flow rates were altered in an effort to increase separation, and with it, the possibility of detecting any other peaks containing product, but none were observed. Taking into account the poor chromatography of the 5-ethynyl fluorescein moiety as a starting material and the difficulties with its synthesis, it was felt that another method of coupling was worth investigating.

6.4.3.3 Synthetic Strategy 3: Click Chemistry

In parallel with the Sonogashira coupling reactions, Click chemistry was also attempted as a possible alternative method to couple fluorophore and nucleoside to each other. This involved the introduction of a phenyl group between both compounds and consequently a loss in some of the rigidity between the base and label but the site of reaction should be more accessible when compared to the previous methods of Suzuki and Sonogashira couplings. The coupling of the aromatic halide (8-BrdG) to the boronic acid may be described by the Suzuki coupling reaction mechanism above, to give the starting materials of 8-(4-ethynylphenyl)-2'-deoxyguanosine and 8-(4-cyanophenyl)-2'-deoxyguanosine in yields of 35% and 96% respectively.

The fluorescein moiety, 5-azidofluorescein, was prepared in a 79% yield. Here, 5-aminofluorescein (an aromatic primary amine) quickly reacts with the amyl nitrite to form the corresponding diazonium salt, which then decomposes in the presence of sodium azide to produce the desired 5-azidofluorescein product in a nucleophilic aromatic substitution reaction.

6.4.3.3.1 Click Chemistry Results

1, 3-dipolar cycloaddition reaction (also known as the Huisgen reaction) is the reaction between an azide and alkyne to link both components via a triazole linker and is an adaptation on the original Sharpless 'Click' chemistry.[5, 32, 61-66] The reaction is characterised by mild and simple reaction conditions and the ability to perform reactions in the presence of oxygen and aqueous conditions.[67-69] Initially the click reaction was attempted with 8-(4-ethynylphenyl)-2'-deoxyguanosine and 5-azidofluorescein to give the linker containing a triazole 5-membered heterocyclic ring. However, due to ease of synthesis and high yields of the starting material 8-(4-cyanophenyl)-2'-deoxyguanosine, it was also worthwhile to attempt the complementary Huisgen-Sharpless reaction between aromatic nitriles and organic azides that would result in a tetrazole 5-membered hetrocyclic ring in the cross-coupling linker.[70-73]

The mechanism of coupling in Figure 6.19 may be used to describe the copper (I) catalysed cycloaddition between the azide and alkyne to form a triazole. First step in the reaction is the coordination of the alkyne (8-(4-ethynylphenyl)-2'-deoxyguanosine) to the copper (I) catalyst, by removal of one of the copper ligands to give the copper acetylide. Next the azide (5-azidofluorescein) replaces another one of the ligands and the copper complex binds to the nitrogen beside the carbon. The terminal nitrogen on this complex proceeds to attack the second carbon of the copper acetylide to form the six-membered copper (III) intermediate. Rearrangement of this ring gives the familiar 5-membered triazole structure. The final step sees the elimination of the compound by reductive elimination and regeneration the original copper (I) species. Figure 6.20, shows the mechanism used to describe the formation the tetrazole heterocyclic ring.

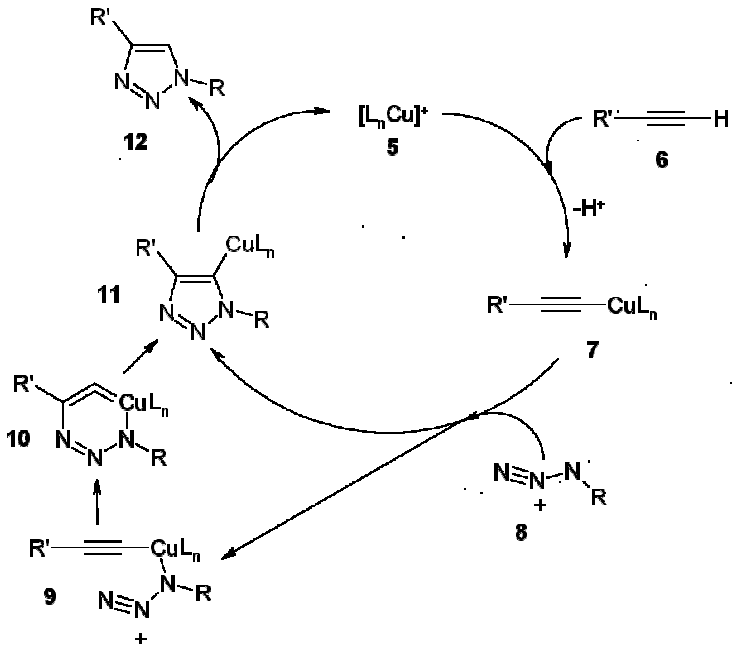

Figure 6.19: Schematic diagram illustrating the general mechanism of reaction for the Huisgen reaction between azides and alkynes to form a triazole linker.[74]

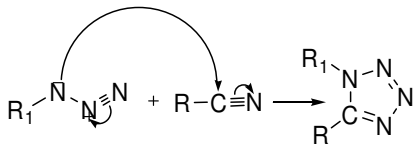

Figure 6.20: Mechanism for the formation of a 1,5-tetrazole cross-coupling linker.

In the preparation of 8-(4-phenyl(1,3-triazole))-5-fluorescein-2'-deoxyguanosine neither NMR or mass spectrometry or TLC analysis of the product indicated that the Click reaction had worked. Alternative reaction conditions used copper iodide as a catalyst with heating to 60 ^{o}C for 12 hours but there was no evidence of the fluorescently coupled product. In another experiment tetrakis(acetonitrile) copper(I) hexaflurophosphate and elementary copper wire were used as catalysts in a solution of dichloromethane : methanol (4:1) with heating to 50 ^{o}C for 12 hours but once again NMR and mass spectrometry analysis proved that the reaction had also not proceeded as intended. The same may be said in the experiment in the synthesis of 8-(4-phenyl(1,5-tetrazole))-5-fluorescein-2'-deoxyguanosine as analysis of the reaction product failed to give any indication that the product had been synthesised.

In a final effort to achieve the fluorescent nucleoside, next to consider was a reaction that required the full protection of the 8-bromo-2'-deoxyguanosine before any coupling reactions would take place. This has the added advantages of the ability to purify the nucleoside at every stage by ordinary silica gel chromatography due to the non-polar nature of the compound. It may also in turn lead to increased yields due to more selective coupling, as the majority of the protected deoxyguanosine molecules should be in cis confirmation leaving the site of reaction more accessible for coupling reactions to take place. Also, for incorporation of any nucleoside into a sequence of DNA by polymerase chain reaction (PCR), the corresponding phosphoramidite must first be synthesised. In order for this to occur, certain functional groups of the nucleoside must be protected. Choosing to protect the nucleoside before any coupling reactions take place, would eliminate many further (de)protection reactions using a novel compound, and hence, may lead to a decrease in yields with every synthetic step. The Buchwald-Hartwig reaction was the final coupling reaction to be attempted.

.

6.4.3.4 Synthetic Strategy 4: Buchwald-Hartwig coupling:

Buchwald-Hartwig coupling is a coupling reaction between an aryl halide and amine in the presence of palladium catalyst and base to form a carbon-nitrogen bond.[75-83] There are many examples throughout the literature of Buchwald-Hartwig reactions to link molecules to the C-8 position of purine bases in high yields.[17-20, 84-86]

For the successful amination of the N^2-isobutyryl- O^6-benzyl-8-bromo-3',5'-O-bis(tert-butyldimethylsilyl)-2'-deoxyguanosine and 5-aminofluorescein one must fully protect the deoxyguanosine nucleoside prior to Buchwald-Hartwig coupling. The O-silylation of the 3' and 5' hydroxyl on the sugar moiety was performed using conditions described by Ludovic *et al*.[20] with relatively high yields of over 70%.

Next step was the protection of the O^6 atom on the base. Initially 4-cyanophenylethyl was used as the protecting group for the O^6-postion as this group may be removed after the oligonucleotide synthesis using 1,8-diazabicycloundec-7-ene (DBU) and as a result would avoid a further deprotection step before phosphoramidite synthesis.[19] Hence, the O^6-(4-cyanophenyl)ethyl-8-bromo-3',5'-O-bis(tert-butyldimethylsilyl)-2'-deoxyguanosine was synthesised and isolated in a 52% yield [results not shown]. However, having researched the synthesis further it is the benzylalcohol O^6-protecting group that is more widely used throughout the literature.[17, 18, 20, 85, 86] Even though yields of both O^6-protection were comparable, it was decided to use the benzylalcohol as the protecting group and the corresponding O^6-benzyl-8-bromo-3',5'-O-bis(tert-butyldimethylsilyl)-2'-deoxyguanosine was prepared in 60% yield.

Finally the exocyclic amino group was protected using isobutyric anhydride, however, as the reaction proceeded it was only the starting material of O^6-benzyl-8-bromo-3',5'-O-bis(tert-butyldimethylsilyl)-2'-deoxyguanosine that was returned and reaction failed to work satisfactorily. The stronger isobutyic chloride was then employed and the fully protected N^2-isobutyryl- O^6-benzyl-8-bromo-3',5'-O-bis(tert-butyldimethylsilyl)-2'-deoxyguanosine was isolated in a 50% yield.

Buchwald-Hartwig Catalytic Cycle:

The palladium (II) catalyst ($Pd_2(dba)_3$) is initially reduced with the BINAP ligand to give the active palladium (0) species. The catalytic cycle starts when the arly halide coordinates to the palladium (0) species in an oxidative addition reaction. Next, coordination of the amine to the palladium complex occurs to give species number 3 in Figure 6.21. A strong base is then required to abstract a proton from the amine of this species. Under initial reaction conditions, K_3PO_4 was used as base but the reaction did not show any signs of progress by TLC. It was only when the stronger base of NaOtBu was used that the reaction showed evidence of proceeding. This intermediate then gives the desired aryl amine coupled product and regeneration the Pd(0)(BINAP) species by reductive elimination. At this final reductive elimination step there may be a couple of undesired side reactions including β-hydride elimination to the arene compound or elimination of the imine compound. In either case the zerovalent palladium species is regenerated and the catalytic cycle continues.[77, 80]

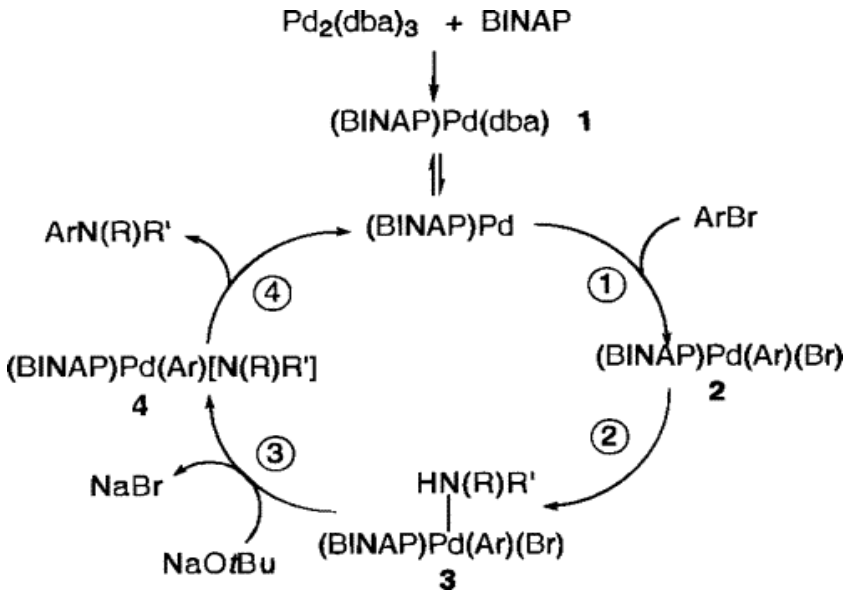

Figure 6.21: Schematic diagram illustrating the general mechanism of Buchwald-Hartwig coupling reactions.[75]

6.4.3.4.1 Buchwald-Hartwig Results:

HPLC method development:

The following HPLC conditions were found to give the best separation of starting materials to determine their retention times and for the analysis of the coupled compound.

Time (min)	Flow Rate (ml/min)	% Methanol	% MilliQ Water
0	1.8	85	15
10	1.8	90	10
20	1.8	95	5
25	1.8	100	0
35	1.8	100	0

Table 6.6: Mobile phase gradient for the isolation of N^2-isobutyryl- O^6-benzyl-8N-(5-aminofluorescein)-3',5'-O-bis(tert-butyldimethylsilyl)-2'-deoxyguanosine.

Injection of starting materials:

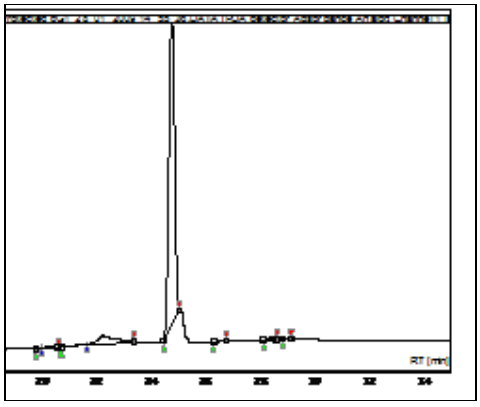

Figure 6.22: HPLC chromatogram of N^2-isobutyryl- O^6-benzyl-8-bromo-3',5'-O-bis(tert-butyldimethylsilyl)-2'-deoxyguanosine using a detector wavelength of 254 nm. Rt = 24.8mins.

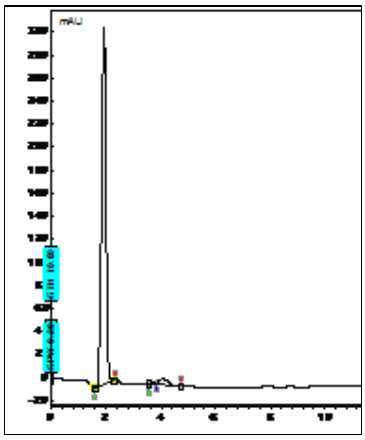

Figure 6.23: HPLC chromatogram of 5-aminofluorescein using a detector wavelength of 254 nm. Rt = 1.9mins.

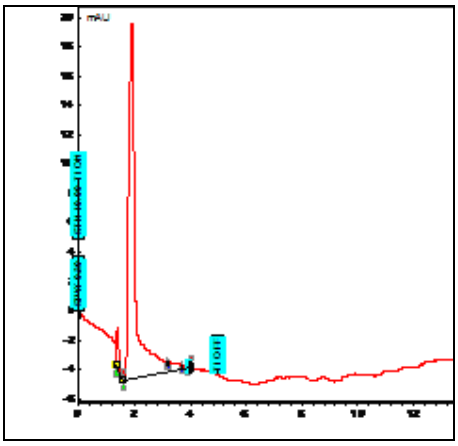

Figure 6.24: HPLC chromatogram of 5-aminofluorescein using a detector wavelength of 490 nm. Rt = 1.9mins.

As with many of these coupling reactions, the conditions used are often very sensitive to the success of the coupling reaction and no more so than with the Buchwald-Hartwig amination. Meyers *et al.*[87] even suggest that the supplier and particle size of the base can have an effect on the reaction mechanism. However, it was felt that the choice of solvent can have the most profound effect on the amination reaction,[88] and hence, 5 small scale reactions were set-up using 5 different solvents covering a majority of the possibilities of polar aprotic, polar protic and nonpolar solvents. The reactions were only analysed by HPLC in order to determine the best solvent, if any, to continue with this method of synthesis. The anhydrous solvents used

in the coupling reactions were toluene (nonpolar), xylene (nonpolar), 1,4-dioxane (polar aprotic), methylpyrrolidone (polar aprotic) and dimethoxyethane (polar aprotic). Results suggested that it is toluene that gives cause for most optimism and the formation of the coupled product, and therefore, this solvent was used for the scaled up production of the fluorescently labelled nucleoside.

The progress of the reaction was monitored by HPLC analysis, by diluting 1 µl of the reaction mixture into 2 ml of mobile phase and injecting onto the HPLC system. The reaction was deemed to be finished when the ratio of the two starting material peaks did not alter anymore, which was after a period of 48 hours. The extraction of the reaction mixture into diethylether and methanol prior to injection onto the HPLC removed large quantities of the unreacted 5-aminofluorescein and catalytic mixture. In order to identify the peak containing the product of interest, the HPLC was set up to collect multiple injections of the crude product in 6 different fractions (Figure 6.25). These were then evaporated to dryness and sent for NMR analysis. Fraction 6, with a retention time of 29-33 minutes (Figure 6.25) also shows absorbance at 254 nm and 490 nm. This might be potentially expected from a chromatographic peak containing both the fluorescein and nucleoside moieties.

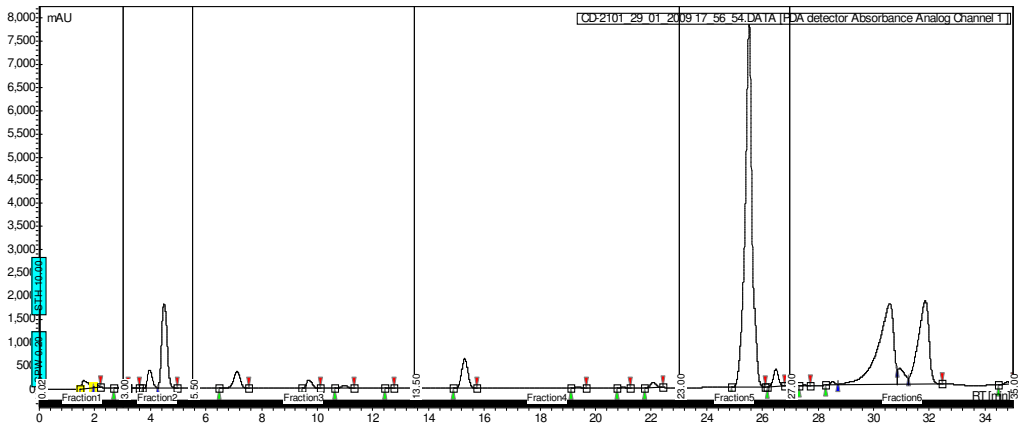

Figure 6.25: HPLC chromatogram of N^2-isobutyryl- O^6-benzyl-8N-(5-aminofluorescein)-3',5'-O-bis(tert-butyldimethylsilyl)-2'-deoxyguanosine crude reaction mixture using a detector wavelength of 254 nm.

Following proton NMR analysis, the fractions were thought to contain the following compounds:

Fraction 1 (ret. time: 0-3 minutes): evidence of 5-aminofluorescein.
Fraction 2 (ret. time: 3-5.5 minutes): evidence of catalytic mixture.
Fraction 3 (ret. time: 5.5-13.5 minutes): nothing detected.
Fraction 4 (ret. time: 13.5-23 minutes): nothing detected.
Fraction 5 (ret. time: 23-27 minutes): N^2-Isobutyryl- O^6-benzyl-8-bromo-3',5'-O-bis(tert-butyldimethylsilyl)-2'- deoxyguanosine
Fraction 6 (ret. time: 27-35 minutes): evidence of the product N^2-isobutyryl- O^6-benzyl-8N-(5-aminofluorescein)-3',5'-O-bis(tert-butyldimethylsilyl)-2'-deoxyguanosine.

As fraction 6 was thought the most likely to contain the product, the fraction was then taken and re-injected to isolate the two peaks separately and both were sent for further NMR and mass spectrometry analysis. Both NMR's still showed evidence of product but they were still far from pure for incorporation into a sequence of DNA. However, it is the second peak of fraction 6 that gives most cause for optimism as the mass spectrum results in Figure 6.26 and the corresponding identification of peaks in Table 6.7 highlight.

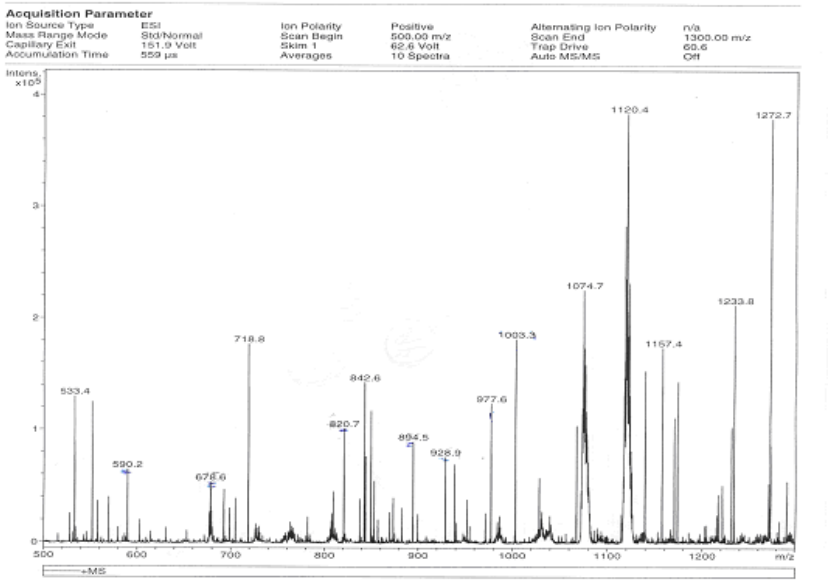

Figure 6.26: Mass spectra of HPLC fraction 6 (peak 2) with retention time of 32 minutes in the preparation of N^2-isobutyryl- O^6-benzyl-8N-(5-aminofluorescein)-3',5'-O-bis(tert-butyldimethylsilyl)-2'-deoxyguanosine.

Mass Spec Peak	***Comments***
1074.7 m/z	N^2-Isobutyryl- O^6-benzyl-8N-(5-Aminofluorescein)-3',5'-O-bis(tert-butyldimethylsilyl)-2'-deoxyguanosine plus 2 chlorine ions
1003.3 m/z	N^2-Isobutyryl- O^6-benzyl-8N-(5-Aminofluorescein)-3',5'-O-bis(tert-butyldimethylsilyl)-2'-deoxyguanosine. (product of interest)
928.9 m/z	Product minus exocyclic amino protecting group.
894.5 m/z	Product minus O^6 Benzyl protecting group.
820.7 m/z	Product minus exocyclic amino and O^6 Benzyl protecting groups.
678.6 m/z	Product minus fluorescein moiety.
590.2 m/z	Fully unprotected dG with coupled fluorescein.

Table 6.7: Analysis of fragmentation patterns found for fraction 6 (peak 2) in the preparation of N^2-isobutyryl- O^6-benzyl-8N-(5-aminofluorescein)-3',5'-O-bis(tert-butyldimethylsilyl)-2'-deoxyguanosine.

Fraction 6 (peak 2) was once again re-injected in an effort to achieve improved purity of the coupled product. However, both NMR and mass spectrometry still showed an impure product. It is felt that the actual amount of pure product (if any) will prove to have a very low conversion yield overall making this labour intensive synthetic route difficult to justify the time and effort required. Furthermore, a minimum of 100 mg of pure fluorescently coupled product would be required for incorporation of the fluorescent nucleoside into a sequence of DNA by PCR.

6.5 Conclusion

There have been many difficulties encountered throughout the duration of this aspect of the thesis leading to the inability to isolate the final coupled nucleoside in good yields for DNA sequencing. This is despite having tried well known techniques such as Suzuki, Sonogashira, Click and Buchwald-Hartwig methods of coupling. The sole commercially available internally labelled fluorescein nucleoside is illustrated in Figure 6.27 below. However, the length of the linker is too long for its intended purpose and may only lead to self quenching of the fluorophores due to their close proximity to one another in the model photoantenna assembly.

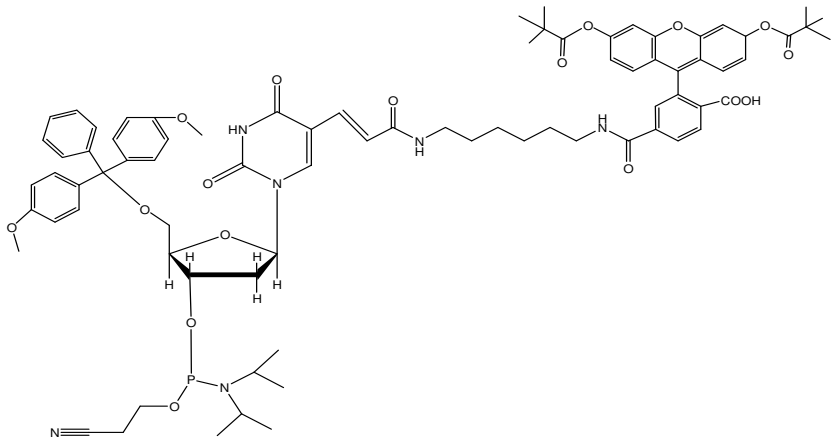

Figure 6.27: Chemical structure of a commercial fluorescein modified deoxythymidine phosphoramidite.

** Contact was made and numerous discussions held with companies who specialise in DNA modifications worldwide about the possibility of a purchasing a commercial fluorescent nucleoside. Not one had anything similar in their catalogue or were willing to take on the project for less than 50,000 euro to achieve what was attempted here.*

The shortest internally labelled fluorescent nucleoside commercially available is a carboxyltetramethylrhodamine (TAMRA) dye conjugated to a deoxycytosine phosphoramidite (Figure 6.28). As discussed above, this could prove to be quite useful as TAMRA is a well known FRET energy acceptor from a fluorescein donor molecule. As a result this may be used as the 'black hole quencher' located towards the terminal of the complimentary strand.

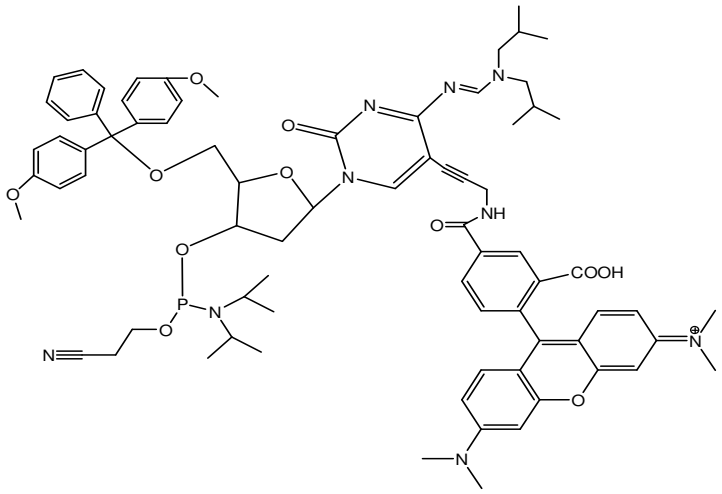

Figure 6.28: TAMRA modified deoxycytosine.

The synthetic aspect of the project has proven to be far more challenging than first considered and may take many more years before a fluorescein coupled phosphoramidite ready for DNA integration, via a short rigid linker, is achieved in manageable yields. It has been shown that the coupling reaction itself has been somewhat successful with mass spectra analysis for both Sonogashira and Buchwald-Hartwig coupling reactions indicating formation of the fluorescently conjugated nucleoside. However, the significant difficulties in purification of the fluorescent nucleoside and associated low yields to date have resulted in the termination of this project within the group. Should the coupling of a fluorescein molecule ever be achieved to the C-8 position of a nucleoside it would open up an area of synthetic chemistry that is very under researched and could have potential applications in a broad

range of scientific areas from photodynamic therapy for cancer research to light harvesting devices

If this synthetic route is to be successful more time and resources will have to be spent experimenting on a small scale initially with different reaction conditions including changing solvents, bases, additives, catalysts and in turn varying all of their chemical equivalences. Or even the possibility of altering the base to a more reactive nucleoside or changing the fluorescent molecule itself, all of which will entail a significant body of work. Above all, it is the Buchwald-Hartwig method of coupling that has shown the most promise out of all the coupling reactions attempted and there is no reason to suggest that another method of coupling might provide superior results.

6.6 References

(1) Wang, S.; Gaylord, B. S.; Bazan, G. C. *J. Am. Chem. Soc.* **2004***, 126*, 5446-5451.

(2) Vrabel, M.; Pohl, R.; Klepetarova, B.; Votruba, I.; Hocek, M. *Org. Biomol. Chem.* **2007***, 5*, 2849-2857.

(3) Jager, S.; Rasched, G.; Kornreich-Leshem, H.; Engeser, M.; Thum, O.; Famulok, M. *J. Am. Chem. Soc.* **2005***, 127*, 15071-15082.

(4) Tyagi, S.; Kramer, F. R. *Nat Biotech* **1996***, 14*, 303-308.

(5) Salic, A.; Mitchison, T. J. *Proceedings of the National Academy of Sciences* **2008***, 105*, 2415-2420.

(6) Pray, L. *Nature Education* **2008***, 1*.

(7) Sabanayagam, C. R.; Eid, J. S.; Meller, A. *J. Chem. Phys.* **2005***, 123*, 224708.

(8) Sykora, M.; Maxwell, K. A.; DeSimone, J. M.; Meyer, T. J. *Proceedings of the National Academy of Sciences* **2000***, 97*, 7687-7691.

(9) Gust, D.; Moore, T. A.; Moore, A. L. *Acc. Chem. Res.* **2001***, 34*, 40-48.

(10) Konishi, T.; Ikeda, A.; Shinkai, S. *Tetrahedron* **2005***, 61*, 4881-4899.

(11) Western, E. C.; Shaughnessy, K. H. *J. Org. Chem.* **2005***, 70*, 6378-6388.

(12) Western, E. C.; Daft, J. R.; Johnson, E. M.; Gannett, P. M.; Shaughnessy, K. H. *J. Org. Chem.* **2003***, 68*, 6767-6774.

(13) Collier, A.; Wagner, G. *Org. Biomol. Chem.* **2006***, 4*, 4526-4532.

(14) Saito, Y.; Matsumoto, K.; Bag, S. S.; Ogasawara, S.; Fujimoto, K.; Hanawa, K.; Saito, I. *Tetrahedron,* **2008***, 64*, 3578-3588.

(15) Saito, Y.; Matsumoto, K.; Bag, S. S.; Ogasawara, S.; Suzuka, I.; Saito, I. *NUCLEIC ACIDS SYMP SER (OXF)* **2007***, 51*, 147-148.

(16) Firth, A. G.; Fairlamb, I. J. S.; Darley, K.; Baumann, C. G. *Tetrahedron Letters,* **2006***, 47*, 3529-3533.

(17) Wang, Z.; Rizzo, C. J. *Org. Lett.* **2001***, 3*, 565-568.

(18) Boge, N.; Krueger, S.; Schroeder, M.; Meier, C. *Synthesis-Stuttgart* **2007**, 3907-3914.

(19) Meier, C.; Grasl, S. *Synlett* **2002**, 802-804.

(20) Gillet, L. C. J.; Scharer, O. D. *Org. Lett.* **2002***, 4*, 4205-4208.

(21) He, G. -.; Krawczyk, S. H.; Swaminathan, S.; Shea, R. G.; Dougherty, J. P.; Terhorst, T.; Law, V. S.; Griffin, L. C.; Coutre, S.; Bischofberger, N. *J. Med. Chem.* **1998***, 41*, 2234-2242.

(22) Ogasawara, S.; Maeda, M. *Angewandte Chemie International Edition* **2009**, *48*, 6671-6674.

(23) Ogasawara, S.; Maeda, M. *Angewandte Chemie* **2008**, *120*, 8971-8974.

(24) Flasche, W.; Cismas, C.; Herrmann, A.; Liebscher, J. *Stuttgart* **2004**, 2335-2341.

(25) Vrabel, M.; Pohl, R.; Votruba, I.; Sajadi, M.; Kovalenko, S. A.; Ernsting, N. P.; Hocek, M. *Organic & Biomolecular Chemistry* **2008**, *6*, 2852-2860.

(26) Hurley, D. J.; Tor, Y. *J. Am. Chem. Soc.* **2002**, *124*, 13231-13241.

(27) Thoresen, L. H.; Jiao, G.; Haaland, W. C.; Metzker, M. L.; Burgess, K. *Chemistry - A European Journal* **2003**, *9*, 4603-4610.

(28) Telser, J.; Cruickshank, K. A.; Morrison, L. E.; Netzel, T. L. *J. Am. Chem. Soc.* **1989**, *111*, 6966-6976.

(29) Cuppoletti, A.; Cho, Y.; Park, J.; Strsssler, C.; Kool, E. T. *Bioconjug. Chem.* **2005**, *16*, 528-534.

(30) Skorobogatyi, M. V.; Malakhov, A. D.; Pchelintseva, A. A.; Turban, A. A.; Bondarev, S. L.; Korshun, V. A. *ChemBioChem* **2006**, *7*, 810-816.

(31) Singleton, S. F.; Roca, A. I.; Lee, A. M.; Xiao, J. *Tetrahedron,* **2007**, *63*, 3553-3566.

(32) Seo, T. S.; Li, Z.; Ruparel, H.; Ju, J. *J. Org. Chem.* **2003**, *68*, 609-612.

(33) Sigmund, H.; Pfleiderer, W. Nucleotides. Part LXXI. *Helv. Chim. Acta* **2003**, *86*, 2299-2334.

(34) Jiao, G.; Han, J. W.; Burgess, K. *J. Org. Chem.* **2003**, *68*, 8264-8267.

(35) Murata, M.; Oyama, T.; Watanabe, S.; Masuda, Y. *J. Org. Chem.* **2000**, *65*, 164-168.

(36) Han, J. W.; Castro, J. C.; Burgess, K. *Tetrahedron Letters,* **2003**, *44*, 9359-9362.

(37) Baudoin, O.; Guenard, D.; Gueritte, F. *J. Org. Chem.* **2000**, *65*, 9268-9271.

(38) Jiao, G.; Thoresen, L. H.; Burgess, K. *J. Am. Chem. Soc.* **2003**, *125*, 14668-14669.

(39) Rotman, A.; Heldman, J. *Biochemistry* **1981**, *20*, 5995-5999.

(40) Rotman, A.; Heldman, J. *FEBS Letters,* **1980**, *122*, 215-218.

(41) Margulies., *nature materials* **2005**, *4*, 768.

(42) Ueno, T.; Urano, Y.; Setsukinai, K.; Takakusa, H.; Kojima, H.; Kikuchi, K.; Ohkubo, K.; Fukuzumi, S.; Nagano, T. *J. Am. Chem. Soc.* **2004**, *126*, 14079-14085.

(43) Joseph R. Lakowicz In *Principles of Fluorescence Spectroscopy;* Springer: 2006.

(44) Jiao, G.; Thoresen, L. H.; Kim, T. G.; Haaland, W. C.; Gao, F.; Topp, M. R.; Hochstrasser, R. M.; Metzker, M. L.; Burgess, K. *Chemistry - A European Journal* **2006***, 12*, 7816-7826.

(45) Christophersen, C.; Begtrup, M.; Ebdrup, S.; Petersen, H.; Vedso, P. *J. Org. Chem.* **2003***, 68*, 9513-9516.

(46) Fang, H.; Kaur, G.; Yan, J.; Wang, B. *Tetrahedron Letters,* **2005***, 46*, 1671-1674.

(47) Borylation Catalytic Cycle. *www.organic-chemistry.org* (accessed 05/27/2009).

(48) Capek, P.; Vrabel, M.; Hasnik, Z.; Pohl, R.; Hocek, M. *Synthesis-Stuttgart* **2006**, 3515-3526.

(49) Hobley, G.; Gubala, V.; Rivera-Sanchez, M. D.; Rivera, J. M. *Synlett* **2008**, 1510-1514.

(50) Hosoya, T.; Inoue, A.; Hiramatsu, T.; Aoyama, H.; Ikemoto, T.; Suzuki, M. Facile *Bioorg. Med. Chem.* **2009***, 17*, 2490-2496.

(51) Suzuki, A. *Journal of Organometallic Chemistry* **1999***, 576*, 147-168.

(52) Miyaura, N.; Suzuki, A. *Chem. Rev.* **1995***, 95*, 2457-2483.

(53) Gannett, P. M.; Heavner, S.; Daft, J. R.; Shaughnessy, K. H.; Epperson, J. D.; Greenbaum, N. L. *Chem. Res. Toxicol.* **2003***, 16*, 1385-1394.

(54) Suzuki Couling Catalytic Cycle. *www.organic-chemistry.org* (accessed 05/27/2009).

(55) Chen, Y.; Lee, G.; Peng, S.; Yeh, C. *Tetrahedron Letters,* **2005***, 46*, 1541-1544.

(56) Hikishima, S.; Hashimoto, M.; Magnowska, L.; Bzowska, A.; Yokomatsu, T. *Bioorganic & Medicinal Chemistry Letters,* **2007***, 17*, 4173-4177.

(57) Hocek, M.; Stepnicka, P.; Ludvik, J.; Cisarova, I.; Votruba, I.; Reha, D.; Hobza, P. *Chemistry-a European Journal* **2004***, 10*, 2058-2066.

(58) Kaucher, M. S.; Davis, J. T. *Tetrahedron Letters,* **2006***, 47*, 6381-6384.

(59) Xiao, Q.; Ranasinghe, R. T.; Tang, A. M. P.; Brown, T. *Tetrahedron,* **2007***, 63*, 3483-3490.

(60) Sonogashira Coupling Catalytic Cycle. *www.organic-chemistry.org* (accessed 08/14/2009).

(61) Cassidy, M. P.; Raushel, J.; Fokin, V. V. *Angewandte Chemie-International Edition* **2006***, 45*, 3154-3157.

(62) Gierlich, J.; Burley, G. A.; Gramlich, P. M. E.; Hammond, D. M.; Carell, T. *Org. Lett.* **2006***, 8*, 3639-3642.

(63) Kolb, H. C.; Sharpless, K. B. *Drug Discov. Today* **2003***, 8*, 1128-1137.

(64) Tron, G. C.; Pirali, T.; Billington, R. A.; Canonico, P. L.; Sorba, G.; Genazzani, A. *Med. Res. Rev.* **2008**, *28*, 278-308.

(65) Weller, R. L.; Rajski, S. R. *Org. Lett.* **2005**, *7*, 2141-2144.

(66) Barral, K.; Moorhouse, A. D.; Moses, J. E. *Org. Lett.* **2007**, *9*, 1809-1811.

(67) Seela, F.; Sirivolu, V. R.; Chittepu, P. *Bioconjug. Chem.* **2008**, *19*, 211-224.

(68) Seela, F.; Sirivolu, V. R. *Nucleosides, Nucleotides and Nucleic Acids* **2007**, *26*, 597.

(69) Seela, F.; Sirivolu, V. R. *Helv. Chim. Acta* **2007**, *90*, 535.

(70) Demko, Z. P.; Sharpless, K. B. *Angewandte Chemie* **2002**, *114*, 2214-2217.

(71) Finnegan, W. G.; Henry, R. A.; Lofquist, R. *J. Am. Chem. Soc.* **1958**, *80*, 3908-3911.

(72) Shie, J.; Fang, J. Microwave-Assisted One-Pot Tandem Reactions for Direct Conversion of Primary Alcohols and Aldehydes to Triazines and Tetrazoles in Aqueous Media. *J. Org. Chem.* **2007**, *72*, 3141-3144.

(73) Demko, Z. P.; Sharpless, K. B. *J. Org. Chem.* **2001**, *66*, 7945-7950.

(74) Click Chemistry Catalytic Cycle. *www.organic-chemistry.org* (accessed 07/03/2009).

(75) Wolfe, J. P.; Wagaw, S.; Buchwald, S. L. *J. Am. Chem. Soc.* **1996**, *118*, 7215-7216.

(76) Wolfe, J. P.; Rennels, R. A.; Buchwald, S. L. *Tetrahedron* **1996**, *52*, 7525-7546.

(77) Wolfe, J. P.; Wagaw, S.; Marcoux, J. F.; Buchwald, S. L. *Acc. Chem. Res.* **1998**, *31*, 805-818.

(78) Ge, N.; Szombati, Z.; Meier, C. *Nucleosides Nucleotides Nucleic Acids* **2007**, *26*, 705-708.

(79) Böge, N.; Jacobsen, M. I.; Szombati, Z.; Baerns, S.; Pasquale, F. D.; Marx, A.; Meier, C. *Chemistry - A European Journal* **2008**, *14*, 11194-11208.

(80) Hartwig, J. F., *Metal Complexes as Catalysts for Carbon-heteroatom Cross-coupling Reactions;* J. A. McCleverty, T. J. Meyer, Eds.; Comprehensive Coordination Chemistry II; Pergamon: Oxford, **2003**, 369-398.

(81) Hartwig, J. F. *Acc. Chem. Res.* **1998**, *31*, 852-860.

(82) Harvey, R. G.; Dai, Q.; Ran, C. Z.; Lim, K.; Blair, I.; Penning, T. M. *Polycycl. Aromat. Compd.* **2005**, *25*, 371-391.

(83) Meier, C. *Nucleosides Nucleotides Nucleic Acids* **2003**, *22*, 1119-1121.

(84) Schoffers, E.; Olsen, P. D.; Means, J. C. *Org. Lett.* **2001**, *3*, 4221-4223.

(85) Boege, N.; Graesl, S.; Meier, C. *J. Org. Chem.* **2006**, *71*, 9728-9738.

(86) Boege, N.; Schroeder, M.; Meier, C. *Synlett* **2008**, 1066-1070.

(87) Meyers, C.; Maes, B. U. W.; Loones, K. T. J.; Bal, G.; Lemiare, G. L. F.; Dommisse, R. A. *J. Org. Chem.* **2004***, 69*, 6010-6017.

(88) Christensen, H.; Kiil, S.; Dam-Johansen, K.; Nielsen, O.; Sommer, M. B. *Organic Process Research & Development* **2006***, 10*, 762-769.

Chapter 7: Conclusions and Future Work

"There are three types of people in this world: those who make things happen, those who watch things happen and those who wonder what happened" – Mary Kay Ash.

7.0 Conclusions and Future Work

This thesis focussed on the assembly of supramolecular bioconjugates of metal complexes and also of fluorescein for application in cellular imaging and as model solar antennae respectively. Chapter 3 detailed the synthesis and a detailed comparative study of the spectroscopic, photophysical and redox characterisation of a series of three water soluble photoactive ruthenium (II) polypyridyl complexes containing bipyridyl ligands and only differed in their terminal functionality on the pH sensitive phenthroline based ancillary ligand. These complexes had been synthesised previously but this is the first study to compare their electronic and photophysical properties. The carboxyl and amino functional derivatives displayed many similar properties including long aqueous lifetime, red emission characteristics, large Stokes shifts and pH/oxygen sensitivity. In contrast, the nitro functionalised complex, $[Ru(bpy)_2(picNO_2)]^{2+}$, exhibited very weak emission intensity and short excited state lifetime attributed to the electron withdrawing ability of the nitro group which lead to an increase in non-radiative decay.

The purpose of synthesising amino and carboxy functionalised luminophores was to aid conjugation of these complexes into extended supramolecular structures for cell imaging probes via amide linkages. In the second part of Chapter 3, the amino functionalised ruthenium (II) complex was conjugated to polyethylene glycol linkers of approximately 3 nm and 13 nm chain lengths with thiol termini to permit their assembly to 50 nm gold nanoparticles. This allowed for the efficient transport, of an otherwise non-permeable luminophore, across the cellular membrane of mammalian cells. Preliminary studies on the influence of chain length on the photophysics of these assembly showed that at a distance of 3 nm from the gold metal substrate the luminescence of the ruthenium dye decreased, however, emission was not completely quenched. Interestingly, both emission intensity and lifetime of the probe was enhanced at a distance of 13 nm (in linear conformation) from nanoparticle to luminophore, suggesting the close-packed nature of the monolayer rather than the nanoparticles itself exerts the greatest influence on the photophysics of the luminophore. The nanoparticle conjugates were water soluble which aided study of their interactions with mammalian SP2 cells without the need to permeabalise the cell's membrane. Results showed that whereas the parent dye was unable to transport across the cell's lipid bilayer the PEG

conjugated complex and the functionalised gold nanoparticles, were readily uptaken by the cells and distrubuted throughout the cytoplasm.

Chapter 4 detailed the synthesis and characterisation of a series of novel water insoluble iridium (III) polypyridyl complexes. It had been reported that many iridium (III) complexes exhibited favourable characteristics such as longer phosphorescent lifetimes, larger quantum yields and tunable emission from blue to red when compared to ruthenium metal complexes. This proved to be the case with $[Ir(dfpp)_2(picCOOH)]^+$ as it displayed lifetimes and quantum yields in organic media above that of other ruthenium complexes synthesised as part if this thesis. However, in aqueous solution this iridium complex did not exhibit lifetimes on par with other ruthenium complexes. This suggests that such an iridium probe may not be as well suited for the analysis of biological samples and furthermore, the wavelength of excitation necessary may not be as amiable to tissue sample as the ruthenium dyes synthesised. However, $[Ir(dfpp)_2(picCOOH)]^+$, displayed pH sensitivity in both Raman spectra and lifetimes and Chapter 5 detailed its conjugation to a CPP for use as a molecular imaging probe.

Unfortunately, the lifetimes and quantum yields of the other iridium (III) complexes synthesised, $[Ir(dfpp)_2(napthNO_2)]^+$ and $[Ir(dfpp)_2(napthNH_2)]^+$, were not as great as their unfunctionalised parent complex suggested. Furthermore, without a pH sensitive ligand present, the use of such a luminescent molecular probe is limited and it was decided not to continue in efforts to label biomolecules with these particular iridium dyes. However, to date there is very little published on the characterisation, especially Raman and FTIR characterisation, of iridium (III) complexes. With this in mind, the three iridium complexes are currently undergoing DFT calculations and along with the existing photophysical and vibrational spectroscopy results a paper will be submitted to serve as a template for similar iridium complexes.

Chapter 5 discussed the conjugation of ruthenium (II) and novel iridium (III) polypyridyl complexes synthesised in Chapters 3 & 4 to a CPP. The conjugation of the carboxyl functionalised ruthenium complex to octarginine has been reported by our group previously as an efficient multimodal molecular probe in determining intercellular pH and oxygen levels within SP2 myeloma cells. However, this is the first time to our knowledge that an iridium (III) probe has been successfully conjugated to a

CPP for the purposes of cellular imaging. In SP2 and CHO cells, results showed how the lone parent dye complexes failed to transport efficiently across the cell membrane. However, upon conjugation to the octarginine peptide both ruthenium and iridium luminophores showed internalisation within the cell without the need for permeabalising the cellular structure. One concern published in the literature on metal complexes in cellular imaging is the use of organic solvents, such as DMSO and ethanol, to aid solubility issues in cellular uptake experiments. This concern is confirmed by experiments performed in Chapter 5 that illustrated the cytotoxic effect of such solvents towards SP2 and CHO cell lines.

Conjugation of the iridium (III) dye to the polypeptide dramatically increased its aqueous solubility and with it, its ability to diffuse across the cell membrane of the mammalian cells without the need for organic solvents. However, the ruthenium probe remains the more attractive proposition for use as a molecular imaging probe when compared to the iridium equivalent. The ruthenium conjugate displayed an aqueous lifetime more then five times greater, however, its quantum yield is only 60% that seen for the iridium conjugate.

Furthermore, the cytotoxicity of the iridium probe is far greater when compared to the ruthenium conjugate. Extensive cell death was also exhibited in both SP2 and CHO cells at a final iridium conjugate concentration of 70 μM in times as short as 10 minutes under 375 nm irradiation. This was confirmed using a DRAQ7 localising dye, which only stains the nucleus of dead cells. However, the ruthenium dye-peptide also exhibited increased cell death as a result of 375 nm irradiation when compared with 458 nm excitation. Interestingly, when no dye is present under continuous excitation at 375 nm and 458 nm there is minimal evidence of cell death, as observed with the viability dye DRAQ7. This suggests that the increased cell death of the iridium complexes is a result of the energy of excitation and also potentially due to a light activated process, which most likely thought to be the generation of singlet oxygen ($^1O_2$) through an electron and energy transfer process. This is further supported by preliminary experiments using ascorbic acid as a singlet oxygen scavenger which has resulted in a reduction in cell cytotoxicity of the iridium peptide from 50% to 5% under similar experimental conditions preformed here. Other explanations for its increased cytotoxicity may include the fluorination of the cyclometalating ligands, the larger

iridium metal centre and longer phosphorescent quantum yields and lifetimes under particular conditions that will also have an impact on the generation of singlet oxygen.

Finally, the most ambitious synthetic aspect of this thesis saw the attempt in creating a model photoantenna based on an interfacial DNA scaffold in Chapter 6. It was hoped that the immobilisation of a fluorescently modified DNA sequence would yield a supramolecular assembly capable of the conversion of light energy into electrical energy. Unfortunately, the conjugation of the fluorescein moiety to deoxyguanosine via a short and rigid linker proved problematic. Despite attempting many coupling techniques such as Suzuki coupling, Sonogashira coupling, click chemistry and Buchwald-Hartwig coupling the fluorescent nucleoside was never isolated in sufficient quantities for incorporation into a sequence of DNA.

Future work to emerge from this thesis will focus on extending and quantifying the application of the probes produced here in cellular imaging. For the supramolecular ruthenium-PEG modified nanoparticles, this work demonstrated that stable nanoparticles assemblies incorporating the ruthenium centres can be formed by the approached outlined here and that depending on chain length, the metal complex retains its photophysical properties. The potential for these materials in multimodal SERS /luminescence imaging will be the main focus of future work in these materials as well as detailed studies of cellular uptake, cell viability and cell localisation studies.

For the ruthenium and iridium peptide conjugates further work is ongoing concerning the attachment of target specific peptides to existing cell penetrating dye peptides with the intention of selectively targeting certain cell organelles. In addition, it is proposed to study the singlet oxygen generating ability of these transition metal complexes that may possibly result in the targeted cell death of tumour cells. Further experiments would include assessment of the iridium conjugate as a multimodal imaging probe to determine intracellular pH and oxygen levels using Raman and FLIM measurements respectively. Additional experiments could also include photostability and bleaching studies of the molecular imaging probe.

For the DNA model photoantenna work, dye to the complexity of the synthesis, this work was terminated within the group but any potential future work on this aspect of the research should involve looking at using an alternative more reactive base, such as thymine, as guanine is known to be the most unreactive of the four bases. Synthetic conditions such as reaction times, base used, catalytic equivalences etc. will also have to be studied in greater detail as they are known to play a critical role in the coupling reactions. However, it is the Buchwald-Hartwig method of coupling that gives rise to the most promise and it is recommended that this method of coupling is pursued.

Many of the supramolecular synthetic strategies attempted in this thesis have shown potential applications in solar energy conversion, enhancing emission efficiencies of photoactive components, increasing aqueous solubility of metal complexes and using inorganic complexes as multimodal imaging probes. Of particular interest, this thesis detailed the ongoing intense efforts to come up with new dyes and multimodal strategies to aid biochemical understanding of cellular processes and medical diagnostics and described potential molecular probes capable of making advances in these areas.

From solar energy conversion to biomedical diagnostics to multimodal cellular imaging, both inorganic and organic photoactive supramolecular assemblies have provided numerous fascinating applications in every aspect of science. With the push to find alternative fuels, more sensitive and selective diagnostic devices and improving on existing technologies the research into photoactive supramolecular assemblies will only continue to intensify well into the future.

Appendix 1: NMR and Mass Spectrometry Results

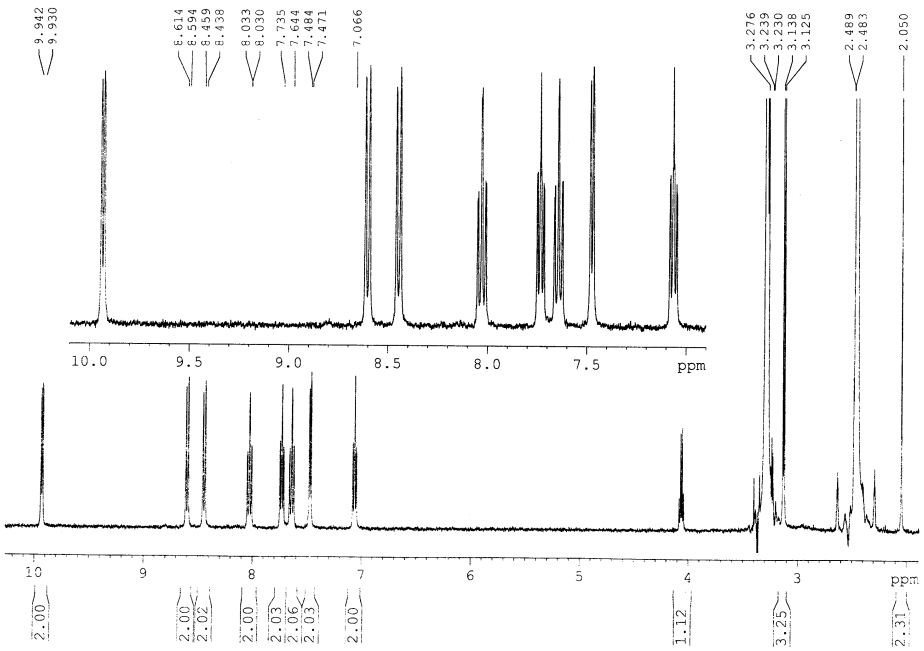

Figure A1: ^{1}H-NMR of $[Ru(bpy)_2Cl_2)]^{2+}$ in DMSO-d_6.

bpy proton	**$[Ru(bpy)_2Cl_2]$ ppm**
H_3	9.94 (d, 2H)
$H_{3'}$	8.60 (d, 2H)
H_6	8.45 (d, 2H)
$H_{4'}$	8.03 (t, 2H)
H_4	7.74 (t, 2H)
H_5	7.64 (t, 2H)
$H_{6'}$	7.47 (d, 2H)
$H_{5'}$	7.07 (t, 2H)

Table A1: ^{1}H-NMR resonances for $[Ru(bpy)_2Cl_2]$, carried out in DMSO-d_6. The integration and peak splitting are shown in brackets.

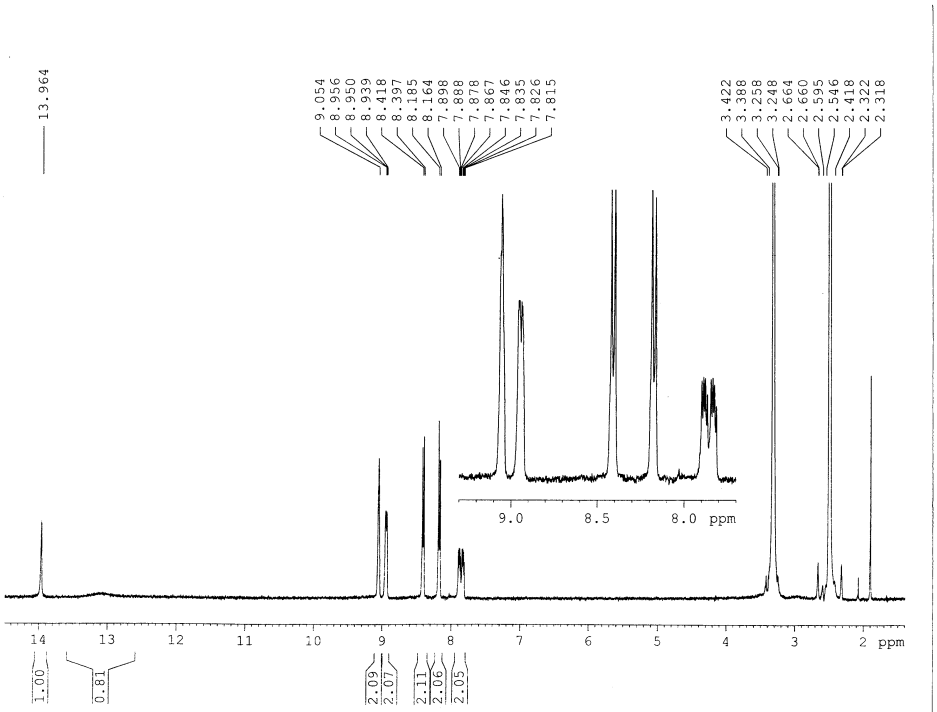

Figure A2: ^{1}H-NMR of [picCOOH] ligand in DMSO-d_6.

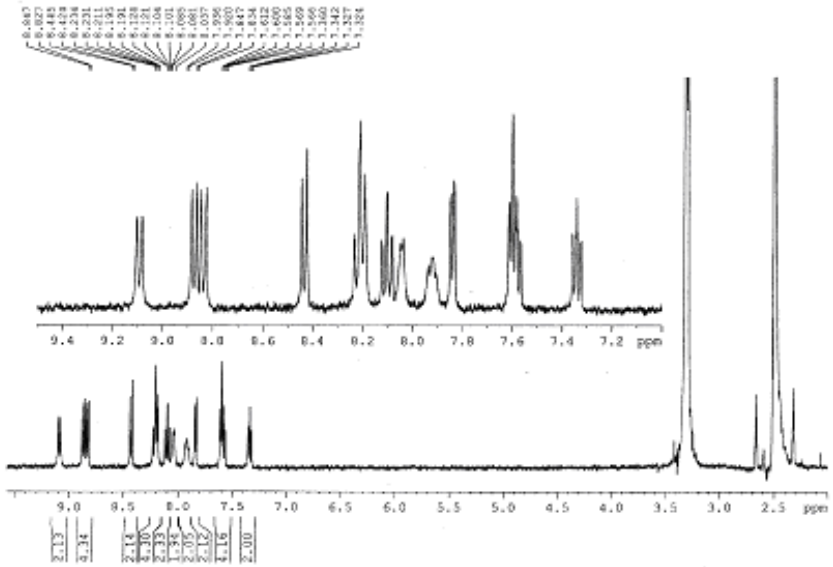

Figure A3: ^{1}H-NMR of $[Ru(bpy)_2(picCOOH)]^{2+}$ in DMSO-d_6.

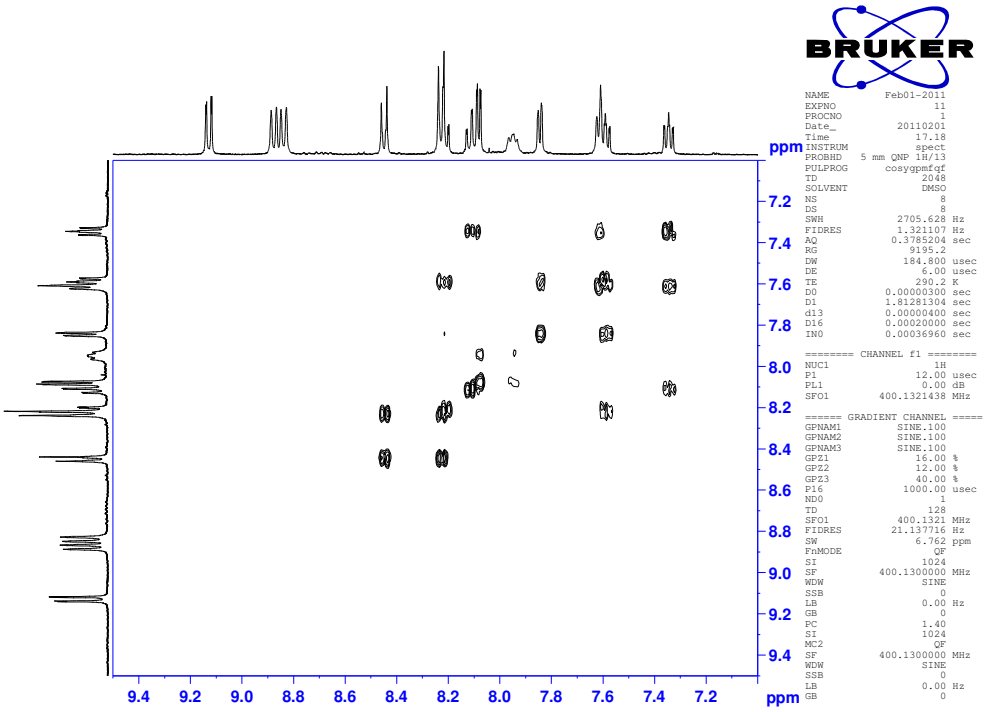

Figure A4: COSY 45 spectrum of $[Ru(bpy)_2(picCOOH)]^{2+}$ in DMSO-d_6.

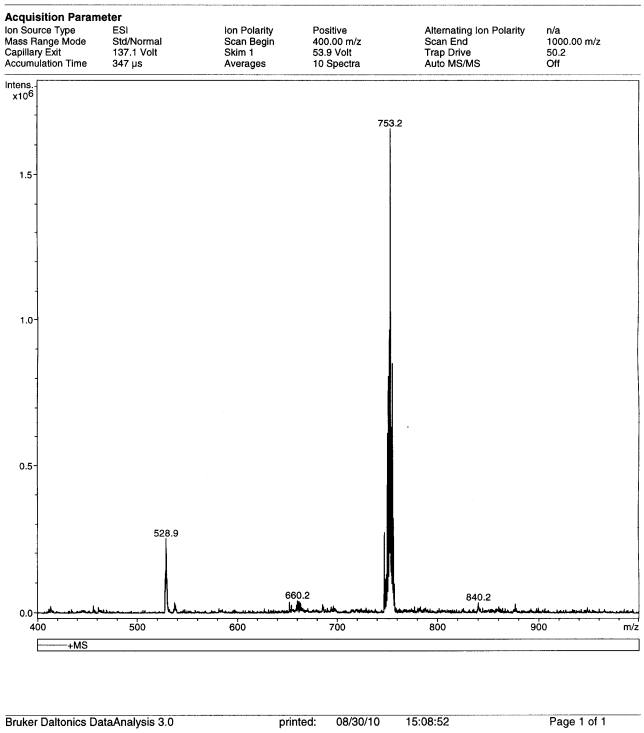

Figure A5: Mass spectrum of $[Ru(bpy)_2(picCOOH)]^{2+}$.

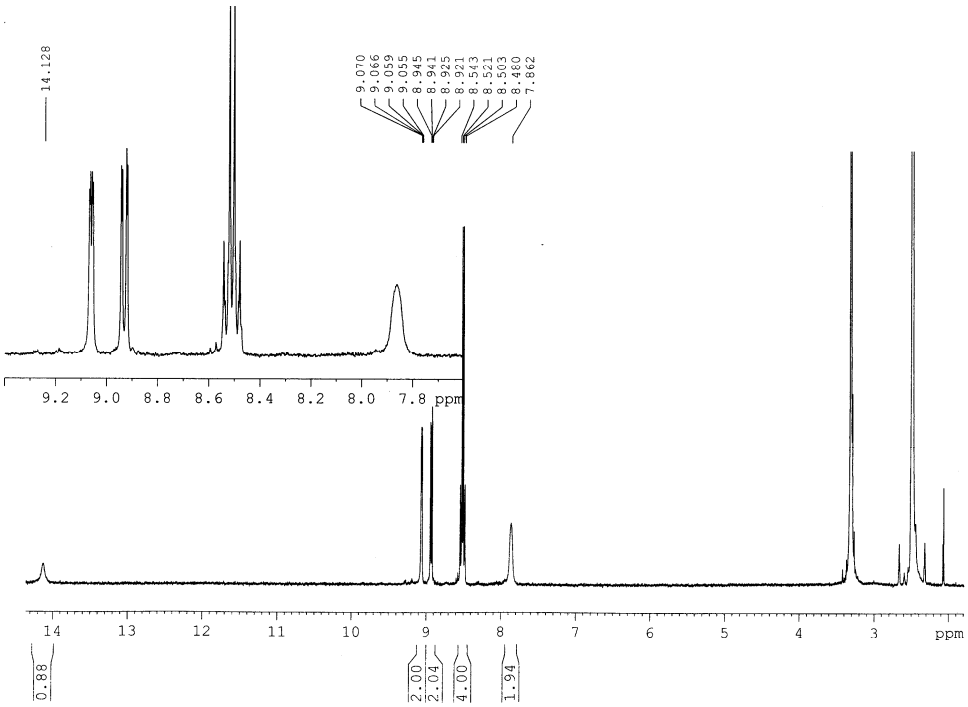

Figure A6: ^{1}H-NMR of [picNO$_2$] ligand in DMSO-d$_6$.

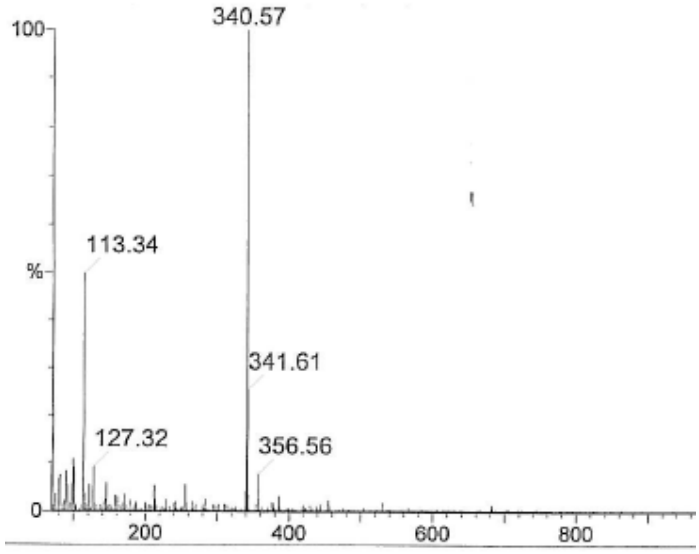

Figure A7: Mass spectrum of [picNO$_2$] ligand.

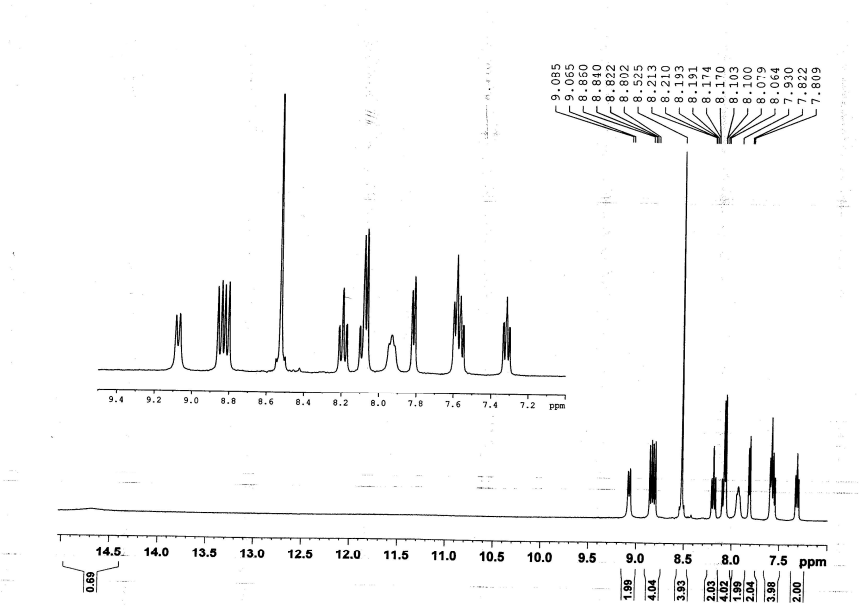

Figure A8: ^{1}H-NMR of $[Ru(bpy)_2(picNO_2)]^{2+}$ in DMSO-d_6.

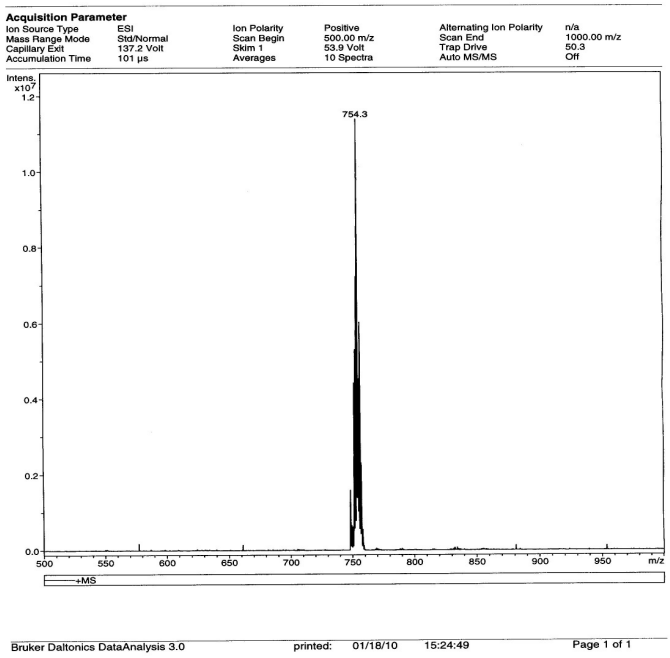

Figure A9: Mass spectrum of $[Ru(bpy)_2(picNO_2)]^{2+}$.

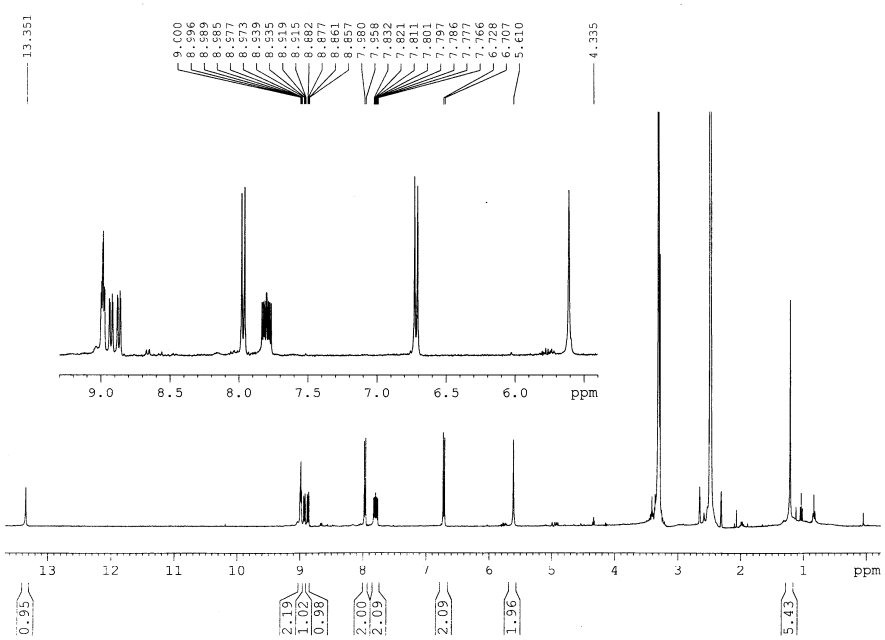

Figure A10: ^{1}H-NMR of [picNH$_2$] ligand in DMSO-d$_6$.

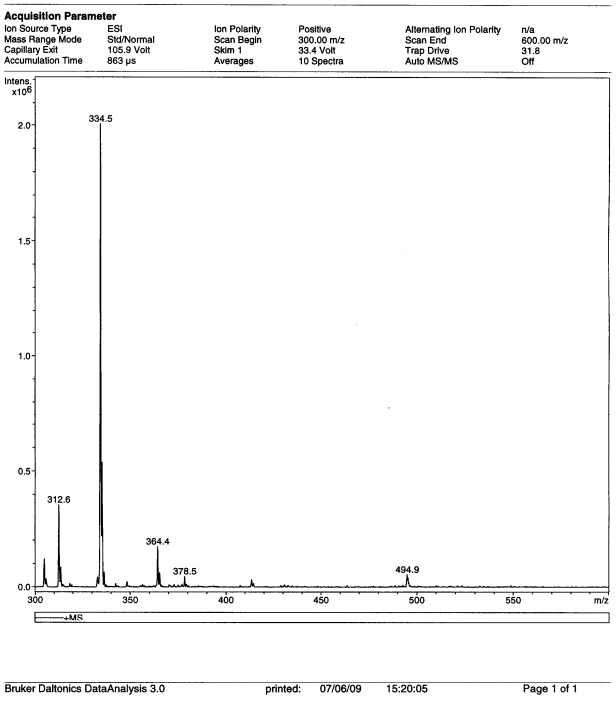

Figure A11: Mass spectrum of [picNH$_2$] ligand.

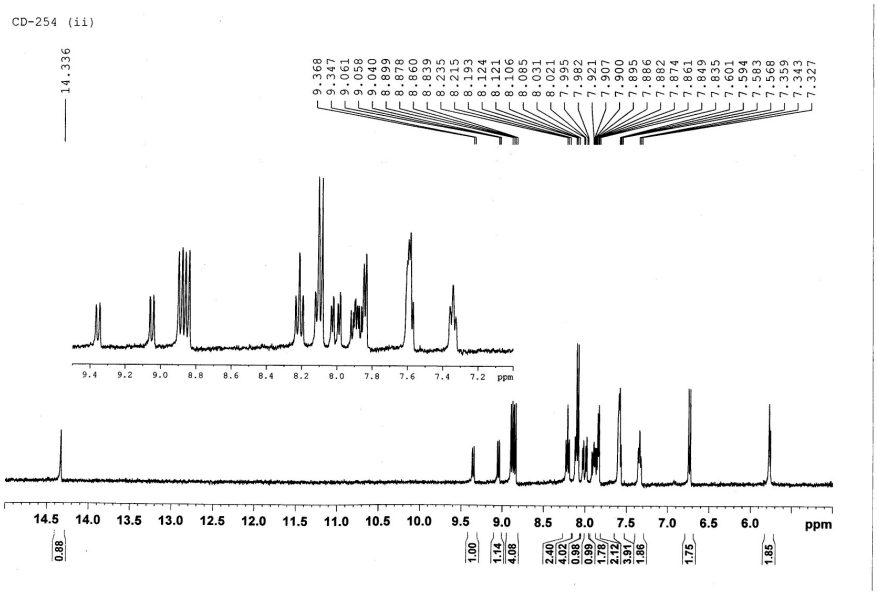

Figure A12: ^{1}H-NMR of $[Ru(bpy)_2(picNH_2)]^{2+}$ in DMSO-d_6.

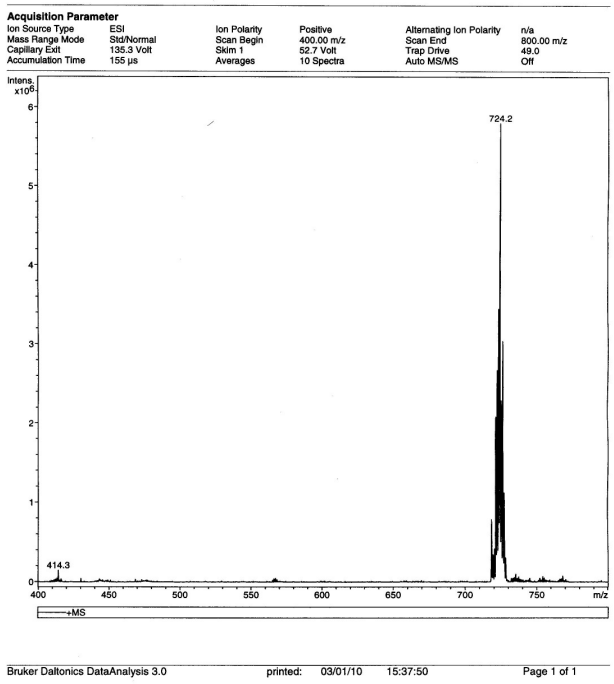

Figure A13: Mass spectrum of $[Ru(bpy)_2(picNH_2)]^{2+}$.

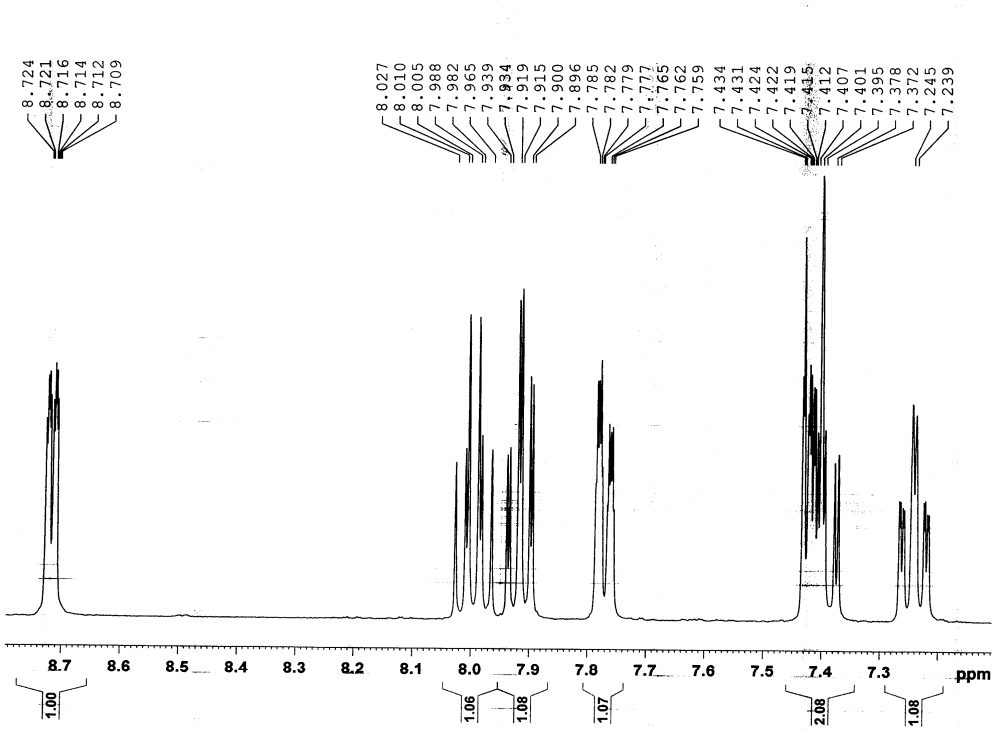

Figure A14: [1]H-NMR of 2-(4,6-difluorophenyl)pyridine [dfpp] in DMSO-d_6.

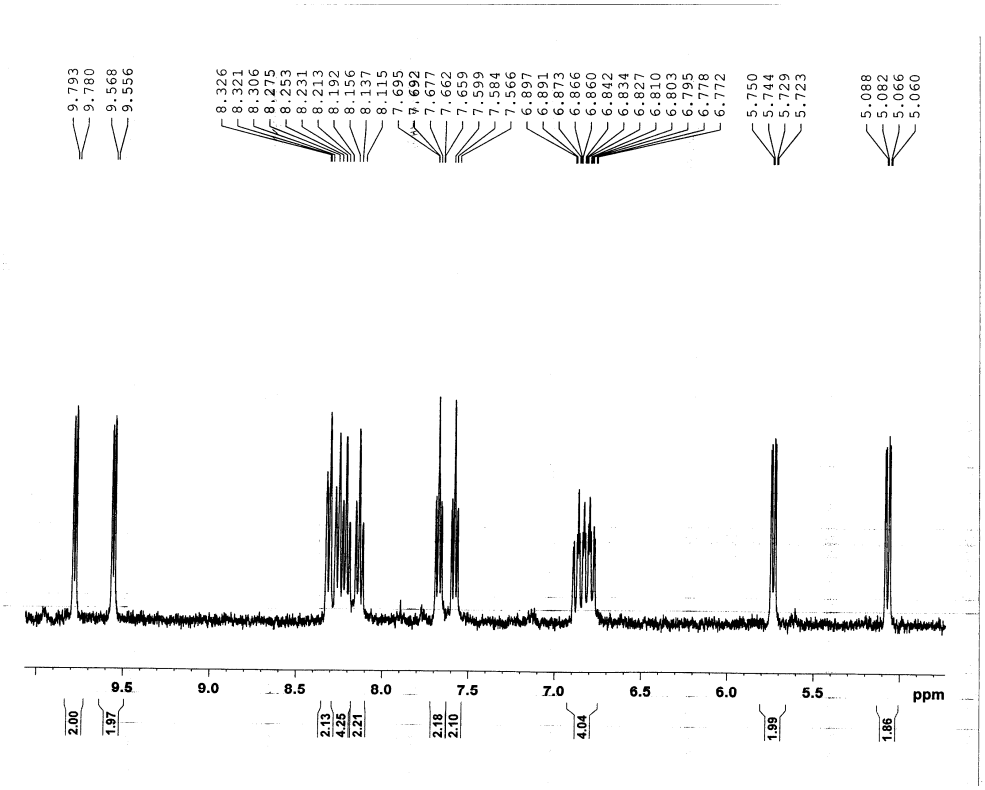

Figure A15: [1]H-NMR of [$Ir_2(dfpp)_4(Cl_2)$] in DMSO-d_6.

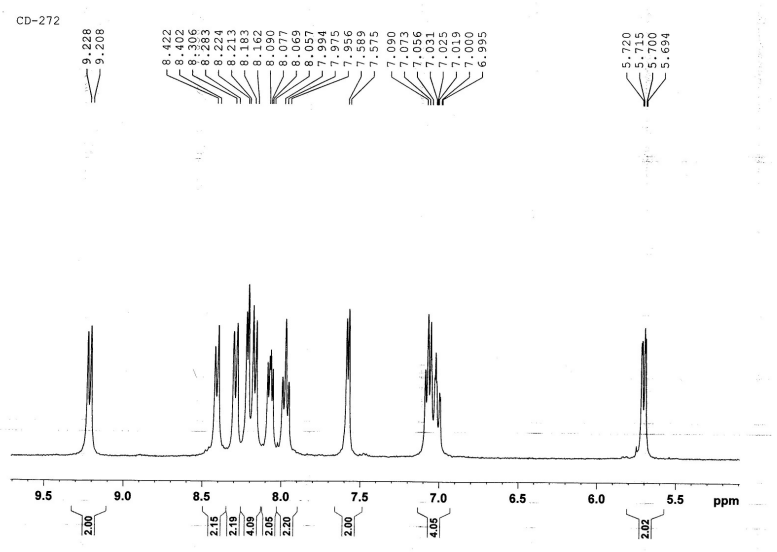

Figure A16: ^{1}H-NMR of [Ir(dfpp)$_2$(picCOOH)]$^+$ in DMSO-d_6.

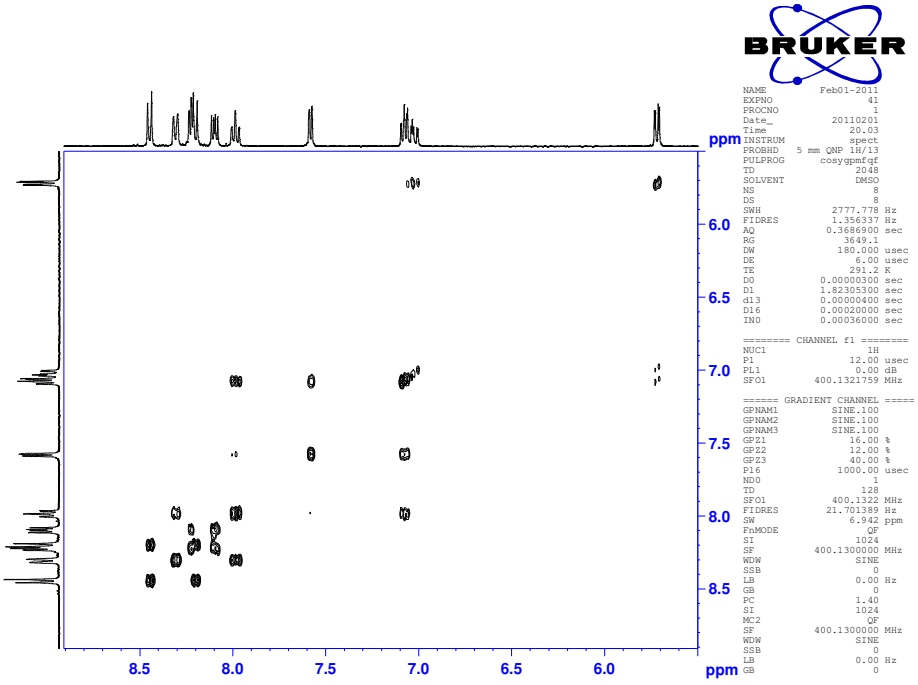

Figure A17: COSY 45 spectrum of [Ir(dfpp)$_2$(picCOOH)]$^+$ in DMSO-d_6.

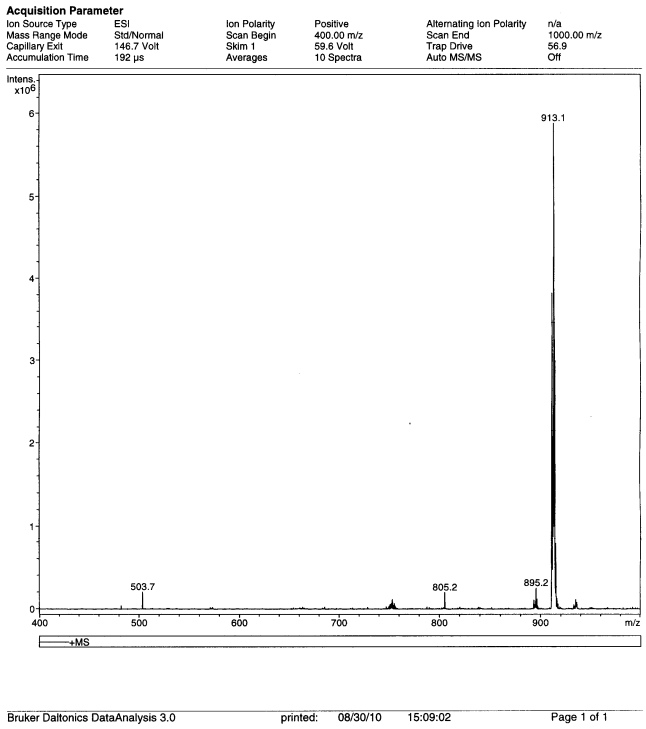

Figure A18: Mass spectrum of $[Ir(dfpp)_2(picCOOH)]^+$.

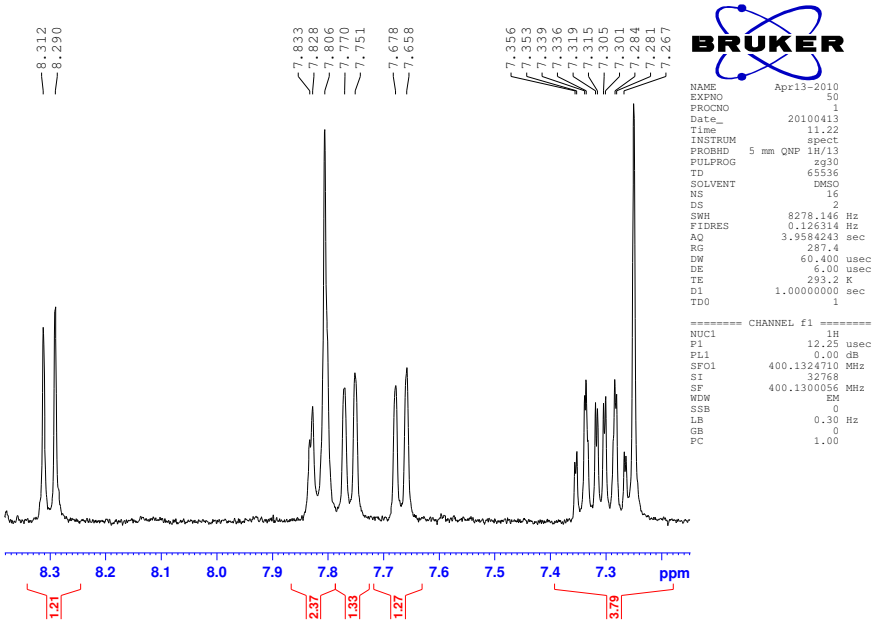

Figure A19: ^{1}H-NMR of $[NapthNO_2]$ ligand in DMSO-d_6.

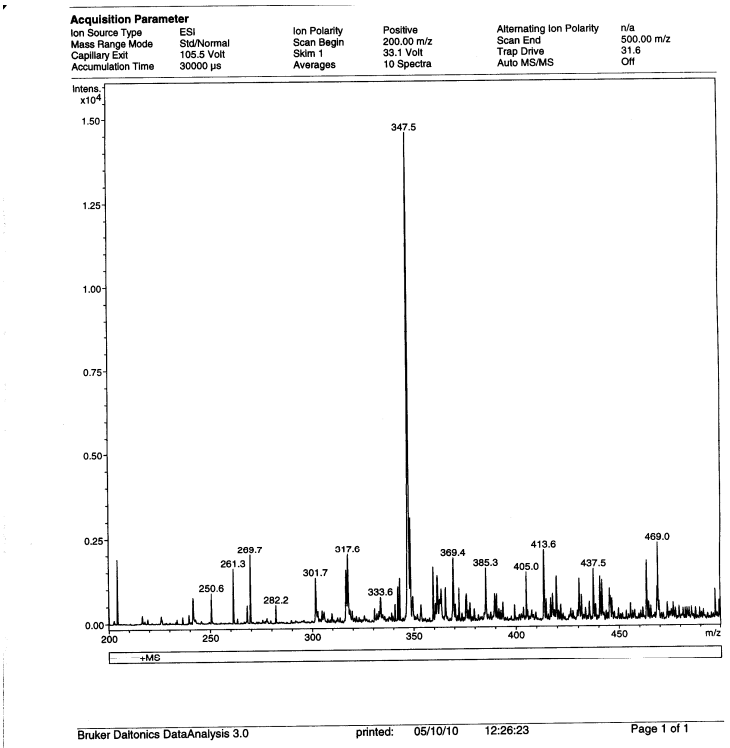

Figure A20: Mass spectrum of [NapthNO$_2$] ligand.

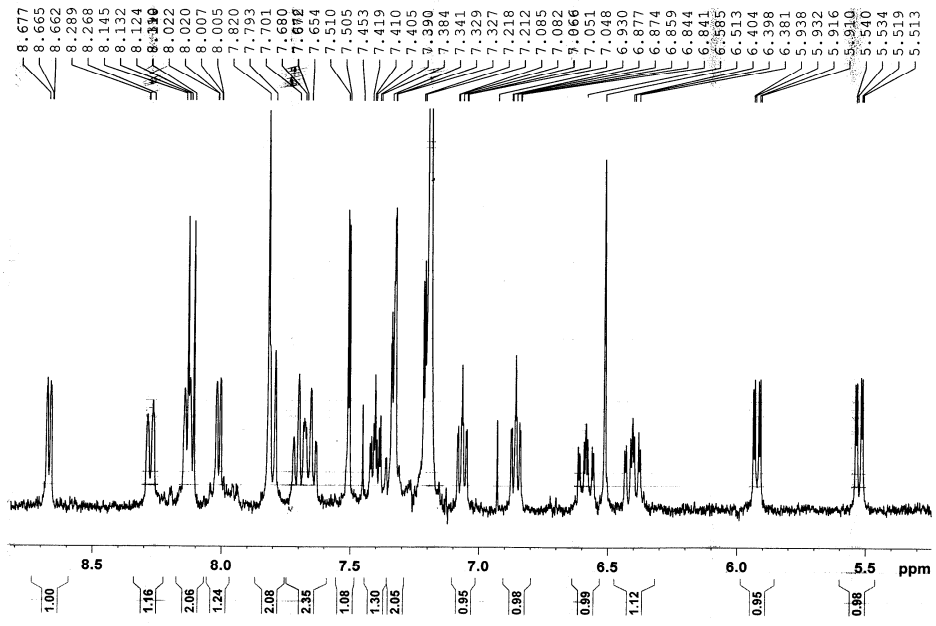

Figure A21: ^{1}H-NMR of [Ir(dfpp)$_2$(napthNO$_2$)] in CDCl$_3$.

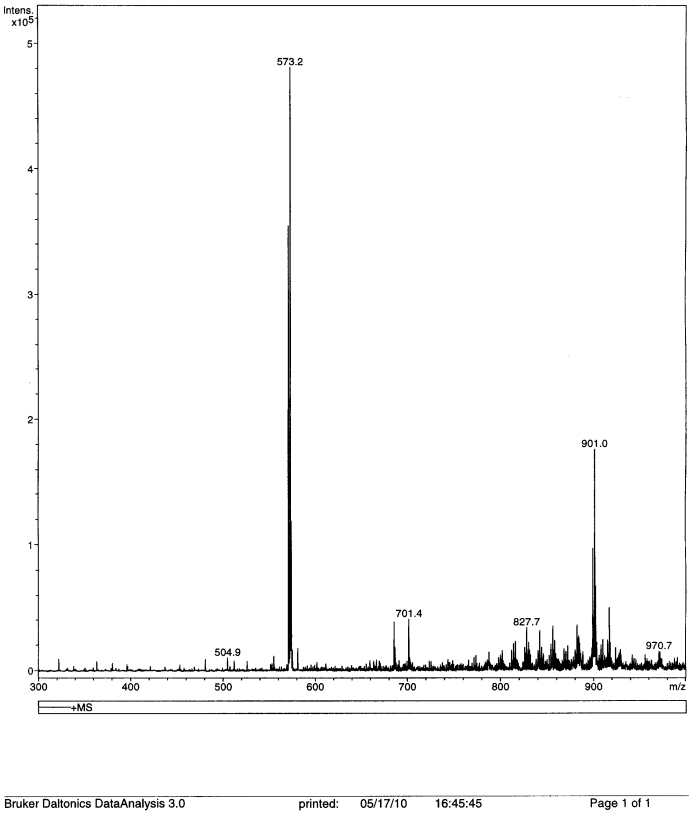

Figure A22: Mass spectrum of [Ir(dfpp)$_2$(napthNO$_2$)].

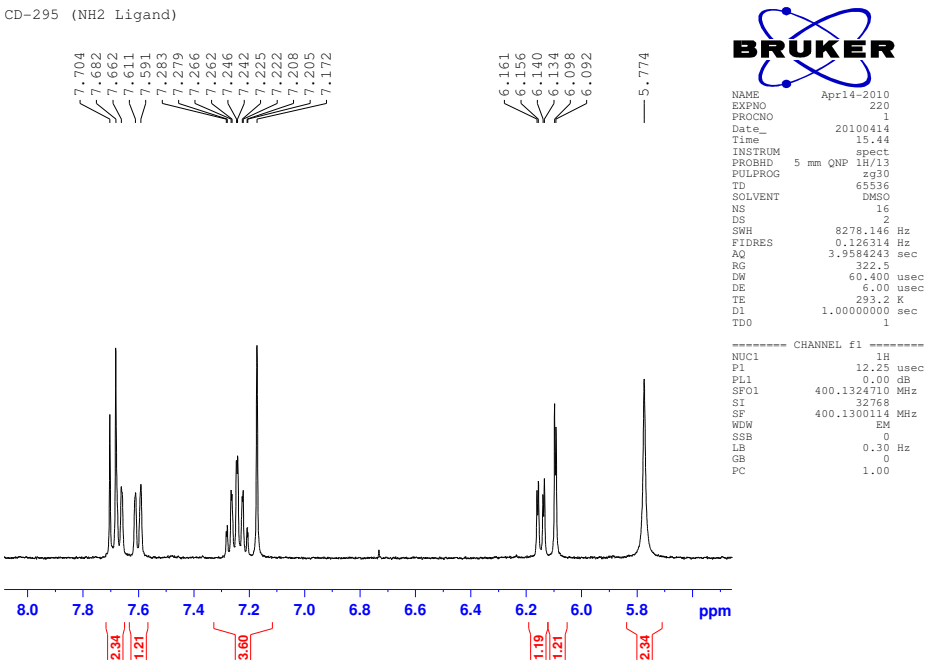

Figure A23: ^{1}H-NMR of [NapthNH$_2$] ligand in DMSO-d$_6$.

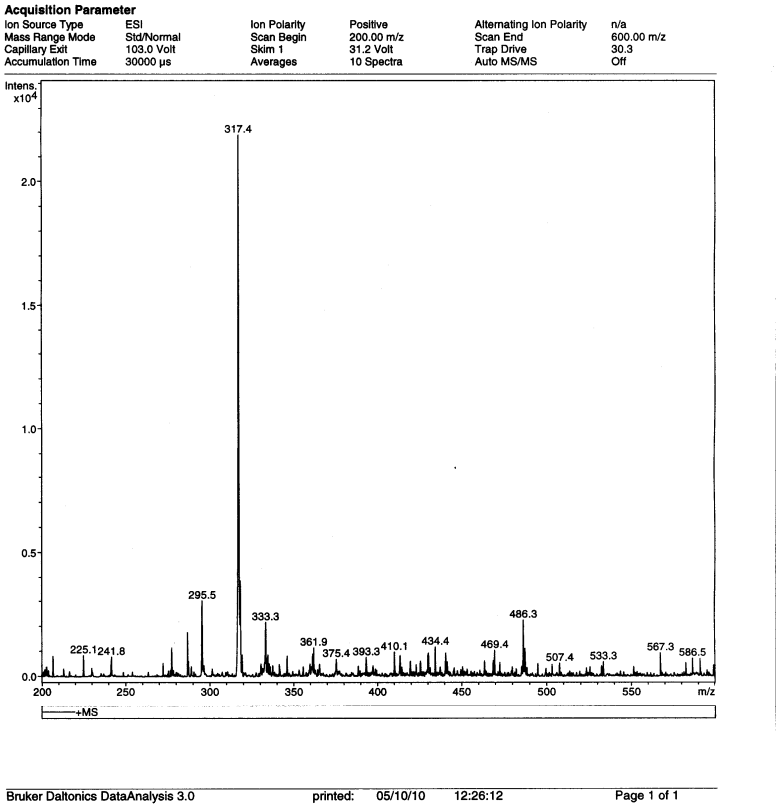

Figure A24: Mass spectrum of [NapthNH$_2$] ligand.

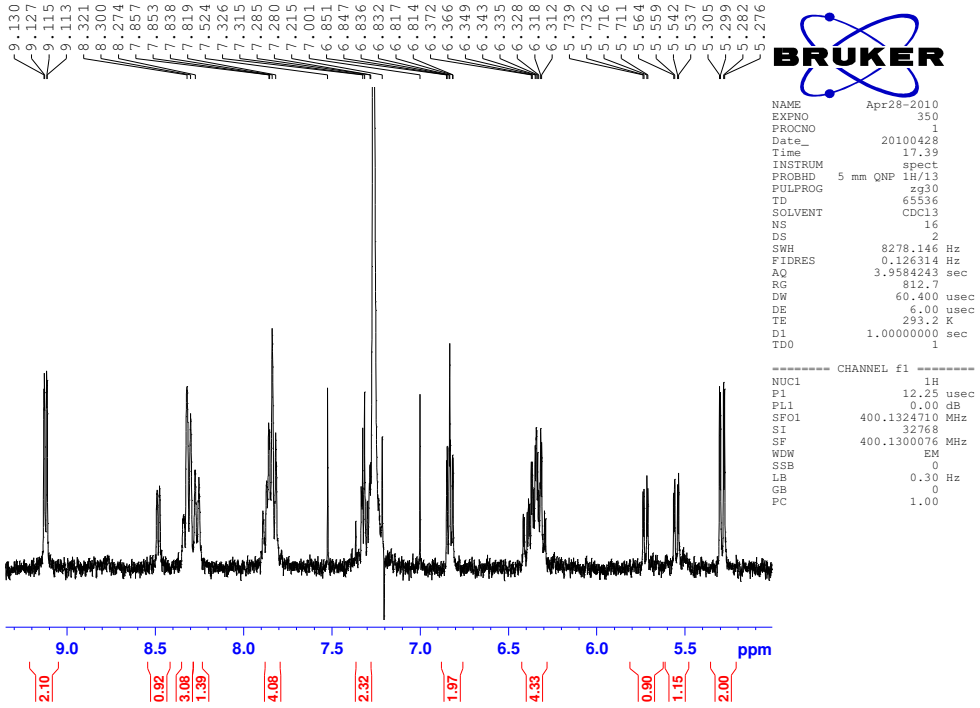

Figure A25: ^{1}H-NMR of [Ir(dfpp)$_2$(napthNH$_2$)] in CDCl$_3$.

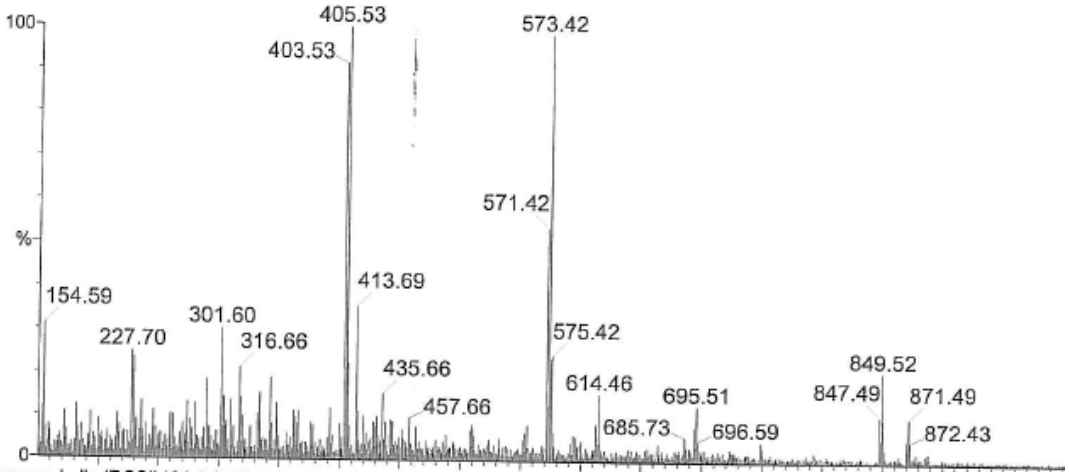

Figure A26: Mass spectrum of [Ir(dfpp)$_2$(napthNH$_2$)].

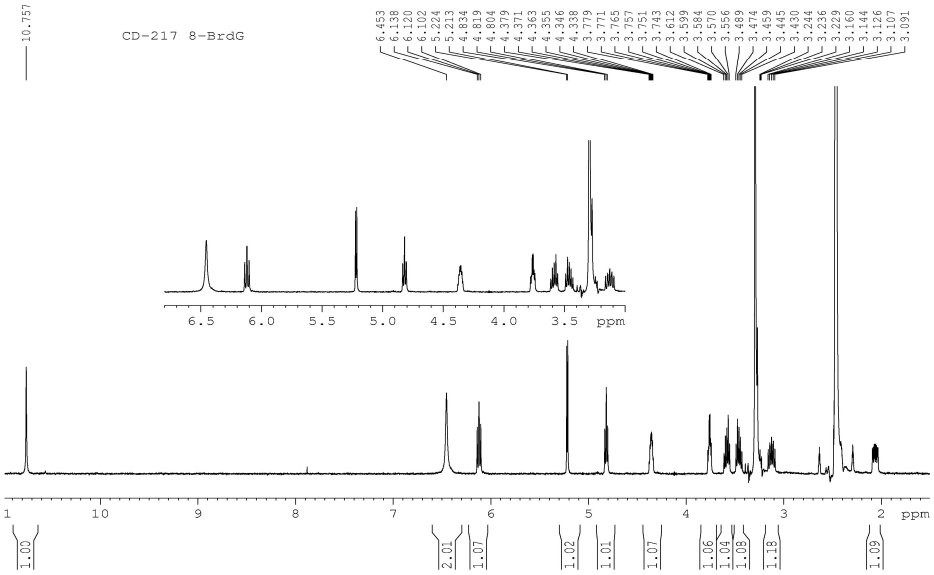

Figure A27: ^{1}H-NMR of 8-bromo-2'-deoxyguanosine in DMSO-d$_6$.

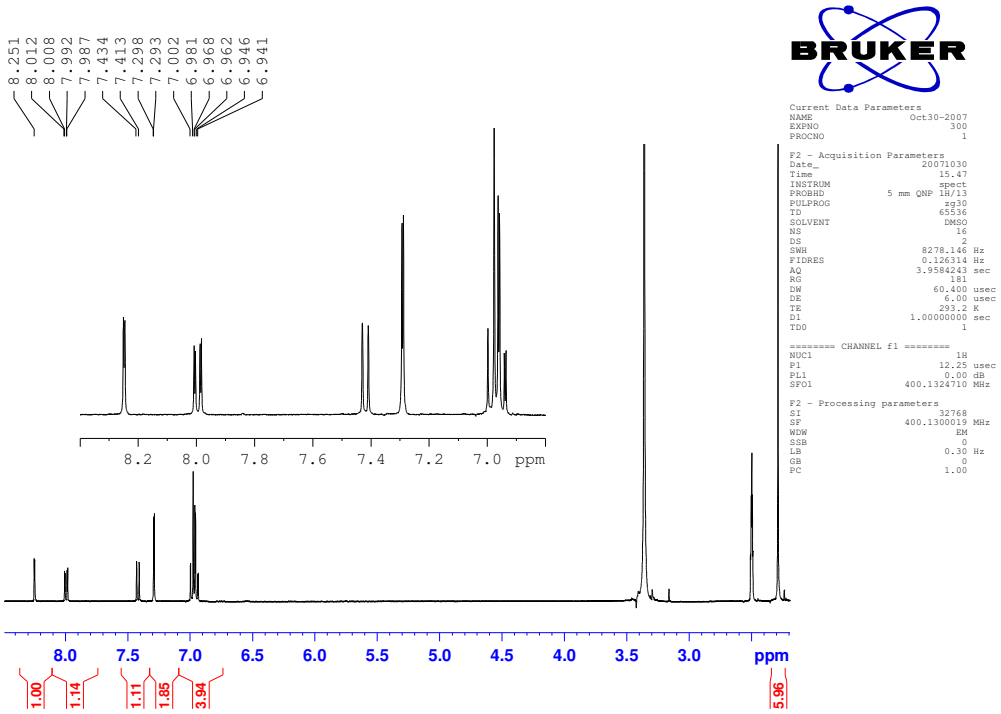

Figure A28: [1]H-NMR of 5-bromofluorescein diacetate in DMSO-d_6.

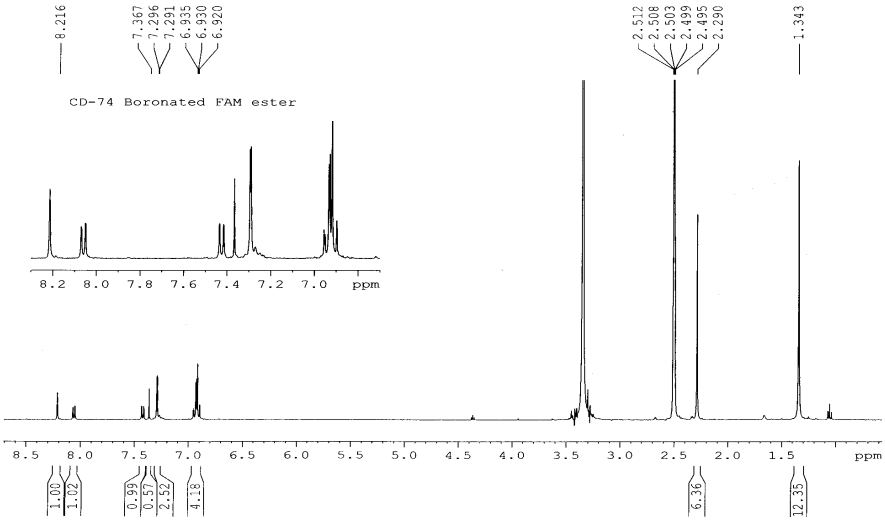

Figure A29: [1]H-NMR of 5-(4,4,5,5-tetramethyl-1,3,2-dioxaborolan-2-yl)fluorescein diacetate in DMSO-d_6.

.

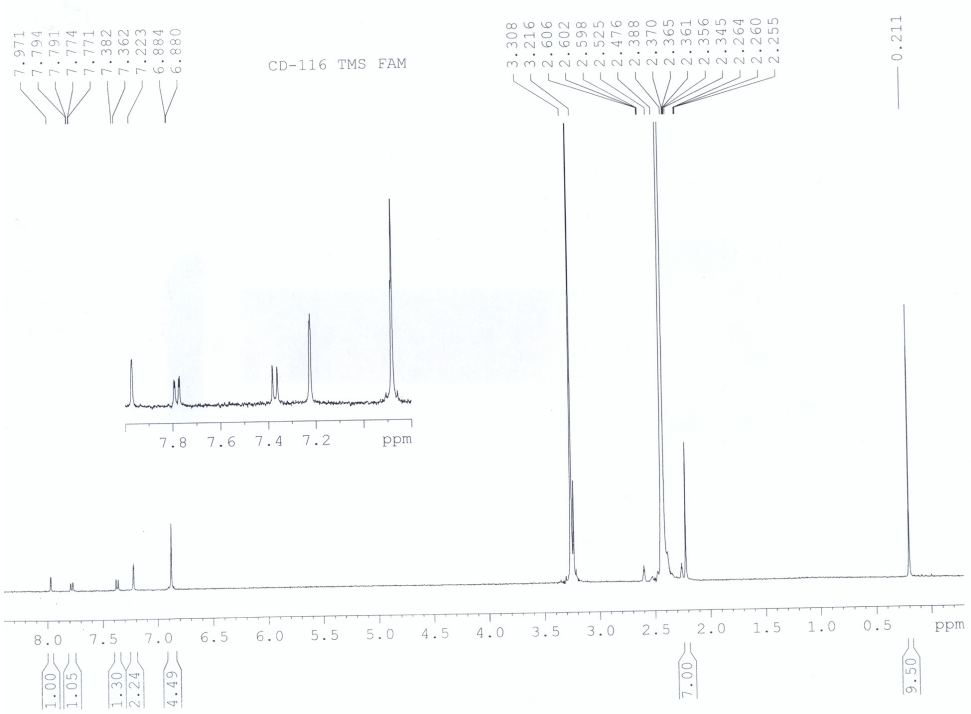

Figure A30: [1]H-NMR of 5-(2-trimethylsilylethynyl)fluorescein diacetate in DMSO-d_6.

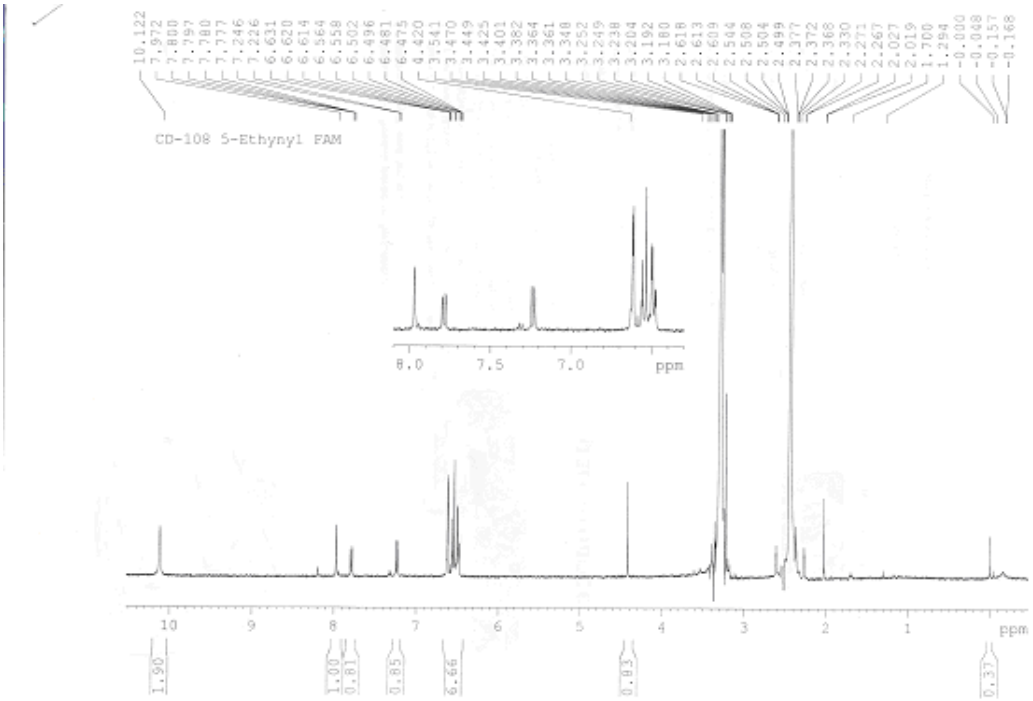

Figure A31: [1]H-NMR of 5-ethynylfluorescein in DMSO-d_6.

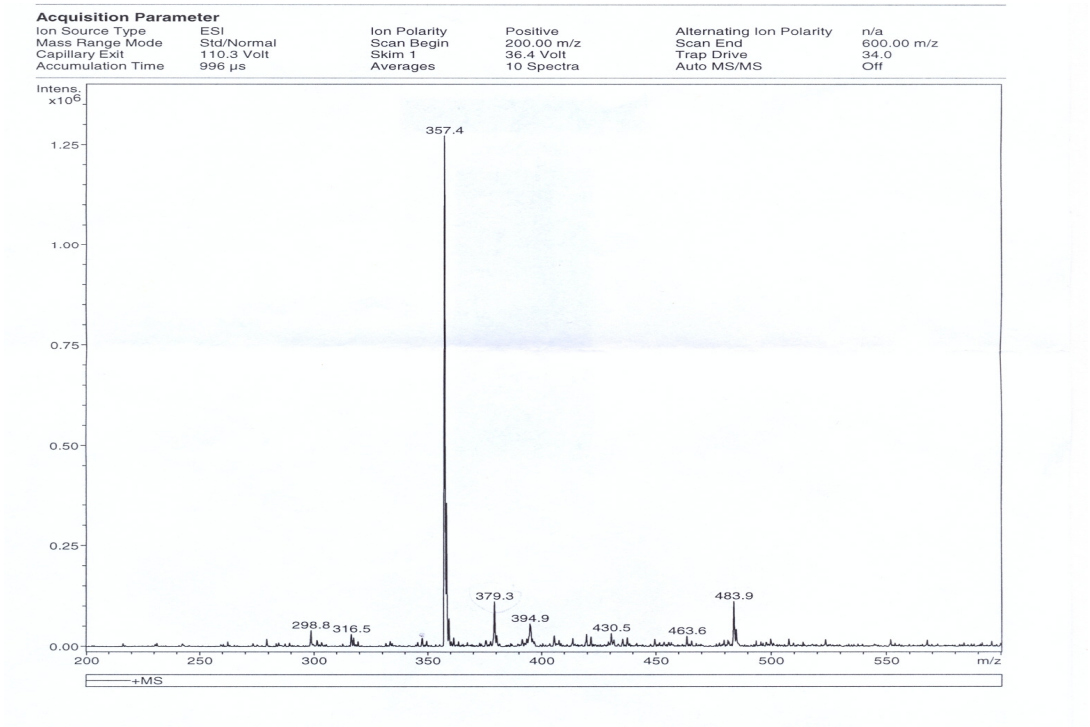

Figure A32: Mass spectrum of 5-ethynylfluorescein.

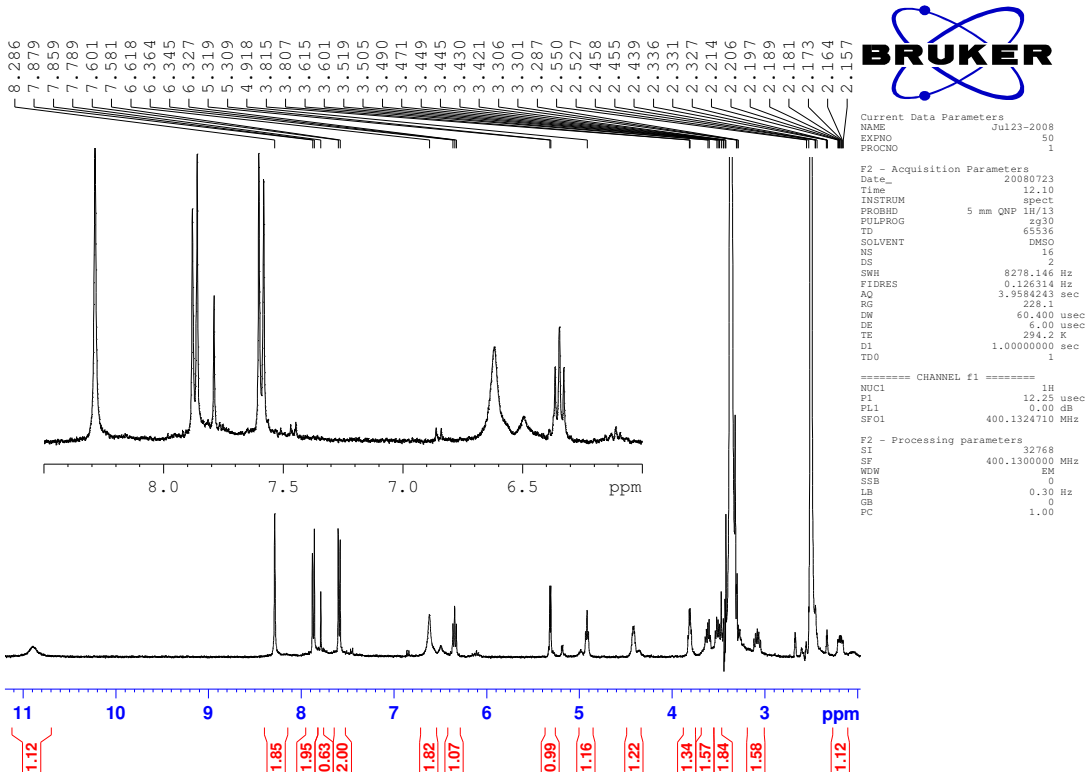

Figure A33: ^{1}H-NMR of 8-(4-ethynylphenyl)-2'-deoxyguanosine in DMSO-d_6.

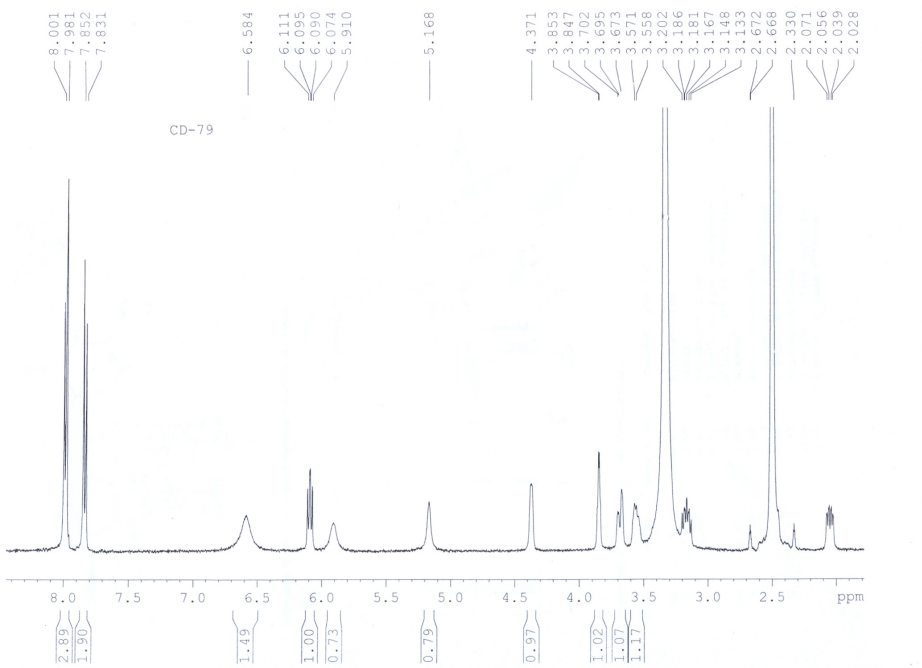

Figure A34: ^{1}H-NMR of 8-(4-cyanophenyl)-2'-deoxyguanosine in DMSO-d_6.

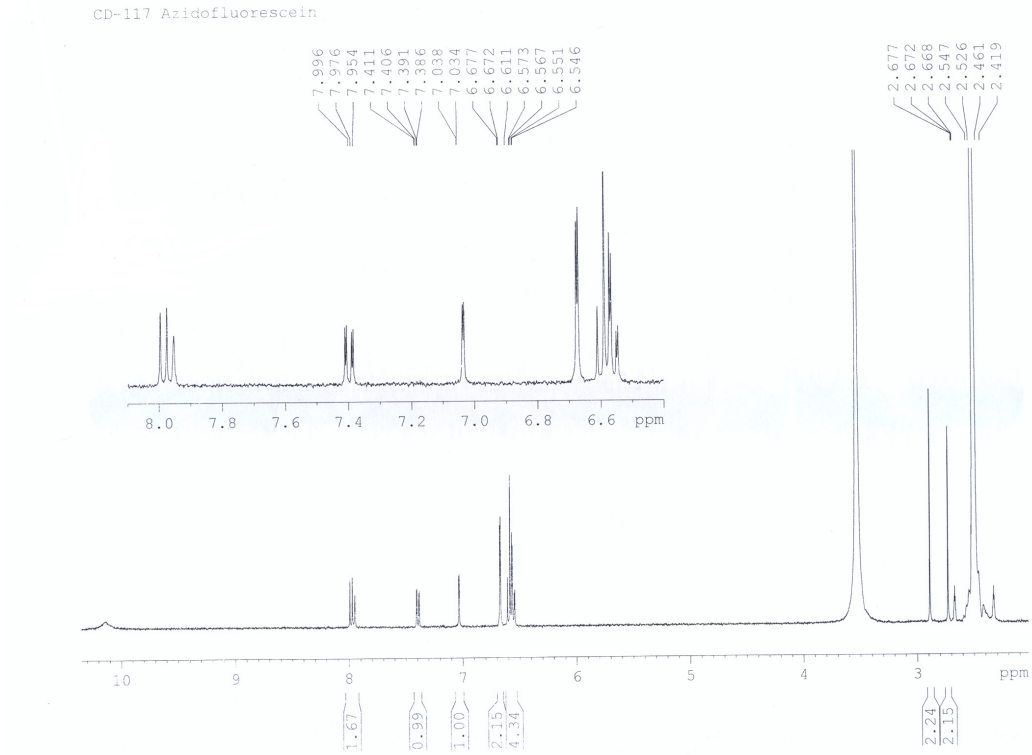

Figure A35: ^{1}H-NMR of 5-azidofluorescein in DMSO-d_6.

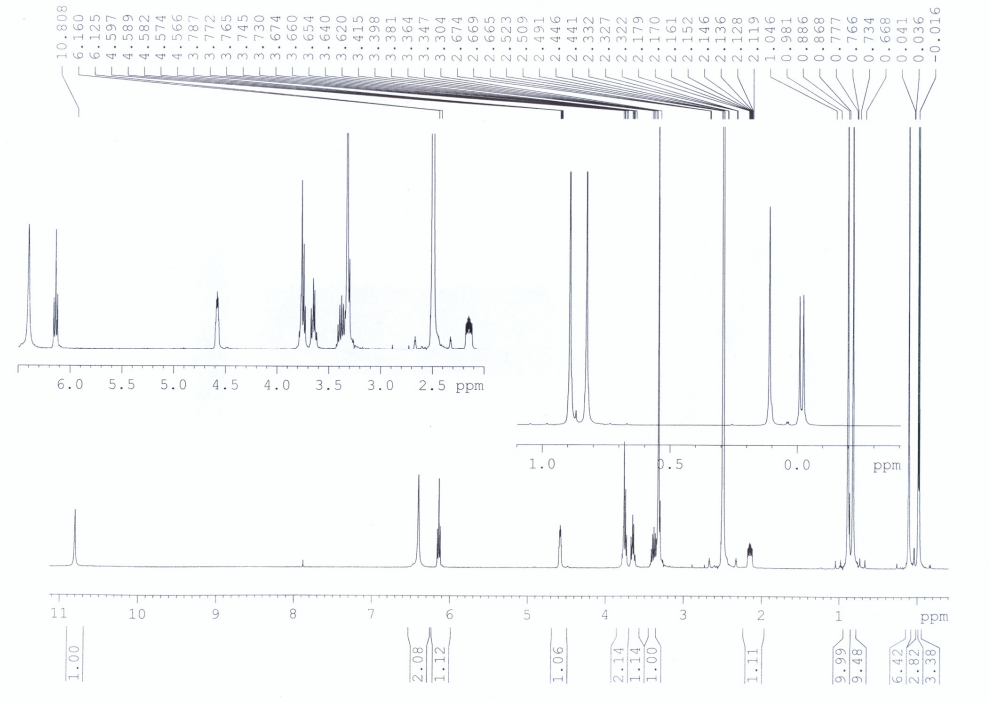

Figure A36: [1]H-NMR of 8-bromo-3',5'-O-bis(tert-butyldimethylsilyl)-2'-deoxyguanosine in DMSO-d_6.

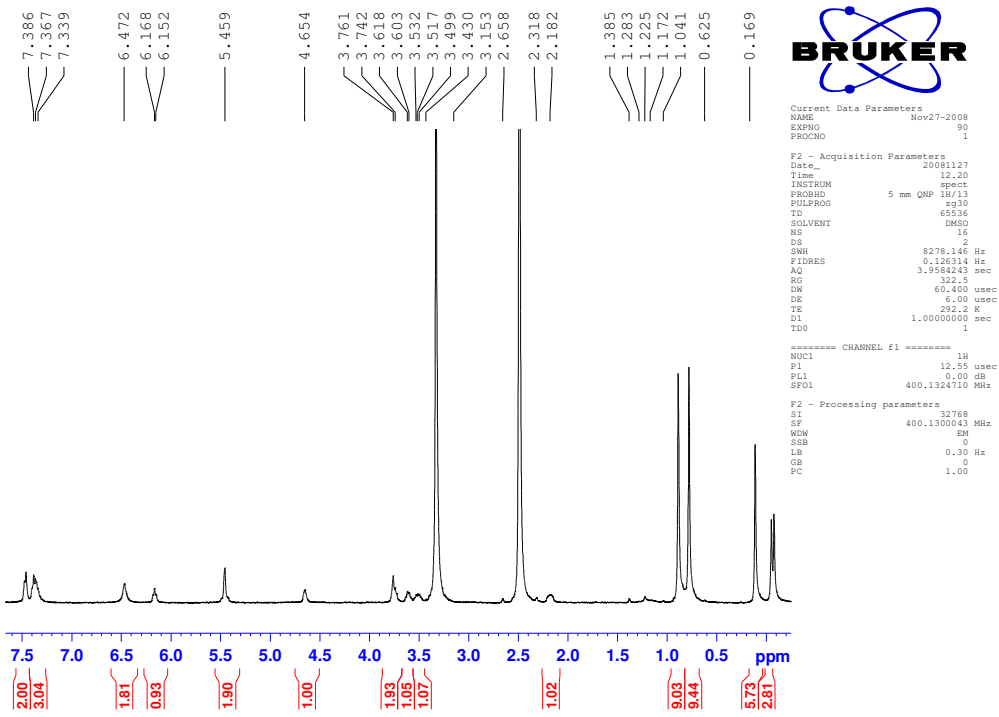

Figure A37: [1]H-NMR of O^6-benzyl-8-bromo-3',5'-O-bis(tert-butyldimethylsilyl)-2'-deoxyguanosine in DMSO-d_6.

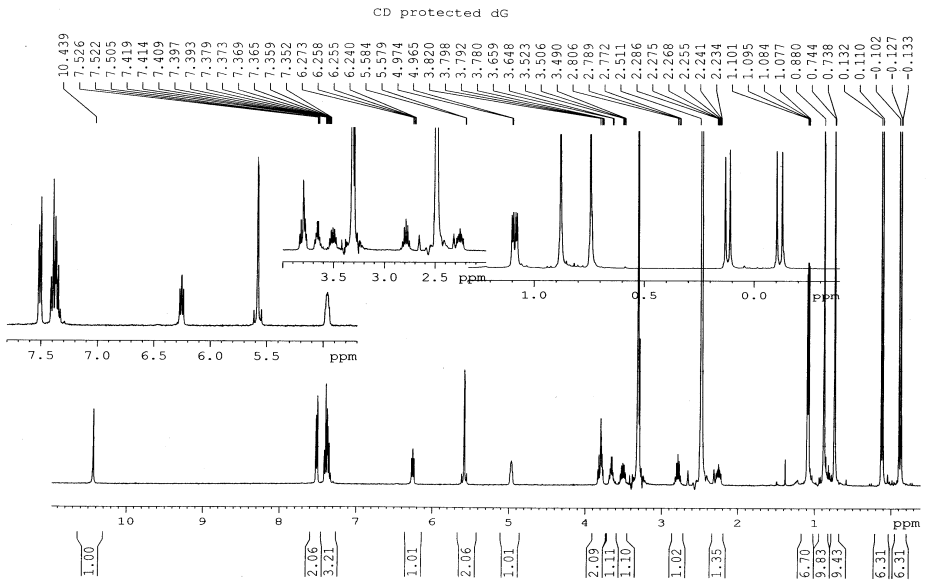

Figure A38: ^{1}H-NMR of N^2-isobutyryl- O^6-benzyl-8-bromo-3',5'-O-bis(tert-butyldimethylsilyl)-2'-deoxyguanosine in DMSO-d_6.

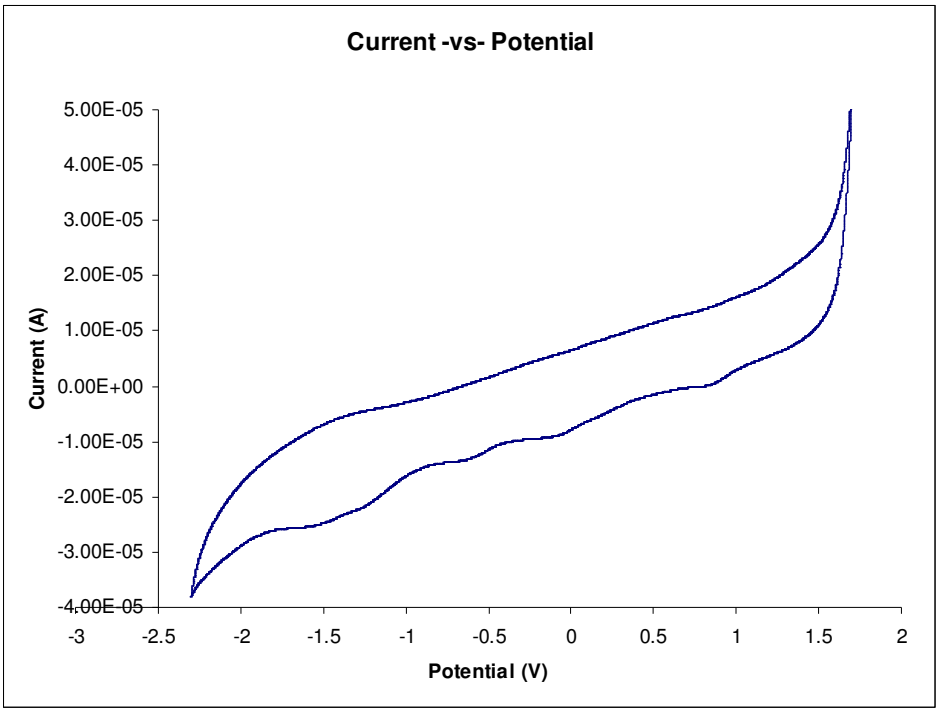

Figure A39: Control cyclic voltammogram of acetonitrile (containing 0.1M TBA as electrolyte) with 1.5 mm glassy carbon working electrode and referenced against Ag/AgCl. Scans were started in a positive direction from an initial potential of 0 V.

Publications and Posters

Publications

- 'Synthesis and Photophysics of a Novel Iridium (III) Dye-Peptide for Cellular Imaging', Dolan, C., Moriarty, R., Devocelle, M., Forster, R.J., Keyes, T.E., *Publication in preparation.*
- 'Targeting Environmentally Sensitive Phosphors within Cells', Blackmore, L., Dolan, C., Cosgrave, L., Forster, R.J., Keyes, T.E., Devocelle, M. (2010), *Peptide Science, 5th International Peptide Symposium., - Conference Proceedings.*
- 'Dyes for Imaging the Sub-cellular Localization of Peptides', Blackmore, L., Dolan, C., Moriarty, R., Forster, R.J., Keyes, T.E., Devocelle, M., *Publication in preparation for JACS.*
- 'Synthesis and Characterisation of Hybrid Silica Nanoparticles Containing an Oxygen-Sensitive Ruthenium Complex', Wencel, D., Dolan, C., Keyes, T.E., McDonagh, C., *Submitted to The Analyst for publication.*
- 'Vibrational Characterisation of [Ir(dfpp)$_2$(napth-R)] Complexes', Lemma, T., Dolan, C., Forster, R.J., Keyes, T.E., *Publication in preparation for The Journal of Raman Spectroscopy.*

Posters

- 'Synthesis and Photophysics of a Novel Iridium (III) Dye-Peptide for Cellular Imaging', Irish Peptide Workshop 2010, 25th-26th May 2010, Royal College of Surgeons in Ireland.
- 'Synthesis and Photophysics of a Novel Iridium (III) Dye-Peptide for Cellular Imaging', 62nd Postgraduate Chemistry Colloquium, 1st-2nd July 2010, Queens University Belfast.
- 'Synthesis and Photophysics of a Novel Iridium (III) Dye-Peptide for Cellular Imaging', BioPhotonics and Imaging Conference (BioPIC) 2010, 18th-20th October 2010, Dunboyne Castle Hotel, Meath, Ireland.